J. Astrophys. Astr. (1987) **8,** 1–16

Stellar Orbits in Elliptical Galaxies with Relativistically Active Nuclei

N. Spyrou & H. Varvoglis *Astronomy Department, University of Thessaloniki, 54006 Thessaloniki, Greece*

Received 1986 August 22; accepted 1986 November 5

Abstract. In a model galaxy composed of a relativistically active nucleus, a main body, and a halo, all three components considered as homogeneous prolate ellipsoids, we explore the probable association of the internal characteristics of the nucleus and the observed orbits of the stars near the surface of the main body. Using the authors' theoretical framework of post-Newtonian general relativistic galactic dynamics, proposed earlier, we prove that a fast-rotating and possibly expanding or contracting nucleus affects the distribution of the box-type orbits near the surface of the main body resulting in a flattening of the main body. The nuclear rotation always results in a flattening, and the contraction contributes less to the flattening than the expansion. However, the contributions of a rotating and changing nucleus are not additive. The study of the post-Newtonian effects in the nucleus on the stellar orbits in the main body, and the consequent modifications of the corresponding non-relativistic results, could in principle provide useful information concerning the kinematical and dynamical characteristics of the nuclei of the elliptical galaxies. The explanation (of at least the post-Newtonian part) of the flattening of elliptical galaxies attempted here seems to be the first theoretical one proposed in the literature.

Key words: galaxies, prolate elliptical—galaxies, active nuclei—galaxies, dynamics and kinematics

1. Introduction and motivation

In a previous paper (Spyrou & Varvoglis 1982; hereinafter quoted as Paper I), we made an effort to establish the theoretical framework of the relativistic galactic dynamics. In that paper, which can be considered (Contopoulos 1983) as the first approach to the problem of the relativistic galactic dynamics, we studied the motion of a star (test particle) in the near zone of the four-dimensional spacetime of a perfect-fluid galaxy with certain symmetries. All the internal characteristics of the galaxy (kinetic energy, internal specific energy, potential energy, and pressure) were properly taken into account, consistently to the first post-Newtonian approximation of general relativity. These characteristics are not taken into account in the corresponding Newtonian approach (see *e.g.* Contopoulos 1960), where only the galaxy's mass-density distribution is considered. The relativistic corrections to the motions of the star are negligible for normal galaxies but non-negligible for elliptical galaxies of large mass and small

linear dimensions. More precisely, for important effects on the star trajectories, the galaxy should be characterized by an extremely fast (rigid-body) rotation, a property of elliptical galaxies not yet observed (Binney 1976; Bertola & Capaccioli, 1978; Bertola 1981). On the other hand, if the galaxy is not to be disrupted by centrifugal forces due to such high rotational velocities, and for the post-Newtonian effects to have their largest possible value and influence, the galaxy's dimensions *have to* be kept small, making it a dwarf galaxy in its dimensions.

In view of the results of Paper I, the question is posed on the possible effect of the post-Newtonian modifications of stellar orbits in a galaxy on the observable properties. In the case of a single galaxy, like the one considered in Paper I, the required rotational velocities are extremely large for a manifestation of such effects. Obviously, the region where we expect such conditions to hold, is the galaxy's nuclear region. Consequently, from the single-body galaxy of Paper I we are naturally led to a composite galaxy containing more than one major constituent, dynamically distinct from each other, the relativistic contributions being due mainly to the innermost constituent.

The idea of a composite elliptical galaxy appears attractive and natural on observational grounds (Bertola 1981). Also, it is very probable that the relativistic effects in the galaxy's nuclear region are not negligible (Gerhard & Binney 1985). This suggests the possibility of investigating the kinematical and dynamical characteristics of a galaxy's nuclear region, by picking out this region's post-Newtonian effects on the star trajectories of the outer part of the galaxy's visible body. Since the galaxy's internal characteristics enter the post-Newtonian part of the metric tensor, they are expected to modify the properties of the star trajectories in the outer parts of the galaxy as predicted by the Newtonian theory of gravity (which ignores the internal characteristics of the gravitating body). The outer parts of the galaxy are, in principle, easier observed than its nucleus, so that the properties of star trajectories affecting the mass-energy distribution there, may be able to tell something about the properties of its nucleus, This is precisely the purpose of the present paper, namely, applying the theoretical framework of Paper I, to examine the probable association, between the relativistic nucleus of an elliptical galaxy on one hand, and the observed star trajectories and mass-energy distribution in the main body on the other. As it will appear, the fast rotation of the nucleus and its probable expansion or contraction affect the properties of the box-type trajectories of the stars of the main body, and can cause a flattening of the main body (Spyrou & Varvoglis 1983). It should be emphasized that this flattening is a post-Newtonian result and thus it cannot by itself explain the observed flattening of normal elliptical galaxies, which is currently attributed to accidents of their birth and not to their rotation (Bertola 1981).

The structure of the paper is as follows: In Section 2 we describe the physics of the model galaxy used, and in Section 3 we describe the evaluation of the coefficients of the Hamiltonian. The numerical results are presented and discussed in Section 4. Finally, some useful formulae and auxiliary calculations have been collected in an Appendix at the end. The reader is assumed to be familiar with the notation and content of Paper I.

2. The physics of the model galaxy

The model galaxy used here is dictated by the observation of stable, *prolate* elliptical galaxies (Bertola & Galletta 1978). In our opinion these galaxies present a possible

mass-energy distribution that, in principle, could give rise to relativistic effects on at least the star trajectories. These galaxies rotate about their *major axis* of symmetry and are thought to be composed generally of three parts, the nucleus, the main body, and the halo. We tried to be as careful as possible with our description of the model galaxy, but we made a few important simplifications. Thus we assume that these three constituents of the galaxy are homeothetic prolate ellipsoids rotating about their common major axis. Each of them is homogeneous and rotates in a rigid-body manner independently of the other two, so that the whole galaxy is characterized by time-independent and axially symmetric distributions of mass and velocities. The change of the velocity and matter distributions from the inner to the exterior ellipsoids is assumed continuous. However, a problem that will not be addressed here, in spite of its obvious importance, is the friction between the three constituents of the galaxy (van Albada & Sanders 1982).

The nucleus, whose linear dimensions are much smaller than those of the body and the halo, is superdense and superheavy, and due to its small dimensions, can rotate very fast with no disruption problems, as compared to an oblate nucleus. The existence of fast rotating cores, as in our model, depends critically on the existence of supermassive elliptical galaxies, which is not strongly supported by current observations (see, however, Biermann, Strom & Bartel 1985). On the other hand, it must be emphasized that masses as high as $10^{15}\ M_{\odot}$ are possible (Danks & Materne 1984), depending on the value of the mass-luminosity relation (Hoffman & Salpeter 1982). In any case the existence of such supermassive galaxies cannot be ruled out on theoretical grounds, because, *e.*g., a generally accepted value of the Jean's mass for galaxy formation is of the order $10^{16}\ M_{\odot}$, its lower limit being $\sim 10^{12}\ M_{\odot}$.

Moreover, the stars whose trajectories we shall be interested in, namely those near (inside or outside) the surface of the main body, lie closer to the nucleus, than in an oblate (main-body) galaxy, and therefore are expected to experience stronger relativistic effects. The dynamical influence of the nucleus on the properties of the box-type orbits of the stars in the main body has been discussed by Gerhard (1985) in the case of a spiral galaxy with a black-hole nucleus. (For theoretical models of active galactic nuclei with a central black hole see Blandford 1984.)

The main body and the halo have masses comparable to the mass of the nucleus, but, due to their larger dimensions, their relativistic effects are not important compared with those due to the nucleus; in addition, there is observational evidence that they are not necessarily rotating rapidly (Bertola 1981). Moreover, the whole galaxy will be assumed to be in a state of an overall expansion or contraction. Since only the mass-distribution and not the internal characteristics of the main body and the halo will be assumed, this property of the galaxy refers only to its nucleus. Thus a violent expansion of the nucleus in the past could have caused a still continuing expansion of the galaxy. Analogous results could be due to an analogous violent implosion of the nucleus. Here we shall assume that the nucleus is currently in a state of a steady expansion or contraction, and this property will enable us to examine the influence of a possible expansion or contraction on the stellar trajectories in the main body. The assumption of a steadily changing nucleus is not completely unjustified. Actually, in view of the presence of strong emission in certain elongated galaxies in the direction of elongation, such an explosive event has been used in explaining the galaxy's elongated optical shape (Bertola & Galletta 1978). More recently, Bergvall & Johansson (1985) suggested that inflow or outflow mass motions in the active (double) nucleus of the southern galaxy ESO 148-IG02 could partially justify the radial velocities corresponding to the

observed absorption lines. Finally, we recall that even in the Milky Way the observed asymmetry, between its two hemispheres, in the distribution of the radial velocities of stars could be explained as a result of an explosive event, that occurred in the centre of the Milky Way a few million years ago and still continues (Tayler 1978).

Finally we shall assume that the (prolate) nucleus is similar to the (oblate) galaxy of Paper I, the main body is a typical elliptical galaxy in its linear dimensions, and the halo is much less dense than the main body. More precisely, the masses, semi-axes, densities and oblatenesses are:

$$\left.\begin{aligned} &m = 1.0 \times 10^{15}\, M_\odot \\ &a_1 = a_2 = 1\ \text{kpc}, \quad a_3 = 2\ \text{kpc} \\ &\rho = 8.1 \times 10^{-18}\ \text{g cm}^{-3}, \quad \varpi = 0.5 \end{aligned}\right\} \text{for the nucleus,} \tag{1a}$$

$$\left.\begin{aligned} &m = 2.0 \times 10^{15}\, M_\odot \\ &a_1 = a_2 = 4\ \text{kpc}, \quad a_3 = 8\ \text{kpc} \\ &\rho = 2.5 \times 10^{-19}\ \text{g cm}^{-3}, \quad \varpi = 0.5 \end{aligned}\right\} \text{for the main body,} \tag{1b}$$

$$\left.\begin{aligned} &m = 2.0 \times 10^{15}\, M_\odot \\ &a_1 = a_2 = 8\ \text{kpc}, \quad a_3 = 16\ \text{kpc} \\ &\rho = 3.2 \times 10^{-20}\ \text{g cm}^{-3}, \quad \varpi = 0.5 \end{aligned}\right\} \text{for the halo.} \tag{1c}$$

Obviously the linear dimensions of this elliptical galaxy are close to typical ones. The total mass is about an order of magnitude larger than the masses, of the most massive galaxies known today. Finally, note that the three ellipsoids have the same oblateness.

3. Evaluation of the coefficients of the Hamiltonian

The basic properties of the composite galaxy used here (axially symmetric and time-independent distributions of mass and velocity of the gravitating source) are the same as in Paper I. So in both cases the general form of the Hamiltonian function describing slightly perturbed, equatorial circular, orbits of equilibrium is the same (see Equations 3.12 and 2.9 of Paper I; the notation is obvious)

$$\begin{aligned} H = {} & \frac{1}{2}(R^2 + Z^2) - \frac{1}{2}\left[(W_{,rr})_0\, \xi^2 + (W_{,zz})_0\, z^2\right] + \frac{4}{c^2}(U_{r,r})_0\, \xi\, R \\ & - \frac{1}{6}(W_{,rrr})_0 \xi^3 - \frac{1}{2}(W_{,zzr})_0\, \xi\, z^2 + \frac{2}{c^2}(U_{r,rr})_0\, \xi^2\, R \\ & + \frac{2}{c^2}(U_{z,rr})_0\, \xi^2\, Z + \frac{2}{c^2}(U_{r,zz})_0\, z^2\, R + \frac{2}{c^2}(U_{z.zz})_0 z^2\, Z \\ & - \frac{1}{c^2}(U_{,r})_0\, \xi (R^2 + Z^2) + \text{Newtonian and post-Newtonian} \\ & \text{terms of order four in } \xi,\ z,\ R,\ Z \end{aligned} \tag{2a}$$

with

$$W = U - \frac{J^2}{2r^2} + \frac{1}{c^2}\left(U^2 + 2F + \frac{J^2 U}{r^2} - \frac{4JU_\varphi}{r}\right) \tag{2b}$$

where all the symbols have the same meaning as in Paper I.

In the present case all the potentials appearing in Equation (2b) have contributions from the three ellipsoids of the composite galaxy, so that for each potential, we may write symbolically

$$Q = Q_n + Q_b + Q_h \tag{3}$$

where the subscripts n, b and h refer to the nucleus, main body and halo, respectively.

We shall mainly be interested in equilibrium orbits far from the nucleus and near the surface of the main body, either inside or outside it (and, of course, inside the halo). Therefore, the contribution Q_n is evaluated in the far region of the nucleus, the contribution Q_b is evaluated near the surface of the main body, either interior to it (along the lines of Paper I) or exterior to it, and the contribution Q_h is evaluated interior to the halo.

Under the above conditions, as it is outlined in the Appendix at the end, Equation (2b) takes the form

$$W = W_n + U_b + U_h \tag{4}$$

where W_n, the internal analogue of W, is the nucleus' total (namely, Newtonian and post-Newtonian) contribution and U_b, U_h, the Newtonian gravitational potentials due to the body and halo, are the only contributions of the latter two constituents to W. Obviously the internal characteristics of the body and halo-ellipsoids are negligible compared with the other terms of W.

Moreover, the Newtonian gravitational potential due to a homogeneous, prolate ellipsoid, at a point interior to the ellipsoid, is given by Equation (A2) in the Appendix of Paper I, e*g.*

$$U_b(\text{interior}) = \pi G \rho_b \left[A_1 (2a_1^2 - r^2) + A_3 (a_3^2 - z^2)\right]_b \tag{5}$$

with a similar expression for U_h (interior), where the coefficients A_1, A_2, as functions of the eccentricity e of the ellipsoid, are defined by Equations (A6) and (A7) in the Appendix. On the other hand, as outlined in the Appendix, for a point external to the ellipsoid.

$$U_b(\text{exterior}) = \pi G \rho_b (a_1^2 a_3)_b (I_1 - r^2 I_2 - z^2 I_3)_b \tag{6}$$

where I_1, I_2 and I_3 are certain functions of r, z defined by Equations (A l0a, b, c).

Furthermore, for the evaluation of the superpotential W_n, we notice that the values of the *velocity potential* U_r, U_φ, U_z are required. In the Appendix it is proved that, if the distribution of the three-velocities of the fluid motions of the prolate ellipsoid, for $|x| < \alpha_{l_n}$, is of the form

$$\mathbf{v}(\mathbf{x}, t) = \boldsymbol{\Omega} \times \mathbf{x} + (\boldsymbol{\Omega} \times \mathbf{x}) \times \boldsymbol{\lambda}, \tag{7}$$

where the nuclear angular-velocity vector of rigid-body rotation, $\boldsymbol{\Omega}$, and the constant vector λ are along the positive z-axis,

$$\boldsymbol{\Omega} = \Omega \hat{\mathbf{z}}, \quad \boldsymbol{\lambda} = \lambda \hat{\mathbf{z}}, \tag{8}$$

then

$$U_r = \lambda U_\varphi, \quad U_z = 0, \tag{9}$$

where U_φ and λ are defined, respectively, through Equation (A14) and

$$\dot{r} = \lambda \Omega r \, (r \leqslant |\mathbf{x}| \leqslant a_1). \tag{10}$$

Obviously $\lambda > 0 (\lambda < 0)$ implies an *expansion* (*contraction*) of the nucleus taking place on its equatorial (x, y) plane (apart, of course, from the general circular equilibrium motions, described by the first term on the right of Equation 7). It is of some interest to note that according to the basic assumptions of Paper I concerning the motion of the fluid (see Equation 14.4) λ is of the order of unity.

Finally for the evaluation of W_n in the far region of the nucleus, and in order to take into account its internal characteristics, we must use the inertial-mass density of the source [see Equation (31) of Contopoulos and Spyrou (1976) and Equation (3.22) of Spyrou (1977)]. Then, as proved in the Appendix, by simple Taylor expansion we obtain to the lowest order

$$W_n(\text{far region}) = \frac{Gm_n}{|\mathbf{x}|} - \frac{J^2}{2r^2} + \frac{1}{c^2}\left(\frac{G^2 m_n^2}{|\mathbf{x}|^2} + \frac{J^2}{r^2}\frac{Gm_n}{|\mathbf{x}|} - \frac{4G}{|\mathbf{x}|^3} J I \Omega\right) \tag{11}$$

where m_n is the inertial mass of the nucleus.

As a final remark we notice that a direct consequence of Equation (10) and of the fact that in the interior of the nucleus all the internal characteristics (v^2, U, Π and p/ρ in the notation of Paper I) are smaller than Gm_n/L, is that at the equatorial surface ($r = \alpha_{1_n}$) of the nucleus

$$\lambda \leqslant \Omega_{max}/\Omega, \tag{12}$$

where

$$\Omega_{max} = (Gm_n \alpha_{1_n}^{-3})^{1/2} \tag{13}$$

is the Newtonian break-up angular velocity of the nucleus. In view of the condition (12), the constant number λ takes a specific physical meaning. A direct consequence of Equation (12) and the time-integrated Equation (10) is the equation

$$r(t > t_0) = r(t_0) \exp[\lambda \Omega (t - t_0)] \leqslant r(t_0) \exp[\Omega_{max}(t - t_0)] \tag{14}$$

describing the time-evolution, of α_{1n} due to the expansion or contraction of the nucleus.

All the previous results permit the evaluation of the coefficients of the Hamiltonian function (2a). Specifically, Equation (5) for both the body and the halo, and (11) for the nucleus, are suitable for equilibrium orbits near the interior to the surface of the body. Also, Equation (6) for the body, Equation (5) for the halo, and Equation (11) for the nucleus, are suitable for equilibrium orbits near the surface of the body and exterior to it. The coefficients of the Hamiltonian are summarized at the end of the Appendix.

4. Numerical results and their discussion

In choosing the combination of dimensions and masses of the model galaxy (see Equation 1), and the initial conditions of the orbits of the test particle (star), we have restricted our attention to the 'generic' case of box-type orbits on a meridian plane of the galaxy. In this way our results are as free as possible from resonant phenomena due

to the existence of periodic orbits of low commensurability, which could obscure the effects of post-Newtonian terms of the Hamiltonian.

In the above model galaxy, we calculated two types of nearly circular orbits lying (i) just outside, and (ii) just inside the surface of the main body. We have not calculated orbits crossing the surface of the main body, because the Newtonian gravitational potential U_b is not differentiable there. The general characteristics of both types of orbits and their dependence on the internal characteristics of the nucleus were found to be qualitatively similar, the only difference being that the post-Newtonian effects were weaker on the orbits of type (ii), due to their larger mean distance from the nucleus. For this reason we present here only the results for orbits inside the main body, which, in addition, were faster to integrate numerically.

As in Paper I, the box-type orbits considered here fill only a curvilinear rectangle (see Equation I4.10) inside the zero-momentum curve, due to the existence of a second KAM-type integral of motion, beyond the Hamiltonian (2a). The width $\Delta\xi$ and the height Δz of this rectangle were used as a measure of the changes induced in the orbit by the rotation and expansion (or contraction) of the nucleus. (For a discussion on the possible complications of the use of this rectangle, see Binney, Gerhard & Piet 1985.

The integrated orbits are perturbations of equatorial circular orbits of radius

$$r_0 = 3.7 \text{ kpc}, \tag{15}$$

and are of two types (a) and (b). A type (a) orbit stays close to the equatorial plane and has initial conditions

$$\xi_0 = 0.3 \text{ kpc}, \; z_0 = 0, \; R_0 = 0, \; Z_0 = 30 \text{ km s}^{-1}, \tag{16}$$

and a type (b) orbit departs from the equatorial plane and has initial conditions

$$\xi_0 = 0.05 \text{ kpc}, \quad z_0 = 0, \; R_0 = 0, \quad Z_0 = 1300 \text{ km s}^{-1}, \tag{17}$$

The results are presented in Figs 1a–4a for type (a) orbits and Figs 1b–4b for type (b) orbits. In Figs 1 and 2 we plot $\Delta\xi$ and Δz, respectively, as functions of the angular velocity of nuclear rotation (Ω) for a constant value of the relative rate of change of its *r/r* (or, equivalently, $\lambda\Omega$; see Equation 10). In Figs 3 and 4 we plot $\Delta\xi$and Δz, respectively, as functions of *r/r* for a constant value of Ω. It is interesting to note a fundamental difference between Figs 1 and 2 on the one hand and Figs 3 and 4 on the other. At first sight Figs 1 and 2 imply a linear dependence of $\Delta\xi$ and Δz on Ω, while Figs 3 and 4 imply a quadratic dependence of the same quantities on $\lambda\Omega$. In addition, Figs l(a, b) imply that the effect of a nonzero value of $\lambda\Omega$ is simply superimposed on the effect of a finite Ω, which would imply the independence of the two processes from one another. However, on a more careful look, small deviations of the 'experimental' points from the straight line can be detected, a feature more prominent in Figs 2 (a, b). Those deviations are well within the accuracy of the orbit-integration routine; and should therefore be taken as real. In this way the functions $\Delta\xi(\Omega; \lambda\Omega = \text{const})$ and $\Delta\xi(\lambda\Omega; \Omega = \text{const})$ are linear functions only to a first approximation. Since the slopes of the curves in Figs 1 (a, b), describing $\Delta\xi(\Omega)$, for the orbits of types (a) and (b) respectively, are of opposite sign, the only simple conclusion that can be deduced from Figs 1 and 2 is that an increase of Ω compresses the height of the box-type orbit in this galaxy. These results are in agreement with Paper I and if the box-type orbits are the back-bone of this galaxy (Gerhard & Binney 1985), it implies that *the high angular velocities of the nucleus contribute to the flattening of the galaxy.* We recall that

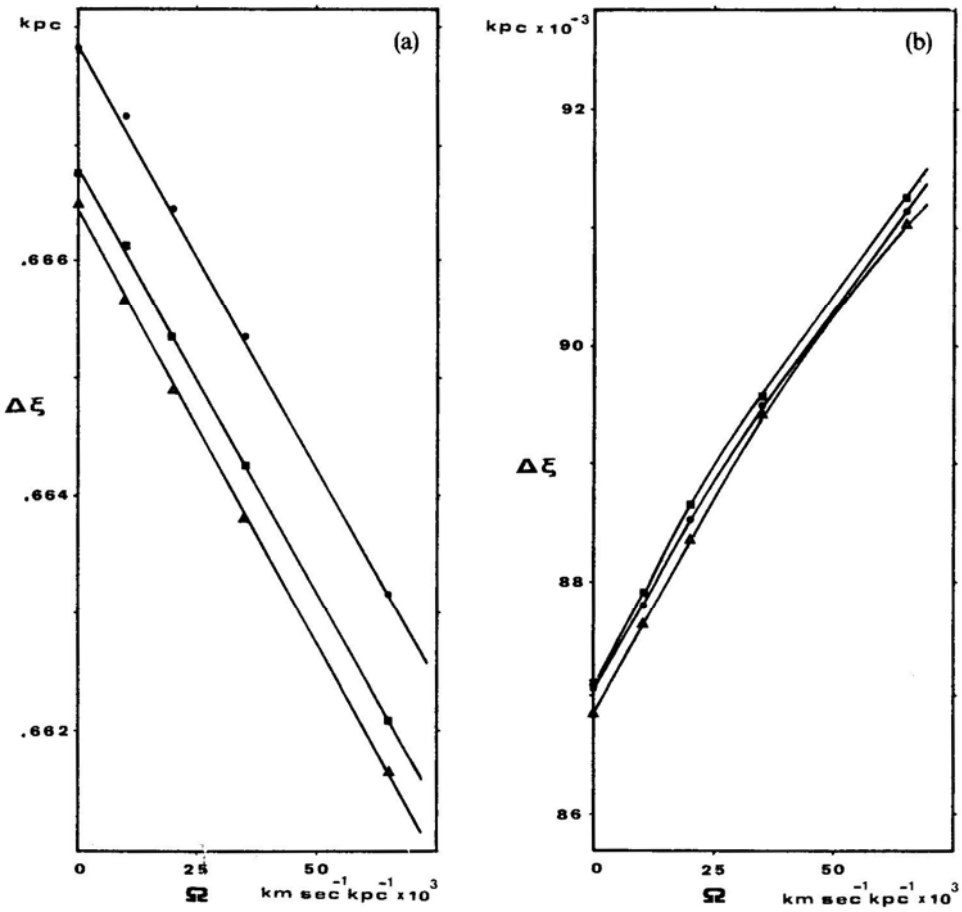

Fig. 1. Width $\Delta\xi$ of a box-type orbit with (a)ξ_0 = 0.3 kpc, and (b)ξ_0 = 0.05 kpc, as a function of Ω, for constant r/r and three values of λ ($\lambda = 3.5\times10^5$ for circles ●, $\lambda = -2.5 \times 10^5$ for squares ■, and $\lambda = 0$ for triangles Δ).

similar argument has already been used in explaining the solar oblateness (Dicke & Goldenberg 1967).

With regard to the expansion or contraction of the nucleus, we observe that they both contribute to an increase of both $\Delta\xi$ and Δz, but not by the same amount, the contribution of the contraction being larger. It should be noted also that the inclusion of a nonzero angular velocity of the nucleus tends to cancel out the differences between r/r of opposite signs. Therefore, the effects of Ω and r/r are not additive, even in a first approximation, and this is more pronounced in Fig. 4b.

A final remark is necessary on the dependence of our results on the initial conditions of the trajectories. As were marked at the end of Section 2, the nuclear mass was selected high, in order to produce easily detectable effects. However, in the course of our numerical calculations we found that the action of the main body and the halo on a test star tends to suppress the post-Newtonian effects of the nucleus in a rather complicated

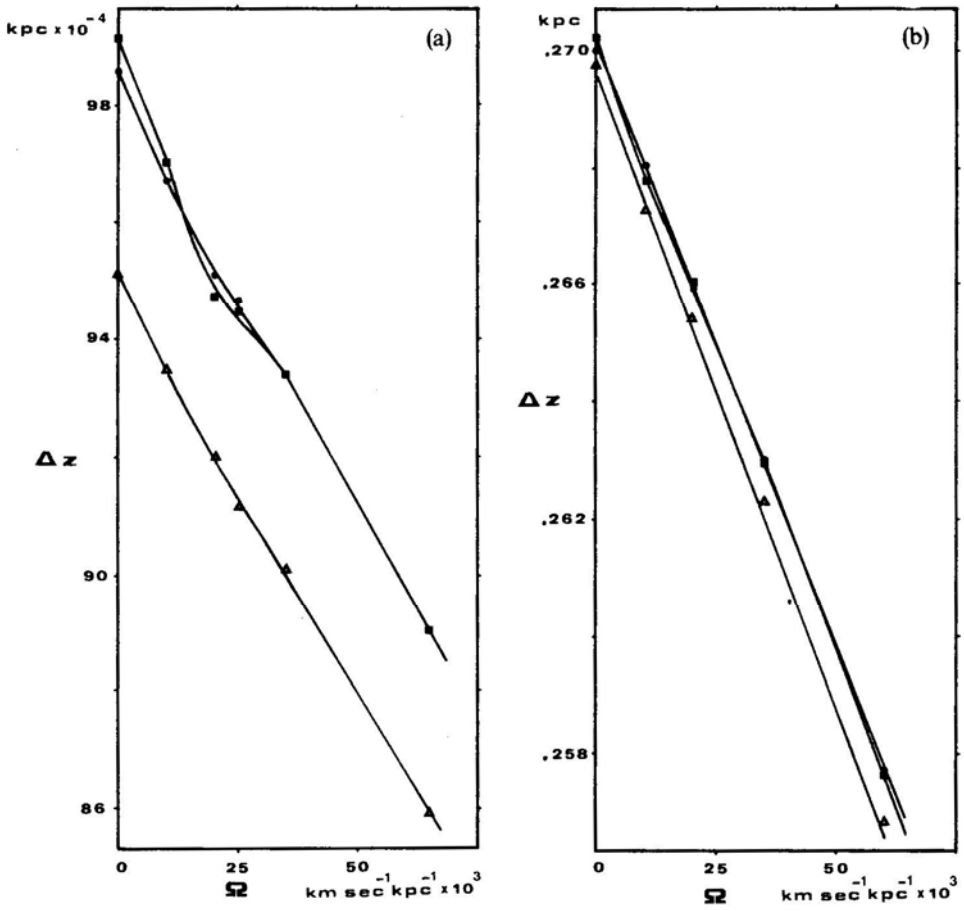

Fig. 2. Height Δz of a box-type orbit with (a) ξ_0= 0.3 kpc and (b) ξ_0 = 0.05 kpc, as a function of Ω, for constant $\dot{r}/r$ and the three values of λ as in Fig. 1.

way, depending on the initial conditions of the trajectory. The net result of this effect is that, if the masses of our model galaxy are reduced by an order of magnitude and the nuclear rotation and expansion (or contraction) velocities as well as the initial conditions of the trajectories are scaled down accordingly in a consistent way, we get post-Newtonian effects that are qualitatively the same and of the same order of magnitude as the ones presented in this work.

Hence, in view of all the above, the results of the present paper can be summarized as follows: (i) We have studied the dynamics of a massive elliptical galaxy, composed of a relativistically active nucleus, a main body and a halo. (ii) We have proved that to post-Newtonian accuracy the internal characteristics of the nucleus (rotation and expansion or contraction) affect the properties of the box-type orbits near the surface of the main body, (iii) The post-Newtonian modifications indicate a flattening of the galaxy, in accordance with observations.

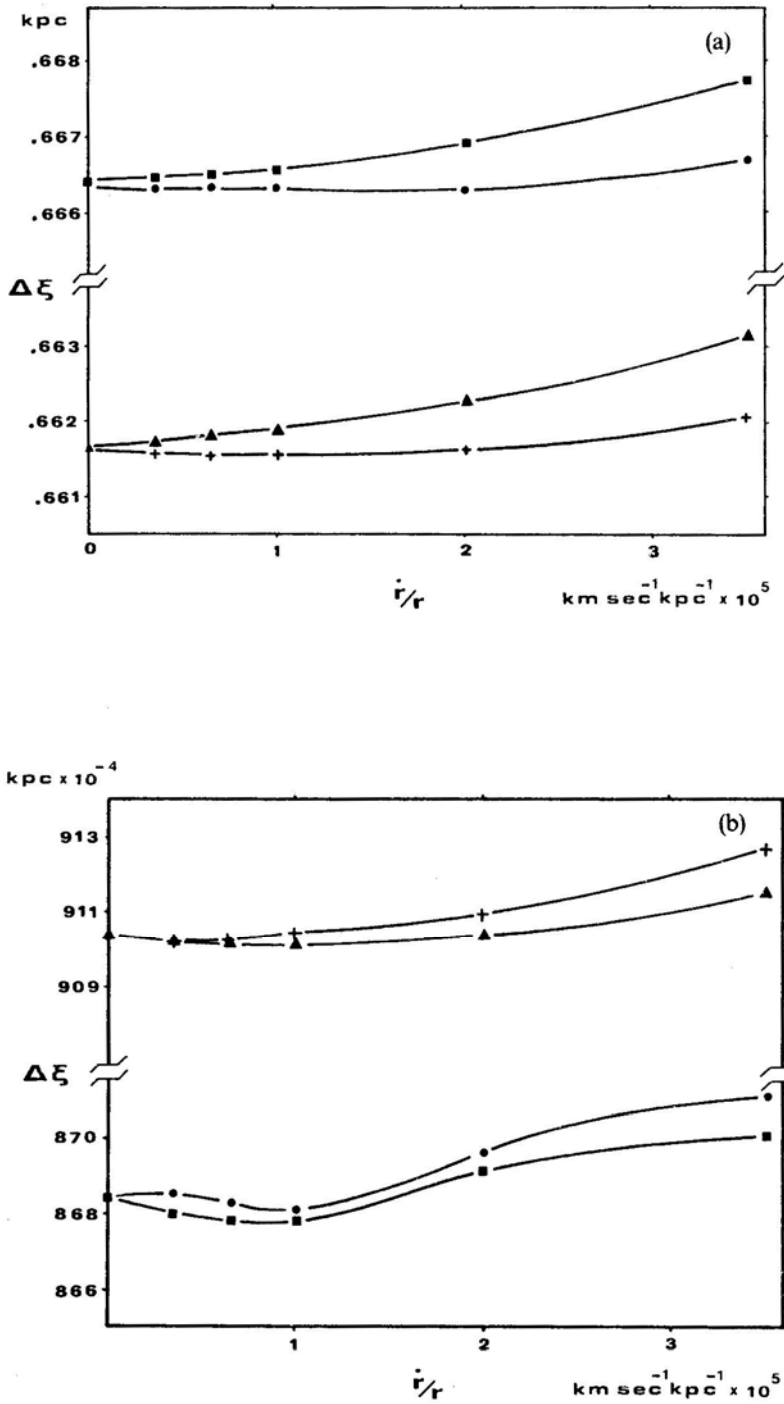

Fig. 3. Width of a box-type orbit with (a) $\xi_0 = 0.3$ kpc, and (b) $\xi_0 = 0.05$ kpc, as a function of r/r for constant Ω ($\lambda > 0$, $\Omega = 6.5 \times 10^4$ for circles ●; $\lambda < 0$, $\Omega = 6.5 \times 10^4$ for squares ■; $\lambda > 0$, $\Omega = 0$ for crosses +; $\lambda < 0$, $\Omega = 0$ for triangles ▲).

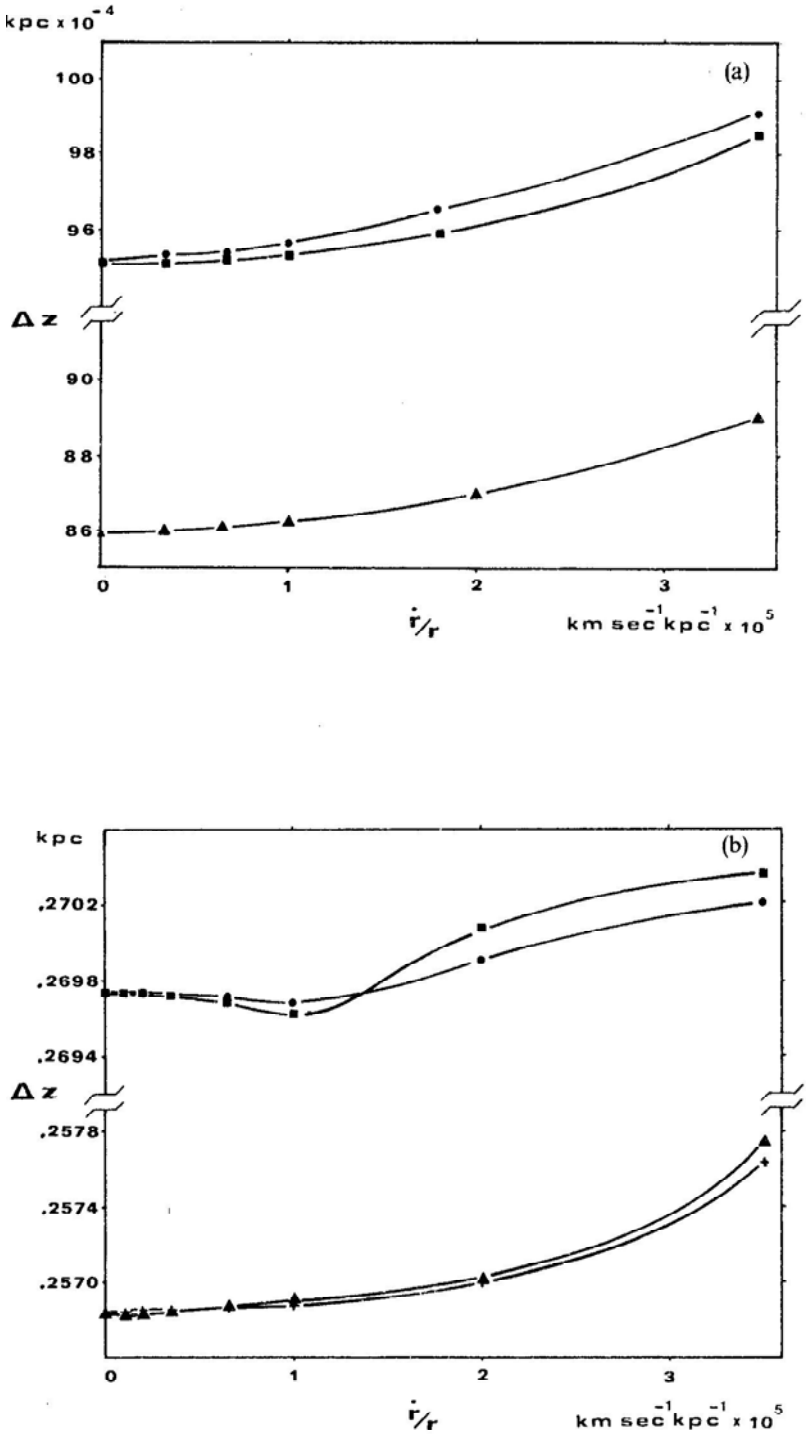

Fig. 4. Height Δz of a box-type orbit with (a) ξ_0 = 0.3 kpc, and (b)ξ_0 = 0.05 kpc, as a function of r/r, for constant Ω and the four pairs of values of λ and Ω as in Fig. 3.

Appendix

I

In view of Equation (3) in the text, Equation (2a) is written

$$\begin{aligned} W &= W_n + W_b + W_h \\ &= W_n \\ &\quad + U_b + \frac{1}{c^2}\left(U_b^2 + 2F_b - \frac{J^2 U_b}{r^2} - \frac{4J}{r} U_{\varphi_b}\right) \\ &\quad + U_h + \frac{1}{c^2}\left(U_h + 2F_h - \frac{J^2 U_h}{r^2} - \frac{4J}{r} U_{\varphi_h}\right) \\ &\quad + \frac{2}{c^2}(U_n U_b + U_b U_h + U_h U_n). \end{aligned} \tag{A1}$$

The assumed parameters of the three ellipsoids imply the following order-of-magnitude relations between Newtonian (N) and post-Newtonian (PN) parts

$$(W_n)_{PN}/c^2 (W_n)_N \sim U_n/c^2 \sim 10^{-3}, \tag{A2}$$

$$(W_b)_{PN}/c^2 (W_b)_N \sim U_b/c^2 \sim 10^{-6}, \tag{A3}$$

$$(W_b)_N/c^2 \sim (U_n/c^2)^2, \tag{A4}$$

$$W_h \sim (W_h)_N \ll (W_b)_N, \tag{A5}$$

according to which the Newtonian contribution of the body to W is of the same order of magnitude as the post-Newtonian contribution of the nucleus. Consequently the terms in the last parenthesis of Equation (Al) are all smaller than $(U_n/c^2)^3$ and Equation (4) follows.

II

As far as the Newtonian gravitational potentials U_b and U_h are concerned, it is rather straightforward to prove that Equation (40) of Chandrasekhar (1969; or Equation (A2) in the Appendix of Paper I), in the case of a point interior to a homogeneous prolate ellipsoid ($\alpha_1 = \alpha_2 < \alpha_3$), reduces to Equation (5) in the text, with

$$A_1 = A_2 = \frac{1}{e^2} - \frac{(1-e^2)}{2e^3} \log\left(\frac{1+e}{1-e}\right), \; A_3 = 2(1 - A_1), \tag{A6}$$

and

$$e = \left(1 - \frac{a_2^2}{a_3^2}\right)^{1/2}. \tag{A7}$$

III

Moreover, at a point exterior to a homogeneous, prolate, triaxial ellipsoid, the Newtonian gravitational potential is (see Equation (70) of Chandrasekhar 1969)

$$U(\text{exterior}) = \pi G\rho\, a_1 a_2 a_3 \int_{\vartheta}^{\infty} \left(1 - \sum_{i=1}^{3} \frac{x_i^2}{a_i^2 + u}\right) \Delta^{-1}\, \mathrm{d}u, \tag{A8a}$$

where x_i are the Cartesian coordinates of the field point,

$$\Delta^2 = (a_1^2 + u)\,(a_2^2 + u)\,(a_3^2 + u), \tag{A8b}$$

and the value of the ellipsoidal coordinates ϑ is found as the solution of the equation

$$\sum_{i=1}^{3} \frac{x_i^2}{a_i^2 + \vartheta} = 1. \tag{A8c}$$

In the special case of a prolate ellipsoid, Equation (A8c) reduces to a binomial equation in ϑ, whose acceptable solution is

$$2\vartheta = (r^2 + z^2 - a_1^2 - a_3^2) + \left[(a_3^2 - a_1^2 + r^2 - z^2)^2 + 4r^2 z^2\right]^{1/2}, \tag{A9}$$

and it is a matter of some algebra to verify that Eq. (A8a) reduces to Eq. (6) in the text, with

$$I_1 = \frac{1}{ea_3} \log\left[\frac{(a_3^2 + \vartheta)^{1/2} + ea_3}{(a_3^2 + \vartheta)^{1/2} - ea_3}\right], \tag{A10a}$$

$$I_2 = \frac{1}{(a_3^2 - a_1^2)}\left[\frac{(a_3^2 + \vartheta)^{1/2}}{a_1^2 + \vartheta} - \frac{I_1}{2}\right], \tag{A10b}$$

$$I_3 = 2\left[\frac{1}{(a_1^2 + \vartheta)\,(a_3^2 + \vartheta)^{1/2}} - I_2\right], \tag{A10c}$$

e and ϑ being given by Equations (17) and (A9) respectively.

IV

Generally, in view of Equation (7), Chandrasekhar's (1969) velocity potential U_a (in Cartesian coordinates centred at the ellipsoid's centre of symmetry) and in the far region of the nucleus, by a simple Taylor expansion, reduces, to lowest order, to

$$\begin{aligned} U_a(\mathbf{x}, t) &= G \int_V \rho(\mathbf{x}', t) v_z(\mathbf{x}', t)\, |\mathbf{x} - \mathbf{x}|^{-1}\, \mathrm{d}^3 x' \\ &\sim G\,|\mathbf{x}|^{-3}\, x^{\delta}\left[\varepsilon_{\alpha\beta\gamma}\Omega^{\beta} I^{\gamma\delta} - \Omega^{\alpha}\lambda^{\mu} I^{\delta\mu} + (\boldsymbol{\lambda}\cdot\boldsymbol{\Omega})\, I^{z\delta}\right] + \cdots, \end{aligned} \tag{A11}$$

where

$$I^{\alpha\beta} = \int_V \rho(\mathbf{x}, t)\, x^{\alpha} x^{\beta}\, \mathrm{d}^3 x, \qquad I^{\alpha\beta} = 0 \quad \text{for} \quad \alpha \neq \beta \tag{A12}$$

is the moment of inertia of the nucleus. In order to determine the velocity potentials in cylindrical coordinates U_r and U_φ we compare Equation (All) for α = 1 and α= 2,

respectively, with the first and second of Eqs (21) of Spyrou & Dionysiou (1973). Thus we verify that the values of U_r and U_φ determined in these two cases are compatible with each other, provided that

$$I^{xx} = I^{yy} \equiv I \tag{A13}$$

This condition is obviously satisfied for the assumed nucleus. More precisely we recover the first of Equation (9) with

$$U_\varphi = G\Omega I |\mathbf{x}|^{-3} r. \tag{A14}$$

In a similar way for $\alpha = 3$ we find

$$U_3 = -G|\mathbf{x}|^{-3}[(x\lambda_x + y\lambda_y) I^{xx}\Omega + z(\Omega\lambda - \boldsymbol{\Omega}\cdot\boldsymbol{\lambda}) I^{zz}] \tag{A15}$$

from which we recover the second of Equations (9) provided that Equation (8) is valid.

V

In evaluating W_n we simply substitute in Equation (2) ρ by the inertial-mass density and Taylor expand, thus obtaining

$$\begin{aligned} W_n \text{ (far region)} = {} & \frac{Gm_n}{|\mathbf{x}|}(1+O_2) - \frac{J^2}{2r^2} \\ & + \frac{1}{c^2}\left\{\left[\left(\frac{Gm_n}{|\mathbf{x}|}\right)^2 + \frac{J^2}{r^2}\frac{Gm_n}{|\mathbf{x}|}\right](1+O_2)\right. \\ & \left. - \frac{4G}{|\mathbf{x}|^3} J I \Omega + \frac{G}{|\mathbf{x}|}\frac{d^2 I^{\rho\rho}}{dt^2}\right\}, \end{aligned} \tag{A16}$$

where the symbol O_n stands for terms of order n in the small parameter L/D, L and D being in orders of magnitude the linear dimensions of the nucleus and $|x|$, respectively. We point out that the vanishing of the last term on the right of Equation (A16)is exactly the Newtonian *virial theorem* for a bounded perfect-fluid configuration (Spyrou 1977; Spyrou 1978). The validity of the virial theorem does not contradict the assumption of a contracting or expanding nucleus, because the fluid's velocity ν appearing in the occupation

$$\frac{1}{2}\frac{d^2 I^{\rho\rho}}{dt^2} = \int_V \rho\left(v^2 - \frac{1}{2}U + \frac{3p}{\rho}\right) d^3x \,(=0) \tag{A17}$$

is the *total* velocity (see Equation 7).

Furthermore, the validity of the virial theorem in the present case can be inferred from the following considerations. Noticing that the lowest-order term in Equation (A16) (apart from the one with d^2I^{pp}/dt^2) is $-4GJI\Omega/|x|^3$, and if the time-scale associated with the change of I^{PP} is T, then the last term of Equation (A 16) will be negligible compared to the previous one, provided that

$$T \gg T_{\min}(L/D)^{-3/2}, \tag{A18}$$

where

$$T_{\min} = 2\pi/\Omega_{\max}. \tag{A19}$$

For the model galaxy considered here the condition (A18) is valid, i.e. the timescale

associaed with the changing nucleus is much larger than a typical timescale characterizing the nucleus. Under such conditions Equation (A16) reduces to Equation (11).

VI

Using the previous results we find

$$(W_{n,rr})_0 = \frac{2Gm_n}{r_0^3} - \frac{3J^2}{r_0^4} + \frac{1}{c^2}\left(\frac{6G^2m_n^2}{r_0^4} + \frac{12J^2Gm_n}{r_0^5} - \frac{48GJI\Omega}{r_0^5}\right), \tag{A20a}$$

$$(W_{n,zz})_0 = -\frac{Gm_n}{r_0^3} + \frac{1}{c^2}\left(\frac{2G^2m_n^2}{r_0^4} - \frac{J^2Gm_n}{r_0^5} + \frac{12GJI\Omega}{r_0^5}\right), \tag{A20b}$$

$$(W_{n,rrr})_0 = -\frac{6Gm_n}{r_0^4} - \frac{12J^2}{r_0^5} + \frac{1}{c^2}\left(-\frac{24G^2m_n^2}{r_0^5} - \frac{60J^2Gm_n}{r_0^6} + \frac{240GJI\Omega}{r_0^6}\right), \tag{A20c}$$

$$(W_{n,zzr})_0 = \frac{3Gm_n}{r_0^4} + \frac{1}{c^2}\left(\frac{8G^2m_n^2}{r_0^5} - \frac{5J^2Gm_n}{r_0^6} - \frac{60GJI\Omega}{r_0^6}\right), \tag{A20d}$$

$$(U_{r,r})_0 = \frac{2G\lambda\Omega I}{r_0^3}, \tag{A21a}$$

$$(U_{r,rr})_0 = -\frac{6G\lambda\Omega I}{r_0^4}, \tag{A21b}$$

$$(U_{r,zz})_0 = -\frac{12G\lambda\Omega I}{r_0^4}, \tag{A21c}$$

$$(U_{,r})_0 = -\frac{Gm_n}{r_0^2}. \tag{A22}$$

The corresponding derivatives of U_b (interior) and U_n (interior) are evaluated in the same way as in Paper I, while those of U_b (exterior), although evaluated, on the basis of the recurrent formulae (A 10a, b, c) are not given here due to their complexity and length.

Reference

Bergval, N., Johansson, L. 1985, *Astr. Astrophys.*, **149,** 475.

Bertola, F. 1981, *Sky Telesc,* **61,** 380.

Bertola, F., Capaccioli, M. 1978, *Astrophys. J.*, **219,** L95.

Bertola, F., Galleta, G. 1978, *Astrophys.* J., **226,** L115.

Biermann, P., Strom, R., Bartel, N. 1985, *Astr. Astrophys.*, **147,** L27.

Binney, J. 1976, *Mon. Not. R. Astr. Soc.*, **177,** 19.

Binney, J., Gerhard, O. E., Piet, H. 1984, Max-Planck-Institut für Astrophysik Green Report No. MPA 134.

Blandford, R. D. 1984, in *Proc. Active Galactic Nuclei,* (Manchester) Caltech Goldenrod Preprint No. GRP-021.

Chandrasekhar, S. 1969, *Ellipsoidal Figures of Equilibrium,* Yale Univ. Press, New Haven.

Contopoulos, G. 1960, *Z. Astrophys.*, **49,** 273.

Contopoulos, G. 1983, in *IAU Symp.* 104: *Early Evolution of the Universe and its Present Structure,* Eds G. O. Abell & G, Chincarini, D. Reidel, Dordrecht, p. 417.
Contopoulos, G., Spyrou, N. 1976, *Astrophys. J.,* **205,** 592.
Danks, A. C, Materne, J. 1984, *Astr. Astrophys.,* **139,** 455.
Dicke, R. H., Goldenberg, H. M. 1967, *Phys. Rev. Lett.,* **18,** 313.
Gerhard, O. 1985, Max-Planck-Institut für Astrophysik Green Report No. MPA 187.
Gerhard, O., Binney, J. 1985, Max-Planck-Institut für Astrophysik Green Report No. MPA 175.
Hoffman, G. L., Sapleter, E. E. 1982, *Astrophys. J.,* **263,** 485.
Spyrou, N. 1977, *Gen. Relativ. Grav.,* **8,** 463.
Spyrou, N. 1978, *Celest. Mech.,* **18,** 351.
Spyrou, N., Dionysiou, D. 1973, *Astrophys. J.,* **183,** 265.
Spyrou, N., Varvoglis, H. 1982, *Astrophys. J.,* **255,** 674 (Paper I).
Spyrou, N., Varvoglis, H. 1983, in *Proc. Seventh European Regional Astronomy Meeting,* Florence.
Tayler, R. J. 1978, *Galaxies: Structure and Evolution,* Wykeham Publ., London.
van Albada, T. S., Sanders, R. H. 1982, *Mon. Not. R. ast. Soc,* **201,** 303.

J. Astrophys. Astr. (1987) **8,** 17–31

N-Body Simulations of Tidal Encounters between Stellar Systems

P. Devadas Rao* & N. Ramamani *Centre of Advanced Study in Astronomy, Osmania University, Hyderabad 500007*

Saleh Mohammed Alladin† *International Centre for Theoretical Physics,* 34100 *Trieste, Italy*

Received 1986 August 1; accepted 1986 November 17

Abstract. ***N***-Body simulations have been performed to study the tidal effects of a primary stellar system on a secondary stellar system of density close to the Roche density. Two hyperbolic, one parabolic and one elliptic encounters have been simulated. The changes in energy, angular momentum, mass distribution, and shape of the secondary system have been determined in each case. The inner region containing about 40 per cent of the mass was found to be practically unchanged and the mass exterior to the tidal radius was found to escape. The intermediate region showed tidal distension. The thickness of this region decreased as we went from hyperbolic encounters to the elliptic encounter keeping the distance of closest approach constant. The numerical results for the fractional change in energy have been compared with the predictions of the available analytic formulae and the usefulness and limitations of the formulae have been discussed.

Key words: stellar systems, tidal encounters—stellar dynamics

1. Introduction

The study of encounters between galaxies has received much attention after the discovery of peculiar galaxies. Photographs of interacting galaxies by Vorontsov-Velyaminov (1959, 1977), Arp (1966) and others show that many pairs of galaxies have peculiar morphological features. Toomre & Toomre (1972) using the restricted three-body approach, showed that the tidal forces play a vital role in the dynamics of interacting galaxies and lead to the formation of such features. Ostriker, Peebles & Yahil (1974), Faber & Gallagher (1979) and Gunn (1980) have discussed dynamical evidence for the galaxies being surrounded by large haloes, often extending up to 100 kpc. This has increased our estimate for the frequency of galactic collisions and has considerably stimulated research in galaxy interactions.

* Permanent Address: Department of Mathematics, M.G.M. College, Udupi.
† Permanent Address: Centre of Advanced Study in Astronomy, Osmania University, Hyderabad 500007.

The effects of the tidal forces are not merely peripheral. The overall structure of the galaxies is also affected. The fractional increase in the total internal energy of a galaxy, $\Delta U/|U|$ provides a good measure of the change in its structure (Alladin 1965). If this is equal to or greater than unity, the galaxy would be appreciably disrupted. This ratio has been estimated by many workers using the impulsive approximation (IA) wherein the motion of the stars in the test system is neglected in comparison with the orbital motion of the systems. This approximation gives good results for energy changes even in slow hyperbolic collisions (Toomre 1977; Dekel, Lecar & Shaham 1980; Aguilar & White 1985). However, for a detailed study of the changes in the shape and mass distribution of a colliding stellar system, a self-consistent method such as the method of *N*-Body simulations is needed. This method has been extensively used to study mergers of galaxies (see Tremaine 1981, and White 1983 for reviews). Borne (1984) has determined merger times of binary galaxies using multiple three-body algorithm. In this paper we shall not consider mergers. Here we shall restrict ourselves to the cases of non-penetrating tidal encounters.

Studies of encounters between stellar systems may be divided into two categories: (a) those in which the two systems are of comparable mass, and (b) those in which there is great disparity in mass. In this paper we shall study the second category. It is convenient in this case to designate the more massive system as the primary and the less massive as the secondary (satellite). The primary has disruptive effects on the secondary while the secondary accelerates the stars in the outer parts of the primary and this leads to dynamical friction on the motion of the satellite. The former (disruptive) effect becomes more important than the latter (merging) effect as the ratio ρ/ρ_R (where ρ is the density of the satellite system and ρ_R is the Roche density) decreases (Alladin, Ramamani & Meinya Singh 1985). The case of $\rho \geqslant \rho_R$ where dynamical friction and merging are more important than disruption has been studied by Lin & Tremaine (1983) and others. In this paper we shall study the case in which the density of the satellite is close to the Roche density. We ignore the effects of dynamical friction and concentrate on how the tidal field of the primary changes the mass distribution, energy and angular momentum of the secondary. We confine ourselves to non-penetrating encounters and treat the primary as a mass point. We investigate to what extent the results of the analytic formulae derived under the assumption that the stars remain stationary (Spitzer 1958; Alladin & Narasimhan 1982; Narasimhan & Alladin 1983) agree with the numerical experiments.

In Section 2 we describe the method used and the initial conditions employed in the present simulations. The numerical results are given and discussed in Section 3. In Section 4 we give the main conclusions.

2, The Method and the Initial Conditions

2.1 *The Method*

In *N*-Body simulations we solve a system of N second-order differential equations of motion of N particles in a system simultaneously. The motions are governed by

$$\frac{\mathrm{d}^2\mathbf{r}_i}{\mathrm{d}t^2} = -G \sum_{\substack{j=1 \\ i \neq j}}^{N} \frac{m_j}{r_{ij}^3}\mathbf{r}_{ij}, \tag{1}$$

where $\mathbf{r}_{ij} = \mathbf{r}_i - \mathbf{r}_j$, m_i and $\mathbf{r}_i$ are the mass and position vector of particle *i*, G is the constant of gravitation. A problem arises in near collision of two particles due to the singularity when $r_{ij} \to 0$. Also on account of the restriction that N should be small to save computer time, relaxation time is reduced and the system may not mimic a real system. The relaxation time is increased by using a softened potential, given by

$$\Phi_i = -G \sum_{\substack{j=1 \\ i \neq j}}^{N} \frac{m_j}{(r_{ij}^2 + \varepsilon^2)^{1/2}} \tag{2}$$

The *N*-BODY 1 Code of S. J. Aarseth was used to compute the orbits of the particles interacting via this potential.

2.2 *The Initial Conditions*

We studied the disruption of the secondary stellar system (satellite system) of mass M due to the tidal effects of the primary system of mass $M_1 = 10^5 M$. The satellite system was modelled by 124 particles each of unit mass distributed randomly within a sphere of radius $R = 20$ units with the mass distribution $M(r) \propto r$. Each particle was then given a velocity equal to the circular velocity at the distance and the directions of the velocity vectors were chosen *randomly* as in ISO model of White (1978). The system so generated had zero angular momentum. Its half-mass radius R_h was nearly 10 units and with $G = 1$, V_{rms} was 2.3 units and the crossing time was about 8 units. Following White (1978) we chose $\varepsilon = 1$ in Equation (2).

The system was allowed to evolve by itself for about 7 crossing times to give a well-mixed, dynamically stable system. This system had its half-mass radius almost unchanged. The values of R_{rms} and V_{rms} were nearly 20.0 and 2.2 respectively. The radius containing 90 per cent mass was about $3R_h$. The ratio of the rms radial and tangential velocities $Vr_{,\,rms}/Vt_{,\,rms}$ was 0.83 indicating that the model also had elongated orbits.

In order that the density of the system may be close to the Roche density when it is at its closest approach p we chose $p = 100\ R_h$ The orbital plane was chosen as the *xy*-plane with the *x*-axis in the direction of the closest approach. Four non-penetrating encounters were simulated with encounter parameters chosen as in Table 1. V_p is the magnitude of the velocity at closest approach and e is the eccentricity of the orbit.

M_1 was placed in the orbit at a distance $r = 2p$. Beyond this distance the tidal effects are negligible. The initial relative velocity at this distance was obtained from the two-body formulae. The positions and velocities of the particles in the test system and of the point-mass perturber were computed in the centre-of-mass frame of the entire system. These were taken as the input for the *N*-BODY 1 Code. At various times, the essential data containing the positions and velocities of all the particles were stored for the latter processing. The computation was stopped when the system showed no further change in its properties.

3. Numerical results and discussion

The position and velocity data obtained at various times was used to study the structural changes of the system during the encounter. We found the internal energy

Table 1. Simulation parameters.

Model	e	P/R_h	V_p/V_{rms}	M/M_1
H1	3.0	100	101	10^{-5}
H2	2.4	84	101	10^{-5}
P	1.0	100	72	10^{-5}
E	0.5	100	62	10^{-5}

(binding energy), the angular momentum, the mass loss, and the change in the shape, at the end of the encounter.

Due to the strong tidal forces acting on the system during the encounter, the system loses spherical symmetry. Thus the mass distribution and shape cannot be conveniently studied with respect to the centre of mass of all the particles in the system. For this purpose we took a reference frame with its origin at the centre of mass of the most dense region defined as the region containing those particles with energy less than—rather than the average energy of—the bound particles. A particle was considered to be bound or be an escaper depending on whether

$$E_i = \frac{1}{2} m_i v_i^2 - G m_i \sum_{\substack{j=1 \\ i \neq j}}^{N} \frac{m_j}{(r_{ij}^2 + \varepsilon^2)^{1/2}} \tag{3}$$

was negative or positive. We determined the structure of the system in this frame designated as the effective frame. The mass loss was estimated from the number of escaping particles.

3.1 *Energy Increase and Mass Loss*

Fig. 1 gives the fractional energy increase $\Delta U/|U|$ and the mass loss $\Delta M/M$ as a function of time for the four models. C indicates the time of closest approach. It may be noted that the energy increase is somewhat symmetric about the closest approach. This is expected from Spitzer's (1958) theory based on impulsive approximation which leads to

$$(\Delta U)_{\text{half}} = \frac{M}{2} \int_{-\infty}^{0} (\Delta \mathbf{V})^2 \, dt = \frac{M}{2} \left(\frac{G M_1}{p^2 V_p} \right)^2 \frac{4}{3} R_{\text{rms}}^2 = \frac{1}{2} (\Delta U)_{\text{Total}}. \tag{4}$$

On the other hand, Ahmed & Alladin (1981) found that the energy transfer in a head-on collision between two identical galaxies is asymmetric with respect to the closest approach, the transfer in the second half being double that of the first half. This was because of the dynamical friction, the relative velocity of the galaxies was slower in the second half. In our case the deceleration due to dynamical friction is very small and was not considered.

In the case of parabolic and elliptic encounters we found that most of the energy increase occurred when $-\pi/2 < \theta < \pi/2$ (taking $\theta = 0$ at closest approach). This does not agree with the analytic formulae obtained under IA (Alladin & Narasimhan 1982; Narasimhan & Alladin 1983) which predict that the energy increase in this range is half the total ($-\pi < \theta < \pi$). Since $\Delta U/|U|$ predicted by these formulae for the total

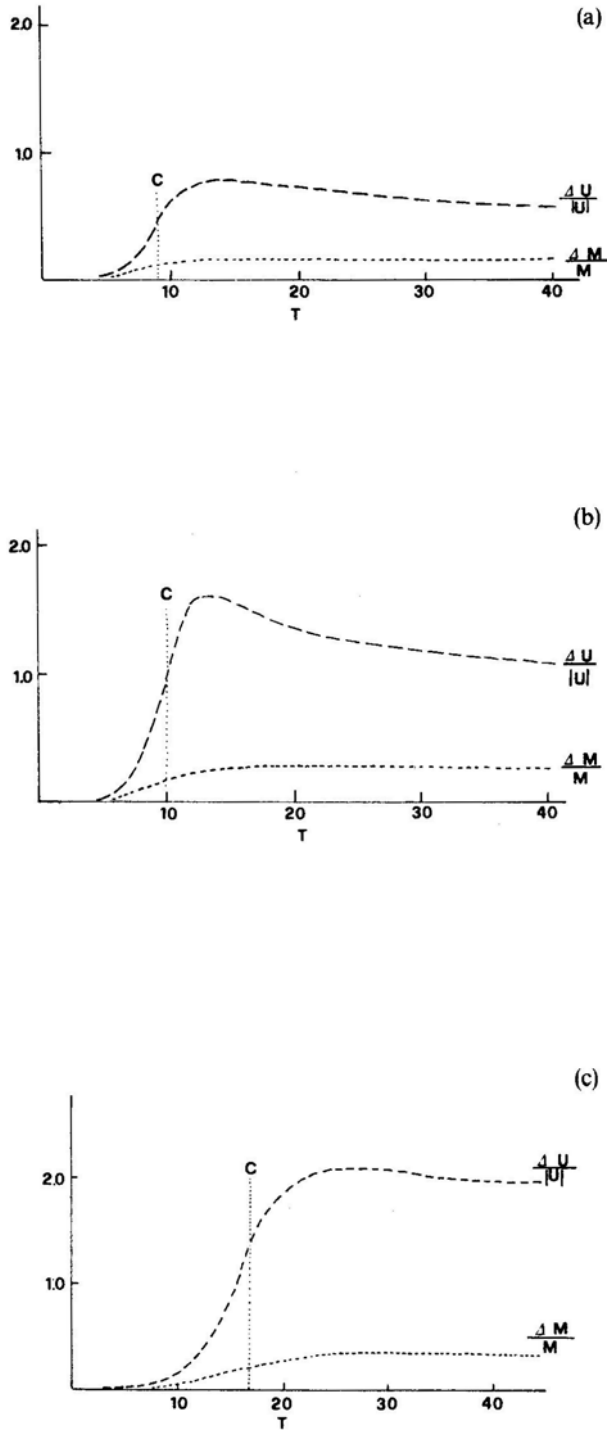

Figure 1. Fractional change in energy and fractional mass loss as a function of time for the four models (a) H1, (b) H2, (c) P, and (d) E.

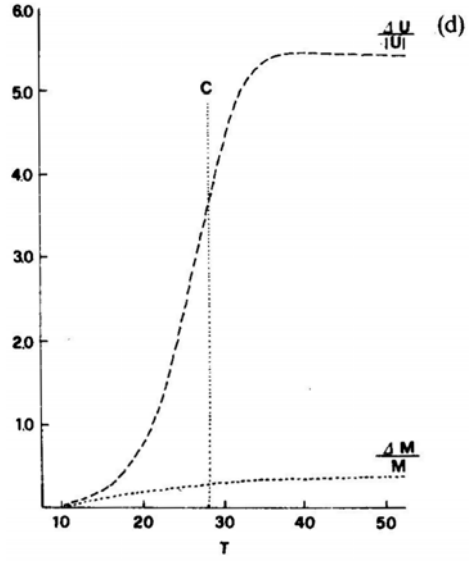

Figure 1. Continued.

encounter is reasonable, as will be discussed subsequently, it follows that IA underestimates the tidal effects near the perigalacticon and overestimates on the far side.

In Table2, we compare the values of ΔU / $|U|$ obtained in the various models with those predicted from the analytical formulae derived under IA. For fast encounters, assuming the relative orbit to be rectilinear, Dekel, Lecar & Shaham (1980) obtained from Spitzer's (1958) theory

$$\frac{\Delta U}{|U|} = \frac{8}{3}\frac{G^2 M_1^2}{p^4 V_p^2}\left(\frac{R_{\rm rms}}{V_{\rm rms}}\right)^2. \tag{5}$$

From Alladin & Narasimhan (1982) and Narasimhan & Alladin (1983), we obtain for the conic orbit

$$\frac{\Delta U}{|U|} = \frac{2\pi^2}{(1+e)^2}\frac{G^2 M_1^2}{p^4 V_p^2}\left(\frac{R_{\rm rms}}{V_{\rm rms}}\right)^2 \qquad \text{for} \quad e \leqslant 1, \tag{6}$$

$$\frac{\Delta U}{|U|} = (1+e)\langle e_i^2 \rangle \frac{G^2 M_1^2}{p^4 V_p^2}\left(\frac{R_{\rm rms}}{V_{\rm rms}}\right)^2 \quad \text{for} \quad e > 1, \tag{7}$$

Table 2. Fractional increase in the energy, fractional mass loss, and the ratio of the radii containing 90 per cent mass of the bound system to that of the whole system. $(\Delta U/|U|)_{\rm Sp}$ is obtained from Equation (5). $(\Delta U/|U|)_{\rm N+A}$ is obtained from Equations (6) or (7).

Model	$(\Delta U/\lvert U\rvert)_{N\text{-Body}}$	$(\Delta U/\lvert U\rvert)_{\rm Sp}$	$(\Delta U/\lvert U\rvert)_{\rm N+A}$	$(\lvert\Delta M\rvert/M)$	$(\Delta U_{\rm B}/\lvert U\rvert)$	$(R_{\rm B}/R)_{0.9}$
H1	0.61	0.70	0.72	0.19	0.24	0.30
H2	1.12	1.40	1.60	0.27	0.27	0.44
P	1.96	1.40	2.60	0.39	0.36	0.58
E	5.48	1.90	6.00	0.40	0.43	0.71

where

$$\langle e_i^2 \rangle = (e_1^2 + e_2^2 + e_3^2)/3,$$

$$e_1 = \frac{1}{(e+1)^{1/2}}\left[\frac{1}{(e+1)}\cos^{-1}(-e^{-1}) + \frac{2e^2-1}{e^2}\left(\frac{e-1}{e+1}\right)^{1/2}\right],$$

$$e_2 = \frac{1}{(e+1)^{1/2}}\left[\frac{1}{(e+1)}\cos^{-1}(-e^{-1}) + \frac{1}{e^2}\left(\frac{e-1}{e+1}\right)^{1/2}\right],$$

$$e_3 = \frac{2}{(e+1)^{1/2}}\left[\frac{1}{(e+1)}\cos^{-1}(-e^{-1}) + \left(\frac{e-1}{e+1}\right)^{1/2}\right]. \tag{8}$$

Equations (6) and (7) are derived on the assumption that the relative orbit is the unperturbed two-body orbit. Equation (5) is of much simpler form since the relative motion is assumed to be rectilinear with constant speed. $\Delta U/|U|$ predicted by the analytical formulae (5) and (7) agree well with the results of numerical experiments for models H1 and H2. For model P, Equation (5) underestimates $\Delta U/|U|$ while Equation (6) overestimates it. The computed value lies almost exactly in between these two estimates. For model E the numerical value is in good agreement with that predicted by Equation (6). Equation (5) underestimates it by a factor of about 3 in this case.

In Table 2 we also give $\Delta U_B/|U|$ where U_B is the binding energy of the final bound part, $\Delta M/M$, the fractional mass loss, and $(R_B/R)_{0.9}$ the ratio of the radii containing 90 per cent mass of the bound system to that of the total system. We find a linear relation of the form (Fig. 2):

$$\frac{\Delta U_B}{|U|} \simeq \frac{\Delta M}{M} \simeq 0.6\left(\frac{R_B}{R}\right)_{0.9}.$$

The first part of the result was earlier noted by Dekel, Lecar & Shaham (1980) for their A model.

The range in $\Delta U_B/|U|$ is considerably smaller than the range in $\Delta U/|U|$. This is because a large part of the transferred energy is carried away by the escaping particles, a result earlier noted by Richstone (1975). An interesting point is that as we go from the hyperbolic to the parabolic case keeping p fixed, $\Delta U/|U|$ and $\Delta M/M$ both go on increasing. But when we go from the parabolic to the elliptic case $\Delta M/M$ remains almost unchanged, but $\Delta U/|U|$ increases drastically. This is because the escaping particles in the elliptic encounter carry away much larger energy than in the case of the parabolic encounter. White (1978) found that more particles escape from parabolically colliding systems than from initially bound systems for equal mass encounters.

Aguilar & White (1985) have written a comprehensive paper on tidal interactions between spherical galaxies in which the changes in binding energy and mass are obtained both by the methods of IA and *N*-body simulations. They have considered galaxies of comparable mass and concentrated on interpenetrating collisions. They have found that Spitzer's distant-encounter formula is valid only for impact parameters exceeding 10 times the effective radius of the test galaxy. In the hyperbolic and parabolic cases that we have studied, this condition is always satisfied since the separation is much larger. Thus, Equation (5) gives good agreement with the results of numerical experiments for hyperbolic and parabolic orbits as expected.

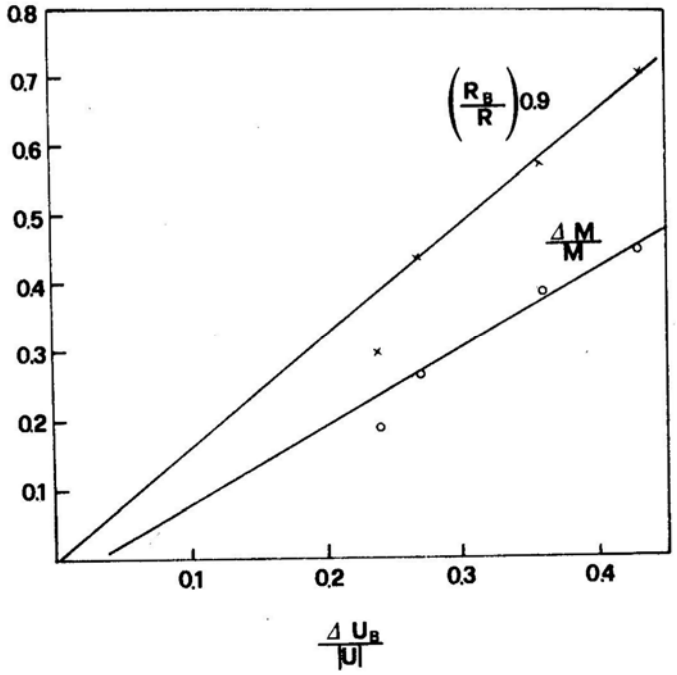

Figure 2. Relation between changes in energy, mass and size.

3.2 *Gain in the Angular Momentum*

As a result of tidal interaction, the satellite system acquires angular momentum from the orbital angular momentum of the pair. In Table 3 we give the orbital angular momentum $(L_Z)_{orb}$ of the pair, the spin angular momentum for the total system $(S_z)_{total}$ and for the bound part $(S_z)_{bound}$ after the encounter. It can be seen that only a very small fraction of the orbital angular momentum is transferred, and that most of the transferred angular momentum is carried away by the escaping particles as earlier noted by White (1979) in simulations of merging galaxies. We also note that the escapers carry away small angular momentum in large angular momentum encounters and vice-versa. Thus the angular-momentum transfer is inversely related to the orbital angular momentum.

Table 3. Angular momentum transfer from the orbital motion to the test system.

Model	$(L_z)_{orb}$	$(S_z)_{Total}$	$(S_z)_{bound}$
H1	2.8(+7)	4.0(+3)	3.6(+2)
H2	2.3(+7)	7.6(+3)	2.1(+2)
P	2.0(+7)	2.1(+4)	1.3(+2)
E	1.7(+7)	6.0(+4)	2.3(+2)

3.3 *Particle Orbits*

An idea of the change in the nature of the stellar orbits can be had from the values of $(V_r)_{rms}$ and $(V_t)_{rms}$ after the encounter. These are given for the total system and for the bound part in Table 4. Both the radial and the transverse velocities of the stars are increased as a result of the tidal interaction. Hyperbolic and parabolic encounters favour the radial motion more than the transverse motion. In bound-orbit encounters both are almost equally affected. The bound part has more transverse orbits than radial orbits even compared with the initial system. It follows that the stars in radial orbits preferentially escape.

3.4 *Radial Mass Distribution*

To study how the radial distribution of mass changes due to the encounter we find the radii containing 10 per cent, 20 per cent, *etc.* of the total mass in the effective frame. This is done for the initial system and the final system including the escapers. The results are given in Table 5. In Fig. 3 $M(r/R_h)/M$ is plotted against r/R_h where M and R_h are the initial mass and half-mass radius of the system.

We distinguish three regions in the final system: (1) the inner region containing about 40 per cent of the mass which remains practically intact; (2) the intermediate tidally distended region which extends up to the tidal radius; and (3) the region exterior to the tidal radius which is found to escape. Dekel, Lecar & Shaham (1980) also observed that the mass distribution within R_h almost remained intact and there was expansion for $r > R_h$. The figure shows that there is not much difference in the final mass distribution between models P and E.

Table 4. Radial and transverse velocities.

	Total			Bound		
Model	$(V_r)_{rms}$	$(V_t)_{rms}$	$(V_r)_{rms}/(V_t)_{rms}$	$(V_r)_{rms}$	$(V_t)_{rms}$	$(V_r)_{rms}/(V_t)_{rms}$
Initial	1.41	1.70	0.83	1.41	1.70	0.83
H1	1.82	1.81	1.00	1.05	1.84	0.57
H2	2.37	1.81	1.31	1.03	1.85	0.56
P	2.84	2.38	1.91	1.19	1.93	0.62
E	2.58	4.69	0.76	1.06	2.00	0.53

Table 5. Mass distribution before and after the encounter.

	$M(r/R_h)/M$									
Model	0.1	0.2	0.3	0.4	0.5	0.6	0.7	0.8	0.9	1.0
Initial	0.12	0.26	0.45	0.67	0.95	1.35	1.83	2.66	3.15	7.8
H1	0.18	0.30	0.46	0.70	1.06	1.59	2.64	5.91	9.4	35
H2	0.16	0.30	0.46	0.75	1.19	2.28	3.75	8.6	13.1	40
P	0.14	0.28	0.40	0.71	1.39	3.26	9.2	13.2	17.5	36
E	0.15	0.29	0.56	0.79	1.93	3.38	7.9	16.1	21.3	35

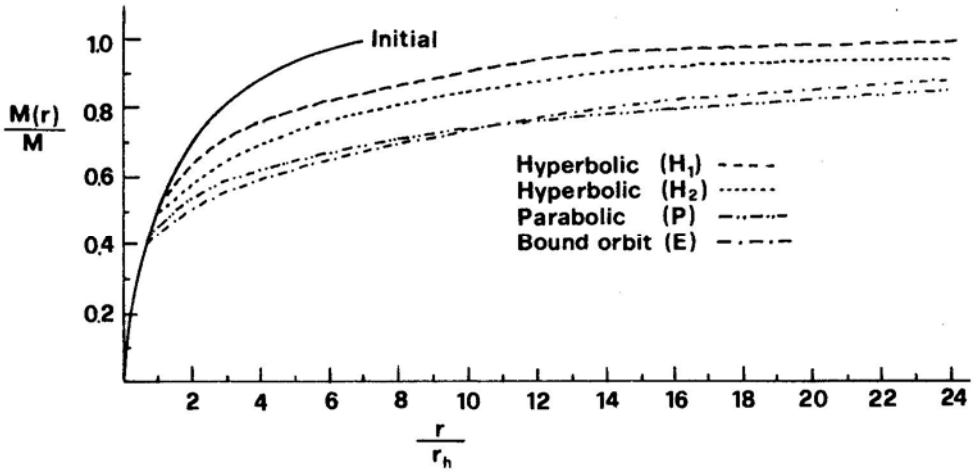

Figure 3. Mass distribution before and after the encounter for the four models.

3.5 *Tidal Radius*

The tidal radius obtained from numerical experiments is compared with those predicted from analytic formulae in Table 6. $(R_t)_{N\text{-Body}}$ is defined as the radius of the initial test system, beyond which the mass escapes in the numerical experiment. $(R_t)_{\text{King}}$ is obtained from King's (1962) formula

$$R_t = p\left(\frac{M}{M_1(3+e)}\right)^{1/3}, \tag{9}$$

and $(R_t)_{IA}$ is taken as the value of R_{rms} in Equation (6) or (7) for which $\Delta U/|U| = 1$. We note that $(R_t)_{N\text{-Body}}$ agrees well with $(R_t)_{IA}$ for hyperbolic and parabolic encounters and with $(R_t)_{King}$ for parabolic and bound-orbit encounters as expected. We also give in the table the radius of the intact sphere measured in the unit of the tidal radius. It may be noted that this fraction is smaller for the hyperbolic encounters which implies that the size of the intermediate region which produces tidal distension decreases as we go from hyperbolic encounter to elliptic encounter keeping the distance of closest approach constant. If we keep p constant, the intermediate region becomes thinner with decreasing e.

It is of interest to compare the result of the present work with that of Angeletti, Capuzzo-Dolcetta & Giannone (1983) who studied analytically the tidal linear stability

Table 6. Tidal radius and the radius of the intact sphere.

Model	$(R_t)_{N\text{-Body}}$	$(R_t)_{King}$	$(R_t)_{IA}$	R_{intact}/R_t
H1	26	15	24	0.4
H2	18	13	16	0.5
P	13	15	12.5	0.6
E	13	15	8	0.6

of a homogeneous star cluster considered as a galactic satellite. They indicated the regions of stability and instability in the v, e plane where

$$v = \frac{M_c}{M_g}\left(\frac{a}{R_c}\right)^3,$$

M_c, M_g, a, R_c, being respectively, the mass of the cluster, the mass of the Galaxy the semi-major axis of the orbit and the radius of the cluster. For a given e, three regions of v may be distinguished: (a) the region of instability when $v < v_{min}$, (b) the region of stability, where $v > v_{max}$, and (c) the transition region $v_{max} > v > v_{min}$ containing zones of both stability and instability. This work shows that in the case of the circular orbit, there is a sharp transition between regions of stability and instability and the width of the transition region increases with e.

3.6 *Change in Shape*

We can make a crude quantitative estimate for the shape of a system of particles from the values of $\langle|x|\rangle$, $\langle|y|\rangle$, $\langle|z|\rangle$. These are given for the total system and for the bound part in Table 7. We also give in the table, the expansion parameters E_x, E_y, E_z defined by

$$E_x = \frac{\langle|x_f|\rangle - \langle|x_i|\rangle}{\langle|x_i|\rangle} \quad etc.,$$

where f and i denote final and initial values. We note that the maximum expansion is always in the x direction and the least in the z direction. At the encounter we have a system flattened in the orbital plane, consistent with the gain in angular momentum in the z direction. The final bound part is, however, almost spherical in shape.

It may be noted that for the hyperbolic encounters, the expansions in the y and z directions are nearly equal. But in the case of parabolic and elliptic encounters the expansion in the z direction is considerably smaller than that in the y direction. We can summarize our results as

$$E_x \gg E_y \simeq E_z \quad \text{for} \quad e \simeq 3,$$
$$E_x > E_y \gg E_z \quad \text{for} \quad 0.5 < e \leqslant 1.0.$$

We expect E_x , E_y, E_z to be proportional to the energy increments in the x, y, z, directions. According to Spitzer's (1958) formula if $e \gg 1$ then $\Delta V_x^2 = \Delta V_z^2$ and $\Delta V_y^2 = 0$. According to Alladin & Narasimhan (1982), for $e \leqslant 1$, $\Delta V_x^2 = \Delta V_y^2 = \frac{1}{4}\Delta V_z^2$

Table 7. Expansion parameters in the three directions.

Model	Total			Total			Bound		
	$\langle\|x\|\rangle$	$\langle\|y\|\rangle$	$\langle\|z\|\rangle$	E_x	E_y	E_z	$\langle\|x\|\rangle$	$\langle\|y\|\rangle$	$\langle\|z\|\rangle$
Initial	6.6	6.6	6.6				6.6	6.6	6.6
H1	24	11	12	2.6	0.6	0.8	7.4	7.3	6.2
H2	32	15	15	3.9	1.2	1.2	6.5	5.2	5.5
P	42	26	11	5.4	3.0	0.7	4.5	3.4	4.5
E	48	32	8	6.3	3.9	0.2	4.5	4.5	4.5

A comparison of the prediction of the analytic formulae with the numerical results indicates that IA overestimates $(\Delta V_z)^2$ in every case. Since the overall estimate for ΔU predicted by IA agrees with the numerical results, it follows that IA underestimates $\Delta V_w^2 = \Delta V_x^2 + \Delta V_y^2$. The IA estimate agrees with the numerical results in predicting that $E_x \gg E_y$ for $e = 3$ but does not agree in predicting that $E_x > E_y$ for $0.5 < e \leqslant 1.0$.

IA is not satisfactory for predicting ΔV_z^2 in slow hyperbolic or bound orbit encounters. Agreement with numerical results may be achieved in a fast hyperbolic encounter. It may be noted that in IA, the term $\mathbf{V}\cdot\Delta\mathbf{V}$ is neglected and that ΔV_Z is negative for a star on the positive z-axis. The negative sign of ΔV_z acts in the direction of reducing the expansion in the z direction. That the tidal expansion in the z direction is small is consistent with Chandrasekhar's (1942) analysis for the tidal disruption of a star cluster, which shows that the disruption does not occur on account of tidal instability in the z direction.

3.7 *Escaping Particle*

In Fig. 4 we plot the number of escaping particles in each quadrant at different times. The circle on the relative orbit represents the position of the perturber. The number in each quadrant is the number of particles beyond a distance of 30 units. Almost all of them are escapers, The system first tends to get elongated towards and away from the perturber. This direction slowly rotates following the perturber's motion. A similar scenario was also observed by Miller (1984) in his study of the tidal effects on a satellite system. The satellite system was seen to get elongated towards and away from the perturber and the particles were seen to escape from the end of the bulges. Dekel, Lecar & Shaham (1980) observed that in interpenetrating encounters, the escaping particles had a preferred direction which was opposite to the direction of closest approach, whereas in distant encounters, particles escaped both towards and away from the perturber.

4. Conclusions

The main conclusions of this work are as follows:

1. The thickness of the shell between the inner intact sphere and the outer stripped region decreases as we go from a hyperbolic orbit to a bound orbit encounter, keeping the distance of closest approach fixed.
2. The estimate for $\Delta U/|U|$ obtained under IA for a conic orbit (Equations 6 and 7) is in fairly good agreement with that obtained by the numerical method for $e \geqslant 0.5$. Spitzer's formula holds for $e \geqslant 1$.
3. Although IA gives good estimates for the overall energy transfer, it does not predict correctly the components of the stellar velocity perturbations. Unless $e \gg 1$, $(\Delta V_Z)^2$ is always overestimated. In a bound orbit encounter, the error is large. The expansion parameters obtained from the numerical experiments satisfy the relations $E_x \gg E_y = E_z$ for $e \simeq 3$ and $E_x > E_y \gg E_z$ for $e \leqslant 1$. On the other hand, the IA formulae suggest $E_x = E_z \quad E_y$ for $e \quad 1$ and $E_z > E_x = E_y$ for $e \leqslant 1$.
4. In the case of bound-orbit encounter, IA underestimates the energy increase during the encounter on the perigalacticon side and overestimates on the apogalacticon side.

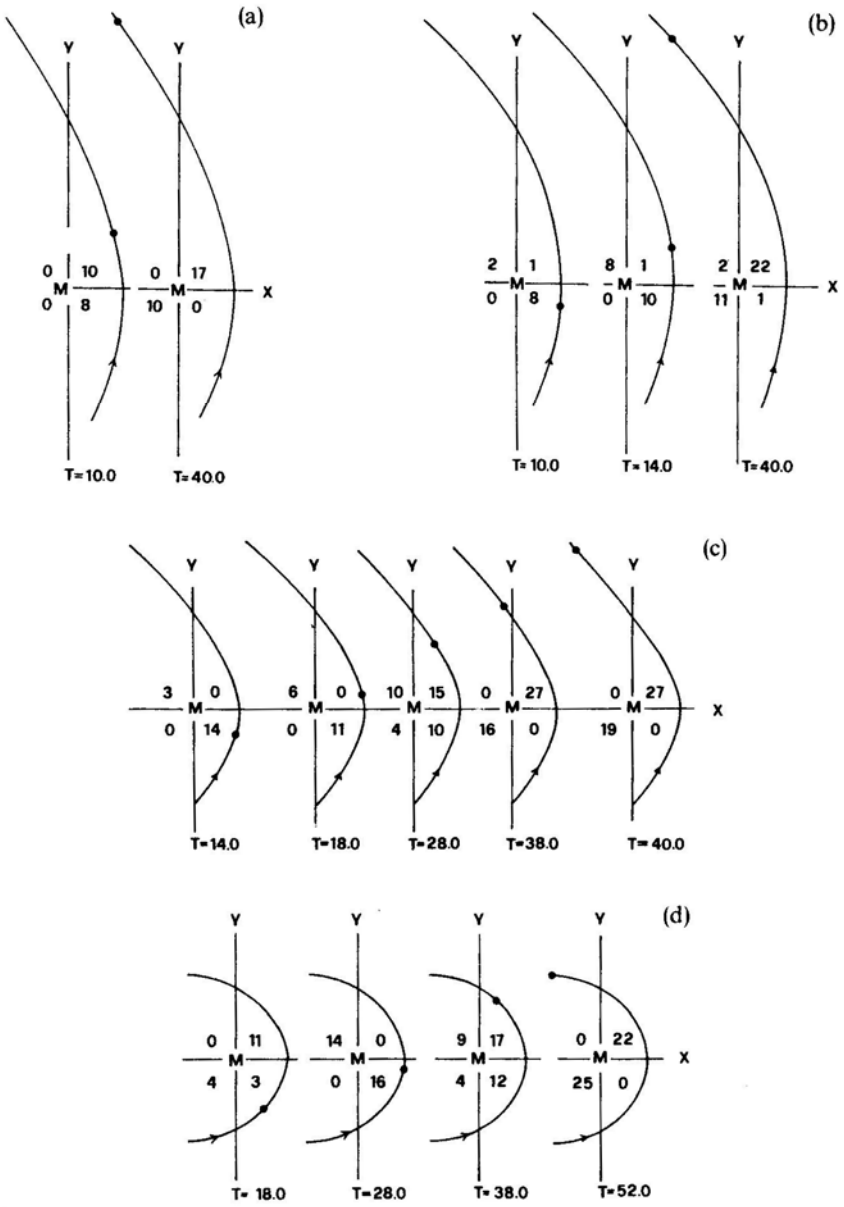

Figure 4. Number of escaping particles from various quadrants at various times for the models (a) H1, (b) H2, (c) P, and (d) E.

5 As we go from hyperbolic to parabolic encounters keeping p constant, the energy and the mass loss both increase, whereas as we go from parabolic to elliptic encounter, the energy increase continues but the mass loss remains constant.

6 An effect of the encounter is to impart spin angular momentum to the system in the same sense as that of the relative orbit. Most of this angular momentum is carried away by the escapers.

7 Tidal encounters elongate the stellar orbits in the system. Escaping stars leave the system in radial orbits. The stellar orbits in the bound part after the encounter have more circular motions than the initial system.

Many results of the present experiment are consistent with those reported by earlier workers. Detailed comparison between the results of the experiments and the predictions of the analytic formulae appears to be new.

Acknowledgments

The authors are grateful to Dr S. J. Aarseth for kindly making available the *N*-BODY 1 Code and to Dr R. K. Bhatia for useful discussions. PDR thanks the University Grants Commission, New Delhi, for providing him with a Teacher Fellowship, and to M.G.M. College, Udupi, for permitting him to make use of this opportunity. SMA is grateful to the University Grants Commission, New Delhi, for providing him with a National Fellowship. He also thanks Professor Abdus Salam, the International Atomic Energy Agency, and the UNESCO for the hospitality extended to him at the International Centre for Theoretical Physics, Trieste, where part of the work was done. He also benefitted from discussions with Professor D. W. Sciama and other scientists at the International School for Advanced Studies, Trieste.

References

Aguilar, L. A., White, S. D. M. 1985, *Astrophys. J.,* **295,** 374.
Ahmed F., Alladin, S. M. 1981, *Bull astr. Soc. India,* **9,** 40.
Alladin, S. M. 1965, *Astrophys. J.,* **141,** 768.
Alladin, S. M., Narasimhan, K. S. V. S. 1982, *Phys. Rep.,* **92,** 339.
Alladin, S. M., Ramamani, N., Meinya Singh, T. 1985, *J. Astrophys. Astr.,* **6,** 5.
Angeletti, L., Capuzzo-Dolcetta, R., Giannone, P. 1983, *Astr. Astrophys.,* **121,** 183.
Arp, H. C. 1966, *Astrophys. J. Suppl. Ser.,* **14,** 123.
Borne, K. D. 1984, *Astrophys. J.,* **287,** 503.
Chandrasekhar, S. 1942, *Principles of Stellar Dynamics,* Univ. Chicago Press.
Dekel, A., Lecar, M., Shaham, J. 1980, *Astrophys. J.,* **241,** 946.
Faber, S. M., Gallagher, J. S. 1979, *A. Rev. Astr. Astrophys.,* **17,** 135.
Gunn, J. E. 1980, *Phil. Trans. R. Soc.* **A, 296,** 313.
King, I. R. 1962, *Astr. J.*, **67,** 471.
Lin, D. N. C, Tremaine, S. 1983, *Astrophys. J.,* **264,** 364.
Miller, R. H. 1984, *ESO preprint* No. 343.
Narasimhan, K. S. V. S., Alladin, S. M. 1983, *Bull. astr. Soc. India,* **11,** 221.
Ostriker, J. P., Peebles, J. P. E., Yahil, A. 1974, *Astrophys. J.,* **193,** L11.
Richstone, D. O. 1975, *Astrophys. J.,* **200,** 535.
Spitzer, L. 1958, *Astrophys. J.*, **127,** 17.
Toomre, A., Toomre, J. 1972, *Astrophys. J.,* **178,** 623.
Toomre, A. 1977, in *The Evolution of Galaxies and Stellar Populations,* Eds B. M. Tinsley & R. B. Larson, Yale Univ. Observatory, p. 401.
Tremaine S. D. 1981, in *The Structure and Evolution of Normal Galaxies,* Eds S. M. Fall & D. Lynden-Bell, Cambridge Univ. Press, p. 67.
Vorontsov-Velyaminov, B. A. 1959, *Atlas and Catalogue of Interacting Galaxies,* Sternberg astronomical Institute, Moscow.

Vorontsov-Velyaminov, B. A. 1977, *Astr. Astrophys. Suppl.,* **28**, 1.
White, S. D. M. 1978, *Mon. Not. R. astr. Soc.,* **184**, 185.
White, S. D. M. 1979, *Mon. Not. R. astr. Soc.,* **189,** 831.
White, S. D. M. 1983, in *IAU Symp.* 100; *Internal Kinematics and Dynamics of Galaxies,* Ed. E. Athanassoula, D. Reidel, Dordrecht, p. 337.

J. Astrophys.Astr.(1987) **8,** 33–50

On the Interpretation of the Observed Angular-Size–Flux-Density Relation for Extragalactic Radio Sources

V. K. Kapahi *Tata Institute of Fundamental Research, Post Box No. 1234, Bangalore 560012*

V. K. Kulkarni *Radio Astronomy Centre, Tata Institute of Fundamental Research, Post Box No. 8, Ootacamund 643001*

C. R. Subrahmanya *Tata Institute of Fundamental Research, Post Box No. 1234, Bangalore 560012*

Received 1986 August 21; accepted 1986 December 15

Abstract. The interpretation of the observed relation between median angular sizes (θ_m) of extragalactic radio sources and flux density at 408 MHz has been examined. The predicted θ_m–S relations based on well-observed strong sources in parent samples selected at 178 and 1400 MHz, and existing models of the evolving radio luminosity function can be made to fit the observed relation only by invoking cosmological evolution in linear sizes even for the $q_0 = 0$ universe. Predictions based on a parent sample at 2.7 GHz are shown to overestimate the contribution of steep-spectrum, compact (SSC) sources in low-frequency samples unless the downward curvature in the spectra of such sources is taken into account. When approximate corrections are made for this effect, predictions based on the 2.7 GHz parent sample cannot obviate the need for linear size evolution as claimed in the literature.

Key words: radio sources, extragalactic—angular-size-flux-density relation—cosmology—radio sources, evolution

1. Introduction

The epoch dependence of the largest physical sizes of extended extragalactic radio source can be investigated using the observed angular-size-redshift (θ–z) or angular-size-flux-density (θ–S) relations. The θ–z relation for radio quasars indicates that angular sizes fall off faster with z than expected in uniform world models in which the maximum physical sizes (l) are independent of epoch *(e.* g. Miley 1971; Wardle & Miley 1974; Ekers & Miley 1977; Wills 1979). The straightforward interpretation of the θ–z relation is that there is cosmological evolution in physical sizes—maximum sizes being smaller at earlier epochs. For simple epoch dependence of the form $l_z \propto l_0(1 + z)^{-n}$, values of the size evolution parameter, n, in the range of 1 to 2 are generally required, depending on the world model ($q_0 = 0$ model requiring the least amount of evolution). But because of the strong correlation between z and radio luminosity, P, in flux-limited samples of quasars, the θ–z relation has also been interpreted to imply an inverse correlation between l and P (e.g. Stannard & Neal 1977; Hooley, Longair & Riley 1978;

Masson 1980). It must be noted, however, that there is no compelling evidence for such an inverse relationship. By considering samples of radio galaxies of similar luminosity at different redshifts, Kapahi (1985; 1986) has in fact shown recently that the sizes of radio galaxies at least are much more likely to be epoch dependent rather than being luminosity dependent in the sense postulated.

The study of the θ–S relation has the advantage that large and complete samples of sources can be used, but the interpretation of the relation requires knowledge of the epoch dependence of the radio luminosity function. Following the first investigation of the θ–S relation (Swarup 1975; Kapahi 1975) based on the comparison of weak sources from the Ooty occultation surveys with stronger known sources, the relation has been confirmed and extended to lower flux levels using data from aperture synthesis observations (*e.* g. Ekers & Miley 1977; Kapahi & Subrahmanya 1982; Fielden *et al.* 1983; Windhorst, van Heerde & Katgert 1984). The θ–S relation has been best determined at 408 MHz where the samples are made up almost exclusively of steep-spectrum extended sources. The median value of angular size, θ_m, appears to fall rather sharply from ~100 arcsec at S_{408} ~ 20Jy to around 15 arcsec at S_{408} ~ 3 Jy and decreases much more gradually at lower flux levels reaching ~ 8 arcsec at S_{408} ~ 0.1 Jy. Early interpretations based on simple density evolution schemes for the luminosity function and a distribution of linear sizes derived from nearby sources in the 3CR sample, indicated (Kapahi 1975, 1977; Swarup & Subrahmanya 1977; Katgert 1977) that the values of θ_m predicted by uniform world models at low flux levels were considerably larger than observed; the data could be fitted only by invoking linear size evolution for all radio sources similar to that inferred from the θ–z relations for quasars.

A somewhat different method was employed by Downes *et al.* (1981) who used the observed properties (S, z,α and θ) of individual sources in the 3CR sample of strong sources selected at 178 MHz to estimate, using a V/V_m type of analysis, the space distributions of such sources and hence the expected distributions of their angular sizes at different flux-density levels. Apart from considering the epoch dependence of the luminosity function according to the evolutionary models successful in explaining the observed source counts, this method has the advantage that it automatically takes into account any correlation between P and l present in the 3CR sample. The method, of course, assumes that all the types of sources seen in low flux-density samples are adequately represented in the strong parent sample, which is a reasonable assumption over the flux-density range of interest. On the basis of such predictions Downes *et al.* (1981) concluded that for the evolutionary models of Wall, Pearson & Longair (1980), no single value of the evolution parameter, n, provided a tolerable fit to the observed median values of θ over the entire available flux-density range. An estimation of the predictions by Kapahi & Subrahmanya (1982) using the same technique and data showed, however, that values of n between 1 and 1.5 provided good fits not only to the observed values of θ_m but also to the θ distributions at different flux levels. The discrepancy in these results was subsequently traced by us to a computational oversight in Downes, Longair & Perryman (1981).

It was further suggested by Downes, Longair & Perryman (1981) that many of the weak sources (0.1 to 1 Jy) at 408 MHz could be similar to the steep-spectrum, compact (SSC) sources that form a substantial fraction of the strong-source surveys at high frequencies (Kapahi 1981; Peacock & Wall 1982) but are poorly represented in surveys at metre wavelengths because of low-frequency turnovers in their spectra. The possibly

large redshifts of weak sources at 408 MHz would imply selection at a high emitted frequency so that it may be more appropriate to compare the observed θ distributions at low flux levels at 408 MHz with the predictions made from strong source samples selected at high frequencies. Such predictions using a parent sample selected at 2.7 GHz (Peacock & Wall 1981: PW) and the multifrequency evolutionary models for the luminosity function (Peacock & Gull 1981) have lead Downes (1982), Fielden *et al.* (1983) and Allington-Smith (1984) to conclude that linear size evolution may not be necessary in order to explain the observed θ–S relation.

In this paper we have compared the observed θ–S relation at 408 MHz with predictions made using parent samples of strong sources selected at several frequencies and using several models for the evolution of the radio luminosity function. Several inadequacies associated with the use of a high frequency survey to estimate angular size distributions for sources selected at low frequencies are first pointed out in Section 2. Predictions made after approximately allowing for some of these effects (Sections 3 and 4) show that size evolution is indeed necessary to fit the data. Our conclusions are summarized in Section 5.

2. Problems of using a high-frequency parent sample

There are several problems associated with using a high-frequency parent sample in general, and the 2.7 GHz PW sample in particular, to predict the distributions of θ at different flux levels at 408 MHz, that have either been totally ignored or not paid adequate attention to by earlier workers.

(i) Although the use of the 2.7 GHz parent sample appears to predict values of θ_m similar to those observed at low flux levels ($S_{408} < 1$ Jy) without introducing size evolution, it fails to predict the fairly rapid fall observed in θ_m between about 20 Jy and 2 Jy at 408 MHz. Rather low values of θ_m are predicted even at high flux levels, the fit with observations getting progressively worse with increasing S_{408} above ~ 2 Jy (*e.g.* Allington-Smith 1984). The reason is easily understood; the presence of a large number of SSC sources in the 2.7 GHz sample, together with the assumption in all evolutionary models that sources have spectral indices independent of frequency, leads to an overestimation of the contribution of such sources in bright-source samples at low frequencies, thereby predicting low values of θ_m. In reality, the spectra of SSC sources must of course turn over at low frequencies since such sources are known to be much less abundant in low-frequency surveys (Kapahi 1981; Peacock & Wall 1982). The overestimate of the number of SSC sources is, in fact, very likely to extend to even the weakest flux levels in the θ–S relation at 408 MHz unless the weak sources have extremely high redshifts of the order of ~ 10. This is because most of the SSC sources are seen at fairly large redshifts (typically $z \sim 1$) even in the parent PW sample. They are therefore effectively selected at an intrinsic frequency of ~ 5 GHz. Only for redshifts of the order of 10 or 12 would the weak sources at 408 MHz be also selected at this high frequency.

(ii) Because the 2.7 GHz sample is based on finding-surveys with telescopes with rather narrow half-power beamwidths, it is likely to discriminate against large radio sources. A comparison of the sample with the well-studied 3CR-LRL sample (Laing, Riley & Longair 1983, and preprint incorporating revisions upto 1983 October 31)

confirms this bias. Although the two samples cover nearly the same area of the sky and have a comparable sensitivity (for steep-spectrum sources) there are 10 sources with $\theta \gtrsim 500$ arcsec in the 3CR-LRL sample but only 3 such sources in the PW sample. From the available spectral information in the literature we find that the 7 large sources listed in Table 1 have flux densities $S_{2.7\ \mathrm{GHz}} \geqslant 1.5$ Jy but are not included in the PW sample, presumably because of their large sizes. All of these are listed in the 3CR-LRL sample.

(iii) Surveys at high frequencies would be expected to discriminate against very-steep-spectrum sources. In the 3CR-LRL sample there are 19 sources with $\alpha_{178}^{750} \geqslant 1.0$, none of which are strong enough at 2.7 GHz to be in the PW sample. These are typically sources of high radio luminosity and have a median linear size of ~ 200 kpc (for q_0 = 0.5 and H_0 = 50kms^{-1} Mpc^{-1}).Most of the sources of this type would be seen with $\theta \gtrsim 24$ arcsec even at low flux levels.

(iv) High-frequency surveys would also be expected to discriminate against sources whose spectra steepen considerably at high frequencies. From the known values of S_{178} and α_{178}^{750} we find that 16 3CR-LRL sources should have $S_{2.7} \geqslant 1.5$ Jy, but are not in the PW sample. While 5 of these are large sources that we have already dealt with, the remaining 11 are not in the PW sample because their spectra steepen considerably at high frequencies. These are again mostly of high radio luminosity and have a median linear size of ~ 190 kpc.

All the above-mentioned problems are likely to affect the θ–S predictions from the PW parent sample, with the first two points being the most significant. While it is quite simple to take care of the second effect by adding the large sources to the parent sample, it is difficult to take care of the other effects that arise due to spectral curvature.

The redshift distributions of steep-spectrum ($\alpha_{2.7}^{5} \geqslant 0.5$) radio sources in the PW 2.7 GHz sample are shown in Fig. 1 for the extended as well as the compact sources (angular sizes $\lesssim$ 2 arcsec in most cases as defined in PW). A much larger fraction of the SSC sources is seen to be associated with quasars. The median value of redshift for the SSC sources ($z_{\mathrm{m}} \sim 0.83$) is also very significantly higher than that for the extended sources ($z_{\mathrm{m}} \sim 0.23$). The SSC sources in the 2.7 GHz survey are therefore typically seen at an emitted frequency of ~ 5 GHz. The use of a 2.7 GHz parent sample to predict the θ distributions at low flux levels in 408 MHz surveys would therefore be appropriate only if the latter had typical redshifts of ~ 12. Although such large redshifts cannot totally be ruled out, it must be noted that the largest redshift known for a quasar is only 3.8 and several recent investigations have indicated a sharp decline in the space density of quasars beyond z = 2.5 or 3 (see Osmer 1986 for a review). Recent work on the space distribution of radio sources using the Leiden–Berkeley deep radio and optical surveys suggests (Windhorst 1984) that there may be a cutoff also in the distribution of radio galaxies at $z \sim 2$. If the typical redshifts of weak SSC sources at 408 MHz are indeed less than 2 or 3, their emission frequencies would match those of SSCs in strong source surveys at frequencies between about 0.7 and 1 GHz. We have therefore also considered a parent sample at 1.4 GHz selected from the BDFL catalogue (Bridle *et al.* 1972) for which reasonably complete data on source structures and redshifts is available in the literature. The details of this sample are given in Section 3.1.

Another point to be noted is that while many SSC sources have curved radio spectra (α decreasing continuously with decreasing frequency) the computations based on the PW parent sample have always used the values of α (assumed independent of

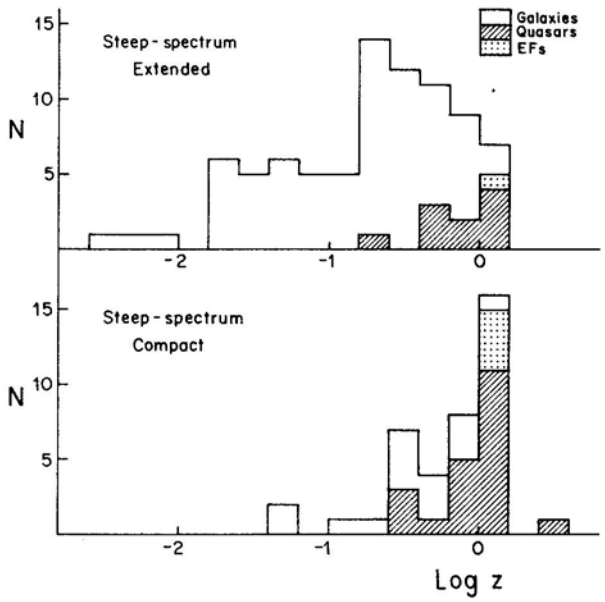

Figure 1. Redshift distributions of extended and compact sources with steep spectrum ($\alpha_{2\,7}^{5}$ > 0.5) in the PW 2.7 GHz sample. Redshifts for some galaxies have been estimated from their optical magnitudes. Empty fields (EFs) and quasars with unknown z are assumed to have z >1.

frequency) listed in the PW catalogue, which are obtained from the measured flux densities at 2.7 GHz and the higher frequency of 5 GHz. This results in a further overestimation of the numbers of SSC sources in low frequency samples because the extrapolated flux densities at low frequencies turn out to be too high so that such sources can be seen out to large volumes of space at lower flux levels. To investigate the magnitude of this effect we have carried out the computations using two-point spectral indices between 1.4 and 2.7 GHz for the SSC sources as described in Section 3.1.

3. θ–S predictions

3.1 *Parent Samples Used*

We have considered three parent samples of strong radio sources selected at frequencies of 178, 1400 and 2700 MHz as follows.

3.1.1 *The* 3*CRL-RL sample* ($S_{178} \geqslant 10$ Jy)

The redshift information for this sample of 174 sources is now extremely good. We use the values of S_{178}, α_{178}^{750} and z listed in LRL. The values of θ have been tabulated by Allington-Smith (1984). The following corrections are however necessary for three sources; 3C16:θ = 60 arcsec (Riley, Longair & Gunn 1980), 3C200: θ = 17 arcsec (Jenkins, Pooley & Riley 1977), 3C457:θ = 190 arcsec (Laing, Riley & Longair 1983).

3.1.2 *The BDFL sample* ($S_{1400} \geqslant 2.5$ Jy)

Although the BDFL catalogue (Bridle *et al.* 1972; Bridle & Fomalont 1974) has a completion limit of $S_{1400} = 2$ Jy, information on z and θ is not available for many sources, particularly near the lower flux limit. We have therefore restricted the sample to the 151 sources with $S_{1400} \geqslant 2.5$ Jy and $|b| > 20°$. The sources with the relevant information are listed in Table 2. Redshifts are known for ~ 83 per cent of the sources and could be estimated from the magnitudes of the identified galaxies for another 10 per cent (values shown in brackets in Column 7 of Table 2). Only 75 (50 per cent) of the sources in this sample are common to the 3CR-LRL sample and 86 (57 per cent) are common to the PW sample (Columns 2 & 3 of Table 2). The values of θ have been taken from a search of the literature. The values of α for a majority of the sources have been taken from the spectral fits given by Kühr *et al.* (1981). For sources with curved spectra we have used the slope of the best fit log S-log ν curve at 1.4 GHz. This was obtained in most cases from the polynomial fits given by Kühr *et al.* (1981).

3.1.3. *The PW* 2.7 *GHz sample* ($S_{2700} \geqslant 1.5$ Jy)

To the original sample of 168 sources defined by PW we have added the 7 large sources listed in Table 1. The values of θ have been tabulated by Allington-Smith (1984). A comment is necessary about the values of spectral indices.

For the steep-spectrum extended sources and for the flat-spectrum sources we have used the two-point spectral indices between 2.7 and 5 GHz listed in PW, but for SSC sources we have used the values of α between 1.4 and 2.7 GHz (as discussed in Section 2) determined from the best fits to the flux density information at a large number of frequencies tabulated by Kühr *et al* (1981) for most sources. For 21 of the 35 SSC sources in PW, the value of α estimated as above appeared to differ significantly from the values listed in PW; the original and revised values for these sources are shown in Table 3. In several cases the differences are seen to be quite large and the revised values of α are often < 0.5. Not all the differences arise from spectral curvature. An examination of the spectral plots shows that two sources (*viz.* 1600+33 & 1749+70) clearly belong to the flat-spectrum class and have been misclassified due to errors in fluxes at 2.7 or 5 GHz, or due to variability. Three other sources (*viz.* 0223 + 34, 0319 +12 and 2247 +14) have a straight sprectrum with $\alpha < 0.5$ and should also be classified in the flat-spectrum class. The remaining sources show varying degree of

Table 1. Large sources added to the PW 2.7 GHz sample.

source name	$S_{2.7}$ Jy	α	z	LAS (arcsec)
0745 + 56 (DA 240)	2.84	0.78	0.035	2040
0945 + 73 (4C 73.08)	1.70	0.85	0.0581	1100
1232 + 21 (3C 274.1)	1.55	0.93	0.422	150
1549 + 20 (3C 326)	2.05	0.83	0.0895	1170
1637 + 82 (NGC 6251)	2.17	0.70	0.024	4320
2212 + 13 (3C 442A)	1.67	1.05	0.0263	270
2247 + 11 (NGC 7385)	1.70	0.66	0.0243	720

Table 2. The BDFL source sample at 1.4 GHz.

Source (1)	3CR (2)	PW (3)	$S_{1.4}$ Jy (4)	α (5)	Opt. Id. (6)	z (7)	LAS arcsec (8)
0003 − 00			3.54	0.79	Q	1.037	6
0019 − 00			2.73	0.44	G	(0.6)	< 1
0034 − 01			4.30	0.75	G	0.073	22
0035 − 02			6.25	0.72	G	0.220	10
0038 + 32	✓	✓	3.12	0.84	G	0.482	9.6
0038 + 09			4.26	0.75	G	0.188	47
0055 − 01			5.22	0.67	G	0.045	150
0104 + 32	✓	✓	5.22	0.66	G	0.017	3600
0106 + 13	✓	✓	12.59	0.70	G	0.059	250
0116 + 31		✓	2.54	0.37	G	0.059	< 1
0123 − 01			6.42	0.93	G	0.018	1260
0123 + 32	✓	✓	3.49	0.73	G	0.794	23
0125 + 28	✓	✓	2.64	0.82	G	0.395	28
0127 + 23	✓	✓	2.78	0.76	Q	1.459	1.5
0128 + 03			2.52	1.00	G	(0.32)	359
0133 + 20	✓	✓	3.68	0.97	Q	0.425	69
0134 + 32	✓	✓	15.29	0.81	Q	0.367	< 1
0138 + 13	✓	✓	2.69	0.82	G	0.621	1
0154 + 28	✓		2.50	0.96	G	0.240	72
0202 + 14		✓	3.40	0.37	G?	(1.0)	< 1
0218 − 02			3.32	1.00	G	0.175	< 15
0219 + 08			2.51	0.83	G	(0.4)	134
0221 + 27	✓	✓	2.94	0.81	G	0.310	2
0240 − 00			4.87	0.75	G	0.003	9
0255 + 05			6.22	0.75	G	0.024	221
0300 + 16	✓	✓	2.60	0.68	G	0.032	45
0305 + 03			7.24	0.57	G	0.029	110
0307 + 16	✓	✓	4.59	0.97	G	0.256	87
0316 + 16		✓	7.60	0.48	G?	(1.0)	2.5
0320 + 05			2.86	0.83	G	(0.5)	< 15
0325 + 02			4.85	0.67	G	0.030	150
0331 − 01			2.72	1.04	G	0.139	93
0340 + 04			2.84	0.90	G	0.358	25
0347 + 05			3.25	0.71	G	(0.68)	65
0356 + 10	✓	✓	9.56	0.72	G	0.031	295
0404 + 03			4.93	0.70	G	0.089	265
0410 + 11	✓	✓	4.09	0.75	G	0.306	90
0430 + 05			5.48	0.0	G	0.032	< 1
0440 − 00			3.18	0.0	Q	0.844	< 1
0511 + 00			2.80	0.83	G	0.127	130
0651 + 54	✓	✓	3.66	0.90	G	0.238	9
0703 + 42		✓	2.82	0.75	G	0.060	360
0744 + 55	✓		4.74	0.78	G	0.035	2040
0755 + 37		✓	2.54	0.55	G	0.043	140
0802 + 24	✓	✓	4.89	0.73	G	0.060	190
0809 + 48	✓	✓	13.85	0.90	Q	0.871	5
0821 + 39			2.65	0.25	Q	1.216	20

Table 2. Continued.

Source (1)	3CR (2)	PW (3)	$S_{1.4}$ Jy (4)	α (5)	Opt. Id. (6)	z (7)	LAS arcsec (8)
0831 + 55		√	8.04	0.0	G	0.242	< 1
0906 + 43	√	√	3.76	0.46	Q	0.668	1
0917 + 45	√	√	8.02	0.93	G	0.174	147
0923 + 39		√	2.52	− 1.0	Q	0.698	< 1
0936 + 36	√	√	3.35	0.77	G	0.137	250
0939 + 14	√	√	3.00	0.94	G	(0.6)	5
0945 + 07			7.40	0.79	G	0.086	178
0947 + 14	√	√	3.47	0.83	G	(0.6)	45
0949 + 00			3.03	0.90	EF	(1.0)	7
0951 + 69	√	√	7.94	0.54	G	0.001	50
0954 + 55		√	3.52	0.23	Q	0.901	< 1
0958 + 29	√	√	5.35	0.96	G	0.185	110
1003 + 35	√	√	3.24	0.66	G	0.099	2340
1005 + 07			6.25	0.88	G	(0.78)	47
1008 + 06			2.93	0.90	G	(1.0)	< 15
1030 + 58	√	√	3.74	0.97	G	0.428	53
1039 + 02			2.84	0.76	EF	(1.0)	5
1040 + 12	√	√	3.07	0.64	Q	1.029	5
1055 + 01			3.10	0.0	Q	0.888	4
1056 + 43	√	√	2.91	0.86	G	0.750	13
1059 − 01			2.56	0.95	EF	(1.0)	18
1106 + 37			3.20	0.40	G	0.346	< 2
1111 + 40	√		3.05	1.00	Q	0.734	13.2
1137 + 66	√	√	2.98	0.85	Q	0.652	44
1140 + 22	√	√	2.96	0.96	G	0.360	5.8
1142 + 19	√	√	5.78	0.83	G	0.021	100
1148 − 00			3.06	0.22	Q	1.982	< 1
1142 + 31	√		2.80	1.00	G	0.811	78
1153 + 31		√	2.77	0.77	Q	1.557	17
1203 + 64	√	√	3.53	0.83	G	0.371	1.3
1213 + 53			2.65	0.78	Q	1.065	33
1216 + 06			17.50	0.53	G	0.007	303
1218 + 33	√	√	2.50	0.82	Q	1.519	12
1222 + 13	√	√	5.80	0.61	G	0.003	120
1226 + 02			38.84	0.0	Q	0.158	21
1228 + 12	√	√	214.0	0.82	G	0.004	460
1232 + 21	√		2.97	0.94	G	0.422	150
1239 − 04			3.34	0.84	G	0.480	< 15
1241 + 16	√	√	2.81	0.76	Q	0.557	14
1251 + 27		√	2.89	0.69	G	0.086	22
1254 + 47	√	√	5.08	0.87	G	0.996	13
1323 + 32		√	4.56	0.50	G	(0.32)	8.4
1328 + 25	√	√	6.72	0.60	Q	1.055	< 1
1328 + 30	√	√	14.78	0.53	Q	0.846	< 1
1330 + 02			3.02	0.59	G	0.216	63

Table 2. Continued.

Source (1)	3CR (2)	PW (3)	$S_{1.4}$ Jy (4)	α (5)	Opt. Id. (6)	z (7)	LAS arcsec (8)
1336 + 39	✓	✓	3.32	1.00	G	0.246	11.5
1345 + 12		✓	5.01	0.48	G	0.122	< 1
1350 + 31	✓	✓	4.42	0.72	G	0.045	85
1358 + 62		✓	4.32	0.70	G	(0.54)	< 1
1409 + 52	✓	✓	22.18	0.90	G	0.461	4.3
1414 + 11	✓	✓	4.32	0.65	G	0.024	360
1416 + 06			5.66	1.10	Q	1.439	< 1
1419 + 41	✓	✓	2.95	0.87	G	0.367	< 1
1420 + 19	✓	✓	3.44	0.92	G	0.270	96
1425 − 01			3.30	0.90	G	0.308	< 15
1434 + 03			2.86	0.69	EF	(1.0)	< 15
1448 + 63	✓	✓	2.94	0.88	G	0.041	3.4
1502 + 26	✓	✓	7.67	1.18	G	0.054	250
1508 + 08			3.65	0.87	G	0.461	134
1511 + 26	✓	✓	3.87	0.85	G	0.108	200
1514 + 07			5.35	1.30	G	0.035	30
1517 + 20	✓		2.50	0.93	G	0.752	< 1
1518 + 04			4.01	0.63	G	(1.0)	< 18
1529 + 24	✓	✓	3.59	0.88	G	0.090	290
1548 + 05			2.52	0.26	Q	(1.0)	< 2
1549 + 20	✓		3.54	0.83	G	0.090	1170
1549 + 62	✓	✓	3.62	0.94	G	(0.70)	16
1559 + 02			8.95	0.87	G	0.104	209
1602 + 01			4.07	1.01	G	(0.6)	11
1607 + 26		✓	4.43	0.35	G	(0.7)	< 1
1609 + 66	✓	✓	6.98	0.86	G	0.549	56
1611 + 34		✓	2.92	0.10	Q	1.401	< 1
1622 + 23	✓		2.71	1.00	Q	0.927	22
1626 + 39	✓		3.53	1.22	G	0.030	41
1627 + 44	✓	✓	2.97	0.88	G	0.630	43
1634 + 62	✓	✓	5.17	0.83	Q	0.988	< 1
1637 + 62	✓	✓	4.66	0.89	G	0.750	< 1
1641 + 39		✓	6.30	0.0	Q	0.594	2.1
1641 + 17	✓	✓	3.64	0.68	G	0.161	2.3
1648 + 05			44.43	1.06	G	0.154	115
1658 + 47	✓	✓	3.18	0.79	G	0.205	82
1704 + 60	✓	✓	3.30	0.79	Q	0.371	58
1726 + 31		✓	2.72	0.80	G	0.166	80
1807 + 69		✓	2.59	0.0	G	0.050	3.3
1819 + 39		✓	3.39	0.75	G	(0.4)	< 2
1828 + 48	✓	✓	14.11	0.60	Q	0.691	5
1832 + 47	✓	✓	3.79	0.77	G	0.161	69
1842 + 45	✓	✓	5.57	0.87	G	0.092	31
2128 + 04			3.98	0.34	EF	(1.0)	< 1
2134 + 00			3.13	−0.76	Q	1.936	< 1

Table 2. Continued.

Source (1)	3CR (2)	PW (3)	$S_{1.4}$ Jy (4)	α (5)	Opt. Id. (6)	z (7)	LAS arcsec (8)
2145 + 15	√	√	2.84	0.88	EF	(1.0)	34
2145 + 06			2.97	−0.21	Q	0.990	< 1
2203 + 29	√	√	2.51	0.85	G	0.707	33
2210 + 01			2.60	0.57	EF	(1.0)	< 1
2212 + 13	√	√	3.29	1.05	G	0.027	270
2221 − 02			5.59	0.81	G	0.057	485
2223 + 21			2.59	0.40	Q	1.959	< 15
2230 + 11		√	6.01	0.36	Q	1.037	< 1
2251 + 15	√	√	11.84	0.0	Q	0.859	5.4
2252 + 12	√	√	2.93	0.91	Q	0.543	3.2
2309 + 09			2.51	0.88	G	0.233	< 15
2310 + 05			2.70	0.81	G	0.290	161
2314 + 03			4.17	1.01	G	0.220	8
2335 + 26	√	√	7.51	0.90	G	0.030	530

Table 3. Revised α for 21 sources considered SSC in PW.

source	$\alpha^{5}_{2.7}$ in PW	α (revised)
0221 + 27	0.99	0.83
0223 + 34	0.53	0.43
0316 + 16	0.89	0.60
0319 + 12	0.59	0.37
0428 + 20	0.50	0.30
1150 + 49	0.55	0.42
1153 + 31	0.92	0.80
1203 + 64	0.97	0.88
1225 + 36	1.17	0.52
1345 + 12	0.51	0.45
1413 + 34	0.60	0.33
1419 + 41	0.92	0.87
1442 + 10	0.68	0.44
1600 + 33	0.63	0.25
1607 + 26	0.89	0.44
1634 + 62	0.95	0.85
1749 + 70	0.89	0.10
1819 + 39	0.98	0.78
1829 + 29	0.80	0.67
2230 + 11	0.50	0.35
2247 + 14	0.62	0.47

spectral curvature at $\nu < 2.7$ GHz, the curvature being strong enough in many cases to cause $\alpha^{2.7}_{1.4}$ to become < 0.5. We have, however, retained the steep-spectrum classification for such sources while estimating their space distribution at different flux levels according to the evolutionary models which treat the evolution separately for sources

classified as 'steep' and 'flat'. Changing the classification of such sources to 'flat' reduces their contribution at low flux levels even further.

In all the three parent samples, sources without optical identifications or those identified with quasars with unknown redshift were assumed to have $z = 1$. The results are not very sensitive to this assumption because of the small number of sources involved and the nearly flat relation between θ and z at $z \sim 1$ in Friedman cosmologies.

3.2 *Evolutionary Models for the RLF*

We have considered the following three classes of models for the evolution of the radio luminosity function (RLF) available in the literature. All the models allow the RLF to be translated from one frequency to another.

3.2.1 *Peacock & Gull* (1981; *PG*) *models*

In these models the RLF at 2.7 GHz for both steep-spectrum and flat-spectrum sources is expressed as a power series expansion in log $(1+ z)$. While the flat-spectrum sources are assumed to have $\alpha = 0$ independent of P, a P–α correlation is assumed for the steep-spectrum sources. The values of q_0 and z_c (redshift cutoff) assumed for the four PG models are as follows:

PG1: $q_0 = 0.5$, $z_c = 100$,

PG2: $q_0 = 0.5$, $z_c = 5$,

PG3: $q_0 = 0$, $z_c = 100$,

PG4: $q_0 = 0$, $z_c = 5$.

3.2.2 *Subrahmanya* & *Kapahi* (1983) *model*

This is a parametric model in which the density evolution is assumed to be luminosity dependent. The model assumes $\alpha = 0$ for flat-spectrum sources and a P–α, correlation for the steep spectrum ones. The local RLF is specified at a frequency of 408 MHz. Other assumptions are $q_0 = 0.5$ and $z_c = 3.5$.

3.2.3 *Condon* (1984) *model*

This is also a parametric model that combines both density and luminosity evolution. Two separate Gaussian functions specify the distribution of spectral indices for flat and steep-spectrum sources, the latter distribution being a function of redshift. The local RLF is specified at a frequency of 1.4 GHz and values of $q_0 = 0.5$ and $z_c = 9$ are assumed.

The above models cover a wide range of permitted behaviour of the RLF consistent with the observed counts of radio sources and a variety of other available information on radio sources such as luminosity distributions, optical identification statistics, spectral index distributions *etc.*

4. Results and discussion

Using the different parent samples of bright sources and models for the evolution of the RLF, the predicted distributions of θ at different flux levels were estimated following the method described in detail by Allington-Smith (1984). The calculations were carried out both with and without evolution in the linear sizes. Size evolution was assumed to be of the form $l(z) \propto (1+z)^{-n}$ and values of n = 1,1.5 and 2 were tried out. The results for n = 0 (no size evolution) and a value of n that came closest to fitting the observational data are shown in Figs 2 to 6. The observed θ–S relation shown in the figures is reproduced from Kapahi & Subrahmanya (1982) with the following additions at low flux levels. The point at S_m = 0.25 Jy and θ_m = 9.5 arcsec is based on recent VLA observations of 42 5C6 and 5C7 sources with 0.2 Jy < S_{408} < 0.35 Jy (Gopal-Krishna personal communication). The point for 0.055 Jy < S_{408} < 1 Jy from Downes et al. (1981) based on only 24 sources from the 5C6 and 5C7 has been replaced by the point at $S_m \simeq$ 0.2 Jy and θ_m = 7.5 arcsec from the observations of 44 sources from the 5C7 and 5C12 surveys in the range of 0.1 to 1 Jy reported by Fielden *et al.* (1983). For clarity, we have not shown in Figs 2 to 6 the range in S covered by each θ_m value shown (see Kapahi & Subrahmanya 1982) and also the errors in the predicted θ_m–S curves due to the finite number of sources in the parent samples. For all the parent samples and evolutionary models used by us (except model PG-2, see discussion below) the estimated uncertainities in the predictions (as defined by Allington-Smith 1984) over the entire flux density range of the data (10 Jy < S_{408} < 0.2 Jy) are considerably smaller than the

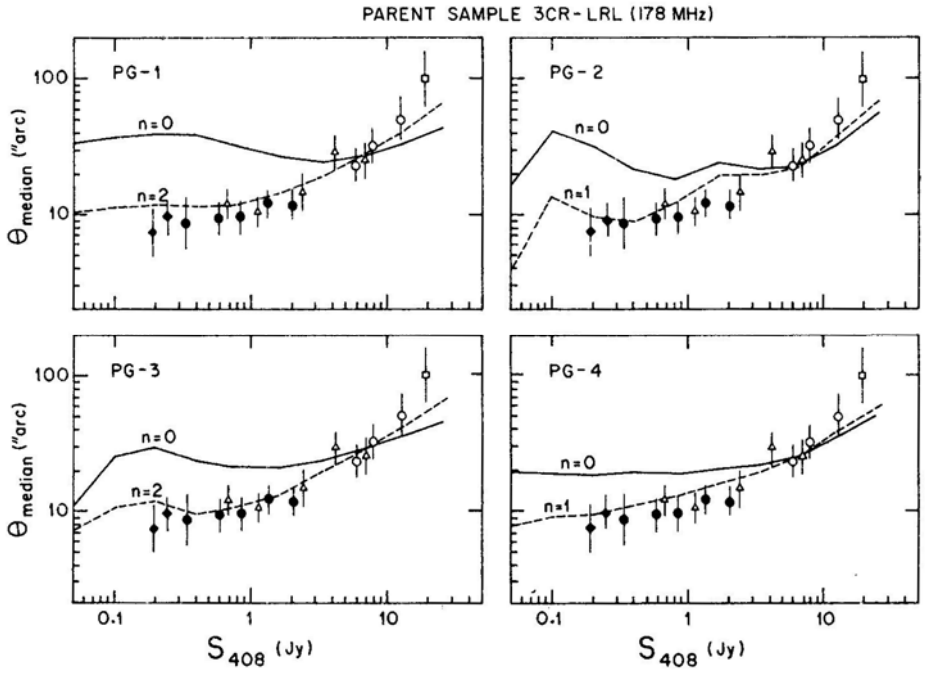

Figure 2. Comparison of the observed θ_m–S relation with predictions based on the 3CR-LRL parent sample for the 4 evolutionary models of Peacock & Gull (1981: PG).

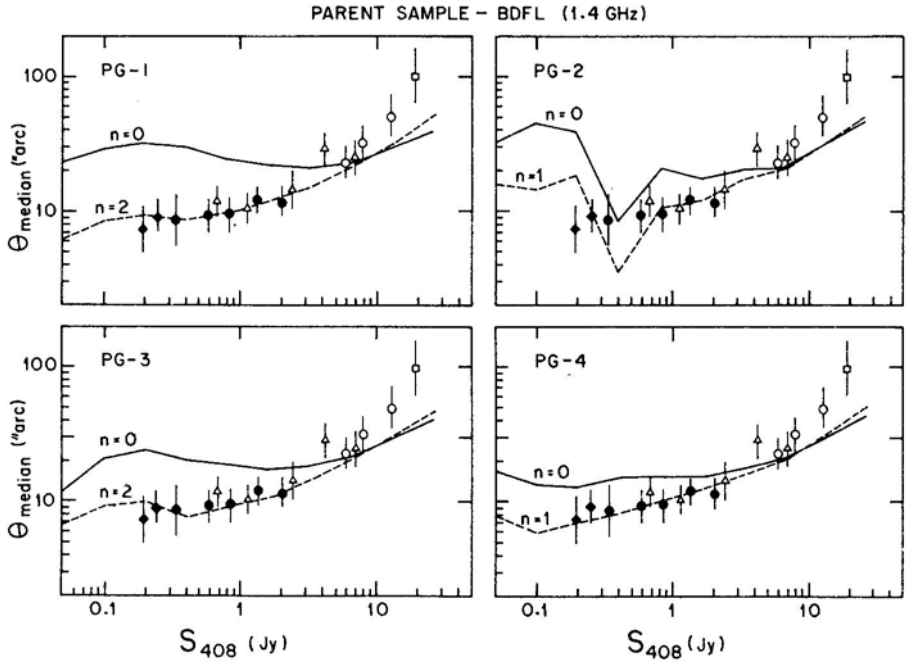

Figure 3. Predictions based on the BDFL parent sample for the PG evolutionary models.

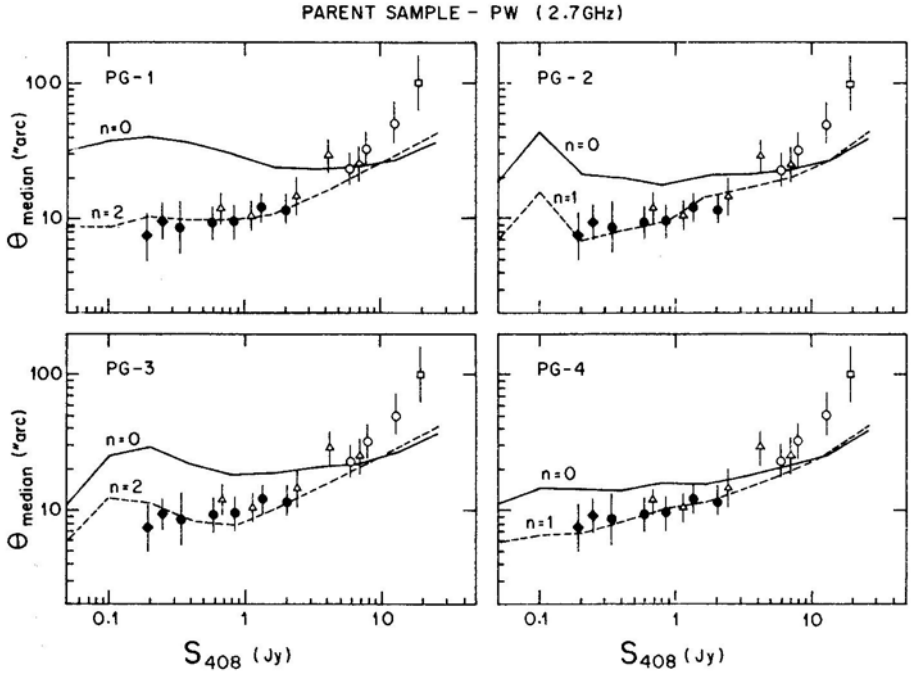

Figure 4. Predictions based on the PW 2.7 GHz parent sample for the PG evolutionary models.

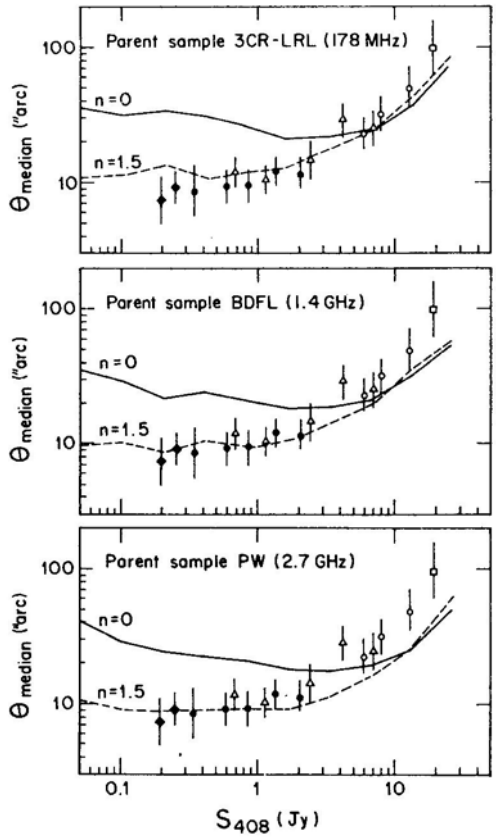

Figure 5. Predictions of the Subrahmanya & Kapahi (1983) evolutionary model using parent samples at different frequencies.

errors in the individual data points. Prediction-errors start becoming increasingly important only at $S_{408} \lesssim 0.1$ Jy where low luminosity sources, not well represented in the parent samples begin to make a significant contribution. It is also worth noting that in view of the good angular resolution of the observations used in determining the θ_m–S relation and the good agreement in the data obtained with different techniques and telescopes, it is very unlikely that the observed character of the θ_m–S relation is seriously affected by instrumental effects.

It is clear from Figs 2 to 6 that in no case do the predictions fit the data without size evolution. While the least amount of evolution ($n \sim 1$) appears to be required for the evolutionary model PG-4 ($q_0 = 0$) used with the PW 2.7 GHz parent sample (Fig. 4), the largest amount of evolution ($n \sim 2.25$) is needed for Condon's (1984) model (Fig. 6). The PG-3 model, which is the only other available model for $q_0 = 0$, requires $n \sim 2$ to fit the observations.

We note from Figs 2 to 4 that compared to other PG models the model PG-2 does not predict a smooth variation of θ_m with S. Closer examination shows that the sharp changes in the θ–S relation for this model arise because of abnormally large contributions made at some flux levels by just one or two sources in the parent samples.

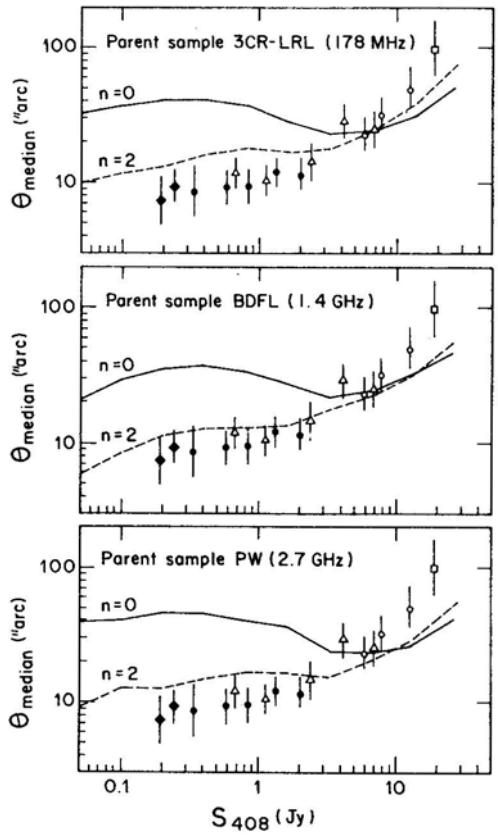

Figure 6. Predictions of the Condon (1984) evolutionary model using different parent samples.

The reason for this is clear from Fig. 7 where we show the evolution functions (ratio of space density at z to the corresponding density at $z = 0$) for different luminosities as a function of redshift in the four PG models. The evolution function for model 2 appears to exhibit a rapid change in slope at high redshifts which causes the contribution of one or two high luminosity sources to dominate at some flux levels. Model 2 of PG does not also appear to fit the observed source counts as noted earlier by Danese, De Zotti & Mandolesi (1984) and Kapahi & Kulkarni (1986).

Although the values of n indicated by predictions based on the 3CR sample and those based on the BDFL and PW samples do not appear to differ significantly, contrary to the conclusions of Fielden *et al.* (1983) and Allington-Smith (1984), the 3CR sample provides a better fit to the data at high flux densities compared to the high-frequency parent samples which predict considerably smaller values of θ_m compared to observations. This is not surprising and is clearly due to the presence of a larger number of SSC sources in the high-frequency samples, whose contribution at 408 MHz is being overestimated by ignoring spectral curvature at low frequencies. Kapahi & Kulkarni (1986) have shown recently that this is likely to be responsible also for the fact that the PG models do not fit the observed flux-density-spectral-index relation for bright sources in the 408 MHz samples.

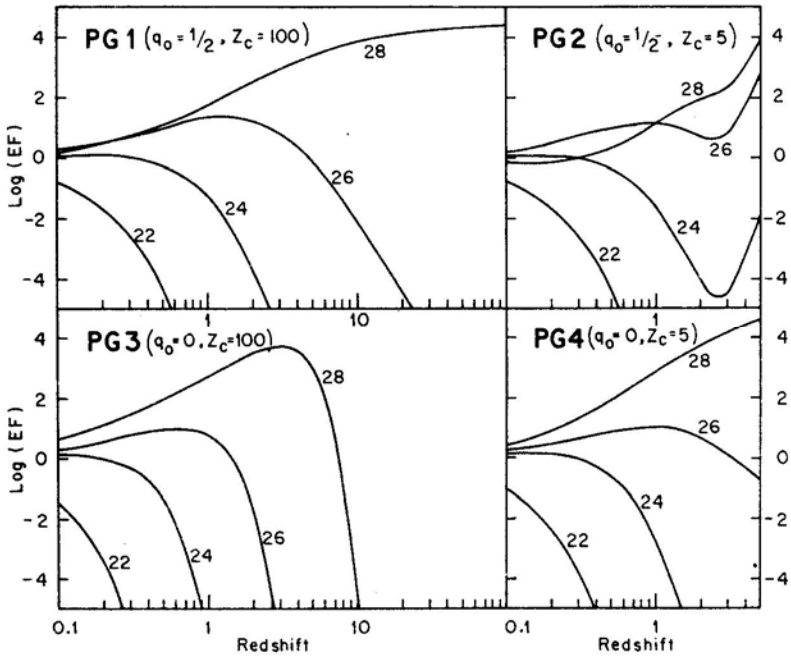

Figure 7. Plots of the evolution functions for steep-spectrum sources as a function of redshift in the 4 evolutionary models of Peacock & Gull (1981) for different values of log *P*.

Most of the difference between the predictions presented here and those reported by earlier workers using the PW parent sample and PG models seems to arise from the use of spectral indices between 1.4 and 2.7 GHz used by us for many of the SSC sources compared to those listed in PW, which are considerably steeper. We have argued in Section 3.1 that the use of the latter spectral indices for extrapolating the flux density of SSC sources from 2.7 GHz to 408 MHz is inappropriate and leads to lowering the values of θ_m at all flux levels. If the weak sources in 408 MHz samples have typical redshifts of say 2.5, then the appropriate spectral index that should be used in translating the flux density of sources from 2.7 GHz to 408 MHz is likely to be the value near an emitted frequency of ~ 1.4 GHz. The value of α between the observed frequencies of 1.4 and 2.7 GHz used by us corresponds typically (for $z_m \sim 0.8$) to emitted frequencies of 2.5 and 4.9 GHz. Even our revised α values are therefore likely to have overestimated the contribution of SSC sources and hence underestimated the evolution in linear sizes. This is likely to be so also in the case of predictions based on the BDFL sample because here again we have used values of α at the observed frequency of 1.4 GHz.

The omission of large sources (Table 1), which should legitimately be included in the PW sample, has also contributed, but to a much smaller extent, in decreasing the predicted values of θ_m at low flux levels in the earlier work. It thus seems clear that the larger contribution of SSC sources in low flux density samples is unlikely to obviate the need for linear size evolution, as claimed in the literature, unless the weak sources in low-frequency samples have unusually large redshifts of 10 or greater. Finally, we note that one of the important reasons for the suggestion by Downes, Longair & Perryman

(1981) and Fielden *et al.* (1983) that many of the weak sources in the 408 MHz samples may be similar to SSC sources seen in strong source samples at high frequencies was that they found a large fraction (~ 35 per cent) of the 5C sources to be unresolved with the VLA. However, recent high-resolution VLA observations of a comparable sample of 5C6 and 5C7 sources (with 0.2 Jy < S_{408} < 0.35 Jy) at both 1.4 and 5 GHz by Gopal-Krishna *et al.* (1986) show only 13 per cent of the sources to be compact ($\theta \leqslant 3$ arcsec), a fraction similar to that in the 3CR sample. The work of Gopal-Krishna *et al.,* in fact, suggests that the much larger fraction of SSC sources in the earlier study may have resulted from inadequate sensitivity (of the 'A' array observations at 5 GHz) to even moderately extended components.

5. Conclusions

From a comparison of the observed θ–S relation at 408 MHz with the predicted relations based on well-observed parent samples of strong sources at different frequencies and several models of the evolution of the radio luminosity function, we have shown that cosmological evolution in linear sizes of extragalactic radio sources is required in order to fit the data. This result is independent of any correlation between radio luminosity and linear size. We have examined the claim in the literature that the observed θ–S relation may be interpreted without need for size evolution if a substantial fraction of the weak sources in 408 MHz samples are of the steep-spectrum, compact variety that are well represented in bright samples at high frequencies. We find that the available predictions of θ–S relations based on the 2.7 GHz parent sample do not satisfactorily take account of the pronounced curvature in the spectra of SSC sources at low frequencies, thus overestimating their contribution at all flux levels in low-frequency samples. Approximate corrections for spectral curvature, assuming that most radio sources at low flux densities do not have redshifts in excess of 3 or 4, lead us to conclude that size evolution is indeed necessary. The amount of evolution is found to be similar to that inferred from the θ–z relations for quasars and radio galaxies.

Acknowledgements

We thank Dr Gopal-Krishna for useful discussions.

References

Allington-Smith, J. R. 1984, *Mon. Not. R. astr. Soc.,* **210,** 611.
Bridle, A. H., Davis, M. M, Fomalont, E. B., Lequeux, J. 1972, *Astr. J.,* **77,** 405.
Bridle, A. H., Fomalont, E. B. 1974, *Astr. J.,* **79,** 1000.
Condon, J. J. 1984, *Astrophys. J.,* **287,** 461.
Danese, L., De Zotti, G., Mandolesi, N. 1983, *Astr. Astrophys.,* **121,** 114.
Downes, A. J. B. 1982, in *IAU Symp.* 97: *Extragalactic Radio Sources,* Eds D. S. Heeschen & C. M. Wade, D. Reidel, Dordrecht, p. 393.
Downes, A. J. B., Longair, M. S., Perryman, M. A. C. 1981, *Mon. Not. R. astr. Soc.,* **197,** 593.
Ekers, R. D., Miley, G. K. 1977, in *IAU Symp.* 74: *Radio Astronomy and Cosmology*, Ed. D. L. Jauncey, D. Reidel, Dordrecht, p. 109.

Fielden, J., Downes, A. J. B., Allington-Smith, J. R., Benn, C. R., Longair, M. S., Perryman, M. A. C. 1983, *Mon. Not. R. astr. Soc.,* **204,** 289.

Gopal-Krishna, Saripalli, L., Saikia, D. J., Sramek, R. A. 1986, in *IAU Symp.* 119: *Quasars,* Eds G. Swarup & V. K. Kapahi, D. Reidel, Dordrecht, p. 193.

Hooley, T. A., Longair, M. S., Riley, J. M. 1978, *Mon. Not. R. astr. Soc.,* **182,** 127.

Jenkins, C. J., Pooley, G. G., Riley, J. M. 1977, *Mem. R. astr. Soc,* **84,** 61.

Kapahi, V. K. 1975, *Mon. Not. R. astr. Soc.,* **172,** 513.

Kapahi, V. K. 1977, in *IAU Symp.* 74: *Radio Astronomy and Cosmology,* Ed. D. L. Jauncey, D. Reidel, Dordrecht, p. 119.

Kapahi, V. K. 1981, *Astr. Astrophys., Suppl. Ser.,* **43,** 381.

Kapahi, V. K. 1985, *Mon. Not. R. astr. Soc.,* **214,** 19p.

Kapahi, V. K. 1986, in *Highlights of Astronomy,* Vol. 7, Ed. P. A. Swings, D. Reidel, Dordrecht, p. 371.

Kapahi, V. K., Kulkarni, V. K. 1986, *Astr. Astrophys.,* **165,** 39.

Kapahi, V. K., Subrahmanya, C. R. 1982, in *IAU Symp.* 97: *Extragalactic Radio Sources,* Eds D. S. Heeschen & C. M. Wade, D. Reidel, Dordrecht, p. 401.

Katgert, P. 1977, *Ph.D. Thesis,* University of Leiden.

Kühr, H., Witzel, A., Pauliny-Toth, I.I. K., Nauber, U. 1981, *Astr. Astrophys., Suppl. Ser.,* **45,** 367.

Laing, R. A., Riley, J. M., Longair, M. S. 1983, *Mon. Not. R. astr. Soc.,* **204,** 151.

Masson, C. R. 1980, *Astrophys. J.,* **242,** 8.

Miley, G. K. 1971, *Mon. Not. R. astr. Soc.,* **152,** 577.

Osmer, P. S. 1986, in *IAU Symp.* 119: *Quasars,* Eds G. Swarup & V. K. Kapahi, D. Reidel, Dordrecht, p. 447.

Peacock, J. A., Gull, S. F. 1981, *Mon. Not. R. astr. Soc.,* **196,** 611.

Peacock, J. A., Wall, J. V. 1981, *Mon. Not. R. astr. Soc.,* **194,** 331.

Peacock, J. A., Wall, J. V. 1982, *Mon. Not. R. astr. Soc.,* **198,** 843.

Riley, J. M., Longair, M. S., Gunn, J. E. 1980, *Mon. Not. R. astr. Soc.,* **192,** 233.

Stannard, D., Neal, D. S. 1977, *Mon. Not. R. astr. Soc.,* **179,** 719.

Subrahmanya, C. R., Kapahi, V. K. 1983, in *IAU Symp.* 104: *Early Evolution of the Universe and Its Present Structure,* Eds G. O. Abell & G. Chincarini, D. Reidel, Dordrecht, p. 47.

Swarup, G. 1975, *Mon. Not. R. astr. Soc.,* **172,** 501.

Swarup, G., Subrahmanya, C. R. 1977, in *IAU Symp.* 74: *Radio Astronomy and Cosmology,* Ed. D. J. Jauncey, D. Reidel, Dordrecht, p. 125.

Wall, J. V., Pearson, T. J., Longair, M. S. 1980, *Mon. Not. R. astr. Soc.,* **193,** 683.

Wardle, J. F. C, Miley, G. K. 1974, *Astr. Astrophys.,* **30,** 305.

Wills, D. 1979, *Astrophys. J., Suppl. Ser.,* **39,** 291.

Windhorst, R. A. 1984, *Ph.D. Thesis,* University of Leiden.

Windhorst, R. A., van Heerde, G. M., Katgert, P. 1984, *Astr. Astrophys., Suppl. Ser.,* **58,** 1.

J. Astrophys. Astr. (1987) **8,** 51–56

Alpha Cygni as a Radial-Velocity Variable

M. Parthasarathy* & David L. Lambert *Department of Astronomy, University of Texas, Austin, Texas 78712-1083, USA*

Received 1986 July 23; accepted 1986 December 16

Abstract One hundred and twentythree radial velocities for α Cyg are derived between December 1977 and October 1982. These photospheric velocities are derived from N I lines near 8700 Å. Semiregular variations in radial velocities are present with periods of 7 to 20 days. The range of variation of 14.3 kms^{-1} observed in the present radial velocities of α Cyg is close to the sum of the amplitudes (10.44 kms^{-1}) of all the pulsation periods from 7 to 101 days (Lucy 1976a) and is also approximately equal to micro and macro-turbulent velocities.

Key words: stars, radial velocities—supergiants—stars, pulsation

1. Introduction

Alpha Cygni (Deneb, spectral type A2 Iae) shows quasi-periodic variations of radial velocity (Paddock 1935). Such variations are characteristic of early-type Ia supergiants for which Abt (1957) showed that the time scale of variations was 10–100 days with an amplitude of about 10 km s^{-1}. For α Cyg, Paddock found a mean quasi-period of 11.7 days and an amplitude of ± 4.2 km s^{-1}. Lucy's (1976a) analysis of more than 400 radial velocities obtained by Paddock between 1927 and 1935 provided 16 modes with periods from 6.9 to 100.8 days, as well as a longer-term (~ 800 days) variation suggestive of orbital motion. Lucy (1976b) proposed that the 'macroturbulence' in the atmospheres of these supergiants is due to multiperiodic nonradial oscillations. Other recent studies of the radial velocity of α Cyg include those by Rosendhal (1972) and Inoue (1979).

Our study, which began as an attempt to monitor α Cyg's radial velocity during selected intervals of 14 to 21 days, was motivated by two factors. First, α Cyg is so bright that a spectrum of excellent quality is obtainable in a few minutes and, hence, regular observations of the star are possible without any interference with other observing programs. Second, since observations in the near-infrared are possible in daytime, the star may now be observed throughout the year from the northern hemisphere. In this paper we report the radial velocities of α Cyg derived from near-infrared N I lines.

2. Observations

Alpha Cygni was observed at the McDonald Observatory with the 2.7 m reflector and the coudé spectrometer. A spectral interval of about 100 Å centred at 8700 Å was

* Present address: Indian Institute of Astrophysics, Bangalore 560034

recorded with a Reticon detector (Vogt, Tull & Kelton 1978). For daytime observations our observing procedure was to follow the short (about 5 minutes) exposure on α Cyg with an exposure of equal length on the adjacent sky. The latter was subtracted from the former (star plus sky) and the difference (stellar) spectrum was recorded. In typical seeing conditions, the sky brightness was about 10 to 20 per cent of the stellar continuum. Day time observations were made only when the sky was devoid of clouds. Observations of Vega were made to check on systematic errors.

The 8700 Å region was chosen because it provides several high excitation lines of N I which are strong in Deneb (and Vega), but weak in the solar spectrum. Hence, all but major fluctuations of the sky brightness change the apparent continuum level of the 'stellar' spectrum, but not the stellar radial velocity. The radial velocities are based on the N I lines at 8680.283, 8683.401, 8686.149, 8703.248, 8711.707, and 8718.826 Å.

Radial velocities were derived using a cross-correlation program written by Dr. J. Tomkin. Velocities for Vega were determined by cross-correlation against a spectrum obtained on 1977 December 23. The velocity for that date was derived using the stellar N I lines and lines from a Fe-Ne hollow cathode lamp observed following the stellar observations. This reference spectrum of Vega was adopted for the cross-correlations with the Deneb spectra. Small changes in the instrumental setting were measured by cross-correlating the Fe-Ne spectra obtained following each observation of Deneb. Heliocentric radial velocities for Vega and Deneb are given in Table 1 and Table 2 respectively.

3. Discussion

The 13 observations of Vega give a mean radial velocity of = –13.67 kms $^{-1}$ (the standard deviation of an individual radial velocity measurement is 0.88 km s^{-1}), a value consistent with the velocity (–13.9 kms^{-1}) recommended by Wilson (1953) in his catalogue. Our observations of Vega during the period 1977 December to 1980 June show that the radial velocity is constant. However there have been reports on the

Table 1. Radial velocities of Vega from N I lines near 8700 Å.

Date		Time (UT) h	m	Radial velocity (km s^{-1})
1977	December 23	22	21.5	−13.9
	December 25	00	13.0	−14.7
	December 30	00	33.5	−12.4
1978	May 16	11	41.0	−13.4
	November 25	00	38.0	−15.0
	November 26	22	12.0	−14.9
	November 27	01	02.0	−12.6
1979	December 31	19	35.0	−14.5
1980	May 28	12	36.0	−13.4
	May 29	12	39.0	−13.6
	May 30	12	52.0	−12.6
	June 2	12	21.0	−13.6
	June 25	10	24.0	−13.2

Table 2. Radial velocities (V_r) of Deneb from N I lines near 8700 Å.

Date JD 2440000 +	V_r km s^{-1}	Date JD 2440000 +	V_r km s^{-1}	Date JD 2440000 +	V_r km s^{-1}
3501.441	−2.6	4537.612	−5.5	4677.409	−9.0
3502.514	−3.6	4539.598	−4.6	4681.023	−4.2
3507.526	−3.1	4540.566	−4.4	4683.025	−3.3
3644.976	−3.6	4542.530	−5.5	4683.976	−3.1
3837.539	−4.2	4543.529	−4.5	4704.115	−8.8
3839.415	−6.3	4572.551	−4.2	4704.234	−7.8
3839.554	−6.0	4573.545	−3.6	4720.150	−8.6
4239.323	−5.9	4574.562	−3.2	4741.981	−9.8
4241.309	−3.3	4575.526	−2.5	4742.976	−5.7
4379.975	0.0	4576.517	−2.2	4744.985	−8.6
4388.043	−5.9	4600.517	−6.8	4745.971	−8.8
4389.037	−3.8	4602.550	−8.1	4746.980	−7.8
4390.047	−2.0	4604.550	−5.2	4771.921	−2.4
4393.023	−2.7	4606.549	−3.5	4772.865	−4.5
4394.025	−3.4	4632.202	−3.7	4773.902	−4.0
4415.941	−4.2	4632.217	−3.5	4774.913	−4.0
4439.977	−2.2	4632.234	−5.5	4805.812	−6.8
4441.004	−0.2	4632.299	−4.4	4807.856	+3.2
4441.987	−0.7	4632.372	−3.7	4838.763	+2.2
4442.901	−1.6	4632.404	−4.1	4862.813	+0.2
4444.979	−4.4	4632.415	−4.2	4865.592	−2.9
4446.000	−6.2	4632.439	−4.4	5207.647	−0.2
4446.990	−3.2	4633.200	−3.4	5207.665	−0.5
4447.818	−1.7	4634.334	−5.7	5208.901	+0.8
4448.899	−1.5	4634.397	−3.3	5210.629	+1.1
4448.979	−1.8	4634.467	−2.2	5212.594	−1.3
4455.812	−4.2	4650.328	−5.2	5215.659	−1.2
4455.877	−3.8	4652.323	−5.4	5216.827	−1.3
4474.819	−6.0	4657.355	−8.0	5217.695	−0.9
4475.905	−4.2	4657.411	−8.0	5218.679	+0.6
4476.892	−5.4	4658.030	−7.8	5219.682	+3.1
4477.722	−5.3	4658.046	−8.0	5220.609	+3.2
4478.862	−4.3	4659.310	−7.7	5221.644	+4.5
4480.740	−7.3	4660.183	−6.7	5224.577	+2.1
4481.759	−7.9	4660.234	−5.9	5225.592	+1.6
4482.780	−6.8	4660.276	−5.3	5247.557	−0.9
4483.779	−5.2	4660.319	−5.1	5249.572	+0.2
4484.694	−2.9	4660.359	−4.7	5250.786	+1.1
4484.934	−3.8	4661.251	−5.0	5251.555	+0.9
4502.661	−1.5	4665.026	−4.2	5252.551	+1.8
4503.613	−0.9	4666.032	−1.7	5253.544	+1.9

possibilities of variations in radial velocity and spectrum of Vega. Wisniewski & Johnson (1979), and more recently Hayes (1985, p. 238), have summarized all the observations on the variability of Vega. Johnson & Wisniewski (1978) reported the detection of violet-shifted emission components in the near-infrared lines of O I and Ca II. However, Griffins (1978) have obtained very-high-dispersion (0.8Å–1.8Å mm^{-1}) spectrum of Vega and found no trace of emission in the lines. Barker *et al.,* (1978) also found no evidence for emission components in their Reticon spectra of the O I and Ca II

near-infrared lines. There appear to be no emission lines in the spectrum of Vega and the features seen by Johnson & Wisniewski (1978) are probably introduced by their instrument. In summarizing all the observations of Vega, Hayes (1985, p. 238) concluded that there is no evidence for variability in Vega. Our standard deviation of 0.88 km s^{-1} in a radial-velocity observation corresponds to about one-quarter of a Reticon diode and is a plausible value for our spectra with 8 useful stellar lines in the window adopted for the cross-correlation, each line having a width (FWHM) of about 13 diodes. The N I lines are far stronger in Deneb's spectrum, and hence the stronger signal from a cross-correlation provides an even smaller uncertainty.

The Radial velocities for Deneb between JD 2444440 and JD 2445260 are plotted in Fig. 1. Solid lines connect points which appear to belong to a common pulsation; broken lines appear where a bolder interpolation seems necessary. Radial-velocity variations with the characteristics described by Paddock are obviously present. The

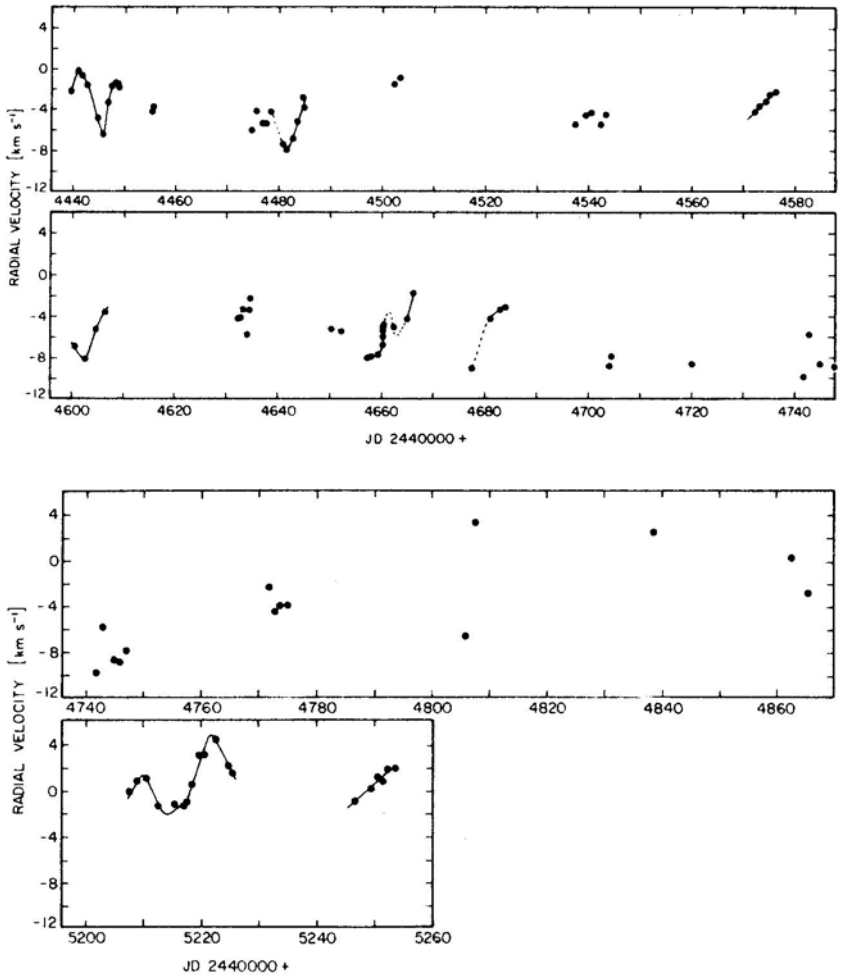

Figure 1. The radial velocity of α Cyg from JD 2444440 to JD 2445260.

mean velocity of the pulsation is apparently varying reaching a minimum around JD 2444700 and a maximum around JD 2445222.

The predominant feature of the radial velocities is the quasi-periodic pulsation with periods of 5 to 20 days documented by Paddock (1935), and analysed by Lucy (1976a). Lucy found 16 significant modes with periods from 6.9 to 100.8 days. As our coverage is less intensive than Paddock's, we have not attempted to mimic Lucy's analysis, but it may be safely asserted that several modes must again be invoked. Our radial velocity observations of Deneb are nearly continuous during the interval JD 2444440 to JD 2444449 and JD 2445207 to JD 2445226, and show the periods of 7 and 12 days (Fig. 1) respectively. In addition to identifying 7–101 day pulsation periods, Lucy (1976a) also proposed that α Cyg is a spectroscopic binary, with an orbital period of 850 days. We find that the long-period radial-velocity variation of Deneb in our data is similar to that shown in Fig. 2 of Lucy's (1976a) paper.

On the timescale of one day or less, the regular pulsations may provide a detectable variation of the radial velocity: a 1 km s^{-1} day^{-1} change is fairly characteristic of the pulsations. We found two occasions on which this acceleration was exceeded. On JD 2444446 and JD 2444741, 3–4 km s^{-1} variation occurred in one day. On JD 2444634, a 3.5 k m s^{-1} change occurred in 3 hours. On JD 2444660, a 2.0 k m s^{-1} change took 4 hours. There are similar intervals when no significant change of velocity was detected: e.g., on JD 2444632, 8 observations combine for a mean velocity of – 4.2 km s^{-1} and 6 of the 8 are within –0.2 to + 0.7 km s^{-1} of the mean. To establish conclusively that the rapid accelerations are not, in part, of instrumental origin, either spectra should be acquired with an imposed set of absorption lines (Campbell & Walker 1979) or observations of Deneb and Vega (or another radial velocity standard star) should be interlaced.

The unweighted mean of our 123 velocities is – 3.6 km s^{-1}. Our radial velocity observations of Deneb show a minimum value of — 9.8 k m s^{-1} and a maximum value of + 4.5 kms^{-1}(a range of 14 kms^{-1}). This value is close to the sum of the amplitudes (10.44 kms^{-1}) of all the pulsation periods from 6.9 to 100.8 days (Lucy 1976a). Recently, de Jager, Mulder & Kondo (1984) derived micro- and macro-turbulent velocities in the atmosphere of Deneb to be 15.0 ±0.5 km s^{-1} and 14.2 ± 2.5 km s^{-1} respectively. They find that the larger macroturbulent velocities determined by Groth (1961:28 kms^{-1}), Gray(1975:36 kms^{-1}), and others, are in compatible with their data. Lucy (1976b) suggested the possibility of variation in macroturbulent velocity as due to the multiperiodic nonradial oscillations corresponding to surface harmonics of degree 3–4. A measurement of the radial velocity from a cross-correlation provides a one parameter description of the profile changes induced by pulsations/oscillations. Analysis of accurate line profiles for lines formed at differing depths may provide more detailed information on the pulsations. Inspection of our profiles shows no major features such as have been seen in the B stars experiencing nonradial oscillations (cf., Smith 1986).

4. Concluding Remarks

Supergiants such as α Cyg with a complex pattern of radial-velocity variations continue to present a considerable challenge to the observer. The present and earlier series of observations show that the radial-velocity variations need to be monitored continu-

ously for a longer period of time on a variety of spectral lines in order to understand the atmospheric pulsations and velocity field effects of the Ia supergiants of all spectral types (*cf.* Abt 1957; Maeder 1980; Sterken 1977; de Jager 1980).

We thank Drs Fred Sanner, Myron A. Smith, and Brenda Young for obtaining several spectra. This research has been supported in part by the U.S. National Science Foundation (grant AST 83–16635).

References

Abt, H. A. 1957, *Astrophys. J.,* **126,** 138.
Barker, E. S., Lambert, D. L, Tomkin, J., Africano, J. 1978, *Publ. astr. Soc. Pacific,* **90,** 514.
Campbell, B., Walker, G. A. H. 1979, *Publ. astr. Soc. Pacific,* **91,** 540.
de Jager, C. 1980, *The Brightest Stars,* D. Reidel, Dordrecht, p. 340.
de Jager, C, Mulder, P. S., Kondo, Y. 1984, *Astr. Astrophys.,* **141,** 304.
Gray, D. F. 1975, *Astrophys, J.,* **202,** 148.
Griffin, R. & R. 1978, *Publ. astr. Soc. Pacific,* **90,** 518.
Groth, H.- G. 1961, *Z. Astrophys.,* **51,** 206.
Hayes, D. S. 1985, in *IAU Symp.* 111: *Calibration of Fundamental Stellar Quantities,* Eds D. S. Hayes, L. E. Pasinetti & A. G. Davis Philip, D. Reidel, Dordrecht, p. 225.
Inoue, M. O. 1979, *Publ. astr. Soc. Japan,* **31,** 11.
Johnson, H. L., Wisniewski, W. Z. 1978, *Publ. astr. Soc. Pacific,* **90,** 139.
Lucy, L. B. 1976a, *Astrophys. J.,* **206,** 499.
Lucy, L. B. 1976b, in IAU Coll. 29: *Multiple Periodic Variable Stars: Contributed Papers,* Ed. W. S. Fitch, Akadémiai Kiadó, p. 105.
Maeder, A. 1980, *Astr. Astrophys.,* **90,** 311.
Paddock, G. F. 1935, *Lick Obs. Bull.,* **17,** 99.
Rosendhal, J. D. 1972, *Astrophys. J.,* **178,** 707.
Smith, M. 1986, *Astrophys. J.,* **304,** 728.
Sterken, C. 1977, *Astr. Astrophys.,* **57,** 361.
Vogt, S. S., Tull, R. G., Kelton, P. 1978, *Appl. Optics,* **17,** 574.
Wilson, R. E. 1953, *Carnegie Inst. Washington Publ. No.* 601.
Wisniewski, W. Z., Johnson, H. L. 1979, *Sky Telesc,* **57,** 4.

J. Astrophys. Astr. (1987) **8,** 57–68

ST-FOC Observations of Globular Clusters: Simulations

A. Bragaglia, F. R. Ferraro & F. Fusi Pecci *Dipartimento di Astronomia, Universitá di Bologna, I-40100, Bologna, Italy*

R. Buonanno, C. E. Corsi, I. Ferraro & G. Iannicola *Osservatorio Astronomico, I-00136, Roma, Italy*

Received 1986 October 7; accepted 1986 January 1

Abstract. Using a first approximation to the Hubble space telescope point-spread function, the problems concerning observation and reduction of globular clusters in the Andromeda nebula are analysed through a simulation procedure in order to study the feasibility of accurate photometry of individual stars in the clusters.

Key words: Hubble space telescope—globular clusters—simulations

1. Introduction

The astronomical community is devoting growing attention to the forthcoming launch of the Hubble space telescope (ST). Considering that the scientific results achievable from the observations depend not only on the performance of the instruments but also on the technical ability to decode the information stored in the data, we have begun to equip ourselves with the ability to plan and execute an observational programme on ST, and to analyse the data that would be acquired. If the sources of noise are properly considered, simulated observations may provide grounds for more stringent tests of reduction techniques than the observational data. Such simulations also provide the possibility of defining the scientific objectives better, with quantitative estimates of the final precision of measurements.

Our current interest in the scientific use of ST is concerned with the determination of the age of the globular clusters in order to estimate the value of the Hubble constant H_0. Particular attention was paid to the study of problems inherent to the photometry of stars in crowded fields taking into account the induced background noise. The observations were thought to be done using the Faint Object Camera (f/96, 512 × 512 pixels, 1 pixel = 0.022 arcsec) and, in part, with the Planetary Camera (f/30, 1600 × 1600 pixels, 1 pixel = 0.044 arcsec). The study was undertaken with the following objectives:

1. to investigate the possibility of planning a project of photometry in highly crowded fields observed with ST;
2. to define possible targets within each cluster (or galaxy) in view of the strong gradient of contamination level and sampling of stellar population;
3. to establish the exposure times;

4. to adapt our current data reduction software to the new requirements presented by ST characteristics;

5. to study the errors in the measurements and to investigate the influence of each component of these global errors on the immediate scientific aims.

2. Simulations

2.1 *Choice of the Point-Spread Function*

As the images of ST will be almost diffraction limited, the study of the points-pread function (PSF) is of fundamental importance. A detailed study of the PSF properties of the Hubble space telescope has been made by Bendinelli *et al.* (1985). For a monochromatic, on-axis image with no jittering, Bendinelli *et al.* give the following normalized expression of PSF:

$$\varphi(\lambda,\rho) = \frac{a^2}{(1-m^2)\pi}\left[\frac{J_1(a\rho) - m\,J_1(ma\rho)}{a\rho}\right],$$

where $a = 2\pi R/(206265\lambda)$, R is the mirror external radius, mR is the mirror internal radius, J_1 is the Bessel function.

A simpler, smoothed, normalized function which does not take into account the possible diffraction rings (and represents a zero-order approximation) has been proposed by King (1983). Figs la, b show the comparison between these two functions

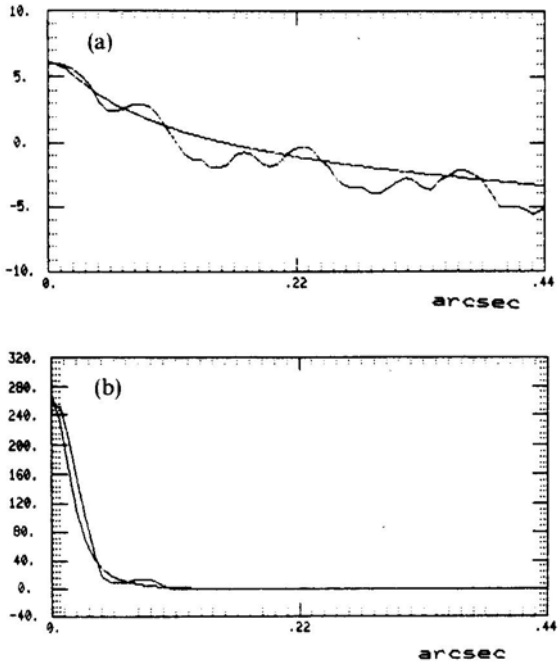

Figure 1. Comparison between the PSFs given by King (1983) and Bendinelli *et al.* (1985); (a) in the units of mag arcsec^{-2}; (b) in intensity units. King's PSF is the smoother of the two.

expressed in mag arcsec^{-2} and in intensity units, respectively. It is evident from the figure that King's function smooths out the diffraction rings and shows higher concentration of light at the centre. In the simulation, the choice of the PSF has the obvious meaning of selecting the weight function to distribute the photons coming from each single star. The two calculated weight functions are given in Fig. 2.

2.2 *Selecting the Exposure Times*

I. R. King (personal communication) has kindly made available to us a table giving the limiting magnitude (in the V and B bands) needed to detect one count per second, as a function of spectral type of the source. The reflectivity, transmission, and efficiency of the FOC detector (August 1985) have been taken into account by King. Using these data we have derived $V_{\rm lim}$ and $B_{\rm lim}$ (as defined above) versus colour index. From the table, the exposure times required to detect a given number of photons from a star of given magnitude and colour can readily be calculated. It is also important to stress the presence of a strong but definite colour equation (particularly in B) which strongly influences exposure times when colours of the stars in the target change.

2.3 *Choice of the Field*

The radial behaviour of many properties in a globular cluster (like for instance the luminosity function) is not known well. The proper simulation of a cluster thus requires particular care. As a first step in the simulation, we used, as hypothetical target, the galactic globular cluster M 15. For this cluster, from a careful photometric analysis (Buonanno *et al.* 1983), we derived $U\,BV$ magnitudes and positions for all the stars in a given region up to a magnitude limit of B=18.6. Considering M 15 as a 'typical' globular cluster, we scaled the magnitudes and coordinates of all the stars to the distance of M 31 (globular clusters in which are proposed to be observed with ST), thus obtaining the 'granular' contribution to the simulated field. In synthesis, this means that we have adopted, as resolved component of the cluster population, all the stars with $B < 18.6$ ($B < 27.6$ when shifted to M31).

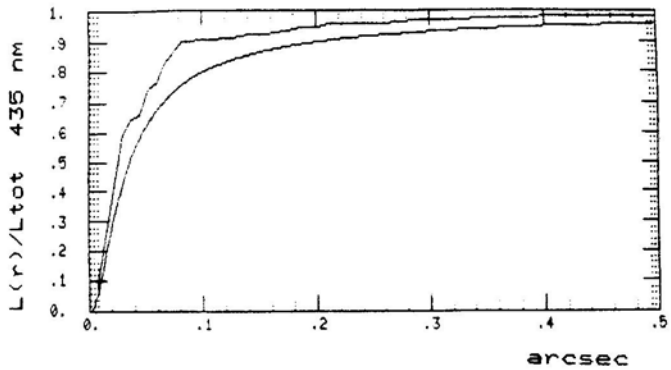

Figure 2. Companion between the weight functions obtained from the PSFs due to King (smoother curve), and Bendinelli *et al.*

2.4 *Contribution due to the Background*

In order to properly take into account the luminosity of the unresolved component of the cluster, we used the brightness profile described by King (1962), adopting for the structural parameters (k, r_c, r_t) those derived by Peterson & King (1975) (scaled to the distance of M 31). This brightness profile can be expressed in photons arcsec^{-2}, and after the subtraction of the resolved contribution, it gives the background contribution due to the unresolved stellar component.

Two additional components of the background have also been considered: zodiacal light and stray light. At this stage, for both these components we referred to the figures provided by the ST Science Institute (ESA SP–1028).

The noise added to the data has been considered as only due to photon statistics and, therefore, given by $L + bA$, where L is the signal (number of counts for a star of a given luminosity), b is the number of photons given by the total background for unit area, and A is the considered area.

A typical simulated field is shown in Fig. 3 where King's PSF has been used. The array here is only 64×128 pixels (instead of the 512×512 anticipated for ST).

3. Reductions

3.1 *Determination of the PSF*

The data have been reduced using the Rome code (Buonanno *et al.* 1979), a technique based on a two-dimensional multipeak fit to the digital array which makes the full use of available information. Dealing with a method for stellar photometry, which requires

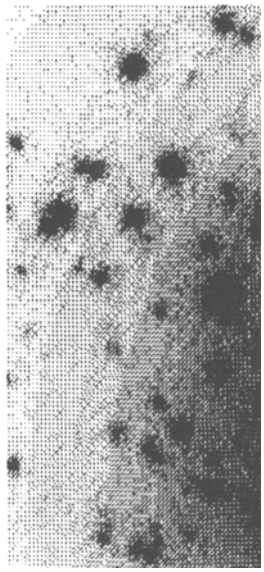

Figure 3. Map of a simulated field: matrix of 64 pixels × 128 pixels.

the knowledge of stellar profiles, the obvious question arises: what is the accuracy required in describing the PSF? Figs 4a, b give a first-order answer. The figures show the results of reduction of two different simulations: the first field has been simulated using in the 'observation' phase the approximate PSF given by King (1983), the second one (identical in the stellar and nonstellar content) has been created making use of the more accurate PSF given by Bendinelli *et al.* (1985). Both fields have then been reduced using Moffat's (1969) curve

$$I = I_0(1+r^2/R^2)^{\beta}$$

for the PSF. In other words, the first field has been reduced adopting a fairly 'realistic' PSF. As King's PSF is a particular case of Moffat's curve, both 'observations' and reductions are based on similar PSFs. In the second case, the adopted PSF represents only a rough approximation of the 'unknown' original PSF. The comparable dispersion shown by the data in Figs 4a and 4b indicates that a relatively low accuracy is sufficient for describing the PSF during the reduction phase. Therefore, we can draw the first conclusion: although the real PSF of the ST will not be described by a simple expression, however, when dealing with photometric reductions it can be approximated by a much simpler function.

3.2 *The Searching Phase*

Unlike in the 'observation' phase, the choice of different PSFs makes a great difference in the results during the searching phase. In fact,

1. the interference of the secondary maxima due to different stars having different magnitudes and colours (present only if a sufficiently accurate description of the PSF is provided), and

2. the shape of the pixels themselves can create spurious images (see Fig. 5) which appear as 'ghost' stars or can lead to losses, particularly in the search for the faintest objects. In order to eliminate this bias, we therefore devised a hierarchical searching

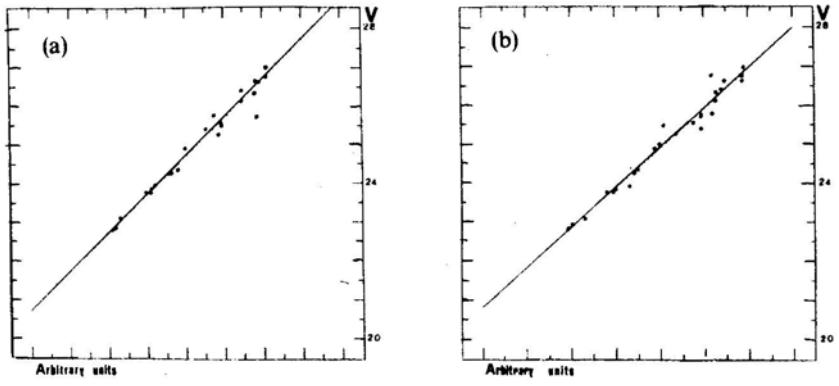

Figure 4. Results of the reduction of the field in Fig. 3 simulated with the PSFs given by: (a) King (1983) (σ = 0.13 mag after discarding the two largest deviants); (b) Bendinelli *et al.* (1985) (σ = 0.19 over the interval V = 20–28 and σ = 0.12 over the interval V = 2025)

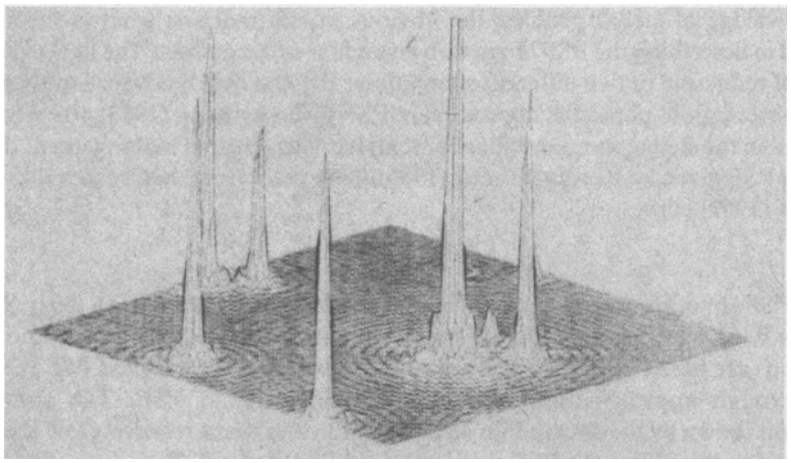

Figure 5. Interference effects amongst different images: the faint, starlike image between two bright objects (in the right part of the map) is a 'ghost' star produced by a positive interference of the secondary maxima of the two bright objects.

procedure. After having experimentally derived the PSF of stars in the frame, the algorithm finds the most luminous star and subtracts from the frame a star of known profile and intensity equal to the detected maximum (centred on the maximum). If all the stars were properly subtracted, the final residuals should be negligible. A first, very rough, approach led to a final mapping of the residuals shown in Fig. 6a. Since most of the effect is essentially due to errors in the definition of the position of the selected stars, we improved the procedure by finding the position of each star via a simple Gaussian fitting of the central maximum of the diffraction-limited image and then making the hierarchical subtraction. The results of this second method are illustrated in Fig. 6b.

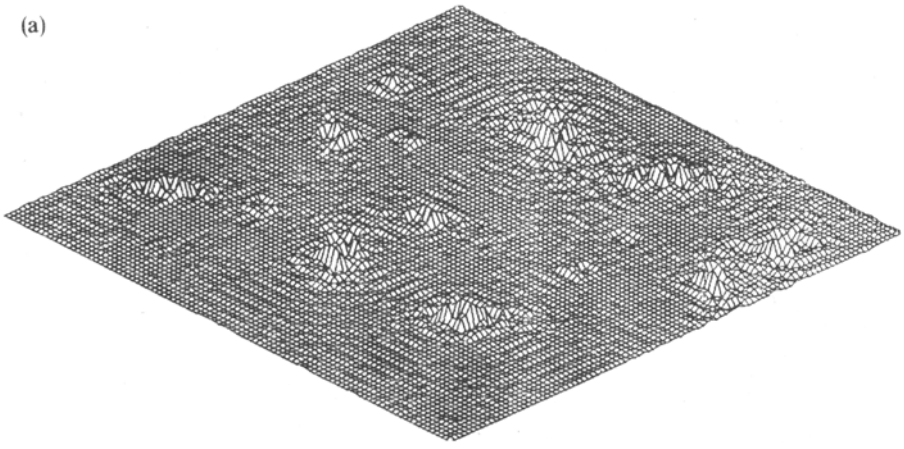

Figure 6. Map of the residuals after subtracting stars from the image frame; (a) with a rough determination of star positions; (b) after a hierarchical subtraction of Gaussian components.

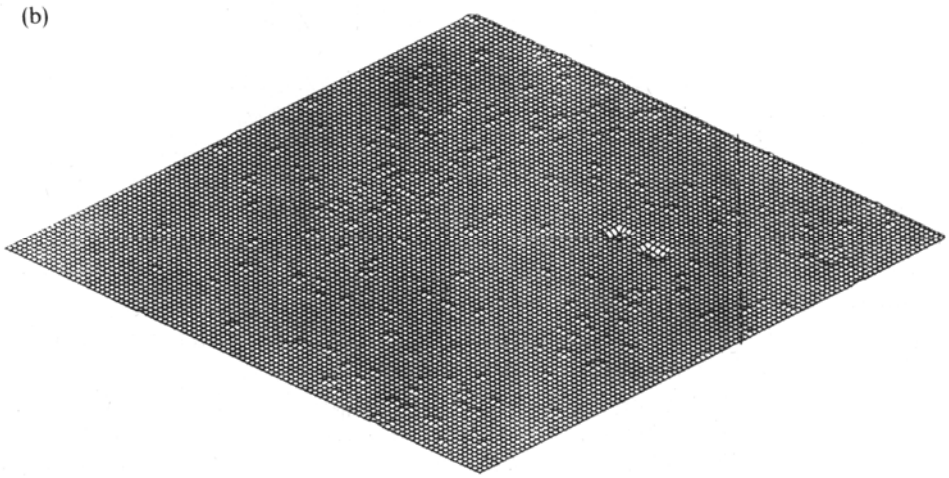

Figure 6. Continued.

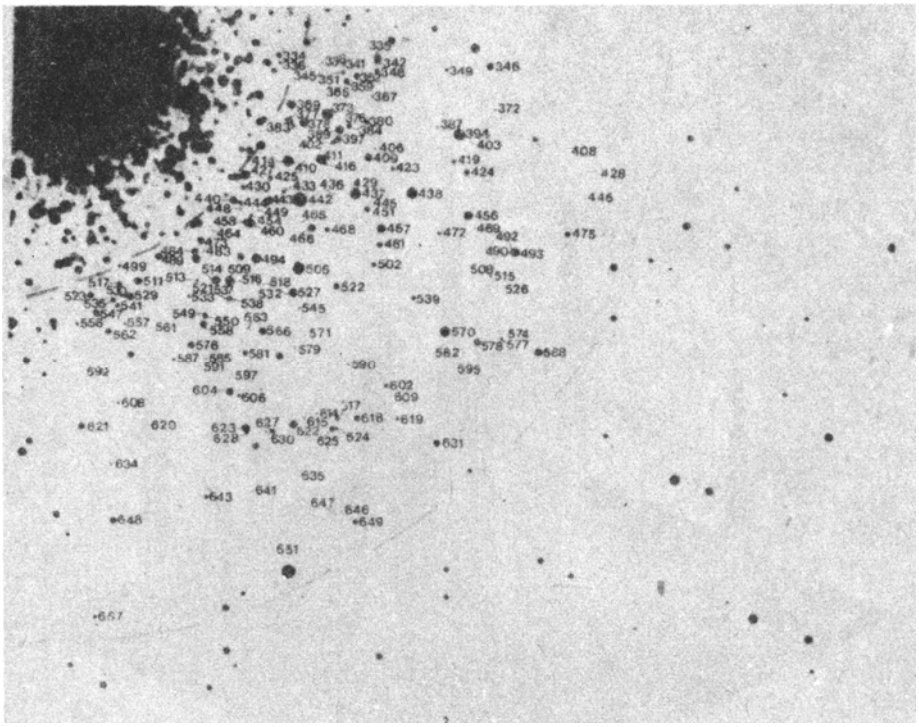

Figure 7. The region of M 15 used for the simulation; the region with $1.9 < r$ (arcmin) < 5.0 corresponds to $1.8 < r$ (arcsec) < 4.6 at the distance of M 31.

3.3 '*Observations*' *and Errors*

After considering all these aspects, we were able to apply the entire procedure, starting from the simulation of a well-studied globular cluster moved at the distance of M 31, up to the reduction of the data as if 'observed' via ST-FOC. Fig. 7 shows the region of M 15 selected for the simulation. The 'observed' output is then presented in Fig. 8 for a small area in the outer regions. Two exposures have been simulated: one in *B* (4200s) and the other in *V* (3600 s) bands. The degree of crowding can be deduced from the estimate of the mean number of pixels per star in the frame. In the considered region this number turns out to be 250 pixels/star. The results obtained from the reduction of the simulated observations are then shown in Fig. 9 where the original *C–M* diagram of M 15 (Fig. 9a) and that obtained after simulated ST-observations (Fig. 9b) are shown.

It is important to note here that we started the simulation not from an 'ideal' *C–M* diagram but from an experimental one, where each star is plotted with its own photometric error. Thus, as a first approximation, the measure of the errors due to the 'observation' (and reduction) with ST is represented by the increased scatter found along the main branches and by the residual colour effects still present in the final *C–M* diagram.

A quantitative estimate of the error due to both 'ST-observation' and reduction procedure can be drawn from Fig. 10 where the plots of residuals ('original' — 'measured') versus measured *B* and *V* magnitudes are presented.

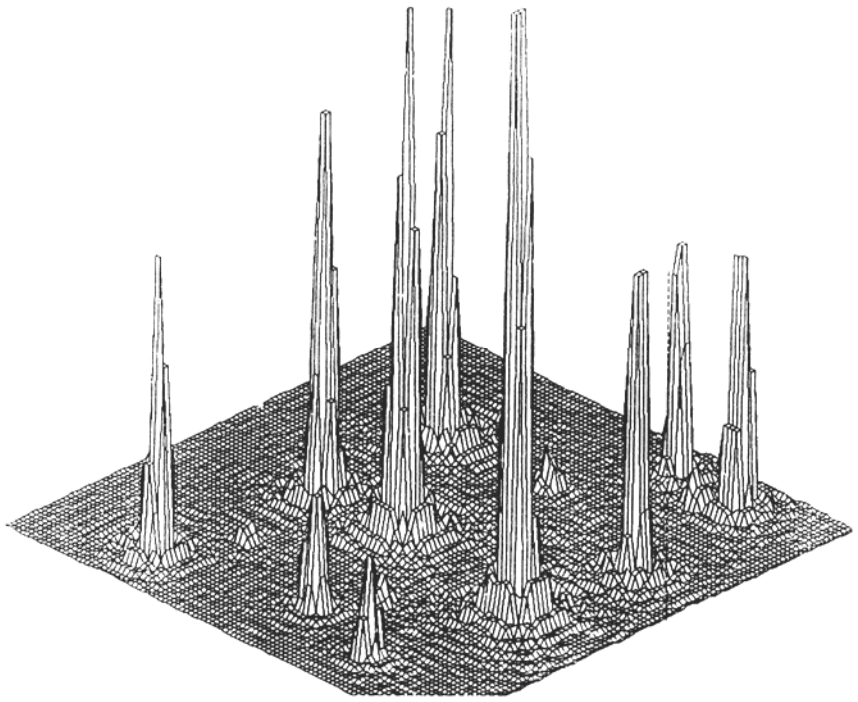

Figure 8. 3-D map of a small outer field.

3.4 *Photometric Sampling*

A few words are needed here on the problem of photometric sampling. For each object this problem is a physical feature intrinsically related to the telescope–detector combination. We cannot act on it, but we can—at least—handle the data correctly. In fact, when we fit a curve through the experimental points, in general, we equate the mean value of the function within a pixel to the value of the function at the mean point of the pixel. This is essentially correct if the pixel is small in comparison with the typical size of the stellar image. When the image is insufficiently sampled, we should ascribe to each pixel the integral of the function within the pixel area and fit this integral against the experimental points. This requires integrating the PSF over each pixel area.

We have applied this procedure (using King's expression of the PSF) in two cases: 1 pixel = 0.022 arcsec (FOC) and 1 pixel = 0.044 arcsec (WF/PC) respectively. Whereas in the first case we did not notice any significant variation in passing from the first to the second approach (which confirms a sufficient sampling of the stellar

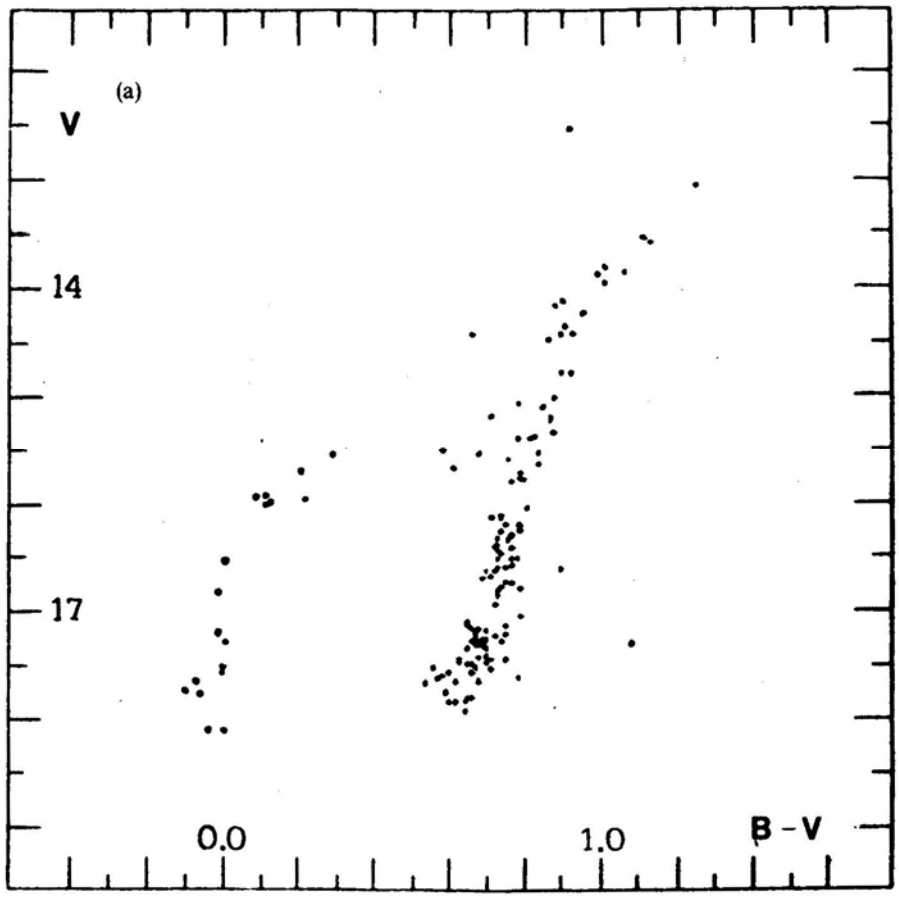

Figure 9. *C–M* diagrams of M 15 obtained from the stars in the field analyzed: (a) data from Buonanno *et al.* (1983); (b) after the simulated shift to the distance of M 31. Exposure times are 3800 s in *B*, and 4200 s in *V*.

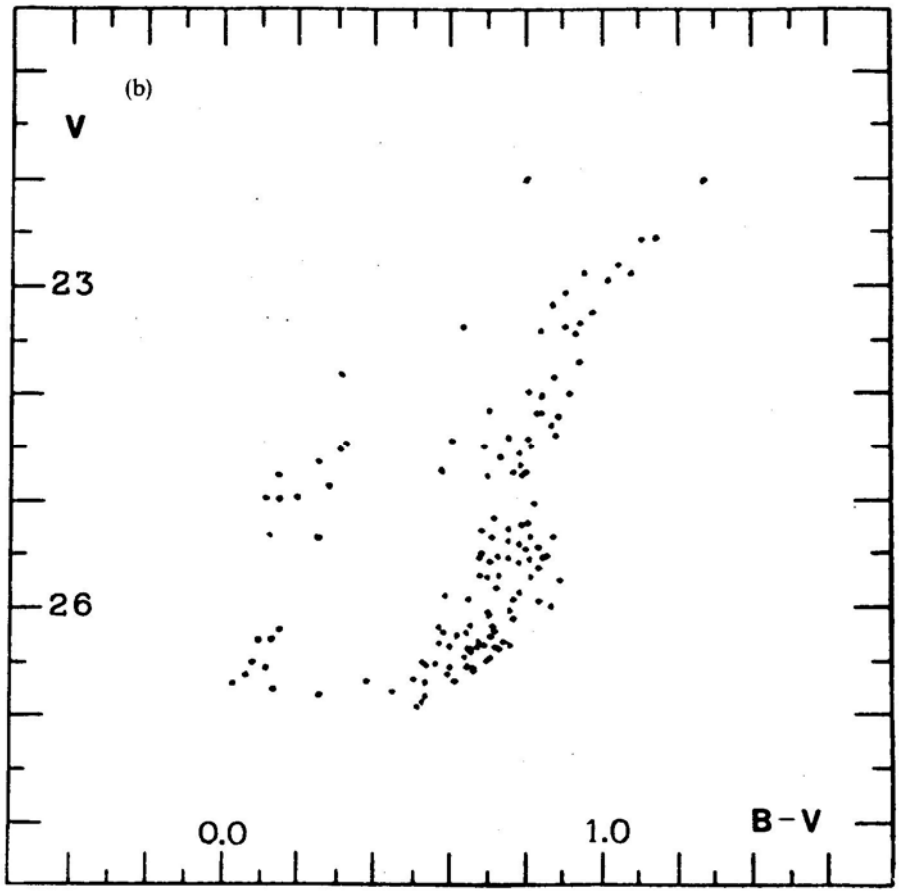

Figure 9. Continued.

images), a clear photometric improvement is noticed while dealing with WF/PC data. The significance of the improvement is apparent from Fig. 11 where the derived magnitudes are plotted against the 'input' magnitudes for both cases: the rms decreases from $\sigma = 0.22$ to $\sigma = 0.10$, when the integral is computed.

4. Conclusions

In summary, the results obtained through this simulation seem useful for planning observations (and reductions) with ST. The adopted procedure is still rather rough and only qualitative conclusions can be drawn. However, ST-observations of individual stars in globular clusters in M 31 seem feasible with the required photometric accuracy ($\sigma = 0.1$ mag) down to the blue extreme of the Horizontal Branch. Updated data on the optical system, detectors, and filters are necessary to properly simulate future observation. We plan to revise and extend the present procedure as soon as definitive data on ST performance become available.

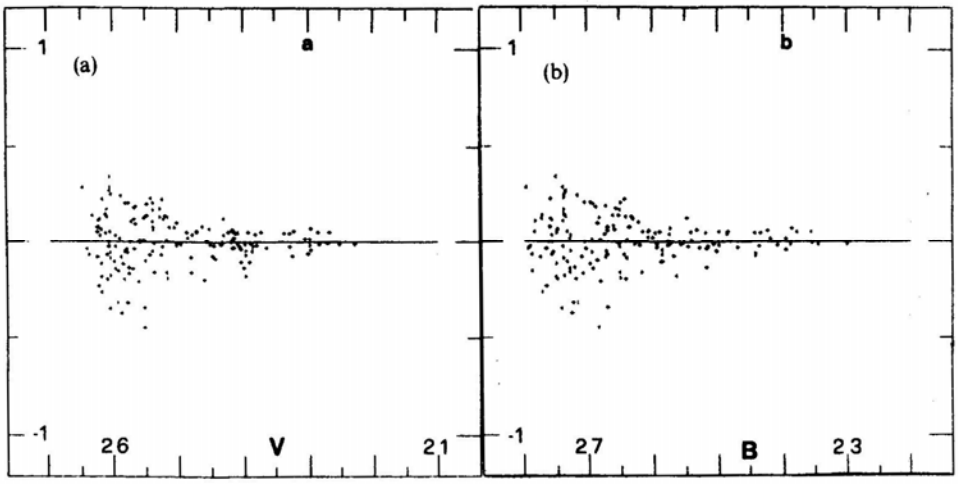

Figure 10. Plots of residuals (original – measured) against (a) measured *V* magnitudes, (b) measured *B* magnitudes.

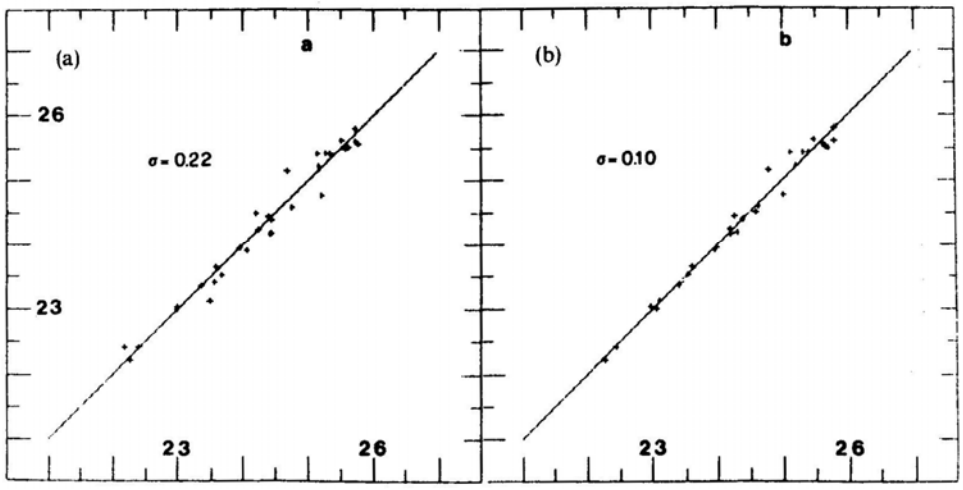

Figure 11. Derived magnitudes versus input magnitudes (in the case of WF/PC): (a) giving the mean value of the function to each pixel, and (b) giving the mean value of the integral of the function to each pixel.

Acknowledgements

The authors are indebted to Drs Bendinelli, Di Iorio, Parmeggiani and Zavatti for making their results available prior to publication, and to Professor I. R. King for sending data on the ST performance.

References

Bendinelli, O., Di Iorio, A., Parmeggiani, G., Zavatti, F. 1985, *Astr. Astrophys.,* **153,** 265.

Buonanno, R., Corsi, C. E., De Biase, G. A., Ferraro, I. 1979, in *Proc. Image Processing in Astronomy,* Eds G. Sedmak, M. Capaccioli & R. J. Allen, Oss. astr. Trieste, p. 354.

Buonanno, R., Buscema, G., Corsi, C. E., Fusi Pecci, F., Iannicola, G. 1983, *Astr. Astrophys. Suppl.Ser.,* **51,** 83.

King, I. R. 1983, *Publ. astr. Soc. Pacific,* **95,** 163.

Moffat, A. F, J. 1969, *Astr. Astrophys.,* **3,** 455.

Peterson, C. J, King, I. R. 1975, *Astr. J.*, **80,** 427.

J. Astrophys. Astr. (1987) **8,** 69–78

Very High Energy Gamma Rays from the Crab Pulsar

P. R. Vishwanath *Tata Institute of Fundamental Research, Homi Bhabha Road, Bombay 400005*

Received 1986 July 29; accepted 1986 December 11

Abstract. The Ooty data on VHE (> 600 GeV) γ-rays from the Crab pulsar have been used to look at possible emission on three different timescales, *viz.* years, minutes and hours. When averaged over three years of observation, there is no significant time-averaged emission. But interesting aspects are revealed when the data are subdivided into miniruns of one-minute duration. Minutes with moderate γ-ray activity were isolated with a χ^2 analysis. The summed phasogram of such minutes shows two strong peaks coinciding with the radio main pulse and the interpulse respectively. The probability that these are due to chance is small. The phasogram has a bimodal distribution which indicates some emission from the middle region between the two phases. In general, there is no significant emission on the timescale of a few hours. However, the main pulse, as well as the bimodal distribution, were seen also in the total data of two nights of simultaneous observation at two sites during 1984–1985.

Key words: γ-ray astronomy—pulsars, VHE γ−rays—Crab pulsar

1. Introduction

Observations with ground-based atmospheric Cerenkov technique have been on since 1969 for the detection of very high energy (VHE) γ-rays from the Crab pulsar. In recent years, two types of emission from the pulsar have been reported. The first is a weak ($\sim 4\sigma$) time-averaged emission: a signal aligned with the radio main pulse was seen (a) in 1983–1984 by the University of Durham group (Dowthwaite *et al.* 1984), and (b) in 1984 by the Iowa State University–JPL collaboration (Turner *et al.* 1985). The other type of emission, stronger ($> 5\sigma$) and short-lived (15 minutes), was seen (a) in 1983 October by the University of Durham group (Gibson *et al.* 1984), and (b) in 1985 January by the Tata Institute of Fundamental Research (TIFR) group (Bhat *et al.* 1986). The phase of the signal seen by the TIFR group agreed with that of the radio main pulse, whereas there was no absolute phase information for the burst seen by the University of Durham group. Thus, according to the available information, the Crab pulsar is a steady emitter of weak flux of γ-rays and a very infrequent emitter of large bursts. In this paper, we explore the possibility of emission on three different timescales, *viz.,* years, minutes and hours. At first, we put together all data available from the TIFR observations for which absolute phase is available, in order to see whether there is any time-averaged emission. Later, we ask the question whether there is any phenomenon which is different in timescale and intensity from either the time-averaged emission or

the 15-min emission. Thus, we explore the possibility of γ-ray emission in a scenario different from those explored till now.

2. The time-averaged emission

The atmospheric Cerenkov array at Ooty, described elsewhere in detail (Gupta *et al.* 1985), was used with all the mirrors close to each other in 1979–1980 and 1982–1983. In 1984–1985, the array was split up with 8 large mirrors at site G and 10 small mirrors at site C, separated from site G by 11 km (Bhat *et al*). The four data sets—1979–1980, 1982–1983, 1984–1985 (C), and 1984–1985 (G) (referred to hereafter as I, II, III and IV observations)—had energy thresholds of 3000, 600, 2200 and 800 GeV with exposures of 70.6,45.8,31.8 and 26.6 hours respectively. The phasograms for all the four data sets were obtained in the standard manner as described in earlier papers of the Ooty group (for *e.g.* Bhat *et al.*). Because we have absolute phase for all the four data sets, these data can be summed in phase. Fig. l(a) shows the total time-averaged phasogram for 174.8 hours. There is no dominant peak (> 3 σ) in the phasogram. Therefore, we derive an upper limit of 4.6×10^{-12} cm^{-2} s^{-1}for the time-averaged emission from the Crab

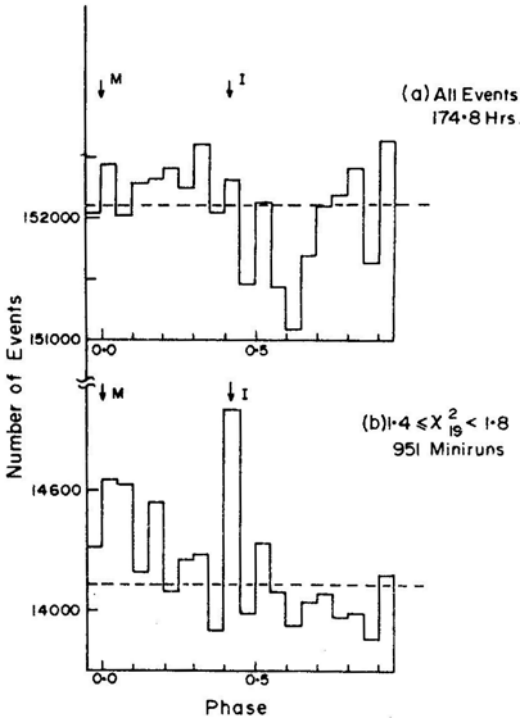

Figure 1. (a) The total phasogram of all the data sets with absolute phase. The dashed line represents the average of all the events in the phasogram. M and I refer to the position of the radio main pulse and interpulse respectively, (b) The summed phasogram of miniruns with $1.4 < \chi^2_{19} \leq 1.8$. The dashed line shows the average of the phasogram after substracting the events in the main and the interpulse region. Phase region 0.950–0.45 is called the region A and the remaining region is called the region B.

pulsar. This limit is not in disagreement with the flux seen by Dowthwaite *et al.* However, three of the above four data sets do show independently a very weak peak (~ 1.5 σ) at the position of the radio main pulse. Data sets I, III and IV together give a peak of 2.3 σ at the radio main pulse phase, while no other bin shows such excess. But the data set II (1982–1983), which is at the lowest threshold energy did not show any excess.

3. Emission on the timescales of minutes

We have already noted in the introduction that strong emission on timescales of 15 min has been found by two groups. The traditional way to look for such a signal is to group the data into relevant timescales and see whether there is a large excess in any bin in the phasograms (*e.g.* Bhat *et al.*). Another method was reported in an earlier paper (Vishwanath 1982) where we had shown the possibility of occasional VHE γ-ray emission in the intervals of minutes. In that analysis, we had considered positive deviation of any bin in the phasograms over timescales of minutes, but we did not have absolute phase information for that data. Both these methods have shortcomings. In the first method, the signal has to be well above the background and if there is less intense emission it would not be noted. The second method does not consider negative deviations. Negative deviations may be interesting since low-level signals could be revealed when the cosmic ray background has statistically downward fluctuation. The new analysis is based on the assumption that the signal, if present, may show up in phasograms with moderate to high χ^2 . While such a χ^2 can also be due to upward or downward statistical fluctuation of one or more bins, the total fluctuation in the signal region may be due to both statistics and presence of a signal, whereas in the background region it will be due only to statistics. The method adopted here will be to group the miniruns over minutes according to their, χ^2 values. The resultant χ^2 of the group phasogram is expected to have a large value if the deviations are not entirely due to statistics. Thus there is a possibility of a signal only in a group phasogram having a large χ^2. We should note here that in the low-energy γ-ray observations of the Cos-B group, no emission was seen in one-half of the phase plot (Wills *et al.* 1982). This possibility exists in the VHE γ-ray region also. (In fact, the excess seen by Dowthwaite *et al.* is above the mean of those bins in the phase region 0.48–0.96.) While the initial selection would be done with the 20-bin phasograms, it is interesting to use only 2 bins if the group phasogram shows a large difference between two halves of the phasogram. While χ^2_{19} (19 degree of freedom) criterion highlights individual bins with signal if there are any, χ^2_1 (1 degree of freedom) reveals whether the two phase regions have real differences. The timescale we consider here is of minutes since the earlier analysis showed the possibility of emission with this timescale.

To find whether such emissions over timescales of minutes exist, the present data were divided into miniruns of one-minute duration and phasogram for each minirun was obtained. The total number of miniruns was 10489 and the average rate per minirun was 289. χ^2 was computed for each minirun and divided by 19 to get χ^2_{19} , the reduced chi-square. Each minirun was grouped as to its χ^2_{19} . Fifteen groups were tried for χ^2_{19} *viz.* 1.0–1.1, 1.0–1.2, 1.0–1.3, 1.0–1.4, 1.0–1.6, 1.0–1.8, 1.0–1.4, 1.4–1.8, 1.2–1.6, 1.6–2.0, 1.3–1.6,1.6–1.9, > 1.8, > 1.9, and > 2.0. The group with $1.4 < \chi^2_{19}$ 1.8 had the highest resultant χ^2_{19} of 2.7. The highest grouping viz., > 1.8, > 1.9 and > 2.0 had

resultant χ^2_{19} of 1.8, 1.5 and 1.5 respectively. The phasogram for the group $1.4 < \chi^2_{19} \leqslant 1.8$ is shown in Fig. 1 (b). The expected number of miniruns in this χ^2_{19} group was 1016 whereas the observed number is 951. Both the main and the interpulses are quite prominent, whereas the bins in phase region 0.45–0.95 have, in general, lower number of events. When we divide the phasogram into two regions—region A (phase 0.95–0.45), and region B (phase 0.45–0.95)—and apply Wilcoxon's rank test (Frodesen, Skeggestad & Tofte 1980), we find the probability that the events in the two regions stem from the same population is lower than 1 per cent. There are several disparities between regions A and B. The mean rates for regions A and B in this selected group are 152.0 ± 0.4 and 149.6 ±0.4 per minirun. If we demand that the region have at least n (any n) bins showing positive excess in a minirun, 55, 28 and 8 per cent in region A and 49, 22 and 4 per cent in region B satisfy this criteria for n = 5,6 and 7. If we further demand that at least 5 bins have excess in one region and deficiency in the other, 34 per cent of the miniruns have excess in A and deficiency in B, whereas 28 per cent have excess in B and deficiency in A. Therefore, it is possible that in VHE γ-ray studies, region B is populated by background events due to cosmic rays only, whereas the rest of the phase plot has events due to γ-rays also. A comment is in order about the non inclusion of the high χ^2_{19} group ($\chi^2_{19} > 1.8$). As mentioned above, the resultant χ^2_{19} of the phasogram in this group is not high. Further, the rank parameter is 106, giving a high probability that the two regions come from the same population. Therefore, it appears that the constituent miniruns of this group owe their high χ^2_{19} essentially to statistical fluctuations. We also note that if we remove the events from the main pulse and the interpulse regions from each minirun and then compute the χ^2_{17}, the summed phasogram of the miniruns in the $1{\cdot}4 < \chi^2_{17} \leqslant 1.8$ interval is flat.

For exploring further the differences between regions A and B, events in each minirun with $1.4 < \chi^2_{19} \leqslant 1.8$ were placed either in region A or in region B depending on their phase. For the two-bin phasogram thus obtained, χ^2_1 was computed. While three different ($\chi^2_1 > 1.$, 1.5, 2.) cuts were tried out, Fig. 2 displays the $\chi^2_1 > 2$ cut. The phasogram shows considerable excess at both the main and the interpulse phases. The average rate per minirun in regions A and B in Fig. 2 are 155.03 ± 0.80 and 147.90 ± 0.80 respectively. The average normal background rate (shown by the dashed line) was derived by ignoring the bins in the phase interval 0.95–0.10 and 0.40–0.45. This average rate for Fig. 2 is 149.9 ± 0.4 for half of the phase plot. Another measure of the normal background rate is obtained by comparing the rates before and after the 263 miniruns selected for Fig. 2. The pharograms of two miniruns just before and two miniruns just after the selected miniruns were pulled out and added up and the mean-rate obtained for either region was 148.9 ± 0.6. (Miniruns just before and after the selected minutes have better sensitivity to variations of atmospheric transparency and zenith angle.)

We consider here the reasons for high rate in region A. The value of δ, the excess number of events in region A was computed for each minirun. Miniruns with $+\delta$ and $-\delta$ were labelled as Type I and Type II respectively. R, the ratio of number of Type I to Type II miniruns, is 1.33 ± 0.16. At $\delta > 20$, R is 1.73 ± 0.27. Therefore, there are more Type I miniruns and that too with a higher rate in region A. Next, we compare the rate in each selected minirun with normal background average rate of 4 min which encompass it. The percentage of miniruns where region A (B) has fluctuated upward by $> 2\sigma$ is 17 (12) and downward by $> 2\sigma$ is 8 (18). The fluctuation of the normal cosmic ray background was computed and it was found that 20 per cent and 5 percent of the normal miniruns fluctuate beyond 1σ and 2σ for both A and B. (These differ slightly

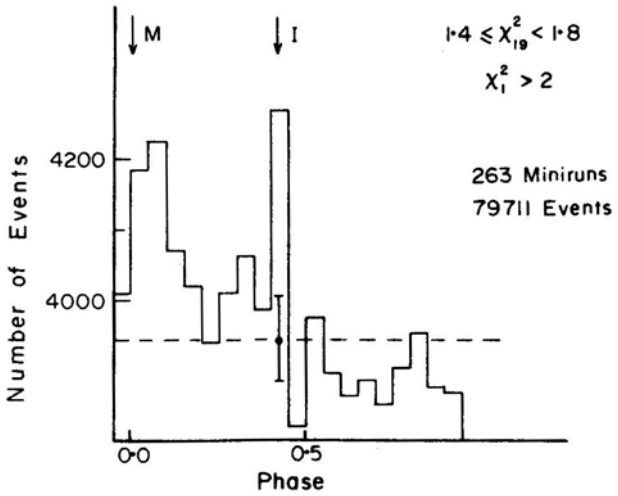

Figure 2. The summed phasogram of 263 miniruns which survive both the χ^2 cuts. The bimodal distribution is due to a dominant signal riding over the background due to cosmic rays.

from Poisson fluctuation because atmospheric transparency and extraneous lights play an important role in atmospheric Cerenkov methods.) The selected miniruns in which the total rate is lower than the normal cosmic ray background rate account for 42 per cent and 28 percent, of the excess seen in main pulse and interpulse respectively. Thus, the selection process has preferentially picked out miniruns where regions A and B have shown significant upward and downward fluctuation respectively.

We did a Monte Carlo simulation to see the probability of getting the distribution shown in Fig. 2. The observed average rate of 288 was chosen and each bin was given a Poisson fluctuated value, and thus a 20 bin phasogram was constructed. 10489 miniruns were generated as in the data and cuts identical to those made on the data were also applied to the simulated minutes. For each trial, a phasogram similar to Fig. 2 was obtained. We made a total of 1000 trials. While it was possible to get a distribution with one-half of the phasogram showing considerably large number of events compared to the other half (3 out of 1000 trials), this did not translate to significant peaks as seen in the data. Only one trial showed a single peak of statistical significance similar to those in Fig. 2. Therefore, to get at least two peaks of similar significance, the probability is 1×10^{-5} (Eadie *et al.* 1971). When we further demand that the two peaks be separated by 0.43 in phase, the probability is reduced to 1×10^{-6}. The higher-rate region was picked up for each trial and an average rate was obtained which was equal to 149.9 ± 0.4 per minirun. This rate, incidentally, is the same as that obtained by ignoring the peaks in the phasogram.

With this background rate, the Gaussian strengths of the main pulse and the interpulse in Fig. 2 are 5.9σ and 5.2σ. 142 out of 6146 miniruns at higher energy threshold (data sets I and III) and 123 out of 4343 miniruns at lower energy threshold (data sets II and IV) contribute to the phasogram in Fig. 2. The main pulse at low-and high-energy thresholds is at significance levels of 5.7σ and 1.9σ respectively. The interpulse at the low- and high-energy thresholds is at significance levels of 4.5σ and 3.0σ respectively. Fig. 3(a) shows the VHE γ-ray light curve from the present analysis for the lower threshold energy. The ordinate represents the number of events over and

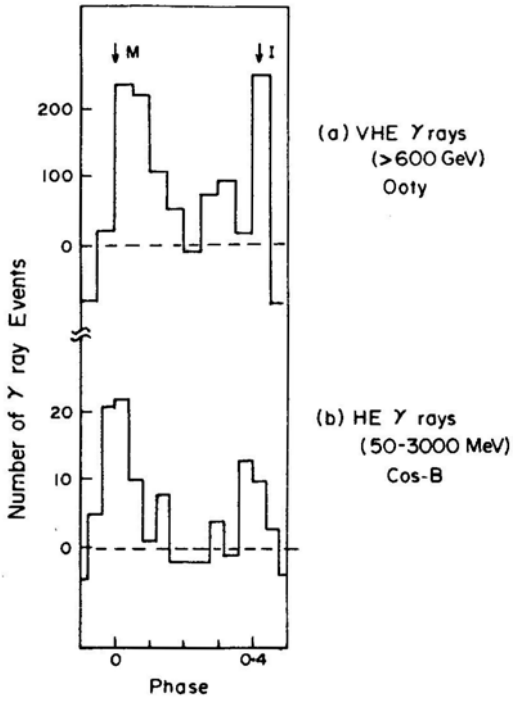

Figure 3. (a) The summed phasogram of miniruns at low-energy threshold (>600 GeV) which satisfy the criteria. The number in each bin is calculated after subtracting the background as mentioned in the text, (b) The light curve of high-energy γ-rays obtained by the Cos-B group in September 1980.

above the background, determined as explained in the earlier paragraph. Fig. 3(b) represents the rebinned light curve from the 1980 observations of the Cos-B group (Wills *et al.* 1972). The shapes of the two light curves are quite similar. While Dowthwaite *et al.* have a weak evidence for the interpulse, the present analysis is the only one to have shown the interpulse clearly at VHE γ-ray energies. The main pulse is wider (< 3.3 ms) than in the low-energy studies. In the VHE range there is no consensus about the width of the signal. Regarding time-averaged emission, Dowthwaite *et al.* saw a pulse with width less than 1 ms, whereas Tumer *et al.* reported the width to be 6 ms. In the burst measurements, Bhat *et al.* reported a width of 1.65 ms, whereas Gibson *et al.* had a much larger width. As for the possible smearing of the pulse due to inaccurate timekeeping, we would like to note that the Ooty time calibrations were done with a radio signal before 1984 and with a NNSS satellite time receiver after 1984 with timekeeping accuracies of ± 0.5 ms and 0.03 ms respectively. Further, the interpulse which is narrower appears in the same bin in all the 4 data sets. Therefore, it is quite possible that varied phenomena with slightly different widths are present.

The flux of VHE γ-rays from the Crab pulsar was obtained for energy thresholds of 600 Gev and 2200 Gev using the results of minirun analysis. The flux due to the main pulse alone is $(1.6 \pm 0.3) \times 10^{-10}$ cm^2s^{-1} and $(2.1 \pm 1.1) \times 10^{-11} cm^2s^{-1}$ at E > 600 GeV and > 2200 GeV respectively. The main pulse flux at both energies agrees well with the expectations from Cos-B observations (at least 70 per cent of the Cos-B flux is due to the main pulse). In the observations on bursts (Bhat *et al.* 1986 and Gibson *et al.*

1983) and in the present work, the flux of the main pulse is $\geqslant 10^{-10}$cm^{-2} s^{-1}. We note that the time-averaged flux from the Crab pulsar is generally less than what is expected from observations at low energies. The agreement of a transient flux at TeV energies with what is expected from a time-averaged flux at low energies suggests (Porter 1983) that the Crab pulsar is capable of emitting considerable flux of VHE γ-rays.

4. Emission in individual runs

There were 65 runs in the whole data representing 65 independent nights of observation. When we consider the phasogram of individual runs, we find that the frequency with which the bin corresponding to either the main pulse or the interpulse is dominant ($>n\ \sigma$, with n= 1,2,3) is not much different from that for the other bins. Therefore, on the basis of this statistics, it is difficult to consider any particular run as being rich in γ-rays. However, special mention must be made of 4 complete runs from the 1984–1985 observations, where the phase region A had excess events on the same two nights at both the places. The summed phasograms for each site on these two nights (1985 January 23 and 1985 February 14) are shown in Figs 4(a, b). The total observation times at sites C and G were 150 min and 210 min respectively with overlap of 105

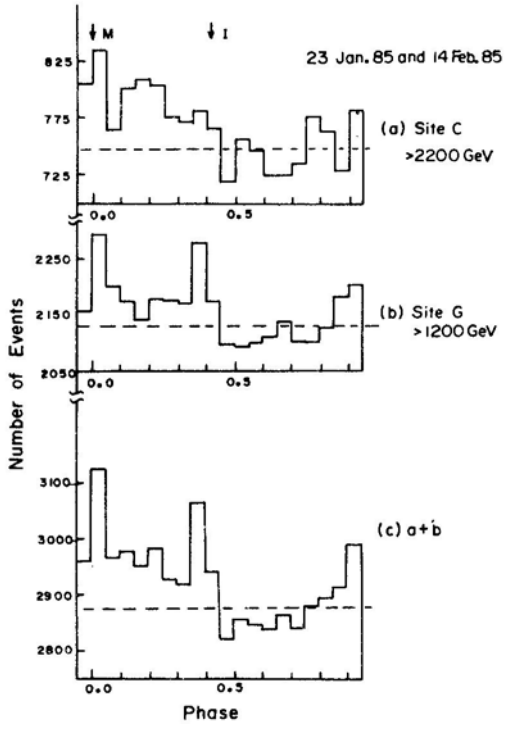

Figure 4. (a) The summed phasogram of all the data taken on two nights (see text) at site C where the energy threshold was 2200 GeV. (b) The summed phasogram of all the data taken on the same two nights at site G where the energy threshold was 1200 GeV. (c) The summed phasogram of data taken at sites C and G.

minutes. These two phasograms are further summed and the total phasogram for these two nights is shown in Fig. 4(c). The Wilcoxon's rank parameter is 56 for region A in Fig.4(c). If we consider the cosmic ray background to be given by the mean of region B then the main pulse is at 3.1 σ and 3.6 σ for the phasograms in Figs 4(a, b). The probability of occurrence of peak at the main pulse due to chance at both the sites is 4×10^{-6}. However, there were 7 nights of simultaneous observations and there are 21 ways of selecting two nights from the total of 7 nights. Therefore, the final probability of observing the main pulse in the season (1984–1985) when we had simultaneous observations is 8×10^{-4}. We should also note that the 15 min burst seen by Bhat *et al.* occurred on 1985 January 23.

5. Discussion

As for the time-averaged emission, the combined data of 4 data sets with absolute phase do not show any dominant peak. However, the upper limit in the present analysis does not disagree with the flux seen by Dowthwaite *et al.* at these energies. At the higher threshold energies (Data sets I, III and IV), there is a hint of a signal at the main pulse. There could be two reasons for the lowest threshold data not showing any signal: (a) The steady emission has seasonal variations and the Crab pulsar did not have, any emission during that season. (b) The lowest threshold also meant a higher trigger rate (because of use of all mirrors and a larger aperture) and it is possible that more noise (cosmic rays) was admitted into the system. We should, however, note that while the University of Durham group did find a signal in 1982–1983, 34 hours of observation in 1981 did not show any such signal.

We would like to note that one-minute activities reported here do not refer to the strong emission from the pulsar. The nomenclature 'burst' traditionally refers to the activity of the pulsar over and above the normal background (*cf.* Bhat *et al.* 1986; Gibson *et al.* 1982). The present analysis does not require a high signal level. In fact, out of the 263 miniruns selected for the final plots, the ratio of the number of miniruns with any bin in region A having $> n\,\sigma$ peak (with n =1,2,3) to the number with any bin in region B showing a similar peak, decreases from 1.26 ±0.7 at n = 1 to 1.1 ±0.2 at n= 3. Thus, most of the events in the signal come from miniruns where the peak is present but not at any high intensity. Therefore, it is the low-level transient emission which gets picked up by this method. It is interesting that while most of the earlier efforts look for a transient signal in a region with higher emission rate (*e.*g., Gibson *et al.*), the method outlined here searches for minutes with low rates also. However, one should note that this analysis is not expected to pick out constant and weak signals. The flux seen by Dowthwaite *et al.* (1984) results in about one γ-ray event in 17 minutes and will not be detected irrespective of how low the background may fluctuate.

As for the emission over timescales of a few hours, the data on individual runs show that such emission is in general not present. However, our 1984–1985 observations were done at two well separated sites (Bhat *et al.*) and two out of seven nights of observation did show the main pulse at a level $> 3\,\sigma$. It is interesting to compare Fig. 4(c) and Fig. 2 since both display a main pulse and a rather bimodal distribution. Fig.2 is a result of the minirun analysis and all the data sets contribute to it. Fig.4(c) represents the complete data of two nights. While Fig. 2 is a possible result of both the presence of a signal in region A and a statistical downward fluctuation of the cosmic ray background, it is

highly unlikely that the background has fluctuated downward on both the nights and at both the sites. Therefore, Fig. 4(c) can be accounted for only by increased γ-ray activity on those two nights. Another interesting aspect of these two phasograms is that there seems to be some emission from the middle phase regions also. The number of events in the middle phase region is much higher than the background. In effect, regions A and B can be considered to be the 'on' and the 'off' regions for the pulsar. However, the emission is from the pulsar and not from the nebula since periodicity has been invoked.

6. Conclusions

In summary, a new analysis of the Ooty data has shown that it is more likely that the Crab pulsar emits VHE γ-rays on a shorter timescale rather than on a larger timescale. While the emission over a timescale of years is barely detectable, the analysis has evidence for emission over timescales of minutes and possibly hours. The analysis shows the main pulse and the inter pulse from the Crab pulsar with a low probability that they are due to chance. These pulses have been seen at both low- and high-energy thresholds and in all four data sets. The analysis has located minutes where the pulsar is active. It is easier to discern low-level activity when the background undergoes a downward fluctuation. As for emission over a few hours, our most recent observations on Crab pulsar also showed the main pulse on two nights of simultaneous observations. In the emission over both minutes and hours, there are γ-rays from in between the main and interpulse region. The observed flux in the miniruns, which is similar to transient fluxes determined in observations on bursts, shows that the pulsar iscapable of emitting considerable amount of γ-rays.

Acknowledgements

It is a pleasure to thank Professors P.V. Ramanamurthy, M. V. S. Rao, B. V. Sreekantan and Dr B. K. Chaterjee for useful discussions on the manuscript. Professors P. V. Ramanamurthy and S. C. Tonwar, and Drs P. N. Bhat and S. K. Gupta are thanked for their contributions to the observation and analysis. Mr A. R. Apte is thanked for designing and setting up the array and also for assistance during the observations. Messrs N. V. Gopalakrishnan, R. Mahalingam, R. Ramani, S. Swaminathan and M. Venkateshwarlu are thanked for the design and testing of electronics and assistance during the observations. Drs P. T. Wallace and A. J. Lyne graciously provided the pulsar elements.

References

Bhat, P. N., Ramanamurthy, P. V., Sreekantan, B. V., Vishwanath, P. R. 1986, *Nature,* **319,** 127.

Dowthwaite, J.C, Harrison, A. B., Kirkman, I.W., Macrae, H. J., McComb, T. J. L., Orford, K.J., Turver, K. E., Walmsley, M. 1984, *Astrophys. J.,* **286,** L35.

Eadie, W. T., Drijard, D., James, F. E., Roos, M., Sadaoulet, B. 1971, *Statistical Methods in Experimental Physics,* North Holland, Amsterdam.

Frodesen, A. G., Skeggestad, O., Tofte, H. 1979, *Probability and Statistics in Particle Physics,* Universitetsforlaget, Bergen, 453.

Gibson, A. I., Harrison, A. B., Kirkman, I. W., Lotts, A. P., Macrae, J. H., Orford, K. J., Turver, K. E., Walmsley, M. 1982, *Nature,* **296,** 833.

Gupta, S. K., Ramanamurthy, P. V., Tonwar, S. C, Vishwanath, P. R. 1985, *Astrophys. Space Sci.,* **115,** 163.

Porter, N. A. 1983, in *Proc. of XVIII Int. Conf. on Cosmic Rays,* **12,** 435.

Tumer, O. T., Wheaton, W. A., Godfrey, C. P., Lamb, R. C. 1985, in *Proc. IX Int. Conf. on Cosmic Rays,* **1,** 139.

Vishwanath, P.R.1982, in *Proc. Int. Workshop on Very High Energy Gamma Ray Astronomy,* Eds. P. V. Ramanamurthy & T. C. Weekes, TIFR, Bombay, p. 21.

Wills, R. D., Bennet, K., Bignami, G. F., Buccheri, R., Caraveo, P. A., Hermsen, W., Kanbach, G., Masnou, J. L., Mayer-Haselwander, H. A., Paul, J. A., Sacco, B. 1982, *Nature,* **296**,723.

Preface

The meeting of IAU Commission 29 on the topic 'Nucleosynthesis in the Galaxy from the study of low-mass stars' was held on 27 November 1985 during the XIX General Assembly of the International Astronomical Union, New Delhi. A dozen papers were presented and discussed. The papers presented were of considerable interest, contained many new results and covered several aspects of nucleosynthesis in the Galaxy as inferred from the study of low-mass stars. Infact, it is the first meeting to focus attention on the elemental abundances of low-mass stars.

We publish here ten out of twelve papers presented during the meeting and also an excellent summary and concluding remarks of the meeting presented by Professor B. Gustafsson. We are grateful to the Indian Academy of Sciences for encouragement and support in the publication of these proceedings in the *Journal of Astrophysics and Astronomy*.

G. Cayrel de Strobel
M. Parthasarathy

J. Astrophys. Astr. (1987) **8,** 81–82

Abundances of the Very Light Elements D, He, Li and their Cosmological Implications

Jean Audouze *Institut d'Astrophysique du CNRS, 98 Bis BLVD Arago, F-75014 Paris, France* and *Laboratoire René Bernas, F-91405 Orsay Campus, France*

Abstract. The abundances of very light elements D, ^{3}He, ^{4}He and ^{7}Li in low-mass stars and their cosmological implications are discussed.

Key words: abundances, light elements:—low-mass stars—cosmology

1. Introduction

The very light elements (D, ^{3}He, ^{4}He and ^{7}Li) are known to be likely produced during the early phases of the universe. The relation between the results of the big bang nucleosynthesis and cosmology has been discussed in other sessions of the Delhi IAU Assembly (J. Audouze, B. E. J. Pagel, G. Steigman). The few remarks I would like to make here regarding this very important problem deal with the relations between the relevant observations in the low-mass stars and the primordial abundances of these very light elements. They concern mainly ^{4}He and ^{7}Li since D has been destroyed in these stars and is only observed in the interstellar medium and the solar system. Given the lack of information regarding ^{3}He, it would be most useful to measure its abundance in low-mass stars for reasons which are presented in the sequel.

2. ^{4}He and ^{7}Li observations in low-mass stars

Concerning ^{4}He afew observations have been made by Carney (1983) in low-mass stars who quotes $Y_P \sim 0.19 \pm 0.05$. This value can be compared with that deduced by Pagel (1986) who from the analysis of blue compact (metal-poor) galaxies derives a primordial ^{4}He abundance $Y_p \sim 0.235 \pm 0.005$. Should the primordial abundance of He be as low as the value reported by Carney (1983), the standard big bang model would be in serious difficulty: *i.e.*, prediction of too low a baryonic density from ^{4}He compared to that deduced from D and ^{7}Li, and number of neutrino families < 3 being a value determined by the particle physicists.

In the case of ^{7}Li, Spite & Spite (1982) and Spite, Maillard & Spite (1984) have used their observations of the Li abundance in very old and very metal-poor population II stars, and derived the primordial abundance of ^{7}Li to be Li/H ~ l – 2× 10^{-10}. Boesgaard & Steigman (1985), in their recent review, estimate the upper limit to the primordial ^{7}Li to be Li/H <8 × 10^{-10}.

3. Implications

From the primordial abundances of D, ^{3}He, ^{4}He and ^{7}Li (Y~ 0.235, $X(D+{}^3\mathrm{He}) \sim 10^{-4}$ and $X(^7\mathrm{Li}) \sim 5 \times 10^{-10}$) and their comparison with the canonical (sim-

plest) big bang nucleosynthesis models one concludes that the baryonic cosmological parameter $\Omega_B \sim 0.10$ and that one should not observe another type of leptons (or neutrinos) than those already known (see *e.g.* Boesgaard & Steigman (1985) and Steigman (1985) for reviews). Our group (Audouze 1986a, b) is currently arguing that the baryonic cosmological parameters Ω_B deduced from ^{4}He and D are consistent only in the case where specific models of chemical evolution of galaxies apply (Delbourgo-Salvador *et al.* 1985). These models assume a large destruction of D during the galactic life. The observation of the ^{3}He abundance in the atmosphere of low-mass stars could carry valuable information in that respect: if the abundance of D decreases strongly with time one should determine some relatively large ^{3}He abundance ratio at the surface of such old stars resulting from the transformation of a large initial D content.

4. Concluding remarks

Low-mass stars cannot by themselves provide all the information which is needed to determine all the primordial abundances of the very light elements D, ^{3}He, ^{4}He and ^{7}Li. Nevertheless they play a basic role in establishing the primordial abundance of ^{7}Li and they may provide useful constraint on the chemical models of our Galaxy such as those designed by Delbourgo-Salvador *et al.* (1985) to reconcile the baryonic densities deduced respectively from ^{4}He and D. Moreover they might constrain the primordial abundance of He and force the cosmologist to adopt a low value for it which may be inconsistent with the prediction of the Standard big bang nucleosynthesis.

Dr Giusa Cayrel deserves my admiration for having been so persistent in making me write this short contribution.

References

Audouze, J. 1986a in *Dark Matter in the Universe,* Ed. J. Kormendy, D. Reidel, Dordrecht, in press.

Audouze, J. 1986b, *Highlights in Astronomy,* **7,** 377.

Boesgaard, A. M., Steigman, G.1985, *A. Rev. Astr. Astrophys.,* **23,** 319.

Carney, B. W.1983 in *Primordial Helium,* Eds P.A. Shaver, D. Kunth & K. Kjar, ESO, Garching, p. 179.

Delbourgo-Salvador, P., Gry, C., Malinie, G., Audouze, J. 1985 *Astr. Astrophys.,* **150,** 53.

Pagel, B. E. J. 1986, *Highlights in Astronomy,* **7,** 551.

Spite, F., Spite, M.1982, *Astr. Astrophys.,* **115,** 357.

Spite, M., Maillard, J.P., Spite, F.1984, *Astr. Astrophys.,* **141,** 56.

Steigman, G. 1985 in *Nucleosynthesis,* Eds W. D. Arnett & J. W. Truran, Univ. Chicago Press, p. 48.

J. Astr. Astrophys. (1987) **8,** 83–87

Li Production in the Big Bang

Douglas K. Duncan *Mt Wilson and Las Campanas Observatories of the Carnegie Institution of Washington, 813 Santa Barbara St., Pasadena, CA 91101, USA*

L. M. Hobbs *Yerkes Observatory, University of Chicago, Post Box 258, Williams Bay WI 53191, USA*

Abstract. Li abundance is determined for 23 halo subdwarfs. About half of the stars show [Fe/H] < –1.4 and a space velocity V > 160 km s $^{-1}$. Li appears to be present in all our halo stars, with an abundance within about ± 0.2 dex of the value log n (Li) = 2.0 found by Spite & Spite (1982). Thus our results provide confirmation of the main conclusion of Spite & Spite.

Key words: abundances, Li—cosmology—stars, halo subdwarfs

1. Introduction

Accurate measurements of the abundance of lithium in the surface layers of old and young stars and in the interstellar medium can increase our knowledge of stellar structure, Galactic element production, and big-bang nucleosynthesis. The latter topic has recently been reviewed by Boesgaard & Steigman (1985). Standard models of the hot big bang (*e.g.*, Yang *et al.* 1984) predict the formation of D, ^{3}He, ^{4}He, and ^{7}Li in an epoch of primordial nucleosynthesis of a few minutes duration. If the abundances so produced can be measured, they may be used to probe the conditions of the big bang, and to place constraints on particle physics and cosmology.

The primordial abundance of ^{7}Li is last of these quantities to be probed, in large part because it seemed unlikely that primordial lithium could be detected. Li is the easiest of all elements to destroy. If subjected to temperatures in excess of 2.5×10^6 K, it is rapidly destroyed by (p,α) reactions. Such temperatures are reached at the base of the convection zones of cool stars, and the Li in these stars is continuously destroyed. The present Li abundance in the Sun is approximately 100 times less than that in the matter from which it formed.

Thus it was a surprising and extremely important discovery by Spite & Spite (1982; hereinafter SS) that Li is present in halo stars of approximately solar temperature, in quantities approximately 10 times larger than in the Sun. Surveying old disc and halo stars, SS, and Spite, Maillard & Spite (1984; hereinafter SMS) found basically that Li is present in stars which have [Fe/H] < 1.0, and log T_e = 3.74–3.80. When detected, the Li abundance was in all cases between 1.9 and 2.2, on the scale log n(H) = 12.0. The age of the stars and the uniformity of the Li abundance led SS to conclude that they were observing Li produced by the big bang and not modified since then.

The explanation of how such halo stars could presently have more Li than the Sun, despite their greater age, is apparently related to their metallicities. Calculations by Dappen (1984, personal communication) show that as metal abundance is reduced at

fixed log T_e, convection zones become thinner and the temperature at their base less. The rate of Li destruction, being extremely temperature-dependent, may be greatly lessened.

What may be a related effect was first noted by Duncan (1981). In studying two phenomena associated with age in solar-type stars, chromospheric activity and Li abundance, he found that although most stars either exhibited high activity and high Li abundances, indicating youth, or low activity and low Li abundance, indicating that they were old, perhaps 15 per cent showed a discrepancy. In all cases the discrepancy was in the sense of low chromospheric activity and high Li abundance. Duncan tentatively concluded that the stars were probably in fact old, and had somehow avoided destroying their Li. The anomalous stars included the most metal-poor stars in Duncan's sample, but no star was more metal-poor than [Fe/H] = –0.6, and not all of the anomalous stars were metal-poor.

Stimulated by the results of SS, the present authors independently set out in 1983 to examine a larger number of subdwarfs chosen to be as homogeneously old as possible. Since both temperature and metal abundance could be expected to effect Li destruction, we set out to survey a large region of the [Fe/H], log T_e plane. We have combined our data, and now have spectra of the Li I λ6707 doublet at a resolution of typically 0.2 Å for a group of 23 subdwarfs with iron abundances [Fe/H] $\leqslant -0.6$ and space velocities $\geqslant 100$ km s^{-1}. About half of these stars in fact show [Fe/H] $\leqslant -1.4$ and $V \geqslant 160$ km s^{-1}.

A very preliminary report on some of the most interesting stars is presented here.

2. Observations

A typical spectrum is presented in Fig. 1. Signal-to-noise ratios are generally 100–200. Agreement between our spectra and those of SS are very good. For eleven stars in which we both measured equivalent widths, the mean difference is 2 ± 5 mÅ. Every one of our stars which is clearly a halo object shows measurable Li λ6707.

3. Temperatures

We have paid particular attention to accurate temperature determination for the stars in our sample. Since Li I λ6707 is the resonance line of the neutral species of an atom which is almost completely ionized in these stars, it is very temperature sensitive, and accurate stellar temperatures are needed to derive accurate Li abundances. Peterson & Carney (1979, and additional data in Carney 1983) derived temperatures for most of these stars from matching spectrophotometric scans covering 5,000–8,400 Å to ATLAS6 model-atmosphere surface fluxes, and also from $R - I$ and $V - K$ colours. These three sets of determinations are independent, so random errors should be reduced by averaging them. The discussion which follows concerns differences between stars, in which random errors are the most important ones. Peterson & Carney estimate a random error of 80 K in their temperatures, and a possible 80 K systematic error or zero-point uncertainty. Intercomparison of their three sets of temperatures for each star indicates random errors of approximately 80 K in any one determination from a

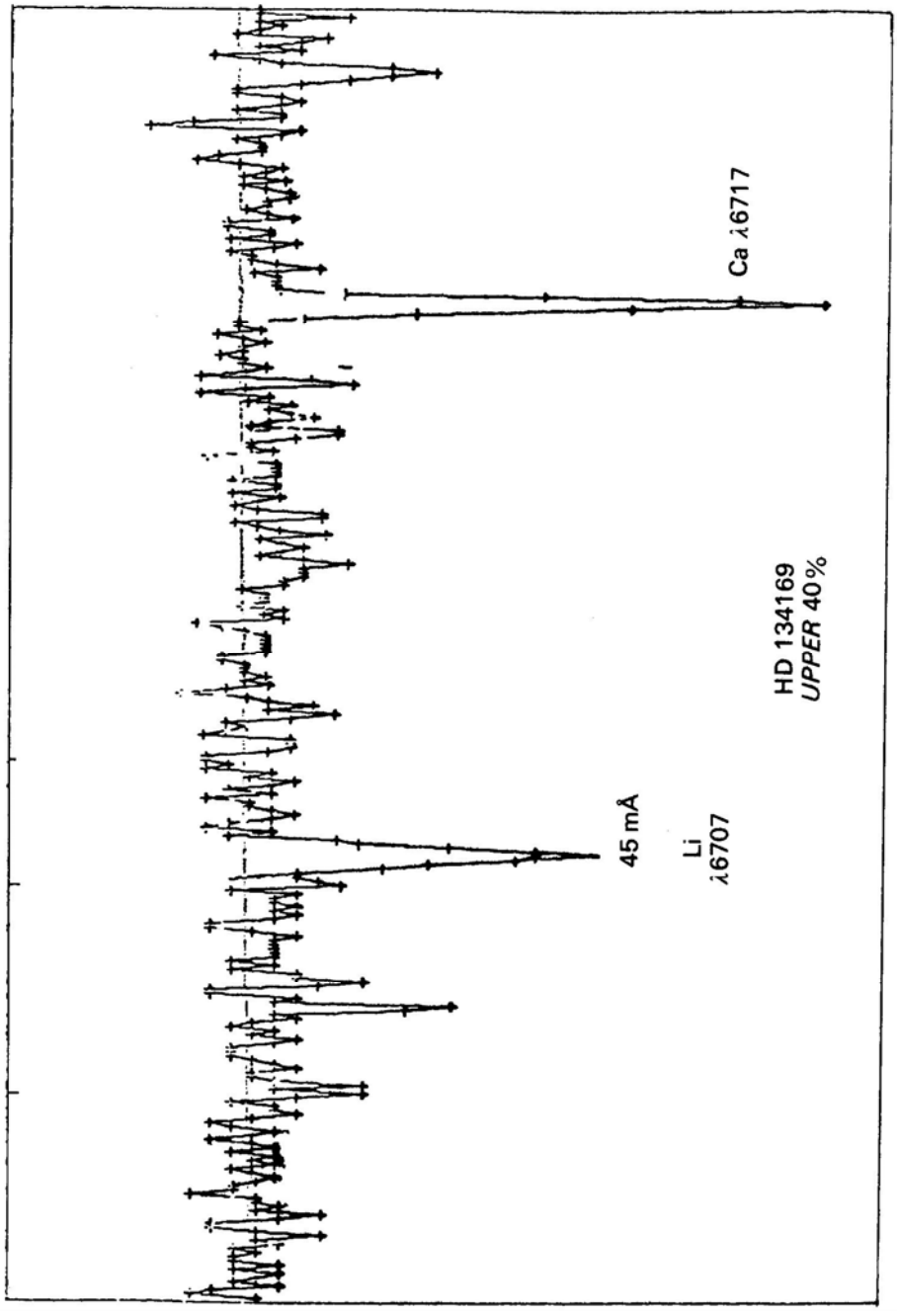

Figure 1. Spectrum of HD 134169 showing the upper 40 per cent of the flux.

colour or scan. It appears that Peterson and Carney's estimate of random errors of 80 K in the average of three measurements is conservative.

We conclude that random errors in the present temperature determinations, which are typically based on three independent sets of data, are approximately 60 K. It follows that we can estimate temperature differences between stars with a typical accuracy of about 80 K.

4. Abundances

Curves of growth for Li were computed using the program WIDTH6 (R. L. Kurucz 1983, personal communication) and model atmospheres of Bell *et al.* (1976). Computations were made for T_e =4500K, 5000K, 5500 K, and 6000 K; [Fe/H] =0, –1, and 2; log g= 4.5 and 3.75. The Li line was treated as a singlet although it is actually a close doublet since previous computations (Duncan 1981) showed this causes negligible error. Atomic parameters were the same as in Duncan (1981). Though there may be small systematic errors in the curves of growth, the dominant source of relative error is the temperature uncertainty. A typical error of 60 K in a star of temperature 5800 K and Li equivalent width 30 mÅ causes an abundance error of 0.06 dex.

5. Discussion

Li appears to be present in all our halo stars, with an abundance within about ± 0.2 dex of the value log *n*(Li) = 2.0 found by SS. Thus our results provide significant confirmation of their main conclusion, that in the halo stars one sees Li which was probably produced in the big bang.

However, we are less certain that it is an *unaltered* big bang product. Some halo stars of almost exactly the same temperature show differences in Li which may be real. Three examples are listed in Table 1. Although the stars are very similar physically, the Li abundances differ. However, since the temperature uncertainty contributes signify-cantly to the inferred Li abundance, we consider this evidence of differences to be marginal.

The abundance of Li in a wide variety of galactic locations has been found to be approximately log *n*(Li) = 3.0. These include the interstellar medium, young galactic clusters such as the Hyades (Cayrel *et al.* 1984), the T-Tauri stars, and also lunar samples (Dreibus, Spettel & Wanke 1976), and carbonaceous chondrites (Nichiporuk & Moore 1974). The Pleiades stars which show the least Li depletion (late F stars: Duncan & Jones 1982) also have the same abundance of approximately log *n*(Li) = 3.0. Thus the galactic Li abundance appears constant over at least the last 5 billion yr. The simple monotonic increase suggested by SS (Fig. 5) cannot be correct—it ignores the

Table 1. Observed and derived parameters for three stars from the sample.

HD	$R-I$	$V-K$	T_{scan}	T_{R-I}	T_{V-K}	$T_{adopted}$	[Fe/H]	W_{Li}(mÅ)
19445	0.34	1.39	5820	5770	5850	5810	−2.1	38±4
201891	0.33	1.42	5810	5830	5810	5810	−1.4	27±3
134169	0.33	1.46	—	5840	5780	5800	−1.3	46±3

meteoritic and lunar evidence. If the primordial big bang production of Li is approximately 2.0, a substantial galactic source of Li must have raised the abundance relatively early to log n(Li) = 3.0, but not increased it over the last 5 billion yr.

It also seems possible to us that the big bang production was log n(Li) = 3.0, and that the halo stars have in fact suffered some depletion (10 ×), but not as much as the Sun (100 ×). This, of course, depends on the star-to-star differences being real. The star-to-star differences would then represent scatter about the mean depletion curve, (*cf.* the scatter in Fig. 2 of Cayrel *et al.* 1984). We suggest that the value log n(Li) = 2.0 be taken as a lower limit to the big bang production.

References

Bell, R. A., Eriksson, K., Gustafsson, B., Nordlund, A. 1976, *Astr. Astrophys. Suppl.*, **23,** 37.
Boesgaard, A. M. 1985, *Publ. astr. Soc. Pacific*, **97,** 784.
Boesgaard, A. M., Steigman, G. 1985, *A. Rev. Astr. Astrophys.*, **23,** 319.
Carney, B. W. 1979, *Astrophys. J.*, **233,** 211.
Carney, B. W. 1983, *Astrophys. J.*, **88,** 623.
Carney, B. W., Peterson, R. C. 1981, *Astrophys. J.*, **251,** 190.
Cayrel, R., Cayrel de Strobel, G., Campbell, B., Dappen, W. 1984, *Astrophys. J.*, **283,** 205.
Dreibus, G., Spettel, B., Wanke, H., 1976, in *Proc. 7th Lunar Sci. Conf.*, New York, p. 3383.
Duncan, D. K. 1981, *Astrophys. J.*, **248,** 651.
Duncan, D. K., Jones, B. F. 1982, *Bull. am. astr. Soc.*, **14,** 866.
Hobbs, L. M. 1984, *Astrophys. J.*, **286,** 252.
Hobbs, L. M. 1985, *Astrophys. J.*, **290,** 284.
Nichiporuk, W., Moore, C. B. 1974, *Geochim. Cosmochim. Acta*, **38,** 1691.
Peterson, R. C., 1981, *Astrophys. J.*, **244,** 989.
Peterson, R. C, Carney, B. W. 1979, *Astrophys. J.*, **231,** 762.
Spite, F., Spite, M. 1982, *Astr. Astrophys.*, **115,** 357.
Spite, M., Maillard, J. P., Spite, F. 1984, *Astr. Astrophys.*, **141,** 56.
Wilson, R. E. 1953, in *General Catalogue of Stellar Radial Velocities*, Carnegie Institution of Washington, p. 601.
Yang, J., Schramm, D. N., Steigman, G., Rood, R. T. 1979, *Astrophys. J.*, **227,** 697.

Present address of Douglas K. Duncan: The Space Telescope Science Institute, 3700 San Martin Dr., Baltimore, MD 21218, USA.

J. Astrophys. Astr. (1987) **8,** 89–92

Recent Work on CNO in Dwarfs and Subdwarfs

Robert P. Kraft *Lick Observatory, Board of Studies in Astronomy and Astrophysics, University of California, Santa Cruz, California 95064, USA*

Abstract. The recent results on CNO in dwarfs and subdwarfs are discussed. The value of [O/Fe] $\simeq$ 0.0 at solar abundances but gradually increases with decreasing [Fe/H]. The value of [C/Fe] is constant at $\simeq 0 \,.\, 0^{+1}_{-2}$ as [Fe/H] declines from + 0.5 to –2.0; for [Fe/H] < – 2.0, [C/Fe] increases somewhat reaching a mean value near + 0.2 or + 0.3 dex. All the investigations agree that N has a strong primary component.

Key words: abundances, CNO—stars, dwarfs and subdwarfs

1. Preliminary remarks and caveats

In attempting to reconstruct the temporal behavior of the CNO group, students of galactic nucleosynthesis would like to have information on the abundances of these elements as closely as possible to the epoch of the formation of the Galaxy. The best the observers can do is to provide data from abundance analyses of the oldest stars. We must be careful, however, to study only those stars in which the atmospheres are uncontaminated by the dredge-up of nuclearly processed material from the interiors. Thus we reject giants and deal only with dwarfs and subdwarfs.

A review (Kraft 1985) of this problem was given only last May at the ESO Workshop on the *Origin and Distribution of the CNO Elements* where many of the results discussed here are plotted in graphical form. The reader is referred to that article for an extended discussion. Here, I provide only a summary and evaluation of the most recent results.

It must not be supposed that the derivation of CNO abundances is easy: there are many pitfalls and the stumbling blocks are probably greater for N than for C and O. Consequently, results for C and O can be quoted with greater certainty than for N. Briefly, we can catalogue the caveats by element, as follows:

For O: In the hotter subdwarfs, one analyzes the O I triplet near λ 7770, but the lower level of these lines lies at high excitation potential (9 eV) and thus the strengths are particularly sensitive to errors in temperature (recalling that kT~½ eV). For the cooler subdwarfs, one can use the [OI] pair near λ6300, but high spectral resolution is required: in the most metal-poor stars the equivalent widths are of order 10 mÅ. Recently some exciting new results have been derived from the study of the OH molecular features near λ3100, in the extreme (ground-based) ultraviolet. These will be discussed later in this session (Bessell & Norris 1987).

For C: C is mostly derived from the CH (G-band) feature (λ4300) which is strong and spectroscopically accessible in these stars. A small amount of work using atomic C I lines has been done, but the atomic lines suffer the same difficulty encountered in the

case of O I lines. Low resolution CH studies can be very reliable if spectrum synthesis is employed, but one has to give up any hope of deriving $^{12}C/^{13}C$-ratios.

For N: N has sometimes been derived from combining analyses of the CH (G-band) and CN (λ3880) features, but this approach is ill-advised, since a systematic error in C-abundances could introduce a spurious anticorrelation between C and N. Non-LTE effects are especially severe for CN (λ3880), but also may play a role in the analysis of the CH-feature already cited and the NH-feature at λ3360. The latter is far in the (ground-based) ultraviolet and, since the stars are rather red, high signal-to-noise spectra are obtained only with difficulty. Moreover, the dissociation potentials of both NH and CN are imperfectly known. However, low spectral resolution can be employed in the study of both the NH and CN bands if spectrum synthesis is available.

Finally, we note that CO-formation is an important consideration when deriving CH-band-based Cabundances for dwarfs with $T_{\rm eff} \lesssim 5500$ K, in constrast to giants in which CO formation plays no role above $T_{\rm eff} \sim 4500$ K because of reduced atmospheric pressure.

2. Results for oxygen

There is fundamental work by the Texas group on O (summarized by Clegg, Lambert & Tomkin 1981, but see Sneden, Lambert & Whitaker 1979 for the most metal-poor objects), in which the major result is that [O/Fe] $\simeq$ 0.0 at solar abundance but gradually increases with decreasing [Fe/H] to a more-or-less constant value near +0.6 when [Fe/H] < –1.0. Bessell & Norris (1987) will report later in this session that [O/Fe] is ~ +1.3 in the super metal-poor star CD – 38° 245, so there is a slight additional rise with decreasing [Fe/H]. However, [O/Fe] shows some scatter at a given [Fe/H] which is probably real and the present results, based as they are on a sample of only 20 or so stars, need to be supplemented. Systematic errors are difficult to assess, especially since only one group has extensively attacked the oxygen problem, but Gratton & Ortolani (1984) report a study of one metal-poor subdwarf in which they find [O/Fe] = + 0.3.

3. Results for carbon

The leading recent investigations have been those by Tomkin & Lambert (TL, 1984: high spectral resolution, small sample), Laird (1985: intermediate spectral resolution, sample size > 100 stars), and Carbon *et al.* (1985: low spectral resolution, ~·80 stars). In a plot of [C/Fe] as a function of [Fe/H], these investigations essentially agree in giving [C/Fe] ~ 0.0^{+1}_{-2} as [Fe/H] declines from +0.5 to – 2.0. The range quoted represents an estimate of the size of possible systematic errors, based on a comparison of investigations, but does not take into account possible errors of analysis that might be common to all (for example, errors introduced by non-LTE effects and from the fact that C and Fe are formed in rather different atmospheric layers).

The Carbon *et al.* investigation contains a significant sample of subdwarfs with [Fe/H] < – 2.0 (about 30 stars), whereas almost no very-metal-poor stars are found in the other two samples. This introduces a new element, *viz.*, that for [Fe/H] < – 2.0, [C/Fe] increases somewhat, to a mean value near +0.2 or +0.3 dex. Thus it appears

that carbon does not quite perfectly track Fe at very low metallicities, which suggests a partial return to the early Talbot/Arnett (Arnett 1978) nucleosynthetic scenario (*cf.* Tinsley 1979). In the past few days, I received from Chris Sneden a plot of [C/Fe] *vs* [Fe/H] based on recent high-resolution work by the Texas group which confirms the Lick group finding amongst very metal-poor subdwarfs, so that this carbon 'turn up' now seems quite firmly established.

On the basis of the low-metallicity sample of the Lick group, one finds that the slope of the mean relation between [C/Fe] and $T_{\rm eff}$, as $T_{\rm eff}$ decreases, depends on the choice of oxygen abundance through CO-formation: the slope is slightly positive if [O/Fe] = + 0.6 and negative if [O/Fe] = 0.0. The plot is horizontal if [O/Fe] = + 0.3. This result should be compared with the directly derived oxygen abundances and associated caveats cited above, *viz.*, [O/Fe] = + 0.6, for stars in this metallicity regime.

Summarizing, we conclude that the run of carbon-to-iron with decreasing [Fe/H] is quite well established, based as it is on a total sample of nearly 200 dwarfs and subdwarfs. The various investigations satisfactorily agree that [C/Fe] $\simeq$ 0.0, independent of metallicity from [Fe/H] = + 0.5 to – 2.0, but below – 2,0 there is some evidence for a small increase in [C/Fe] of 0.20.3 dex.

4. Results for nitrogen

Since the NH and CH bands are formed in the same atmospheric layers, we adopt [N/C] and [C/H] as dependent and independent variables, respectively. This is nearly equivalent to using [Fe/H] as independent variable, but not quite (Section 3). However, the situation in the case of nitrogen is not so firm as for carbon. The best that can be said is that all investigators (Barbuy 1981, 1983; Tomkin & Lambert 1984; Laird 1985; Carbon *et al.* 1985) agree on the main result, *viz.*, that nitrogen has a strong *primary* component. However, determination of the precise *ab initio* value, *i.e.*, [N/C] when [C/H] is below –2.0, depends strongly on each particular investigation. Both the Barbuy and TL samples are quite small and do not penetrate the domain of lowest metallicities. Altogether in the other two samples, over 150 stars were measured for N-abundance using the NH-bands. They are in reasonable agreement with each other (and are in agreement with TL) for [C/H] values above –1.5; below this value, $\langle$[N/C]$\rangle$ gradually increases to ~ +0.4 in the Laird investigation, but contrariwise $\langle$[N/C]$\rangle$ gradually decreases to ~ – 0.4 in the Carbon *et al.* investigation. In either case, there is simply too much nitrogen early on to maintain the proposition that N is a 'secondary' element (relative to carbon or iron), following the simple formulation [N/C] ~ [C/H].

Although a satisfactory explanation for the differences between investigators has not been found, all probably suffer from certain systematic errors. One in particular is actually shared by TL, Laird, and Carbon *et al.* All show a systematic decrease of $\langle$[N/C]$\rangle$ with decreasing $T_{\rm eff}$; the slope is the same for all and amounts to Δ [N/C] $\simeq$ 0.4 dex over the range 6250 K $\gtrsim T_{\rm eff} \gtrsim$ 5000 K. The differing spectral resolution employed by the investigators, ranging as it does from R ~ 100,000 down to R ~ 1000, does not seem to have much to do with it: unless one wants to believe that the abundance of N is a function of $T_{\rm eff}$ (or equivalently M_v) along the main sequence, one has to conclude that some error of analysis afflicts all the investigations in more-or-less the same way.

Finally, a few words about 'supernitrogen' stars. In a sample of ~ 25 subdwarfs and dwarfs, Bessell & Norris (1982) uncovered two metal-poor stars with nitrogen abundances enhanced by factors of 10 or more, giving rise to the expectation that such objects might form a quite significant component of the subdwarf population. However the much larger samples of Laird, and Carbon *et al.* taken together have revealed only two or three additional objects of this kind —four or five altogether —so the actual fraction is in the 1–5 per cent range. Carbon *et al.* speculated that these stars might have escaped from globular clusters, but evidence cited in the open discussions at New Delhi (Carney) suggests they are members of binary systems, as originally proposed by Bessell and Norris.

References

Arnett, W. D. 1978, *Astrophys. J.*, **219,** 1008.
Barbuy, B. 1981, *Astr. Astrophys.*, **101,** 365.
Barbuy, B. 1983, *Astr. Astrophys.*, **123,** 1.
Bessell, M. S., Norris, J. 1982, *Astrophys. J.*, **263,** L29.
Bessell, M. S., Norris, J. 1987, *J. Astrophys. Astr.*, **8,** 000.
Carbon, D., Barbuy, B., Kraft, R., Friel, E., Suntzeff, N. 1985, in preparation.
Clegg, R., Lambert, D., Tomkin, J. 1981, *Astrophys. J.*, **250,** 262.
Gratton, R., Ortolani, S. 1984, *Messenger*, No. 37, 3.
Kraft, R. 1985, in *Proc. ESO Workshop: The Origin and Distribution of CNO Elements.*, Eds I. J. Danziger, F. Matteucci & K. Kjar, ESO, Garching-bei-Munchen, p. 21.
Laird, J. 1985, *Astrophys. J.*, **289,** 556.
Sneden, G, Lambert, D., Whitaker, R. 1979, *Astrophys. J.*, **234,** 964.
Tinsley, B. 1979, *Astrophys. J.*, **229,** 1046.
Tomkin, J., Lambert, D. 1984, *Astrophys. J.*, **279,** 220.

J. Astrophys. Astr. (1987) **8,** 93–97

Nitrogen Enhancement in Metal-Poor Dwarfs: From Inside or Outside?

F. Spite & M. Spite* *Observatoire de Paris, Section de Meüdon, F 92195 Meudon Cedex, France*

Abstract. The five known metal-poor dwarfs with an enhanced N/Fe ratio have been observed spectroscopically. Two of these dwarfs have no lithium line; the absence of lithium is most probably accounted for by the usual convective destruction. The three other dwarfs have the same lithium abundance as the normal metal-poor dwarfs (Spite, Maillard & Spite 1984). This excludes the deep mixing process as the general source of nitrogen enhancement, since lithium is destroyed in deep (hot) layers. Deep mixing had been previously found unlikely in metal-poor dwarfs (Da Costa & Demarque 1982). The discussion stresses the remarkable uniformity of the lithium abundance in metal-poor dwarfs, and shows that the N-rich contaminating matter has a high N/H ratio. Finally, the Al abundance is not greatly enhanced in these five stars.

Key words: halo dwarfs—nitrogen abundance—lithium abundance—mixing

1. Introduction

Recently, Laird (1985) made a survey of nitrogen abundance anomalies in dwarfs, and among about 40 halo dwarfs he found 4 'nitrogen-rich' dwarfs. We have to clear here immediately two points about the vocabulary. We arbitrarily define halo dwarfs as those that have a metallicity lower than [Fe/H] = –1.0; this limit has already been proposed by Carney (1979), and Spite & Spite (1982). Following Laird, we call the stars 'nitrogen-rich' when the abundance ratio N/Fe is enhanced by more than about a factor of 3 (*i.e.* $\geqslant$0.5 dex). Obviously, since iron is very deficient in the stars discussed here, nitrogen is also deficient: it is only less deficient than the average.

In this way, Laird (1985) confirmed the discovery of two N-rich dwarfs by Bessell & Norris (1982) and added two more dwarfs. Laird proposed three explanations for these anomalies: primordial nitrogen enhancement, binary mass transfer and internal deep mixing.

2. Previous observations

It so happened that, in the course of a program of determination of lithium abundance (Spite &Spite 1982; Spite, Maillard & Spite 1984), we had already observed two of these stars: HD 25329 (Pagel & Powell 1966; Harmer & Pagel 1973) and HD 97916. The lithium line was absent in the spectra of these stars. As a first guess we thought that the

* Based on observations collected at ESO and CFHT.

enhancement of the N/Fe ratio was produced by the mixing of surface with deep layers of the dwarf (near the core) where nitrogen is formed. This would explain the absence of the lithium line, since lithium is destroyed in moderately deep layers of the stars, and more so in very deep layers. However this idea is not very appealing. Such a mixing is expected in globular cluster giants (Sweigart & Mengel 1979), but it seems practically impossible in dwarfs (Da Costa & Demarque 1982). Moreover, the absence of lithium in HD 25329 is normal for such a cool star: the other halo dwarfs of similar temperature have also a low lithium abundance. (Spite, Maillard & Spite 1984; Boesgaard & Steigman 1985).

The case of HD 97916 is more complicated. In an earlier work (Spite& Spite 1982) we found that an empirical limit seemed to exist at about [Fe/H] = – 1.0. The dwarfs which had a lower metallicity than this limit (*i.e.* [Fe/H] < –1.0) suffered no lithium destruction for $T_{\rm eff}$ > 5700 K. The dwarfs which had a larger metallicity than the limit (*i.e.* [Fe/H]> –1.0)were in the usual situation found in normal or slightly metal-poor stars: some suffered lithium destruction, some not.

The star HD 97916, with a metallicity [Fe/H] = –1.1 does not support the hypothesis of a limit at exactly [Fe/H] = –1.0. Hence Spite, Maillard & Spite (1984) proposed that the limit be pushed to –1.1, or preferably, that some kind of progressive effect be considered. Among dwarfs around solar temperature and solar metallicity, about 50 per cent have no detectable lithium (Spite 1982; see also Duncan 1981). Among dwarfs with intermediate metallicity, *i.e.* –1.3 < [Fe/H] < − 0.3, about 30 per cent have no detectable lithium; among very metal-poor dwarfs, *i.e.* [Fe/H] < –1.3, none is known, up to now, without a 'normal' lithium abundance (see also Duncan & Hobbs 1987; this issue).

These facts can be explained by noting that when the metallicity decreases, the opacity also decreases, which implies that the convection zone becomes shallower, which in turn leads to a smaller chance of lithium destruction. More specifically, the computations of W. Däppen (1982, personal communication; see also Cayrel 1986) show that the internal structure of metal-poor dwarfs is significantly different from the structure of normal dwarfs and should produce an effect similar to the observed one. It is also interesting to note that the limit at [Fe/H] = –1.0 previously proposed by Spite & Spite (1982) was linked with the opacity and internal structure problem. This limit also coincides, by chance, with the value of metallicity that discriminates (although not sharply) between halo and disc stars: such a limit was considered by several authors (see *e.g.* Carney 1979); this limit is thus linked with the chemical and dynamical evolution of the Galaxy. If we consider now a progressive effect, about the lithium destruction, and no specific limit, the problem of confusion between the two different limits does not arise any more.

Coming back to HD 97916, the lithium destruction in this star is not surprising, since it is only very slightly below the metallicity limit, the difference in metallicity being smaller than the error bar, and lithium destruction has been observed in many other stars at or slightly above the limit. Thus the observation of these two stars leads to inconclusive results, and it appeared interesting to observe the other members of the list of metal-poor N-rich dwarfs.

3. Observations

We observed the two N-rich dwarfs listed by Laird (1985) and the N-rich dwarf also noted by Carbon *et al.* (1986) who insist that such N-rich stars are very rare (only a few

per cent of the halo dwarfs). One of these stars was observed at the coudė spectrograph of the CFH 3.6 m telescope and the other two with the CASPEC spectrograph of the ESO 3.6 m telescope. The description of these stars may be found in Table 1.

The analysis of the stars was made by using a grid of model atmospheres by B. Gustafsson (1981, personal communication; Gustafsson *et al.* 1975). More details about the analysis may be found in another paper (Spite & Spite 1986).

The result is that the three stars (Table 2) have the 'normal' lithium abundance of the metal-poor dwarfs (Spite & Spite 1982; Spite, Maillard & Spite 1984). In other words, 4 of the nitrogen enhanced halo dwarfs including HD 25329 have about the same lithium abundance as the nitrogen-normal halo dwarfs of the same temperature. The lithium abundance of the star HD 97916 is easily compatible with the idea that, within error limits, it is not deviating from the lithium abundance of a nitrogen-normal metal-poor star of similar metallicity.

These results point to the conclusion that the lithium abundance has the same behaviour in metal-poor dwarfs either nitrogen-enhanced or not (Fig. 1). This discards any general explanation of nitrogen-enhancement by mixing of the surface with very deep layers of the dwarfs, and some other process has to be responsible for the nitrogen enhancement. Our observations also bring out an interesting information: in order to increase the N/Fe ratio without lowering the Li abundance (the Li/H ratio) the contaminating nitrogen-rich matter had necessarily to have a high N/H ratio.

As previously noted, the nitrogen enrichment observed in some giant stars in globular clusters may be attributed to mixing, but such a mixing should be different from the mixing considered for the dwarfs. Such giants have enhanced sodium and

Table 1. Main characteristics of nitrogen-rich stars.

	$\log T_{\rm eff}$	$\log g$	[Fe/H]	Ref.	[N/Fe] (Laird)	[N/Fe] (Carbon)
HD 25329	3.685	4.0	−1.5	(1, 6)		+0.45
HD 74000	3.794	4.5	−1.8	(2)	+1.7	+0.9
HD 97916	3.787	4.0	−1.1	(3)	+0.8	
HD 160617	3.768	3.5	−1.6	(4)	+1.7	
HD 166913	3.787	4.3	−1.8	(5)	+0.7	

References:
(1) Spite, Maillard & Spite (1984)
(2) Peterson (1978a)
(3) Peterson (1978b)
(4) Perrin (1986)
(5) Laird (1985)
(6) See also Pagel & Powell (1966); Harmer & Pagel (1973) for nitrogen abundance of HD 25329

Table 2. Abundance of lithium in nitrogen-rich halo dwarfs.

	$W_{\rm Li}$	$N_{\rm Li}$
HD 25329	<3	<0.0
HD 74000	24.5	2.16
HD 97916	<3	<1.2
HD 160617	42	2.20
HD 166913	40	2.17

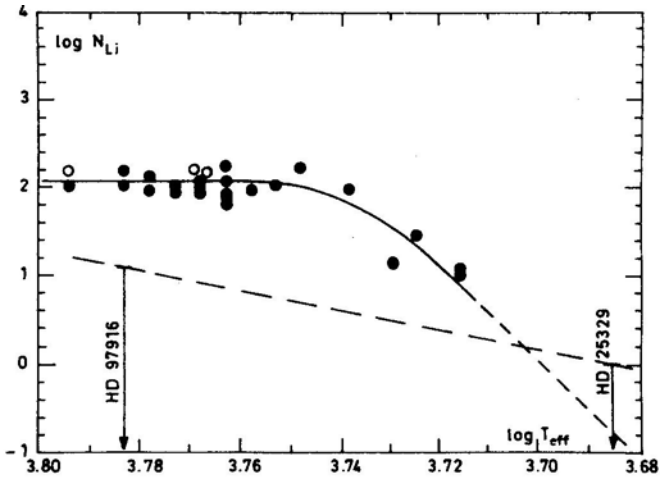

Figure 1. The lithium abundance log N_{Li} (in the standard scale where log N_H = 12) in halo dwarfs, according to Spite, Maillard & Spite (1984) with a few additional stars. The nitrogen-rich metal-poor stars are represented by open symbols when their lithium abundance is measurable; when the lithium line is not detected, an arrow is drawn, originating at the maximum possible abundance. The dashed line represents the detection limit on our CFHT spectra (*i.e.* the lithium abundance corresponding to an equivalent width W_{Li}=3 mÅ)

aluminium abundances (Cottrell & Da Costa 1981). It is interesting to check if this effect is also present (and stronger) in the N-enriched dwarfs.

In four of the dwarfs, the red Al doublet is not detectable, as it should be if the Al abundance is not greatly enhanced. In HD 97916 the Al doublet is measurable and leads to an abundance [Al/Fe] = + 0.12 (Francois 1986), which is normal for halo dwarfs. These observations show that the aluminum abundance is not *greatly* enhanced in the N-enriched halo dwarfs.

4. Conclusion

The observations described above show that

1. Lithium is present with 'normal' abundance in three of the nitrogen-enhanced metal-poor dwarfs, absent in the coolest one (as expected) and, not surprisingly, absent in the fifth star. Generally speaking, lithium behaves similarly in N-enhanced and in 'normal' metal-poor dwarfs. This excludes mixing as a general explanation of nitrogen enhancement, since lithium is destroyed in deep layers.

   At this IAU meeting (New Delhi 1985) Bruce Carney and David Latham announced that the metal-poor dwarfs with an enhanced N/Fe ratio are spectroscopic binaries or suspected binaries, so that the final (general) explanation for N enhancement is probably the binary mass exchange.
2. As previously noted (Spite, Maillard & Spite 1984) the lithium abundance of metal-poor dwarfs is noticeably constant and independent of the temperature (for T_{eff} > 5500K), mass, metallicity (for [Fe/H] < –1.0 or –1.1), galactic orbit and eccentricity of the star. These observations show that this abundance is also independent of the N/Fe ratio.

3. The contaminating (N-rich) matter has therefore a high N/H ratio, in order to be able to enhance the nitrogen abundance in the star without lowering the lithium abundance.
4. The A1/Fe ratio is not *greatly* enhanced in these stars.

Acknowledgments

It is not so often that several conclusions may be drawn from the analysis of only 5 stars. This was only possible owing to the work of those who built efficient telescopes, spectrographs and detectors, and maintained them, and also because of those who made extensive surveys and selected the stars which are of special interest. We are especially indebted to R. Cayrel, W. Däppen and P. Francois for communication of results before publication.

References

Bessell, M. S., Norris, J. 1982, *Astrophys. J.*, **263,** L29.
Boesgaard, A. M., Steigman, G. 1985, *A. Rev. Astr. Astrophys.*, **23,** 319.
Carbon, D. F., Barbuy, B., Kraft, R. P., Friel, E. D., Suntzeff, N. B. 1986, in press.
Carney, B. W. 1979, *Astrophys. J.*, **233,** 211.
Cayrel, R. 1986, in preparation.
Cottrell, P. L, Da Costa, G. S. 1981, *Astrophys. J.*, **245,** L79.
Da Costa, G. S., Demarque, P. 1982, *Astrophys. J.*, **259,** 193.
Duncan, D. K. 1981, *Astrophys. J.*, **248,** 651.
Duncan, D. K., Hobbs, L. M. 1987, *J. Astrophys. Astr.*, **8,** 83.
Francois, P. 1986, *Astr. Astrophys.*, **160,** 264.
Gustafsson, B., Bell, R. A., Eriksson, K., Nordlund, A. 1975, *Astr. Astrophys.*, **42,** 407.
Harmer, D. L., Pagel, B. E. J. 1973, *Mon. Not. R. astr. Soc*, **165,** 91.
Laird, J. B. 1985, *Astrophys. J.*, **289,** 556.
Pagel, B. E., J., Powell, A. L. T. 1966, *R. Obs, Bull.* No. 124.
Perrin, M. N. 1986, *Astr. Astrophys.*, **159,** 239.
Peterson, R. 1978a, *Astrophys. J.*, **222,** 181.
Peterson, R. 1978b, *Astrophys. J.*, **222,** 595.
Spite, M., Maillard, J. P., Spite, F. 1984, *Astr. Astrophys.*, **141,** 56.
Spite, M., Spite, F. 1982, *Astr. Astrophys.*, **115,** 357.
Spite, F., Spite, M. 1986, *Astr. Astrophys.*, **163,** 140.
Sweigart, A. V., Mengel, J. G. 1979, *Astrophys. J.*, **229,** 624.

J. Astrophys. Astr. (1987) **8,** 99–102

Relative Elemental Abundances in Extremely Metal-Deficient Stars

M. S. Bessell & John Norris *Mount Stromlo and Siding Spring Observatories, The Australian National University, Private Bag, Woden P.O. ACT 2606, Australia*

Abstract. The relative elemental abundances in an extremely metal-deficient star CD – 38° 245 with [Fe/H] ~ – 4.5 and in similar stars are discussed.

Key words: stars, abundances—stars, metal-deficient

1. Introduction

The composition of field halo stars was recently summarized in an excellent review by Spite & Spite (1985). In this report we will supplement that review by discussing our published results for CD – 38° 245, a giant star with [Fe/H] ~ – 4.5 (Bessell & Norris 1984), and some unpublished results on nickel and oxygen abundances in extremely metal-deficient ([Fe/H] < –2.0) stars.

Most of the exciting new results in abundance analyses recently have come from the high signal-to-noise red-sensitive detectors such as the reticon and the CCD; however, we have been using a very-blue-sensitive photon-counting system (IPCS) in the ultraviolet ($\lambda\lambda$ 3100 –λ3500) to measure primarily, molecular lines of OH, CH, and NH (Bessell & Norris 1982), and low excitation lines of Ni I, Cr II, Mn II, Ti II, and V II in GK stars of low metallicity. The preliminary results from that work will be discussed here.

There is considerable evidence that oxygen is less deficient than iron in metal deficient objects (*cf.* Sneden 1985). The abundance of oxygen in cool stars is normally derived from the forbidden O I lines (λ6300, λ6363) in giant stars, and from the O I triplet (λ7772–λ7775) in hotter dwarf stars. These lines are generally weak in normal stars, either because they are forbidden, or because the excitation potentials of the permitted lines are so high. In metal-deficient stars they become vanishingly small; HD 122563 (T_e = 4500 K, [Fe/H] = –2.6) has a [O I] λ6300 line of only 6 mÅ equivalent width. Bessell, Hughes & Cottrell (1984) computed synthetic spectra of OH lines in GK giants and dwarfs, and showed that these lines can be very strong in extremely metal-deficient models and would serve as a valuable way to derive oxygen abundances when the normal methods are impractical. With the AAT 3.9 m telescope and the IPCS detector we now have OH observations at 3.3 Å mm^{-1} dispersion or 0.15 Å resolution for eight stars (2 dwarfs, 6 giants) with [Fe/H] < – 2.2, including three with [Fe/H] < –3.0. In addition, we determined to derive Ni abundances in CD –38° 245 and other extreme stars to examine the results of Luck & Bond (1983), who found Ni to be overabundant with respect to Fe by up to 0.5 dex at [Fe/H] ~ –2.5. Luck & Bond used Ni lines in the red, but we chose to use the strong Ni lines near λ3400 which Would be easily seen in stars as deficient as CD –38° 245. These ultraviolet spectral regions also contain lines of the alpha-rich nuclei Ti, V, Cr, Mn whose relative abundances are of interest in metal-poor stars.

2. Discussion

Ground-based ultraviolet observations are normally considered difficult because of atmospheric absorption; however, although the base extinction is higher than in the blue, the additional ozone absorption component comprises broad shallow bands which are easily removed using the spectrum of a continuous source, such as a broad-line B star. The worse problem is normally the efficiency of the gratings. Most commonly available gratings are blazed for the first or the second order wavelengths in the blue or yellow, and have very low efficiency in the violet; we obtained high efficiency by using a 1200-line grating blazed at λ3300 in the third order.

A list of metal lines was selected for the region λ3100 –λ3200 from the Utrecht Solar Atlas (Moore, Minnaert & Houtgast 1966). Oscillator strengths were taken from references given by Miller, Fuhr & Martin (1980), or if unavailable, from Kurucz & Peytremann (1975). This short list was adequate for the hotter (T_e> 4700 K) and most metal-deficient stars, but for the stronger-line stars it was apparent that a more complete list of metal lines was necessary. Kurucz (1986, personal communication) recently has kindly sent us a provisional list based on his computations, and we will use this data for the final analyses. The OH line list was described in Bessell, Hughes & Cottrell (1984), and was taken from Goldman & Gillis (1981).

In Fig. 1 is shown a part of the observed spectrum for the extreme subdwarf HD 140283, [Fe/H] = –2.65, T_e = 5650 K, log g = 3.50, in the vicinity of the CH C – X

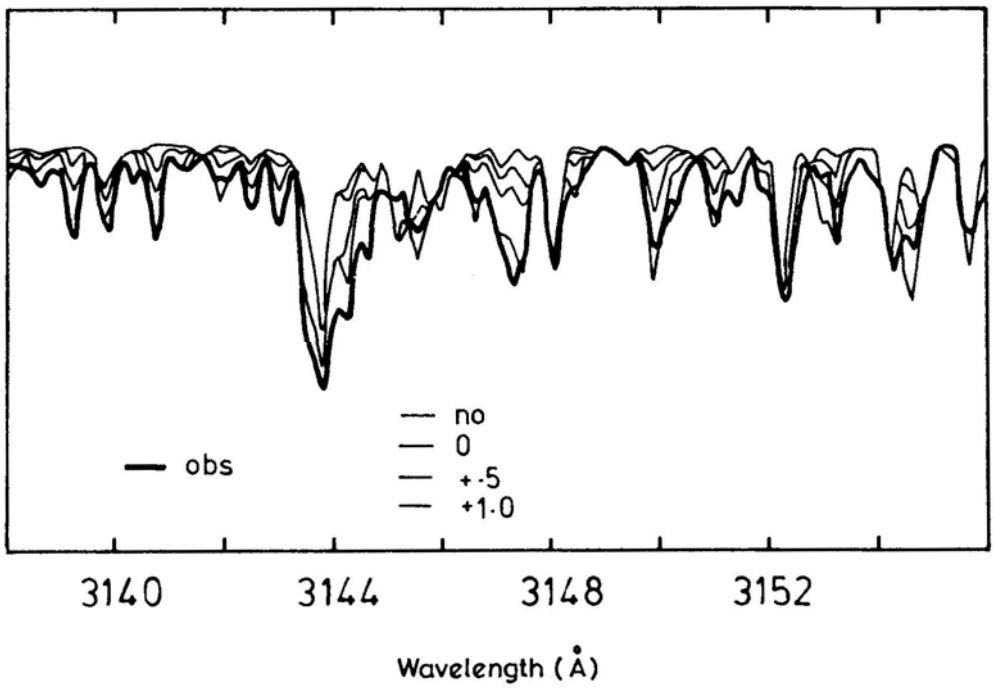

Figure 1. Observed spectrum of HD 140283 (heavy line) compared with a series of synthetic spectra with [O/Fe]= –2.0, 0.0, +0.5 and +1.0 dex. The best fitting synthetic spectrum has [O/Fe] ~ + 0.9 dex.

band; many strong OH lines from the (0, 0) and (0, 1) bands dominate the spectrum. Superimposed are the synthetic spectra corresponding to four values of [O/Fe], –2.0 dex (zero oxygen), + 0, + 0.5, and + 1.0 dex. Clearly an overabundance of [O/Fe] ~ + 0.9 is indicated. Six other halo stars with similar Fe abundance gave similar O overabundance and in a very exciting observation we detected OH in CD –38° 245 (T_e = 4500 K, log g = 2.0, [Fe/H] = – 4.5). yielding [O/Fe] = +1.3.

Fine-analyses using WIDTH6 (Kurucz 1975, personal communication) were made for individual unblended lines of Ni I, Ti II, Cr II, Mn II and V II measured in the λ3360– λ3500 and λ3100 –λ3200 regions. No evidence was found for Ni overabundance in any of the stars observed, including two found most overabundant by Luck & Bond (1983). Barbuy, Spite & Spite (1985, and references therein), and Leep & Wallerstein (1981) also find no evidence for Ni overabundance in three very-metal-poor stars. The alpha-rich elements showed the expected odd-even abundance effect, and the overabundance of Ca and Ti, relative to Fe, seen in previous analyses of metal-poor stars is seen to be the case for the alpha-rich elements in general.

In Fig. 2 are plotted schematically the relative abundances of HD2796 an archetypal [Fe/H] = –2.4 giant, and CD–38° 245. The data are taken from Bessell & Norris (1984), supplemented with the data discussed here. It is clear that the character of the relative abundances in the two stars is similar and that we are probably seeing the underlying trends of element synthesis in the early stages of galactic chemical enrichment. We are continuing the search for more extreme metal-poor stars [Fe/H] < – 3.0, to find how uniform these chemical enrichment processes were in the field. The increasing use of echelle spectrographs and the possibility of using high signal-to-noise blue-sensitive CCDs will produce remarkable improvements in our knowledge of abundances of metal-poor systems in the next few years.

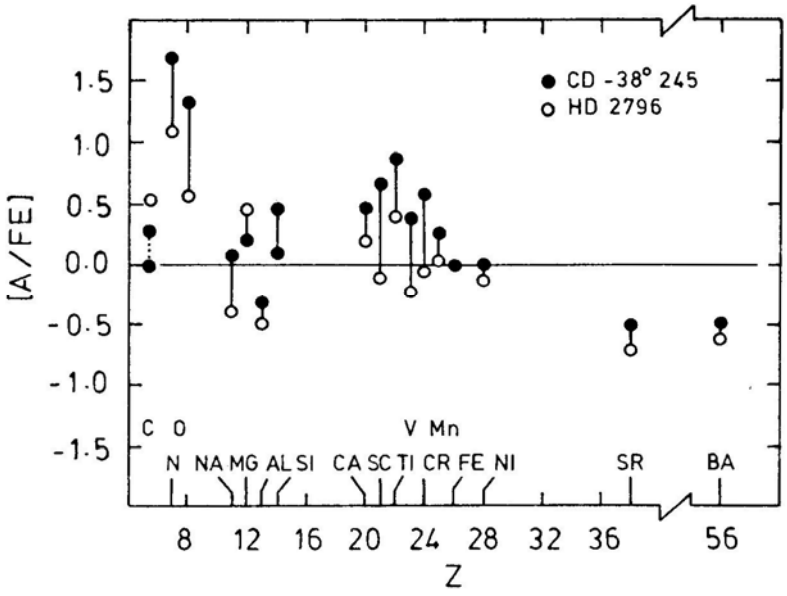

Figure 2. Relative abundances of HD 2796 and CD –38° 245.

References

Barbuy, B., Spite, F., Spite, M. 1985, *Astr. Astrophys.*, **144,** 343.
Bessell, M. S., Hughes, S., Cottrell, P. L 1984, in *proc. astr. Soc. Australia,* **5,** p. 547.
Bessell, M. S., Norris, J. E. 1982, *Astrophys. J.,* **263,** L29.
Bessell, M. S., Norris, J. E. 1984, *Astrophys. J.,* **285,** 622.
Goldman, A., Gillis, J. R. 1981, *J. quantit. Spectrose. radiat. Transfer,* **25,** 111.
Kurucz, R. L., Peytremann, E. 1975, *SAO Special Rep.* 362.
Luck, R. E., Bond, H. E. 1983, *Astrophys. J.,* **271,** L75.
Miller, B. I, Fuhr, J. R., Martin, G. A. 1980, *N BS Special Publ.,* **505,** Suppl. 1.
Moore, C. E., Minnaert, M. G. J., Houtgast, J. 1966, *NBS Monograph* no. 61.
Sneden, C. 1985, in *Proc. ESO Workshop: The Origin and Distribution of CNO Elements,* Eds I. J, Danziger, F. Matteucci & K. Kjär, ESO, Garching-bei-München, p. 1.
Spite, M., Spite, F. 1985, *A. Rev. Astr. Astrophys.,* **23,** 225.

J. Astrophys. Astr. (1987) **8,** 103–122

Chemical Evolution of the Galaxy: Abundances of the Light Elements (Sodium to Calcium)

David L. Lambert *Department of Astronomy, University of Texas, Austin, Texas 78712-1083, USA*

Abstract. The abundances of the light (Na to Ca) elements in disc and halo stars are reviewed. New analyses are emphasized. Elements considered are the α-nuclei (Mg, Si, and Ca), and the odd-even nuclei (Na and Al, also ^{25}Mg and ^{26}Mg).

The α-nuclei are overabundant (relative to Fe) in the old disc and halo stars. Halo stars ([Fe/H] < —1.2) have [α/Fe] ~ 0.3 with extreme halo ([Fe/H] $\lesssim -$ 2.0) stars showing possibly higher overabundances. The scatter in [α/Fe] at a given [Fe/H] is small. To within the observational errors, the abundance patterns for Mg, Si, and Ca are identical.

For disc stars, the Na and Al abundances relative to Mg are almost independent of the [Fe/H]. Halo stars ([Fe/H] < –1) show [Na/Mg] < 0 and [AI/Mg] < 0, but the form of the mean relation and the scatter about the relation between [odd-even/Mg] and [Fe/H] remains uncertain.

Key words: Galaxy, chemical evolution—abundances, light elements

1. Introduction

This brief review examines the status of determinations of the abundances of the light elements—sodium to calcium—in stars of differing metallicities (*i.e.*, iron abundance). The review may be timely in as much as new results of unprecedented precision are becoming available as high quality, high resolution spectra are obtained and analysed in increasing numbers. Application of solid-state detectors such as the Reticon and charge-coupled device are revolutionizing quantitative stellar spectroscopy. For the galactic disc population which is well represented by bright stars, the revolution is providing abundances of high accuracy; an aim of this review is to illustrate this accuracy. For the halo population, the initial impact of the revolution will be to enlarge the sample of analysed stars with reliably determined abundances.

Throughout the review, 'the *X* abundance' is taken to be the ratio of *X* to hydrogen by number of atoms. I denote this ratio by $\varepsilon(X)$ and usually give log e(*X*) on the standard scale such that log ε(H) = 12.0. For convenience, stellar abundances are often referenced to the solar values. Then, the standard notation

$$[X] = \log \varepsilon(X)_{\rm star} - \log \varepsilon(X)_{\rm sun}$$

is adopted. In much of the discussion, I examine how the abundances of the light elements vary with respect to iron, *i.e.*, I consider the change of [light/Fe] with [Fe/H].

Iron is a spectroscopically convenient choice as a representative of the iron-peak. Reference of the light elements to the iron-peak is a significant step because the two groups may well have different nucleosynthetic origins. I define 'light elements' to be bounded by Na and Ca.

Too little information is available on the evolution of the He abundance over its big-bang level. Lithium, beryllium and boron abundances reflect a different set of production and destruction processes to those betrayed by the light elements. Carbon, nitrogen, and oxygen abundances in metal-poor stars are discussed by Kraft (1987) in this volume. Fluorine and Ne are omitted for lack of information on their abundances in stars. With a study of the light elements in stars of differing metallicity (*i.e.*, determinations of [light/Fe]), the iron-peak is brought within the scope of the review; I do not, however, discuss the metallicity-age relation.

The main thrust here is to pose and answer a few simple questions about the abundances of the light elements:

What is the mean relation between [light/Fe] and [Fe/H] in the disc and the halo?

Is the scatter in [light/Fe] at a given [Fe/H] significantly greater than the measurement errors?

Do the even-even (or α) nuclei (*e.g.*, ^{24}Mg, ^{28}Si) and odd-even nuclei (*e*.g., ^{23}Na, ^{27}A1, ^{25}Mg) show different trends with metallicity?

Few interpretive remarks are provided to relate the abundances to the theory of stellar nucleosynthesis. The emphasis is on new results for the light element abundances. I omit P, S (Clegg, Lambert & Tomkin 1981), C1, Ar, and K (Gratton & Sneden 1986) for which little or no information is available. In a concluding section, I sketch the variation of [*X*/*Fe*] with [Fe/H] for the light elements as well as additional groups of elements (CNO, the *s*- and *r*-process heavy elements) in both disc and halo stars.

2. A survey of the abundances

2.1 *Recent Investigations*

With the advent of new spectrometers of high sensitivity, several studies of the abundances in metal-poor stars have been completed recently. Although constraints of time and space discourage me from attempting a complete cataloguing and critical discussion of the many earlier publications on the abundances in metal-poor stars, I must emphasize that the gross systematics of the abundance variations were uncovered long ago. Certain key references are provided. I apologize to any author whose papers have been (apparently) overlooked.

Five recent papers are the basis for my discussion:

1. Tomkin, Lambert & Balachandran (1985, hereinafter TLB): High-resolution red and near-infrared Reticon spectra from the McDonald Observatory were used with scaled solar (Holweger & Müller 1974) models and solar g*f*-values to derive Na, Mg, Al, Si, Ca, Sc, and Fe abundances for 20 F, G, or K dwarfs of the galactic disc ([Fe/H] $\gtrsim$ –0.9). Effective temperatures were taken from colours and the Hβ index and published calibrations (see Clegg, Lambert & Tomkin 1981, hereinafter CLT). Surface gravities were computed from the absolute magnitudes, the effective temperatures, and estimates of the stellar mass (see CLT)

2. Luck & Bond (1985, hereinafter LB): Image-tube echelle spectrograms of 36 metal-poor field red giants, solar g*f*-values, MARCS model atmospheres (Gustafsson *et al.* 1975; Bell *et al.* 1976), and a LTE line analysis program provide abundances for a range of elements from oxygen to europium. The appropriate $T_{\rm eff}$ and log g for the model were determined from the Fe I and Fe II lines by the usual means. Of the light elements, Mg and Ca are best represented, with useful data also provided for Si. Unfortunately, the odd-even pair—Na and Al—are represented by just one or two lines and in only a few of the 36 stars. The value of the sample is that all but two of the stars belong to the halo; *i.e.*, [Fe/H] < –1.0 with a minimum and a mean abundance of –3.0 and –1.9, respectively.

3. Nissen, Edvardsson & Gustafsson (1985, hereinafter NEG): High-resolution Reticon spectra from ESO's coudé echelle spectrometer (CES) provide high S/N spectra of 29 disc dwarfs of F type in selected intervals from which abundances of a selection of light through heavy elements are derived using MARCS models and solar g*f*-values. The basic parameters—$T_{\rm eff}$ and *log g*—are computed from Strömgren photometric indices.

This analysis appears to be the most precise of the quintet highlighted here; for example, the rms scatter of the [Fe/H] values from about 20 Fe I lines is only 0.05 dex for a typical star—*all* values fall within ±0.10 dex of the mean. The light elements available are Na, Mg, Al, Si, and Ca. Titanium which behaves much like an α-element was also included along with Ni, and the heavy elements Y and Ba.

4. Francois (1986, hereinafter F): High-resolution Reticon spectra from the CES at ESO and the coude spectrometer of the CFHT provide abundances of Na , Mg, Al, Si, and Fe in up to 36 field dwarf stars including a few halo stars. Defining parameters—$T_{\rm eff}$ and log g—were taken from published analyses as provided by the 'Catalogue of [Fe/H] Determinations' (Cayrel de Strobel *et al.* 1985). MARCS models with solar g*f*-values were adopted for the abundance analysis.

5. Gratton & Sneden (1986, hereinafter GS): This ambitious survey of the light elements examined 62 stars of types F, G, K and luminosity classes V to III with known iron abundances, and belonging to the metal-rich disc to the extreme halo. Approximately half of the sample belong to the halo (*i.e.*, [Fe/H] < – 1)and one quarter to the extreme halo (*i.e.*, [Fe/H] < –2). High resolution spectra were acquired at the McDonald and ESO observatories using various detectors (Reticon, Digicon, CCD). The method of abundance analysis incorporates MARCS models and solar g*f*-values. A star's $T_{\rm eff}$ was derived from colour indices. The surface gravities for dwarfs were calculated from the M_V's, bolometric corrections, and an assumption about the stellar mass (0.7 to 1.0 $M_\odot$ according to absolute luminosity). For the giants, the surface gravities appear to be based primarily on the stellar spectroscopists' customary insistence that neutral and ionized lines of the same element (often, Fe) yield the same abundance. Light elements generally examined were Na, Mg, Al, Si, Ca, and K(also Ti). The iron peak was represented by Fe in all stars, Ni in almost all stars, and Sc and V in many stars.

Space (and time) limitations prevent me from providing a critical assessment of these abundance analyses. I shall let the plots of the abundance variations ([*X*/Fe] versus [Fe/H]) portray the remarkably high degree of agreement and betray the few remaining irritating inconsistencies between these (and other) investigations of the evolution of light elements.

2.2 *The α-Elements*

The α-elements provided to varying levels of completeness by the five sources are Mg, Si, and Ca. In Fig. 1, 1 show [Si/Fe] versus [Fe/H] for four of the samples; the fifth (LB) is the only sample to be based on photographic spectra. Each of the α-elements shows a similar trend with declining Fe abundance. In an attempt to reduce the scatter, I computed the mean abundance (see Fig. 2). This mean is based on at least two of the three α-elements. Inspection of these two figures shows that the scatter at a fixed [Fe/H] is reduced noticeably in Fig. 2 relative to Fig. 1.1 suggest that this reduction results from a partial cancellation of measurement errors when the mean [α/Fe] is computed. In Figs 3 and 4, I compare the Mg and Ca abundances given by the two sources (LB and GS), that provide a thorough sample of halo stars, and by Peterson (1981, hereinafter P), whose careful analyses are based on photographic high-dispersion spectra of old disc and halo dwarfs. Finally, Fig. 5 compares the mean [α/Fe] abundances versus [Fe/H] for the LB and GS samples; the contributors to the means are Mg and Ca, for LB's sample, and Mg, Si, and Ca, for GS's samples.

How does the abundance of α-elements vary relative to the iron abundance in disc and halo stars? Examination of Figs 2 and 5 suggests the following variations:

In stars of approximately solar metallicity, [α/Fe] is apparently constant. The mean value may be slightly positive; *i.e.*, the Sun is apparently slightly deficient in the α-elements. The scatter in [α/Fe] is small.

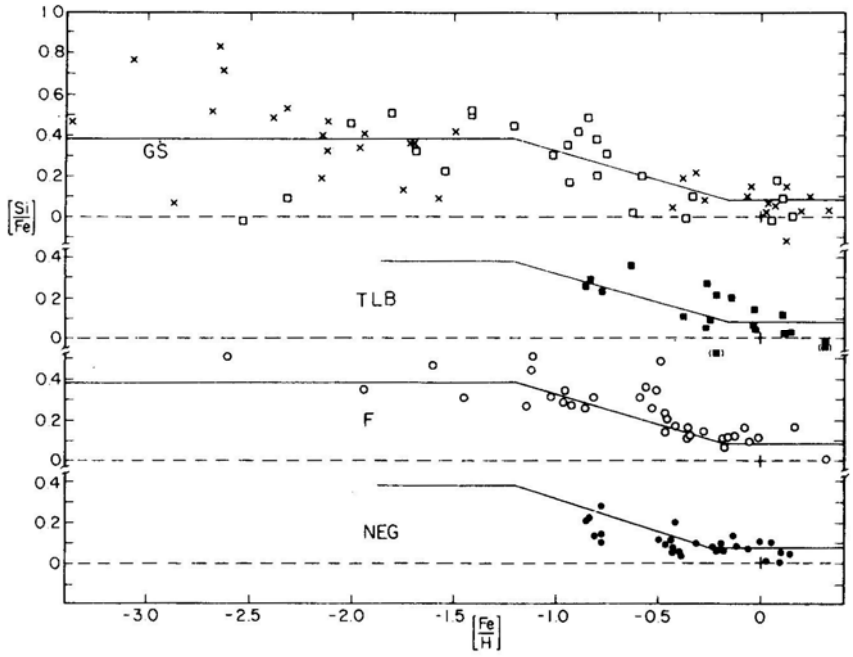

Figure 1. [Si/Fe] as a function of [Fe/H] for the samples analysed by GS, TLB, F, and NEG. Giants (log g <3.0)in GS's sample are denoted by crosses, and dwarfs and subgiants (log g $\geqslant$3.0) by open squares. The points corresponding to the two K0 dwarfs in TLB's collection of dwarfs are placed in parentheses. The identical lines drawn through the data are approximate fits, not least-squares solutions.

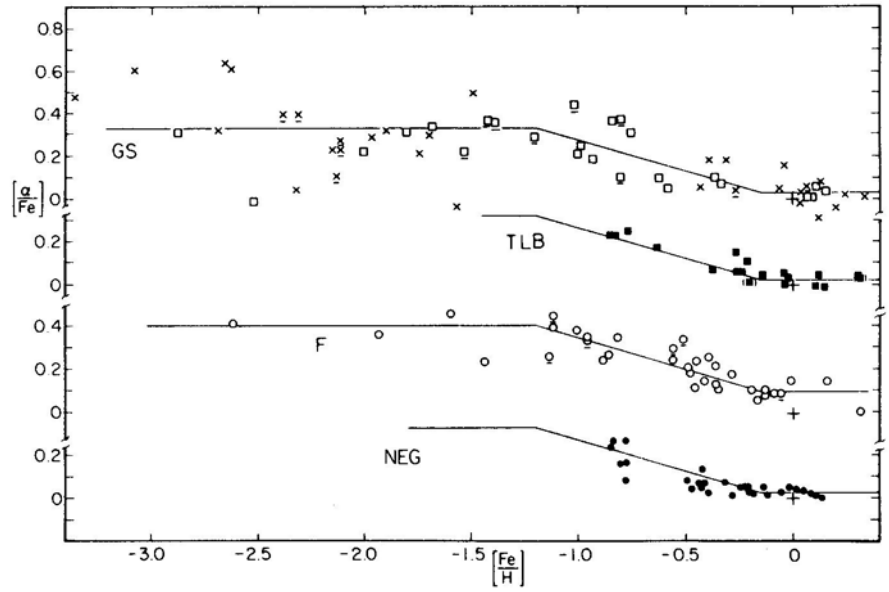

Figure 2. [α/Fe] as a function of [Fe/H] for the samples analysed by GS, TLB, F, and NEG. See caption to Fig. 1 for comments on the symbols. The elements contributing to [α/Fe] are Mg, Si, and Ca for the GS, TLB, and NEG samples and Mg and Si for F's samples. For those stars where the abundance of one of the contributors to the mean [α/Fe] was unavailable, the symbol is underlined. Several stars for which GS provide just one of the three contributing abundances are not plotted. The lines drawn through the data are approximate fits and are identical except for slight offsets in [α/Fe].

In metal-poor disc stars, [α/Fe] increases approximately linearly with decreasing [Fe/H]. This increase begins at [Fe/H] = –0.2 ± 0.1 and terminates at [Fe/H] = –1.2 + 0.1. The scatter in [α/Fe] at a given [Fe/H] is small.

In halo stars, [α/Fe] is approximately constant with that [α/Fe] = +0.3 ± 0.05 relative to its value in stars of solar metallicity. The scatter (Fig. 5) in [α/Fe] at a given [Fe/H] may be larger than in the disc stars.

On the figures, we represent this variation of [α/Fe] by lines constructed according to the prescription

$$[\alpha/\mathrm{Fe}] = A_\alpha \quad \text{for } [\mathrm{Fe/H}] \geqslant -0.15,$$

$$[\alpha/\mathrm{Fe}] = A_\alpha - 0.286\,([\mathrm{Fe/H}] + 0.15) \quad \text{for } -1.2 \leqslant [\mathrm{Fe/H}] \leqslant -0.15,$$

$$[\alpha/\mathrm{Fe}] = A_\alpha + 0.30 \quad \text{for } [\mathrm{Fe/H}] < -1.2.$$

The constant A_α =0.05 appears to fit most of the data; *i.e.*, the Sun appears to be slightly α-poor relative to the majority of stars of the same metallicity. However, systematic errors are likely to be of the same order of magnitude; *e.g.*, a revision of the temperature scale by about 100 K suffices to reduce A_α to zero for Mg and Si. Furthermore, the many similarities between the five (and other) selected recent analyses ensure that all may be afflicted by similar systematic errors. It would be interesting to undertake a detailed analysis of the Sun and stars in order to determine both A_α and the intrinsic

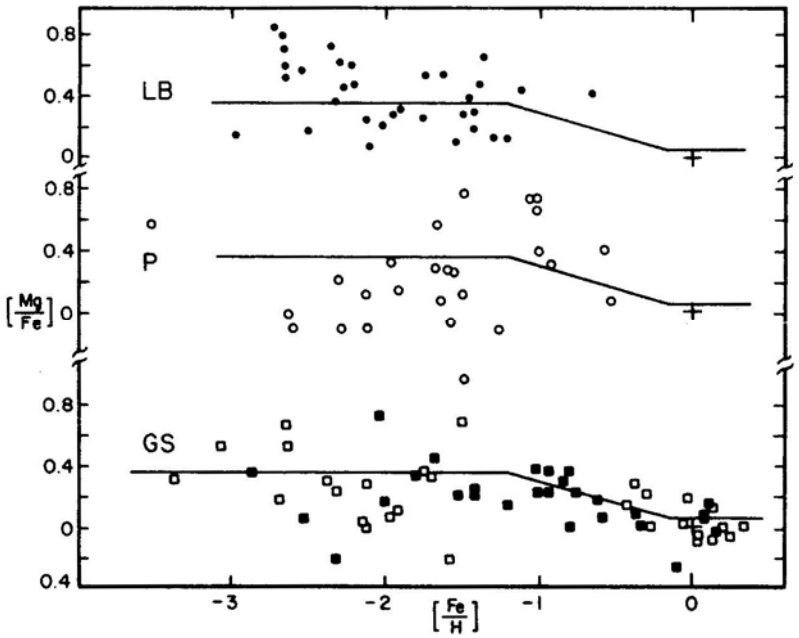

Figure 3. [Mg/Fe] as a function of [Fe/H] for the samples analysed by LB, GS and Peterson (1981; hereinafter. P).Giants (log g < 3.0) in GS's sample are denoted by open squares, and dwarfs and subgiants (log g $\geqslant$3.0) by filled squares. The identical lines drawn through the data are approximate fits based on data in Figs 2 and 5.

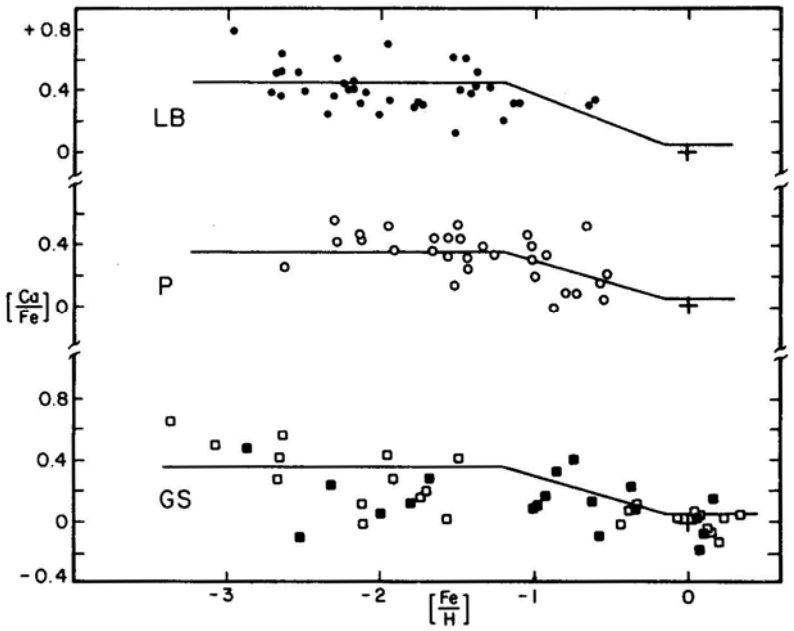

Figure 4. [Ca/Fe] as a function of [Fe/H] for the samples analysed by LB, GS, and P. See caption to Fig. 3 for comments on the symbols and the lines.

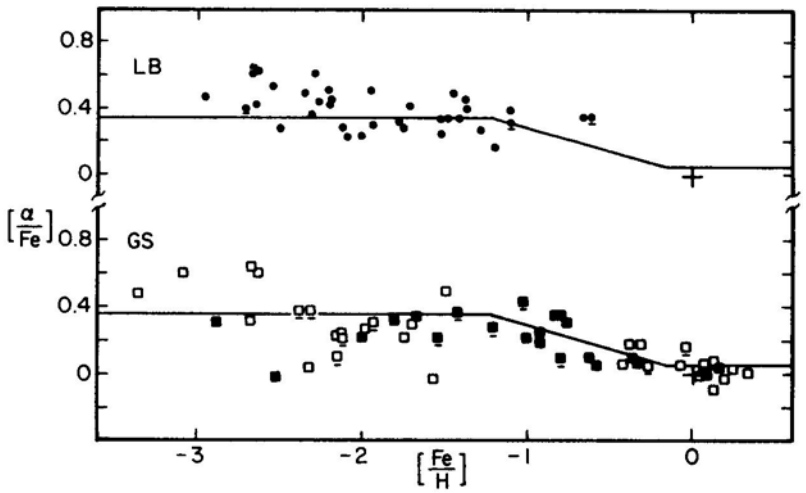

Figure 5. [α/Fe] as a function of [Fe/H] for the samples analysed by LB and GS. See caption to Fig. 3 for comments on the symbols and the lines. The explanation of the underlined symbols is provided in the caption to Fig. 2.

scatter in [α/Fe] at[Fe/H]~ 0.0. On the present evidence (Fig. 2), the scatter in [α/Fe] is less than about ±0.03 dex, a value certainly dominated by the measurement errors, and A_α apparently differs from the mean [α/Fe] by an amount exceeding 0.03 dex. The remarkably small intrinsic scatter must constrain theories of stellar nucleosynthesis.

The increase of the α/Fe abundance ratio in metal-poor disc stars is *not* a novel result of the recent analyses. An increase was noted first (?) by Wallerstein (1962) from an analysis of 31G dwarfs. Many studies on a variety of stellar samples have now provided evidence for the mean trend summarized in our figures and by the formulae given above. The most recent analysis of Mg (Laird 1986) appeared as the final draft of this paper was being prepared. Laird derives the Mg abundance from synthetic spectra fitted to 43 Å mm $^{-1}$ image-tube spectra providing the Mg I b lines in 111 dwarfs. For approximately 90 disc stars ([Fe/H] > – 1), Laird's least-squares fit gives

$$[\mathrm{Mg/Fe}] = -(0.28 \pm 0.02)[\mathrm{Fe/H}] - 0.06(\pm 0.02).$$

The coefficient (–0.28) is identical to mine. The offset (my A_α) is here negative rather than positive. However, such a difference may well reflect the systematic errors, as Laird's analysis in contrast to others is based exclusively on lines that are very strong in field disc dwarfs. Inspection of Laird's results shows that they permit a transition to [α/Fe] = A_α at [Fe/H] ~ –0.2. For the halo ([Fe/H] < –1), Laird obtains a mean [α/Fe] = + 0.24 ± 0.13 (s.d.) from 22 stars and, hence, to a 0.30 increase above the value at [Fe/H] = 0.0, an increase precisely equivalent to that given by our prescription.

Perhaps, the leading outstanding questions about the α/Fe ratio concern its behaviour in the halo. The simplest assumption consistent with most of the published abundances is that [α/Fe] is constant below [Fe/H] ~ –1 with an observed scatter which is small (say, ± 0.15 dex) and is dominated by the measurement errors. Figs 1 through 5 confirm this assumption except for two deviations:

1. The scatter in [α/Fe] according to GS is rather larger than assumed. The scatter is ±0.4 dex in [Mg/Fe] (Fig. 3) and ±0.3 dex in [α/Fe] (Fig. 2).

2. LB's result show [α/Fe] to increase slightly in the extreme halo stars ([Fe/H] < –2) (Fig. 5).

An assumption that the intrinsic scatter in [α/Fe] for halo stars is small is not necessarily compatible with the theories of Galactic chemical evolution. If the α-elements and the iron-group are synthesized in different stars, and gas clouds in the early Galaxy were poorly mixed, one may expect, as earlier and earlier generations of stars are examined, [α/Fe] to show an increasing scatter with decreasing [Fe/H]. Also, halo stars now in the solar neighbourhood and having the same [Fe/H] may have come from more diverse birthplaces than the disc stars. Is the scatter portrayed by GS's results for halo stars a reflection of an intrinsic scatter? First, we note that some earlier studies based on spectra of ostensibly inferior quality do not show such a large scatter; note Fig. 5 where the scatter in [α/Fe] for LB's sample is slightly smaller than for GS's sample. Second, we draw attention to the sudden onset of the scatter that is seen clearly in Figs 1 and 3 where the small scatter in [Si/Fe] and [Mg/Fe] for disc stars is insufficient to mask the trend with [Fe/H], but the scatter in the halo suddenly and dramatically increases below [Fe/H] ~ –1.5. A dominant contributor to the scatter is the set of abundances based on CASPEC CCD-spectra. Infact, GS place low weight on the abundance derived from ESO's CASPEC and even omit the 'CASPEC' abundances from several plots. The lines of Mg I, Si I, and Ca I are extremely weak and the available spectra are too noisy to permit reliable measurements. The problems are not inherent to the CCD-equipped CASPEC because several investigators have lauded its ability to provide high quality spectra (see Spite, Francois & Spite 1985). We suggest that the totality of present evidence does not demand that the scatter in [α/Fe] at a given [Fe/H] be markedly greater in halo than in disc stars.

If GS's 'CASPEC abundances are disregarded, LB's study is the only one to provide data on more than just one or two extreme halo stars. Fig. 5 offers a hint that [α/Fe]in the halo increases either steadily with declining [Fe/H] below [Fe/H] ~ –1 or more rapidly below [Fe/H] ~ –2 after remaining level between [Fe/H] = – 1 and –2. We offer this hint as an incentive to observers. By way of supporting evidence, we note that the [Fe/H] ~ –2 is also the point below which LB report a steady increase in [Ni/Fe] (see also Luck & Bond 1983), and a slight decline in [Ti/Fe]. Other changes occur at or near this metallicity. There is a deficiency of *s*-process elements beginning near [Fe/H] = –1.5 (Spite & Spite 1978; Spite 1983, and LB). Carbon appears to increase in abundance relative to iron beginning at [Fe/H] ~ –1.8 (Tomkin, Sneden & Lambert 1986). There is contrary evidence on some of these changes. In particular, the [Ni/Fe] trends have been challenged. Magain (1985) reports [Ni/Fe] = + 0.05 for HD 19445 with [Fe/H] = – 2.33, and +0.08 for HD 140283 with [Fe/H] = – 3.00. LB's expected results for these stars are [Ni/Fe] = +0.2 and +0.6 respectively.

2.3 *Na and Al*

Nucleosynthetic yields of odd-even nuclei such as Na and Al are expected (from carbon burning) to be lower than the yields of the even-even or α-nuclei such as Mg and Si. Both Arnett's (1971) theoretical study of explosive C burning and more recent

calculations by Woosley & Weaver (1982) of hydrostatic C burning in massive stars predict lower yields for Na and A1 Even with the new abundance analyses, the observational picture on the ratio of the odd-even/even-even nuclei such as ^{23}Na/^{24}Mg and ^{27}Al/^{28} Si is cloudy. Both ^{22}Na and ^{27}A1 are the sole stable nuclides of these elements. Although ^{24}Mg and ^{28}Si are the most abundant nuclides, the atomic lines necessarily provide the total elemental abundances—*i.e.*, Mg= ^{24}Mg+ ^{25}Mg + ^{26}Mg and Si= ^{28}Si+ ^{29}Si + ^{30}Si. However, the heavier isotopes provide only about 20 per cent(Mg) to 8 percent (Si) of the elemental abundance instars of near solar metallicity, and this fraction is known to decline with decreasing metallicity (see below). Therefore, we may identify Mg, Si, and Ca as effectively pure α-elements.

Prior to the completion of some of the recent analyses, one could claim that the longstanding confusion about the Na and Al abundances in halo stars was close to resolution. Fig. 6 from TLB provides the basis for this claim. With the sole exception of two stars analysed by Spite & Spite (1980), [AI/Mg] fits the following prescription:

$$[\mathrm{Al/Mg}] = A_{\mathrm{Al}} \quad \text{for } [\mathrm{Fe/H}] \geqslant -1.0,$$
$$[\mathrm{Al/Mg}] = [\mathrm{Fe/H}] + 1.0 + A_{\mathrm{Al}} \quad \text{for } -2.5 \leqslant [\mathrm{Fe/H}] \leqslant -1.0,$$
$$[\mathrm{Al/Mg}] = -1.0 + A_{\mathrm{Al}} \quad \text{for } [\mathrm{Fe/H}] \leqslant -2.0.$$

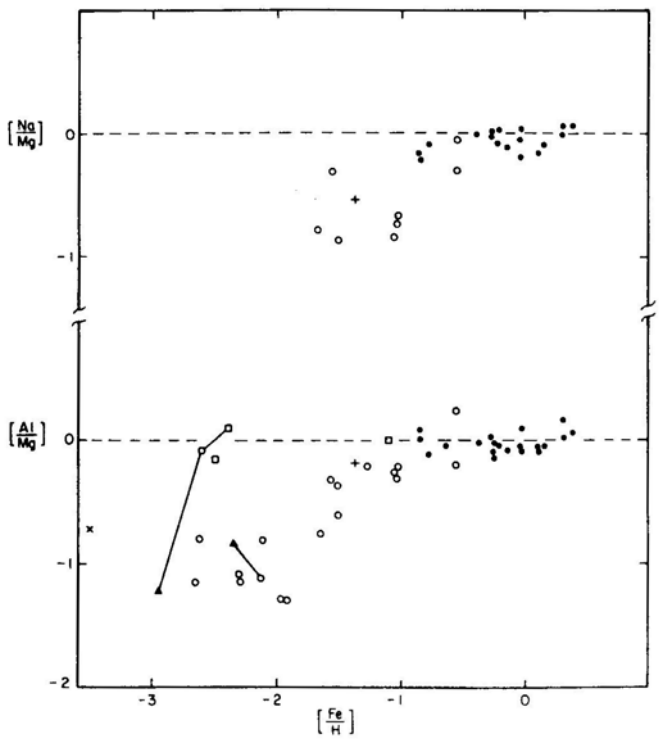

Figure 6. [Na/Mg] and [Al/Mg] as a function of [Fe/H] for the F and G dwarfs analysed by TLB (filled circles) and others (open circles: Peterson 1981; open squares: Spite & Spite 1980; filled triangles: Arpigny & Magain 1983; plus sign: Tomkin & Lambert 1980; cross: Carney & Peterson 1981). Lines join the points for HD 19445 and HD 140283, which have been the subjects of multiple investigations; HD 140283 is the more metal-deficient of the two stars.

where $A_{Al} \simeq 0.0$. Note that [Fe/H] ~ – 2 again appears as the point at which a change of the chemical composition of the extreme halo occurs.

In providing this prescription and the accompanying assumption that the scatter in [A1/Mg] at a given [Fe/H] is small, we dismiss the two points near [Al/Mg] ~ 0.0 contributed by Spite & Spite (1980). The third such star analysed by them was HD 140283 which was reanalysed by Arpigny & Magain (1983; see also Magain 1985) who discovered that one of the two Al I resonance lines used by Spite & Spite and by others is blended with a CH line. For this and other reasons, Arpigny & Magain (see Fig. 6) obtained a much lower [A1/Mg] value for HD 140283. TLB supposed that the halo stars showing [Al/Mg] $\simeq 0$ would, on reanalysis, conform to the simple prescription, and show [Al/Mg] ~ –1. With the limited data on Na available to TLB, one can claim no more than that to [Fe/H] ~ –1.5, [Na/Mg] ~ [Al/Mg].

After this introduction, I return to the new studies. In Fig. 7, I show [Na/Fe] versus [Fe/H] from the samples considered by GS, TLB, F, and NEG. For disc stars, the four studies provide concordant results. Only GS and F considered halo stars, and the latter's sample is perhaps too small for a meaningful check on the large scatter formed by GS for halo stars. Since Na, Al and the α-elements, but not Fe, are formed in the same sites, a ratio such as [Na/Mg] is more meaningful than [Na/Fe]; later, we comment on [Mg/H] as an alternative to [Fe/H]. Fig. 8 shows [Na/α] versus [Fe/H] for the samples considered by GS, F, and NEG. Fig. 9 gives the equivalent plot for [Al/α].The lines fitted by eye to the data follow the prescription given above with A_{Al} (or A_{Na}) as the

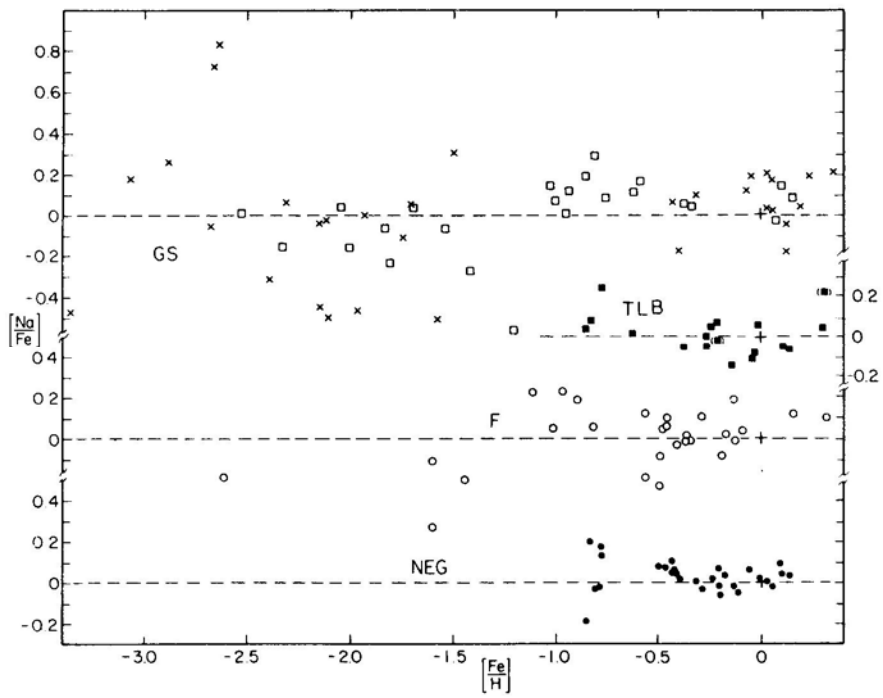

Figure 7. [Na/Fe] as a function of [Fe/H] for the samples analysed by GS, TLB, F, and NEG. See caption to Fig. 1 for comments on the symbols.

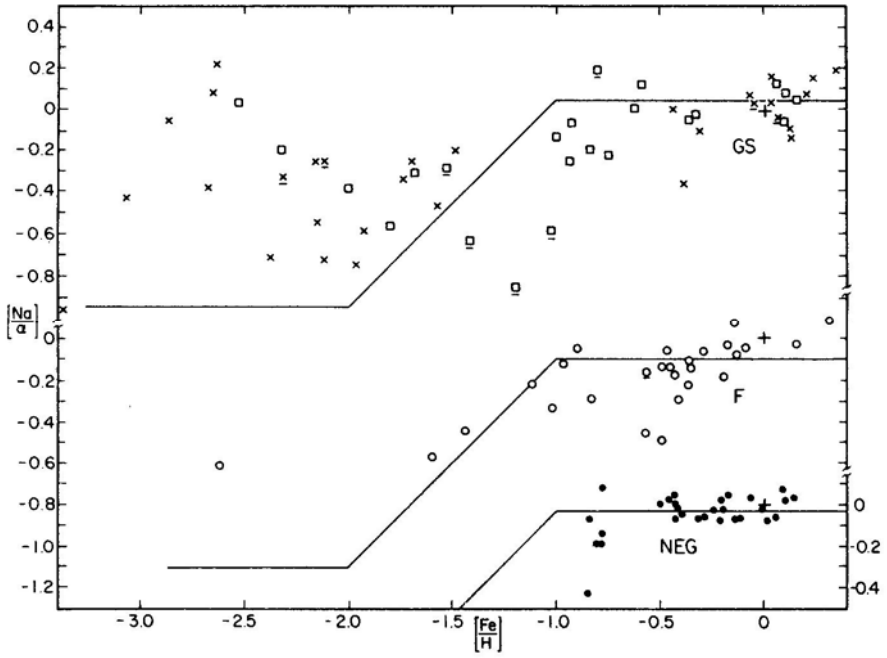

Figure 8. [Na/α] as a function of [Fe/H] for the samples analysed by GS, F, and NEG. See captions to Figs 1 and 2 for comments on the symbols. The line fitted by eye to the points (the disc stars are emphasized here) is described in the text. It is an approximate fit to the points plotted in Fig. 6.

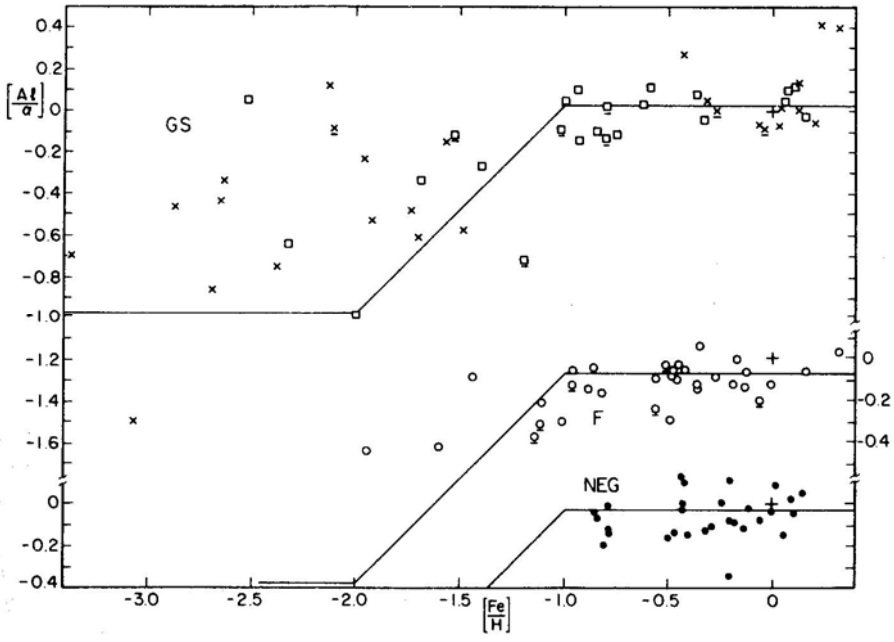

Figure 9. [Al/α] as a function of [Fe/H] for the samples analysed by GS, F, and NEG. See caption to Fig. 8 for explanation of the symbols and the line.

sole free parameter. The fits are made emphasizing the disc stars for which all studies are in broad agreement.

Comparison of Figs 6, 8, and 9 suggest that the new studies have not clarified the evolution of the Na and Al abundances through the halo to the disc. Fair agreement now exists on these abundances in the disc ([Fe/H] $\geqslant -1$): [Na/α] and [Al/α] are independent of[Fe/H]. One cannot exclude a slight increase of the ratios with [Fe/H], say by 0.1 dex between [Fe/H] of –1 and 0. The scatter in [Na/α] reported by GS and F is presumably attributable to measurement errors. Certainly, this scatter exceeds that exhibited by TLB's and NEG's samples. Frangois's few halo stars deviate slightly from the prescription based on Fig. 6. If his stars are representative and the scatter in composition among halo stars is small, minor modifications to the prescription suffice to achieve a compromise; say, adopt [Fe/H] ~ –2.5 as the point below which [Al/α] and [Na/Mg] assume an approximately constant value. A far larger deviation from the prescription is provided by GS's sample. It would appear that the prescription is a fair fit to the lower envelopes of GS's points in both Figs 8 and 9. If the stars with [Fe/H] $\lesssim$ – 2.0 were rejected from the sample, GS's results would fit the prescription with one of the possible minor modifications suggested by F's results. GS remark that their Na abundances for[Fe/H]< –2.0 are based on the Na I D lines which, being on the flat portion of the curve of growth, are less than ideal as abundance indicators. GS do not identify a similar specific reason for supposing that the Al abundances of the extreme halo stars be assigned a low weight; the one unblended A1 I resonance line may be partially blended at the lower resolution of the CASPEC spectra. I suspect that the dominant contribution to the scatter in the results both [Na/α] and [Al/α] for extreme halo stars is observational rather than intrinsic. I note that GS omit those points based on the CASPEC spectra in compiling several plots showing abundance trends.

LB's analyses of Na and Al provide little additional information because the pair are 'poorly represented' on the echelle spectra. For Na, LB have 10 stars with –1.5 < [Fe/H]< –1.0 which provide mean values of [Na/α] = –0.24 and [Fe/H] = –1.33 (or [Na/α] = –0.34 if one very discrepant star is dropped). These values fall close to the prescription. Two stars with [Fe/H] < – 2.0 have [Na/α]>0 and apparently fall well above the prescription. For Al, the means in the same ranges are [Al/α] = +0.13 (4 stars with a mean [Fe/H] = –1.31) and –0.37 (4 stars with a mean [Fe/H] = – 2.35). The [Al/α] value for the extreme halo drops to – 0.67 when one star with an apparently discrepant value (+ 0.54) is discarded; the other three values are –0.62, –0.56, and –0.83. These [Al/α] values are about 0.3 dex above the value derived using the prescription.

Any odd-even isotope of a light element should serve to test the predictions of stellar nucleosynthesis. Recently, attempts have been made to extract the $^{24}Mg/^{25}Mg/^{26}Mg$ ratios from the Mg H *A–X* transition whose lines are present in cool stars. The isotopic ratios were earlier obtained for sunspots (Sotirovski 1971), and K and M giants (Boesgaard 1968; Bell & Branch 1970; Tomkin & Lambert 1976, 1979). An initial attempt to examine a metal-poor dwarf was made by Tomkin & Lambert (1980) who reported upper limits on the ^{25}Mg and ^{26}Mg abundances which were less than the solar/terrestrial values: $^{i}Mg/^{24}Mg < 7$ per cent, but $^{i}Mg/^{24}Mg = 13$ per cent for terrestrial samples (here ^{i}Mg denotes one of the heavier isotopes, *i.e.*, i = 25 or 26). Lambert & McWilliam (1986) set a lower limit to $^{i}Mg/^{24}Mg$ ($\leqslant 3$ per cent) for the subgiant *v* Ind with [Fe/H] = –1.52. Barbuy (1985) provides estimates of ^{i}Mg for a

selection of (mainly) metal-poor dwarfs and giants. McWilliam & Lambert (1986) rediscuss stars first analysed by Tomkin & Lambert (1980).

In Fig. 10, I show currently available results for $^{i}Mg/^{24}Mg$ versus [Fe/H] in dwarfs and subgiants; the abundance of the neutron-rich isotopes ^{25}Mg and ^{26}Mg declines with increasing metal-deficiency, approximately as predicted by theories of stellar nucleosynthesis. The scatter in $^{i}Mg/Mg$ at a given [Fe/H] is probably dominated by observational errors. The decline in $^{i}Mg/Mg$ may begin at a higher metallicity than is evident in the [Na/α] and [Al/α] results. Arnett's (1971) calculations of explosive nucleosynthesis predict the more rapid decline for $^{i}Mg/Mg$: [Na/Mg] and [Al/Mg] drop by about 0.6 dex, but $[^{25}Mg/^{24}Mg]$ and $[^{26}Mg/^{24}Mg]$ drop by 2.0 and 1.8 dex respectively as the adopted neutron excess declines by an order of magnitude from the solar value. Woosley & Weaver (1982) predict a qualitatively similar result.

The yield of the odd-even nuclei such as ^{27}Al is predicted to be controlled by the neutron excess at the site of stellar nucleosynthesis. In explosive nucleosynthesis, the neutron excess is controlled by the ^{14}N abundance, or the neutron-rich isotopes ^{18}O and ^{22}Ne synthesized from ^{14}N, but, thanks to a prior phase of H burning, the internal ^{14}N (or ^{18}O, ^{22}Ne) abundance is set by the sum of the initial C, N, and O abundances. Calculations for massive stars suggest that the effective neutron excess is less strongly tied to the initial composition because of additional processing following the helium-burning phase. However, the predicted yields for Population I and II 25 $M_{\odot}$ stars differ by about the same amount as Arnett's less realistic calculations of explosive nucleosynthesis (Woosley & Weaver 1982).

Through this tie to the CNO abundances, we may anticipate that the correlation of [Al/Mg] should be tightest when plotted against [(C + N + O)/H] rather than either [Mg/H] or [Fe/H]; the CNO abundances were calculated from the mean relations for these stars and not the values derived for the individual stars. Of course, one should really employ a weighted mean of the CNO abundances over the several generations of stars prior to the formation of the observed star. The scatter is probably reduced (see Fig. 11 from TLB). (The fact that the scatter is quite obviously larger when [A1/Fe] is plotted against [Fe/H] shows that Al and Fe are synthesized in rather different sites.)

In summary, the variation of odd-even nuclei relative to the α-nuclei through the disc

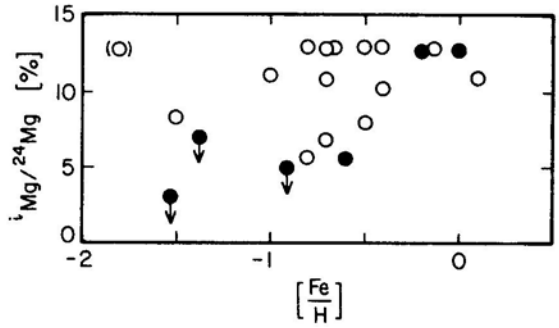

Figure 10. ^{i}Mg) istopic abundances as a function of [Fe/H]. Observations (here $^{i}Mg = {}^{25}Mg$ or ^{26}Mg) are taken from Barbuy (1985—open circles) and Tomkin & Lambert (1980), Lambert & McWilliam (1986), and McWilliam & Lambert (1986)—solid symbols for the latter three references. The symbol in parentheses is based on a spectrum described as 'bad' by Barbuy.

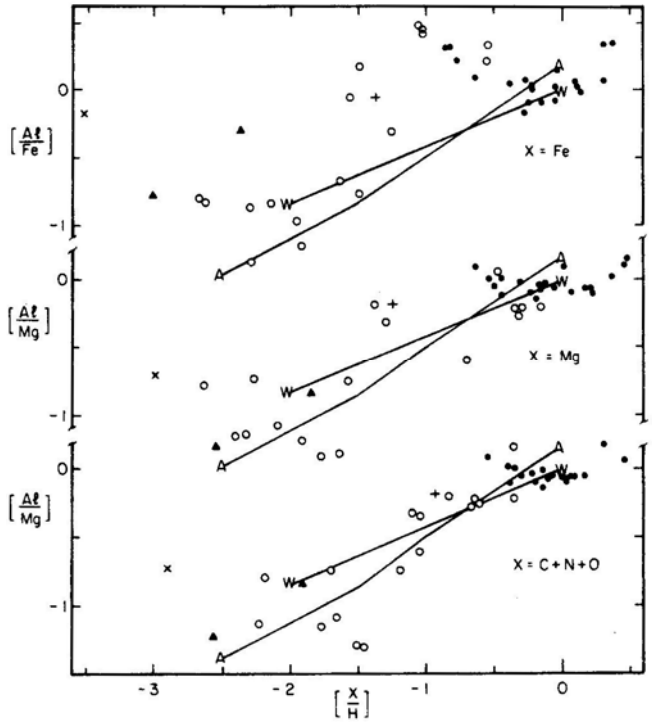

Figure 11. Aluminium in the halo and disc. The three plots show [Al/Fe] versus [Fe/H] (top), [Al/Mg] versus [Mg/H] (middle), and [Al/Mg] versus [(C +N + O)/H] (bottom). The key to the observations is given in the caption to Fig. 6. Theoretical predictions are by Arnett (1971; lines terminated by A) and Woosley & Weaver (1982; lines terminated by W).

to the halo appears to match rather well the predictions of nucleosynthesis occurring in either explosive or hydrostatic C burning. Abundances of odd-even nuclei (here, Na and Al) in halo stars remain uncertain. To [Fe/H] ~ –1.5, recent analyses suggest that our prescription overestimates the Na and Al abundances. Below [Fe/H] ~ –1.5, the Na and Al abundances must be considered uncertain. I suspect that they are approximately constant in the extreme halo with a much smaller scatter than is suggested by a casual inspection of Figs 7, 8, and 9. One must not forget persistent reports that Al (and Na) are enhanced in globular cluster 'CN-strong' stars.

3. Summary

3.1 *Disc-to-Halo Abundance Variations*

As a ready guide for the busy theoretician, I present in Figs 12 and 13 my impressions of the mean trends of [el/Fe] (or[el/α])with [Fe/H] for a selection of elements: C, N, and O; the α-nuclei (Mg, Si, Ca), the odd-even nuclei (Na, Al—see Fig. 13 where [odd-even/α] is given); the light *s*-process (Sr), the heavy *s*-process (Ba), and the *r*-process (Eu). Solid-lines denote those portions of the relations which appear to be well

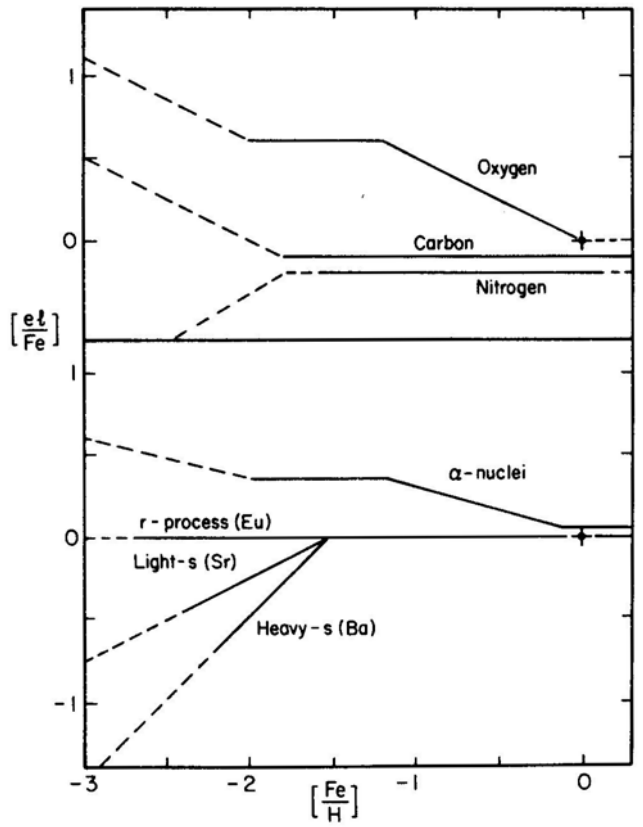

Figure 12. [el/Fe] as a function of [Fe/H] for C, N, O, α-nuclei (Mg, Si, Ca), and *s*-and *r*-process nuclei. Observes trends are represented here by connected straight lines with broken lines denoting uncertainty because the observations are spare or less accurate.

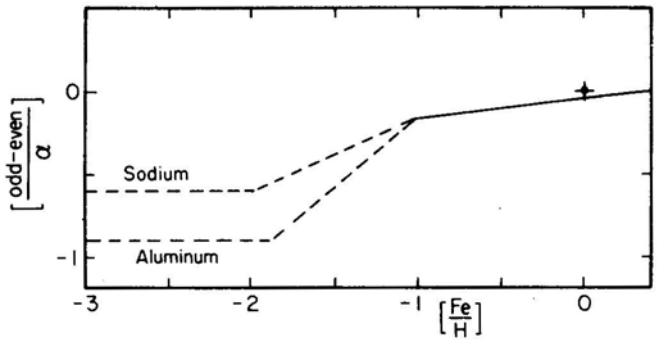

Figure 13. [odd-even/α] as a function of [Fe/H] for Na and Al. See caption for Fig. 12.

determined and exhibit little scatter. Broken lines denote those portions where considerable uncertainty remains as to the mean relation and/or the scatter. The relations are described by linear segments for convenience only. Undue emphasis should not be placed on the fact that most of the relations do not pass through the point

(el/Fe] = 0 and [Fe/H] = 0; as noted above, a thorough scrutiny of potential sources of systematic errors will be necessary before it can be claimed that particular elements are slightly underabundant (*e*.g., Mg, Si) or slightly overabundant (*e*.g., C, N) in the Sun relative to a sample of dwarfs of solar metallicity. To complete the crude summary, one should add Ni([Ni/Fe] > 0 for [Fe/H] < –2) and Ti ([Ti/Fe] declines for [Fe/H]< 2)—see LB.

In the variation of [el/Fe] with [Fe/H], a change of slope may occur at up to three metallicities. The most obvious change of slope is that between the disc and halo at [Fe/H] = –1.2 ± 0.1, which is evident in the oxygen and α-nuclei plots, and apparently also in the Na and Al plots. In the disc, there is evidence for a change of slope at [Fe/H] = –0.2 ± 0.1 in the α-nuclei plots. Oxygen may show a change of slope at a slightly higher metallicity, say [Fe/H] = 0.0. In the extreme halo, [Fe/H] ~ – 2 marks a change of slope for several elements: carbon, α-nuclei, and, perhaps, the odd-even nuclei (Na and Al), Ti, Ni, as well as the *s*-process elements. An obvious goal for the future is to examine more stars in the extreme halo in order to define the abundance variations for [Fe/H]≲–2.

For Na and Al, [el/α] is plotted because the yields of the odd-even and α-nuclei should be rather closely coupled (see Fig. 11 and the accompanying text). As emphasized in Section 2.3, the observational evidence on Na and Al abundances in halo stars is confusing. My suggested trends are weighted heavily towards the results provided by Peterson (1981), Magain (1985), and a few other references providing abundances for just one or two stars each. I assume, too, that the scatter in the Na or Al abundances is small for a given [Fe/H]. GS, and to a lesser degree LB, provide abundances which suggest that my relations in Fig. 13 are lower bounds to a distribution which is bounded at the upper end by [odd-even/α] ~ 0.0 for [Fe/H] < – 2. The evidence that [Na/α] > [Al/α] in the extreme halo is weak. For [Fe/H] > — 1, I show [odd-even/α] to increase with [Fe/H], but the evidence for this is inconclusive; [odd-even/α] ~ 0.0 is an acceptable alternative.

3.2 *'Primary' and 'Secondary' Elements*

In discussions of the chemical evolution of the Galaxy, the labels 'primary' or 'secondary' are attached to elements. Often, the iron-group elements are taken to be the quintessential 'primary' ones; *i.e.*, stellar nucleosynthesis of iron begins with hydrogen as the raw material. Other elements are termed 'primary' by the observers when

$$\left[\frac{\mathrm{el}}{\mathrm{H}}\right]=\left[\frac{\mathrm{Fe}}{\mathrm{H}}\right],\ \textit{i.e.},\ \left[\frac{\mathrm{el}}{\mathrm{Fe}}\right]=0.$$

This result follows for simple models of the Galaxy's chemical evolution when, among several simplifying assumptions, the element (el) may be synthesized from hydrogen with a yield that is approximately a constant fraction of the Fe yield.

An element is labeled 'secondary' by observers when

$$\left[\frac{\mathrm{el}}{\mathrm{Fe}}\right]=\left[\frac{\mathrm{Fe}}{\mathrm{H}}\right].$$

In the simple models, this relation follows when the element cannot be synthesized from hydrogen, but from a heavier element which was synthesized in earlier generations of stars.

Nitrogen is perhaps most frequently cited as an example of a secondary element. (It may also be synthesized as a primary element.) 'Secondary' because ^{14}N, the dominant isotope, is synthesized in H burning within a star when the CNO-cycles converts existing ^{12}C to ^{14}N, and, also, ^{16}O to ^{14}N in the deeper hotter layers. In many stars, this ^{14}N may be ejected into the interstellar medium with a yield which depends on the C abundance of the star as its formation. With the assumption that C is primary ([C/Fe]~0), simple models predict

$$\left[\frac{N}{Fe}\right]=\left[\frac{Fe}{H}\right].$$

Stars may synthesize ^{12}C from H when H burning is followed by He burning with ^{12}C as the principal product. If some of this ^{12}C is exposed to H burning, the resultant ^{14}N is a 'primary' product and, if several simple assumptions are valid, one may expect [N/Fe] = 0.

Inspection of Fig. 12 shows that

$$\left[\frac{N}{Fe}\right]\sim\left[\frac{N}{C}\right]\sim 0 \quad \text{and} \quad \left[\frac{N}{O}\right]\leqslant\left[\frac{O}{H}\right]$$

for nitrogen in disc stars. The first relations suggest that N is a 'primary' element relative to C, Fe, and many other elements showing [el/Fe] ~0. Two sites for primary production of N were discussed by Bessell & Norris (1982): (i) AGB stars in which fresh C is converted to N by hot protons; (ii) very massive (~500 $M_{\odot}$) stars.

The second relation suggests that N is a 'secondary' element relative to O. If existing O (and C) were converted to N by hot proton in significant amounts within a star and this processed material were ejected, this relation might be explained. No stellar models satisfy these requirements. Earlier, we (Tomkin & Lambert 1984) suggested that N is in fact primary, and this second relation is simply a numerical accident resulting from combining [O/H]~0.5 [Fe/H] and [N/Fe]~0.

This last discussion shows that a classification of elements as 'primary' or 'secondary' must involve more than the inspection of plots of [el/Fe] versus [Fe/H]. The puzzling case of the *s*-process elements (Tinsley 1979) provides a second example. The *s*-process elements in the disc would appear to be 'primary' elements (see Fig. 12). If we were to prefer oxygen as the 'primary' reference element, we note that

$$\left[\frac{s}{O}\right]=\left[\frac{O}{H}\right]$$

for disc stars and, perhaps, most of the halo stars; *i.e.*, the *s*-process elements should now be referred to as 'secondary'. Moreover, one can offer a plausible nucleosynthetic origin for this relation.

The production site of the *s*-process elements with $70 < A < 204$ is believed to be the convective shells of thermally pulsing intermediate-mass stars on the asymptotic giant branch (Iben & Truran 1978). The predicted yields show that a solar abundance pattern is produced. The source of neutrons for the *s*-processing is predicted to be the $^{22}Ne(\alpha,n)^{25}Mg$ reaction, where the ^{22}Ne is synthesized by the chain

$^{14}N(\alpha,\gamma)^{18}F(\beta^+,\gamma)^{18}O(\alpha,\gamma)^{22}Ne$, and the ^{14}N is produced during H burning by CNO cycling of the initial CNO nuclei. The neutron supply is thus proportional to the sum of the initial CNO abundances. If the neutron supply is the factor that limits the production of *s*-process elements—inspection of Truran & Iben's (1977) results suggests that it is—the *s*-process yield will also be proportional to the sum of the initial CNO abundances (in effect, the O abundance because the O abundance dominates). It is therefore more instructive to consider [*s*/O] rather than [*s*/Fe]. In the absence of infall of metal-poor gas, standard relations predict

$$\left[\frac{s}{O}\right]=\left[\frac{O}{H}\right].$$

This is, in fact, the observed relation for [Fe/H] $\gtrsim -1.5$ (see above and Fig. 12).

A third example of possible dual assignment of 'primary' and 'secondary' is Na or Al where [Na/Fe] ~ [A1/Fe] ~0 with considerable scatter, a result earning Na and Al the label 'primary'. But as we showed with Fig. 11, [Na/Mg] and [A1/Mg] are better correlated with [(C + N + O)/H] which is a stand-in for the neutron excess in the C-burning zones in which Na and Al are predominantly 'secondary' products.

I urge care in the christening of elements as 'primary' and 'secondary'!

For the extreme halo stars, Truran (1981) suggested that the *r*-process dominates production, and detailed abundance analyses (Sneden & Parthasarathy 1983; Sneden & Pilachowski 1985) indeed find that the *r*-process—not the *s*-process—can account for the relative abundances. This cannot be the complete story, because whether the *r*- or *s*-process (or both) are effective, the observed abundances of Sr, Ba, and many other heavy elements decline in the extreme halo relative to Fe and Eu (an *r*-process element). Some variable factor is needed (*e.g.*, the pattern of *r*-process yields must vary with metallicity) or, as Magain (1985) notes, [*s*/Fe] would have constant negative value in the halo (the limited observations do not yet exclude this possibility for [Fe/H] $\lesssim -2.5$). The stars examined in detail by Sneden and colleagues have [Fe/H] = –2.6 and – 2.3. Before the metallicity of the disc was reached, the *s*-process must have begun to dominate.

In these last paragraphs, I have apparently strayed from my terms of reference. My excuse is that the nucleosynthesis of the elements from the light to the heavy are linked and, hence, the full understanding of their nucleosynthesis may come only when observers and theoreticians recognize the elements as an ensemble. My principal goal in preparing this review will have been met if a few observers are stimulated to go to a telescope with an observing program designed to address the glaring deficiencies in our knowledge of the abundances of the light (and other) elements.

Acknowledgements

I thank Drs P. Francois, P. E. Nissen, and C. Sneden for providing important results in advance of publication. My research on the light elements is supported in part by the U.S. National Science Foundation (grant AST 83-16635) and the Robert A. Welch Foundation.

References

Arnett, W. D. 1971, *Astrophys. J.*, **166,** 153.
Arpigny, C., Magain, P. 1983, *Astr. Astrophys.*, **127,** L7.
Barbuy, B. 1985, *Astr. Astrophys.*, **151,** 189.
Bell, R. A., Branch, D. 1970, *Astrophys. J.*, **5,** L203.
Bell, R. A., Eriksson, K., Gustafsson, B., Nordlund, Å., 1976, *Astr. Astrophys. Suppl Ser.*, **23** .37.
Bessell, M. S., Norris, J. 1982, *Astrophys. J.*, **263,** L101.
Boesgaard, A. M. 1968, *Astrophys. J.*, **154,** 185.
Carney, B. W., Peterson, R. C. 1981, *Astrophys. J.*, **245,** 238.
Cayrel de Strobel, G., Bentolila, C., Hauck, B., Duquennoy, A. 1985, *Astr. Astrophys. Suppl. Ser.*, **59,** 145.
Clegg, R. E. S., Lambert, D. L., Tomkin, J. 1981, *Astrophys. J.*, **250,** 262 (CLT).
Francois, P. 1986, *Astr. Astrophys.*, in press (F).
Francois, P. 1986, preprint.
Gratton, R. G., Sneden, C. 1986, preprint (GS).
Gustafsson, B., Bell, R. A., Eriksson, K., Nordlund, Å. 1975, *Astr. Astrophys.*, **42,** 407.
Holweger, H., Müller, E. A. 1974, *Solar Phys.*, **39,** 19.
Iben, I., Jr., Truran, J. W. 1978, *Astrophys. J.*, **220,** 980.
Kraft, R. P. 1987, *J. Astrophys. Astr.*, **8,** 89.
Laird, J. B. 1986, *Astrophys. J.*, **303,** 718.
Lambert, D. L., McWilliam, A. 1986, *Astrophys. J.*, **304,** 436.
Luck, R. E., Bond, H. E. 1983, *Astrophys. J.*, **271,** L75 (LB)
Luck, R. E. 1985, *Astrophys. J.*, **292,** 559.
Magain, P. 1985, *Astr. Astrophys.*, **146,** 95.
McWilliam, A., Lambert, D. L. 1986, in preparation.
Nissen, P. E., Edvardsson, B., Gustafsson, B. 1985, in *Production and Distribution of C: N, O Elements*, Eds I. J. Danziger, F. Matteucci & K. Kjär, ESO, Garching, p. 131 (NEG).
Peterson, R. C. 1981, *Astrophys. J.*, **244,** 989(P).
Sneden, C., Parthasarathy, M. 1983, *Astrophys. J.*, **267,** 757.
Sneden, C., Pilachowski, C. A. 1985, *Astrophys. J.*, **288,** L55.
Sotirovski, P. 1971, *Astr. Astrophys.*, **14,** 319.
Spite, F. 1983, *Mem. Soc. astr. Ital*, **54,** 283.
Spite, F., Francois, P., Spite, M. 1985, *The Messenger*, No. 42,p.14.
Spite, M., Spite, F. 1978, *Astr. Astrophys.*, **67,** 23.
Spite, M., Spite, F. 1980, *Astr. Astrophys.*, **89,** 118.
Tinsley, B. M. 1979, *Astrophys. J.*, **229,** 1046.
Tomkin, J., Lambert, D. L. 1976, *Astrophys. J.*, **208,** 436.
Tomkin, J., Lambert, D. L. 1979, *Astrophys. J.*, **227,** 209.
Tomkin, J., Lambert, D. L. 1980, *Astrophys. J.*, **235,** 925.
Tomkin, J., Lambert, D. L. 1984, *Astrophys. J.*, **279,** 220.
Tomkin, J., Lambert, D. L., Balachandran, S. 1985, *Astrophys. J.*, **290,** 289 (TLB).
Tomkin, J., Sneden, C, Lambert, D. L. 1986, *Astrophys. J.*, **302,** 415.
Truran, J. W. 1981, *Astr. Astrophys.*, **97,** 391.
Truran, J. W., Iben, I., Jr., 1977, *Astrophys. J.*, **216,** 797.
Wallerstein, G. 1962, *Astrophys. J. Suppl Ser.*, **6,** 407.
Woosley, S. E., Weaver, T. A. 1982, in *Essays in Nuclear Astrophysics*, Eds C. A. Barnes, D. D. Clayton & D. N. Schramm, Cambridge University Press, p. 377.

Note added in proof

Of the several significant developments since my talk in New Delhi in December 1985, two should be noted:

(i) The extensive study by Gratton & Sneden will appear in a slightly revised form as two papers in *Astronomy and Astrophysics.* Relative to the preliminary results discussed in my review, the revisions conform in the main to my suggested trends (Figs 12 and 13), but the scatter about those trends is reduced significantly.

One particular new result deserves emphasis. Gratton & Sneden now show that potassium behaves like the α-elements Mg, Si, and Ca; *i.e.*, [K/Fe] increases with decreasing metallicity to reach [K/Fe] ~ 0.4 for [Fe/H] < – 1. Potassium with stable isotopes ^{39}K and ^{41}K might have been expected to have followed the other odd-even nuclei in showing a lower abundance (relative to either Mg or Fe) in halo stars. Potassium's differing nucleosynthetic behaviour may be a clue to the origin of the Na and Al enrichments reported for some stars in certain globular clusters. If the strengthening of Na I and Al I lines in these stars is due to a change of atmospheric structure, the K I resonance lines at 7664 and 7699 Å might be expected to show a similar strengthening. On the other hand, if the Na and Al enrichments are real and produced by the same nucleosynthetic process responsible for the overall enrichment in the Galaxy, one would not expect K enrichments in the Na and Al enriched globular cluster stars.

(ii) Magain (1987, *Astr. Astrophys.*, in press) provides abundances of α(Mg, Si, Ca) and odd-even (Na, Al) elements "on the basis of literature data reanalysed in an homogeneous way". His results generally confirm my suggested trends. For the α-elements, the mean abundances for this sample in which all stars belong to the halo (the most metal-rich star has [Fe/H] = –0.87) are [Mg/Fe] = 0.43 ± 0.02 (17 stars), [Si/Fe] = 0.39 ± 0.05 (8 stars), and [Ca/Fe] = +0.50 ± 0.04 (14 stars). The mean values do not differ sensibly when the sample is divided at [Fe/H] = – 2. Gratton & Sneden's sample of 13 extremely metal-poor stars ([Fe/H]$\leqslant$– 1.3) yields the following mean values: [Mg/Fe] = 0.34 ± 0.03, [Si/Fe] = 0.50 ± 0.06, and [Ca/Fe] = 0.31 ± 0.09. (I give the formal errors of the mean values.) Magain's reanalysis of published data suggests that the α-elements (relative to Fe) are slightly more abundant than any recommended trend would suggest, and confirms my suggestion that the scatter in [el/Fe] about the mean value is very small, even in the halo; Magain's sample is concentrated between about –1.5 to –2.5 in [Fe/H]. More importantly, his results do not support my tentative suggestion that [α/Fe] may increase again in the extreme halo ([Fe/H] < –2).

The few stars which pass Magain's stringent selection criteria show the decline of [A1/Mg] with declining [Mg/H] to be similar to that indicated by Fig. 11 and the combination of Figs 12 and 13.

The papers by Francois have now appeared in print: *Astr. Astrophys.*, **160,** 264 (F), and *Astr. Astrophys.*, **165,**183.

J. Astrophys. Astr. (1987) **8,** 123–139

Past and Present Metal Abundance Gradient in the Galactic Disc

M. Grenon *Observatoire de Geneve, CH-1290 Sauverny, Switzerland*

Abstract. A critical discussion of some determinations of metal abundance gradient in the galactic disc is presented with an attempt to homogenize the results related to local and large-scale gradients. A new estimation of the palaeogradient in intermediate and old disc population is presented. The gradient is found to depend on galactocentric distance, and to be nearly constant with time during the lifetime of the galactic disc.

Key words: Galaxy, metal abundance gradient

1. Introduction

Several reviews have been dedicated to the topic of abundance gradient in the galactic disc (see Pagel 1975; Peimbert 1974, 1977, 1979; Janes 1979; and more recent work of Luck 1982; Shaver *et al.* 1983 for the abundances in the interstellar matter).

A wide variety of objects have been used for gradient determinations: the nearby stars, the G and K giants, the F stars (for the local gradient $\delta[M/\mathrm{H}]/\delta\varpi$ at $\varpi_\odot$, the solar galactocentric distance), the yellow supergiants and the Cepheids, the open clusters, the H II regions, the planetary nebulae *etc.* for abundance estimates *in situ* at large distances.

Selected values of abundance gradients deduced from stellar samples are given in Table 1. They refer to young, intermediate, old, or mixed stellar populations. The extreme values range between 0.00 and –0.13 kpc $^{-1}$. The various approaches differ by the techniques used and the observational material, the sampling conditions, the basic assumptions and the volume of space investigated.

Part of differences between gradients deduced from *in situ* observations and those obtained from kinematical considerations originates in the adopted solar galactocentric distance and are reduced when the recommended value $\varpi_\odot = 8.5$ kpc is adopted. The gradients by Janes & McClure (1972), Grenon (1972, 1977), Mayor (1976) have then to be multiplied by a factor 1.18; a factor of the same order has to be applied to gradients from H II regions with distance deduced from rotation curve assuming $\varpi_\odot = 10$ kpc. In the following, $\varpi_\odot = 8.5$ kpc will be assumed.

Observations *in situ* are clearly to be preferred for the young disc objects as they allow both a gradient determination independent of any dynamical models of the Galaxy, the galactocentric distances being relative to that of the Sun, and a detailed picture of the abundance distribution as a function of the distance to the galactic centre.

As the [N/Fe] ratio in stars appears independent of [Fe/H] for a wide range of [Fe/H], at least those typical of the galactic disc (*cf.* Matteucci & Tornambe 1985), the [N/H] ratio deduced from H II regions may be used as an additional estimator of

Table 1. Metal abundance gradient determinations based on stellar observations

Object	Age	Parameter	$\delta p/\delta\varpi$	Reference
gG-gK	mixed	[CN/H]	−0.02	Janes & McClure 1972
dG-dK	mixed	[*M*/H]	−0.05	Grenon 1972
dF	young to intermediate	[*M*/H]	−0.0	Clegg & Bell 1973
gG-gK	mixed	[*M*/H]	0.0	Jennens & Helfer 1975
dF-dG	young	[*M*/H]	−0.10	Mayor 1976
	old	[*M*/H]	−0.05	Mayor 1976
G-K	old	[*M*/H]	−0.07	Grenon 1977
gG-gK	intermediate	[CN/H]	−0.05	Janes 1979
open clusters	young	[*Z*/X]	−0.095	Panagia & Tosi 1981
Cepheids	young	[*M*/H]	−0.07	Harris 1981
G-K Ib	young	[Fe/H]	−0.13	Luck 1982

metallicity at large distances from the Sun. Various [N/H] gradients are summarized in Table 2. They are steeper than the [*M*/H] gradients deduced from stars; typically δ[N/H]/$\delta\varpi$ = –0.15 kpc $^{-1}$.

Planetary nebulae abundances, intermediate between those of the local interstellar medium and those of the stellar ejecta, will not be discussed here as their ages and birthplaces of their progenitors are difficult to determine.

All abundance gradient determinations are highly sensitive to the distance scale adopted, to the possible coupling between luminosity and metallicity, to the sampling and its possible dependence on age and/or abundance.

In the following sections we will attempt to produce a global picture of the radial metal abundance distribution in our Galaxy, at the present time and in the past. This tentatively uses the published data after discussion and homogenization and also uses new observational material.

Table 2. Nitrogen abundance gradient in interstellar medium.

Objects	δ[N/H]/$\delta\varpi$	Reference
H II regions	−0.10	Hawley 1978
	−0.14	Peimbert 1979
	−0.08	Talent & Dufour 1979
	−0.23	Peimbert, Torres-Peimbert & Rayo 1978
Planetary nebulae	−0.13	d'Odorico *et al.* 1976
	−0.18	Torres-Peimbert & Peimbert 1977
	−0.27	Peimbert & Serrano 1980
Supernovae remnants	−0.095	Binette *et al.* 1982

2. The definition of stellar samples

The reliability of a gradient, defined for a given epoch and galactocentric distance, is conditioned by the quality of the stellar or nonstellar sample used and by the validity of the methods applied to the gradient determination. The constitution of an unbiased sample is indeed a nontrivial process as most of relations between the physical, the photometric and the spectroscopic parameters defined for objects in the solar vicinity are generally no longer valid at large distances where the metal abundances are expected to be significantly different. In the solar neighbourhood itself, abundance effects on the stellar classification and also evolutionary effects may lead to serious biases. In the case of a stellar sample, the following conditions must be verified:

1. The stellar ages should be known either from their evolutionary stage, or at least from the kinematical properties. A mixing of ages leads to a flattening of the gradient (*cf.* Section 5). Problems arise with the red giants and the G and K dwarfs.
2. The metal abundance estimator should not show residual effects of temperature or reddening. If it does, we may expect spurious dependence of the metallicity on the age in the first case and a bending of the relation [M/H] versus ϖ in the second.
3. The objects should be situated at the same galactocentric distances as they had at the time of their formation. If not, the galactocentric distances of their birthsites have to be evaluated. All objects more than a few billion years old are problematic in this respect.
4. The sample itself should not be biased in favour of particular abundances or ages. Rather surprisingly, this last condition is almost never verified and most selection criteria are more or less dependent on metallicity and age. As an example, a selection of F-type stars excludes practically all old metal-rich stars (*cf.* Section 7).

3. Large-scale gradient in the young disc

The modelling of the galactic chemical evolution requires a knowledge of the metal abundance distribution over the whole range of galactocentric distances. Most determinations of gradient are defined over a small range of distances—typically $\varpi_{\odot} \pm 2$ kpc.

At large distances the information on the metallicity distribution relies mainly on the galactic clusters, the bright yellow and red supergiants (Cepheids included), and on the C, N, O abundances in H II regions.

3.1 *Open Clusters*

The intermediate-age open clusters have several unique advantages for the gradient determination. Their HR diagrams allow a precise estimation of their evolutionary age, typically 0.5 to 3 billion years. The luminosity of red giants in core He-burning phase is almost invariant with the age and metal abundance (*cf.* Cannon 1970). Clump stars are probably the best distance estimators in the Galaxy. The number of red giants is generally sufficient for an accurate evaluation of the mean metallicity of each cluster.

The pioneering investigation by Janes (1979)using DDO photometry of 41 clusters

indicates a gradient δ[CN/H] /$\delta\varpi$ = – 0.05 kpc^{-1} when the clusters data were combined with those of field K giants observed towards the galactic centre and anticentre in order to extend the range of galactocentric distances.

Returning to the original data we see (Fig. 1) that the abundances in clusters show a marked dependence on ϖ although some scatter is present. This scatter exceeds the dispersion in abundances observed in young populations in the solar vicinity. In addition to the uncertainties due to measurement errors and reddening corrections, the factors contributing to the observed scatter are the dispersion in the abundances in the interstellar medium at a given galactocentric distance and the fact that old clusters would have moved away from their birthsites by several kiloparsecs in the radial direction, (see *e.g.* the galactic orbits computed for M67 and NGC 188 by Keenan, Innanen & House 1973). The mean gradient is however not significantly altered by this uncertainty on the birth-distances: It appears to be constant over 6 kpc, from $\varpi_{\odot}$–1.7 to $\varpi_{\odot}$+ 4.2 kpc with a mean value of δ [CN/H]/$\delta\varpi$= –0.11 kpc^{-1}.

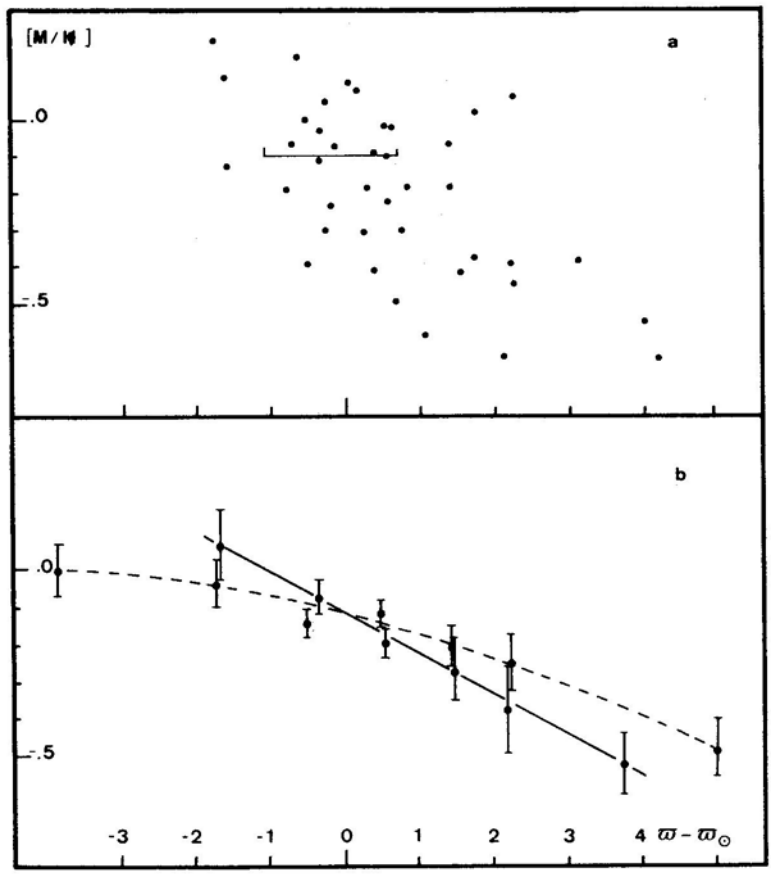

Figure 1. (a) The distribution of metal abundances of open clusters deduced from CN parameter by Janes (1979), and (b) themean abundance distribution of clusters(solid line) and of clusters plus field giants (dashed line). In panel (a) the horizontal line shows the amplitude of epicyclical motion of M67 according to Keenan (1973).

The inclusion of field stars with uncertain distances, apparently overestimated, leads to a flattening of the abundance distribution which is more pronounced towards the galactic centre. The gradient from the clusters appears to be the most reliable for intermediate-age population in the range of ages 0.5×10^9 to about 4×10^9 yr.

Intermediate-age to old open clusters are not identified at distances exceeding 2 kpc towards the galactic centre, probably a consequence of their shorter lifetimes in the regions where tidal evaporation becomes intense. Other metal abundance indicators have then to be used for the inner disc and bulge populations.

3.2 *Supergiants*

Supergiants with ages much smaller than that of the galactic disc are excellent tracers of the present abundance distribution in the interstellar matter. The F to M/supergiant spectra show a sufficient number of spectral features usable as abundance estimators or even allow direct [Fe/H] determinations through high-dispersion analysis. Their intrinsic brightness allows [*M*/H] determinations at very large distances from the Sun.

Cepheids form a subset with the advantages of detection, even in crowded areas, and the accuracy of their absolute luminosities. They have been used by Harris (1981) for a determination of abundance gradient. The distribution of [*M*/H] as a function of ϖ

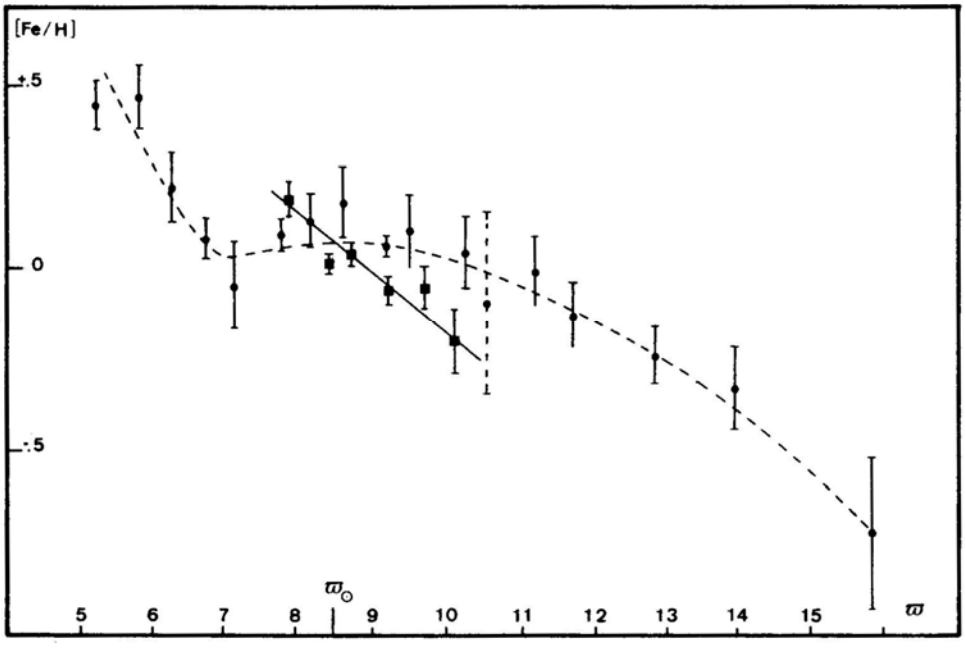

Figure 2. Mean metal abundances of classical Cepheids (dots; Harris 1981) and of F–M supergiants (Luck 1982; squares).

appears somewhat irregular (*cf.* Fig. 2), with some flattening between 6.5 to 9.5 kpc, a steep increase towards the galactic centre and a slope of – 0.11 kpc^{-1} outside 10 kpc, the mean gradient being about – 0.07 kpc^{-1}.

A spectroscopic investigation of non-variable F to M supergiants by Luck (1982) leads to a steeper local gradient of – 0.13 kpc^{-1} over 2.5 kpc, in conflict with the results of Harris. In both the cases, the star samples have essentially the same ages and should have shown similar abundance distribution. As several supergiants are members of stellar associations with well-defined distances, Luck's distance scale is not questionable. But as mentioned by the author, some uncertainty remains concerning the metallicity of M supergiants. As a matter of fact, when [Fe/H] values are plotted as a function of spectral type, a systematic trend exists at given galactocentric distance, in the sense that cooler stars appear more metal deficient. As the ratio of K-M to F-G supergiants increases towards the anticentre, this effect leads to an overestimation of the gradient. If tentatively we correct the [Fe/H] ratios by +0.05, +0.11 and +0.23 for K0, K5, M0 stars respectively, the gradient becomes δ[Fe/H]/$\delta\varpi$= – 0.09 kpc^{-1} with a mean [Fe/H] ratio at solar galactocentric distance = + 0.095. Although the zero point of the [Fe/H] scale remains somewhat uncertain, this local ratio is consistent with that observed in young stellar groups indicating that the mean abundances in newly formed stars do not exceed 0.1 dex with respect to that of the Sun.

When compared with the [N/H] distribution (*cf.* Section 3.3) or with the cluster abundances, the distribution derived by Harris appears excessively metal-rich at large galactocentric distances. Several sources of uncertainty are present and complicate the interpretation of this distribution. One might suspect that the luminosities of short-period Cepheids on which the abundances beyond 13 kpc are primarily based could have been overestimated (*cf.* Schmidt 1980). In order to check this point, the period-luminosity relation of SMC Cepheids has been used as their [*M*/H] are similar to that expected in the galactocentric distance interval 13 to 15 kpc, assuming a distance modulus of 18.5 for SMC. The gradient then becomes only slightly steeper, *i.e.* – 0.13 to – 0.14 kpc^{-1} between 11 and 16 kpc, leading to A =¼ $A_\odot$ at ϖ= 15 kpc.

The most critical point is the effect of the variation of the reddening law with the galactocentric distance. We may expect the galactic interstellar matter to behave similarly to that of M 31 where the ultraviolet extinction increases with galactocentric distance for a given $E(B\text{-}V)$ excess. At ϖ =13–14 kpc, the reddening law could be close to that observed in SMC by Lequeux *et al.* (1984), and at ϖ = 10–11 kpc close to that found in LMC by Nandy *et al.* (1980), if the CNO abundances in the outer parts of the Galaxy vary in a similar way as in Magellanic clouds. With a steeper extinction in the ultraviolet Harris' metallicity parameter overstimates the metal abundance at a rate increasing with the gas metal-deficiency and then with the distance. Harris' (1981) distribution should then be considered as an upper limit outside the solar circle. The steepening towards the galactic centre seems to result mainly from the choice of [*M*/H] = +0.3 (Luck 1979) for the most metal-rich Cepheids, a value revised downwards since (Luck 1982).

The difficulties pointed out here are not specific to the photometric system employed, but affect all determinations of abundances based on violet or ultraviolet excess measured with intermediate or broadband filters. The stellar distances themselves are not totally reliable as there is some evidence that the ratio $R= A_v/E(B\text{-}V)$ is also dependent on the gas metal content (see *e.g.* Fitzpatrick 1985).

3.3 *Interstellar Matter*

A discussion of the elemental abundance gradients in the interstellar matter is beyond the scope of this paper. Nevertheless, abundances observed in H II regions are extremely useful as they complete our knowledge on abundance distribution at short galactocentric distances and they may be used as a check of abundances derived from young stars. In the range of metallicities occurring in the portion of the disc investigated until now (+ 0.5 > [*M* /H] > –1.0), the nitrogen abundance is expected to follow that of the iron peak elements (*cf.* Matteucci 1986). For a comparison with the metallicity gradients we will adopt [N/H] = [*M* /H].

C, N, O, and He abundance gradients were discussed by Peimbert (1979). The oxygen and nitrogen gradients were –0.10 kpc $^{-1}$ in the distance range 8 to 14 kpc assuming $\varpi_\odot$= 10 kpc. More recently, Shaver *et al.* (1983) derived abundances from electron temperatures over a wider range of galactocentric distances (*cf* Fig. 3). The distances to H II regions were obtained from radial velocities using the Schmidt (1965) rotation curve with $\varpi_\odot$= 10 kpc. The derived oxygen and nitrogen gradients are –0.07 ± 0.015 and –0.09 ± 0.015 kpc $^{-1}$ respectively. With the Sun at 8.5 kpc, the nitrogen gradient would be –0.105 ± 0.02, but this value appears quite dependent on the models of galactic potential adopted. When the distances are deduced from Schmidt (1965) rotation curve the gradient tends to steepen slightly outside the solar circle, and the [N/H] distribution fits almost perfectly those of open clusters and supergiants (*cf* Fig. 4). As the Schmidt curve is known to be somewhat unsatisfactory at large

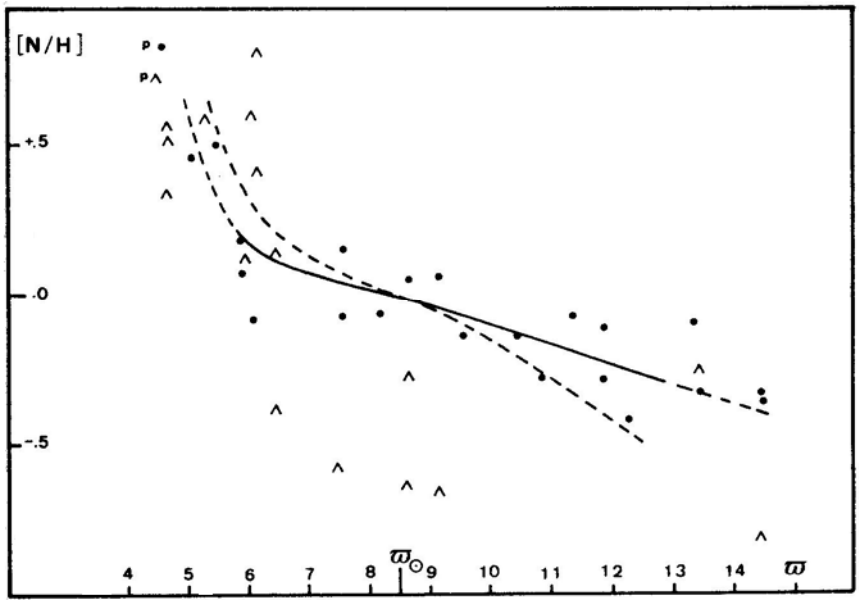

Figure 3. The nitrogen abundance distribution adopted from Shaver *et al.* (1983). Symbols: Λ lower limits; p: peculiar H II regions. The galactocentric distances are deduced from a Sc-like rotation curve by Bahcall *et al.* (1982). The mean sequence is given in full line. The dashed sequence is that obtained with Schmidt (1965) rotation curve.

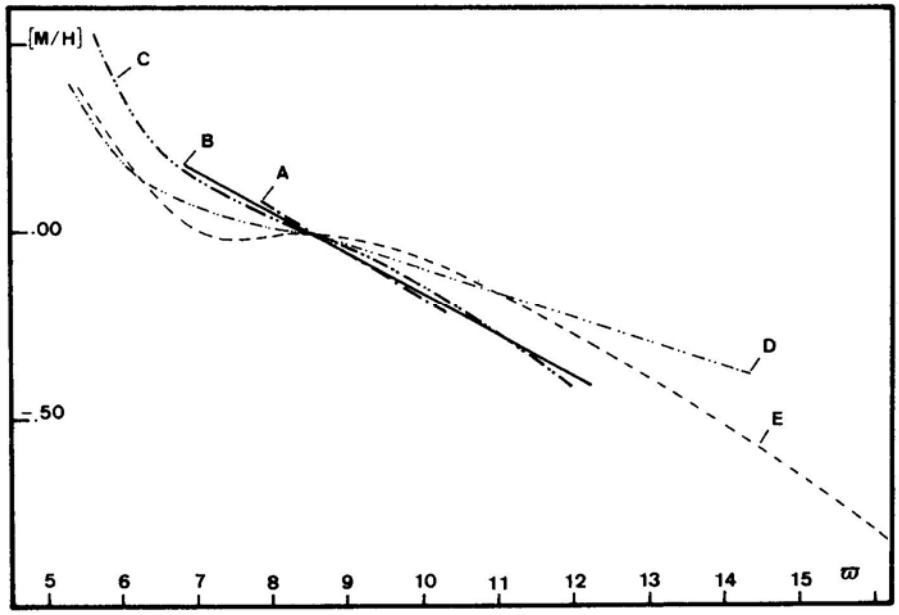

Figure 4. Mean gradients in the young galactic disc. A: supergiants (Luck 1982); B: open clusters (Janes 1979); C: nitrogen abundances in H II regions with distances derived using Schmidt (1965) rotation curve (Shaver *et al.* 1983); D: the same, but distances derived using Bahcall *et al.* (1982) rotation curve; E: classical Cepheids (Harris 1981). All abundances are forced to [*A*/H]=0 at $\varpi_\odot$ = 8.5 kpc.

galactocentric distances, it may be tempting to re-evaluate the gradient using the Bahcall *et al.* (1982) rotation curve, which is flat in the region 40–60 kpc and is similar to those observed in Sc galaxies. As the kinematical distances are increased, especially at large ϖ, the gradient becomes more nearly constant, and also smaller, *i.e.* – 0.066 kpc $^{-1}$ over 8 kpc. This value is inconsistent with that deduced from stars with well-known distances. The agreement with Harris' distribution (Fig. 4) may be considered as partially spurious remembering the reservation on the validity of photometric abundances.

An additional evidence for a gradient of about – 0.10 dex kpc^{-1} at $\varpi_\odot$ is provided by the distribution of abundances in Supernovae remnants. Binette *et al.* (1982) found a nitrogen gradient of – 0.103 ± 0.03 or – 0.087 ± 0.03 (if the nitrogen is primary or secondary, respectively), the mean value – 0.095 ± 0.03 being a suitable value to adopt.

4. Old disc stars: birthplaces and ages

The basic difficulty with old stars is the fact that—since these stars follow non-circular orbits—they are presently observed at galactocentric distances which are often different from those at the time of their birth. This is a consequence of both their initial space motions and of the diffusion of their orbits with time.

The effects of isotropic diffusion of the stellar orbits have been investigated by Wielen (1977) and more recently by Wielen & Fuchs (1985). Although the origin of this

diffusion is not fully explained, a semi-empirical approach shows that the amplitude of epicyclical motions increases as $t^{½}$. After a few billion years (*cf.* Fig. 5), the star's galactocentric distance may differ by several kpc from its initial value whereas the mean galactocentric distance $\varpi = ½ (R_a + R_p)$, the mean between apo- and pericentric distances, remains fairly close to the initial value ϖ_i

In order to derive an abundance gradient in the disc at a given epoch in the past, it is then necessary to replace each star or object at its right initial galactocentric distance, and hence to define their galactic orbits.

The necessary ingredients are evidently the distances, the proper motions, and the radial velocities. The need on significant proper motions restricts the volume of investigation to a few hundred parsecs from the Sun.

As the solar vicinity is visited by stars showing a wide variety of orbits, eccentricities, and mean galactocentric distances, it is possible to trace back in the past the distribution of [*M*/H] as a function of ϖ provided that some discrimination on age is made. Mayor (1976) has shown that an age criterion is necessary for decoupling the effects of a gradient at a given epoch and of the metal enhancement with time at a given galactocentric distance.

Except for subgiants and for a few main-sequence stars for which Ca II K line intensities are known, no individual stellar ages are available. Especially for the oldest populations, the number of stars with known ages is clearly insufficient for a statistically accurate determination of palaeogradients of abundances. We have then to rely on kinematical age estimators.

The space velocities dispersions σ_u, σ_v, σ_w are known to be increasing functions of age. A calibration of σ_w versus age has been worked out by Mayor (1976).

An age ranking using orbit eccentricities has been frequently used in the past. For small-eccentricity stellar samples, part of the spread in age and abundance results from the inclusion of stars with non-negligible perpendicular motions (or orbital inclinations). It is possible to refine the age ranking by taking into account not only the

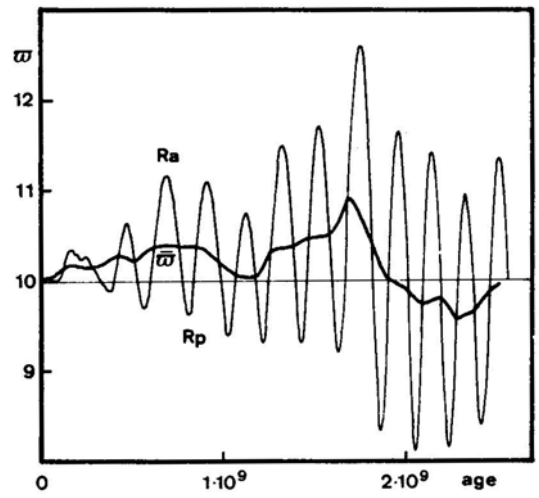

Figure 5. Example of diffusion orbit from Wielen (1977). The thick line shows the variation of the mean distance to the centre $\bar{\varpi}$ as a function of the age.

eccentricity but also the *W* velocity component, which is a sensitive function of age. The following function will be used here for the constitution of groups of kinematical ages:

$$f = \frac{1}{C}\left[\frac{(U_c)^2}{\sigma_u} + \frac{(V_c)^2}{\sigma_v} + \frac{(W_c)^2}{\sigma_w}\right]^{1/2}$$

with $U_c = U - 10$, $V_c = V + 6$, $W_c = W + 6$, and *U, V, W* the velocity components relative to the Sun. The values σ_u, σ_v, σ_w were taken equal to those observed by Vyssotsky in an unbiased sample of dK–dM stars. The constant *C* is adapted in such a way that for $W_c = 0$, and for small eccentricities e, $f = e$. The *f* function becomes:

$$f = (1/300)(U_c^2 + 2.5\ V_c^2 + 3.5\ W_c^2)^{1/2}.$$

An *f* value exceeding a given threshold f_0 is a sufficient condition for an age $a > a_0$, but as for the eccentricity, it is not a necessary condition and a partial mixing of ages is then unavoidable especially for small *f* samples.

An age grouping according to/parameter (or *e*) makes the implicit hypothesis that stars sharing the same *f* value should have the same age whatever their birth-distance could be. This assumption would be correct only if the mechanism of diffusion of orbits would have the same efficiency at all the galactocentric distances. It is probably not true as regards the perturbations by molecular clouds whose density shows a strong dependence on ϖ. We may suspect that stars at $\varpi < \varpi_\odot$ are somewhat younger than those at $\varpi > \varpi_\odot$ for a given value of *f*.

The orbital parameters R_a, R_p, $\bar{\varpi}$ are deduced from space velocities with the help of a galactic potential model. The model adopted here was built by P. Magnenat (personal communication, 1984) and fits the second Sc-like rotation curve by Bahcall *et al.* (1982). It is a three-component model assuming $\varpi_\odot = 8.0$ kpc, a circular velocity at the Sun equal to 228.7 km s^{-1} and a local density $0.15 M_\odot$ pc $^{-3}$. The implications of this particular choice will be discussed in the next section.

The derivation of abundance gradients from distributions of [*M*/H] versus ϖ also assumes the conservation of $\bar{\varpi}$ with time. This hypothesis is approximately true as regards the diffusion of the orbits but not as concerns the effect of a variation of the galactic potential consecutive to the slow building up of the disc. The non-conservation of $\bar{\varpi}$ for the oldest stars will affect the gradient value less than that of the mean [*M*/H] ratio as a function of time at $\varpi_\odot$, in the interval of $\bar{\varpi}_\odot = 7$ to 12 kpc covered by the present investigation.

5. The NLTT sample

Stars from Luyten's NLTT catalogue with $m_R \leqslant 11.5$ belonging to the decimation zone +10° to –10° have been observed photometrically in the Geneva system from La Silla, Chile, and partly with Coravel, from Haute Provence Observatory, for radial velocities.

This sample, with proper motions exceeding 0.19 arcsec yr $^{-1}$, is tangential-velocity limited, *e.g.* $V_T \leqslant 90$ km s^{-1} at l00 pc, but not directly metal abundance biased. It consists of a mixture of nearby stars, old disc and halo stars.

The stellar physical parameters are deduced from calibrations of Geneva system for late-type stars by Grenon (1978, 1981). Stars cooler than about K4 V are not considered here as no reliable [*M*/H] estimator is available. Spatial velocities and

metal abundances have been obtained for 530 stars in the range of distances 20 to 100 pc. The stars closer than 20 pc will be considered separately as nearby stars.

When stars are divided in intervals according to f parameter, we obtain, (*cf.* Fig. 6) the following abundance distributions: for $f < 0.2$ we see a unimodal distribution centred on [M /H]= 0, and similar to that of unevolved nearby G and K stars (Grenon 1984).

The interval $0.3 < f < 0.5$ is characterized by the presence of a bimodal distribution, showing a mild metal poor, and a metal-rich to SMR populations, The mode of the [M/H] distribution is shifted towards low [M/H] with increasing f values showing a smooth transition from population I to II stars. The metallicity distribution of stars with $f \geqslant 1$ is essentially the same as that of globular cluster system.

Fig. 7 shows the distribution of [M /H] versus. ϖ A general increase of the mean [M/H] with decreasing f is patent but also that of the mean $\bar{\varpi}$ with [M/H]. The vast majority of old stars have $\bar{\varpi}$ smaller than $\varpi_{\odot}$. Neglecting the age separation would lead to an almost zero gradient in the interval $6 < \bar{\varpi} < 9$ kpc.

When stars with [M /H] > 0.0 are considered, the mean metallicity increases with decreasing $\bar{\varpi}$, a consequence of the metallicity gradient. As the stars with the smallest $\bar{\varpi}$ and the highest [M/H] are also the oldest, we could deduce that the metallicity has decreased with the time if we neglect to take into account the stellar birthplaces.

The mean [M /H] are plotted as a function of ϖ in Fig. 8a for three intervals of f. The group defined by $f \leqslant 0.20$ contains young to intermediate age stars, typically less than 3

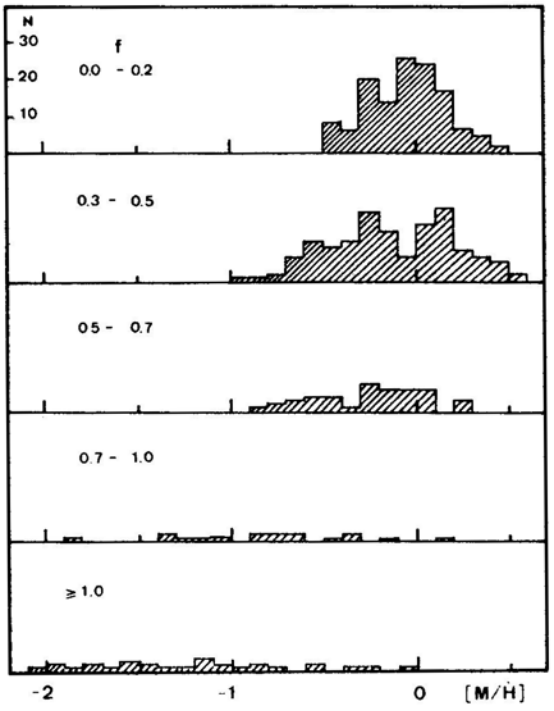

Figure 6. Metal abundance distributions of NLTT stars hotter than K4 V for various f parameter intervals. The Hyades [M/H] is +0.15.

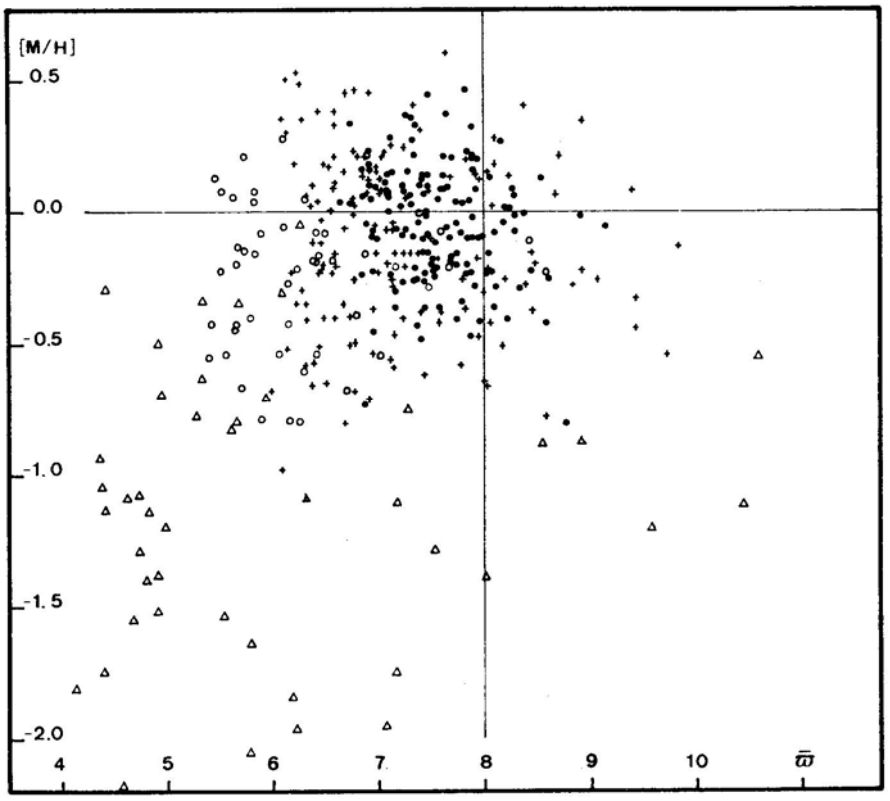

Figure 7. The distribution of [*M*/H] versus the mean galactocentric distance ϖ for NLTT stars with distances 20 to 100 pc. Symbols: • : $f < 0.20$; +: f ε [0.30, 0.50]; O: f ε[0.15, 0.70]; Δ: $f > 0.70$.

to 4 billion years old; the interval 0.20 to 0.35 correspond to ages of about 3–10 × 10^9 yr and the interval 0.35 to 0.70 to ages exceeding 10^{10} yr. The striking feature is that, for the first two age groups, the [M/H] distribution is essentially the same in the domain of overlap, indicating a very small (if any), metal abundance enrichment during the galactic disc lifetime. At $\varpi_\odot$ the oldest group is only 0.10 dex, more metal poor than the young stars which indicate $[M/H]_{\varpi_\odot} = -0.07$. The flattening of the gradient for $\bar{\varpi} < 7.5$ kpc, or even the decrease of [*M*/H] for the oldest group, is a spurious effect. For large eccentricities and small $\bar{\varpi}$, it appears no more possible to discriminate between inner spheroid and old disc stars on the basis of the kinematical criterion alone. The minimum ϖ for SMR stars is about 6.2 kpc (Fig. 7). At smaller $\bar{\varpi}$, the velocity dispersion of disc stars is then not large enough to produce a significant fraction of orbits with apocentric distances $\geqslant \varpi_\odot$. For ϖ less than about 7.5 kpc, the number of SMRs (the high eccentricity fraction of inner old-disc stars) becomes small compared to that of intermediate population stars characterized by a higher velocity dispersion and a lower metallicity. In this range of galactocentric distances the mean [*M*/H] is not appropriate to describe the disc metallicity and underestimates it. The NLTT stars show a gradient of – 0.07 kpc^{-1} for $\bar{\varpi}$ from 7.0 to 8.7 kpc and – 0.14 kpc^{-1} for $\bar{\varpi}_\odot$ from 8.7 to 10 kpc.

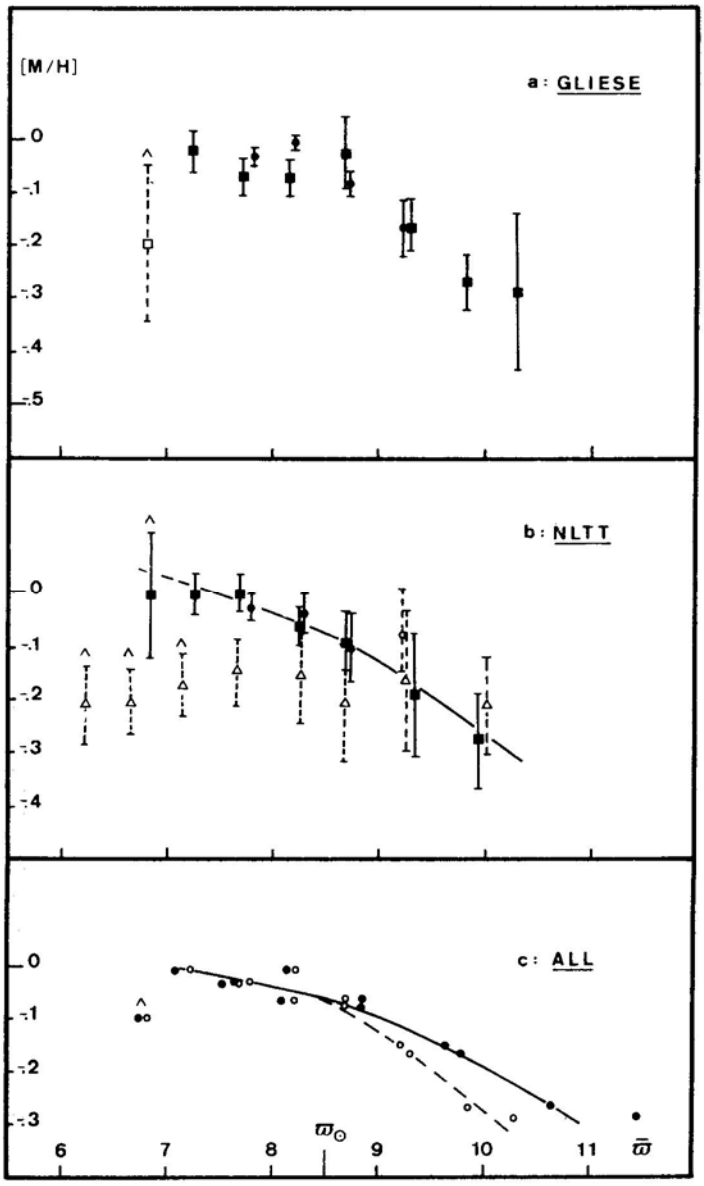

Figure 8. The distribution of the mean metal abundance [*M*/H] as a function of $\bar{\varpi}$. Symbols: ●: f ε[0.0,0.20]; ■: f ε [0.21, 0.35]; Δ :f > 0.35. (a) Glieses' stars with r <20 pc; (b) NLTT stars with r from 20 to 80 pc; (c) all stars; open symbols: Bahcall *et al.* (1982) rotation curve; full symbols: Eggen, Lynden-Bell & Sandage (1962) potential.

6. The stars nearer than 20 pc

The NLTT sample being kinematically biased, it is important to check the results using stars with known proper motion in a distance-limited sample. Gliese's catalogue is believed to be fairly complete down to at least K5 V, and may be considered as a sample complete in volume.

For 648 stars with known radial velocities, photometric [*M*/H] and distances confirmed to be less than 20 pc, orbital parameters are computed in the same way as for stars with known proper motions. For groups with $f \leqslant 0.35$, [*M*/H] versus $\bar{\varpi}$ distribution appears to be essentially the same as for the NLTT sample (Fig. 8b). The number of stars with $f > 0.35$ is insufficient here for a description of the trend of [*M*/H] versus ϖ. The change of slope at $\varpi = 8.7$ kpc is apparent here too and the gradient outside 8.7 kpc is again -0.14 kpc^{-1}, independent of age. The amplitude of this change appears to be quite sensitive to the shape of the galactic potential in the outer regions. When the Eggen, Lynden-Bell & Sandage (1962) potential is adopted, this curvature almost vanishes (Fig. 8c). The condition that gradients deduced from *in situ* observations and from kinematics should be identical for all ϖ, provides a strong constraint on the galactic potential outside the solar orbit.

7. The evolution of metal abundance distribution with time

Previous gradient determinations indicate a gradient steepening for the very-young-disc population (see Mayor 1976; Grenon 1977). The present investigation shows that, except for very old disc stars for which the coarse method applied here is not fully valid, the gradient has not changed significantly during the history of the galactic disc, nor the mean metal abundance at given $\bar{\varpi}$.

The reasons for the discrepancy with previous results are multiple. When gradients are deduced from kinematics, the gradient flattening observed for old disc stars results from population mixing in the case of small $\bar{\varpi}$ (*cf.* Section 5), and from an overestimation of apocentric distances of stars with $\bar{\varpi} > \bar{\varpi}$ when Eggen, Lynden-Bell & Sandage (1962) model is adopted.

When samples of F-type stars are considered, an important selection bias against old solar abundance to SMR stars is made. It is clear from Fig. 9 that a selection of stars with spectral type earlier than G0 retains old stars near the turnoff only if their [*M*/H] ratio is less than -0.30, In the case of SMR stars the spectral type at the turn-off is as late as G7 IV corresponding to a hydrogen-line type G2. The sample of F stars has, as a consequence, an apparent flattening of the gradient for old stars and an excessive dependance of [*M*/H] on time at $\varpi_{\odot}$.

An unbiased sample of stars should contain all subgiants, down to the spectral type K2 IV in order to include the old, evolved, metal-rich and SMR stars. In the case of dwarfs it should be defined by a limiting absolute magnitude, preferably $M_{\mathrm{v}} \geqslant 5.5$, and not by a limiting colour index value.

Samples of field G and K giants are generally free of bias against metal-rich stars. Nevertheless, an age effect was found by Mayor (1976) working on the Hansen-Kjaergaard (1971) sample of K giants. When distances to the giants are deduced from spectroscopic luminosity estimators, a spurious age effect on the gradient may be

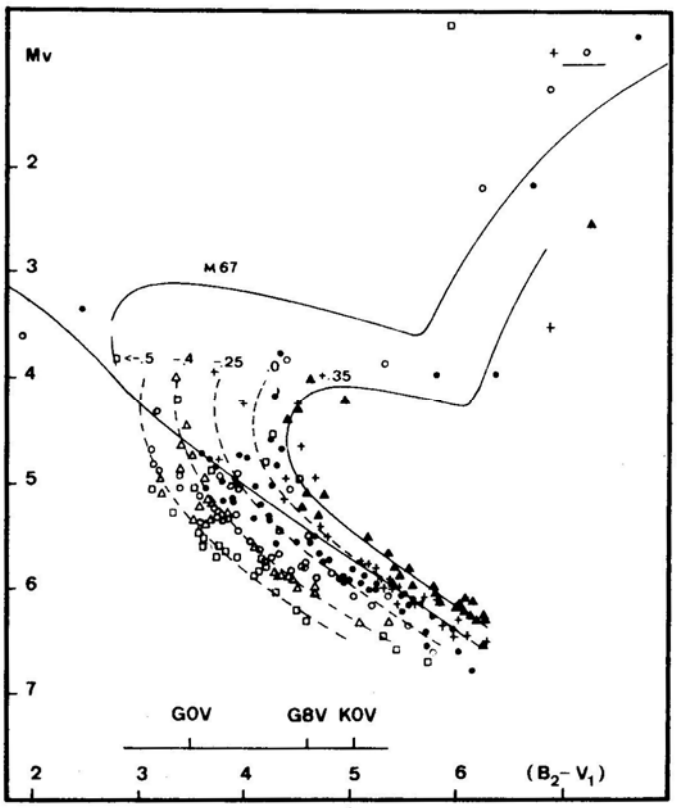

Figure 9. The HR diagram of old NLTT and Gliese stars with *f* parameter from 0.30 to 0.50. Note the abundance effect on the colour and spectral type at the turnoff. Symbols for [*M*/H] intervals: □: $\leqslant$ –.50; Δ: –.49, –.30; O: –.29, .15; ● : –.14, +.14; +:+.15,+.29; ▲: $\geqslant$ + .30.

expected. Because of the spread of masses at given $T_{\rm eff}$ and luminosity, the relations between a gravity parameter and the absolute magnitude are strictly valid only for a given stellar generation (Grenon 1979). If these relations are true for intermediate age stars, distances and space velocities of young massive stars are underestimated whereas those of old giants are overestimated. The amplitude of this effect is as follows: if a true gradient of – 0.10 kpc^{-1} is observed from 1.3 $M_{\odot}$ intermediate age stars, the Hyades generation giants lead to – 0.13 kpc^{-1} and the oldest giants to – 0.08 kpc^{-1} when galactocentric distances are deduced from space velocities.

Local irregularities of the stellar distribution may also affect the gradient determineation. The presence in the solar vicinity of the Hyades cluster and associated group, with an [*M*/H] higher than the mean for their mean ϖ, produces some steepening of the gradient deduced from young stars with eccentricities less than 0.15.

The preceding considerations appear sufficient to explain why the gradient has been found to increase with time in previous investigations. Considering the similarity of the large-scale gradients found from young, massive stars, the open clusters, the interstellar matter, and the old disc stars we may conclude that the gradient did not change significantly in the disc during the last 8 to 10 billion years.

8. A global picture of the abundance distribution

Very few determinations of metal abundances are available for objects located near the galactic centre, *i.e.* for $\varpi < 5$ kpc. A very important set of observations were produced by Withford & Rich (1983) who have observed K giants in Baade's window. The abundance distribution of these inner bulge stars show a bulk of metal-rich stars and about one third of stars with halo metallicities. The mean [*M*/H]of metal-rich stars is + 0.44 ± 0.08 or up to + 0.60 if a less conservative colour excess is adopted.

If we assume that this subpopulation has an age similar to that of SMR stars seen in the solar neighbourhood, *i.e.* about 9×10^9 yr (Grenon 1984), and that it represents the inner extension of the old thick disc, it is possible to produce a global picture of the [*M*/H] distribution in the old disc. The age of SMRs appears quite similar to that of the disc itself at $\varpi_\odot$. For 9-billion-year-old stars, Twarog (1980) gives a mean [M/H] = – 0.30 in the solar vicinity, irrespective of the stellar birthplaces. The old disc NLTT and Gliese stars with *f* between 0.30 and 0.70 show a higher metallicity at $\varpi_\odot$ of about – 0.15 dex. Considering the high velocity dispersion observed near the galactic centre and the associated mixing of orbits, we may expect a flat distribution of [*M*/H] at the centre. Adopting a quadratic law for the relation [M/H] versus ϖ we have, for the old disc, gradients equal to – 0.09 kpc^{-1} for ϖ from 4 to 8 kpc, and – 0.12 kpc^{-1} from 8 to 12 kpc.

The young disc objects, H II regions and Cepheids seem to indicate a steepening of the gradient for $\varpi < 7$ kpc. If real, this abundance increase might result from the intense stellar formation observed in the inner regions and from the gas inflow. In particular, in the so-called 3 kpc arm the present metallicity might well exceed that achieved in the central regions at the end of the bulge formation. In the outer regions the young-disc metal-abundance distribution has a shape very similar to that of old disc stars, with a mean abundance at solar galactocentric distance equal to – 0.05 dex.

References

Bahcall, J. N., Schmidt, M., Soneira, R. M. 1982, *Astrophys. J.*, **258,** L23.
Binette, L., Dopita, M. A., d'Odorico, S., Benvennuti, P. 1982, *Astr. Astrophys.*, **115,** 315.
Cannon, R. D. 1970, *Mon, Not. R. astr. Soc.*, **150,** 111.
Clegg, R. E. S., Bell, R. A. 1973, *Bull am. astr. Soc.*, **5,** 2.
Eggen, O. J., Lynden-Bell, D., Sandage, A. R. 1962, *Astrophys. J.*. **136,** 748.
Fitzpatrick, E. L. 1985, *Astrophys. J.*, **299,** 219.
Grenon, M. 1972, in *IAU Coll.* 17*: L' Age des Etoiles,* Eds G. Cayrel de Strobel & A. M. Delplace, Paris-Meudon Observatory, p. xxix–1.
Grenon, M. 1977, in *Highlights of Astronomy,* **4,** 55.
Grenon, M. 1978, *Publ Obs. Geneve,* **5,** 1.
Grenon, M. 1979, *Dudley Obs. Rep.*, **14,** 171.
Grenon, M. 1981, in *IAU Coll.* 68: *Astrophysical Parameters for Globular Clusters,* Eds A. G. D. Philip & D. S. Hayes, Schenectady, New York, p. 393.
Grenon, M. 1984, *Van Vleck Obs. Contr.*, **1**, 439.
Hansen, L., Kjaergaard, P. 1971, *Astr. Astrophys.*, **15,** 123.
Harris, H. C. 1981, *Astr. J.*, **86,** 707.
Hawley, S. A. 1978, *Astrophys. J.*, **224,** 417.
Janes, K. A. 1979, *Astrophys. J. Suppl. Ser.*, **39,** 135.
Janes, K. A., McClure, R. D. 1972, in *IAU Coll.* 17: *L' Age des Etoiles,* Eds G. Cayrel de Strobel & A. M. Delplace, Paris-Meudon Observatory, p. xxviii-1.

Jennens, P. A., Helfer, H. L. 1975, *Mon. Not. R. astr. Soc.*, **172,** 667.
Keenan, D. W. 1973, in *IAU Symp.* 54: *Problems of Calibration ofAbsolute Magnitudes and the Temperature of Stars*, Eds B. Hauck & B. E. Westerlund, D. Reidel, Dorrecht, p. 68.
Keenan, D. W., Innanen, K. A., House, F. C. 1973, *Astr. J.*, **78,** 178.
Lequeux, J., Maurice, E., Prevost, L., Prevost-Burnichon, M. L. 1984, in *IAU Symp.* 108: *Structure and Evolution of the Magellanic Clouds*, Eds S. van den Bergh & K. S. de Boer, D. Reidel, Dordrecht, p. 405.
Luck, R. E. 1979, *Astrophys. J.*, **232,** 797.
Luck, R. E. 1982, *Astrophys. J.*, **256,** 177.
Matteucci, F. 1986, *Mon. Not. R. astr. Soc.*, **221,** 911.
Matteucci, F., Tornambe, I. 1985, *Astr. Astrophys.*, **142,** 13.
Mayor, M. 1976, *Astr. Astrophys.*, **48,** 301.
Nandy, K., Morgan, D. H., Wills, A. J. Wilson, R., Gondhalekar, P. M., Houziaux, L. 1980, *Nature*, **283,** 725.
d'Odorico, S., Peimbert, M., Sabbadin, F. 1976, *Astr. Astrophys.*, **47,** 341.
Pagel, B. E. J., Patchett, B. E. 1975, *Mon. Not. R. astr. Soc.*, **172,** 13.
Panagia, N., Tosi, M. 1981, *Astr. Astrophys.*, **96,** 306.
Peimbert, M. 1974, in *IAU Symp.* 58: *The Formation and Dynamics of Galaxies*, D. Reidel, Dordrecht, p. 141.
Peimbert, M. 1977, in *IAU Symp.* 45: *Chemical and Dynamical Evolution of our Galaxy*, Eds E. Basinska & M. Mayor, Geneva Observatory, p. 149.
Peimbert, M. 1979, in *IAU Symp.* 84: *The Large-Scale Characteristics of the Galaxy*, Eds W. B. Burton, D. Reidel, Dordrecht, p. 307.
Peimbert, M., Serrano, A. 1982, *Mon. Not. R. astr. Soc.*, **198,** 563.
Peimbert, M., Torres-Peimbert, S., Rayo, J. F. 1978, *Astrophys. J.*, **220,** 516.
Schmidt, E. G. 1980, *Bull. Am. astr. Soc.*, **12,** 457.
Schmidt, M. 1965, in *Galactic Structure*, Eds A. Blaauw & M. Schmidt, Univ. Chicago Press, p. 513.
Shaver, P. A., McGee, R. X., Lynette, M. N., Danks, A. C, Pottasch, S. R., 1983, *Mon. Not. R. astr. Soc.*, **204,** 53.
Talent, D. L., Dufour, R. J. 1979, *Astrophys. J.*, **233,** 888.
Torres-Peimbert, S., Peimbert, M. 1977, *Rev. Mexicana Astr. Astrofis.*, **2,** 181.
Twarog, B. A. 1980, *Astrophys. J.*, **242,** 242.
Wielen, R.1977, *Astr. Astrophys.*, **60,** 263.
Wielen, R., Fuchs, B. 1985, in *IAU Symp.* 106: *The Milky Way Galaxy*, Eds H. van Woerden, R. J. Allen & W. B. Burton, D. Reidel, Dordrecht, p. 481.
Withford, A. E., Rich, R. M. 1983, *Astrophys. J.*, **274,** 723.

J. Astrophys. Astr. (1987) **8,** 141–145

On a Possible Metallicity Gradient in SMR Stars

G. Cayrel de Strobel *Observatoire de Paris, Section de Meudon, 92195 Meudon Cedex, France*

Abstract. The possibility of existence of a metallicity gradient in super-metal-rich (SMR) stars is discussed. It is concluded that the SMR phenomenon was more active in the past than it is now.

Key words: stars, super-metal-rich—Galaxy, metallicity gradient—Galaxy, chuemical evolution

1. Introduction

The enrichment in heavy elements has begun in the universe immediately after its birth and still continues. It is widely accepted that all elements as heavy as—or heavier than—carbon have been formed by nucleosynthesis in stellar interiors or during supernova explosions. At the present time the problem is to find out how the different star-interstellar-matter systems have been enriched in heavy nuclei during the phases of their evolution. From observations we know that the metal enrichment has not been uniform, neither in time, nor in location, in our own Galaxy. We know also that this metal enrichment is tightly bound to the nature of the nucleosynthesis which has acted in supernova explosions and, in much less efficient way, in the centre of red giants. One of the things we still poorly know, is the value of the upper limit of metal enrichment in stars: is it possible to find stars having metal abundances two, three or more times higher than that of the Sun?

Because this meeting is dedicated to low-mass stars, and because my paper is a very short one, I shall speak only of metal-rich solar type subgiants and dwarfs, leaving for another occasion the discussion on super-metal-rich (SMR) G and K giants. The convective zone of the slightly evolved or unevolved solar-type stars is sufficiently developed to prevent diffusion effects of chemical elements, and to avoid the Am-Ap phenomenon. We therefore can assume that in these stars the chemical composition of the atmosphere does reflect the initial chemical composition of the object.

2. Metal-rich G and K stars

Spinrad & Taylor (1969) called a star super-metal-rich if its overall metal to hydrogen ratio [*M*/H], was higher than that of the Hyades:

$$[M/\mathrm{H}]_{\mathrm{SMR}} > [M/\mathrm{H}]_{\mathrm{Hyades}}.$$

This statement came back in my mind while finishing with Roger Cayrel and Bruce Campbell a spectral analysis based on high signal/noise C. F. H. Reticon spectra (Cayrel

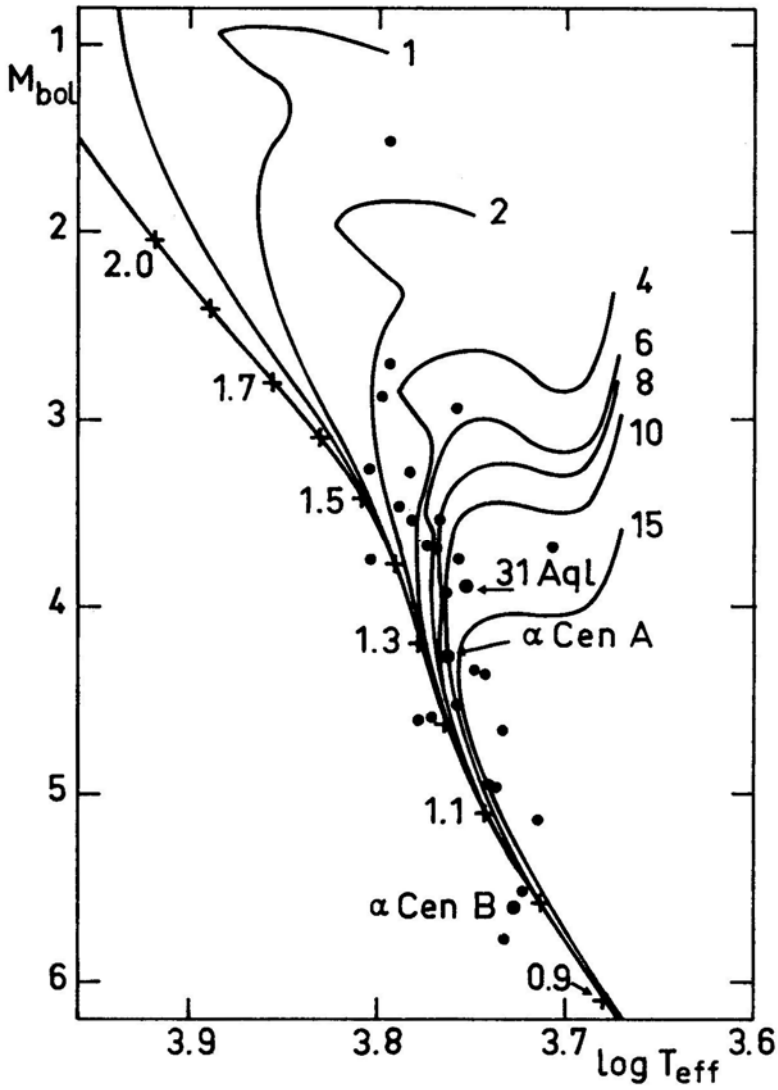

Figure 1. Observational HR diagram for 29 SMR dwarfs and subgiants compared to a metal-rich grid of isochrones (Y = 0.30, Z = 0.034, l/H_P=1.5) extrapolated from VandenBerg (1983) models.

et ah 1985). We obtained accurate abundances for metals (principally iron) in twelve Hyades solar-type dwarfs. The resulting iron abundances are very near solar value for two dwarfs (probably due to a high level of their chromospherical activity); for the remaining 10 stars the mean abundance is:

$$[\mathrm{Fe/H}]_{\mathrm{Hyades}} = +0.12 \pm 0.03 \text{ dex.}$$

We choose the above value for the Fe abundance of the Hyades in selecting SMR candidates in the [Fe/H] Catalogue (Cayrel de Strobel *et al.* 1985). We surveyed the

Table 1. SMR/F, G and K dwarfs and subgiants.

HD	$B-V$	U	V	W	log T_{eff}	M_{bol}	[Fe/H]	Age $Z=0.034$	Age $Z=0.016$
36395	1.47	−20	−57	−11	3.559	8.32	+0.60	D	D
160691	0.70	+15	−6	−3	3.748	4.32	+0.41	>15	⩾15
182572	0.77	+126	−21	−25	3.753	3.89	+0.41	13	12.5
157881	1.36	0	−53	−10	3.602	7.44	+0.40	D	D
1461	0.68	+25	−31	+2	3.743	4.96	+0.39	15	⩾15
10780	0.81	+21	−15	−5	3.734	5.79	+0.36	D	D
121370	0.58	−8	−15	−2	3.794	2.70	+0.30	2.5	3.7
88230	1.37	+8	−19	−35	3.602	7.59	+0.28	D	D
145675	0.90	−23	−7	−9	3.720	5.52	+0.27	D	D
190360	0.73	+10	−47	−92	3.740	4.35	+0.26	>15	⩾15
102870	0.55	−37	+3	+7	3.783	3.56	+0.24	4	7
190248	0.76	—	—	—	3.734	4.66	+0.23	⩾15	⩾15
128620	0.68	+29	+2	+14	3.763	4.27	+0.22	10	12.5
128621	0.88	+29	+2	+14	3.729	5.61	+0.22	D	D
161797	0.75	−19	−33	−5	3.707	3.69	+0.22	12	11
34411	0.63	+77	−45	+5	3.758	3.76	+0.22	11	11
75732	0.87	+37	−19	−10	3.716	5.14	+0.22	⩾15	⩾15
120136	0.48	+33	−20	−7	3.805	3.26	+0.21	1.8	3.5
104304	0.77	−20	−16	−16	3.739	4.96	+0.18	15	15
30652	0.45	+26	−15	+4	3.805	3.74	+0.17	D	3
86728	0.66	+57	−46	+20	3.768	3.71	+0.16	7	9.5
114710	0.57	+45	+11	+8	3.778	4.61	+0.16	D	D
10307	0.62	+37	−28	0	3.773	4.59	+0.15	D	D
30562	0.62	+52	−79	−19	3.768	3.55	+0.13	8	8.3
102634	0.52	—	—	—	3.783	3.30	+0.12	3.5	6.1
107213	0.50	—	—	—	3.799	2.88	+0.12	2.6	3.9
124570	0.54	+38	−31	−26	3.794	1.52	+0.12	1.5	1.4
187691	0.55	+3	−3	−28	3.789	3.47	+0.12	2.5	6.0
187923	0.65	−57	−65	+26	3.758	2.95	+0.12	5.5	5.0
217014	0.67	+14	−28	+15	3.758	4.73	+0.12	D	10.0

D: doubtful.

Catalogue in order to find stars having

$$[Fe/H] \geqslant +0.12 \text{ dex}$$

We used then Spinrad & Taylor definition of SMR's as:

$$[Fe/H]_{SMR} \geqslant +0.12 \text{ dex.}$$

We found that in the Catalogue exist

30 F, G and K dwarfs and subgiants,

and 60 G and K bright yellow giants,

satisfying the above condition.

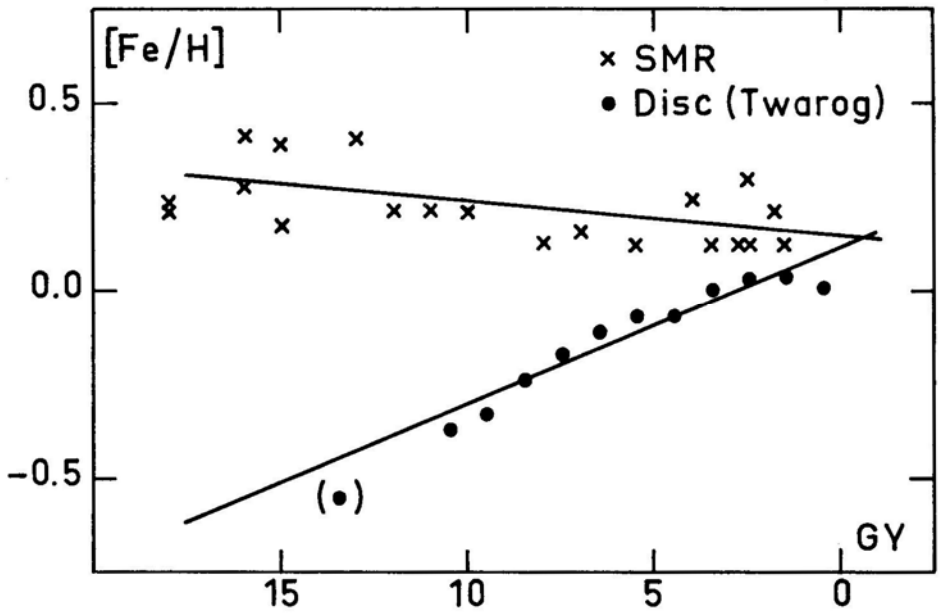

Figure 2. [Fe/H] versus age relations: the upper one refers to SMR subgiants which could be dated, the lower one is the general disc-star relation by Twarog (1980).

These 90 stars represent 17 per cent of all the 539 stars contained in the [Fe/H] Catalogue (edition January 1985).

As already said, today we shall speak only of 30 dwarf and subgiant SMR candidates. Table 1 gives relevant data for these objects: HD number, *B—V,* space velocity components: *U, V, W,* log $T_{\rm eff}$, $M_{\rm bol}$, [Fe/H]. The last two columns of this table contain two age estimations for the programme stars, one with the help of a metal-rich isochrone grid (Z = 0.034) and one with a metal-normal isochrone grid. The metal-normal grid is from VandenBerg (1983), the metal-rich comes from an extrapolation of VandenBerg's grids.

The sample of dwarfs and subgiants contained in Table 1 is by no means a significative SMR star sample in our solar neighbourhood. Certainly many more SMR low-mass M dwarfs do exist. But detailed spectral analyses of such objects are very difficult and abundance results very doubtful. For instance, the only star in Table 1 that is metal-rich by a factor 4, with respect to the Sun, is the M 1 dwarf HD 36395 analyzed by Mould (1978). Besides, only 17 per cent of the sample of 30 stars are 'super-metal-rich' by more than a factor of 2 and less than by a factor of 2.6 with the exception of Mould's star. The other stars are metal-rich by a factor of 2 down to 1,3 with respect to the Sun. It is also interesting to note that the 30 stars have rather high space-velocity parameters, showing that probably all belong to the old disc population.

With the help of the last two columns of Table 1 we tried to attribute a 'turn-off' age to the slightly evolved stars. The ages for the stars contained in the last column are spurious because they have not been obtained with the grid of isochrones computed with the appropriate Z. Fig. 1 reproduces the metal-enhanced grid and the positions in

it of 29 SMR dwarfs and subgiants of which we have determined the bolometric magnitudes and effective temperatures.

The ages contained in the penultimate column have been used in constructing a [Fe/H] versus 'age' diagram., This diagram is shown in Fig. 2. Two different relations are displayed on it; the upper one refers to SMR stars, whereas the lower one comes from Twarog (1980) and is the general disc-star relation.

3. Conclusion

In conclusion we can say, that, there is an indication that the SMR phenomenon was more active in the past than it is now. Following Twarog (1980) we see that, in 10 Gyr the [Fe/H] abundance of disc stars has increased by approximately + 0.4 dex, whereas the [Fe/H] abundance of SMR disc stars has diminished by 'very' approximately – 0.1 dex. However, all along these last 10 Gyr, the SMR phenomenon did exist, but slightly damped.

A possible, but not unique, interpretation of this is that the interstellar medium in our Galaxy became progressively more chemically uniform with time.

References

Cayrel, R., Cayrel de Strobel, G., Campbell, B.1985, *Astr. Astrophys.*, **146,** 249.
Cayrel de Strobel, G., Bentolila, C., Hauck, B., Duquennoy, A. 1985, *Astr. Astrophys. Suppl. Ser.*, **59,** 145.
Mould, J. R. 1978, *Astrophys. J.*, **226,** 923.
Spinard, H., Taylor, B. J. 1969, *Astrophys. J.*, **157,** 1279.
Twarog, B. A. 1980, *Astrophys. J.*, **242,** 242.
VandenBerg, D. A. 1983, *Astrophys. J. Suppl. Ser.*, **51,** 29.

J. Astrophys. Astr. (1987) **8,** 147–152

Chemical Evolution of Galaxies and Abundances in Low-Mass Stars

Jean Audouze *Institut d'Astrophysique du CNRS, 98 Bis Blvd Arago, F-75014 Paris, France* and *Laboratoire Rene Bernas, Orsay Campus, France*

Abstract. The chemical evolution of galaxies is discussed with reference to elemental abundances in low- and intermediate-mass stars.

Key words: galaxies, chemical evolution—stars, low- and intermediate-mass

1. Introduction

Since they are very numerous and they have a long life-time, low-mass stars play a crucial role in the evolution of galaxies. They can be used to determine the metallicity at the beginning of galactic evolution. Moreover, when one compares their abundance ratios with those observed in other sites they lead to a better understanding of the formation and the evolution of many nuclear species. After a very brief presentation of the main parameters which govern the evolution of galaxies like the rate of star formation, the stellar initial mass function and the nuclear yields, I will provide a list of the nuclear species which should be observed in low-mass stars in order to progress in the analysis of such evolutions.

2. The main parameters governing the galactic evolution

2.1 *The Initial Stellar Mass Function*

Salpeter (1955) has been the first to propose a simple relation between the relative number of stars $\phi(m)\mathrm{d}m$ with respect to their mass m at their birth.

$$\phi(m)\mathrm{d}m \sim \int_{m_{\min}}^{m_{\max}} m^{-x}\,\mathrm{d}m \tag{1}$$

where the exponent x depends on m such that $x(m)$ ~0.6 for $m < 1.8 M_{\odot}$ and ~2 for $m > 1.8\ \mathrm{M}_{\odot}$ (see *e.g.* Miller & Scalo 1979; Scalo 1985 and Zinnecker 1986 for a more thorough presentation); $m_{\min}$ and $m_{\max}$ represent respectively the lower and upper limits of the stellar masses represented by this distribution. These two quantities *may not be constant everywhere.* For instance Güsten & Mezger (1983) have proposed a model for the chemical evolution of our Galaxy for which $m_{\min}=0.1\ M_{\odot}$ for the stars formed out of the spiral arms and $m_{\min} = 2M_{\odot}$ for the stars formed inside them: this assumption has been made in order to account for the metallicity gradient with respect to the galactocentric distance. More recently Larson (1985) has built up a bimodal star-formation model fairly similar to the one of Gusten & Mezger (1983) but with no

reference to the galactic arms. Concerning m_{max}, one may argue that $m_{max} \sim 1/Z^{\beta}$ with $\beta \sim 1$ since the largest giant H II region complexes have been observed by Viallefond and collaborators in the external regions of the galactic disc of M101 where the metallicity should be the weakest.

2.2 *The Rates of Star Formation*

The classical Schmidt law $dS/dt \sim \mu^{\alpha}$ such as $1 < \alpha < 2$ where μ and S are respectively the gas and the stellar density is most often used to parametrize the rate of star formation. The Schmidt law has been found to be a valid representation of the rate of star formation in the high-mass range by Guibert, Lequeux & Viallefond (1978) who deduced $\alpha = 2$ from the many tracers of high-mass stars.

It is very difficult to determine directly the rate of formation of low-mass stars. In a still unpublished work, G. Malinie, J. Audouze & M. Dennefeld (see a quotation of this work in Audouze, 1983) are attempting to use the planetary nebulae and the observations of their metallicity to deduce the rate of formation of low-mass stars. From their analysis they would conclude that $S(t) \sim e^{-t/\tau}$ with $\tau \sim 4^{+2}_{-1} \times 10^9$ years.

Audouze, Chiosi & Woosley (1986) are also investigating the possibility of a constant rate of star formation in the beginning of the galaxy evolution.

$$S(t) = S_0$$

for $t < t_c$ and then $dS/dt \sim \mu^{\alpha}$ for $t \geqslant t_c$.

To summarize the remarks on the rate of star formation one should recall that this parameter is not always a continuous function: Bursts of star formation occur often in the course of evolution of a galaxy(see *e.g.* Larson & Tinsley 1978). Moreover, the rate of star formation can be stochastic according to Gerola & Seiden (1982, see also White & Audouze 1983).

2.3 *The Yields*

The yields concern the relative production of a given nuclear species by a distribution of stars. They are indeed related to the different nucleosynthetic contributions of the stars with respect to their mass (see *e.g.* the reviews of Audouze& Tinsley 1976; Tinsley 1980; Audouze 1983). The yields y_i concerning a species i can be written as:

$$y_i = \frac{\sum_{i \neq j} X_j \int_{m_{min}}^{m_{max}} Q_{ij}(m)\phi(m)\mathrm{d}m}{1 - \sum_{i \neq j} X_j \int_{m_{min}}^{m_{max}} Q_{ij}(m)\phi(m)\mathrm{d}m}. \quad (2)$$

In this relation Q_{ij} are the mass fraction of the nucleus j transformed into i in a star of mass m; and X_j are the mass fractions of the element j; $\phi(m)$ is the initial mass function (IMF). The yield y_i of a stellar generation is defined as the mass of newly synthesized species Z_i per fraction of matter that is locked-up in long-living stars and remnants. The yields are also related to the constraints coming from the nucleosynthesis and stellar evolution. Audouze & Tinsley (1976), Güsten & Mezger (1983) and Glisten (1986) give a

list of yields of nucleosynthesis processes. It should be stressed at this point that spectroscopic studies of low-mass stars should provide valuable information regarding the determination of some of these yields.

3. A very quick tour in the nucleosynthetic 'zoo'

Recent general accounts of the progress made in nuclear astrophysics are given in Barnes, Clayton & Schramm (1982), Audouze & Mathieu (1986), and Audouze, Chiosi & Woosley (1986). One can distinguish roughly four different nucleosynthetic sites:

1. Primordial nucleosynthesis is responsible for the formation of D, ^{3}He, ^{4}He, ^{7}Li.
2. The interaction between the galactic cosmic rays and the interstellar medium explains the synthesis of ^{6}Li, ^{9}Be, ^{10}B and ^{11}B.
3. The low-mass stars $m < 5M_{\odot}$ should be able to transform some of the ^{12}C and ^{16}O nuclei into species like ^{13}C, ^{14}N, ^{17}O. They synthesize also the *s*-process elements. Moreover, ^{56}Fe seems to be produced by stars less massive than those which form ^{16}O. Planetary nebulae, novae and possibly Type I Supernovae which can have an active nucleosynthetic role should come from low-mass star progenitors.
4. The high-mass stars are especially responsible for the formation of ^{16}O and related elements between Ne and Ca. They terminate their evolution as Type II Supernovae or/and Wolf-Rayet stars.

4. Relations describing the evolution of abundances and gas density during the galactic evolution

These relations are fairly classical and are described in more details in Vigroux, Audouze & Lequeux (1976) and Tinsley (1980). The evolution of the gas density and the abundances of an element *i* are given by:

$$\frac{\mathrm{d}\mu}{\mathrm{d}t} = -\mu v + \int_{m_{\mathrm{inf}}}^{m_{\mathrm{sup}}} E(m) Q(t-\tau_m) v \mathrm{d}m + \delta_{\mu}. \tag{3}$$

where v is the rate of astration, $E(m)$ the fraction of gas returned at the end of the stellar evolution, τ_m the lifetime of a star of mass m such that $\tau_m = 10^{10}/m^{8} + 10^{6}$ yr (one sees here the crucial role of low-mass stars which have a long lifetime such that τ_m cannot be neglected in the calculations), and δ_{μ} is a term describing the possible accretion of gas in the considered zone

$$\frac{\mathrm{d}(Z_i \mu)}{\mathrm{d}t} = -\mu Z_i v + \int_{m_{\mathrm{inf}}}^{m_{\mathrm{sup}}} p_{Z_i} \phi(t-\tau_m) v \mathrm{d}m + \delta_{Z_i} \tag{4}$$

where Z_i is the mass fraction of the element í in the interstellar medium, p_{Zi} the fraction of this element produced in the stars and δ_{ti} the mass fraction of this element contained in the accreted gas. The study of low-mass stars is not only important because their τ_m is large but also because the determination of the different p_{Zi} depends critically on the abundance determination which concern them.

5. A list of evolutionary problems related to low-mass stars

This list is of course far from complete. The reader is advised to exercise his(her) own wisdom on this topic. One could divide the type of problems in which low-mass stars play a role in two classes—;those concerning the elemental abundances and hopefully those concerning the isotopic ratios.

5.1 *Elemental Abundances*

In the sequel of the joint discussion, interesting remarks have been made by Kraft and other colleagues. I will therefore comment only on two points:

1. The concept of primary and secondary elements which has been introduced *e.g.* by Audouze & Tinsley (1976), might be a bit misleading. Let me recall that primary elements are defined as those which can be produced directly in any star while secondary elements are only formed from a first generation of primary elements. This classification should be replaced by that in which one separates the elements produced in high-mass stars which behave like primary elements and those which are produced in low-mass stars which behave like secondary elements.
2. Recently Matteucci (1986) studied the N problem and concluded that N is both a primary and secondary nucleosynthesis product; the primary N originated from high and intermediate stars, whereas the secondary nitrogen is from lower-mass stars. A consistent explanation for the origin of N is yet to be found. A similar problem exists in the case of *s*-process elements and isotopes (see Spite & Spite 1985; Iben 1985) whose synthesis in intermediate-mass stars or low-mass stars is not yet well-understood.

5.2 *Isotopic Ratios*

Isotopic measurements are especially important in this context because they provide valuable information on the relative contributions and properties of the different nucleosynthetic sites defined above. The synthesis of ^{13}C, ^{15}N and ^{17}O are extremely different from those of ^{12}C, ^{14}N and ^{16}O. Tomkin, Luck & Lambert (1976) find $10 < ^{12}C/^{13}C < 35$ in red giants, much smaller than the terrestrial value. Recently, Sneden & Pilachowski (1986) and Sneden, Pilachowski & VandenBerg (1986) determined carbon isotope ratios in old galactic cluster stars and field population II giant stars. Determination of the oxygen isotope ratios in low and intermediate-mass stars are valuable in understanding the stellar nucleosynthesis and galactic nuclear evolution. Recently, Harris, Lambert & Smith (1985) determined the oxygen isotope ratio in several MS and S stars. Wannier (1980, 1985) reviewed the CNO isotope ratios in red giants and the galactic evolution of the CNO nuclides. Schramm (1985) gave detailed review of the problems connected with the nucleosynthetic interpretations of isotopic anomalies. Clearly, we need more determinations of several isotopic ratios in low-mass and population II stars in order to be able to constrain the present models of stellar and galactic evolution.

Clayton (1985) presented a new analytic model of the chemical evolution of the

galaxy and suggested adopting this model as a reference standard for studies of chemical evolution.

6. Concluding remarks

Low-mass stars are the witnesses of the early phases of the galactic evolution. They should constrain the choice of the parameters governing the chemical evolution of galaxies. But for that purpose progress should be made in the determination of more elemental abundances and especially isotopic ratios which constitute the best input data to deduce the relative yields which are used in the galactic evolution models and also in refining the current analyses of various nucleosynthetic mechanisms.

Binaries are also important in the galactic nucleosynthesis. Since more than half of all stars appear to be members of binary systems it is important to consider the effects of binary evolution on nucleosynthesis, and consequently on galactic chemical evolution.

Acknowledgements

These introductory remarks have been written only to please Giusa Cayrel which is perhaps a sufficient motivation by itself. I thank Marie-Christine Pelletan for her quick and efficient typing of these notes.

References

Audouze, J. 1983, in *Proc. ESO Workshop, Diffuse Matter in Galaxies,* Eds J. Audouze, J. Lequeux, M. Levy & A. Vidal-Madjar, D. Reidel, Dordrecht, p. 95.

Audouze, J., Chiosi, C, Woosley, S. E. 1986, *Saas Fee* (lecture notes) in preparation.

Audouze, J., Mathieu, N. 1986, *Nucleosynthesis and its Implications on Nuclear and Particle Physics,* D. Reidel, Dordrecht.

Audouze, J., Tinsley, B. M. 1976, *A. Rev. Astr. Astrophys.,* **14,** 43.

Audouze, J.,Vangioni-Flam, E., Vigroux, L. 1986, in preparation.

Barnes, C. A., Clayton, D. D., Schramm, D. N. (Eds) 1982, *Essays in Nuclear Astrophysics,* Univ. Cambridge Press.

Clayton, D. D.1985, in *Nucleosynthesis,* Eds W. D. Arnett & Truran, Univ. Chicago Press, p. 65.

Guibert, J., Lequeux, J., Viallefond, F. 1978, *Astr. Astrophys.,* **68,** 1.

Güsten, R. 1986, in *Spectral Evolution of Galaxies,* Eds C. Chiosi & A. Renzini, D. Reidel, Dordrecht, p. 449.

Güsten, R., Mezger, P. G. 1983, *Vistas in Astr.,* **26,** 159.

Harris, M. J., Lambert, D. L, Smith, V. V., 1985, *Astrophys. J.,* **299,** 375.

Iben, I. 1985, in *Nucleosynthesis,* Eds W. D. Arnett & J. W. Truran, Univ. Chicago Press, p. 292.

Larson, R. B. 1985, *Mon. Not. R. astr. Soc.,* **214,** 379.

Larson, R. B., Tinsley, B. M. 1978, *Astrophys. J.,* **219,** 46.

Matteucci, F. 1986, *Mon. Not. R. astr. Soc,* **221,** 911.

Miller, G. E., Scalo, J. M. 1979, *Astrophys. J. Suppl. Ser.,* **41,** 513.

Salpeter, E. E. 1955, *Astrophys. J.,* **121,** 161.

Scalo, J. M. 1986, *Fund. Cos. Phys,* **11,** 1.

Schmidt, M.1959, *Astrophys.. J.,***129,** 243.

Schramm, D. N. 1985, in *Nucleosynthesis,* Eds W. D. Arnett & J. W. Truran, Univ. Chicago Press, p. 106.

Seiden, P. E., Gerola, H. 1982, *Fund. Cos. Phys,,* 7, 241.

Sneden, C, Pilachowski, C. A. 1986, *Astrophys. J.*, **301,** 860.
Sneden, C, Pilachowski, C. A., VandenBerg, D. A. 1986, *Astrophys. J.*, **311,** 826.
Spite, F., Spite, M. 1985, *A. Rev, Astr. Astrophys.*, **62,** 1.
Tinsley, B. M. 1980, *Fund. Cos. Phys.*, **5,** 287.
Tomkin, J., Luck, R. E., Lambert, D. L. 1976, *Astrophys. J.*, **210,** 694.
Vigroux, L., Audouze, J., Lequeux, J. 1976, *Astr. Astrophys.*, **52,** 1.
Wannier, P. G. 1980, *A Rev. Astr. Astrophys.*, **18,** 399.
Wannier, P. G., 1985, in *Proc. ESO Workshop, Production and Distribution of C, N, O Elements*, Eds I. J. Danziger, F. Matteucci & K. Kjär, ESO, Garching, p. 233.
White, S. D. M., Audouze, J. 1983, *Mon. Not. R. astr. Soc.*, **203,** 603.
Zinnecker, H. 1986, in *Highlights in Astronomy*, Ed. J. P. Swings, D. Reidel, Dordrecht, Vol. 7, p. 489.

J. Astrophys. Astr. (1987) **8,** 153–159

A New Interpretation of the Metallicity Histogram of Globular Clusters

R. Cayrel *Observatoire de Paris, 61 Avenue de l'Observatoire, F-75014 Paris, France*

Abstract. A new interpretation is given to the low metallicity peak of the bimodal metallicity histogram of galactic globular clusters. It is proposed that these globular clusters are primordial, *i.e.,* formed out of big-bang matter. Their nonvanishing metallicity is attributed to pollution by supermassive stars like R 136a. The first stellar generation is formed out of the 'dirty' primordial matter.

Key words: globular clusters, formation—globular clusters, metallicity

1. Introduction

It is widely assumed that stars have the same chemical composition as the interstellar medium out of which they are born. However, this statement may well be only partially true because, when a cluster of stars is formed, the chemical composition of the cloud progenitor of the cluster has no reason to escape some degree of heavy elements pollution due to the formation of O-stars evolving very fast into Supernovae (SN) within the cloud. Usually this phenomenon is inconspicuous because if, for example, we assume that 20 per cent of the heavy elements produced by the SNs of a cluster have polluted the cloud, the ensuing increase in metallicity ΔZ for the cloud is of the order of:

$$\Delta Z = 0.2\, yr$$

where y is the yield and r the stellar formation efficiency (fraction of the gas turned into stars in the cloud).

Assuming a stellar formation efficiency, $r \simeq 0.08$, (Cohen & Kuhi 1979), and a yield of 0.02 (Matteucci 1983) gives $\Delta Z \simeq 0.0003$, quite small compared to the present value of Z in the disc ($Z \simeq 0.02$).

However if the initial chemical composition of the cloud is $Z = 0$ (primordial cloud) the resulting Z is of the order of the metallicity of a globular cluster and the whole concept of population III is deeply shaken. In this paper we reconsider the metallicity histogram of the globular clusters according to the view that the clouds, progenitors of globular clusters, are primordial, as initially assumed by Peebles & Dicke (1968).

2. The bimodality of the metallicity histogram for galactic globular clusters

Zinn (1985) has convincingly shown that two stellar populations can be identified within the metallicity histogram of galactic globular clusters (Fig. 1).

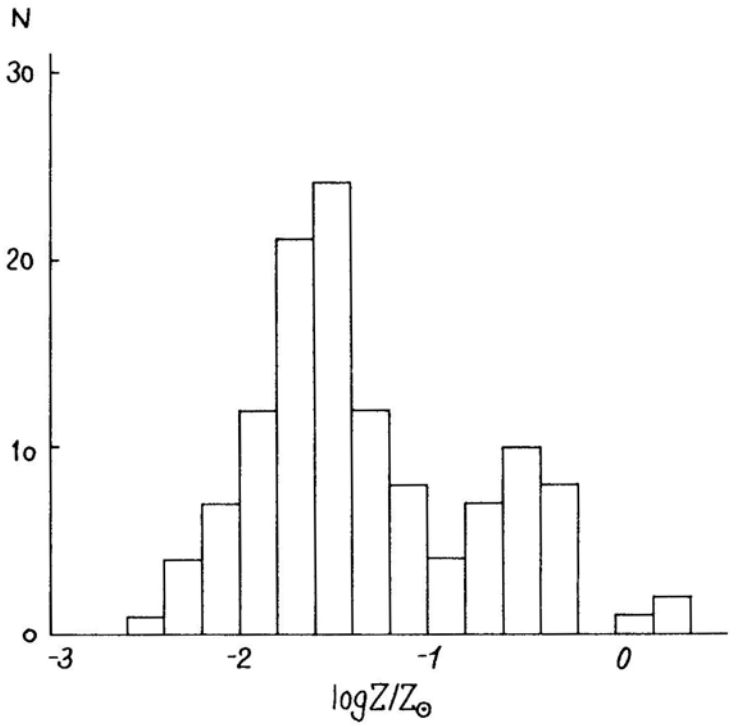

Figure 1. Metallicity histogram of. globular clusters according to Zinn (1985). The two metallicity peaks correspond to two subsets of clusters having very different spatial and kinematical properties.

The low metallicity peak ([Fe/H] = –1.6) in the histogram corresponds to a subset of globulars having a spheroidal distribution and virtually no rotation around the galactic centre. The high metallicity ([Fe/H] = – 0.5) subset has a very substantial degree of flattening and a mean rotation of about 170 km s^{-1} only 25 percent less than the rotation of the disc. We have plotted in Fig. 2 the metallicities of globular clusters as a function of their absolute magnitude (no correlation) and of their distance to the galactic plane. It is clear that the subset within ± 2 kpc from the plane is more metal rich than the subset with distances to the galactic plane between 2 and 4 kpc, and that clusters more distant than 4 kpc from the galactic plane are still less metal rich. If we redraw Zinn's histogram using a linear scale instead of a logarithmic scale (Fig. 3) we see that the metal-poor clusters are highly concentrated near $Z \simeq 0$, whereas the intermediate metallicity clusters have a fairly flat distribution.

We are proposing here that the flattened system reflects the progressive formation of clusters in a protogalaxy in which metallicity increases as the protogalaxy becomes flatter, as evidenced by Fig. 2. It is then quite understandable that the globular clusters of the flat subset have a metallicity comparable to the initial mean metallicity of the disc ($Z \simeq 0.25\ Z_{\odot}$, according to Twarog 1980). This is the 'classical' view of an age-metallicity relationship as suggested by Eggen, Lynden-Bell & Sandage (1962). The absence of younger galactic globular clusters is then explained by the shear of the galactic rotation, preventing the gravitational instability of large structures. We depart

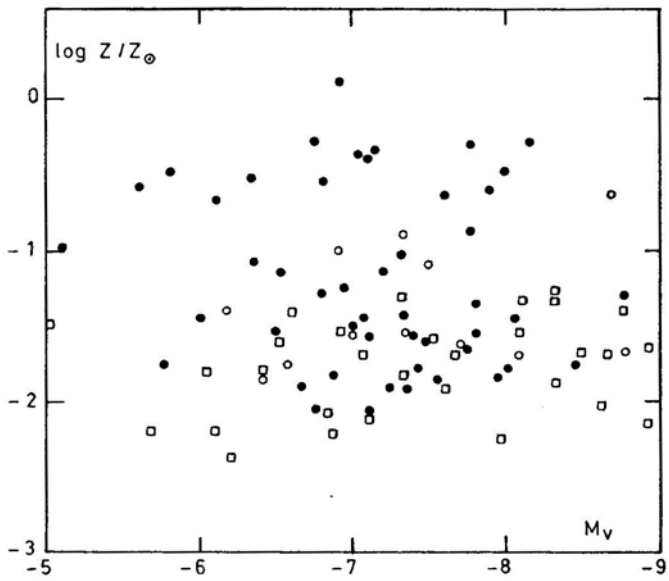

Figure 2. The metallicity of globular clusters as depending upon their visual magnitude and their spatial distribution. Symbols are as follows: ●: globulars within 2 kpc from the galactic plane; O: globulars with distances to the galactic plane between 2 and 4 kpc; □: globulars with distances to the galactic plane larger than 4 kpc.

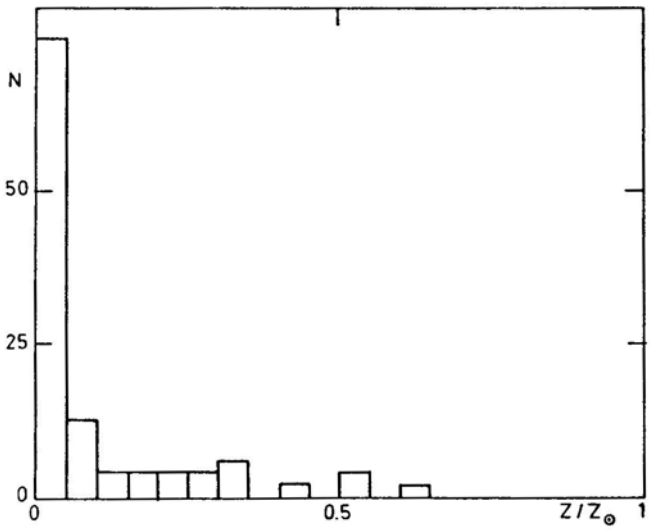

Figure 3. Metallicity histogram of globular clusters according to Zinn (1985). The abscissa is now linear in *Z*.

from the classical view, however, in claiming that the low-metallicity, spheroidal system is primordial, *i.e.*, formed out of big-bang matter as initially proposed by Peebles & Dicke (1968).

The only objection to this concept is that the globular cluster stars should be

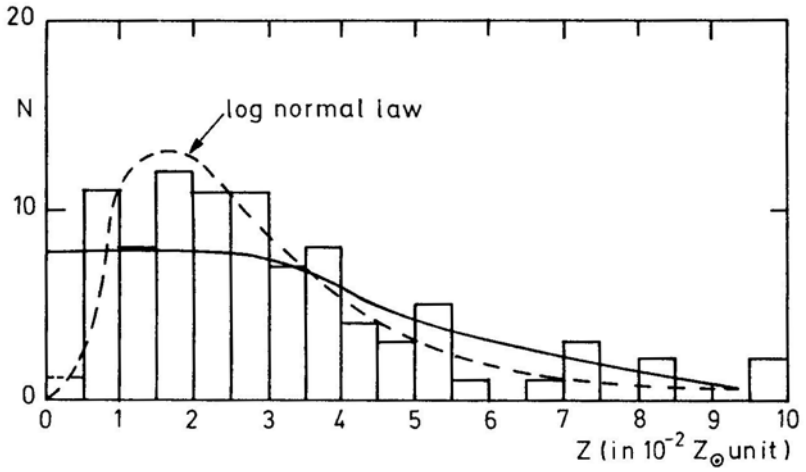

Figure 4. Close-up of the low-metallicity part of the metallicity histogram of globular clusters according to Zinn (1985). The abscissa is linear in *Z*. The dotted curve is a log-normal law of parameters (log $Z/Z_\odot$ = – 1.6, σ = 0.3). The full curve is from a stochastic enrichment model by Searle (1977).

population III stars *i.e.* stars with Z =0 . But as we said in the introduction, the view that a primordial cloud produces stars without any degree of self pollution is rather questionable. In other words the idea that the signature of the first stellar generation is Z = 0, does not take into account the ecology of star formation. As the only stars still visible in globular clusters have masses below 0.9 $M_\odot$, the crucial point is to know if stars of such masses have been (on the average) born before any supernova has contaminated the progenitor cloud, or not. We are actually considering this point in the next paragraph. For the time being we assume that each globular cluster in the spheroidal system has generated its own metals, and that each globular of the spheroidal system is chemcially independent of the others. We compare in Fig. 4 the close-up of the lower metallicity group of the histogram with (i) a theoretical curve obtained by Searle (1977), (ii) a simple log-normal law fitted to the observed distribution. The bin with the lower metallicity (Z = 0 to 0.005 $Z_\odot$) has a crucial importance. If this bin is actually empty, or nearly empty (the only globular cluster in this bin is NGC 5053 and has a poorly determined metallicity) the log-normal law is a better fit than Searle's law, which is based on a progressive enrichment model, but with some stochastic component in it. The purely stochastic log-normal law is quite an acceptable law for a self-pollution model as ours: the number and the masses of the polluting SNs, the dilution factor of the pollution in the primordial gas, *etc.* are stochastic in nature, and it is known that when a variable is expressed as the product (or ratio) of several stochastic variables, this variable tends to have a log-normal distribution. Anticipating the results from the next section we even connect the existence of this first empty bin to a basic process in star formation: if the first bin is actually empty it means that no low-mass stars can form unless an SN has already exploded in the medium.

One must of course question whether the width of the log-normal law is determined by the observational errors in metallicity. The error is actually merely gaussian in

[Fe/H], leading to a log-normal law by itself. However, the width due to the observational error is $\delta\log Z \simeq 0.15$ according to Zinn & West (1984), significantly smaller than the combined width of the intrinsic distribution and of observational errors ($\delta \log Z \simeq 0.3$ in Fig. 4).

To summarize this section, we believe that the low metallicity subset of the galactic globular clusters, *i.e.*, the spheroidal subset, is primordial, with a metallicity histogram resulting from the stochastic self-pollution of the initial zero-metal progenitor cloud having enriched the low-mass stars born a little later in the cloud which are being observed today.

3. The gravitational collapse of a primordial cloud

The cloud progenitors of globular clusters cannot have a mass smaller than the mass of the present-day clusters and, unless star formation was extraordinarily efficient, may very well have been 10 to 50 times more massive. As the typical mass of a present-day globular cluster is $10^5\ M_\odot$ the typical mass of a progenitor must have been in the 10^6–$10^7\ M_\odot$ range. When such a cloud becomes gravitationally unstable it begins to collapse, each layer taking an inward motion towards the centre of the cloud, over timescales corresponding to a free fall under the gravitational pull of all the matter inside this particular layer. Detailed computations (Larson 1978) show that whereas the free-fall model is a good approximation in the central parts of the cloud, a pressure gradient counteracts the gravitational pull in the rest of the cloud, which evolves into a dense core reaching a very high density in a free-fall time $(3\pi/32\ G\rho)^{1/2}$ (where G is the gravitational constant and ρ the density) surrounded by an envelope which evolves slower. In the absence of Eddington instability (role of the radiative force balancing the gravity at the surface of very luminous objects) and the occurrence of fragmentation, the core of a collapsing cloud would likely form a very massive object, the luminosity of which would stop the further accretion of mass from the envelope. We claim that such a (hypothetical) very massve object *must* fragment at least to the level of the most massive existing stars, *i.e.* to the most massive O-stars. Carr, Bond & Arnett (1981), and El Eid, Fricke & Ober (1981) discuss the evolution of, and nucleosynthesis in, such primordial, very massive stars. We propose that the bulk of the low-mass stars is formed in the gigantic shock between the still infalling envelope and the expanding medium formed by the stellar winds and by supernova shells of the fast evolving central massive stars. The fragmentation to smaller masses is then made much easier by the Rayleigh-Taylor instability occurring at the boundary between the expanding central 'bubble' and the cooler infalling medium, by the shock-enhanced density and by the presence of a few heavy elements supplying additional cooling mechanisms. Although this scenario is qualitatively attractive and would explain the first empty bin in the globular cluster histograms, we must admit that the theory of star formation has not yet reached a state that would permit detailed predictions. We believe that the strongest argument in support of the early occurrence of O-stars in the cloud is drawn from observation and will be developed in the next section.

The 'secondary' SNs, formed with the low-mass stars, inject so much energy in the cloud that after its short life as an H II region the cloud is disrupted.

Only a minority of stars have velocities low enough to remain bound to the central cluster, after most of the initial mass has been expelled. So we expect that the main

product of the process is not the cluster but an association whose expansion velocity is drawn from the initial stellar winds and SN explosions at the centre (first star-formation region). The stars of these former associations could be the present field population II.

The complete suggested sequence of events is therefore: gravitational collapse→ cloud with high density core→ cloud with a central cluster of O-stars → association with expanding gas and star system→ globular cluster (still existing or dissolved in the field) + field population II + gas collected by the galactic disc.

4. The cores of 30 Doradus and NGC 3603

We have assumed that the first stellar formation in a collapsing cloud was (i) at the centre, and (ii) rich in massive stars capable of taking control of further evolution of the cloud. If this is true for primordial clouds it should also be true of present-day more metal-rich giant clouds. The nearest giant H II region with a mass $\simeq 10^6\ M_\odot$ is 30 Doradus in the large Magellanic cloud. It is precisely at the centre of 30 Doradus that a supermassive object has been suspected for many years. This central object R 136a has a luminosity of $10^7\ L_\odot$ and is responsible for the ionization of a large part of 30 Doradus. Recent observations (Weigelt 1981; Walker & O'Donoghue 1984) however have shown that the object is multiple and has a composite spectrum of O and Wolf-Rayet stars. It is now believed that R 136a is a compact cluster(diameter < 0.3 pc) of over 20 massive early-type stars. The nearer, but smaller, H II region NGC 3603 has also a still more compact group of O stars at its centre. We think that this observational fact is the strongest argument in favor of our assumption that something similar has happened in population II star-formation regions.

5. Consequences on the chemical composition of population II and the chemical evolution of the galaxy

An immediate consequence of our proposed scenario is that the first low-mass stellar generation has been selectively polluted by ejecta of SNs due to very massive stars. Current observation of H II regions seem to show that the whole burst of star formation does not last longer than $\sim 5 \times 10^6$ years.

The more prominent characteristic of heavy element production in massive SNs is the fact that they produce more oxygen in proportion of the metals as compared to the ratio in the Sun. Although the results for oxygen/iron ratio in globular cluster giants are somewhat scattered, it is a well-known observational fact that population II dwarfs show a O/Fe ratio about four times the solar value (Sneden 1985). An analysis of Arnett (1978) yields shows that such a ratio is expected from SN having progenitor O-stars of mass $\geqslant 50\ M_\odot$. This is in perfect agreement with our scenario, the most massive stars being at the same time the fastest and the most energetic, able to take control of the fate of the collapsing cloud.

The heavy elements caught in globular cluster stars are, however, a very tiny fraction of the total production of heavy elements during the first stellar generation of the Galaxy.

The total amount of population II is likely to be about 10 per cent of the mass of the Galaxy. If the yield for this stellar generation has been $\simeq 0.02$(Matteucci 1983), then the value of Z at the end of the first stellar generation (population II = population III in our view) was $0.1 \times 0.02 = 0.002 = 0.1\ Z_{\odot}$, a value corresponding fairly well to the transition value between actual population II and early disc value. This may also explain the so-called G-dwarf problem (Pagel & Pachett 1975) as the metallicity of the disc having been already brought to a high value by the first stellar generation.

6. Conclusion

We have developed arguments in favour of the concept that a first stellar generation in the Galaxy did originate from 'dirty' primordial matter and comprises of the old-known population II globular clusters, and field population II stars; a large fraction of the metallicity of the early disc is a product of this first stellar generation.

The fact that the first stellar generation is dirty is attributed to the early formation, at the centre of a collapsing massive cloud, of a compact cluster of O-stars like R 136a in 30 Doradus. The heavy elements produced by the Supernovae of this central cluster are thought to be the main pollutant of the first stellar generation. This first population is oxygen-rich.

References

Arnett, W. D.1978, *Astrophys. J.*, **219,** 1008.

Carr, B. J., Bond, J. R., Arnett, W. D.1981, in *Proc. ESO Conf., The Most Massive Stars,* Eds S. D' Odorico, D. Baade & K. Kjär, ESO, Garching, p. 315.

Cohen, M., Kuhi, L. V. 1979, *Astrophys. J. Suppl Ser.*, **41,** 743.

Eggen, O. J., Lynden Bell, D., Sandage, A. 1962, *Astrophys. J,* **136,** 748.

El Eid, M. F., Fricke, K. J., Ober, W. W. 1981, in *Proc. ESO Conf. The Most Massive Stars,* Eds S. D' Odorico, D. Baade & K. Kjär, ESO, Garching, p. 303.

Larson, R. B. 1978, in *Infrared Astronomy,* Eds G. Setti & G. G. Fazio, D. Reidel, Dordrecht, p. 137.

Matteucci, F. 1983, *Mem. Soc. astr. ltal.*, **54,** 289.

Peebles, P. J. E., Dicke, R. H. 1968, *Astrophys. J.*, **154,** 891.

Searle, L. 1977, in *The Evolution of Galaxies and Stellar Populations,* Eds B. M. Tinsley & R. B. Larson, Yale Univ. Obs., New Haven, p. 219.

Sneden, C.1985, in *Proc. ESO Workshop, Production and Distribution of CNO Elements,* Eds I. J. Danziger, F. Matteucci &K. Kjär, ESO, Garching, p.1.

Twarog, B. A. 1980, *Astrophys. J.*, **242,** 242.

Walker, A. R., O'Donoghue,D. E. 1984, *Astr. Exp.*, **1**, 45.

Weigelt, G. 1981, in *Proc. ESO Conf., Scientific Importance of High Angular Resolution at Infrared and Optical Wavelengths,* Eds M. H. Ulrich & K. Kjär, ESO, Garching, p. 35.

Zinn, R. 1985, *Astrophys. J.*, **293,** 424.

Zinn, R., West, M. J. 1984, *Astrophys. J. Suppl. Ser.*, **55,** 45.

J. Astrophys. Astr. (1987) **8,** 161–163

Concluding Remarks

B. Gustafsson *Stockholm Observatory, S-13300 Saltsjöbaden, Sweden*

An obvious impression from this quite interesting session is that the study of abundances of low-mass stars is very essential for several reasons. In particular, the considerable ages of these stars, the possibilities to determine their ages, and the absence for almost all elements of effects of interior nuclear burning on the atmospheric abundances, at least for the dwarfs, make these studies vital in the investigation of the chemical history of the Galaxy and, for He and Li, of the universe as a whole. However, the results and problems presented in this session also demonstrate the need for a high, or improved, accuracy in the abundance determinations. Fortunately, such improvements are within reach with methods already available or soon to come.

The following comments deal with the trends in relative abundances and the scatter around these trends.

Trends. The variations of the relative abundance ratios, as functions of heavy-element abundances, are competently reviewed by Bob Kraft and David Lambert The situation is schematically summarized in Lambert's Figs 12 and 13, where also our imperfect knowledge, in particular for stars with [Fe/H] < -2, is indicated by broken lines.

It seems reasonable to attempt interpretations of these tendencies in terms of nucleosynthesis and galactic evolution. However, several circumstances indicate that caution is well motivated:

Late-type stars with lower overall metal abundance deviate in several important respects from their more metal-rich counterparts, *e.g.,* the metal-poor atmospheres are more transparent, which should make the spectral effects of the hydrogen convection zone more important. Also, the higher transparency in the ultraviolet (due to the weaker spectral-line blocking) increases the possibilities for non-local ionization and excitation.

The risks that these stellar departures from standard plane-parallel local-mixing-length LTE model atmospheres could induce some of the abundance tendencies traced must be remembered and systematically investigated by more realistic model calculations. Such calculations are, at least partially, within reach today (*cf.,* Nordlund 1985; Scharmer & Carlsson 1985). Also, semiempirical modelling should be pursued further (*cf.* Magain 1985). As long as this programme has not been completed one should seek 'independent' empirical confirmation of the abundance tendencies traced (*e.g.,* from other spectral lines, other ions or molecules, other types of stars). Inconsistencies showing up at such checks are interesting as such and should be analysed carefully—probable or possible examples are the disparate Al and Ni abundances, discussed by Lambert and (in the case of Ni) by Bessell & Norris. Other examples of such inconsistencies were reviewed by Gustafsson (1983) who also gave a number of general comments on the determination of abundances for metal-poor stars.

Other abundance trends, *e.g.,* with effective temperature, may also indicate that

something is wrong. Two examples were provided at this session—Kraft discussed the tendency for N/C to change rather drastically with $T_{\rm eff}$, and Grenon mentioned that, at a given galactocentric distance, the cooler supergiants analysed by Luck appear more metal poor than the hotter ones. At least in the latter case one might suspect that the problem is related to the veiling effects of weak molecular bands, thus lowering the quasi-continuum with respect to the model spectra. This possibility, worrying all of us interested in abundances of cool stars, should be studied further.

Finally, however, one should note the reassuring result by Bessell & Norris that their remarkable very metal-poor star CD – 38°245 shows normal population II relative abundances.

Scatter. For various astrophysical problems, the physical star-to-star scatter in an elemental abundance or in an abundance ratio, *e.g.* at a given stellar age, is of great interest. Since this scatter is often not much greater than the normal observational uncertainties an estimate of it requires high accuracy in the abundance analysis and methods for obtaining a realistic estimate of this accuracy.

The problem is clearly illustrated in the papers by Kraft, Lambert, Duncan & Hobbs, and Cayrel de Strobel. In the first two papers the quite important question is whether the considerable scatter in various abundance ratios such as [O/Fe], [α/Fe],[Na/Fe], [AI/Fe] for population II stars is real, or just reflecting the uncertainties in observations and analyses. Lambert suggests that most of it may be 'observational'—obviously more detailed and homogeneous studies are necessary to trace the true chemical inhomogeneities in the early halo gas. Such studies should, however, be feasible with current instrumentation.

Duncan & Hobbs suggest that there is a real scatter in the Li abundances for halo dwarfs at solar temperatures. This would then question the interpretation by Spite & Spite (1982) that these stars show a primordial Li abundance of cosmological significance. The interesting possibility certainly requires further study—however, one should also note the finding that the strength of the solar λ6708 Li line is weak in plages, which may be interpreted as an overionization effect due to the enhanced non-radiative heating (Giampapa 1984). May be that the problem with the discrepant stars that show small chromospheric activity and still strong Li lines, discussed by Duncan & Hobbs, is related to this phenomenon.

Giusa Cayrel de Strobel has selected stars with [Fe/H] > $[Fe/H]_{Hyades}$ from the Cayrel *et al.* catalogue, estimated their ages, and obtained a very interesting diagram (her Fig. 2). She suggests that the SMR phenomenon was more active in the past than now, and that the interstellar medium in the disc may have become gradually more chemically homogeneous with time. One possibility, along the lines of Roger Cayrel's paper, might be that the SMR stars in general were formed in cloud complexes, considerably polluted by their Supernovae before they were dissolved, while the general disc stars were produced in the more well-mixed and gradually enriched interstellar medium. However, these speculations are based on an inhomogeneous set of data, with a considerable and not well-known observational scatter. A more homogeneous and precise sample of data should be obtained to confirm and further illuminate Cayrel de Strobel's result. Note in this connection the bimodal metallicity distribution obtained by Grenon for his age group $0.3 \leqslant f \leqslant 0.5$ (his Fig. 6).

Grenon's study of the overall metallicity gradients in the Galaxy is very instructive. In particular, he demonstrates how vital a precise definition of an unbiased sample of

stars used for tracing an abundance gradient is, how serious the effects of mixing stars of different ages and different places of birth may be, *etc.* The importance of avoiding errors in calibrations of temperature and gravity dependences in [Fe/H] measures is also noteworthy. Independent attempts to verify Grenon's results, *e.g.* from studies based on photometric instead of dynamic age determinations, will be of great interest.

Final remarks. The comments made above have been mainly of methodological character. This should not be taken to imply that the astrophysical results presented in the session were less interesting. The comments by Audouze and Lambert on the unsatisfactory use of the notions 'primary' and 'secondary elements' and on the importance of determining isotopic ratios, the astrophysical implications of the trends discussed by Kraft and Lambert, the result that the nitrogen-rich population II dwarfs seem to be the result of binary evolution that was mentioned by Carney, Kraft and Spite & Spite, the finding by Grenon that the metallicity gradient in the Galatic disc does not seem to change appreciably with time and, not the least, Roger Cayrel's suggestive scenario of star formation and nucleosynthesis in proto-globular-clusters, which at least qualitatively seems to explain the absence of population III, the relatively high oxygen abundances of population II stars and the so-called G-dwarf problem; all these and several other points and results presented during the session made it very valuable, also for the result-oriented astrophysicist. I would like to add to the list the interesting contributions by Cathy Pilachowski which I, however, have no possibility to discuss further here. Thus, it is well motivated, indeed, to thank Giusa Cayrel de Strobel for having arranged the session.

References

Giampapa, M. S. 1984, *Astrophys. J.*, **277,** 235.
Gustafsson, B. 1983, *Publ. astr. Soc. Pacific*, **95**, 101.
Magain, P. 1985, *Astr. Astrophys.*, **146,** 95.
Nordlund, Å. 1985, *Solar Phys.*, **100,** 209.
Scharmer, G. B., Carlsson, M. 1985, *J. Comp. Phys.*, **59**, 56.
Spite, F., Spite, M. 1982, *Astr. Astrophys.*, **141,** 56.

J. Astrophys. Astr. (1987) **8,** 169–181

The Role of a Strong Far-Infrared Radiation Field in Line Excitation and Cooling of Photodissociation Regions and Molecular Clouds

Abdul Qaiyum & S. M. R. Ansari *Department of Physics, Aligarh Muslim University, Aligarh 202001*

Received 1986 February 14; revised 1986 December 10; accepted 1987 January 2

Abstract. We have theoretically studied the influence of a far-infrared radiation (FIR) field from H II region on the cooling by C and O atoms, C^+ ion and CO molecule in a photodissociation region, and a molecular cloud associated with H II region (hereinafter referred as H I region) at low temperatures ($T_k \leqslant 200$ K). Comparisons have been made for cooling with and without FIR for two extreme abundances (10^{-4} and 10^{-7}) of the mentioned species for temperatures ranging between 10 and 200K and an hydrogen particle density range 10 cm$^{-3} \leqslant n_o \leqslant 10^7$ cm^3.

The cooling by the species with low line-splitting (C I, C II and CO) is significantly influenced by the radiation field for temperatures T_k < 100 K while the effect of radiation field on cooling by O I is significant even at higher temperatures (T_k > 100 K). The effect of FIR field on the cooling of CO from low rotational transitions is negligibly small, whereas it is considerable for higher transitions. In general, the cooling terms related to the short-wavelength transitions are more affected by FIR than those related to longer wavelengths.

It is also demonstrated here that in the determination of thermal structure of an H I region the dust grains play an important role in the heating of gas only through photoelectron emission following irradiation by far-ultraviolet (FUV) radiation, as the infrared radiation from the dust is too small to have substantial effect on the cooling. It is found that in the H II /H I interface the FIR field from grains in the H II region is not capable of modifying the temperature of the warmest regions but does so in the inner part where the temperature is low enough.

Key words: molecular clouds, cooling—H I regions—far-infrared radiation

1. Introduction

Low-temperature and high-density media illuminated by far-ultraviolet (FUV) radiation field (photodissociation region) and molecular clouds (hereinafter referred as HI regions) (*of.* schematic drawing shown in Fig. 1) have received considerable attention recently. The line radiations from C and O atoms, C^+ ion and CO molecules

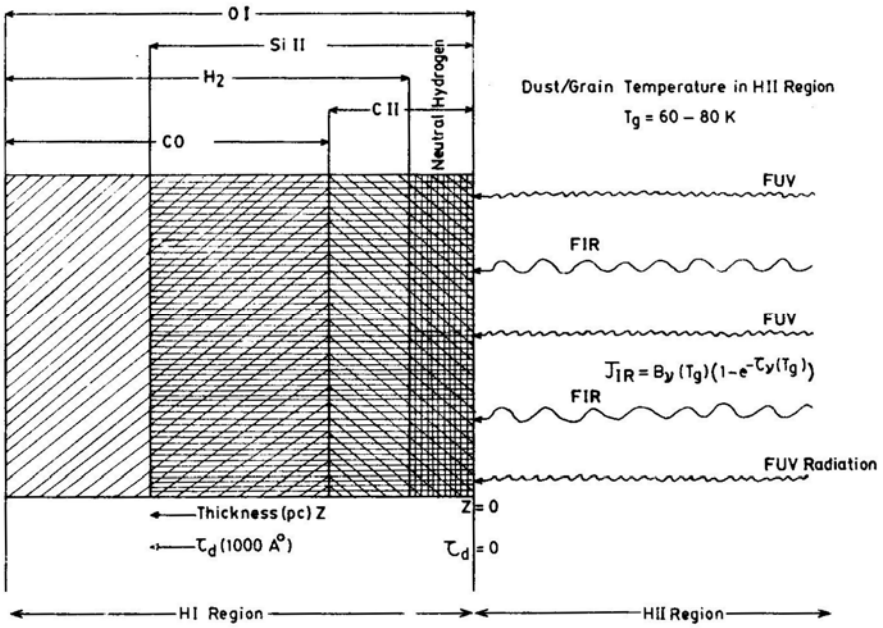

Figure 1. A schematic drawing of one-dimensional plane-parallel slabs of photodissociation region and molecular cloud (referred as H I region).

have greatly modified our ideas and have revealed a large variety of physical conditions in these media (Phillips *et al.* 1979, 1980; Phillips & Huggins 1981; Russell *et al.* 1980; Stracey *et al.* 1983; Werner *et al.* 1984; Crawford *et al.* 1985). Furthermore, molecular line emission, particularly of CO, is expected to play an important role in determining the thermal balance of dense clouds, whereas in diffuse and warm clouds the cooling is predominantly due to ionic and atomic species of C and O.

The dust grains play also a significant role in the interstellar medium in protecting the atoms and molecules from ionization and/or photodestruction by absorbing the ultraviolet radiation from the galactic background or nearest hot stars of associated H II regions. The photoelectrons from dust grains are now known to be potential heating agents in the interstellar medium. Furthermore, the far-infrared radiation (FIR) from the dust grains is considered to be important in determining the level populations of atoms, ions and molecules. As a consequence, the cooling by these species may also be modified.

In this paper, we study the effect of the FIR field from associated H II regions, on the level populations of CO molecules, carbon atoms and its ions, and also oxygen atoms. The coolings from these species are discussed in detail here. Calculations are performed for the level population and cooling over ranges in hydrogen density 10 to 10^7 cm^{-3}, kinetic temperature 10 to 200K, and abundance 10^{-4} and 10^{-7}. The range of parameters are relevant to neutral shells around planetary nebulae, bright-rimmed molecular clouds, reflection nebulae, regions around protostars, and H II/ H I Iinterfaces in general. The grain temperature T_g considered here are 60 and 80 K following Westbrook *et al.* (1976) and Werner *et al.* (1976).

The results obtained are fairly important for cool as well as warm regions with gas temperatures $T_k \leqslant 200$ K. This range of temperature is realistic (Qaiyum & Ansari 1983). The cooling by carbon atom and ion are greatly modified at low temperatures (T_k < 100 K), whereas it is so in the case of oxygen atom even at $T_k \sim 100$ K. Particularly, the level populations of CO molecules for $J > 5$ are greatly affected due to FIR field. As a consequence, the physical conditions of the cloud deduced from the line flux of fine structure transitions of C and O atoms and C II ion, and $J > 5$ transitions of CO molecule may be affected. The emergent cooling radiations are calculated using the escape probability formalism for line radiation.

Although the main aim of the present paper is to show that cooling in H I region by FIR field from associated H II region is largely modified, yet it is also shown here that the dust within cloud (H I region) plays an important role only in the heating of the gas by the photoelectrons from the surface of the dust grain due to FUV radiation. However, the infrared radiation from the dust within the gas is very small as compared to that within the H II region. Therefore its effect on cooling is negligible.

2. Physical processes

2.1 *Collisional Rates*

The intense FUV fluxes from central stars of associated H II regions generally photodissociate the molecules and photoionize the heavy elements with ionization potential less than the Lyman limit (912 Å). Thus, important coolants having appreciable fractional abundances in the interstellar medium are C I, O I, C II, Fe II, Si II, CO and H_2O. Qaiyum & Ansari (1983) have demonstrated that the FUV flux creates a warm layer $T_k > 100$ K heated by the photoelectrons from dust grains. At such temperatures C I, C II and O I are the only important cooling agents because of low excitation energy (temperature equivalent < 300 K) of their hyperfine structure transitions. Further, the temperature falls below 100 K inside the cloud and the carbon is transformed into CO; therefore the gas is cooled mainly by low-lying rotational transitions of CO.

Cooling by fine structure transitions of C I excited by electron and hydrogen have been studied by Penston (1970), Dalgarno and McCray (1972), Launay & Roueff (1977a), but collisional excitation with molecular hydrogen is yet to be studied in detail. The latter has been taken to be 10 times smaller than that with H-atom at the same temperature. In the following we use the rate of excitation of C II by electron and H from Dalgarno & McCray (1972), and Launay & Roueff (1977b), and by H_2 from Chu & Dalgarno (1975), and Flower & Launay (1977 a,b). The de-excitation rates calculated by Green & Thaddeus (1976) combined with the formalism of the De Jong, Chu & Dalgarno (1975) are used to calculate the level population of the CO molecule and its isotopes. Although these rates may not be up to date, we keep them for comparison with the results of Goldsmith & Langer (1978).

2.2 *Radiation Field*

Level populations of atoms/molecules are partly governed by the radiative transitions due to background radiation combined with the local source function. A number of

cool and dense clouds are associated with H II regions and the radiation from these regions may be important. Westbrook *et al.* (1976) observed that in the neighbourhood of H II regions the grain temperature is 60 K. Werner *et al.* (1976) mention the typical value of grain temperature as 75 K. Following Ungerechts & Walmsley (1979), we have attempted here to take into account the FIR field from these associated H II regions which can be approximated as

$$J_{IR}(\nu) = WB_{\nu}(T_g)\,(1 - e^{-\tau_g(\nu)}). \tag{1}$$

In this expression W is the dilution factor taken equal to 0.5. This factor W may be very close to unity at H II / H I interface (see Fig. 1), but it will approach 0.5 as we proceed inside the cloud away from the H II region. The value of W = 0.5 is a slight underestimate for the optical depths < 6, *i.e.*, in the C I, O I and C II regions, and a slight overestimate for optical depths > 6 where carbon is completely locked in CO molecules (see Figs 1 and 2). B_{ν} (T_g) is the Planck function at grain temperature T_g. Two grain temperatures, T_g = 60 and 80 K, are considered in the calculation of FIR field, following Westbrook *et al.* (1976) and Werner *et al.* (1976). τ_g is the dust optical depth which depends upon frequency. The value of t_g = 0.3 at 100 μm (Werner *et al.* 1976) and 0.06 at 400 μm (Hudson & Soifer 1976) near an H II region suggest a wavelength dependence as λ^{-1}. However, in the present calculation we consider the dependence as $\lambda^{-1.5}$ following Mezger, Mathis & Panagia (1982); this dependence is widely accepted at present.

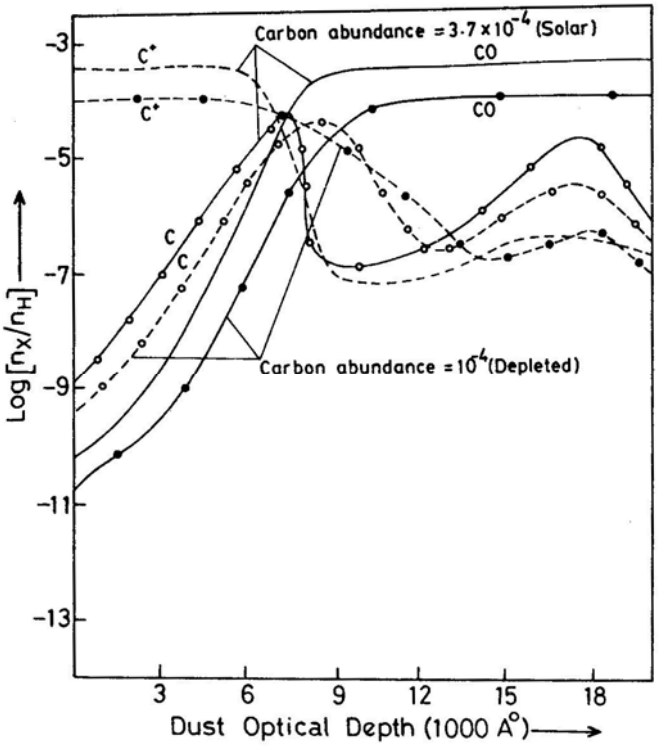

Figure 2. Variation of abundances (relative to hydrogen) of carbon atom and its ion, and CO molecule as a function of dust optical depth for two different abundances.

2.3 *Level Populations and Cooling Rates*

In order to solve for the level population, all the possible populating and depopulating processes of a particular level i are considered. In general, under the assumption of steady state we can write,

$$n_i(x) \sum_j P_{ij}(x) = \sum_j n_j(x)\, P_{ji}(x), \tag{2}$$

where n_i and n_i are the number densities of element x in the levels i and j. P_{ij} is expressible in terms of radiative, induced and collisional rates. The mean radiation field $\langle J_{ij} \rangle$ includes the background radiation 2.7 K radiation, and that from dust and grain of H II region) and the local source function. This mean radiation field may be written as (De Jong, Chu & Dalgarno 1975)

$$\langle J_{ij} \rangle = [1 - \beta_{ij}]\, S_{ij} + \beta_{ij}\, U(\nu_{ij}, T_{2.7}, T_g), \tag{3}$$

where U is the intensity of the radiation at frequency ν_{ij} due to universal background at 2.7 K and due to the grain at T_g, S_{ij} is the local source function and $ß_{ij}$ is the escape probability.

The total cooling rates (erg cm^{-3} s^{-1}) considering all the possible transitions from a particular species x is

$$\Lambda(x) = \sum_j \sum_{i<j} \{n_j(x)[A_{ji} + \beta_{ji}\, U(\nu_{ij})] - n_i(x)\, \beta_{ij}\, U(\nu_{ij})\}\, \beta_{ij}\, (E_j - E_i). \tag{4}$$

3. Results and discussion

The main aim of the present paper is to study how the cooling efficiency in the region with $T_k \leqslant 200$ K is affected in the presence of FIR from the nearest H II regions. We present in this section the calculation of cooling rates by C, O, C^+ and CO, for a hydrogen particle density 10^1–10^7 cm^{-3}, and the grain temperature T_g = 60–80 K.

To find the abundance structure, a time independent chemistry model is used. At the cloud edge the temperature is > 100 K and the main coolants are oxygen atom and carbon ion. For optical depths > 6 the region becomes cool (T_k < 50 K) and most of the carbon is converted into CO molecule. At the edge of the molecular cloud, carbon atom has significant abundance only in a very small region, but further inside—after optical depths > 10—its abundance becomes appreciable again (see Fig. 2). This is in accordance with the observations of Keene, Blake & Phillips (1985). The cooling rates by C I and CO are calculated for kinetic temperatures 10, 20 and 100K (Figs 3 and 7),by C^+ at 40 K and 100 K (Fig. 4) and by O I at 100 and 200 K (Fig. 5). The cooling rates with FIR from grains at T_g = 60 and 80 K with W = 0.5 are compared with those without FIR following Goldsmith & Langer (1978).

3.1 *Cooling by Carbon Atoms and Ions*

At low temperature (T_k = 10 K), and low hydrogen density, the cooling rate by the carbon atom is reduced by a factor ~ 2 in the presence of FIR. At high density of hydrogen, the cooling is reduced by an order of magnitude (Fig, 3). For T_k = 10 K and

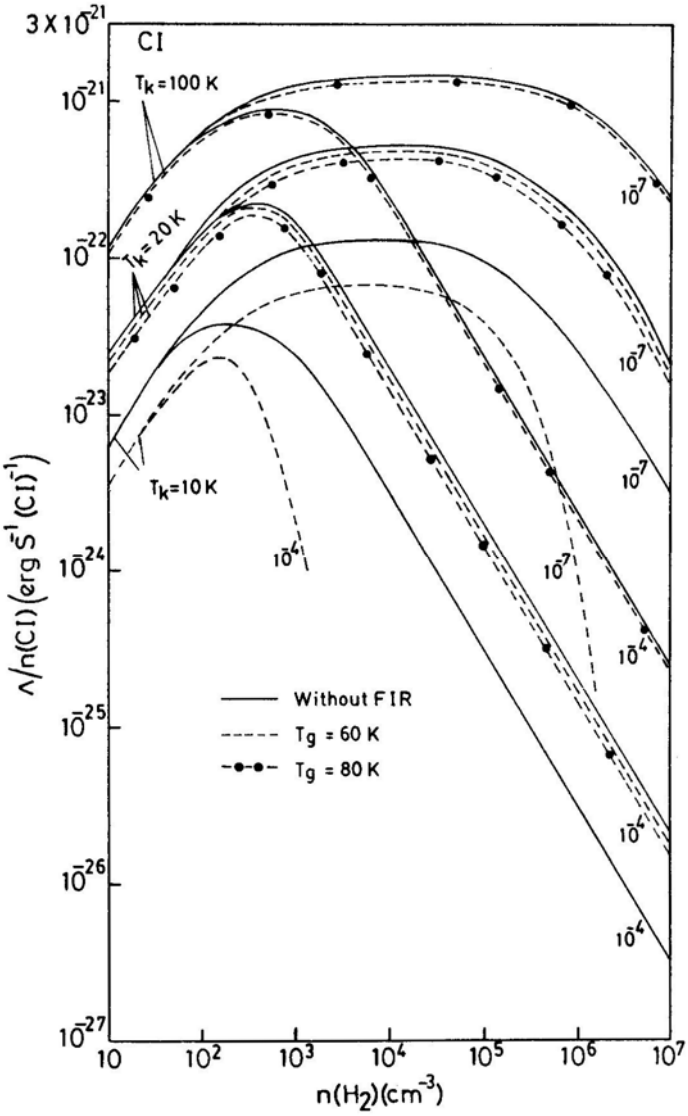

Figure 3. Total cooling rate per atom from the fine structure transitions of the neutral carbon for X (C I)/ (dv/dr) = 10^{-4} and 10^{-7} (km s $^{-1}$ pc $^{-1}$)[1] at kinetic temperatures of 10 K, 20 K and 100 K.

abundances of 10^{-4} and 10^{-7} the dashed curves are incomplete, because when the gas density becomes high enough, absorption of radiation takes place instead of emission from the fine structure transitions. The situation is similar with carbon atom for T_k = 10K and T_g = 80 K. It is also clear from Fig. 3 that an increase in temperature decreases the effect of FIR radiation. At T_k = 20 K the reduction factor of the cooling rates decreases and remains almost constant over the whole range of densities. At T_k = 100 K the effect of FIR is negligibly small. An increase in grain temperature further decreases the rate of cooling. The effect of FIR would be more pronounced if the dust

optical depth dependence is taken as λ^{-1} following Ungerechts & Walmsley (1978).

The cooling by carbon ion (Fig. 4) is also found to be somewhat affected. Again in this case an increase in kinetic temperature decreases the contribution due to FIR. At T_k = 100 K the contribution is small. It should be noted that cooling by carbon ion is largely modified at low temperature (T_k = 40 K) contrary to the cooling by atomic carbon. The higher reduction in the cooling is due to the small collisional rates at low temperature as compared to the radiative rate. At T_k = 10 K only absorption of background radiation would take place and the medium would be heated accordingly.

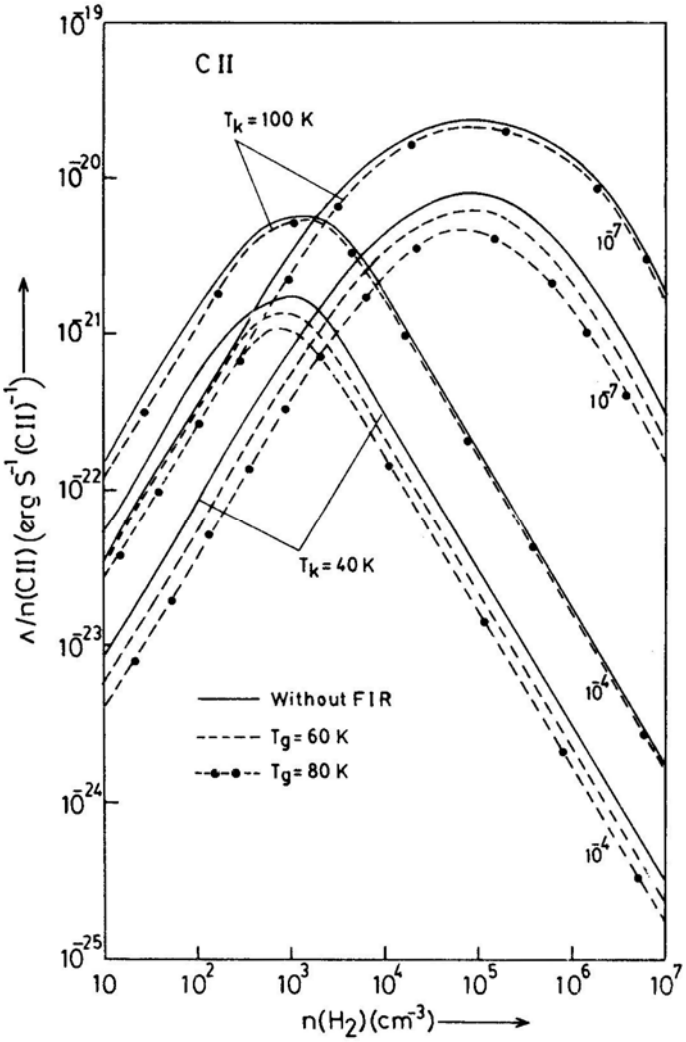

Figure 4. Cooling rate per ion from the fine structure transition of carbon ion for X (C II)/ (dv/dr) =10^{-4} and 10^{-7} (km s^{-1} pc^{-1})$^{-1}$ at kinetic temperatures of 40 K and 100 K.

3.2 *Cooling by Oxygen Atoms*

The cooling rates by oxygen atom are shown in Fig. 5 for T_k = 100 and 200 K. The grain temperatures considered are the same as mentioned earlier. It is clear from the figure that cooling by oxygen atom is not as simple to analyse as those by C I and C II, as it is a complicated function of density, temperature and optical depth in both the lines at 63 μm and at 145 μm. It is found that at moderate temperatures (~ 100 K) and low hydrogen density ($10 < n(H_2) < 10^6$) the cooling in the presence of FIR is enhanced almost by an order of magnitude while at high densities > 10^7 it is the same or even smaller than when only collisions are considered. At moderate densities, radiative transitions dominate over collisional excitation in populating the higher levels which

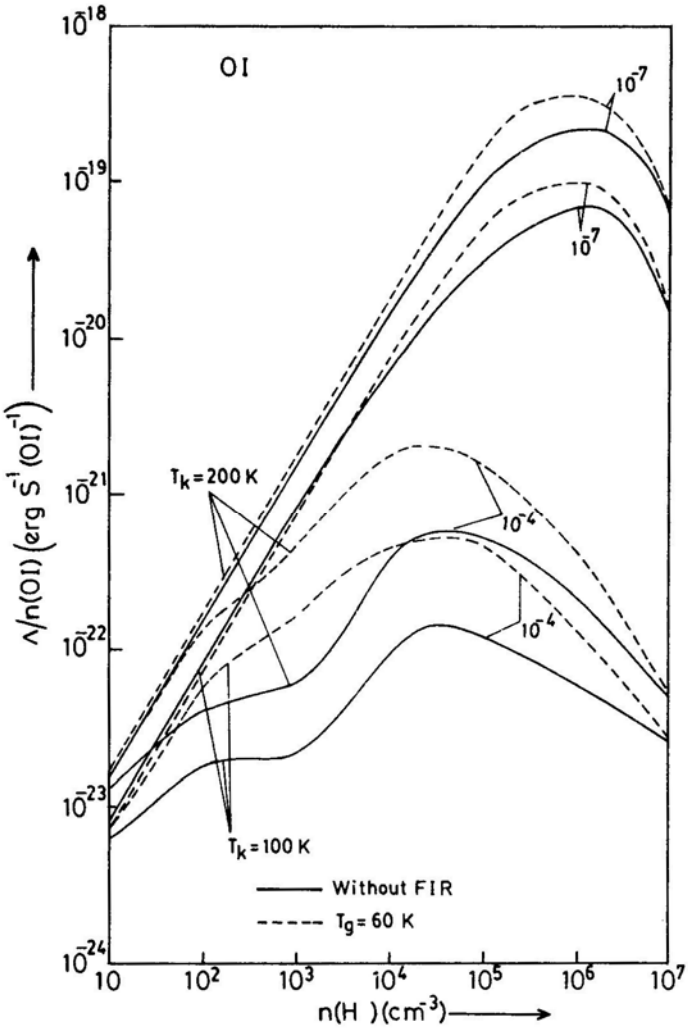

Figure 5. Cooling rate per atom from the fine structure transition of oxygen for X (O I/(dv/dr) = 10^{-4} and 10^{-7} (km s^{-1} pc^{-1})$^{-1}$ at kinetic temperatures of 100 K and 200 K.

causes an increase in the cooling rates. When the density becomes high enough the collisional rates dominate even at moderate temperatures (~ 100 K) and the role of FIR is limited. Further increase of temperature (T_k ~ 200 K) also ensures the domination of collisional rates even at a low density and only small differences exist between the cooling rates obtained with and without FIR.

It should be mentioned here that at T_k < 200 K the cooling rates by C I and C II are larger than those by oxygen atom at similar abundances mainly due to the high collisional rates of these species at low temperature as compared to the oxygen atom.

3.3 *Cooling by CO Molecules*

The reduced cooling rates of various transitions of CO molecule are illustrated in Fig. 6. From this figure it is clear that cooling due to lower transitions dominate at low n (H_2) while at high n (H_2) the higher transitions take over. The cooling rates by higher transitions remain proportional to n (H_2) long after the lower levels are thermalized. It is also seen from the figure that cooling from lower transitions is little affected by FIR because of the low density of radiation at low frequencies. For higher transitions the situation is reversed. Therefore, the cooling by CO molecule in the presence of FIR field is less affected at low n (H_2) as compared to high n (H_2), as is apparent in Fig. 7 where the total rate including all transitions is plotted. It can be seen from this figure that there exists a low hydrogen density region in which the cooling rate per coolant (Λ (CO)/n(CO)) is almost independent of abundance and is proportional to n (H_2), whereas in the high density region the cooling π (CO)/n (CO) decreases with abundance. Also, the cooling rate is affected by FIR field much more at low temperatures (10 and 20 K) than at higher temperatures (100 K) where the effect is negligibly small. It should be mentioned here again that the effect of FIR will be more pronounced if the dust optical depth varies as λ^{-1} as suggested by Ungerechts & Walmsley (1978).

3.4 *Thermal Structure*

In order to demonstrate the effect of FIR field on the thermal structure, the temperature is determined at each depth z of a plane parallel slab (see Fig. 1). The gas temperature is obtained after solving the chemical equilibrium and thermal balance for $n_H = 10^4$ cm^{-3} and T_g = 75 K under the assumption of steady-state equilibrium. This is plotted as a function of optical depth in Fig. 8. The thermal balance in H I is affected by the dust both in H I and associated H II regions. However, it should be emphasized here that the infrared radiation from the dust in H I region is negligible as compared to that from the H II region. We find that, for the cloud of hydrogen column density N_H = N (H) +2N (H_2) = 5 × 10^{22} cm^{-3}, the ratio of infrared radiation of the H I and H II regions J_{IR}(H I)/J_{IR}(H II) < 10^{-4} at 100 μm, whereas it is < .025 at 1000μm; this is the range in wavelength in which most of the cooling lines considered here are lying. Therefore the FIR field from the dust within the H I gas is neglected here.

The heating of the medium is affected strongly by the dust within the gas only through photoelectric emission from the surface of the dust grain (Γ_d) due to UV radiation coming from the adjacent H II regions. It is shown in Fig. 8 that the temperature of the medium changes drastically specially at small optical depths in the

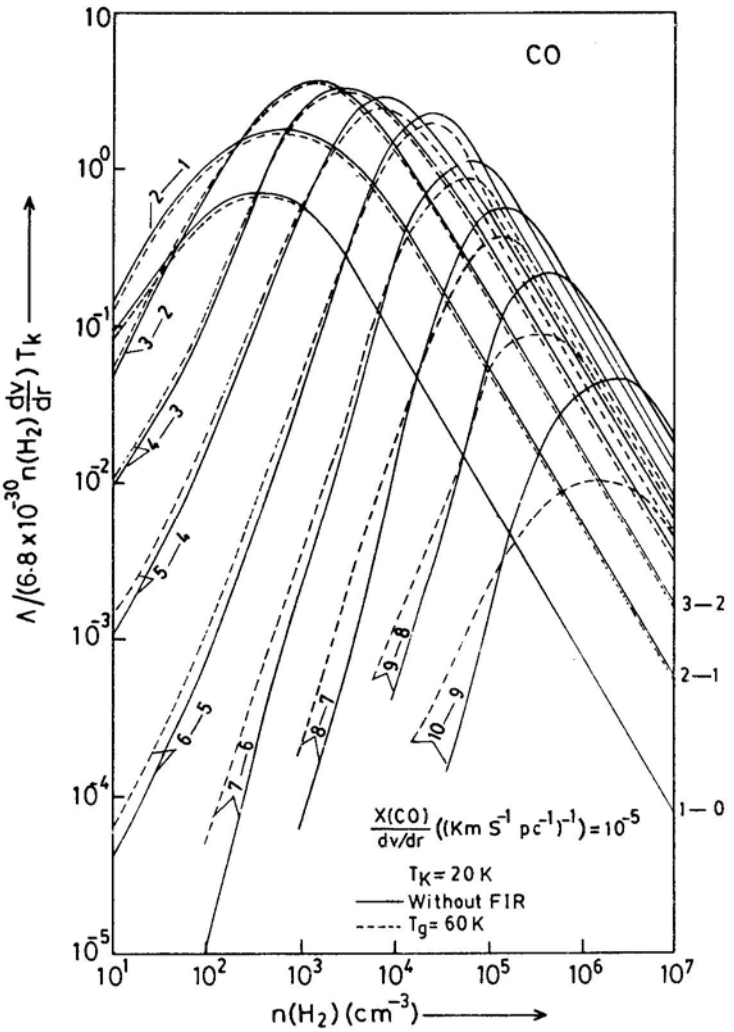

Figure 6. Reduced cooling rates for individual transitions of CO at T_k = 20 K and for X (CO)/(dv/dr) = 10^{-5} (km s^{-1} pc^{-1})$^{-1}$.

absence of FUV fluxes. Beyond a dust optical depth of 10 the temperature is almost constant and the contribution to heating by photoelectric emission becomes negligible because of attenuation of UV radiation by dust.

The dust temperature in the neutral medium (H I) associated with the H II regions follows from the balance between photon absorption and emission. It is found that the gas and grain temperature are very close to each other. Therefore, energy exchange between gas and grain by collision (Γ_{coll}) is $10^{-25} \leqslant \Gamma_{coll} \leqslant 10^{-24}$ for $10 \leqslant T_k \leqslant 20$ K and $n_H = 10^4$ cm^{-3} (of. Equations (l)–(3) of Burke & Hollenbach 1983). It should be mentioned here that cooling rate due to CO alone which has a minimum value in the core of the cloud, is greater than that due to gas grain collisions. The cooling due to CO molecule in the core is 2×10^{-23} erg cm^{-3} s^{-1} at T_k = 10K and 1.5×10^{-22} erg

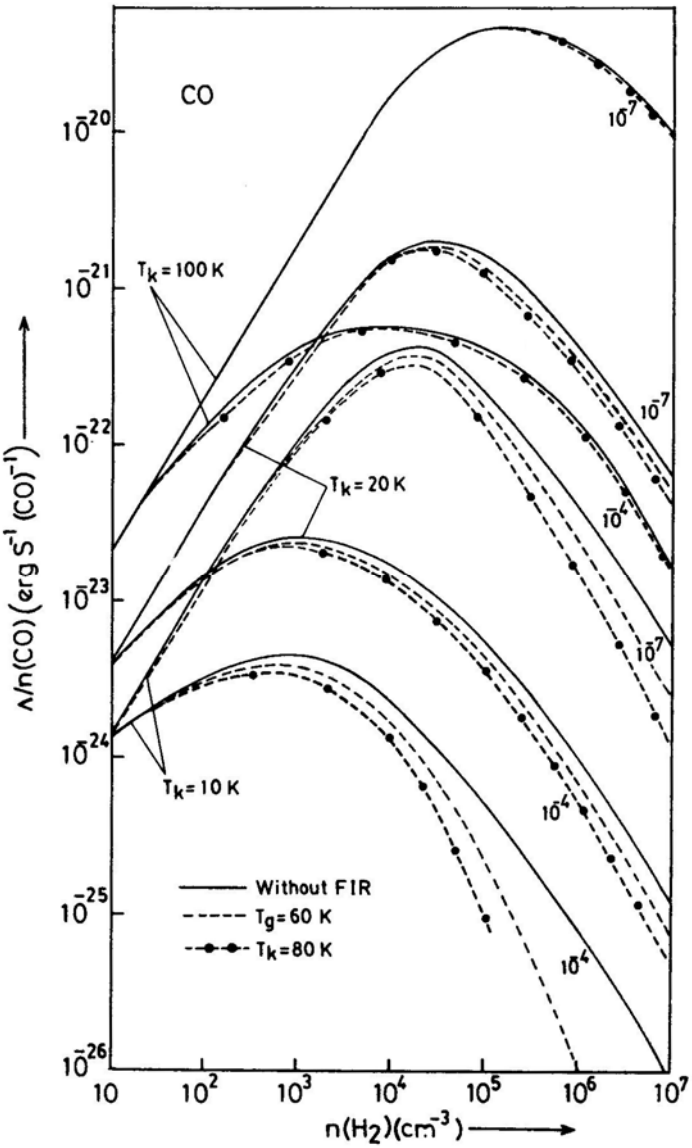

Figure 7. Total cooling rate per molecule from rotational transitions of CO for X (CO)/(dv/dr) 10^{-4} and 10^{-7} (km s^{-1} $pc^{-1})^{-1}$ at kinetic temperatures of 10 K, 20 K and 100 K.

cm^{-3} s^{-1} at T_k = 20K for n_H= 10^4 cm^{-3} and abundance X (CO)/(dv/dr) = 10^{-5} (km s^{-1} $pc^{-1})^{-1}$. Therefore, the temperature structure remains identical even if gas-grain collisions are included.

From Fig. 8 we conclude that close to H II/H I interface the thermal structure remains unchanged even in the presence of FIR, whereas in the inner part, particularly at low temperatures, it may significantly be changed. However, if the density is large enough in this region, the energy exchange by grain-molecule collisions determines the

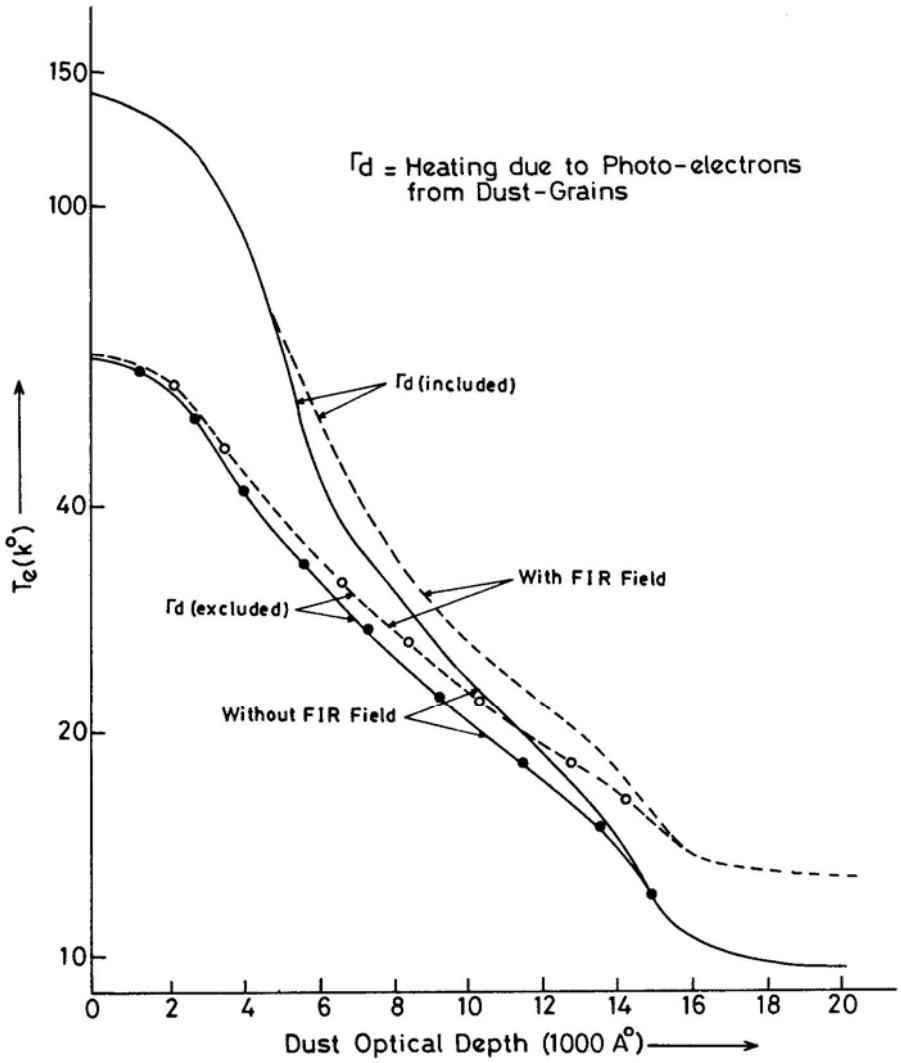

Figure 8. Gas temperature distribution in the cloud with Γ_d and without FIR field (——), with Γ_d and with FIR field (----), without Γ_d and FIR field (–•–) and without Γ_d and with FIR field (----o----).

gas temperature because it is proportional to n_0^2 (Falgarone & Puget 1985); but situation may not always be so. In the present case, the cooling is dominated by carbon species. If the temperature were slightly higher, as it would be if the UV radiation were more intense or shocks were present, when cooling by oxygen would be dominant. In this situation, the total cooling at the interface and also in the interior will be reduced due to which temperature will be increased. Therefore, in the determination of temperature structure of a cloud associated with the H II regions, the FIR field from the H II regions needs to be considered at least in some cases.

Acknowledgements

We would like to thank Professor Mohammad Shafi for providing necessary facilities to carry out this work. We are grateful to Mr Badre Alam for helpful discussions.

References

Burke, J. R., Hollenbach, D. J. 1983, *Astrophys. J.*, **265,** 223.
Chu, S.-I, Dalgarno, A. 1975, *Proc. R. Soc. London*, **A342,** 191.
Crawford, M. K., Genzel, R., Townes, C. H., Watson, D. M. 1985, *Astrophys. J.*, **291,** 755.
Dalgarno, A., McCray, R. A. 1972, *A. Rev. Astr. Astrophys.*, **10,** 375.
De Jong, T., Chu, S.-I, Dalgarno, A. 1975, *Astrophys. J.*, **199,** 69.
Falgarone, E., Puget, J. L. 1985, *Astr. Astrophys.*, **142,** 157.
Flower, D. R., Launay, J. M. 1977a, *J. Phys. B: Atom. mol. Phys.*, **10,** L229.
Flower, D. R., Launay, J. M. 1977b, *J. Phys. B: Atom. mol. Phys.*, **10,** 3673.
Goldsmith, P. F., Langer, W. D. 1978, *Astrophys. J.*, **222,** 881.
Green, S., Thaddeus, P. 1976, *Astrophys. J.*, **205,** 766.
Hudson, H. S., Soifer, B. T. 1976, *Astrophys. J.*, **206,** 100.
Keene, J., Blake, G. A., Phillips, T. G, Huggins, P. J., Beichman, C. A. 1985, *Astrophys. J.*, **299,** 967.
Launay, J. M., Roueff, E. 1977a, *Astr. Astrophys.*, **56,** 289.
Launay, J. M., Roueff, E. 1977b, *J. Phys. B: Atom. mol. Phys.*, **10,** 879.
Mezger, P. G., Mathis, J. S., Panagia, N. 1982, *Astr. Astrophys.*, **105,** 372.
Pankonin, V., Walrasley, C. M. 1976, *Astr. Astrophys.*, **48,** 341.
Penston, M. V. 1970, *Astrophys. J.*, **162,** 771.
Phillips, T. G., Huggins, P. J., Wannier, P. G., Scoville, N. Z. 1979, *Astrophys. J.*, **231,** 720.
Phillips, T. G, Huggins, P. J., Kuiper, T. B. H., Miller, R. E. 1980, *Astrophys. J.*, **238,** L103.
Phillips, T. G., Huggins, P. J. 1981, *Astrophys. J.*, **251,** 533.
Qaiyum, A., Ansari, S. M. R. 1983, *Mon. Not. R. astr. Soc*, **205,** 719.
Russel, R. W., Melnick, G., Gull, G. E., Harwit, M. 1980, *Astrophys. J.*, **240,** L99.
Stracey, G. J., Smyers, S. D., Kurtz, N. T., Harwit, M. 1983, *Astrophys. J.*, **265,** L7.
Ungerechts, H., Walmsley, C. M. 1979, *Astr. Astrophys.*, **80,** 325.
Werner, M. W., Gatley, I., Harper, D. A., Becklin, E. E., Loewenstein, R. E., Telesco, C. M., Thronson, H. A. 1976, *Astrophys. J.*, **204,** 420.
Werner, M. W., Crawford, M. K., Genzel, R., Hollenbach, D. J., Townes, C. H., Watson, D. M. 1984, *Astrophys. J.*, **282,** L81.
Westbrook, W. E, Werner, M. W., Elias, J. H., Gezari, D. Y., Hauser, M. G., Lo, K. Y., Neugebauer, G. 1976, *Astrophys. J.*, **209,** 94.

J. Astrophys. Astr. (1987) **8**, 183–194

The He II Line λ4686 in WN Binaries

B. S. Shylaja *Indian Institute of Astrophysics, Bangalore 560034*

Received 1986 August 19; accepted 1987 February 16

Abstract. The behaviour of the λ4686 line of He II in various WN binaries is studied for variations in total flux as well as radial velocities. It appears that the true motion of the WN component is not depicted by this line especially for short-period binaries. A qualitative explanation is sought in terms of a large, extended line-emitting region and multiple-component line profile.

Key words: stars, emission-line—stars, binaries—stars, WN-type

1. Introduction

The λ4686 line of He II is one of the brightest lines in WR spectra and, therefore, is used as an identifying feature in lowdispersion emission-line surveys. It is the strongest line in the spectra of the WN sub-group in the visible and UV region.

Out of the twenty binaries listed in the catalogue of van der Hucht *et al.* (1981), sixteen have WN components while remaining four have WC components. A more recent list by Hidayat, Admiranto & van der Hucht (1984) includes also the low-mass-function systems and puts the total number to about 35, of which 25 have WN components. The variations in line profiles with orbital phase, have been studied in great detail by Sahade (1958) for many of these binaries. Here we have chosen the binaries with well-determined radial-velocity variations (Table 1) in order to study the effect of the companion on the λ4686 line-emitting region. The study has been restricted to binaries with WN components, because in the WC sub-group this line is blended with the red wing of the stronger line of C III λ4650.

A preliminary report of this study is already published (Shylaja 1986c).

2. Observational data

From a study of WNL systems, it has been shown by Moffat & Seggewiss (1979) that the motion of the WN component in these binaries is best represented by the N IV line at λ4058. This assumption has been extended to all binaries studied here, so that the differences in the behaviour of He II λ4686 line relative to N IV λ4058 can be interpreted as a consequence of the differences in the dynamics of line-emitting regions. For WNE systems N V λ4603 is a better choice and whenever the observations of this line are available, they have been used to decide the anomalous behaviour of λ4686.

Table 1. WN binaries from Hidayat, Admiranto & van der Hucht (1984).

				λ4686		λ4058					
WR No.	Name/HD	Sp. type	P(d)	K	γ	K	γ	log P	R_K	$\Delta\gamma$*	Reference†
155	CQ Cep	WN 7+07	1.64	134	165	297	−53	0.22	2.22	218	Stickland *et al.* 1984
	HD 214419			148	118	313	−61		2.12	179	Bappu & Viswanadham 1977
				165	137	295	−75		1.79	212	Hiltner 1944
						285	−85				Niemela 1980
				181	77	310	−60		1.71	137	Leung, Moffat & Seggewiss 1983
123	HD 177230	WN 8	1.76	17	—	22	—	0.25	1.29	P	Lamontagne, Moffat & Seggewiss 1983
151	CX Cep	WN 5+O8V	2.13	300	—	300	—	0.33	—	—	Massey & Conti 1981
138	HD 193077	WN 6+abs	2.32?	36	69	28	−92	0.34	0.78	161	Lamontagne *et al.* 1982
124	209 BAC	WN 8	2.36	12.7	190	—	—	0.37	—	?	Moffat, Lamontagne & Seggewiss 1982
6	HD 50896	WN 5	3.76	25	147	—	—	0.58	—	P	Firmani *et al.* 1980
43	HD 97950	WN 6+abs.	3.77	72	12	—	—	0.58	∼1	46	Moffat & Niemela 1984
128	HD 187282	WN 4	3.85	∼20	∼130	—	—	0.59	—	P	Antokhin, Aslanov & Cherepashchuk 1982b
40	HD 96548	WN 8	4.16	—	—	—	—	0.62	—	P	Moffat & Isserstedt 1980
139	HD 193576	WN 5+O6	4.21	283	16	303	−42	0.62	1.07	58	Ganesh, Bappu & Natarajan 1967
	V444 Cyg										
148	HD 197406	WN 7	4.32	57	−95	82	−126	0.63	1.44	31	Bracher 1979
				∼60	∼−100	90	−143		1.5	43	Moffat & Seggewiss 1980
				49	−94	86	−134		1.76	40	Drissen *et al.* 1986

136	HD 192163	WN 6	4.5?	13.6	64.9	32.7	−183.4	0.65	2.40	248	Aslanov & Cherepashchuk 1981
31	HD 94546	WN 4+O7	4.9	—	—	290	−130	0.69	—	—	
47	HD E311884	WN 6+O5V	6.34	310	−10	297	−89	0.80	0.96	79	Niemela, Conti & Massey 1980
153	HD 211853	WN 6+O	6.69?	220	15	155	−120	0.83	0.70	135	Ganesh & Bappu 1967
134	HD 191765	WN 6	7.44	20	~85	—	—	0.87	—	P	Antokhin, Aslanov & Cherepashchuk 1982a
71	HD 143414	WN 6	7.69	29	−150	18	−260	0.89	0.62	110	Isserstedt, Moffat & Niemela 1983
21	HD 90657	WN 4	8.2	246	20	221	−33	0.92	0.90	153	Niemela & Moffat 1982
97	HDE 320102	WN 3+O5.7	8.83	—	—	150	0	0.95	—	—	Niemela 1982
127	HD 186943	WN 4+O9.5V	9.56	212	107	167	70	0.98	0.79	37	Ganesh & Bappu 1967
				146	239	—	—	—	—	P	Massey 1981
16	HD 86161	WN 8	10.73	—	—	4.7	−23	1.03	—	P	Moffat & Niemela 1982
141	HD 193928	WN 6	21.64	147	60	135	−64	1.34	0.92	124	Ganesh & Bappu 1967
145	AS 422	WN+WC	22	—	—	—	—	1.34	—	—	Pesch, Hiltner & Brandt 1960
12	CD−45°4482	WN 7	23.9	—	—	130	−34	1.38	~1	P	Niemela 1982
22	HD 92740	WN 7+abs	80.35	~80	—	~70	—	1.91	~0.88	P	Moffat & Seggewiss 1978
133	HD 190918	WN 4.5 +O9.5Ia	112.8	—	—	—	—	2.05	—	—	Hidayat, Admiranto & van der Hucht 1984

* 'P' in this column implies the red shift of $\Delta\gamma$ noticeable in the figures or tables in the corresponding reference, but not necessarily as orbital solutions.

† References correspond to information on R_K and $\Delta\gamma$.

Although hydrogen deficiency is an established phenomenon in some WR stars (Sahade 1980), Balmer lines in absorption have been detected in some binaries and single-line stars. Therefore, it is difficult to estimate the contribution of the companion to some lines like λ6562, λ4860, λ4340, λ4100 etc. Therefore, although in general these lines are considered as due to He II, they cannot be compared with λ4686.

2.1 *Variations in Total Flux*

The flux of λ4686 and λ4058 lines, obtained for two systems CQ Cep (P= 1.64 d) and HD 50896 (P = 3.76 d) as a function of orbital phase, is shown in Fig. 1 (from Shylaja 1986a and b). It may be seen that the flux of λ4686 shows an increase near phases 0.0 and 0.5 corresponding to the eclipse and transit of the components. Although the flux of λ4686 in HD 50896 has considerable scatter, the increase in flux at phase 0.0 is noticeable (Shylaja 1986b). In the case of CQ Cep, not only the N IV λ4058 line, but all the other lines of He II such as λ4860, λ5411 and λ6562, showed a similar behaviour. This was attributed to the complicated structure of the extended atmosphere, arising as a consequence of the proximity of the companion. In the case of HD 50896, the N IV line

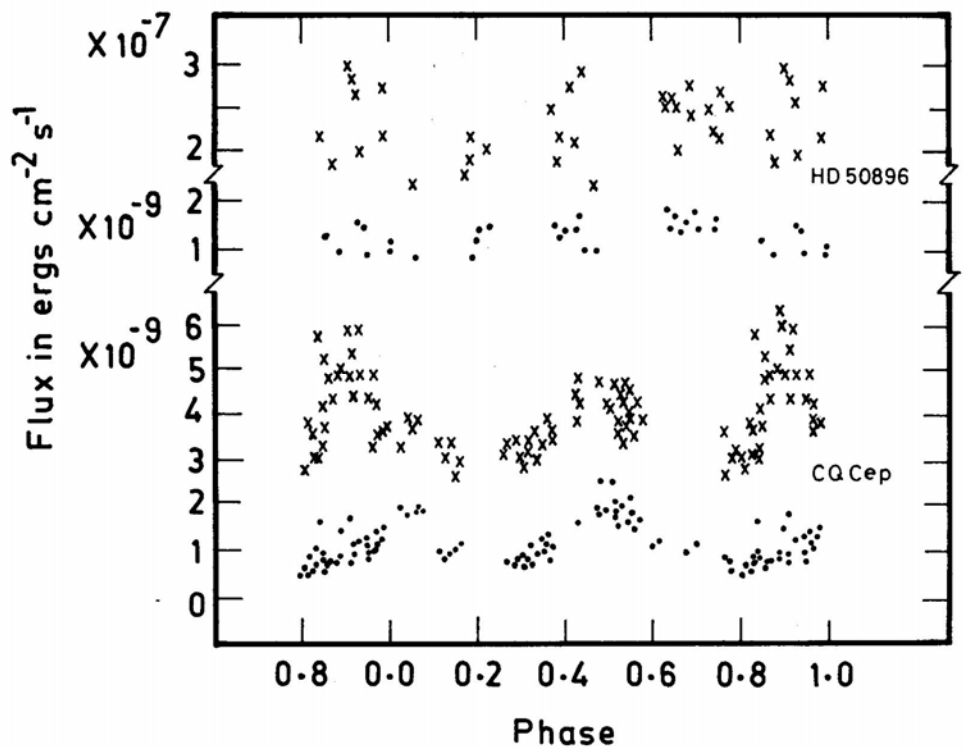

Figure 1. Fluxes of He II λ4686 (crosses) and N IV λ4058 (dots) for two short-period binaries from Shylaja (1986a, b).

at λ4058 and the other lines of He II, like λ4860, λ5411, λ6562 *etc.* show a scatter in flux, and again the behaviour of l4686 is different. The flux measures of other binaries are not available as yet. However, the line profiles of HD 186943 (Ganesh, Bappu & Natarajan 1967) show a large variation from quadratures to conjunctions. It may be inferred that the flux (the total flux measured in absolute quantities and not relating to a normalized continuum) increases at eclipse and transit. In the case of V444 Cyg (Kuhi 1968) the O-type companion is larger and more massive than the WN component unlike the case of CQ Cep. Therefore, all the emission lines showed eclipse effects. However, the eclipse depth of λ4686 is markedly different from those of other lines. This may imply that at phases corresponding to the eclipse and transit of components, the total flux of λ4686 increases, compared to any other emission line so that the net effect is to have a smaller eclipse depth as seen by Kuhi (1968). There are some other systems whose observations may also indicate a similar increase of flux. In the case of HD 90657 (P = 8.26 d), a dip in the light curve at λ4680 is observed (Niemela & Moffat 1982) at phase ~ 0.15, which is attributed to the asymmetric line-emitting region. However, the same curve can also be interpreted as showing an increase in flux at phase 0.5, corresponding to the WN4 component behind the companion. The light variation shown by HD 96548 (Moffat & Isserstedt 1980) is not included here because, only the variations of the continuum are reflected in the λ4686 light curve.

The line profile studies of V444 Cyg have shown that there is a hump superimposed on a smooth profile (Ganesh & Bappu 1967). The movement of this hump was attributed to the contribution from the concentration of line-emitting material between the stars. A similar possibility exists in the case of HD 90657, as mentioned above, where the dip near phase 0.15 may be attributed to reduced contribution from the region between the two stars. In the case of HD 5980 (P = 19.27 d), WN4 + O7 binary in SMC, Breysacher, Moffat & Niemela (1982) have explained the line profile by assuming that a larger amount of material exists near the hemisphere facing the O star.

2.2 *Radial Velocities*

The radial velocity (RV) curves from various sources (Table 1) are reproduced in Fig. 2. The following points are immediately apparent:

1. Considering that the N IV λ4058 represents the true motion of the WN component, *i.e.* the velocity of centre of mass, there is a redshift in γ of He II λ4686 in all cases.
2. The amplitudes of the RV curves K(4686) and K(4058) vary from system to system. The variation of the ratio $R_K = K(4058)/K(4686)$ with orbital period is shown in Fig. 3. For CQ Cep, the shortest orbital period system, R_K is the largest, whereas it becomes unity for systems with orbital period of about 4 d. For still larger orbital periods, the tendency for R_K is to become < 1 or remain near unity.
3. The solutions derived from the RV curve of K(4686) generally give eccentric orbits, especially for short-period systems, whereas solutions from other lines are circular.

The table includes almost all the known binaries with WN components (Hidayat, Admiranto & van der Hucht 1984). For HD 177230 the RV curve is not explicitly available for λ4058, but appears as a 'mean emission'. For CX Cep (P = 2.12 d), the amplitude differences of λ4686 and λ4058 RV curves have been discussed by Massey & Conti (1981) and they have assumed K(4686) = K(4058). However, their RV curve

appears to exclude the possibility $K(4058) < K(4686)$, while there is a suggestion that $K(4058)$ may be greater than K (4686). From Fig. 3 it would appear that for its orbital period the value of R_K may be about 1.7. This can be established only by a better RV curve of λ4058. For the other short-period binary 209 BAC, the RV curve of λ4058 is not available. In the case of HD 97950 (P = 3.77 d), it appears that the amplitudes do not differ greatly (Moffat & Niemela 1984). For HD 311884 (Niemela, Conti & Massey 1980) the RV curve of λ4686 cannot be separated from the mean of all He II velocities. In many other cases λ4058 RV curve is not available.

The redshift of γ for the λ4686 RV curves is a general feature in many systems. In Table 1 the redshift is denoted as $\Delta\gamma = (\gamma(4686) - \gamma(4058))$, whenever both the quantities are available in literature. In many other cases, this redshift is noticeable in the figures

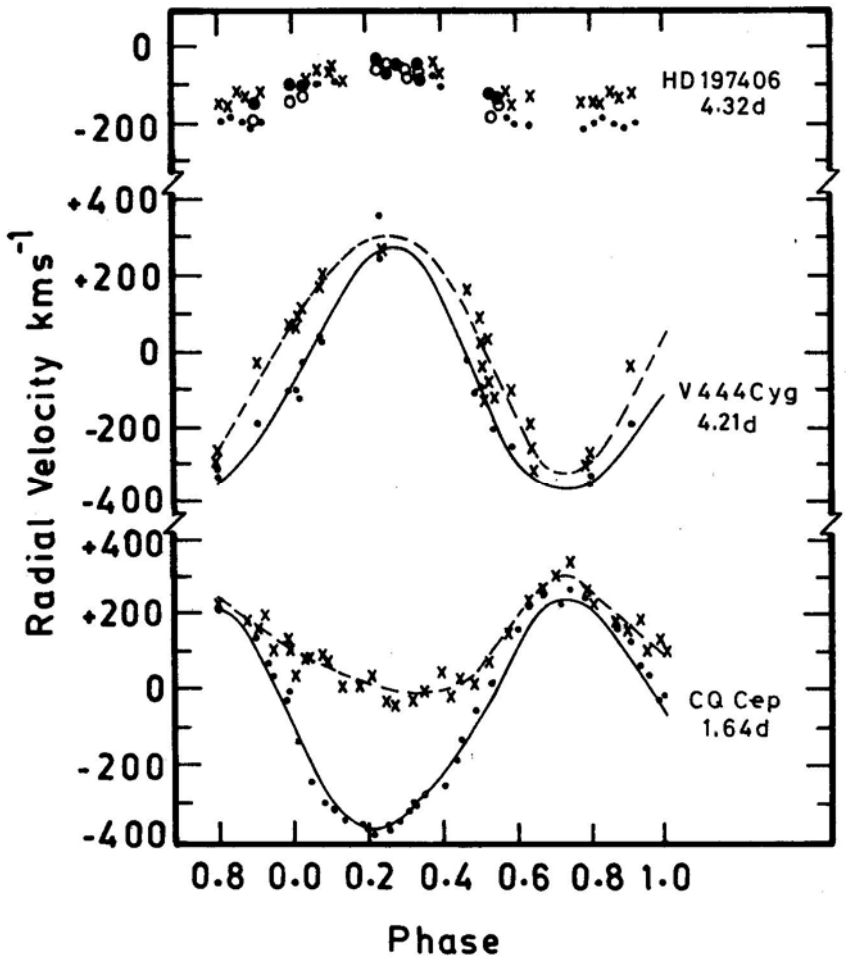

Figure 2. Radial velocity curves of He II λ4686 (crosses) and N IV λ4058 (dots) from various sources indicated in Table 1. The λ4058 points for HD 50896 are from Ebbets (1979). In the case of HD 197406 the observations of Moffat & Seggewiss (1980) are marked by filled (λ4686) and open (λ4058) circles. The curves are hand-drawn for cases where original solutions were not available.

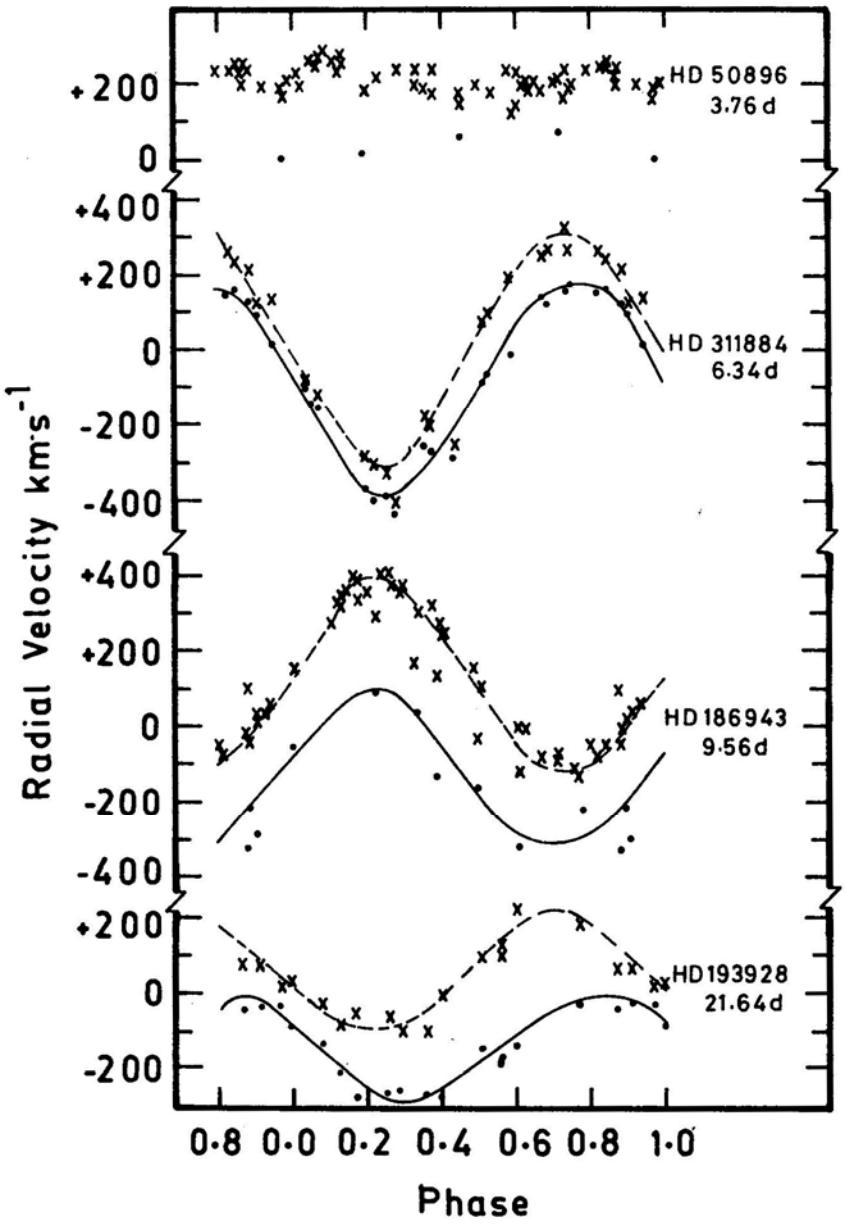

Figure 2. Continued.

and tables provided by the previous investigators, and not necessarily as orbital solutions. These are indicated as 'P' (= present) in the column $\Delta\gamma$. For systems like HD 187282 the redshift is apparent relative to the N V λ4603 RV curve. For HD 191765 the same is true relative to the N III λ4640 RV curve.

3. Discussion

In general, the established companions in many of these binaries are of spectral type O. Therefore, it is possible that there is an absorption superposed on these emission profiles. This implies that such an absorption component may move in an opposite direction so as to indicate the movement of the companion. Attempt made to search for this, revealed that such absorptions are not clearly noticeable. The profiles of the λ4860 line of He II clearly show this type of movement of absorption (Ganesh & Bappu 1967) whereas λ4686 does not show this, although one could think of the double-hump profile being caused by two emissions rather than an absorption. In case of HD 193928 (P = 21.64 d), there is an indication of double-hump structure that is not very well separated.

If we postulate a companion of type Of, the contribution to the emission becomes considerable. This has been discussed in the case of HD 5980 by Breysacher, Moffat & Niemela (1982) who consider three contributors to the emission: (1) the WN component, (2) the companion and (3) the region between the two stars. Assuming such a multi-component profile, they are able to analyze the variation of half-intensity widths of this line. At phases 0.0 and 0.5, the contribution from (3) is diminished, causing a decrease in the half-intensity widths.

The observational evidence thus clearly shows that there are additional contributors to λ4686 relative to λ4058. We may consider different possibilities such as (1) the companion itself, (2) the optical depth effects, and (3) asymmetric distribution of material emitting λ4686.

In the case of binaries with Of companions, therefore, it is possible that there is significant contribution to emission from all the three cases listed above. In medium dispersion spectra, because of the large widths of each contribution, the line profile may become significantly blended resulting in an error in fixing the centre of the profile for RV measurements. This can cause a net reduction in the amplitude of the RV curve.

In the case of binaries with compact companions, although the contribution to the line profile from the companion is not significant, the accretion disc can contribute to the total flux. However, not many samples are available for verifying this aspect. HD 197406 (P = 4.17 d) fits in Fig. 3 very well, but the contribution from the disc cannot be distinguished in the line profile. The interpretation is complicated because of the recent identity of the companion with a black hole (Drissen *et al.* 1986). In the case of HD 50896, the λ4058 line profile is complicated and, therefore, a comparison is not possible.

The redshift of the γ value of He II λ4686 line relative to N IV λ4058 is a general feature in the case of all WN binaries. This aspect has been discussed by many previous investigators (Sahade 1958 and Ganesh & Bappu 1967). The other He II lines like λ4860 and λ4340 have contributions from the companion either in emission or absorption making it difficult to identify the redshift, even if it is present. The effects of electron scattering in radially expanding envelope was investigated by Auer & van Blerkom (1972), who showed that the velocity field preferentially scatters photons to the red. Thus, electron scattering is mainly responsible for the red wing of the He II profiles and this has been confirmed in HD 50896 (Hillier 1984) by both observations and theoretical modelling. Thus, this effect also makes the profile asymmetric, making it difficult to fix the line centre and hence adding to the systematic errors in the RV estimates.

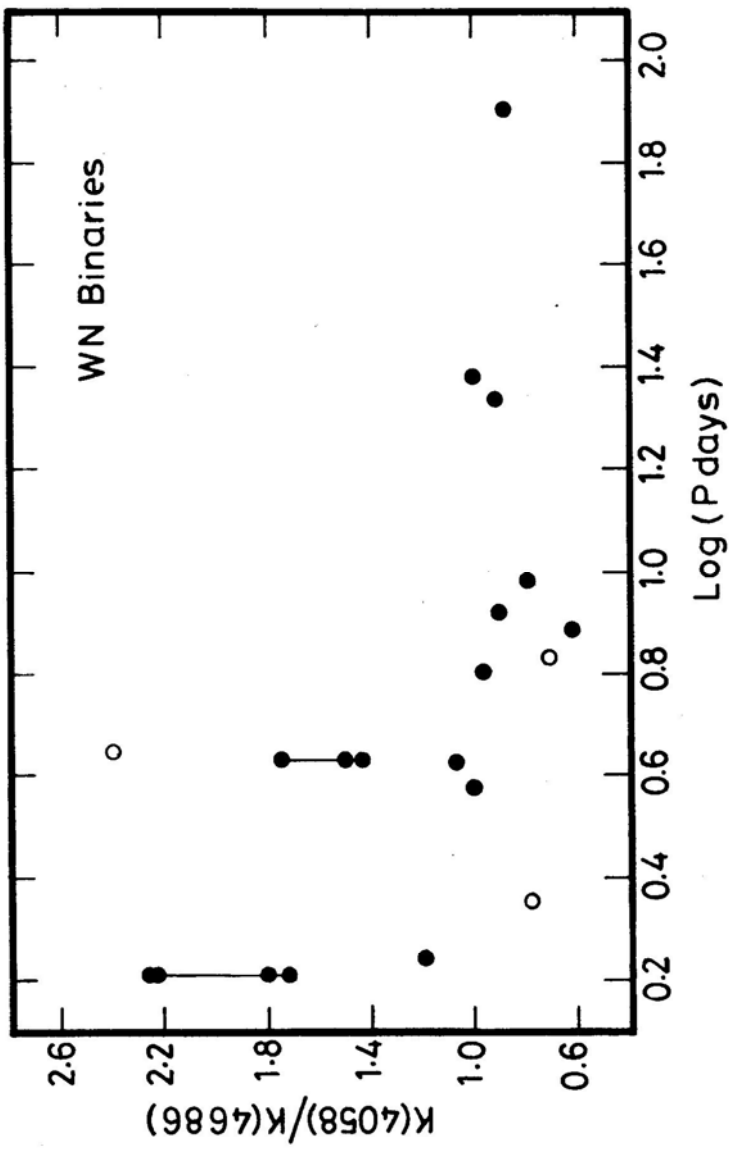

Figure 3. The variation of the ratio, R_K of the amplitudes of RV curves of λ4058 to λ4686 in km s^{-1}, relative to log (orbital period in days). The unfilled circles correspond to the stress cases where the binary nature is questioned (see text).

The effects of the companion and the electron scattering as discussed above are probably common to all WN systems. Therefore, the reduction of the amplitude ratio R_K with orbital period cannot be explained by these two factors.

In Fig. 3, HD 193077, HD 211853 and HD 192163 are indicated by separate symbols. HD l93077 has been identified as a possible triple system (Lamontagne, Moffat & Seggewiss 1983). HD 211853 has been identified with a quadruple system and therefore the λ4686 variation is complicated (Massey 1981). The binary nature of HD 192163 has been debated (Vreux, Andrillat & Gosset). Thus these points suggest that the relation of R_K with orbital period is not linear. It is possible that the binaries with low-mass companions exhibit a different behaviour of λ4686 in comparison to those with OB companions. Therefore, although it is not possible to draw a smooth relation between R_K and log P, it appears that this ratio reaches the value of unity asymptotically for periods longer than 6 days. In many solutions that are used for deriving K, the circular orbit is generally assumed. Hence it is possible that by observing more systems with $p \leqslant 6$ days, a more meaningful relation can be arrived at.

It is known that classical Roche surfaces are not applicable for these binaries with strong winds. The wind-dominant Roche surface calculations have been done by Niemela for V444 Cyg (*of.* Sahade & Wood 1978) which clearly shows the asymmetry of line-emitting region. It is also known that λ4686 has the largest optical depth amongst all He II lines (Hillier 1983) and, therefore, we see the emission from the outermost parts of the line-emitting region. Such regions are, according to the Roche surface calculations of Niemela, asymmetric and, therefore, the flux variation of λ4686 reflects these distorted locations directly. However, the exact distribution of line-emitting material in such a surface will be decided by the density distribution, the velocity law and also the temperature gradient. A qualitative analysis of the asymmetry can lead to the deduction that short-period systems show more complicated line profiles and larger flux variations. As the separation of the companion from the primary increases (*i.e.* the period becomes longer) the magnitude of this effect is reduced.

Thus, the long-period systems ($P \geqslant$6d) may not show an increase of flux and decrease in amplitude of the λ4686 RV curve at phases corresponding to eclipse. It may also be seen from Fig. 3 that only few samples are available with long orbital periods.

We may also consider the effect of an O type or Of type companion on other emission lines as well. N III λ4640 is a possible contributor. However, because these are already 3 unresolved multiplets, the additional contributors cannot be distinguished. In the case of CQ Cep (Shylaja 1986a) it was seen that the behaviour of the N III λ4640 line was also markedly different from other lines. Similar measurements in other systems are not available. The redshift of the line and the reduction of its amplitude are generally noticeable, but any flux variation is not striking for other He II lines *(e.g.* in CQ Cep). It may also be mentioned here that sudden sporadic strengthening of emission lines is reported in many cases. However, it may be noted that when a change in the strength of λ4686 occurs, no corresponding change in λ4860 is seen. This may be caused by one or more of the following: (1) the effect of absorption lines, (2) the small difference in the upper level of excitation, (3) the differences in optical depth effects, (4) the differences in the sizes of the line-emitting regions.

All the lines of He I originate in the outermost regions of the atmosphere (Moffat & Seggewiss 1978) and in many cases do not show phase-dependent variations in flux. The profiles are generally associated with violet absorption edges, whose velocities

usually follow the movement of the WN component, although with large scatter. Therefore, the contribution of the companion is difficult to detect.

Thus, it appears that the contribution from the companion in terms of either emission or absorption, to the line profile of λ4686, is partly responsible for the observed difference in the behaviour of this line relative to λ4058. The large optical depth and the asymmetric distribution of line-emitting material in the atmosphere can also cause the observed variation. Since the proximity of the companion is responsible for the distortion of the line-emitting region and, therefore, of the line profiles, the inequality $K(4686) < K(4058)$ may be valid for very-short-period binaries only. This study emphasizes the need for a study of short-period systems like CX Cep and 209 BAC (relatively faint) more thoroughly for flux and RV variations.

4. Conclusions

The behaviour of the λ4686 line in many WN binaries shows a marked difference relative to nitrogen lines, which are deemed to represent the true motion of the WN component. The differences in the variation of total flux and of radial velocities seem to be inter-related. A qualitative analysis using wind-dominant Roche surfaces shows that asymmetric distribution as well as optical depth effects are significant. Similarly, the contribution from the companion will also have to be taken into consideration, in the case of multiple component line profiles. Since the proximity of the companion is responsible for the distortion of the line-emitting region and, therefore, of the line profiles, it is possible that the large flux variation of λ4686 and the inequality $K(4686) < K(4058)$ are valid for short-period systems and this anomaly gradually reduces at a period of about 6 d.

Acknowledgements

The author wishes to thank Professor J. C. Bhattacharyya for continued guidance in this program. Thanks are also due to Dr N. K. Rao for a critical reading of the manuscript and stimulating discussions. Helpful suggestions by Professors W. Seggewiss, A. F. J. Moffat and an anonymous referee are gratefully acknowledged.

References

Antokhin, I. I., Aslanov, A. A., Cherepashchuk, A. M. 1982a *Soviet Astr. Lett.*, **8**, 156.
Antokhin, I. I., Aslanov, A. A., Cherepashchuk, A. M. 1982b *Soviet Astr. Lett,* **8,** 395.
Aslanov, A. A., Cherepashchuk, A. M. 1981, *Soviet Astr. Lett.*, **7,** 265.
Auer, L. H., van Blerkom, D. 1972, *Astrophys. J.*, **178,** 175.
Bappu, M. K. V., Viswanadham, P. 1977, *Kodaikanal Obs. Bull, Ser. A,* **2,** 89.
Breysacher, J., Moffat, A. F. J., Niemela, V. S. 1982, *Astrophys. J.*, **257,** 116.
Bracher, K. 1979, *Publ astr. Soc. Pacific*, **91,** 827.
Drissen, L., Lamontagne, R., Moffat, A. F. J., Bastien, P., Seguin, M. 1986, *Astrophys. J.*, **304,** 188.
Ebbets, D. 1979, *Publ astr. Soc. Pacific*, **91,** 804.
Firmani, C, Koenigsberger, G., Bisiacchi, G. F., Moffat, A. F. J., Issertedt, J. 1980, *Astrophys. J.*, **239,** 607.

Ganesh, K. S., Bappu, M. K. V. 1967, *Kodaikanal Obs. Bull., Ser. A.,* No. 185, 104.
Ganesh, K. S., Bappu, M. K. V., Natarajan, V. 1967, *Kodaikanal Obs. Bull, Ser. A.,* No. 184, 93.
Hidayat, B., Admiranto, A. G., van der Hucht, K. A. 1984, *Astrophys. Space Sci.,* **99,** 175.
Hillier, D. J. 1983, *Astrophys. J.,* **271,** 221.
Hillier, D. J. 1984, *Astrophys. J.,* **280,** 744.
Hiltner, W. 1944, *Astrophys. J.,* **99,** 273.
Isserstedt, J., Moffat, A. F. J., Niemela, V. S. 1983, *Astr. Astrophys.,* **126,** 183.
Kuhi, L. V. 1968, *Astrophys. J.,* **152,** 89.
Lamontagne, R., Moffat, A. F. J., Koenigsberger, G., Seggewiss, W. 1982a, *Astrophys. J.,* **253,** 230.
Lamontagne, R., Moffat, A. F. J, Seggewiss, W. 1983, *Astrophys. J.,* **269,** 596.
Leung, K. C, Moffat, A. F. J., Seggewiss, W. 1983, *Astrophys. J.,* **265,** 961.
Massey, P. 1981, *Astrophys. J.,* **244,** 157.
Massey, P., Conti, P. S. 1981, *Astrophys. J.,* **244,** 169.
Moffat, A. F. J., Isserstedt, J. 1980, *Astr. Astrophys.,* **91,** 147.
Moffat, A. F. J., Lamontagne, R., Seggewiss, W. 1.982, *Astr. Astrophys.,* **114,** 135.
Moffat, A, F. J„ Niemela, V. S. 1982, *Astr. Astrophys.,* **108,** 326.
Moffat, A. F. J., Niemela, V. S. 1984, *Astrophys. J.,* **284,** 631.
Moffat, A. F. J., Seggewiss, W. 1978, *Astr. Astrophys.,* **70,** 69.
Moffat, A. F. J., Seggewiss, W, 1979, *Astr. Astrophys.,* **77,** 928.
Moffat, A. F. J., Seggewiss, W. 1980, *Astr. Astrophys.,* **86,** 87.
Niemela, V. S. 1980, in *IAU symp.* 88: *Close Binary Stars: Observations and Interpretations,* Eds M. J. Plavec, D. M. Popper & R. K. Ulrich, D. Reidel, Dordrecht, p. 177.
Niemela, V. S. 1982, in *IAU Symp.* 99: *Wolf-Rayet Stars, Observations Physics and Evolution,* Eds C. de Loore & A. J. Wills, D. Reidel, Dordrecht, p. 299.
Niemela, V. S., Conti, P. S., Massey, P. 1980, *Astrophys. J.,* **241,** 1050.
Niemela, V. S., Moffat, A. F. J. 1982, *Astrophys. J.,* **259,** 213.
Pesch, P., Hiltner, W. A., Brandt, J. C. 1960, *Astrophys. J.,* **132,** 513.
Sahade, J. 1958, *Mem. Soc. R. Sci. Liege,* Ser. 4e, **20,** 46.
Sahade, J. 1980, *Rev. Mexicana. Astr. Astrof.,* **6,** 189.
Sahade, J., Wood, F. B. 1978, in *Interacting Binary Stars,* Pergamon press, p. 101.
Shylaja, B. S. 1986a, *J. Astrophys. Astr.,* **7,** 171.
Shylaja, B, S. 1986b, *J. Astrophys. Astr.,* **7,** 305.
Shylaja, B. S, 1986c, in *IAU Symp.* 122: *Circumstellar matter,* Ed. I. Appenzeller, D. Reidel, Dordrecht (in press).
Stickland, D. J., Bromage, G. E., Budding, E., Burton, W. M., Howrath, I. D., Jameson, R., Sherrington, M. R., Willis, A. J. 1984, *Astr. Astrophys.,* **134,** 45.
van der Hucht, K. A., Conti, P. S., Lundstrom, I., Stenholm, B. 1981, *Space Sci. Rev.,* **28,** 227.
Vreux, J, M., Andrillat, Y., Gosset, E. 1985, *Astr. Astrophys.,* **149,** 337.

J. Astrophys. Astr. (1987) **8**, 195–209

Evolution of the Optical Spectrum of SN 1987a in the Large Magellanic Cloud

B. N. Ashoka, G. C. Anupama, T. P. Prabhu, S. Giridhar,
K. K. Ghosh, S. K. Jain, A. K. Pati & N. Kameswara Rao
Indian Institute of Astrophysics, Bangalore 560034

Received 1987 April 13; accepted 1987 April 29

Abstract. The evolution of the spectrum of SN1987a is traced from 1987 February 26 to March 31. Based on the low-resolution spectroscopic data we identify the lines of H, He I, Na I, Fe II, Sc II, Ca II which are known to be present in Type II Supernovae, and also present evidence for the existence of lines of Mg I, Ca I, O I, and N I. We discuss the evolution of the Hα profile, and draw attention to its complex structure around March 30. Close to the rest wavelength of Hα a double-peaked structure appeared in the profile with a peak-to-peak separation of ~ 1400 km s^{-1}, suggestive of an expanding shell or disc of gas.

Using the available broadband photometric information, we also trace the evolution of the photosphere of SN1987a assuming that it radiates like a supergiant.

Key words: Supernovae, spectra—Supernovae, SN1987a

1. Introduction

Supernova (SN) 1987a in the Large Magellanic Cloud (LMC) was discovered on 1987 February 24 at a brightness of m_v = 4.5 (*IAU Circular No.* 4316). Its dramatic rise did not continue for long, and the light curve levelled off initially at about m_v = 4.3, and then began a slow rise by ~ 0.017 mag day^{-1}.

Though the optical spectrum of SN 1987a showed characteristics similar to a typical Type II, the supernova was peculiar in many respects. In the optical region, the striking deviations from a typical supernova are in terms of very high absorption velocities of Balmer lines during the early phases, and a peculiar light curve.

The observations of SN 1987a commenced at the Vainu Bappu Observatory (VBO) Kavalur (latitude = 12°34′), on 1987 February 26. Some spectroscopic measurements have been communicated through (*IAU Circular Nos* 4339, 4340, 4359). We present here a brief description of the nature and evolution of the spectrum between 1987 February 26 and March 31. We also discuss the photometric behaviour based on data gathered mostly from *IAU Circulars.*

2. Observations and reductions

We monitored the spectrum of SN 1987a at reciprocal dispersions ranging from 100 to 250 Å mm^{-1} over a wavelength range of $\lambda\lambda$4000–9000 (wavelengths are expressed in Å units all through). Spectrograms were obtained regularly with the Bhavanagar spectrograph using gratings of 300 and 400 grooves mm^{-1} and a 75-mm camera, at the Cassegrain focus of the 0.75-m reflector. In addition, some spectrograms were obtained also at the Cassegrain focus of the 1-m reflector with the help of Carl-Zeiss UAG spectrograph, using a grating of 651 grooves mm^{-1} and a 110-mm camera. Kodak 098-02 and I-N (hypersensitized) emulsions were employed. Occasionally, a 150-mm camera was used in conjunction with a Varo 8605, single-stage, electrostatistically-focussed image tube and spectra were recorded on Kodak IIa-D plates. All plates were calibrated for relative intensity using an auxilliary calibration spectrograph. A few photoelectric spectrum scans were also obtained with a bandpass of 50 Å at the Cassegrain focus of the 1-m reflector.

The spectrograms were digitized using PDS-1010M microdensitometer, generally at a speed of 2 mm s^{-1}, using a sampling interval of 5 μm. RESPECT software (Prabhu, Anupama & Giridhar 1987) was used for final reductions, though some of the preliminary measurements reported here have been made directly on an auxiliary analogue chart output of the microdensitometer. The interactive reductions using RESPECT software include smoothing by a low-pass filter (cut-off frequency ~15 cycles mm^{-1}), and conversion to intensity scale achieved through the characteristic curve determined as a polynomial of third degree in Baker-transformed densities. The wavelength scale was established as a polynomial using the laboratory comparison spectrum (Fe + Ar or Fe + Ne hollow cathode source) exposed on both sides of the spectrum. The spectra were linearized in wavelength through natural cubic-spline interpolation at regular intervals in wavelength.

3. Optical spectrum and its evolution

The spectrum of SN 1987a conforms to the general characteristics of SN II with hydrogen lines in emission although it is not a typical Type II. Since the time of rapid rise to 4.5 mag on February 24–25, the spectrum evolved from a Balmer-line-dominated one with broad P-Cygni type emission to one with strong blue-shifted absorption features due mostly to Fe II and Na I.

Following Patchett & Branch (1972) we use the absorption features as more reliable means of identification. As pointed out by Kirshner *et al.* (1973), the features in both Type I and Type II Supernovae are essentially the same; hence, the identifications of features in Type I SN 1981b in NGC 4536 (Branch *et al.* 1983), and in Type II SN 1979c in M 100 (Branch *et al.* 1981) were used as a guide. The dominant species identified are due to H, He I, Na I, Fe II, Mg I and perhaps Sc II.

3.1 *The Early Spectrum*

Our first spectrum recorded on February 26.63 (Fig. 1) shows broad Hα emission with strong P-Cygni absorption at a velocity of – 16400 km s^{-1}. The absorption compo-

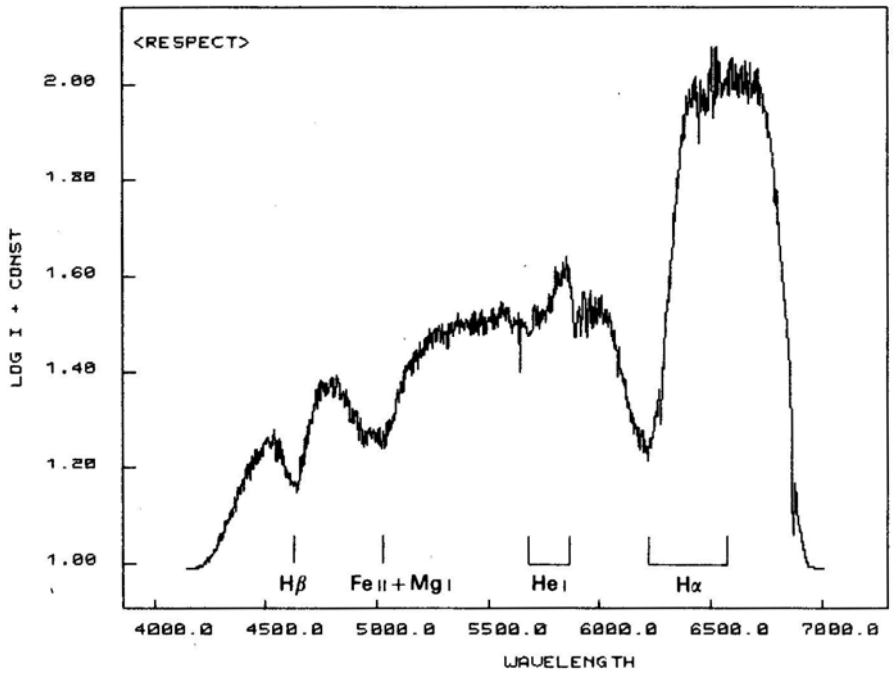

Figure 1. The spectrum of SN 1987a recorded on 1987 February 26.63 at 110 Å mm^{-1} The sharp feature at λ5650 is a plate flaw. The correction for instrumental response has not been applied.

nent reaches the continuum only at – 25500 km s^{-1}. The continuum is fairly strong. We attribute the P-Cygni feature at λ5900 to He I λ5876 instead of Na I D since the latter is not expected to be seen so early in the evolution of the supernova. The absorption velocity of this line is at – 9400 km s^{-1}, considerably smaller in magnitude than the value for Hα. The emission component is severely distorted by interstellar Na I D, and atmospheric absorption lines. He I λ6678 is possibly blended with Hα. Other strong lines in the spectrum are Fe II + Mg I blend at λ5176, and Hβ. The blend at λ5176 has an absorption velocity similar to that of He I whereas the corresponding value of Hβ (– 13000 km s^{-1}) lies in between these and Hα.

The first near-infrared spectrum recorded on February 27.62 shows the Ca II triplet at λ8600 prominently. The P-Cygni absorption is, however, blended with atmospheric absorption due to H_2O. The estimated absorption core velocity was –7900 km s^{-1}, similar to He I and λ5176 features. Some of our early spectra are shown in Fig. 2.

3.2 *Evolution of the Spectrum*

The most striking change in the spectrum of SN 1987a during the period of observation is the continuous decrease of the magnitude of absorption velocity. The measured velocities of different lines and blends are listed in Table 1, and are plotted in Fig. 3. The spectrum also moves continuously to lower excitation and lines of Na I and Fe II begin

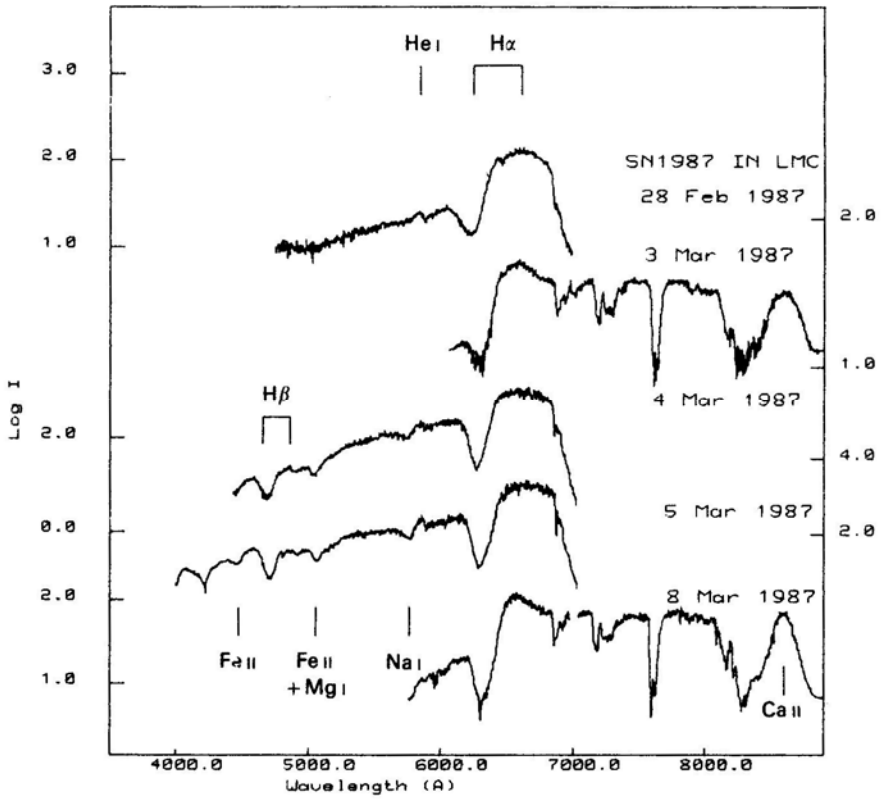

Figure 2. Early spectra of SN 1987a, not corrected for instrumental response. The scale marks alternate between left and right.

to appear and strengthen. We discuss in the following these changes in lines of individual species.

3.2.1 *The Balmer Lines*

The profiles of Balmer lines show flat-bottomed P-Cygni absorption until about March 8 indicating high optical depths. Initially the amount of absorption was roughly equal to emission. With time the absorption component narrowed down and the emission increased relative to absorption. The profile of March 3 compared to that of March 8 in Fig. 4 exemplifies these changes. The peak of the emission component was initially shifted to shorter wavelengths compared to the rest wavelength. With time the emission peak moved toward the rest wavelength.

One can make crude estimates of the radius of the Hα-scattering envelope from the ratios of radial velocities of blue and red extremities of the profile (Kuan & Kuhi 1975). The derived extent is about 1.2 photospheric radii on March 3 and 1.3 on March 8.

The evolution of Hα absorption cannot be traced beyond March 22 due to the increasing strength of P-Cygni profile of Fe II λ6456. A dramatic change in the emission

Table 1. Radical velocities (km s^{-1}) of blueshifted absroption features.

Date 1987	4100 Hδ	4340 Hγ	"4568" Fe II	4861 Hβ	4924 Fe II	5018 Fe II	"5176"	5325.56 Fe II	5535 Fe II	"5675"	5876 He I	5892 Na I	"6135" Fe II	"6263" Fe II	6456 Fe II	6563 Hα
February 26				13000			8600				9400					16400
February 28											7400					14800
March 2			7700	11000		8100	8200					7300				13800
March 3																
March 4			8400	11000		6900	8100		8300			7800				13400
March 5	7800	9000	7400	9800	7400	6500	6600	6200		7500		6600				12300
March 6			7700	9700	6500	6600	6700		6900			6500	5900			12200
March 8		7100	6800	8000	5300	5400	5400	5600	5300	5300		5500	5300	5200		10400
March 9					5400			4300	4800	5400		5500	5100			10300
March 13					4900	4400	4700	4300	4400	4500		4500	4400	4400		9300
March 14									4200	4200		4700	3800			8800
March 15									3700	4100		4700	3700	3900		8300
March 16					3300	3800	3300	3900	3900	4000		4400	3700	3400		8300
March 19					4300	3400	3300	3500	3600	3700		4100	3400	3400		8000
March 22									2700	2800		4200	3200	3100	2800	7700
March 23						3400	4000		3600	3600		4000	3500	3500	3000	
March 25					3200	3000	2900	2200	3200	3300		3700	3600	3200	2800	
March 26						3000	3200	2700	3000	3200		3600		3300	2700	
March 27							3000	2600	3100	3100		4100	3200	2800	2600	
March 29									3200	3100		4200	3400	2400	2500	
March 30										3100		3900	3400	2900	2400	

Velocities are corrected for the radial velocity of LMC. Typical errors are 200 km s^{-1}.

The quotation marks denote the wavelengths of blends: Fe II "4568": 4584, 4549, 4556, 4629; "5176": 5169 of Fe II + 5183 of Mg I, "5675": Sc II (29); "6135": 6149, 6147 of Fe II, 6122 of Ca I (3) blending with Ca I seems to occur from 15 March onwards; "6263": 6248, of Fe II (74), 6280 of Sc II (28).

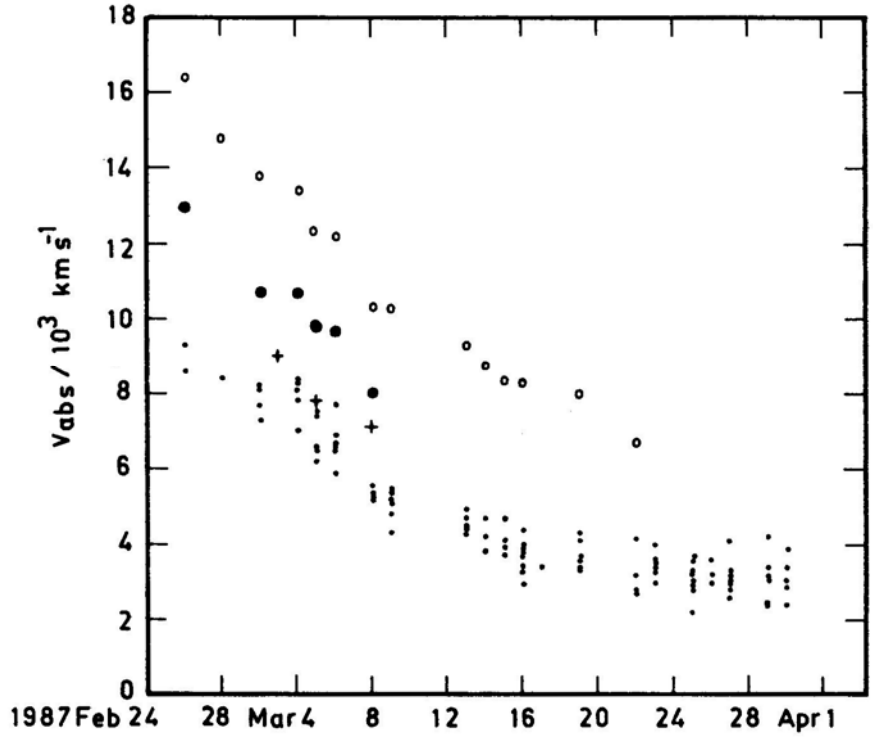

Figure 3. Absorption core velocities as a function of time. Hα: open circles; H*β*: filled circles; H*γ* and H*δ*: crosses: all other lines: dots.

profile, however, was evident on March 30. The profile had changed into a double-peaked one with the central absorption at *λ*6563 (Fig. 5): The two emission-peaks had a separation of 1400 km s^{-1} whereas the width at the base of the emission was 3150 km s^{-1}. The shape of the profile was similar to that in Be stars and novae. Particularly it is reminiscent of nova DQ Her during 1935 January-March (*of.* Fig. 9 of Beer 1973), though the peak-to-peak separation is much larger. The double-peaked Hα emission in DQ Her has been interpreted to be arising in the expanding, recombining shell between the star and the outer scattering shell (Rottenberg 1952).

There was another emission peak present at *λ*6690 since about March 22. This emission was varying in relative intensity with respect to the emission at *λλ*6538–6539. For example, on the photoelectric spectrum scan obtained on March 31 (Fig. 6) *λ*6690 appears brighter than Hα. It is tempting to ascribe this peak to He I *λ*6678. We will return to this feature again while discussing lines due to He I.

The emission due to H*β* was generally weak, though detectable on March 2.62 and 4.62. The absorption cores of Hα, H*β* and H*γ* showed velocities progressively smaller in magnitude (see Table 1).

3.2.2 *Lines due to He I*

He I *λ*5876 was conspicuous during the early evolution of the spectrum until the Na I D *λ*5892 began to dominate over it (March 2). The absorption trough of He I was

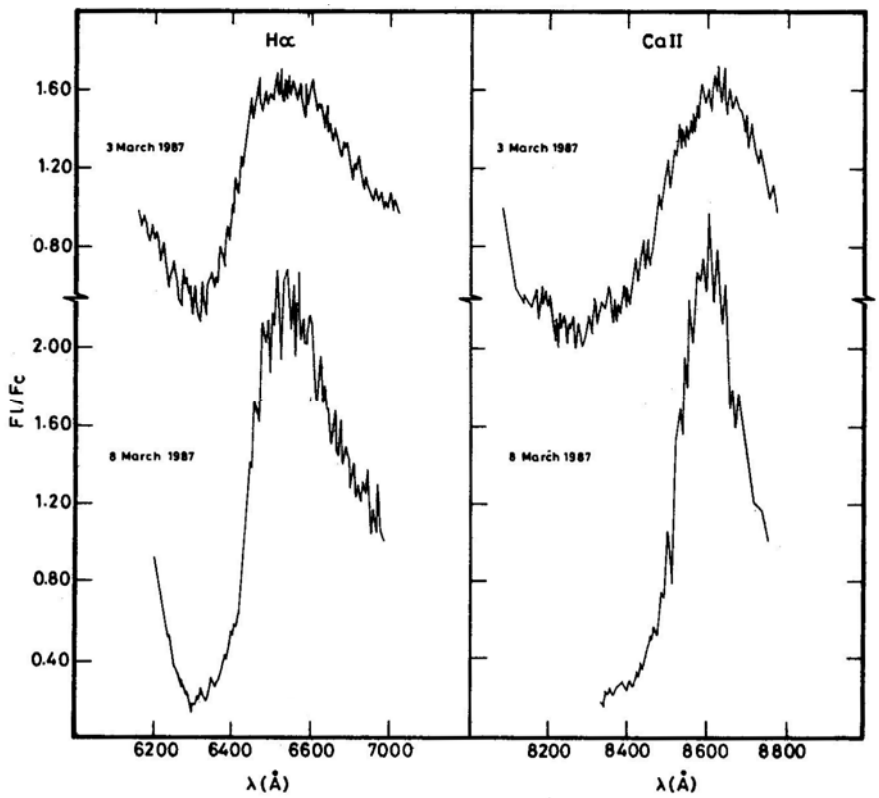

Figure 4. The change in the profiles of Hα and Ca II λ8600, reduced to an estimated continuum, on 1987 March 3 and 8.

shallower, and narrower compared to Hß. This is as expected since the optical depth of Hβ is larger than He I λ5876 at any given point in the atmosphere. The possible identification of He I λ6678 on March 30 raises the question whether the He I lines due to inner recombining shell become visible at the later phase. The other triplet transitions at λ5876 and λ7065 are, however, not very conspicuous. A sharp peak was present at λ5873 in the spectra of both March 29 and 30, superposed over the Na I D line. Some emission was evident around λ7065 on March 27 and 29. The unsmoothed data showed that the λ6678 peak was also double, but with a separation of 750–900 km s^{-1}. If the identification is right, it would imply that the velocity in the linear shell increases with radius as in the shells of novae.

3.2.3 *Lines due to Na I*

Na I D λ5893 dominated over He I λ5875 on March 2.62 and got stronger with time. Its absorption began to get flat-bottomed by March 8. An absorption feature at λ8004 possibly due to Na I $\lambda\lambda$8183, 8194 appeared on March 5 and began its redward migration. It was visible until it merged with the atmospheric absorption due to H_2O. N I (2) λ8212 may also contribute in this region.

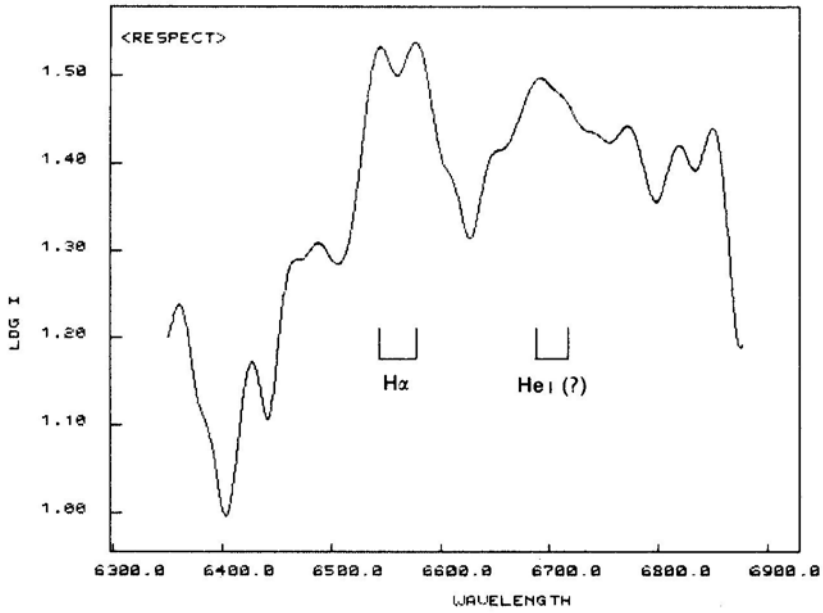

Figure 5. The region around Hα on 1987 March 30. The data has been smoothed considerably.

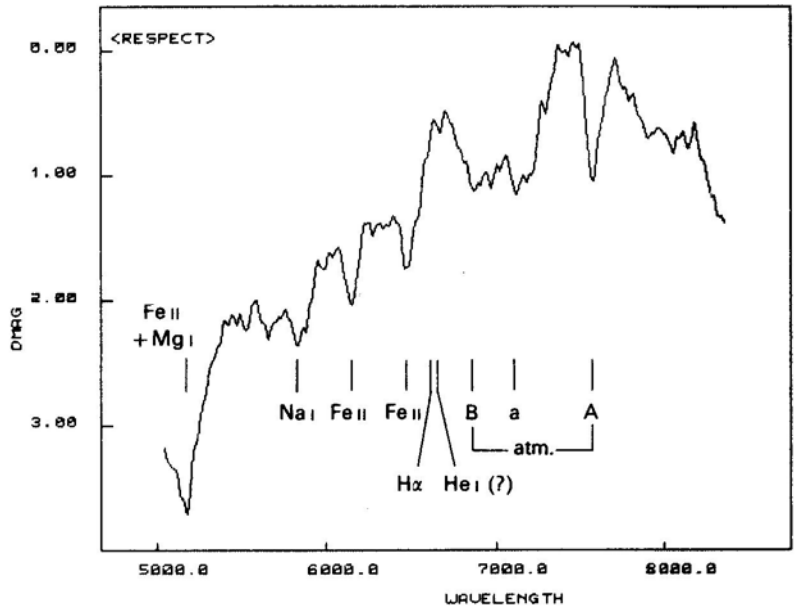

Figure 6. A photoelectric spectrum scan of SN 1987a obtained on 1987 March 31 in the range $\lambda\lambda$4800–8200 with a bandpass of 50 Å. Notice the double-peaked structure near Hα. The left peak is near λ6563, whereas the right one is near λ6678. Both the peaks are further split at higher resolutions.

When Na I D is strong we expect the lines of Mg I and K I also. Mg I λ5176 was blended with Fe II all through. The absorption due to K I $\lambda\lambda$7665, 7699 was probably blended with the blue edge of the atmospheric 'A' band. A measurable dip appeared on March 30 at λ7575 which yields absorption velocities consistent with Na I D line if ascribed to K I λ7665.

3.2.4 *Lines due to Fe II and Sc II*

The earliest Fe II lines to appear were the multiplets 38 and 42 (March 2). An absorption feature at λ5421 appeared on March 4 due to Fe II λ5535. The absorption at λ6032 seen on March 6 is due to Fe II (74) λ6148, 6149. The presence of Fe II (73) $\lambda\lambda$7449, 7462, 7515 was evident on March 8 through its absorption at λ7345 close to atmospheric 'a' band, and excess emission at 7459. There may be some contribution due to N I (3) λ7452 also here.

An absorption feature at λ7393 seen on March 22 is probably due to Fe II (73) λ7475. It implies a velocity of – 3568 km s^{-1}, consistent with other Fe II lines.

An emission feature appeared dramatically at λ6461 around March 16.62, on the red side of the P-Cygni absorption of Hα and close to the expected emission peak of the strong emission line Fe II (74) λ6456. Its P-Cygni absorption component was distinct on March 19 and became flat-bottomed by March 22. The presence of this feature made it impossible to measure the absorption velocity of Hα any longer. All lines of Fe II strengthened with time.

Sc II has been identified by Patchett & Branch (1972) in SN 1959 in NGC 7331. We identify the absorption feature at $\lambda\lambda$5517–5513 seen first on March 4 with Sc II (29) λ5606. It became saturated by March 16.

3.2.5 *Lines due to Cα I and Ca II*

The infrared triplet of Ca II $\lambda\lambda$8498, 8542, 8662 was strong since the very beginning. Its P-Cygni absorption is affected by atmospheric H_2O bands, but it was possible to estimate its velocity as – 7900 km s^{-1} on March 3.62 and – 7700 km s^{-1} on March 5.62. The emission initially narrowed down (see Fig. 4), but later broadened again and began to show some structure by March 16. There were two emission peaks at λ8647 and λ8693. The peaks shifted to λ8666 and λ8716 on March 27.

The relative intensities of the three lines of Ca II is expected to be 1:9:5 in an optically thin case, *i.e.* a centroid wavelength of λ8579. The strong emission at wavelengths much larger than this suggests that there are other contributors to this blend. We suggest in the following subsection that N I is the principal contributor.

According to Kirshner *et al.* (1973) most of the calcium in SN envelopes is expected to be in the form of Ca II. However, one out of 10^4 atoms would still be neutral and thus show their presence particularly when Na I D line is strong and saturated. The likely lines are Ca I (1) λ4226 and Ca I (3) $\lambda\lambda$6127, 6166. Based on the absorption velocities we infer that the latter contributes to Fe II (74) λ6148.

3.2.6 *The Lines of C, N and O*

We have looked for the presence of C I and C II lines in the spectrum of SN 1987a, but could not identify positively even the strongest features expected.

The emission on the red wing of Ca II λ8600 is most likely N I (1) $\lambda\lambda$8680–8747 of which λ8680 is the strongest line. Fe I (60) $\lambda\lambda$8662, 8768 may contribute in this region at later stages; however, their presence is not very likely at the stage observed, since most of iron is in Fe II, and since other lines of the multiplet at $\lambda\lambda$8327, 8387 do not appear to be present. Further, the centroid of the emission was at λ8680 on March 30 suggesting that Ca II had faded considerably by then and the emission was largely due to N I λ8680 (see Fig. 7). The presence of these high-excitation lines in such a strength suggests that N I is overabundant, and hence that the material had undergone CNO-processing before ejection.

The emission due to O I λ7774 was visible on March 8, and was quite prominent on March 16 and 26. The blue-shifted absorption was clearly seen on March 26 at -2306 km s^{-1}.

4. The evolution of the photosphere

If SN 1987a were to exhibit a photometric behaviour typical of Type I or Type II Supernovae, one would have expected it to brighten to at least magnitude 1 at the distance of LMC. Though it brightened very rapidly on February 24, it lingered around $V = 4.5$ and then began to brighten slowly to $V = 4.0$ on March 24.

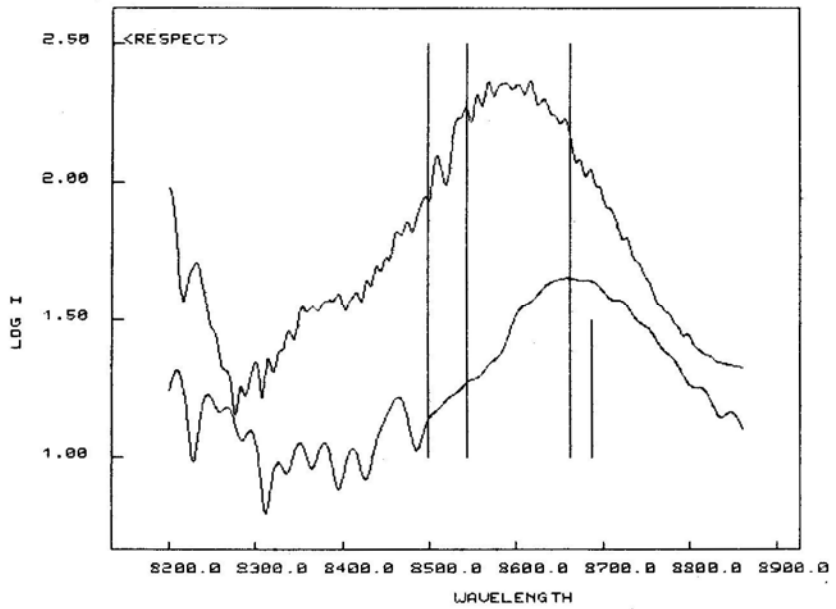

Figure 7. The region around Ca II λ86OO and N I λ8680 on 1987 March 8 (top) and March 30 (bottom). The longer vertical bars are at Ca II λ8498, 8542, 8662, whereas the shorter one is at N I λ8680.

We reproduce in Fig. 8 the *V* and *B* light curves and *U – B, B – V, V – R, V – I* colour curves for the period 1987 February 24–1987 March 25, based on the data published in IAU circulars. Also included is one estimate of *V* from VBO on March 6 (K. E. Rangarajan & K. Jayakumar 1987, personal communication) and a set of *V* magnitudes due to van Vuuren between March 15–21 (M. Feast 1987, personal communication). It is interesting to note that the *B* light curve follows the typical trend and reaches a plateau, but shows signs of further increase in brightness. The plateau is at a magnitude of 5.7, about 1.1 mag below the maximum of February 24. The colour gets redder at a high rate, the change between February 24 and March 24 being from – 0.8 to +2.2 in *U – B*, from 0.0 to 1.6 in *B – V*, from 0.25 to 0.7 in *V – R*, and from 0.35

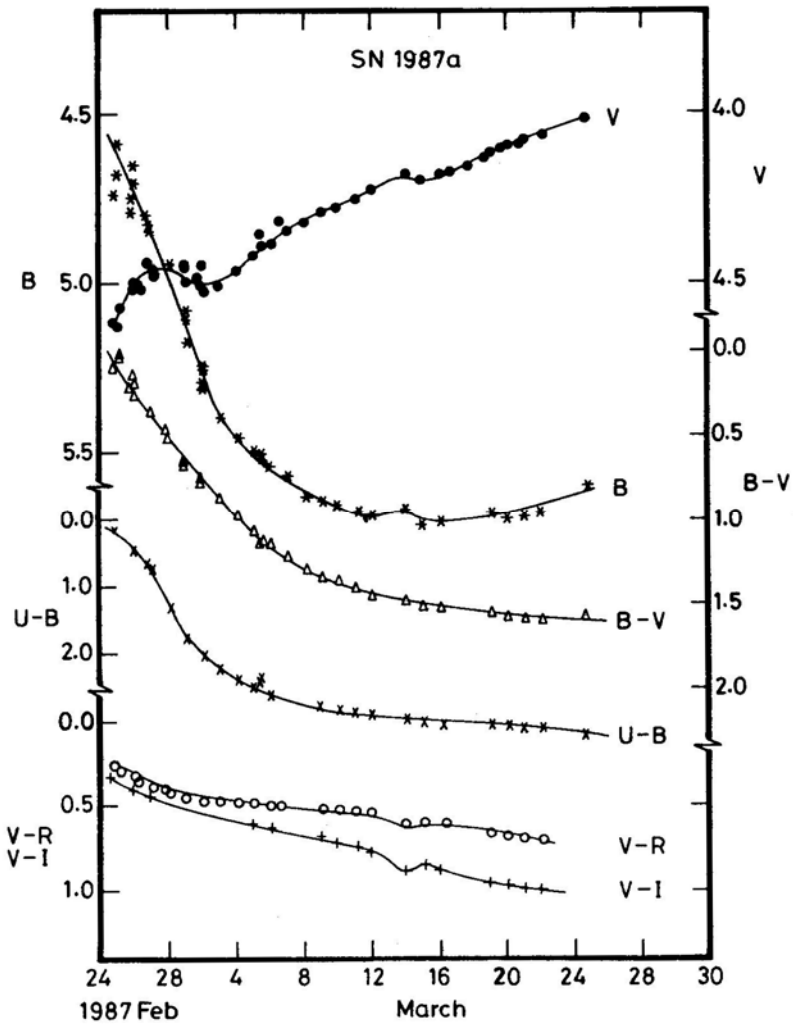

Figure 8. The *B, V* light curves, and *B – V, U – B, V – R, R – I* colour curves of SN 1987a based on the data compiled from various sources. The *R* and *I* bands are on the Cousins system.

to 1.0 in $V - I$ The light curve was hence rising in R and I bands as well, though dropped sharply in U and B before reaching a plateau at $U = 7.7$, $B = 5.7$.

Though this photometric behaviour is so atypical that it is difficult to predict its future course, it is instructive to compare it with the Type II supernova SN 1973r in NGC 3627, sometimes termed subluminous. SN 1973r reached a maximum at $V \simeq 14.2$ and $B \simeq 15.0$ on 1973 December 19. About a month later, the plateau was reached at $V \simeq 14.6$ and $B \simeq 6.5$ (Ciatti & Rosino 1977). Assuming a value of $E(B–V) = + 0.6$, the maximum and plateau correspond to $V_0 = 12.2$, $B_0 = 12.4$, and $V_0 = 12.6$, $B_0 = 13.9$ respectively. The change in $(B - V)_0$ ranges from 0.2 at maximum to 1.3 at plateau.

The distance modulus to NGC 3627 is 29.83 according to de Vaucouleurs (1979). Assuming a distance modulus of 18.5 for LMC, the magnitudes of SN 1973r translated to the distance of LMC would be $V_0 = 0.9$, $B_0 = 1.1$ at maximum, and $V_0 = 1.3$, $B_0 = 2.5$ at the plateau. Clearly, these values are much brighter than the range of magnitudes displayed by SN 1987a so far. On the other hand, the steep colour curve of SN 1987a resembles, to a great degree, that of SN 1973r.

The broad-band colours of SN 1987a can be compared with supergiants, and the effective temperatures determined. The V magnitudes and effective temperatures can be used to estimate the angular radii of the photosphere at different times. The known distance to LMC helps in converting the angular sizes to linear sizes. We have estimated photospheric temperatures by comparison with the colours and temperatures of supergiants as tabulated by Johnson (1967). The $(B - V)_0$ colours were used when $(B - V)_0 \lesssim 0.5$ and the $(V—R)_0$ colours were used above this value. The observed colours were corrected for interstellar extinction estimated as $E(B - V) = 0.17$ and $E(V - R) = 0.15$ using the photometric data on Sk – 69° 202.

The angular radii (θ) were determined using the calibration of Barnes, Evans & Parsons (1976):

$$\log \theta(\text{mas}) = 0.1864 - 0.2 V_0 + 0.855 (V - R)_0$$

The ratio $R = A_v / E(B — V) = 3.2$ was assumed to correct for interstellar extinction. The derived values of photospheric temperatures and radii are listed in Table 2 and plotted in Fig. 9. The radius increases from 4100 $R_\odot$ on February 24 to 17200 $R_\odot$ on March 22, while the temperature decreases from 10500 K to 4500 K. The kink on February 14 results from the hump in the V light curve and dip in $V - R$ colour curve on that day, which is based on a single observation, and hence may need confirmation (see, however, Section 5).

5. Discussion

We have assumed in the calculations of photospheric parameters that the supernova radiates like a supergiant. We believe that this is a better approximation than a blackbody. The available *UBVRI* data suggest that blackbody approximation held good during the early phases, except that the U magnitudes were fainter than predicted by blackbody because of blanketing effects. Also, the derived blackbody temperatures are somewhat higher than the supergiant temperatures in Table 2. As time progresses, it becomes more difficult to fit a blackbody spectrum, the B magnitudes also falling short of blackbody and the R and I bands showing an excess. The supergiant spectra, however, match the *UBVRI* data better all through.

Table 2. Photospheric temperatures and radii.

	Date 1987	V_0	$(B-V)_0$	$(V-R)_0$	Ref.	T_{eff} K	θ mas	$R/R_\odot$
February	24.8	4.09	−0.06	0.25	1	10500*	0.38	4100
	25.9	3.98	+0.06	0.31	1	8600*	0.45	4900
	26.8	3.90	0.19	0.35	1	7500*	0.51	5500
	27.1	3.92	0.21	0.42	2	7400*	0.58	6300
	28.1	3.93	0.22	0.48	2	7300*	0.65	7000
March	1.1	3.94	0.49	0.50	2	6400*	0.67	7300
	2.1	3.96	0.51	0.53	2	6300*	0.71	7600
	3.1	3.97		0.52	2	5800	0.69	7400
	4.1	3.93		0.53	2	5700	0.72	7700
	5.1	3.88		0.54	3	5700	0.75	8100
	6.1	3.84		0.55	3	5600	0.78	8400
	9.1	3.76		0.59	3	5500	0.87	9400
	10.1	3.74		0.60	3	5400	0.90	9700
	11.1	3.72		0.63	3	5300	0.96	10400
	12.1	3.69		0.63	4	5300	0.97	10500
	14.1	3.64		0.74	4	4900	1.24	13400
	15.1	3.66		0.70	4	5100	1.13	12300
	16.1	3.64		0.72	4	5000	1.19	12900
	19.1	3.58		0.79	4	4700	1.41	15200
	20.1	3.56		0.80	4	4700	1.45	15600
	21.1	3.54		0.83	4	4600	1.55	16700
	22.1	3.53		0.84	4	4500	1.59	17200

* Derived using $(B-V)_0$ colour.

References to the photometric data: 1. IAU Circular No. 4352; 2. IAU Circular No. 4332; 3. IAU Circular No. 4341; 4. IAU Circular No. 4352.

Extinction corrections applied: $E(B-V)=0.17$, $E(V-R)=0.15$, $A_V = 0.54$.

$(V-R)$ was transformed from Cousins system to Johnson system using transformations of Taylor (1987).

Inclusion of infrared data helps fitting blackbody curves (*of.* Bouchet *et al* 1987) better. However, the increase in bolometric luminosity may not be as fast as predicted by the blackbody fits. The energy integrated over *UBVRI* bands was 3.1×10^{-10}, 3.1×10^{-10} and 6.2×10^{-10} Wm^{-2} on February 24, March 11 and March 22 respectively. These variations are much smaller in magnitude compared to the variations in total luminosity derived by Bouchet *et al.* between March 1–11 using blackbody fits. Actually, during the latter period, there is a slight fall in the total *UBVRI* flux because of decreasing light in *U* and *B.*

The values of radius and temperature derived in Table 2 are based on *V* light and $V-R$ colour, and would represent the region of wavelengths where the bulk of the energy is radiated. The derived photospheric radii yield a photospheric velocity of 4200 km s^{-1} between February 24 and March 22, consistent with the observed absorption velocities of lines other than hydrogen.

The development of the spectrum of SN 1987a is consistent with the changes in colour and temperature derived from photometry: The continuum energy distribution generally gets redder with time. The evolution in radius and temperature is not smooth; there are kinks around March 3 and March 14. In the latter case, the radius increased faster than usual whereas the temperature decreased. This coincides with a slight enhancement of lines due to neutral metals like Ca I, and the emergence of Fe II λ6456.

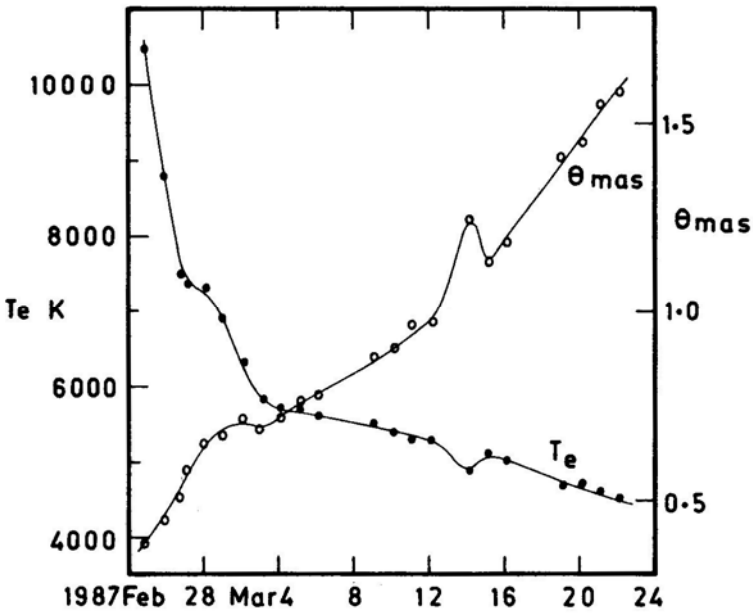

Figure 9. The variation of temperature and angular radius of the photosphere of SN 1987a as a function of time.

The radial velocities of the Na I D feature seem to show a higher value around this time. Such a behaviour is not obvious in the case of Fe II lines.

The radial velocities of the blueshifted absorptions show a redward movement and reach a plateau around March 22 in the case of most of the Fe II lines and possibly also in the case of Na I. The radial velocity of the Hα absorption core starts with a larger magnitude and decreases analogously. It is difficult to estimate its value after March 19 because of the emergence of Fe II λ6456. If the dip seen at λ6487 on March 25 is attributed to the absorption of Hα, the implied velocity is –2673 km s^{-1} which is about the value shown by the Fe II lines. The variation of absorption velocities is consistent with the picture of an expanding, scattering envelope with velocity increasing with distance above the photosphere and the optical depth reducing with time.

Although the *V* light as well as the bolometric luminosity are increasing, the spectrum is getting later and later. Many lines of Fe II and Na I show flat-bottomed absorption indicative of high optical depths in the lines.The similarity with SN II 1973r in NGC 3627 (Ciatti & Rosino 1977) mentioned in Section 4 appears to extend to the spectroscopic evolution too; however, the process is more rapid in SN 1987a and the Fe II lines are much stronger than seen in SN 1973r.

A comparison can be made of SN 1987a with Type II SN 1979c in M100 at a stage when the metallic lines were well developed, and when the photospheric temperatures are roughly the same, i.e., roughly a month after the light maximum of SN 1979c (1979 May 28). Though our spectra of SN 1987a were obtained before the maximum in *V* light, the similarity of the spectra suggests that the physical conditions in the atmosphere of SN 1987a had already reached by March 8 the conditions in SN 1979c

on May 28. The spectrum of 1979c was also matched by Branch *et al.* (1981) with a synthetic spectrum computed by assuming solar abundances and that the lines are formed in a scattering, spherically symmetric, expanding atmosphere with a photosphere that emits like a blackbody. According to Branch *et al.*, the spectrum of SN 1979c was characterized by $T_* \simeq 6000$ *K* and $V_{\exp} \simeq 8000$ km s^{-1} on May 26. In the case of SN 1987a, the Hα velocity is 8000 km s^{-1} and $T_* \simeq 5600$ K around 1987 March 8 and 9. A closer look at the spectra shows that the Fe II and Na I lines were much stronger in SN 1987a than both observed and synthesized ones in SN 1979c, indicating higher optical depths in these lines of SN 1987a. Branch *et al.* estimate the mass of the scattering envelope of SN 1979c as $\simeq 0.58\ M_\odot$. In order to produce higher optical depths in the case of SN 1987a one would require $\gtrsim 0.58\ M_\odot$ of envelope mass, provided the abundances are the same in both the Supernovae (relative to H). It is possible to reduce this limit slightly if the metal abundance is lower in SN 1987a. In such an event, the electron density reduces and consequently so does the continuum opacity. As a result, the contrast between the lines and the continuum will also increase resulting in stronger lines. A more quantitative study is needed to estimate the envelope mass accurately.

Acknowledgements

We would like to express our thanks to many people for their encouragement. Particular thanks are due to Prof. J. C. Bhattacharyya, and several colleagues for generous donation of the 40-inch telescope time for this programme. We thank Dr Sushma Mallik for obtaining some of the spectra and Mr A. Jairaj for digitizing the spectrograms with the PDS microdensitometer. The digital reductions were carried out using the VAX 11/780 systems at VBO, Kavalur, and Raman Research Insitute, Bangalore.

References

Barnes, T. G., Evans, D, S., Parsons, S. B. 1976, *Mon. Not. R. astr. Soc*, **174,** 503.
Beer, A.1973, *Vistas Astr.*, **16**, 179.
Branch, D., Falk, S.W., McCall, M. L, Rybski, P., Uomoto, A. K., Willis, B. J.,1981, *Astrophys. J.*, **244,** 780.
Branch, D., Lacy, C. H., McCall, M. L, Sutherland, P.G., Uomoto, A., Wheeler, J. C, Willis, B. J. 1983, *Astrophys. J.*, **270,** 123.
Bouchet, P., Stanga, R., Le Bertre, T., Epchtein, N., Hamann, W. R., Lorenzetti, D. 1987, *ESO Scientific Preprint* No. 500.
Ciatti, F., Rosino, L. 1977, *Astr. Astrophys.*, **56,** 59.
de Vaucouleurs, G. 1979, *Astrophys. J.*, **277,** 729.
Johnson, H. L.1967, *A. Rev. Astr. Astrophys.*, **4**, 193.
Kuan, P., Kuhi, L. V, 1975, *Astrophys.* J, **199,** 148.
Kirshner, R. P., Oke, J. B., Penston, M. V., Searle, L. 1973, *Astrophys. J.*, **185,** 303.
Patchett, B., Branch, D. 1972, *Mon. Not. R. astr. Soc*, **158,** 375.
Prabhu, T. P., Anupama, G. C, Giridhar, S. 1987, *Bull astr. Soc. India*, (submitted).
Rottenberg, J. A. 1952, *Mon. Not. R. astr. Soc*, **112,** 125.
Taylor, B. J. 1986, *Astrophys. J. Suppl. Ser.*, **60,** 577.

J. Astrophys. Astr. (1987) **8,** 211–217

Dark Spots, Bubbles, and Shells in the Lobes of Extragalactic Radio Sources

Wolfgang Kundt *Institut für Astrophysik der Universität, Auf dem Hügel 71, D-5300 Bonn 1, FRG*

Lakshmi Saripalli *Joint Astronomy Programme, Department of Physics, Indian Institute of Science, Bangalore 560012* and *Radio Astronomy Centre, Tata Institute of Fundamental Research, PO Box 1234, Bangalore 560012*

Received 1986 November 22; accepted 1987 April 3

Abstract. Based on maps of the extragalactic radio sources Cyg A, Her A, Cen A, 3C 277.3 and others, arguments are given that the twin-jets from the respective active galactic nucleus ram their channels repeatedly through thin, massive shells. The jets are thereby temporarily choked and blow radio bubbles. Warm shell matter in the cocoon shows up radio-dark through electron-scattering.

Key words: jets—lobes—shells around galaxies—Cyg A—Her A—radio bubbles

1. Introduction

Maps of extragalactic radio sources with high dynamic range and, radio-optical overlay maps have shown considerable fine structure of the lobes (radio, Cyg A: Perley, Dreher & Cowan 1984; Dreher *et al.* 1984; Her A: Dreher & Feigelson 1984; 3C310: van Breugel & Fomalont 1984; 3C 382: Strom, Willis & Wilson 1978; 3C219: Perley *et al.* 1980; 3C433: van Breugel *et al.* 1983; optical, 3C 277.3: van Breugel *et al.* 1985b; NGC 541: van Breugel *et al.* 1985a; NGC 7385: Simkin, Bicknell & Bosma 1984; Fornax A: Schweizer 1980, Ekers *et al.* 1983;3C293: van Breugel *et al.* 1984).There are clear to likely indications that the radio hotspots are associated with optical continuum radiation (Cyg A: Kronberg, van den Bergh & Button 1977; 3C 33 S: Rudnick *et al.* 1981; Meisenheimer & Röser 1986; 3C273: Röser & Meisenheimer 1986; further: Crane, Tyson & Saslaw 1983).

The radio fine structure of Cyg A shows two (narrow)jets in emission, cylindrical and loop-like emission 'filaments', and two hotspots in each lobe (*cf.* Figs 1a, b). It also shows 'dark spots' associated with the hotspots, and perhaps dark lanes at right angles to the jets (Fig. 1c). We shall interpret these radio-dark features as due to electron-scattering by filamentary matter whose mass amounts to at least $10^{10}M_{\odot}$. The filamentary matter is thought to traverse the halo in the form of thin, heavy partial shells, as evidenced by the mentioned radio-dark lanes in the case of Cyg A, by optical emission in the case of Cen A (Malin, Quinn & Graham 1983) and by radio depolarization in the case of 3C 277.3 (van Breugel *et al.* 1985b). These partial shells appear to be rather common (Malin & Carter 1983; Quinn 1984; Schweizer 1986). In

the case of Cen A, Gopal-Krishna & Saripalli (1984) have presented overlay evidence that the shells interact with the jets. Kundt & Krause (1985) have argued that the shells consist of filamentary matter ejected supersonically by the galactic nucleus during active epochs—which matter is continually reionised by ram-pressure heating and/or background UV.

These thin, massive partial shells in the haloes of galaxies can make their appearance directly, as quasi-circular radio or optical lanes. Indirectly they are indicated by the large mass needed to give rise to the radio-dark spots of Cyg A, and also by the radio 'bubbles' seen in Her A, 3C 310, 3C 277.3,3C 219 and others. Such bubbles are thought to be the results of 'jet-choking' (van Breugel & Fomalont 1984): A thin layer of heavy material temporarily reduces the advance speed of the beam's head considerably, in proportion to $\rho^{-1/2}$. As a result of such temporary choking, or stalling, the beam head does not advance at a constant speed but rather at two very different speeds, like a drill eating its way through a sandwich door (at constant thrust). During shell crossing, a huge amount of beam plasma is dumped in a short beam segment. Its explosive expansion sweeps thermal plasma and magnetic fields out in the shape of a strongly magnetised quasi-spherical layer: a radio bubble. These bubbles are reminiscent of a glass-blower's craft. They are observed to have circumferential magnetic fields, in accordance with the suggested explanation (*e.g.* Dreher & Feigelson 1984; van Breugel & Fomalont 1984). We believe that many observed lobe morphologies can be understood as the result of a steady beam ramming its channel through a strongly inhomogeneous environment.

Another environmental effect, not elaborated in this communication, is channel destruction by shear motion of the IGM, in particular at the edge of a galactic halo.

2. The radio-dark spots of Cyg A

In Fig. 1c we have drawn what we consider dark spots, and dark lanes, in the lobes of Cyg A. Most remarkable is the dark spot in front of radio hotspot B, in the north-preceding component (*cf.* Alexander, Brown & Scott 1984). It has less than 10 per cent of the peak brightness of the adjacent hotspot B, most clearly obtained from an intensity cut (personal communication by John Dreher; see also Fig. 2 of Hargrave & Ryle 1976). It is hugging hotspot B. It may or may not coincide with an optical source of *J*-magnitude 22 (Kronberg, van den Bergh & Button 1977, in particular the erratum; also *R* band CCD image of P. Hiltner 1986, personal communication).

It is highly unlikely that the synchrotron-emitting lobes have cylindrical holes aligned with the line-of-sight and correlated with the hotspots. We interpret the radio-dark spots as (front-side) pockets, or cushions, of warm matter scattering the radio photons out of the line-of-sight. As we shall see, the alternative possibility of free-free absorption would imply intolerably high optical emission.

A scattering screen of optical depth τ reduces the intensity by the factor $e^{-\tau}$. For the dark spot hugging B we need $\tau \gtrsim 1$, hence

$$1 \lesssim \tau_{sc} = \sigma_T \int n_e \, ds = (\int n_e \, ds)_{24.2} \qquad (1)$$

where σ_T=Thomson cross-section and n_e=electron number density. This estimate envisages the dark spot as a combined effect of scattering plus absence of emission, *i.e.,*

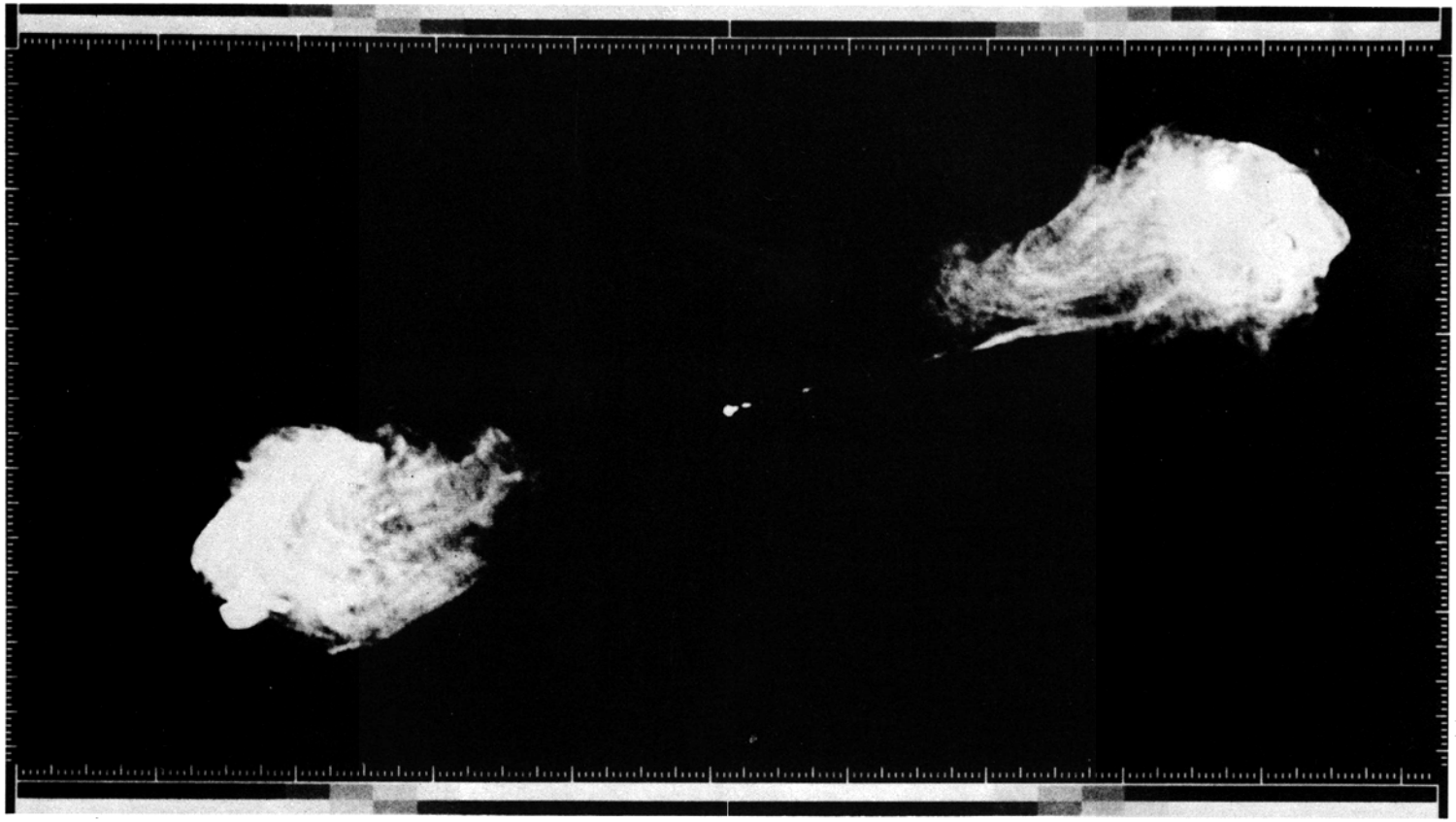

Figure 1a. Radio photograph of Cyg A at 5 GHz, courtesy of John Dreher.

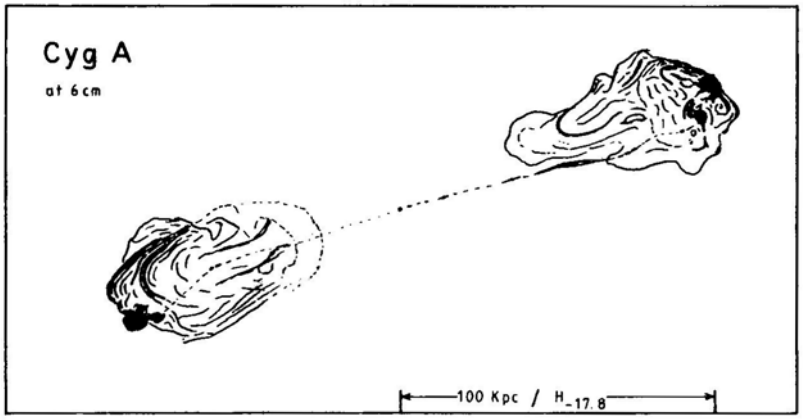

Figure 1b. Our interpretation of the bright emission features in Fig. 1a (as a negative)

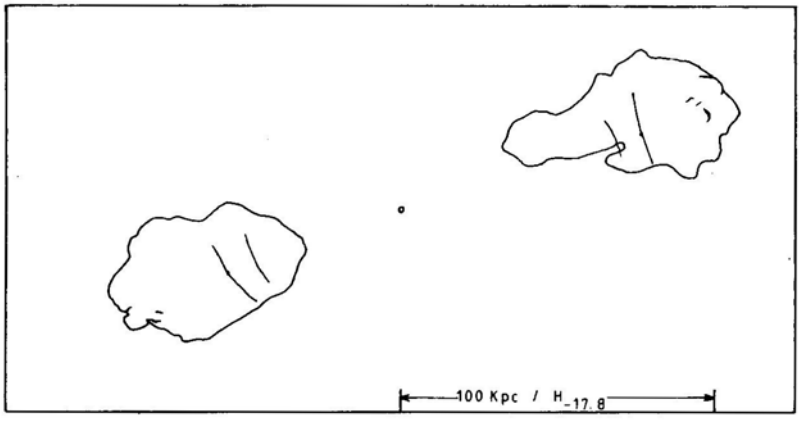

Figure lc. Our interpretation of the (dark) scattering features in Fig. 1a (as a positive). It is not clear whether or not we have overinterpreted the maps in places, but the features show up at different frequencies evaluated both with CLEAN and with maximum entropy algorithm.

absence of relativistic electrons. We approximate the scattering pocket by a cylindrical segment transverse to the beam, of area $A \simeq (3\ \mathrm{kpc}/H_{-17.8})^2$, thickness $d \simeq \sqrt{A}/5$, whence $\int \mathrm{d}s \simeq \sqrt{A}$; ($H$=Hubble constant, $H_{-17.8} := H/50\mathrm{kms}^{-1}\ \mathrm{Mpc}^{-1}$; z(Cyg A) = 0.056). This yields for the average electron density throughout the pocket:

$$\langle n_e \rangle \simeq 10^{2.2}\ \mathrm{cm}^{-3} H_{-17.8}. \tag{2}$$

Here the equality sign need not be trusted: If the pocket is part of an extended shell transverse to the beam, the effective scattering column length $\int \mathrm{d}s$ may be $> \sqrt{A}$, and $\langle n_e \rangle < 10^{2.2}\ \mathrm{cm}^{-3}$ may hold for this longer column. We shall find much lower estimates for $\langle n_e \rangle$ in the next section.

An independent estimate of n_e near hotspot B results from pressure balance with the nonthermal source. From $B^2/8\pi = 2 n_e\, kT$ and $B_{\mathrm{eq}} = 2.2 \times 10^{-4}$ G (Alexander, Brown & Scott 1984) we get

$$n_e \simeq B^2/16\pi kT \lesssim 10^3\ \mathrm{cm}^{-3}/T_4 \tag{3}$$

so that an electron density of $n_e = 10^{2.5}\ \mathrm{cm}^{-3}$ would imply a temperature $T \lesssim 3 \times 10^4$ K of the scattering medium.

An uncertainty in this latter estimate comes from the fact that we do not know the volume filling factor/of the scattering 'pocket'. But the total mass ΔM of the scattering region is determined by the dispersion measure $\int n_e\, \mathrm{d}s$ (*cf.* Equation 1):

$$\Delta M = f m_p n_e A d = m_p \int n_e \mathrm{d}s \sqrt{A}\, \mathrm{d} \simeq 10^{43.7}\,\mathrm{g} \lesssim 10^{10} M_\odot, \tag{4}$$

a mass which is much larger than naively expected near the hotspot. The true thickness d of the layer with $n_e \simeq 10^{2.5}\ \mathrm{cm}^{-3}$ is probably $\ll \sqrt{A}$ Emission shells around isolated elliptical galaxies have estimated column densities of order $N_e \lesssim 10^{21}\ \mathrm{cm}^{-2}$, corresponding to $d \lesssim$ pc (instead of $\sqrt{A}/5 = 0.6$ kpc) (based on QSO absorption lines, and on Hi emission and absorption haloes: Kundt & Krause 1985).

We are thus forced to assume that the dark spot has a larger extent than mapped and a correspondingly smaller (average) electron density. Note that

$$n_e = \rho_{\mathrm{amb}} v^2/2kT \simeq 10\,\mathrm{cm}^{-3} (n_{\mathrm{amb}})_{-3}/T_4 \tag{5}$$

follows for ram pressure balance of a filamentary shell moving transsonically through a hot medium of (hydrogen) number density $n_{\mathrm{amb}} = 10^{-3}\ \mathrm{cm}^{-3}$. This number is probably a better estimate than Equation 2.

What average mass density ρ do we expect in the distant halo of Cyg A? X-ray observations of poor galaxy clusters suggest asymptotic intergalactic medium (IGM) densities n_{IGM} of order $10^{-5}\ \mathrm{cm}^{-3}$ whereas at the centre of a cluster the density can reach $10^{-2}\ \mathrm{cm}^{-3}$ (Canizares *et al.* 1983). Guilbert & Fabian (1986) even suggest IGM densities $\lesssim 10^{-6}\ \mathrm{cm}^{-3}$, based on the assumption of local temperature equilibrium between electrons and protons. For gravitational heating, one would expect compareable velocities of protons and electrons and thus arrive at somewhat higher estimates of the IGM density (Kundt & Krause 1985). But Cyg A lies in a dense environment whose average electron number density at $r \simeq 10^2$ kpc has been determined from X-ray maps as $n_e = 10^{-2.2}\ \mathrm{cm}^{-3}$ (Arnaud *et al.* 1984). This value is likely an overestimate because it ignores clumping, because it would yield too small an advance velocity of the hotspots (heads) and because Faraday depolarization is low (Hargrave & Ryle 1974). We prefer $n_e \lesssim 10^{-3}\mathrm{cm}^{-3}$.

A lower estimate of the mass ΔM in the pocket in front of hotspot B can be obtained from the assumption that the beam head has swept clean (and condensed) a cylindrical volume comparable in length l to its last straight segment:

$$\Delta M \gtrsim \rho_{\rm amb} A l \simeq 10^{39.5}\, {\rm g}(n_{\rm amb})_{-3} \simeq 10^6\, M_\odot . \tag{6}$$

This estimate falls short of the one in Equation (4) needed to get appreciable scattering; we are forced to postulate the presence of much higher mass densities in the distant halo of Cyg A. We could of course invoke a chance encounter of the beam with some (satellite) dwarf galaxy, but the morphology of the south-following head is very similar, and so is the morphology of 3C219 (Perley *et al.* 1980) and others. The presence of a thin, massive shell is much more plausible, particularly in view of the dark lanes probably observed nearer to the central galaxy (Fig. 1c). The dark lanes are also indicated as linear depolarization features in Fig. 8 of Hargrave & Ryle (1974).

Yet another interpretation of the large mass needed would be to invoke substantial mass entrainment by the jets. De Young (1986) estimates that up to $10^9\ M_\odot$ can be entrained by a strong jet. This estimate is, however, based on a heavier jet material than relativistic pair plasma (Kundt & Gopal-Krishna 1981) and appears implausible in view of the very small observed velocities of the channel walls, of order 300 km s^{-1}, and of the metal-poorness of the material emitting near the radio hotspots(*e.g.* van Breugel *et al.* 1985b).

3. Optical constraints on the radio-dark spots of Cyg A

So far we have interpreted the radio-dark features in Cyg A as due to electron scattering and have estimated the required masses to be larger than $10^{10}\ M_\odot$ An alternative interpretation could invoke free-free (ff) absorption (at frequencies reaching up to ν=10^{10} Hz: *cf.* Lang 1978):

$$\tau_{\rm ff} = (\int n_{\rm e}^2\, {\rm d}s)_{26.8} / T_4^{3/2} \nu_{10}^2 . \tag{7}$$

A required $\tau_{\rm ff} \gtrsim 1$ at $1 \lesssim T_4 \lesssim 3$ would therefore ask for an emission measure $\int n_{\rm e}^2\, {\rm d}s = 10^{27.2 \pm 0.5}$ cm $^{-5}$ or $\langle n_{\rm e}^2 \rangle \gtrsim 10^{5.2}$ cm $^{-6}$ which, at first sight, looks consistent with our estimates in Equations (2, 3) (for unit filling factor f).

But an emission measure of order $10^{27.2}$ cm^{-5} would give rise to thermal free-free radiation of power (*cf.* Lang 1978):

$$L_{\rm ff} = 10^{-25} \int n_{\rm e}^2\, {\rm d}s\, T_4^{1/2} (A/5) {\rm erg\, cm^3\, s^{-1}} \simeq 10^{45.5 \pm 0.5} {\rm erg\, s^{-1}} \tag{8}$$

at temperature $T \gtrsim 10^4$ K, and to free-bound (fb) radiation (in particular Lyman and Balmer jump; *cf.* Lang 1978):

$$L_{\rm fb} \gtrsim 10^2 L_{\rm ff} / T_4 \simeq 10^{47.2 \pm 0.5}\ {\rm erg\, s^{-1}} \tag{9}$$

which are much higher than observed, and much higher than available via the beam. Note that a temperature T largely in excess of 10^4 K would imply an intolerably high emission measure through Equation (7), and would at the same time be unexpected because of the shape of the cooling curve which predicts runaway instability above 10^5 K (Gaetz & Salpeter 1983).

Observationally, Kronberg, van den Bergh & Button (1977) put an upper bound of $J \geqslant 22$ mag on the optical power of the dark spot, corresponding to $M_J \geqslant -13.2$

+ 5 log $H_{-17\,8}$ for an estimated (galactic) A_v= 1.2 mag, or $L_J \lesssim 10^{42\cdot5}$ erg s $^{-1}$. In the case of no identification, this estimate would drop by at least two magnitudes, *i.e.*, below 10^{42} erg s $^{-1}$ in the *J*-band. These upper bounds conflict with our estimate (9) by a factor $\gtrsim 10^3$ whereby allowance has been made for a (high) temperature near 3×10^4 K for which most of the ff-(and fb)-radiation would be emitted at higher than *J*-band frequencies. We conclude that $\langle n_e^2 \rangle \lesssim 10^{2\cdot2}$ cm^{-6} must hold, as in Equation (5) above, *i.e.* that ff-absorption of radio power by the warm cushion near hotspot B is insignificant.

Independently of Kronberg *et al.*'s optical constraint, there is the total-available-power constraint: Ram-pressure forcing of the ambient medium by the advancing beam head liberates a maximal power (*cf.* Hobbs *et al.* 1978):

$$L_{\mathrm{ram}} = \rho_{\mathrm{amb}} v_{\mathrm{head}}^3 A \simeq L_{\mathrm{jet}} \beta_{\mathrm{head}} \lesssim 10^{44}\,\mathrm{erg\,s^{-1}} (n_{\mathrm{amb}})_{-3}^{-1/2} \tag{10}$$

(the latter because of $\rho_{\mathrm{amb}} v_{head}^2$ = constant) which must be reduced to $\lesssim 10^{42}$ erg s $^{-1}$ for an encounter with a massive shell, of $n_{\mathrm{amb}} \simeq 10$ cm^{-3}. This estimate agrees with the one by Kronberg *et al.*

In our interpretation, the jet advances at an irregular speed, of over $v_{\mathrm{head}} \simeq 0.1c$ when traversing the average halo medium and some 10^2 times slower when piercing a dense shell. Its average advance speed is therefore given by $0.1c$ multiplied by the fraction of the time during which it is not choked. This fraction may be of order 0.5, in accord with the fact that very bright hotspots are common but not necessarily present in young sources. This estimate is also consistent with the ones by Winter *et al.* (1980) and Alexander, Brown & Scott (1984) which yield $\beta_h = 0.05 H_{-17\cdot8}$ for suitable interpretation.

4. Conclusions

Our interpretation of the dark features and bright features in the lobes of the extragalactic radio sources is based on the assumption that relativistic plasma rams a narrow channel (jet) through the ambient medium (Kundt & Gopal-Krishna 1981; Kundt 1987). At the end of a jet, ram pressure is converted into static pressure across a terminal shock, and subsonic expansion follows supersonic supply. This scenario shares certain features with a glass-blower's art, or with the (imaginary) inflating of a rubber balloon through a straw whose far end is kept near the far end of the balloon. In the case of an extragalactic radio source, the balloon is realized by the cocoon—filled with shocked beam plasma—and observed as the lobe.

In this picture, part of the ambient medium stays near the jet, in the form of a (porous) channel wall, due to Rayleigh-Taylor instabilities during ramming, whereas a large fraction of the ambient medium is swept to the outer edge of the cocoon during the (Rayleigh-Taylor-stable) relaxation phase (of decreasing pressure). The swept-up ambient medium is expected to form cylindrical shells around the jet. Such radio-bright cylindrical shells are indeed indicated in Cyg A, yet offset from the present jets (Fig. 1b). This offset may be a consequence of the swinging of the beam into a new direction, as discussed at length by Kundt & Gopal-Krishna (1986). In the case of Cyg A, both jets have swung south.

The new element introduced in the present paper are the multiple, quasi-spherical partial shells, consisting of ram-pressure confined filaments of mass density

$\rho \simeq 10^{-23}$ g cm^{-3}, which repeatedly choke the ramming beams, give rise to radio bubbles and can make their appearance directly as radio-dark lanes, depolarized lanes, or faint optical emission shells.

Acknowledgements

This work has been launched by a long conversation with John Dreher during which he stressed the possible significance of the radio-dark spots in Cyg A, and presented us the original radio-photograph reproduced in Fig. 1a. Discussions with Robert Laing and Peter Scheuer are likewise acknowledged. One of us (L.S.) gratefully acknowledges the support and hospitality of the Institut für Astrophysik at which this work has been done. Both of us thank Mr. Hutschenreiter for the reproduction of Fig. 1a.

References

Alexander, P., Brown, M. T., Scott, P. F. 1984, *Mon. Not. R. astr. Soc.,* **209,** 851.
Arnaud, K. A., Fabian, A. C., Eales, S. A., Jones, C., Forman, W. 1984, *Mon. Not. R. astr. Soc.,* **211,** 981.
Canizares, C. R., Stewart, G. C., Fabian, A. C. 1983, *Astrophys. J.,* **272,** 449.
Crane, P., Tyson, J. A., Saslaw, W. C. 1983, *Astrophys. J.,* **265,** 681.
DeYoung, D. S. 1986, *Astrophys. J.*, **307,** 26.
Dreher, J. W., Feigelson, E. D. 1984, *Nature,* **308,** 43.
Dreher, J. W., Perley, R. A., Laing, R. A., Scheuer, P., 1984, in Proc. NRAO workshop: *Physics of Energy Transport in Extragalacitic Radio Sources,* Eds A. H. Bridle & J. A. Eilek, Green Bank.
Ekers, R. D., Goss, W. M., Wellington, K. J., Bosma, A., Smith, R. M., Schweizer, F. 1983, *Astr. Astrophys.,* **127,** 361.
Gaetz, T. J., Salpeter, E. E. 1983, *Astrophys. J. Suppl.* **52,** 155.
Gopal-Krishna, Saripalli, L. 1984, *Astr. Astrophys.,* **141,** 61.
Guilbert, P. W., Fabian, A. C. 1986, *Mon. Not. R. astr. Soc.,* **220,** 439.
Hargrave, P. J., Ryle, M. 1974, *Mon. Not. R. astr. Soc.,* **166,** 305.
Kargrave, P. J., Ryle, M. 1976, *Mon. Not. R. astr. Soc.,* **175,** 481.
Hobbs, R. W., Maran, S. P., Kafatos, M., Brown, L. W. 1978, *Astrophys. J.,* **220,** L77.
Kronberg, P., van den Bergh, S., Button, S. 1977, *Astr. J.,* **82,** 315; Erratum: p. 1039.
Kundt, W. 1987, Nato ASIC 208: *Astrophysical Jets and their Engines,* D. Reidel, Dordrecht.
Kundt, W., Gopal-Krishna, 1981, *Astrophys. Sp. Sci.,* **75,** 257.
Kundt, W., Gopal-Krishna, 1986, *J. Astrophys. Astr.,* **7,** 225.
Kundt, W., Krause, M. 1985, *Astr. Astrophys.,* **142,** 150.
Lang, K. R. 1978, *Astrophysical Formulae,* Springer, Berlin.
Malin, D. F., Carter, D. 1983, *Astrophys. J.,* **274,** 534.
Malin, D. F., Quinn, P. J., Graham, J. A. 1983, *Astrophys. J.,* **272,** L5.
Meisenheimer, K., Röser, H.-J. 1986, *Nature,* **319,** 459.
Perley, R. A., Bridle, A. H., Willis, A. G., Fomalont, E. B. 1980, *Astr. J.,* **85,** 499.
Perley, R. A., Dreher, J. W., Cowan, J. J. 1984, *Astrophys. J.,* **285,** L35.
Quinn, P. J. 1984, *Astrophys. J.,* **279,** 596.
Röser, H.-J., Meisenheimer, K. 1986, *Astr. Astrophys.,* **154,** 15.
Rudnick, L., Saslaw, W. C., Crane, P., Tyson, J. A. 1981, *Astrophys. J.,* **246,** 647.
Schweizer, F. 1980, *Astrophys.* J., **237,** 303.
Schweizer, F. 1986, *Science,* **231,** 228.
Simkin, S. M., Bicknell, G. V., Bosma, A. 1984, *Astrophys. J.,* **277,** 513.
Strom, R. G., Willis, A. G., Wilson, A. S. 1978, *Astr. Astrophys.,* **68,** 367.

van Breugel, W., Balick, B., Heckman, T., Miley, G., Helfand, D. 1983, *Astr. J.,* **88,** 40.
van Breugel, W., Filippenko, A. V., Heckman, T., Miley, G. 1985a, *Astrophys. J.,* **293,** 83.
van Breugel, W., Fomalont, E. B. 1984, *Astrophys. J.,* **282,** L55.
van Breugel, W., Heckman, T., Butcher, H., Miley, G. 1984, *Astrophys. J.,* **277,** 82.
van Breugel, W., Miley, G., Heckman, T., Butcher, H., Bridle, A. 1985b, *Astrophys. J.,* **290,** 496.
Winter, A. J. B., Wilson, D. M. A., Warner, P. J., Waldram, E. M., Routledge, D., Nicol, A. T., Boysen, R. C., Bly, D. W. S., Baldwin, J. E. 1980, *Mon. Not. R. astr. Soc.,* **192,** 931.

J. Astrophys. Astr.(1987) **8,** 219–226

A Study of Faint Young Open Clusters as Tracers of Spiral Features in our Gala xy
Paper 3: Collinder 97 (OCl 506)

G. S. D. Babu *Indian Institute of Astrophysics, Bangalore 560034*

Received 1987 January 5; accepted 1987 April 6

Abstract. Photoelectric and photographic photometry of twenty-nine stars was done in the field of the open cluster Collinder 97 ≡ OC1 506. Of these stars, a total of twenty-four have been found to be possible members. There is apparently no interstellar extinction in the direction of this cluster which is in the constellation of Monoceros: its $E(B - V) = 0.0$ mag. This cluster is situated at a distance of 0.63 ± 0.01 kpc, which is well within the local arm of our Galaxy. The age of this cluster is in the range of 1×10^8 to 5.9×10^8 yr, which puts it in an older age group. Thus, it cannot be specifically considered as a spiral-arm tracer in the study of our Galaxy.

Key words: star clusters, open—star clusters, individual—stars, photometry

1. Introduction

A study of faint young open clusters was initiated by the late Professor M. K. V. Bappu with the main aim of utilising them as tracers of spiral features in our Galaxy. A new technique was developed for a rapid selection of the young clusters from among the not-well-studied fainter ones (Babu 1983). Among the clusters selected, the first to be studied was OC1 585 (Babu 1985). Hereafter, these two works will be referred to as Paper 1 and Paper 2 respectively, the present one being the third in this series.

In Paper 1, the observations of two not-well-studied open clusters, picked from the catalogue given by Alter, Balazs & Ruprecht (1970), were also included. In one of them, namely OC1 506, approximate spectral types could be obtained for a total of thirteen stars, using the modified objective-grating technique. These are reproduced in Table 1 for the convenience of the reader. Since the earliest spectral class among the observed ones was of B5 type and since there is an uncertainty inherent in this technique of fixing the spectral subclasses, this cluster was then roughly classified as a marginally young cluster. In view of this, OC1 506 was selected for further photometric work.

This group of stars (Collinder 97≡ Cr 97 ≡ OC1 506 ≡ C 0628 + 059; $l = 205°.37$; $b = -1°.76$) was first listed as a cluster by Collinder (1931), who estimated its distance to be 610 pc. He also gave its angular diameter as 22.5 arcmin with just nine stars in it. He pointed out that this cluster has stars of spectral types B0 and A0 in addition to being a fairly bright cluster ($m_{tot} = 5.3$ mag). It has been classified in the Trumpler system as IV 3 P by Ruprecht (1966), where IV indicates that this is not a well-bound cluster, but is passing gradually into the environs, appearing more like a star-field condensation.

The numeral 3 implies that this cluster is composed of bright and faint stars, while the letter P shows that this is a poor cluster with less than 50 stars in it. The finding chart is given in Fig. 1, where it may be noted that some of the stars in the field are so bright that they have even been included in SAO and BD charts. Thus, it is rather surprising that so far no work has been done on them from the cluster point of view.

In this paper, the results of the photometric observations of OC1 506 are presented, based on which it is found that this open cluster is a little too old to be categorised into the young group and thereby concluded that it is not specifically suitable for use as a spiral-arm tracer.

2. Observations and reductions

The photoelectric observations of seventeen stars in the field of this cluster were obtained using a standard *UBV* photometer mounted on the 61-cm telescope at the Siding Spring Observatory of the Australian National University. A dry-ice-cooled

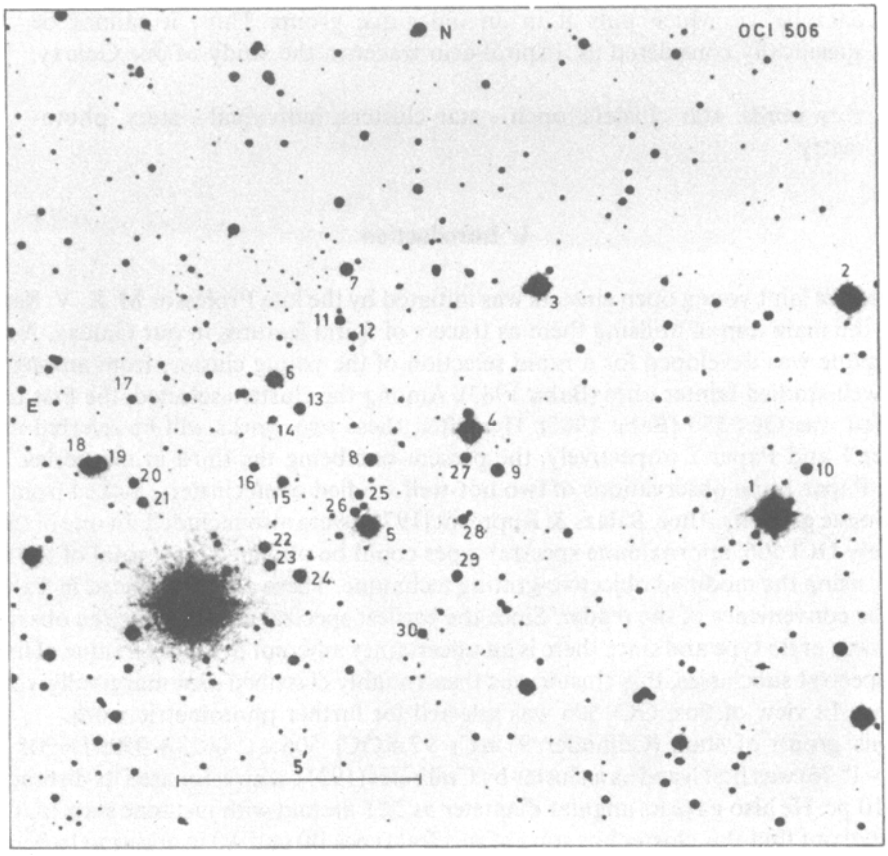

Figure 1. Finding chart for the field of OC1 506, reproduced from the Palomar Observatory Sky Survey (POSS) charts. The identification numbers of the earlier work (Babu 1983) and some extensions introduced in the present work are marked in the chart.

photomultiplier was used along with an on-line computer to collect the data. The instrumental magnitudes, corrected for atmospheric extinction, were standardised with the help of the photometric sequences taken from the work of Landolt (1973). These values are given in Table 1 as V, $(B-V)$ and $(U-B)$. While retaining the same numbers for the stars as in the earlier work (Babu 1983), the numbering has been extended to several more stars in this paper. They are marked in Fig. 1.

The *UBV* photography of this cluster was done using the 102-cm telescope at Kavalur Observatory. The plate and filter combinations are given in Table 2 along with the exposure times. From these plates, the photographic magnitudes in B and V were obtained on an arbitrary scale for a total of twenty-nine stars, using the PDS microdensitometer in conjunction with the computational facilities available at the Mount Stromlo Observatory in Australia. Unfortunately, the U photograph was affected by poor sky conditions. However, since a sufficient number of stars were observed photoelectrically in U, no further attempt was made to obtain the photographic U magnitudes. The stars common to the photoelectric and photographic

Table 1. The observational data for individual stars in the open cluster OC1 506.

Star No.		Sp. type*	V	$(B-V)$	$(U-B)$	Membership
Photoelectric photometry:						
1	(SAO 113979)	B8	8.40	−0.02	0.05	m
2	(SAO 113977)	A0	8.71	0.33	0.01	m
3	(SAO 113987)	K0	8.69	0.99	0.66	m
4	(BD+5° 1274)	B5	9.76	−0.05	−0.23	m
5	(BD+5° 1276)	F5	9.57	0.64	0.27	m
8		A0	12.72	0.38	−0.03	m
9		F0	12.26	0.39	0.04	m
10		K5	12.87	0.85	0.35	—
13		F0	12.73	0.49	0.05	m
14			15.24	0.85	0.78	m
15			14.22	0.73	0.27	m
22			14.10	0.67	0.21	m
23			12.67	1.62	—	—
24			12.62	0.51	0.14	m
25			14.51	0.62	0.05	m
27			13.91	0.74	0.34	m
30			13.81	0.80	0.57	—
Photographic photometry:						
6		B8	10.81	0.15	—	m
7		A0	12.27	0.32	—	m
11		F5	13.34	0.64	—	m
12		G0?	13.63	0.60	—	m
16			13.97	0.65	—	m
17			14.24	1.17	—	—
18			11.84	0.30	—	m
19			12.14	0.45	—	m
20			13.81	0.61	—	m
21			13.71	0.48	—	m
26			14.80	0.67	—	m
28			13.98	0.81	—	—

* From Paper 1.

Table 2. Journal of observations.

Band	Plate	Filter	Exposure time
U	IIa-O	UG 2	35 min
B	103a-O	GG 13	20 min
V	IIa-D	GG 11	40 min

observations were used for standardizing the photographic *B, V* magnitudes of the remaining twelve stars. These magnitudes and colours are also listed in Table 1.

3. Reddening

The colour-colour diagram of the stars in this field, with (*B–V*) against (*U – B*), is given in Fig. 2. In this diagram, the sequence of all the observed stars appears to follow the unreddened curve given by Schmidt-Kaler (1982), indicating that there is no extinction

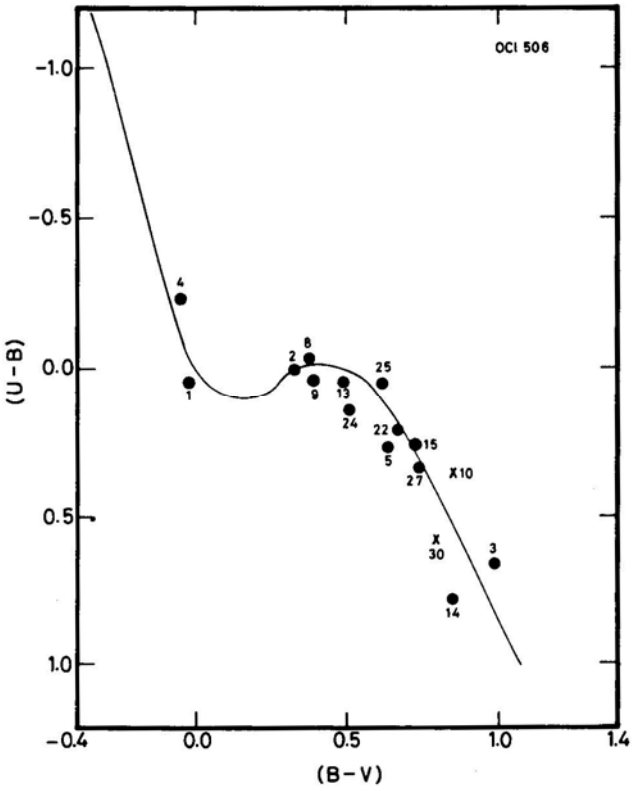

Figure 2. The (*B – V*) versus (*U – B*) diagram of the stars in the field of OCl 506. The filled circles and crosses denote the members and nonmembers respectively. The solid curve is the unreddened main sequence (MS) taken from Schmidt-Kaler (1982). The identification numbers of the stars (*cf.* Fig. 1) are also indicated.

due to interstellar medium between the cluster and the observer. Thus,

$$E(B-V) = 0.0 \qquad \text{and} \qquad E(U-B) = 0.0$$

That is, the observed magnitudes and colours need no further correction by way of interstellar reddening.

4. Membership

The membership of the individual stars in this cluster has been determined with the help of the photometric criteria given by Vogt & Moffat (1972). In this method, the stars of the clear sequence found in the colour-colour diagram are identified on the two colour-magnitude diagrams as well (Figs 3 and 4). The diagram of ($B - V$) versus V (Fig. 3), includes also the data of the photographic photometry on twelve stars. This exercise indicates that a total of twenty-four stars are members, the remaining five (stars 10, 17, 23, 28 and 30) nonmembers. Stars 3 and 5 appear to be belonging to the red-giant branch, whereas stars 1 and 2 show some evolved nature. All the members are denoted by 'm' in Table 1.

5. Distance

In order to determine the distance of this cluster using the present photometric data, the two colour-magnitude diagrams (Figs 3 and 4) have been fitted with the zero-age-main-

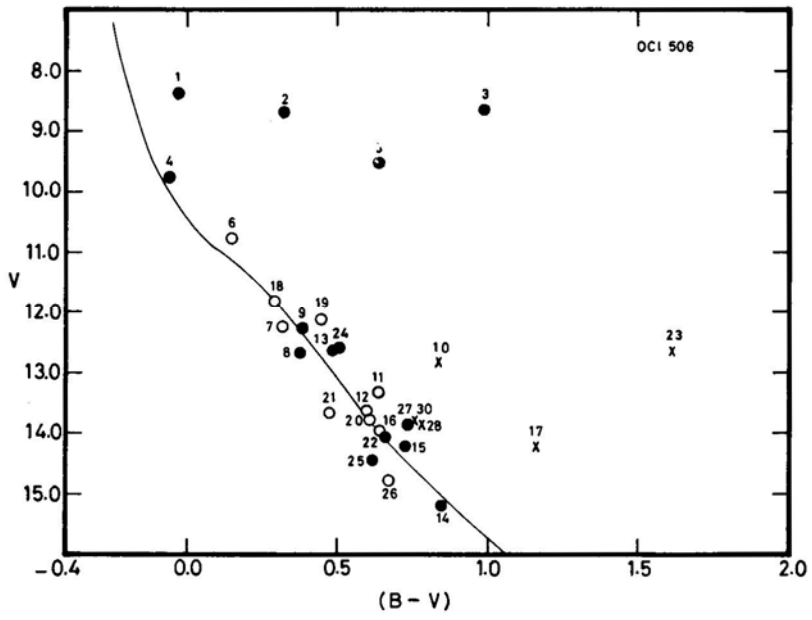

Figure 3. The ($B-V$) versus V magnitude diagram of the stars in the field of OC1 506. The solid curve represents the zero-age-main sequence (ZAMS) (*cf.* Schmidt-Kaler 1982), which is shifted to match with the observations. The unfilled circles indicate the photographically observed members, the rest of the symbols being the same as in Fig. 2.

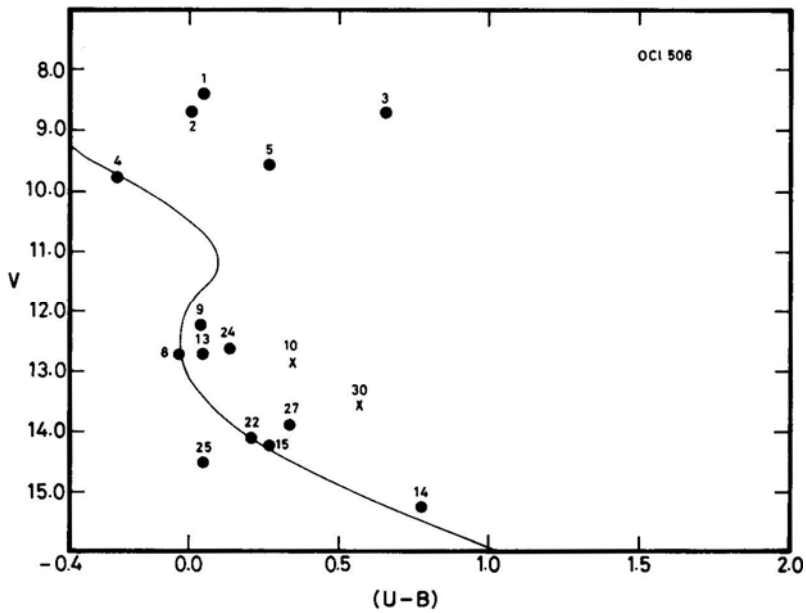

Figure 4. The ($U - B$) versus V magnitude diagram of the stars in the field of OCl 506. The solid curve represents the ZAMS (*cf.* Schmidt-Kaler 1982) which is shifted to match with the observations. The symbols are the same as in Fig. 2.

sequence (ZAMS) given by Schmidt-Kaler (1982). They yielded the distance moduli of 8.95 mag and 9.05 mag from the long and short wavelength colour-magnitude diagrams respectively, giving an average of 9.0 mag. Then, based on the expression $\log D = 0.2\,(V–M)+ 1$, the distance D has been found to be

$$D = 0.63 \pm 0.01\text{kpc},$$

where ($V– M$) is the distance modulus.

6. Age of the cluster

The HR-diagram of this cluster, shown in Fig. 5, is plotted for the true distance modulus of 9.0 mag. When the ZAMS (Schmidt-Kaler 1982) and the post-main sequence isochrones (Barbaro, Dallaporta & Fabris 1969) are superimposed on this diagram, the cluster stars clearly indicate an age range from a little later than 1.25×10^8 to about 5.90×10^8 yr. Further, star 4, being the bluest on the MS with ($B – V$) = – 0.05 gives the age as 1×10^8 yr. Thus, the total dispersion in the age of this cluster appears to be from 1×10^8 to 5.9×10^8 yr.

7. Conclusions

The very fact that this cluster needs no corrections for the interstellar extinction (*cf.* Section 3) indicates that it is a nearby system. Its bright total magnitude and the

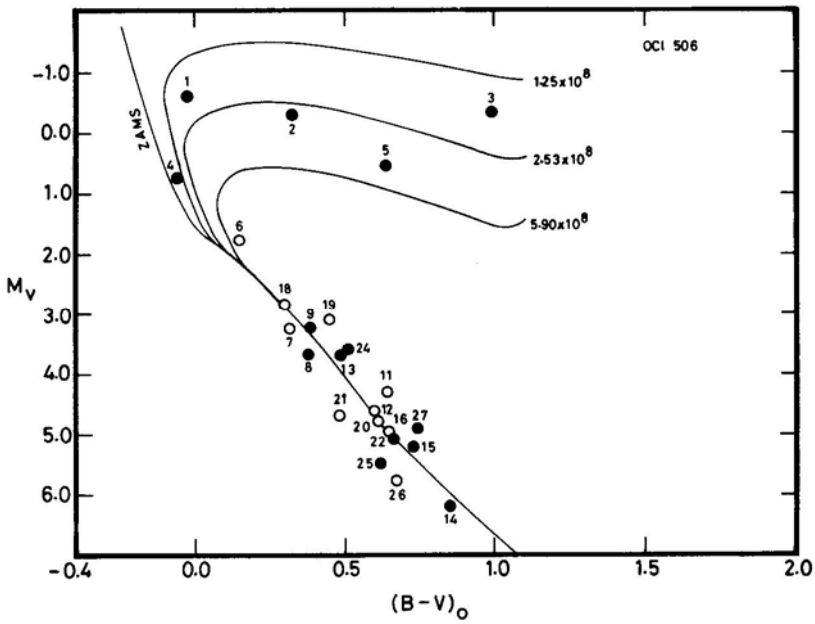

Figure 5. The HR-diagram of the open cluster OCl 506. The ZAMS is the same as in Fig. 3, but drawn for the true distance modules. The post-MS isochrones are from Barbaro, Dallaporta & Fabris (1969), with the ages indicated alongside. The symbols are the same as in Figs 2–4.

large angular diameter (*cf.* Section 1) render support to this inference. In fact, the earlier estimation of distance by Collinder (1931) is very close to the value of 0.63 + 0.01 kpc determined in the present work.

The age of this cluster is found to be in the range of 1×10^8 to 5.9×10^8 yr, which puts it in an older age group. Thus, it cannot be specifically considered as a spiral-arm tracer in the study of our Galaxy, in spite of the fact that its location is sufficiently inside the local Cygnus-Orion arm.

Acknowledgements

I am thankful to Drs D. C. V. Mallik, R. Rajamohan, Professors N. Kameswara Rao, M. B. K. Sarma, R. F. Garrison and G. Lynga for the many helpful discussions and useful suggestions. I gratefully acknowledge the efforts of Dr N. Visvanathan in allotting the telescope time at the Siding Spring Observatory and for all his help to me during my stay in Australia. I also acknowledge the kind hospitality provided to me by the staff of the Mount Stromlo and Siding Spring Observatories. The trip to Australia was financially supported by the Indian Institute of Astrophysics.

References

Alter, G., Balazs, B., Ruprecht, J. 1970, *A Catalogue of Star Clusters and Associations,* 2nd edn., Akademiai Kiado, Budapest.

Babu, G. S. D. 1983, *J. Astrophys. Astr.*, **4,** 235 (Paper 1).
Babu, G. S. D. 1985, *J. Astrophys: Astr.,* **6,** 61 (Paper 2).
Barbaro, G., Dallaporta, N., Fabris, G. 1969, *Astrophys. Space Sci.,* **3,** 123.
Collinder, P. 1931, *Lund Obs. Ann.* No. 2.
Landolt, A. U. 1973, *Astr. J.,* **78,** 959.
Ruprecht, J.1966, *Bull. Astr. Inst.Csl.,* **17,** 34.
Schmidt-Kaler, Th.1982, in *Landolt-Bornstein, Numerical Data and Functional Relationships in Science and Technology,* Eds K. Schaifers & H. H. Voigt, Group VI, Vol. 2, Subvol. b, p. 19 (Table 15).
Vogt, N., Moffat, A. F. J. 1972, *Astr. Astrophys. Suppl. Ser.,* **7,** 133.

J. Astrophys. Astr. (1987) **8,** 227–230

Further VLA* Observations of Hydrogen Deficient Stars

N. Kameswara Rao *Indian Institute of Astrophysics, Bangalore 560034*

V. R. Venugopal & A. R. Patnaik *Radio Astronomy Centre, Tata Institute of Fundamental Research, Post Box 8, Udhagamandalam 643001*

Received 1987 February 18; accepted 1987 April 7

Abstract. VLA observations at 6 cm have been obtained for three hydrogen-deficient objects υ Sgr, V 348 Sgr, and A bell 58. A bell 58 was also observed at 2 cm. Only upper limits to the flux density could be set for these sources. A new radio source at 6 cm was found in the field of υ Sgr.

The upper limit for 6 cm flux density of V348 Sgr sets an upper limit to its reddening as $E(B-V) \leqslant 0.65$. The hydrogen deficient planetary nebula A 58 shows much lower radio flux than expected from the infrared-radio flux density relationship of planetary nebulae.

Key words: stars, hydrogen-deficient—stars, radio observations—stars, individual—planetary nebulae

1. Introduction

In order to study the mass-loss rates and the nebular properties around hydrogen-deficient stars we surveyed six extreme hydrogen-deficient stars with VLA at 2 cm and 6 cm and could place upper limits to the flux density (Rao, Venugopal & Patnaik 1985). Because of the suspicion of variablity of the flux in some of the objects and to include few other hydrogen-deficient nebulae in the sample we have obtained additional observations of three objects V 348 Sgr, υ Sgr and the planetary nebula A 58.

2. Observations

The observations were obtained with VLA (Napier, Thompson & Ekers 1983) in the B/C hybrid configuration on 1985 July 5. V 348 Sgr and υ Sgr were observed only at 6 cm (C-band) whereas A 58 was observed both at 6 and 2 cm (U-band) with a bandwidth of 50 MHz. The data were acquired in both AC and BD Ifs (4835 MHz and 4885 MHz in C band and 14915 and 14965 MHz in U band). The data from the two IFs were combined to make maps. Regions of about 256 arcsec × 256 arcsec at 6 cm and 102 arcsec × 102 arcsec at 2 cm were mapped around these objects. The maps were cleaned and restored using the software package AIPS. We could not detect any source

* National Radio Astronomy Observatory's Very Large Array is operated by Associated Universities Inc. under contract with National Science Foundation, USA.

Table 1. Upper limits to the radio flux densities.

	6 cm			2 cm		
Object	Beam size arcsec	PA	Upper limit (3σ) flux density mJy/beam	Beam size arcsec	PA	Upper limit (3σ) flux density mJy/beam
V 348 Sgr	4.09 × 2.30	−65°	0.15			
υ Sgr	7.03 × 2.01	−62°	0.21			
A 58	4.02 × 1.16	76°	0.15	1.43 × 0.45	75°	0.37

near the position of these objects; however the upper limits to the flux densities are given in Table 1.

3. Discussion of the programme stars

υ *Sgr*: This is one of the four known hydrogen-deficient binaries. The properties and the earlier VLA measurements have been discussed by Rao & Venugopal (1985) and Rao, Venugopal & Patnaik (1985). The present upper limit is a further refinement on the earlier measurements and changes the mass-loss rate to $\lesssim 4.8 \times 10^{-7} \lesssim M_{\odot}$ yr^{-1} for the system. We used the value of the terminal velocity V_{∞}— 813 kms^{-1} as suggested by Parthasarathy, Cornachin & Hack (1986).

There is a source roughly 4 arcmin north of υ Sgr whose 1950 coordinates are:

$$\alpha = 19^{h}\ 18^{m}\ 54^{s}.85 \pm 0^{s}.02, \qquad \delta = -15°\ 59'\ 13''.93 \pm 0''.16.$$

After fitting a single-point gaussian for this source the 6 cm peak flux is 0.89 ± 0.08 mJy/beam and the total flux is 1.135 ± 0.225 mJy. There is no obvious optical candidate to be identified with this source on Palomar Observatory Sky Survey (POSS) prints.

V 348 Sgr: This is one of the hot hydrogen-deficient stars associated with an optical nebulosity. The present upper limit at 6 cm improves the one given in Rao, Venugopal & Patnaik (1985). Purton *et al.* (1982) had earlier observed this object with the Parkes radio telescope in the period 1977–78. Only the 14.5 GHz flux measurement has a smaller probable error and is given as 6 ± 3 mJy. The half-power beam width was however 2.3 arcmin. Our earlier measurements with the VLA at 2 and 6 cm and the present measurement at 6 cm do not show any detectable flux. There is a possibility that the Parkes measurement might have included the galaxy which is 4 arcmin west of V 348 Sgr.

There is considerable uncertainty about the estimate of reddening in the nebulosity. Dahari & Osterbrock (1984) obtained $E(B-V)$ of 1.4 from the Balmer decrement when the star was at minimum light, whereas Houziaux (1986, personal communication) obtained $E(B-V)$ of 0.45 from the Hα/Hβ measurements when the star was at maximum light. Schönberner & Heber (1986) estimates $E(B-V)$=0.60 with 0.15 of this

caused by amorphous carbon dust in the circumstellar environment. The Hβ flux measured by Dahari & Osterbrock (1984) is 4.07×10^{15} erg cm^{-1} s^{-1}. Ifthe 3σ upper limit to the flux density at 6 cm is taken as the upper limit to the free-free flux from the nebula then the flux density S_ν is related to Hβ flux, $F_{H\beta}$ as (The VLA beam size used is about same as the slit size used by Dahari & Osterbrock.)

$$\frac{S_\nu}{F_{H\beta}} = 2.51 \times 10^7 \; T_e^{0.53} \nu^{-0.1} \; Y \; \text{Jy/(erg cm}^{-2}\text{s}^{-1}\text{)}$$

(Pottasch 1984) where

$$Y = \left(1 + \frac{n(H_e^+)}{n(H^+)} + \ldots\right).$$

Using $T_e = 1.5 \times 10^4$ K and Y= 1.13 (Dahari & Osterbrock 1984) the resulting $F_{H\beta}$(cal) is 3.79×10^{-14} erg cm^{-2} s^{-1} and the value of $E(B - V)$ is obtained as $\leqslant 0.65$ using the relation $E(B–V)$ = (l/1.46)log [$F_{H\beta}$ (cal)/$F_{H\beta}$ (obs)] (Pottasch 1984). This value of $E(B—V)$ is in agreement with the reddening estimated by Houziaux (1986, personal communication) and Schönberner & Heber (1986) indicating that most of the reddening is attributable to the interstellar medium.

Abell 58: This is a low-surface-brightness planetary nebula showing an extension of 44 × 36 arcsec on red plates (van den Bergh 1971). However it does not appear on blue POSS prints. On the UK Schmidt *J* plates the nebular filaments near the centre are faintly seen, the nebula is of low-excitation class with [N II] λ 6584 > Hα and λ 5007 λ 4959 of [O III] being very weak (Ford 1971; Pottasch *et al.* 1986). This is also a strong IRAS source with T_{BB} of the dust ~ 122 K. The central object of this nebula was first known as V 605 Aql and became visible in 1917; it reached a magnitude of about 10 in 1919(Lundmark 1921),faded thereafter and was last observed in 1923. The spectrum of the star observed in 1921 showed the characteristics of a hydrogen-deficient star and a very good match to HD 182040 (Bidelman 1973). At present there is a hydrogen deficient nebulous knot near the centre (Pottasch *et al.* 1986; Seitter 1985). There is a very faint star (20 mag) 1 arcsec north of the central nebula which may be what remains of V 605 Aql. The nebular expansion velocity as measured from the line widths of [N II] $\lambda\lambda$ 6548, 6584 and Hα on a CCD spectrum obtained with 3-m Shane telescope is less than 40 km s^{-1}. Thus the nebula has existed much before the 1919 outburst. We planned to look for the remnant of the 1917 outburst if it exists in the radio with the VLA. Secondly, Pottasch *et al.* (1984) showed that for planetary nebulae there is a strong correlation between the total infrared flux as obtained by IRAS measurements and 6 cm radio flux density. With measured infrared flux density (6.0×10^{-2} Wm^{-2}) for A 58 (Pottasch *et al.* 1984) we expected to see about 300 mJy at 6 cm. Surprisingly we could not detect any flux density either at 2 cm or 6 cm and the upper limits for the flux density are given in Table 1. Similar result has also been reported for A 30 and A 78 by Zijlstra (Pottasch *et al.* 1986). The infrared radiation seems to be much higher than expected from the free-free radio emission from hydrogen-deficient nebulae. The present results seem to support the suggestion of Pottasch *et al.* (1986) that this property could probably be used to identify other hydrogen-deficient nebulae.

Acknowledgements

We thank Ms Peggy Perley for her help in obtaining the VLA observations. We also express our thanks to Dr. G. H. Herbig for obtaining the CCD spectrum of A 58 at NKR's request, and for the courtesy of sending a print of Lundmark's spectrum of V605Aql.

References

Bidelman, W. P., 1973, *Bull am. astr. Soc.,* **5,** 442.
Dahari, O., Osterbrock, D. E. 1984, *Astrophys. J.,* **277,** 648.
Ford, H. C. 1971, *Astrophys. J.,* **170,** 547.
Lundmark, K. 1921, *Publ. astr. Soc. Pacific,* **33,** 314.
Napier, P. J., Thompson, A. R., Ekers, R. D. 1983, Proc. IEEE **71,** 1295.
Parthasarathy, M., Cornachin, M., Hack, M. 1986, *Astr. Astrophys.,* **166,** 237.
Pottasch, S. R. (Ed.) 1984, *Planetary Nebulae,* D. Reidel, Dordrecht.
Pottasch, S. R., Baud, B., Beinterna, D., Emerson, J., Habing, H. J., Harris, S., Hauck, J., Jennings, R., Marsden, P. 1984, *Astr. Astrophys.,* **138,** 10.
Pottasch, S. R., Mampaso, A., Manchado, A., Menzies, J. 1986, in *IAU Coli.* **87**: *Hydrogen Deficient Stars and Related Objects,* Eds K. Hunger, D. Schönberner & N. Kameswara Rao, D. Reidel, Dordrecht, p. 359.
Purton, C. R., Feldman, P. A., Marsh, K. A., Allen, D. A., Wright, A. E. 1982, *Mon. Not. R. astr. Soc.,* **198,** 321.
Rao, N. K., Venugopal, V. R. 1985, *J. Astrophys. Astr.,* **6,** 101.
Rao, N. K., Venugopal, V. R., Patnaik, A. R. 1985, *J. Astrophys. Astr.,* **6,** 153.
Schönberner, D., Heber, U. 1986, in *IAU Coll.* 87: *Hydrogen Deficient Stars and Related Objects,* Eds K. Hunger, D. Schönberner & N. Kameswara Rao, D. Reidel, Dordrecht, p. 217.
Seitter, W. E. 1985, *Mitt. astr. Ges.,* **63.** 181.
van den Bergh, S. 1971, *Publ. astr. Soc. Pacific,* **83,** 819.

J. Astrophys. Astr. (1987) **8,** 231–239

3C 120 and the Surrounding Region of Sky

Halton Arp *Max-Planck-Institut für Physik und Astrophysik, Institut für Astrophysik, Karl-Schwarzschild-Str. 1, 8046 Garching bei München, FRG*

Received 1986 November 7; accepted 1987 May 19

Abstract. Image processing performed on a series of photographs of the superluminal Seyfert galaxy, 3C 120, shows the outer optical disc to consist of fragmented segments generally pointing toward the centre. One long arm of peculiar, separated knots comes off to the W and SW. A peculiar companion is seen along the line of the NW radio jet. In the interior, optical jets are detected which are aligned along the direction of the outer radio jets.

A region of the sky 45 × 25 degrees around 3C120 is investigated. It is found that:

1) A nebulous filament about 3/4 degree in length points to 3C 120.
2) Hydrogen clouds of redshift $z = -130$ and -210 km s^{-1} are situated at 3 and 1 degrees on either side of 3C 120.
3) Eleven low-surface-brightness galaxies with $4500 < z < 5300$ km s^{-1} fall within a radius of 8 degrees.
4) Seven quasars with $z \gtrsim 1.35$ and radio fluxes $S_b \gtrsim 0.3$ fall within a radius of 10 degrees.

It is concluded that the concentration of these objects in the vicinity of this unique, active galaxy has a negligible chance of being accidental and that all those objects of diverse redshift are at the same nearby distance. This smaller distance reduces the supposed superluminal motions in 3C 120 to quite precedented ejection velocities.

Key words: galaxies, Seyfert—radio sources, extragalactic—quasars, alignment

1. Introduction

During the course of the earliest radio surveys a strong source with a flat spectrum was discovered at R. A. = $4^h30^m32^s$, Dec. = 5°14'59" (1950). My attention was directed to this object by J. G. Bolton and in 1965 I obtained a photograph with the Mt. Palomar reflector which showed a bright stellar nucleus with faint nebulous material around it. The object later became known as 3C120 and spectra showed that it had broad emission lines redshifted to $z = 0.033$ ($cz = 9900$ km s^{-1}). In redshift, apparent magnitude, morphology and spectral characteristics it formed a transition in properties between active normal galaxies and the extreme quasars (Arp 1968).

Great interest was generated in this object when apparent faster-than-light motions of radio material in the nucleus were discovered in the years 1972 to 1974 (Seielstad *et*

al. 1979). Recently superluminal expansions of greater than 6*c* (for $H_0 = 65$) have been registered in 3C120 (Walker 1984).

In the following we examine the highest resolution, highest signal-to-noise, previously unpublished photographs of 3C120. Image processing to optimize various features is performed. Finally we consider the kinds of objects present in a wide region of the sky around this active object.

2. Image processing of direct photographs

The optical photographs are from a series exposures with the KPNO 4-metre reflector. The exposures were on Kodak IIIa-J emulsion with no filter and went to the limit imposed by sky brightness, about 55 minutes in most cases. The exposures were digitized, added and reproduced with varying degrees of stretching and isocontouring by Jean Lorre with the facilities of the Image Processing Laboratory at JPL (see Arp & Lorre 1976 for discussion of techniques).

Figs 1a and lb here show the single best plate (No. 4405) with contrast, and inner contouring that brings out the inner, fragmented structure of 3C120. The optical jet, strongest in the NW direction and visible as a shorter counter jet in the SE direction, is seen on both of these reproductions which reach into the high intensity levels of the interior regions of 3C 120.

In Figs 2a and 2b six of the best plates in the series were added and reproduced with stretching at faint surface brightness levels. This gives the best view which can be obtained of the outer, faintest regions of 3C120. For additional direct imagery see Wlerick (1981); Arp (1981).

Fig. 2a particularly, shows the numerous bright filaments which exist on the edge of the optical image. These short linear features seem generally to point back toward the centre of 3C120 and many seem to be slightly curved. A very unusual feature is seen in both Figs 2a and 2b, namely a longer linear feature which reaches from the NE side of the outer luminous disc around to the E and southward. This resembles in shape a spiral arm but is composed of individual rather widely spaced knots which are elongated but not along the direction of the arm.

The direct images of 3C 120 emphasize that the morphology of the optical body has a disturbed, generally radial filamentary structure that is unique for a galaxy. This material is distributed around a bright, compact, optical image that was initially described as being stellar, as were the quasars which it resembled. The underlying material, however, is nothing like a normal elliptical or spiral galaxy conventionally postulated to host quasars. But so far this is the only 'host' galaxy which one has been able to observe in any significant detail.

3. Ejection from 3C 120

The radio mapping clearly establishes the fact that 3C120 is ejecting. Fig. 3 shows the radio lobes extending in two opposite directions from the central source. The superposed optical photograph shows a jet and counterjet extending in the same direction as the radio ejection.

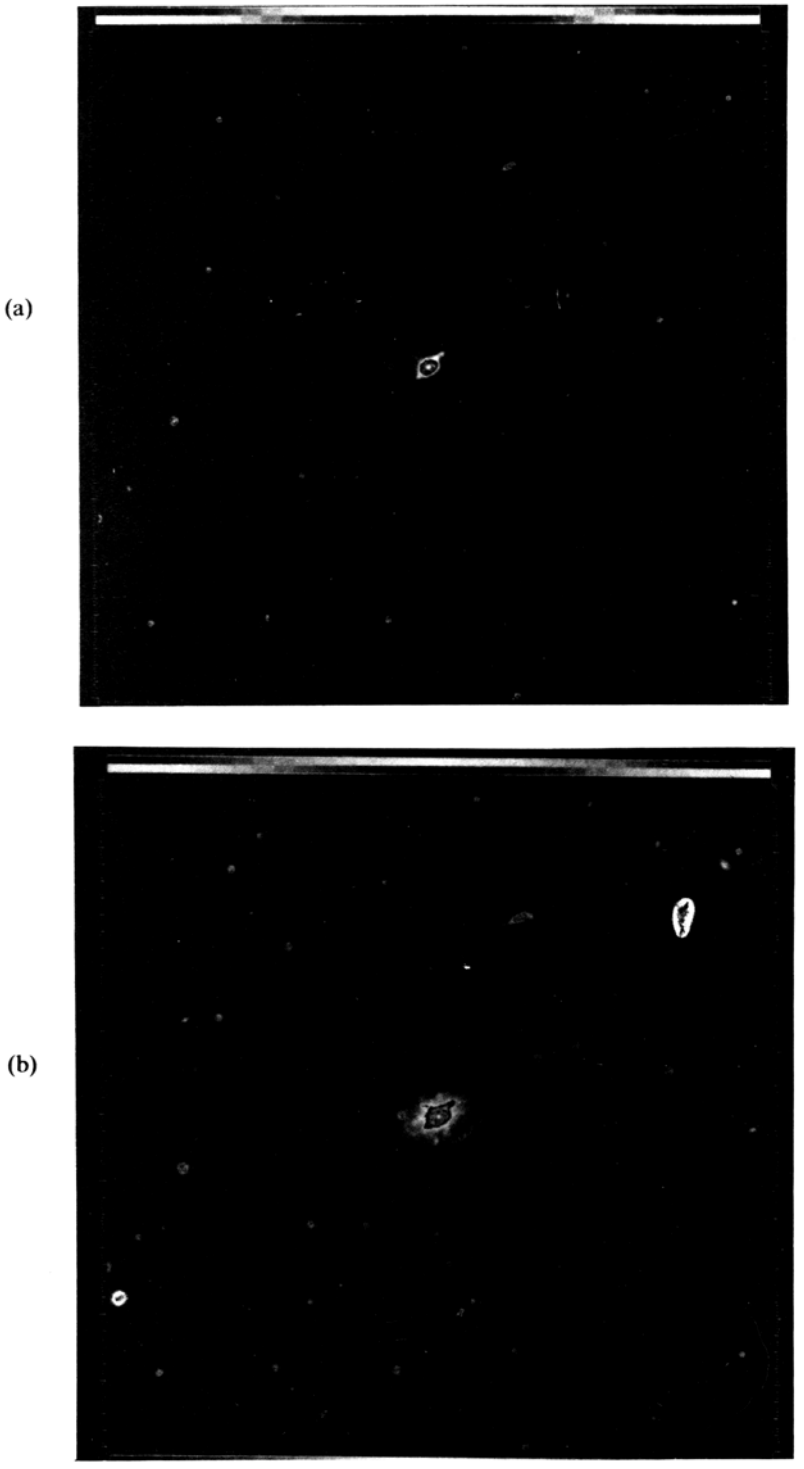

Figure 1. Enhanced contrast and iso-contouring of brighter intensity levels in the best IIIa-J plate(4-m KPNO # 4405) in order to optimize jet and details in the interior of 3C 120. Unusual companion is about 2'NW of 3C120.

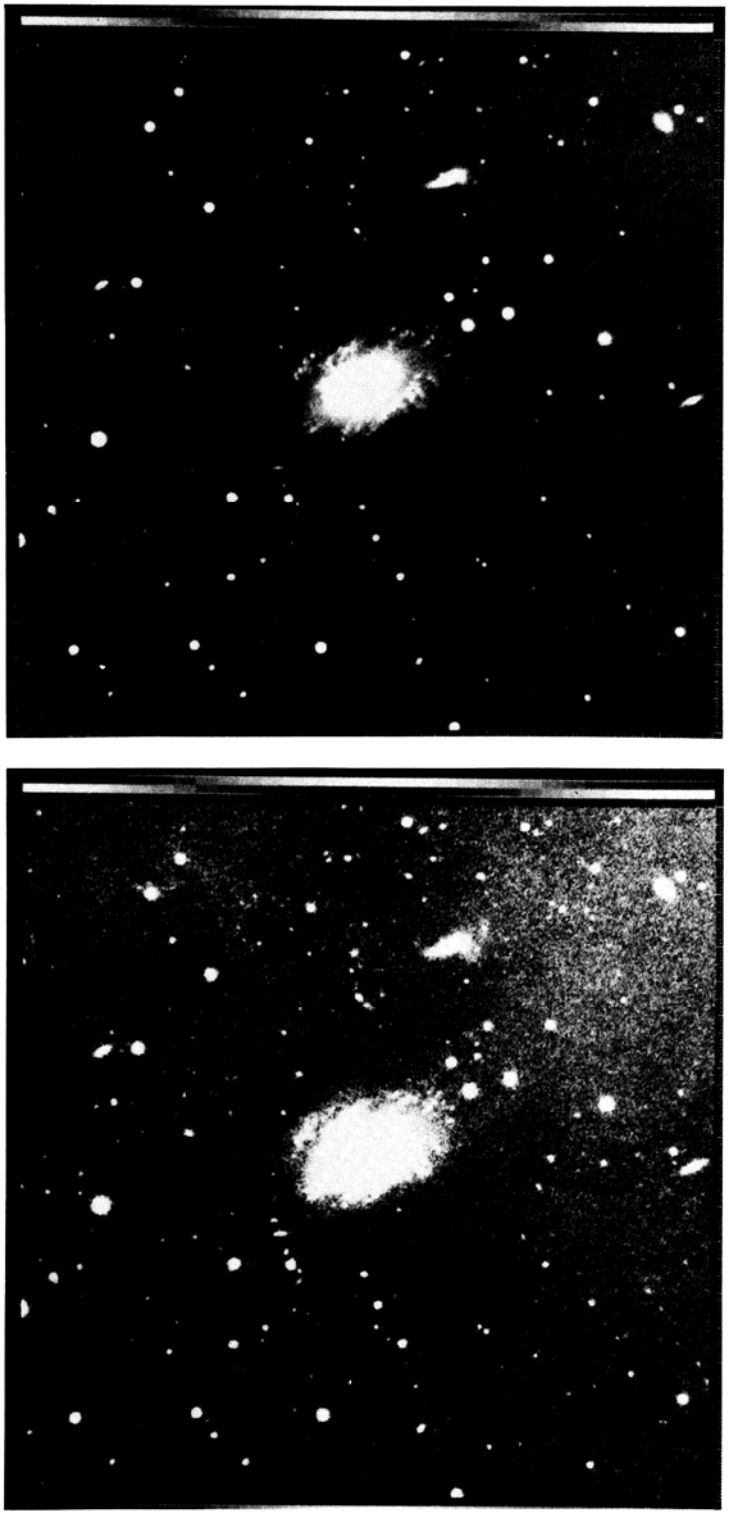

Figure 2. Average of 4-m KPNO photographs nos 4405,4406,4407,1385,1914,4418. Version (b) shows contrast optimized for detection of faintest surface-brightness features.

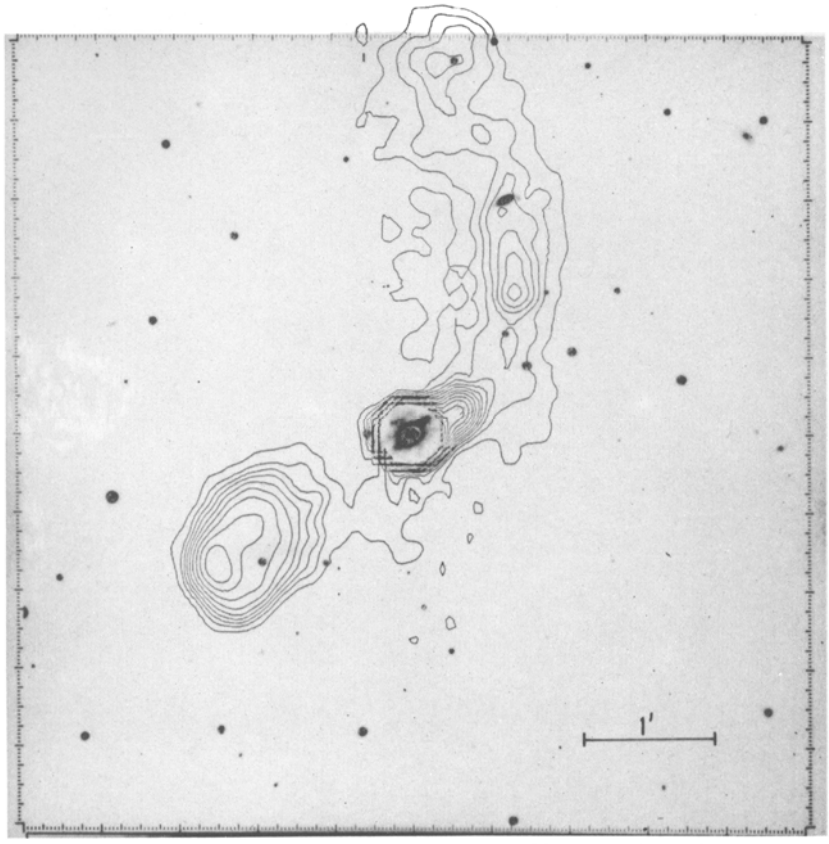

Figure 3. Radio map at 18 cm with VLA (courtesy R. C. Walker) superposed on plate No. 4405. Note approximate alignment of inner optical jet along direction of outer radio ejection.

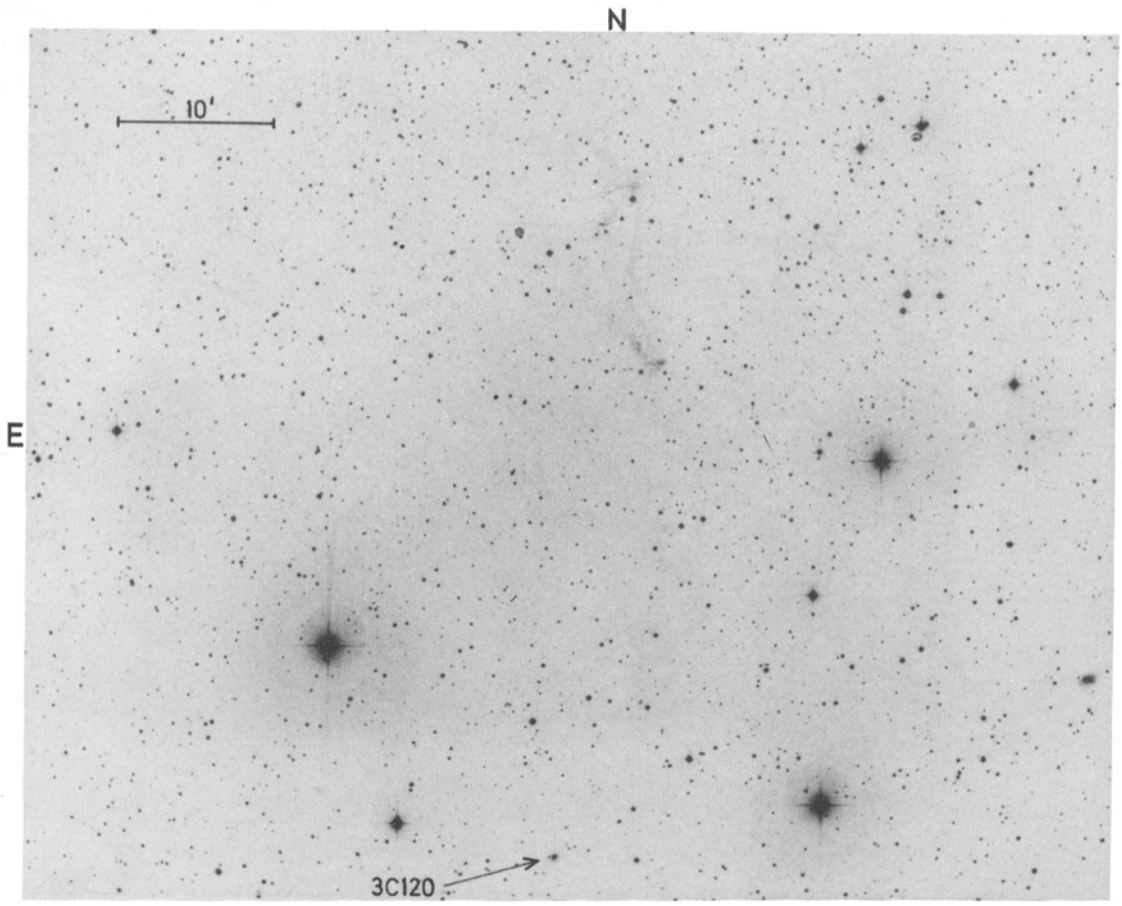

Figure 6. Photograph by Arp with Palomar 1.2-metre Schmidt on Kodak IIIa-J plate. Luminous filament is seen to North and Northwest of 3C 120. Spectroscopic nature of this filament is unknown.

It is noticeable in Fig. 3 that the optical jet seems slightly misaligned from the radio jet. The orientation of the optical photographs was checked and found to have an accuracy of better than ± 1°. The optical image was then superposed on the centre of the radio emission. But if one looks closely at just the radio map it is apparent that, the innermost radio jet does not emerge exactly from the central, circularly distributed radio emission. The meaning of this slight rotation or displacement is not known at this time.

About 2 arcmin to the NNW of 3C 120 there exists a smaller, very unusual galaxy (it can be seen here in Figs 1–2). It is elongated and distorted with a bright, detached, compact component at one end. The galaxy shows [O II], emission and also absorption lines typical of early stellar population which are easily visible to H $_{13}$. Its redshift is cz = 14700 kms^{-1} or about 4800 kms^{-1} greater than that of 3C120 (H. Arp, unpublished observations). In this sense it is typical of companion galaxies which have intrinsic redshifts with respect to the central galaxy in their group. This peculiar companion lies more or less directly in the radio material coming out of 3C 120 to the NNW (Fig. 3). I would suggest that this peculiar companion is a relatively young galaxy which has been ejected from 3C120 (Arp 1978; 1986a, b).

4. Distribution of quasars around 3C120

In studying the distribution of high-redshift ($1.4 < z < 2.7$) quasars on the sky it was noticed that they were much more prevalent in that broad region of the sky which lay in the direction of R. A. $\simeq 0^h$ than a comparable sky area in the direction R. A. $\simeq 12^h$ (Arp 1983, Fig.20).Restricting consideration to radio-emitting quasars, for which measurements are most complete, showed that there existed an elongated concentration originating from the Local Group galaxy, M 33 (Arp 1984, see Fig. 1). In that same general area of the sky a subconcentration of quasars was also apparent at about the position of 3C120.

In 1972 it had been argued that 3C 120 was a member of the Local Group (Arp 1973, p. 55). These observations therefore supported the previous results that high-redshift quasars are relatively nearby, low-luminosity objects, and in particular that these high-redshift quasars are associated with two members of the Local Group, M 33 and 3C120.

In Fig. 4 of the present paper we show in detail how these quasars group around 3C120 within a 45° × 25° area. Quasars outside this redshift and flux range also show this concentration but the parameter range plotted in Fig. 4 shows it most clearly. Utilizing the area immediately around 3C120 that is pictured in Fig. 4 as the most appropriate control area we are enabled to make a simple estimate of the significance of the grouping:

We find all seven of these particular quasars within 10° of 3C120. This radius defines an area of about 0.28 of the pictured region. Each quasar if distributed at random within the pictured area would have a chance of 0.28 of falling this close to 3C 120. To have seven fall this close thus represents a chance, by accident, of only 1×10^{-4}. This simple calculation tells us the same thing a glance at Fig. 4 does—that these quasars clustered in the vicinity of 3C120 are extremely unlikely to occur by chance.

Another way of calculating the improbability of the concentration around 3C120 is to utilize the fact that the total area of the sky is about 40 times larger than the area

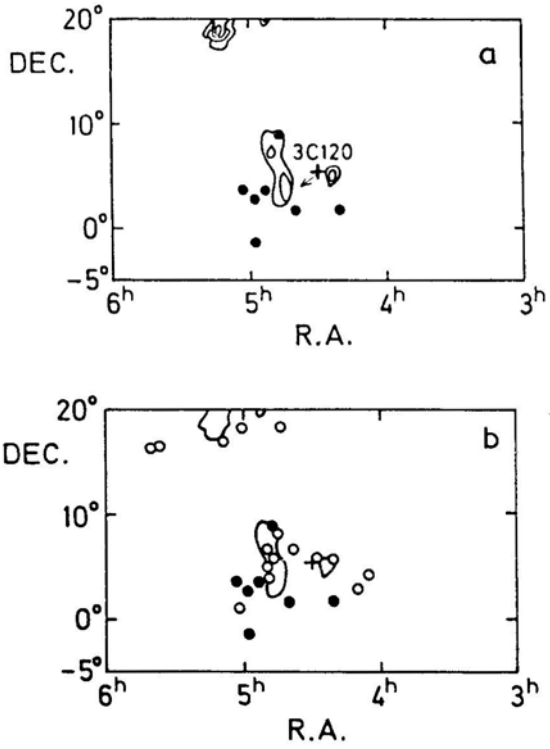

Figure 4. (a) Filled circles denote all quasars with $S_6 \geqslant 0.3$ and $z \geqslant 1.35$ from Catalog of Veron-Cetty & Veron (1984) within pictured area. Isocontours represent low-redshift hydrogen clouds measured by Meng & Kraus (1970). Arrow on 3C120 represents main ejection directions. See Section 5 in present paper, (b) Low-surface-brightness galaxies (LSB) with $4500 \leqslant cz_0 \leqslant 5300$ kms $^{-1}$ measured in survey of Bothun, Beers & Mould (1985) are indicated by open circles. Only outer isocontour lines of hydrogen clouds are shown.

pictured around 3C120 in Fig. 4. That would predict 280 such quasars over the whole sky (an overestimate for these kinds of quasars). To find a concentration of 7 such quasars within an area as small as the one of 10 degrees radius around 3C120 is a probability $P_{28O}(.007) \simeq 10^{-5}$.

It may also be noted that the concentration of radio sources around 3C 120 is conspicuous. Parkes sources in the ±4° zone and in the 4° < Dec. < 25° zone, particularly the quasar candidates, concentrate around 3C 120. The quasars listed in Table 1 and shown in Fig. 4 are a spectroscopically confirmed subset of these radio sources and quasar candidates.

5. Distribution of low-surface-brightness galaxies around 3C 120.

A recent survey of these kind of galaxies (called LSB) by Bothun, Beers & Mould (1985) shows a remarkable inhomogeneity on the sky for galaxies with redshifts $4500 < z < 5300$ km s^{-1}. This distribution is shown here in Fig. 5. In the roughly half of the sky toward the direction of the Local Group of galaxies there are 58 as against

Table 1. Quasars near 3C120 ($S_6 \geqslant 0.3, z \geqslant 1.35$).

QSO	S_6	V	z
PKS 0421 + 019	0.75	17.2	2.048
0442 + 02	0.32	20.0	1.43
0445 + 09	0.53	19.55	2.110
0454 + 039	0.43	16.53	1.345
0457 + 024	1.21	18.5	2.384
0458 − 02	1.65	19.5	2.286
0504 + 03	0.54	18.7	2.453

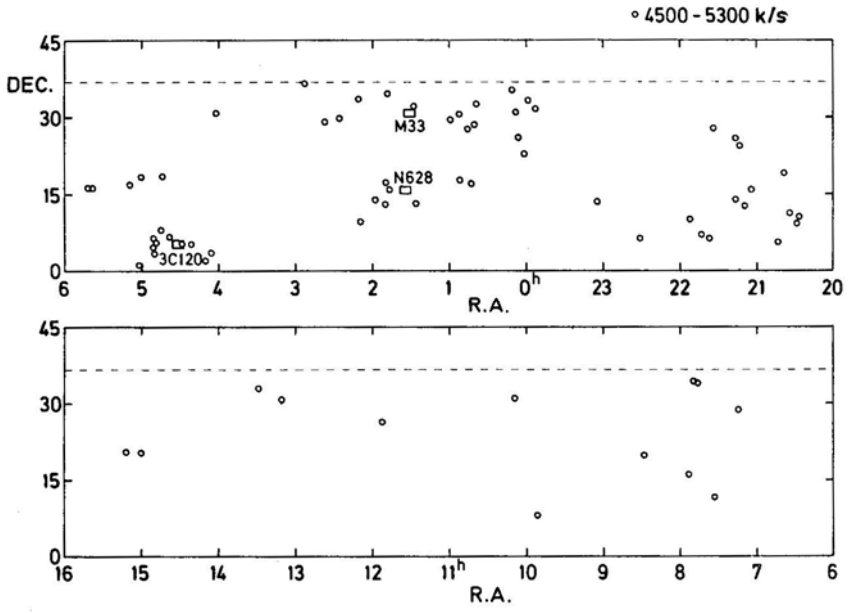

Figure 5. Open circles represent all low-surface-brightness (LSB) galaxies between redshifts $4500 < cz_0 < 5300$ km s^{-1} (from Bothun, Beers & Mould 1985). Horizontal dashed line represents northern limit of Arecibo radio telescope which was used to measure the galaxies.

only 13 in the opposite direction of the sky. In the Local Group direction these LSB galaxies group conspicuously around the bright apparent magnitude galaxies M 33 and NGC 628.

Again, as with the quasars, the imbalance between the R. A. = 0^h and R. A. = 12^h directions in the sky is aparent for broader ranges of redshift But for the particular range of redshift shown in Fig. 5 both the imbalance and the concentration around individual galaxies in the Local Group direction is most conspicuous. M 33, of course, is a traditionally important member of the Local Group of galaxies. NGC 628 has been argued to be a member of the Local Group (Arp 1986a; 1986b and the following paper in this Journal).

The tightest grouping of all, however, is almost exactly centred on 3C120. This is shown in Fig. 4b. Obviously these eleven galaxies must form a related cluster. But in the

entire sky surveyed (approximately 34 × 360°) there is no other LSB cluster this dense. The centre of the cluster falls apparently coincident with 3C120. If we were to assume the cluster centre was 1 degree different in position for calculational purposes, then the chance of such a proximity being accidential would be only $p = \pi \times 1° \times 1° /(34° \times 360°)=3 \times 10^{-4}$

The quasars and LSB galaxies near 3C 120 are listed here in Tables 1 and 2.

6. Hydrogen clouds near 3C120

Many hydrogen clouds have been measured over the sky, principally by the Dutch observers (Hulsbosch 1983). These so-called 'high velocity' clouds have been considered principally as falling into our own Galaxy (Oort 1970), or as distributed throughout the Local Group galaxies (Verschuur 1973; Arp 1985). Two such clouds were discovered very near to 3C 120 by Meng & Kraus (1970). They are indicated by contour lines in Figs 4a and 4b. Hydrogen of similar nature was seen to be associated with M 33 and the high-redshift quasars associated with M 33 (Arp 1985). Here we see the two hydrogen clouds on either side of 3C 120 which appear to be intermingled with the high-redshift quasars. In particular, these hydrogen-cloud outlines encompass the majority of LSB galaxies.

If we just fix our attention on the chance of two such clouds falling within 3° of 3C 120, within the pictured area there is a chance of $(0.025)^2 = 6 \times 10^{-4}$ of accidental occurrence. Again we obtain a very small probability. Moreover this does not take into account the positioning of the clouds on either side of 3C 120 as if they had been ejected. Neither does it take into account the apparent involvement of the clouds with LSB galaxies. We also see LSB galaxies apparently associated with Meng & Kraus H I clouds at the top of the frame in Figs 1a and 1b.

Fig. 6 shows a luminous, nebulous filament stretching about 3/4° across the sky to the north of 3C 120. The filament is strongest at its northern extremity, weakens as it traces southward, makes a bend just in the direction of 3C 120 and then stops, about 10 arcmin short of 3C120 as marked on the Schmidt exposure shown in Fig. 6.

Table 2. Low-Surface-Brightness (LSB) Galaxies near 3C 120 ($4500 \leqslant cz_0 \leqslant 5300$ km s^{-1}).

Galaxy	Position	Type	m_p	cz_0 km s^{-1}
UGC 2963	$04^h05^m +03°51$	Sc	15.3	5265
2983	04 10 +02 14	Sb	15.3	4957
3025	04 21 +05 28	Sd − m	16.0:	4947
3066	04 28 +05 26	Sc/SBc	15.0	4594
3122	04 37 +06 57	SBc	14.8	4653
3162	04 44 +08 13	Sc	16.0	4596
3181	04 48 +05 55	SBb	14.5	4555
3184	04 49 +05 23	S:	16.0:	4498
3186	04 49 +03 35	Sc	16.0:	4505
3187	04 49 +06 45	Sc	15.7	4677
3231	05 00 +00 10	Sc	14.9	4751

It is not known whether this filament contains line emission or reflection or possibly even continuum radiation. The radio material ejected from 3C 120 extends out about 3 arcmin in the approximate direction of this filament. As one approaches very small scales in the interior of 3C 120 the direction of radio ejection rotates rapidly clockwise until one encounters the innermost, supposedly superluminal ejections. It is possible that all this material, including the extended luminous filament pictured in Fig. 1b is a result of directed ejection from 3C120.

7. Discussion

We have seen that a number of different kinds of objects are grouped around 3C120: quasars, low-surface-brightness galaxies. hydrogen clouds and optical filaments. The scale of this grouping, however, is from a few degrees to almost twenty, indicating that all these objects are relatively close to us in extragalactic terms. Some of the same kinds of objects are also grouped around the relatively nearby galaxies M 33 and NGC 628. If we therefore assign a Local Group distance of the order of 1 Mpc to 3C 120 we can compute that the apparent faster-than-light expansions reduce to expansions of ~ 12000 km s^{-1}. This is quite a reasonable velocity of ejection as observed in galaxies whose distances are much more certain.

When apparent superluminal expansions were first discovered in 3C 120 an obvious conclusion would have been that since 3C 120 was so similar to a quasar, that this was another proof that quasars were closer than their redshift distances. At that time, however, an opposite line of reasoning was quickly employed, one that has had long lasting consequences. It was argued that since photographs showed 3C 120 to be a galaxy (at least not an unresolved point source like most quasars at that time), and that all galaxies must be at their redshift distance, that 3C120 had to be at its redshift distance. * It was argued further that this somehow negated other evidence that quasars were closer (M. H. Cohen *et al.* 1977 and personal communication at the time). This latter interpretation inevitably required models involving highly relativistic mass ejection directed at special angles to the observer. In the case of 3C 120 the ejection had to be directed so closely at the observer that there was only a small chance of this happening by accident (Blandford & Königl 1979; M. H. Cohen *et al.* 1979). Yet, as the first section on image processing in this paper reaffirms, 3C 120 is optically such a unique object that it was obvious that this was not likely to be the one member of a large class of objects which happened to have its radio jet pointed toward the observer.

Since it was a unique object it was also obvious that there was no way it could define a Hubble relation. Therefore there was no basis at all for assigning a distance to it. The only evidence as to its distance which could have been adduced was to find other associated objects around it. But a cluster or group of galaxies at cz = 10000 kms^{-1}, the redshift of 3C 120, would have been very conspicuous. Direct photographs showed none. Since galaxies are not isolated (Vettolani, de Souza & Chincarini 1985; Arp 1986a), this in fact, was another piece of evidence that 3C 120 was not at its redshift distance.

* Spectroscopic analysis of 3C 120 led Baldwin *et al.* (1980) to state ". . . it is interesting to note that the widths of the absorption features suggest a smaller velocity dispersion in the disk of 3C 120 than in M 81". But small velocity dispersions of the constituent stars is customarily taken to indicate low luminosity. If 3C 120 were at its redshift distance it could not have low luminosity.

It turns out that objects are actually clumped around 3C 120 on the sky. But they are distributed on a large scale which indicates closer distance than does the 3C 120 redshift and with a wide range of redshifts which requires that the redshifts in this group of objects are not good indicators of distance.

The origin of the various kinds of objects surrounding 3C 120 is difficult to explain on conventional hypothesis of condensation from a diffuse medium. But the evidence for ejection from 3C 120 is very strong. Therefore it is obviously implied that at least some of these surrounding objects originated from ejections within 3C 120, and perhaps the whole ensemble from some nearby low-redshift member of the Local Group. There is considerable supporting evidence from other galaxies that objects of varying amount of redshift arise from ejection processes in active galaxies (see Arp 1978).

Regardless of their origin, however, it is clear that the probabilities of 1×10^{-4}, 3×10^{-4}, and 6×10^{-4} are already individually conclusive. When multiplied together they give a vanishingly small chance of accidental association for these objects of various redshifts. It will be immediately objected that this is an *α posteriori* calculation. But is it *a posteriori*? The identification of 3C 120 as the brightest superluminal object in the sky marked this as a unique centre of interest. It was then found that not objects of similar redshift, but objects of dissimilar redshift clustered around it. Abundant previous evidence for associations of discordant redshift objects has been compiled and these previous cases therefore predict that other cases like the present ones should occur. 3C 120 had been predicted to be Local Group object in 1972 and now further objects identified as Local Group are found around it.

The final, inescapable conclusion of the matter is that if the association of these objects of diverse redshift around 3C 120 is not accidental, but is continued to be believed accidental, then extragalactic research projects will continue to be initiated on, and interpreted in, the light of a fundamental but drastically incorrect assumption.

Acknowledgement

I would like to thank H. C. Thomas for helpful suggestions on the calculation of some of the probabilities involved in the grouping of quasars.

References

Arp, H. 1968, *Astrophys. J.,* **152,** 1101.
Arp, H. 1973, *The Redshift Controversy,* Ed. G. B. Field, W. A. Benjamin, Massachusetts.
Arp, H. 1978, *Problems of Physics and Evolution of the Universe,* Ed. V. L. Mirzoyan, Armenian Acad. Sci., Yerevan, p. 65
Arp, H. 1981, in *Proc. second ESO/ESA Workshop*: *Optical Jets in Galaxies,* ESA, Netherlands, p. 53.
Arp, H. 1983, in *Groups, Concentrations and Associations of Quasars,* Institut d'Astrophysique Univ. Liege, p. 307.
Arp. H. 1984, *J. Astrophys. Astr.,* **5,** 31.
Arp, H. 1985, *Astr. J.,* **90,** 1012.
Arp. H. 1986a, *Preprint,* MPA 236.
Arp. H. 1986b, in IAU Symp. 124: *Observational Cosmology,* Eds A. Hewitt, G. Burbidge & Li Zhi Fang, D. Reidel, Dordrecht, MPA 265.

Arp, H. Lorre, J. 1976, *Astrophys. J.*, **210,** 58.
Baldwin, J. A., Carswell, R. F., Wampler, E. J., Smith, H. E., Burbidge, E. M., Boksenberg, A. 1980, *Astrophys, J.,* **236,** 388.
Blandford, R. D., Königl, A. 1979, *Astrophys. J.,* **232,** 34.
Bothun, G. D., Beers, T. C., Mould, J. R. 1985, *Astr. J.,* **90,** 2487.
Cohen, M. H. *et al.* 1977, *Nature* 268**,** 405.
Cohen, M. H., Pearson, T. J., Readhead, A. C. S., Seielstad, G. A., Simon, R. S., Walker, R. C. 1979, *Astrophys. J.,* **231,** 293.
Hulsbosch, A. 1983, Annual Rep. Netherlands Foundation for Radio Astronomy.
Meng, S. Y., Kraus, J. D. 1970, *Astr. J.,* **75,** 535.
Oort, J. H. 1970, *Astr. Astrophys.,* **7,** 381.
Seielstad, G. A., Cohen, M. H., Linfield, R. P. Moffet, A. T., Romney, J. D., Schilizzi, R. T., Shaffer, D. B., 1979, *Astrophys. J.,* **229**, 53.
Veron-Cetty, M.-P., Veron, P. 1984, *A Catalog of Quasars and Active Nuclei,* ESO Sci. Rep. No. 1.
Verschuur, G. L. 1973, *Astr. Astrophys.,* **22,** 139.
Vettolani, G., de Souza, Chincarini, G. 1985, *ESO Preprint,* No. 388.
Walker, R. C. 1984, in *Proc. NRAO Workshop No.* 9: *Physics of Energy Transport in Extragalactic Radio Sources,* Eds H. H. Bridle & Jo Eilek, NRAO, Green Bank, p. 20.
Wlerick, G. 1981, in *Proc. second ESO/ESA* Workshop: *Optical Jets in Galaxies,* ESA, Netherlands, 1129.

J. Astrophys. Astr. (1987) **8,** 241–255

Additional Members of the Local Group of Galaxies and Quantized Redshifts within the Two Nearest Groups

Halton Arp *Max-Planck-Instiut für Physik und Astrophysik, Institut für Astrophysik, Karl-Schwarzschild-Str. 1, 8046 Garching bei München, FRG*

Received 1986 November 7; accepted 1987 May 6

Abstract. Galaxies of redshift $z \lesssim 1000$ km s^{-1} are investigated. In the South Galactic Hemisphere there are two large concentrations of these galaxies. One is in the direction of the centre of the Local Group, roughly aligned with M 31 and M 33. The other concentration is centred almost 80 degrees away on the sky and involves the next nearest galaxies to the Local Group, NGC 55, NGC 300 and NGC 253.

The large scale and isolation of these concentrations, and the continuity of their redshifts require that they are all galaxies at the same, relatively close distance of the brightest group members. The fainter members of the group have higher redshifts, mimicking to some extent a Hubble relation. But if they are all at the same average distance the higher redshifts must be due to a cause other than velocity.

The redshifts of the galaxies in the central areas of these groups all obey a quantization interval of $\Delta cz_0 = 72.4$ kms^{-1} . This is the same quantization found by William Tifft, and later by others, in all physical groups and pairs which have been tested. The quantization discovered here, however, extends over a larger interval in redshift than heretofore encountered.

The majority of redshifts used in the present analysis are accurate to ± 8 km s^{-1} . The deviation of those redshifts from multiples of 72.4 km s^{-1} averages ±8.2 km s^{-1}. The astonishing result, however, is that for those redshifts which are known more accurately, the deviation from modulo 72.4 drops to a value between 3 and 4 km s^{-1}! The amount of relative velocity allowed these galaxies is therefore implied to be less than this extremely small value.

Key words: redshifts, quantization—galaxies, Local Group—galaxies, Sculptor Group

1. Introduction

The Local Group, being the closest group to us in space, includes the galaxies we know the most about. However, one strange aspect of the Local Group has emerged over the last decades. That is, with the commonly accepted membership, Local Group galaxies only exhibit a range in redshift of a little over 200 km s^{-1} [cz_0 (M 31) = – 86 to cz_0 (NGC404) = + 142 km s^{-1}]. Other groups of galaxies characteristically exhibit

redshift ranges of 800 km s^{-1} or more. (Jaakkola & Moles 1976; Arp 1982, Fig. 1; Huchra & Geller 1982; Sulentic 1984; Arp & Sulentic 1985; Arp 1986b).

Where are those additional Local Group members which should be present? In order to know where to look we note that in all other groups the less luminous galaxies tend to have the higher redshifts. This is strongly true even within the restricted redshift range of the conventional Local Group. Therefore we would naturally look for the additional members among fainter, higher redshift galaxies. It is clear in any case that no lower redshifts are known which could be candidates for the additional members. Even galaxies with redshifts appreciably higher than cz_0 = 142 km s^{-1} are very scarce. We will therefore see that it is easy to distinguish them from more distant background galaxies.

We make the same kind of analysis of the next nearest group to us in space, the Sculptor Group, and find confirmatory results. Finally we investigate quantization in the redshifts of the galaxies in these groups.

2. Distribution of galaxies with $cz_0 < 1000$ kms^{-1} in South Galactic Hemisphere

Table 1 lists all the galaxies known to the author between 17^h < R. A. < 5^h. They have been gathered from two sources:

1) The Revised Shapley Ames Catalog (RSA) by Sandage & Tamman (1981).
2) The Rood Catalog (1980), (H. J. Rood, personal communication).

The RSA lists all galaxies brighter than about apparent magnitude 13 and therefore galaxies likely to have the kind of low redshifts we are considering. The Rood Catalog includes the hydrogen line surveys that detect low redshift galaxies to extremely faint apparent magnitudes (particularly the Fisher-Tully surveys). If any additional galaxies turn up in this redshift range in the future they are likely not to have hydrogen and therefore likely not to have redshifts measurable to a sufficient accuracy for the uses of most of the present analysis.

2.1 *Additional Members of the Local Group of Galaxies*

The filled symbols in Fig. 1 represent the traditional members that make up the Local Group. Also plotted in the figure are all the galaxies known in the pictured area which have redshifts slightly above the redshifts of the presently accepted group members. It is clear that the eight additional galaxies with 300 < cz_0 < 600 km s^{-1} show a conspicuous concentration just in the Local Group direction.

It would be an unlikely coincidence if a background cluster of galaxies accidentally occurred in this exact region of sky. Moreover we will see that the kinds of galaxies involved are not like those in conventional, more distant clusters. Finally we shall see that this concentration consists of galaxies with not one characteristic redshift. Instead it is made up of a range of redshifts running from the value accepted for members of the Local Group to the $\Delta cz_0 \simeq$ 800 km s^{-1} or more that we would expect to be included in a normal group.

Table 1. Galaxies with cz_0 < 1000 km s^{-1} 17^h < R. A. < 5^h (corrected for solar motion of $\Delta v = 251 \sin l \cos b - 20 \cos l \cos b - 5 \sin b$).

Galaxy		R.A. h	R.A. m	Dec. °		cz km s^{-1}	Δv km s^{-1}	cz_0 km s^{-1}
UGC	10669	17	00.7	+70	22	440 ± 8	203	643
	10736	17	08.4	69	33	491 ± 8	204	695
	11000	17	47.7	36	09	300 ± 167		
NGC	6689	18	35.4	70	29	487 ± 8	221	708
	6946	20	33.8	59	59	48 ± 2	246	294
DDO	210	20	44.2	−13	02	−132 ± 8	(150)	(18)
UGC	11891	22	01.5	43	30	461 ± 8	249	710
IC	5201	22	18.3	−46	19	(915 ± 8)	−32	883
DDO	215	22	36.5	−5	02	829 ± 8	(117)	946
NGC	7424	22	54.5	−41	21	951 ± 8	−15	936
	7412 A	22	54.3	−43	05	938 ± 8	−15	923
	7457	22	58.6	29	53	525 ± 90		
NGC	7640	23	19.7	40	34	368 ± 7	236	604
UGC	12588	23	22.3	41	04	425 ± 8	235	660
—		23	24.2	−37	37	690 ± 8	(−4)	(686)
DDO	216	23	26.0	14	28	−178 ± 8	186	8
DDO	217	23	27.6	40	43	424 ± 8	234	658
IC	5332	23	31.8	−36	22	707 ± 8	−2	705
NGC	7713	23	33.6	−38	13	698 ± 8	−15	683
UGC	12713	23	35.7	30	26	289 ± 8	218	507
	12732	23	38.1	25	57	756 ± 8	209	965
—		23	41.4	−32	15	267 ± 8	(17)	(284)
NGC	7741	23	41.4	25	48	750 ± 8	208	958
	7793	23	55.3	−32	51	217 ± 8[a]	5	222
UGC	12894	23	57.9	39	14	339 ± 8	224	563
DDO	221	23	59.2	−15	45	−124 ± 8	(80)	−44
NGC	24	00	07.4	−25	15	561 ± 8	22	583
	45	00	11.4	−23	27	463 ± 3	37	500
	55	00	12.4	−39	28	129 ± 3	−28	101
IC	10	00	17.6	59	02	−348 ± 8		
UGC	290	00	26.5	15	37	763 ± 23	166	929
NGC	147	00	30.5	48	14	−168 ± 10[b]	222	54
NGC	185	00	36.2	48	04	−208 ± 10[b]	220	12
NGC	205	00	37.6	41	25	−239 ± 11	213	−26
M	32	00	40.0	40	36	−200 ± 6	211	11
M	31	00	40.0	41	00	−297 ± 0.4	211	−86
IC	1574	00	40.7	−22	31	361 ± 8	31	392
NGC	247	00	44.6	−21	01	156 ± 4	31	187
	253	00	45.8	−25	34	245 ± 5	14	259
DDO	6	00	47.4	−21	16	303 ± 8	31	334
NGC	278	00	49.2	47	17	640 ± 8	215	855
NGC	300	00	52.2	−37	57	145 ± 2	− 37	108
IC	1613	01	02.4	01	53	−238 ± 90		
UGC	672	01	03.3	44	43	712 ± 8	207	919
NGC	404	01	06.7	35	27	−50 ± 10	192	142
DDO	9	01	07.7	49	20	639 ± 8	215	854
DDO	10	01	18.6	12	09	646 ± 8	129	775
M	33	01	31.1	30	24	−180 ± 0.5	−170	−10
NGC	625	01	32.9	−41	40	404 ± 8	−68	336
NGC	628	01	34.0	15	32	656 ± 2	130	786

Table 1. Contined.

Galaxy		R.A. h	R.A. m	Dec. °	Dec. ′	cz km s^{-1}	Δv km s^{-1}	cz_0 km s^{-1}
DDO	13	01	37.5	15	39	634 ± 8	128	762
UGC	1195	01	39.7	13	43	767 ± 8	122	889
NGC	660	01	40.3	13	23	856 ± 8	120	976
—		01	40.6	19	44	501 ± 8	134	635
A	143	01	42.9	−43	50	394 ± 8	(−86)	326
IC	1727	01	44.7	27	05	339 ± 8	155	494
NGC	672	01	45.0	27	11	413 ± 6	155	568
UGC	1281	01	46.7	32	20	163 ± 8	163	326
NGC	746	01	54.8	44	41	712 ± 8	185	897
	784	01	58.4	28	35	201 ± 8	158	359
UGC	1561	02	01.3	23	58	595 ± 8	126	721
	1807	02	18.0	42	32	631 ± 8	170	801
NGC	891	02	19.3	42	07	530 ± 4	169	699
DDO	19	02	21.9	35	49	577 ± 8	154	731
NGC	925	02	24.3	33	22	554 ± 8	148	702
	949	02	27.8	36	55	610 ± 8	154	764
	959	02	29.3	35	17	609 ± 8	149	758
DDO	22	02	29.8	38	28	570 ± 8	156	726
DDO	25	02	30.3	33	17	611 ± 8	144	755
DDO	24	02	30.6	40	19	581 ± 8	160	741
UGC	2082	02	33.4	25	13	710 ± 8	121	831
NGC	1003	02	36.1	40	40	626 ± 8	158	784
NGC	1023	02	37.2	38	51	(600 ± 16)	153	753
	1036	02	37.6	19	05	(787 ± 27)	101	888
	1058	02	40.2	37	08	520 ± 8	148	668
UGC	2259	02	44.8	37	20	589 ± 8	146	735
	2432	02	54.8	09	55	762 ± ?	61	823
NGC	1156	02	56.8	25	03	374 ± 8	106	480
NGC	1291	03	15.5	−41	19	839 ± 4	−118	721
UGC	2684	03	17.7	17	08	357 ± 8	64	426
NGC	1343 pec	03	32.4	72	24	300 ± 114		
IC	342 Sc	03	42.0	67	57	25 ± 8	178	203
—		03	55.0	66	59	72 ± 8	176	248
NGC	1493	03	55.9	−46	21	1059 ± 8	−150	909
	1507	04	01.9	−02	19	864 ± 8	−27	837
	1512	04	02.3	−43	29	911 ± 8	−147	764
	1569 Irr	04	26.1	64	45	−90 ± 8	161	71
	1560 Sdm	04	27.1	71	48	−28 ± 8	173	145
—	—	04	27.4	63	30	−104 ± 8	(161)	57
NGC	1637	04	38.9	−2	56	726 ± 8	−54	672
DDO	34	04	46.0	0	09	669 ± 8	−48	621
NGC	1679	04	48.1	−32	04	1059 ± 8	(−155)	904
IC	396	04	52.8	68	14	762 ± 137		
NGC	1744	04	57.9	−26	06	742 ± 8	−136	606

[a] Redshifts marked thus, or with less than + 8 km s^{-1} estimated error have been taken from RSA (Sandage & Tamman 1981)

[b] Redshifts taken from Ford, Jacoby & Jenner (1977) but there is a systematic uncertainty of 10 km s^{-1} in their measures. RSA values for v_0 give Δz_0 (N 147) = 148 and Δcz_0 (N185) = 79. In view of value given in RSA. NGC 185 particularly should be remeasured as accurately as possible.

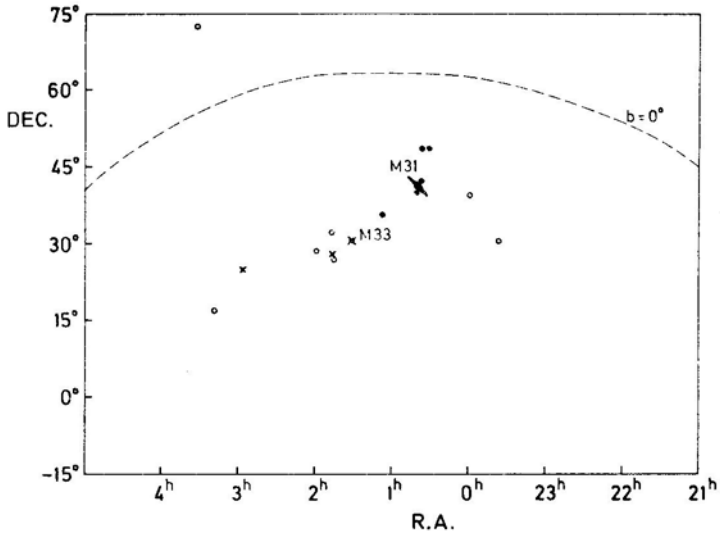

Figure 1. Conventional members of the Local Group (—86 ⩽ cz_0 ⩽ 142 km s^{-1}) are plotted as filled symbols (IC 10 and IC 1613 omitted). Open symbols (dwarfs) and crosses (spirals) represent galaxies from Table 1 which have slightly higher redshifts 300 < cz_0 < 600 kms^{-1}.

2.2 *The M 31–M 33 Line*

Additional confirmation that these higher redshift galaxies belong to the Local Group is evident from their linear distribution on the sky, an alignment which coincides very closely with the distribution of the Local Group members. The alignment of the traditionally accepted Local Group members can be seen from the fact that generally along the minor axis direction from M 31 are distributed the smaller companion members in the Local Group: NGC 147, 185, 205, 221, 404, 598, dwarf spheroidals and peculiar H I clouds (Arp 1987). The coincidence of a background cluster being this elongated and also accidentally this well positioned and aligned with the accepted Local Group would seem to be very small.

2.3 *Testing the Redshift Range of the Members*

Fig. 2 plots all the galaxies in the pictured region which have redshifts cz_0 < 940 k m s^{-1} (with the exception of IC 10 and IC 1613 which are probably very close to our own Milky Way galaxy). We see there is a tight group at high northern declinations, the NGC 1569–IC 342 group, but in addition, more galaxies in this higher redshift range which are concentrated in the general direction of the Local Group and the M 31–M 33 line.

In Fig. 2 we have outlined an elongated region, slightly larger around M 31 and narrowing slightly along a line through M 33 and to the southeast. In the following Section 3 we show that this area contains galaxies with the most significant redshift quantization. But here we simply justify it as the densest area of galaxies in the investigated redshift range (excluding the tight group around NGC 891).

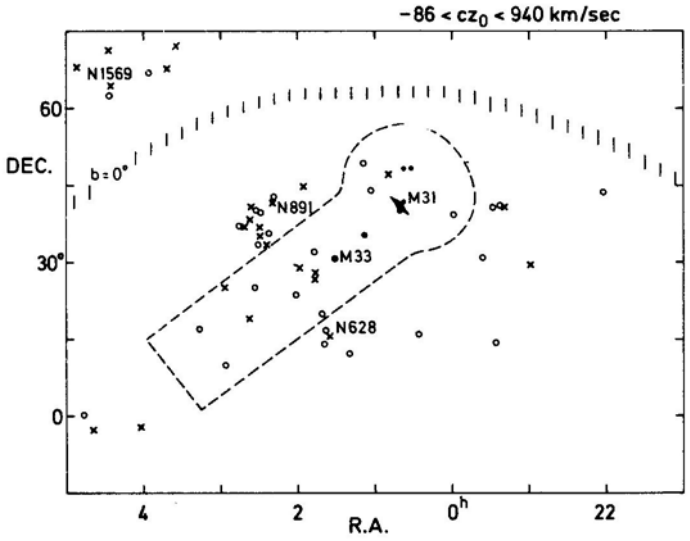

Figure 2. All galaxies with $-86 < cz_0 < 940$ km s^{-1} as listed in Table 1. Symbols are the same as in Fig. 1 except that crosses now represent NGC and IC galaxies, open circles fainter galaxies. Region inside dashed contour is used to test Local Group membership in Fig. 3a and quantization in Fig. 5a.

For the galaxies in this line we now plot Fig. 3a. We see their redshifts are rather evenly spread between $0 < cz_0 < 900$ km s^{-1}. On the hypothesis that this concentrate-ion of galaxies on the sky represented a background group accidentally falling behind the Local Group centre we would expect a peak of redshifts corresponding to that greater distance. Instead we see an even filling in between galaxies of the accepted Local Group redshift and the expected range of a single group membership.

In Fig. 3 the dashed curve shows how numbers of galaxies should increase if they were homogeneously spread through space. The volume sampled should increase as

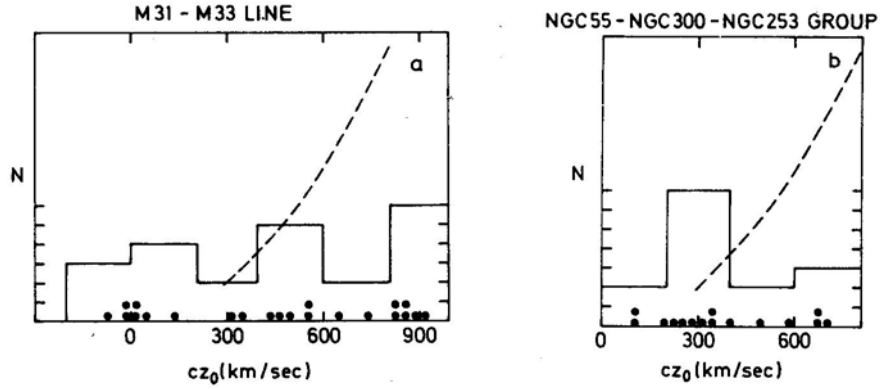

Figure 3. Numbers of galaxies as a function of redshift within Local and Sculptor Groups. a) Within dashed boundary in Fig. 2. b) Within dashed boundary in Fig. 4. Dashed curve illustrates how $N \propto z^3$ (or, in this case how $dN \propto z^2$) would appear.

the cube of the redshift on the redshift-distance assumption. But the observed histograms rule out the possibility that the pictured differential counts increase as z^2. Therefore we conclude that the concentration of galaxies that we see in Figs 1 and 2 is for the most part physically associated with the Local Group and represents the expected range of redshift membership in a group of about $0 \lesssim cz_0 \lesssim 900$ km s^{-1}.

2.4 *Comment on the Hubble Relation*

Table 2 lists the individual galaxies which are considered here to be members of the M 31–M 33 line. It is clear that the fainter galaxies have generally higher redshifts. In this sense they obey a Hubble relation. But if these intrinsically higher redshift galaxies are actually intrinsically less luminous they would still mimic a distance-redshift relation even though all at the same distance. This is unquestionably the case in the galaxies classically considered members of the Local Group ($-86 \leqslant cz_0 \leqslant 142$ km s^{-1}). Those companions define a quite accurate $cz_0 \propto 5 \log m$. relation even though they are all at the same distance (Arp 1987). The fainter members included here in the Local Group could follow a loose Hubble relation until apparent magnitude $\simeq$ 14. Fainter than this the galaxies deviate strongly below a linear Hubble relation. Usually a deviation from a Hubble line is interpreted as a deviation in luminosity. But in fact what it means is that these objects do not themselves define a

Table 2. Galaxies in M 31–M 33 line with $-86 < cz_0 < 1000$ km s^{-1}.

Galaxy	R.A.	Dec.	cz_0[a]	Relative to M 31 Δcz_0	Mod 72.4	mag.	Type
UGC 12894	23 57.9	39 14	563 ± 8	649	9–3	17	Irr v
NGC 147	00 30.5	48 14	54 ± 10[b]	140	2–5	9.96	dE5
NGC 185	00 36.2	48 04	12 ± 10[b]	98	1 + 26	9.73	dE3 pec
NGC 205	00 37.6	41 25	-26 ± 11	60	1–12	8.60	S0/E5 pec
M 32	00 40.0	40 36	11 ± 6	97	1 + 25	8.79	E2
M 31	00 40.0	41 00	-86 ± 0.4	0	reference	3.12	Sb I-II
NGC 278	00 49.2	47 17	855 ± 8	941	13–0	10.85	Sbc II
UGC 672	01 03.3	44 43	919 ± 8	1005	14–9	18	Irr v
NGC 404	01 06.7	35 27	142 ± 10	228	3 + 11	10.96	SO pec
DDO 9	01 07.7	49 20	854 ± 8	940	13–1	17	Irr v
M 33	01 31.1	30 24	-10 ± 0.5	76	1 + 4	5.6	Sc II-III
—	01 40.6	19 44	635 ± 8	721	10–3		Fisher–Tully dwarf
IC 1727	01 44.7	27 05	494 ± 8	580	8 + 4	12.2	Irr I
NGC 672	01 45.0	27 11	568 ± 6	654	9 + 2	10.69	SBc III
UGC 1281	01 46.7	32 20	326 ± 8	412	6–22	13.0	S IV:
NGC 784	01 58.4	28 35	359 ± 8	445	6 + 10	12.1	S dm
UGC 1561	02 01.3	23 58	721 ± 8	807	11 + 11	14.7	Irr I
UGC 2082	02 33.4	25 13	831 ± 8	917	13–24	14.0	Sc
NGC 1036	02 37.6	19 05	888 ± 27			13.5	pec Mark 370
UGC 2432	02 54.8	09 55	$823 \pm ?$			17	S v
NGC 1156	02 56.8	25 03	480 ± 8	566	8–13	11.92	Sm V-IV
UGC 2684	03 17.7	17 08	426 ± 8	512	7 + 5	18–19	dwarf?
NGC 628[c]	01 34.0	15 32	786 ± 2	872	12 ± 3	9.43	Sc I

[a] Values with errors less than ± 8 km s^{-1} have been taken from RSA.
[b] see note to Table 1.
[c] Slightly outside slot in Fig. 1 but predicted to be Local Group member (Arp 1986a).

Hubble line and therefore there is no evidence that these particular galaxies are in fact at their redshift distance.

In Table 2 the morphological types of the galaxies in the M 31–M 33 lines are listed. It is evident that they are almost entirely late type spirals or low surface brightness irregulars. This is not the morphological composition of a normal galaxy cluster. Moreover it is just these kinds of galaxies which have been shown to violate redshift-distance relations because of their intrinsic redshifts (Arp 1986b). In general, the one kind of galaxy for which we have some evidence that a true redshift–distance relationship is obeyed, is Hubble type Sb (like M 31 and M 81). This class is completely unrepresented among the higher redshift members of the M 31–M 33 line.

2.5 *The NGC 55–NGC 300–NGC 253 Group*

Fig. 4 shows a plot in the sky at southern declinations of the galaxies from Table 1 in the redshift interval $100 < cz_0 < 800$ km s^{-1}. This region of the sky includes the well-known Sculptor group of three bright Sc galaxies. Again we see that of all the area possible inside the frame only the region just in the direction of these bright Sculptor spirals is populated by fainter galaxies. As was true of the Local Group, there should be fainter members of the group, and here are the only possible candidates. The Sculptor Group is about 3 times more distant than M 31 and the Local Group, and its apparent diameter on the sky is about 3 times smaller.

Fig. 3b shows the same situation pertains as in the Local Group. The redshifts of the fainter galaxies are not clumped at any particular value but spread evenly between those of the brightest and faintest members. Therefore we see that the Local Group and the next nearest group to us, the Sculptor Group both agree in having companions that range from 700 to 900 km s^{-1} higher redshift than the dominant galaxies in the group.

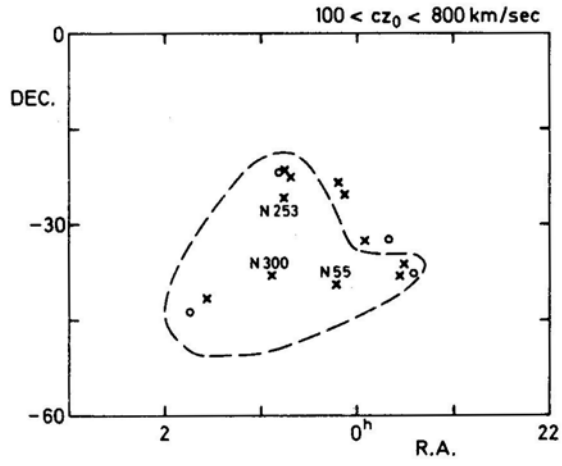

Figure 4. All galaxies in indicated redshift range in Sculptor region of sky. Symbols are as in Fig. 2.

3. Quantization of redshifts

It was shown originally that Local Group galaxies had redshifts quantized in units of 72 km s $^{-1}$ (Tifft 1977). More recently it was shown that the most accurate update of redshifts of companion galaxies in both the traditionally accepted M 31 and M 81 groups were significantly grouped into multiples of 72.4 km s $^{-1}$ (Arp 1986a). In order to demonstrate this quantization a correction for solar motion had to be derived and applied which was more accurate than the correction customarily used. (This correction is principally galactic rotation of the Sun around our galactic centre plus a small component of peculiar motion of our Galaxy.) Particularly for members of groups which are seen in appreciably different directions on the sky, the correction must be very exact or it will degrade any existing quantization of relative redshifts between galaxies.

Therefore in Table 1 all measured redshifts of galaxies, *cz*, have been corrected by the more accurate formula in the beginning of the table to obtain redshifts relative to the mean of Local Group galaxies, the quantity called cz_0 (see Arp 1986a for derivation of new correction formula). For the Local Group galaxies, Table 2 adds the measured redshift of M 31 (86 km s $^{-1}$) to all values of cz_0 to give relative redshifts of the remaining galaxies with respect to M 31.

3.1 *The M31–M33 Line*

Table 2 also lists, for all the galaxies within the area outlined by dashes in Fig. 2, what their relative redshifts are with respect to M 31 in multiples of 72.4 km s $^{-1}$. It is seen that these differential redshifts range all the way from one multiple of 72.4 up to almost 14 multiples. But there is remarkably small deviation from the predicted modulo 72.4! Consider that if the data had no tendency to be quantized, the residuals from mod 72.4 km s $^{-1}$ would be randomly spread between + 36 km s $^{-1}$ and – 36 km s $^{-1}$.

Fig. 5a shows that those 13 companions within the outlined area of Fig. 2 that have redshifts which are 6 to 14 multiples of 72.4, are with but two exceptions accurately quantized. A very nonrandom concentration of points appears near Δcz_0 (mod 72.4) = 0. A crude test of the probability of accidentally finding a concentration of 11 out of 13 Δz's within ± 14 km s^{-1} of $\Delta z = 0$, as pictured in Fig. 5a, is $^{11}P_{13}$ (14/36) $\lesssim$ 10^{-3}. Perhaps even more impressive is the fact that Fig. 5 shows that the majority of points fall within + 8 km s $^{-1}$ of the multiples of 72.4 km s $^{-1}$. But ± 8 km s^{-1} is the accuracy of the measured redshifts so they could not average any closer than this. Extensive power spectrum analyses of periodicities in these data are being performed by W. Napier, B. Guthrie & B. Napier (Royal Observatory Edinburgh).*

In Fig. 5a the lower redshift, traditional members of the Local Group have not been plotted. The reason is that these have already been demonstrated to obey a 72.4 km s $^{-1}$ periodicity (Arp 1985). In fact this is where the more accurate value of 72.4 was derived rather than the previously used value of 72. The important aspect of Fig. 5a is that *the additional* members of the Local Group identified in Fig. 2 and Table 2 *independently* confirm exactly the same value of quantization as the original Local Group members.

*See report in "New Ideas in Astronomy", Istituto Veneto di Scienza, Venice, 5–7 May 1987, Eds F. Bertola, B. Madore & J. W, Sulentic.

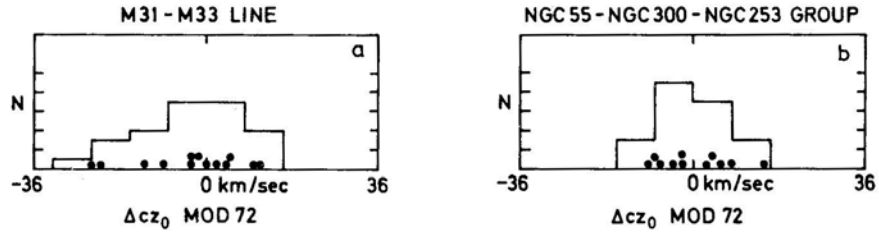

Figure 5. Distribution of residuals from modulus 72.4 km s^{-1} for: a) Galaxies with accuracy ±8 km s^{-1} or better from Table 2. b) Galaxies inside dashed contour in Fig. 4, also listed in Table 3.

3.2 *The NGC 55–NGC 300–NGC 253 Group*

Table 3 extracts the data on the galaxies pictured in Fig. 4. The mod 72.4 column shows that these Sculptor galaxies are generally shifted in zero point with respect to M 31. But this is to be expected since the Sculptor Group is a separate group from the Local Group and it would be expected that there might be some peculiar motion between the groups, or offset in zero point between the redshift of the two groups. For now we will consider the Sculptor group to be approaching the Local Group with a velocity of – 34 km s^{-1}. Adding this velocity to all the Sculptor Group galaxies gives the values listed finally in Table 3. Fig. 5b shows the Sculptor galaxies now have redshifts with only one exception within + 9 km s^{-1} of modulo 72.4 km s^{-1}.

A dashed line in Fig. 4 outlines a contiguous area within which all the galaxies obey the modulo 72.4 law. Four galaxies are excluded on the edge of this area which have a different zero point for their redshifts. They are excluded from Fig. 5b and listed at the end of Table 3. These four are perfectly quantized with respect to our own Local Group without any correction of 34 km s^{-1}. It is not known what significance, if any, this fact has.

Table 3. Galaxies in NGC 55–NGC 300–NGC 253 group ($100 < cz_0 < 800$ km s^{-1}).

Galaxy		R.A.		Dec.		cz_0	Mod 72.4	+34 km s^{-1}	$B_T^{0,i}$	Type
—		23	24.2	−37	37	686±8	9+34	10–4		Fisher–Tully dwarf
IC	5332	23	31.8	−36	22	705±8	10–19	10+15	10.87	Sc II-III
NGC	7713	23	33.6	−38	13	683±8	9+13	10–7	11.08	Sc II-III
NGC	55	00	12.4	−39	28	101±3	1+29	2–9	7.35	Sc
IC	1574	00	40.7	−22	31	392±8	5+30	6–8		Irr
NGC	247	00	44.6	−21	01	187±4	3–30	3+4	8.88	Sc III-IV
NGC	253	00	45.1	−25	34	259±5	4–31	4+3	7.38	Sc
DDO	6	00	47.4	−21	16	334±8	5–28	5+6		dwarf
NGC	300	00	52.5	−37	57	108±2	1+36	2–2	8.31	Sc II
NGC	625	01	32.9	−41	40	336±8	5–26	5+8	11.91	Im III
A	143	01	42.9	−43	50	326±8	5–36	5–2	(13.1)	Irr
—		23	41.4	−32	15	284±8	4-6			Fisher–Tully dwarf
NGC	7793	23	55.3	−32	51	222±8	3+5		9.25	Sd IV
NGC	24	00	07.4	−25	15	583±8	8+4		11.35	Sc II-III
NGC	45	00	11.4	−23	27	500±3	7–7		11.69	Scd III

In order to test the significance of the quantization in the Sculptor Group we use the largest, low-redshift normal-appearing galaxy in the group, NGC 300, as a redshift reference. This is the same procedure as in the Local Group. Table 3 shows that 9 of the 14 remaining members fall within ± 10 km s $^{-1}$ of modulo 72.4. This gives a probability of $^{9}P_{14} = 4\times 10^{-3}$ that the remaining members would accidentally be quantized this closely with respect to NGC 300. Of course the small subgroup of four galaxies is very tightly grouped in Δz and in a very small area on the edge of the Sculptor Group. If we are allowed to choose the central region of the Sculptor Group as drawn in Fig. 4, the probability of accidental quantization in Fig. 5b is only $^{9}P_{10} = 7 \times 10^{-5}$.

3.3 *How Exact is the Quantization?*

For most of the redshifts listed in Tables 2 and 3 the quoted error of determination is ± 8 km s $^{-1}$. These are almost entirely values described by Rood as "Very high quality 21 cm redshifts [that] are assigned the nominal (and realistic) value of ± 8 km s^{-1}" Fig. 6 shows that if we consider only redshifts with this rms error then the average residual from modulo 72.4 is just 8.2 km s^{-1}. We appear to confirm that 8 km s^{-1} is actually the accuracy with which these redshifts have been measured.

But now Fig. 6 additionally shows that for 7 redshifts which are known with greater accuracy than ± 8 km s $^{-1}$, their residual deviations from modulo 72.4 are dramatically smaller. In fact, Fig. 6 shows that the true accuracy of quantization for the redshifts considered here reaches to within at least ± 3 to ± 4 km s $^{-1}$! Since peculiar, relative velocities of more than this amount would destroy this accurate quantization, the startling implication is that these groups of galaxies have internal motions that are less than ± 3 to ± 4km s $^{-1}$!!

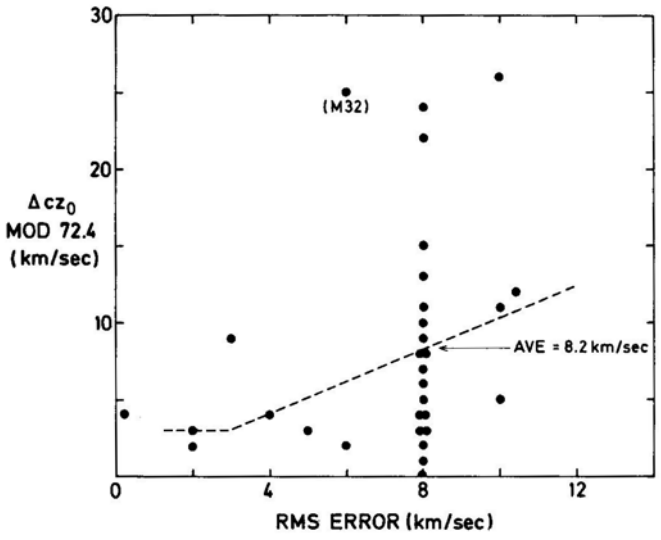

Figure 6. Residuals from modulus 72.4 km s^{-1} as a function of the rms error of measurement of the redshifts. Average residual for measures which are accurate to ±8 km s^{-1} comes out to be ± 8.2 km s^{-1}. M 32 is discussed in text.

There are two further comments to be made about Fig. 6. First, the one point with accuracy better than ± 8 km s^{-1} which falls far from modulo 72.4 is M 32. M 32 is so close to the disc of M 31 that it is clearly warping the disc of M 31 (Arp 1964). A gravitational interaction of M 31 and M 32 is therefore implied. This, in turn, would seem to require an appreciable component of relative velocity to be reflected in the redshift of M 32.

Secondly, the one point slightly outside the slot in Fig. 1 which is plotted in Fig. 6 is NGC 628 (added to the bottom of Table 2). NGC 628 is one of the brightest apparent-magnitude Sc spirals in the region and several pieces of evidence placed it as a member of the Local Group (Arp 1986b). Now we see that its accurately measured redshift, compared to the accurate redshift of M 31, confirms to a high accuracy its quantized value of redshift and thus gives quantitative confirmation of its membership in the Local Group.

3.4 *Remark on the Value of the Hubble Constant, H_0*

Regardless of whether or not the universe is expanding, the general existence of an apparent-magnitude-redshift relation (the Hubble Relation) for Sb galaxies (Arp 1986b) implies there is a redshift–distance relation in the universe. The Tully–Fisher relation for galaxies (excluding those with intrinsic redshifts) yields, H_0 = 55 km s^{-1} Mpc^{-1} (see Arp 1986b, Fig. 10 and accompanying discussion). It is interesting to see how the value of this Hubble constant which everyone has worked so hard to measure fares in a universe which has non-velocity and quantized redshifts.

Table 4 summarizes the situation for the three nearest, major groups of galaxies. The distance modulus for M 31 is taken from the RSA (μ = 24.2 mag), as well as the distance modulus for NGC 300 (μ = 26.8 mag). For M 81, however, the RSA value of μ= 27.7 mag was later superseded by a much more distant value of μ = 28.8 mag (Sandage 1984). However the discussion of M 81 and the Tully–Fisher relation in Arp 1986b indicated an intermediate modulus of μ .= 28.0 mag was more likely. That is the value adopted here although the exact value is not critical to the argument which follows.

The redshift of the dominant galaxies in each group are corrected for the solar motion listed at the head of Table 1 and indicated as cz_0 in the third column of Table 4. Immediately we see that the measured redshifts of these three groups are much too small to give a reasonable H_0 at their known distances. Their average H_0 would actually be negative because of the large negative redshift of M 31. But we know that in order to have M 31 agree with even its most immediate neighbours we must add 72 km s^{-1}, one quantization unit, to its measured redshift value. After doing that, and if

Table 4. Hubble constant and peculiar velocity for nearest three galaxy groups.

Galaxy	distance (Mpc)	cz_0	H_0	after type corr.	H_0	for H_0	required pec vel.
M 31	0.7	−86	−124	+72	−20	$H_0 = 0$	−14
NGC 55–NGC 300	2.3	101, 108	45	0	45	$H_0 = 55$	−22
M 81	4.0	89	22	+72(144)	40(59)	$H_0 = 55$	−58 (+15)

H_0 = 0 within the Local Group, then M 31 and our own Milky Way Galaxy would have a true differential velocity of only –14 km s $^{-1}$.

For NGC 55–NGC 300 the measured cz_0 divided by the adopted distance yields H_0 = 45. If H_0 were actually H_0 = 55, then NGC 55–NGC 300 would have to have a peculiar velocity of – 22 km s $^{-1}$. But this is nearly the peculiar velocity needed in Section 3.2 to bring the quantization of Sculptor Group into zero point agreement with the quantization of the Local Group redshifts! Since this latter value could have come out anywhere between – 36 and +36 km s $^{-1}$, it is possibly not a coincidence.

Finally the low measured cz_0 and large distance of M 81 yield a pitifully small H_0 = 22 km s^{-1} Mpc^{-1} for this important system. But, as in M 31, we must make a type correction of 72 km s $^{-1}$ for the dominant Sb (M 81) relative to our Sc (companion type) galaxy. Then the derived H_0 = 40 km s^{-1} Mpc^{-1}. If the type correction were two multiples of quantization (2×72.4= 145 km s^{-1}) then the H_0 derived from M 81 would be H_0 = 59 kms^{-1} Mpc^{-1} . In these two cases the peculiar velocity of M 81 needed to give H_0 = 55 would be reduced from – 131 km s $^{-1}$ to – 59 or even possibly + 15 km s $^{-1}$. *The bottom line is that if the Hubble constant which is characteristic of extragalactic space is really H_0 =55, the corrections to the observed redshifts required by the quantization yields much more believable peculiar motions for the three nearest galaxy groups.*

One comment on the NGC 55–NGC 300 group is that since these two galaxies are type Sc they would not be expected to have any relative quantization correction to our own (approximately) type Sc galaxy. It is just the NGC 55–NGC 300 group which, without correction, gives the most reasonable value of H_0 = 45.

Another comment is that NGC 253 at about 154 km s^{-1} higher redshift in the NGC 55–NGC 300 group is very bright in apparent magnitude. This is reminiscent of the situation with M 82, which is attached by hydrogen bridges to M 81. M 82 is + 285 km s^{-1} relative to M 81 but is very bright for such a relatively highly redshifted companion. Like M 82, NGC 253 is an active, ejecting galaxy of peculiar, mottled appearance and very little resolution into stars. It is suggested here that both are fainter, intrinsically redshifted galaxies which are temporarily in a bright phase.

4. Summary and discussion

Quantization of galaxy redshifts was first discovered by Tifft in 1972. He noticed that redshifts of galaxies in the Coma Cluster when plotted in an apparent-magnitude-redshift diagram formed bands, separated by discrete values of redshift. In 1976 he analyzed individual spiral galaxies and concluded that the discrete redshift interval was between 70–75 km s $^{-1}$ (Tifft 1976). In 1977 he confirmed this quantization in redshifts of double (binary) galaxies. In this same paper, by identifying redshift bands separated by several multiples in the Coma Cluster, he calculated the value mod Δcz_0 = 72.46 km s^{-1} (Tifft 1977). By 1980 accurate hydrogen redshifts had been measured by others for a new sample of double galaxies and the 72 km s^{-1} periodicity was confirmed even more strongly (Tifft 1980).

The largest and most accurate sample, an independent sample of galaxies in groups, was then reported by Arp & Sulentic (1985). The quantization of 72 km s $^{-1}$ was again, inescapably confirmed. Finally, analysis of the most accurate redshifts available in the

close-by M 31 and M 81 groups, with a new and more accurate solar motion correction, yielded a quantization value of 72.4 km s^{-1} (Arp 1986a, Fig. 4).

It is this value of 72.4 which has been used in the present analysis and which so accurately fits the observed redshifts. Even up to the large redshift represented by 14 multiples of the mod 72.4 value, the fit is extremely good. The goodness of this fit attests to the accuracy of the number in the last decimal place of the derived quantization value.

It should also be emphasized that the full value of 72.4 was taken from concurring previous analyses and applied as a *prediction* to the present data. The fit of this predicted value is shown in Figs 5a and 5b. *But these are redshifts of galaxies not previously tested for this quantization effect,*

It should be commented that Tifft & Cocke (1984) test a model of the universe in which the redshifts are globally quantized. They conclude that a general quantization pertains overall, including between groups, but that the intervals are submultiples of 72.46 km s^{-1}. In the present paper I only test quantization within groups. The groups in my sample can have arbitrary relative redshifts or peculiar motions between themselves. Their differential offsets, however, should be smaller than about ± 50 km s^{-1} in order to agree with a 'quiet' Hubble flow (Tamman, Sandage & Yahil 1980).

As for the cause of the effect, there is as yet no physical theory which will quantitatively account for the redshift periodicity observed. Mathematical descriptions of quantum operators on velocity have been discussed (Cocke 1985; Nieto 1986). But the systematically higher redshifts of fainter galaxies in the M 31 and Sculptor Groups which were demonstrated in the present paper require that redshifts higher than that of the dominant galaxy cannot be due to velocity.

The companion galaxies in each group would have to be receding away from the dominant members of the group just in the direction we happen to be looking. This is a *reductio ad absurdum* and shows the fainter galaxies in each group must have higher redshifts due to some other cause than recessional Doppler shift. This excess redshift for fainter galaxies in groups has been established in many separate investigations over the years with independent samples of galaxies (see for review Arp 1976; Arp & Sulentic 1985; Arp 1982; Arp 1986b, d). The critically important consequence is that the observed excess redshifts cannot be, to any appreciable extent, caused by velocities. If one believes that velocities cannot be quantized then the observed quantization is simply another proof that the redshifts are not velocity redshifts. Moreover, whatever is actually causing the intrinsic redshift could then be quantized.

The combination of intrinsic redshift with its strict quantization points, in My opinion, to the properties of matter which constitute these various galaxies as the causative factor. For example, particle masses might be smaller or clocks run slower in the excess redshift galaxies. But regardless of the physical cause of the intrinsic redshifts, if galaxies in groups can be motionless With respect to each other down to values as small as 3 to 4 kms^{-1} then all current assumptions about masses of galaxies and masses of clusters of galaxies will have to be reexamined.

Undoubtedly many galaxies and peculiar objects will have to be moved closer after allowance for intrinsic redshift effects. Consequently we will have reduced distances and reduced masses. Perhaps this long overdue reexamination of basic assumptions will yield a smaller universe but one with a larger range in the ages of its constituent matter.

Acknowledgements

I would like to thank J. E. Wampler and W. G. Tifft for critical reading of the manuscript and helpful suggestions.

References

Arp, H. 1964, *Astrophys. J.,* **139,** 1045.
Arp, H. 1976, in *IAU Coll. 37: L'Evolution des Galaxies et ses Implications Cosmologique,* Eds C. Balkowski & B. E. Westerlund, No. 263, C. N. R. S., Paris, p. 377.
Arp, H. 1982a, *Astrophys. J.,* **256,** 54.
Arp, H. 1986a, *Astr. Astrophys.,* **156,** 207.
Arp, H. 1986b, MPA 236.
Arp, H. 1986c, in IAU Symp. 124: *Observational Cosmology,* Eds A. Hewitt, G. Burbidge & Li Zhi Fang, D. Reidel, Dordrecht; MPA 265.
Arp, H. 1987, *Quasars, Redshifts and Controversies,* Interstellar Media, California.
Arp, H., Sulentic, J. W. 1985, *Astrophys. J.,* **291,** 88.
Ford, H. C, Jacoby, G., Jenner, D. C. 1977, *Astrophys. J.,* **213,** 318.
Huchra, J. P., Geller, M. J. 1982, *Astrophys. J.,* **257,** 423.
Jaakkola, T., Moles, M. 1976, *Astr. Astrophys.,* **53,** 389.
Sandage, A. R. 1984, *Astr. J.,* **89,** 621.
Sandage, A. R., Tamrnan, G. A. 1981, *A Revised Shapely-Ames Catalog of Bright Galaxies,* Carnegie Institution, Washington.
Sulentic, J. W. 1984, *Astrophys. J.,* **286,** 442.
Tamman, G. A., Sandage, A., Yahil, A. 1980, *Phys. Scripta,* **21,** 630.
Tifft, W. G. 1972, *Astrophys. J.,* **175,** 613.
Tifft, W. G. 1976, *Astrophys.* X, **206,** 38.
Tifft, W. G. 1977, *Astrophys. J.,* **211,** 31.
Tifft, W. G. 1980, *Astrophys, J*., **236,** 70.
Tifft, W. G., Cocke, J. 1984, *Astrophys. J*., **287,** 492.

J. Astrophys. Astr. (1987) **8,** 257–262

Do *H*-functions always increase during Violent Relaxation?

S. Sridhar *Joint Astronomy Programme, Department of Physics, Indian Institute of Science, Bangalore 560012*

Received 1987 April 30; accepted 1987 June 3

Abstract. Recent work on the violent relaxation of collisionless stellar systems has been based on the notion of a wide class of entropy functions. A theorem concerning entropy increase has been proved. We draw attention to some underlying assumptions that have been ignored in the applications of this theorem to stellar dynamical problems. Once these are taken into account, the use of this theorem is at best heuristic. We present a simple counter-example.

Key words: collisionless stellar systems, violent relaxation—entropy increase

1. Introduction

A long-standing and well-known problem concerns the distribution of light (and hence of stars) in elliptical galaxies. The stars seem to be so smoothly distributed that it is widely believed that these systems are 'relaxed'. There is very little gas in ellipticals and the dynamics is governed by the mutual gravitational attraction between stars. So it is natural to look for some relaxation process that leads self-gravitating systems to some equilibrium state.

Just like the motion of molecules in gases, the motion of stars in galaxies is described by the Boltzmann equation. There are so many stars in a galaxy that the time over which collisions are effective turns out to be much longer than the galaxy's age. So galaxies are well-approximated as collisionless stellar systems and any relaxation process should be collisionless. Lynden-Bell (1967) suggested that if the stars were initially distributed in a state very far from equilibrium, large fluctuations in the galaxy's mean field could scatter stars, allow them to exchange energy and equilibrate. He called this 'violent relaxation'.

In the kinetic theory of gases, the form of the collision term in the Boltzmann equation singles out Boltzmann's *H*-function as the unique function that increases with time. While the Boltzmann equation is inherently irreversible in nature, the equation that describes galaxies does not have the collision term and is symmetric under time-reversal. Tremaine, Henon & Lynden-Bell (1986, hereinafter THL) have addressed the problem of entropy increase for collisionless stellar systems during processes like violent relaxation. THL consider entropy functions of a more general form than Boltzmann's *H*-function. They have proved a theorem concerning entropy increase. We disagree with their interpretation and its application to stellar dynamics. We give a summary of THL's proof of their theorem in Section 2 and discuss the assumptions in

Section 3. A simple example that invalidates THL's interpretation is presented in Section 4.

2. The *H*-theorem of THL

The time evolution of collisionless stellar systems is governed by the collisionless Boltzmann equation (CBE):

$$\frac{\mathrm{d}f}{\mathrm{d}t} \equiv \frac{\partial f}{\partial t} + \mathbf{v} \cdot \frac{\partial f}{\partial \mathbf{x}} - \frac{\partial \phi}{\partial \mathbf{x}} \cdot \frac{\partial f}{\partial \mathbf{v}} = 0 \tag{1}$$

where f (x, v, t) dx dυ is the mass in phase volume dx dυ arid ϕ is the mean gravitational potential

$$\phi(\mathbf{x}, t) = -G \int \frac{f(\mathbf{x}', \mathbf{v}', t)}{|\mathbf{x} - \mathbf{x}'|} \mathrm{d}v'. \tag{2}$$

Unlike the Boltzmann equation for gases, the CBE is symmetric under time-reversal. Very few properties of the time-dependent and nonlinear CBE are known. So any general result is very useful.

THL define *H*-functions as

$$H[f] = -\int C(f)\, \mathrm{d}x\, \mathrm{d}\upsilon \tag{3}$$

where C is a convex function with $C(0) = 0$. Time evolution governed by the CBE conserves phase volumes and densities. So the contribution of any phase 'element' of density f and volume dx dυ to H does not change with time. Therefore $H[f]$ is conserved in time:

$$\frac{\mathrm{d}}{\mathrm{d}t} H[f] = 0. \tag{4}$$

Incidentally, the convex property of C is not necessary for (4) to be true; it is enough that C is a function of f alone.

THL partition phase space into macrocells each of volume $\Delta x \Delta \upsilon$. They average f (x, v, t) over these phase volumes to obtain a coarse-grained distribution function F (x, v, t). The convex property of C implies that at any time

$$H[F] \geqslant H[f] \tag{5}$$

regardless of how exactly phase space is partitioned. To prove their theorem THL assume that the system was prepared in a state for which $f = F$ at some initial time $t = t_1$. This implies that

$$H[F(t_1)] = H[f(t_1)]. \tag{6}$$

At some later time $t_2 > t_1$, $F(t_2) \neq f(t_2)$. So, from (5) we have

$$H[F(t_2)] \geqslant H[f(t_2)]. \tag{7}$$

Frm (4) we know that

$$H[f(t_2)] = H[f(t_1)]. \tag{8}$$

so

$$H[F(t_2)] \geqslant H[F(t_1)]. \tag{9}$$

THL argue that inequality (9) implies that $H(t)$ is a monotonically increasing function

of t and that 'the direction of the arrow of time has been determined by the assumption that $f = F$ at $t = t_1$'. They use their theorem as a basic criterion that must be satisfied by the evolution of stellar systems during processes like violent relaxation and their paper contains many examples. Further, they prove a theorem on mixing during violent relaxation. We discuss their proof and applications in the next section.

3. Comments on the *H*-theorem of THL

Although we agree with THL's derivation of (9), we disagree with their interpretation and applications of the same theorem. It is not clear to us that the particular choice of initial state $f = F$ is the natural one and we note that the validity of inequality (9) hinges on the assumption that $f = F$ at $t = t_1$ *Even if* $f=F$ is a reasonable initial state, we disagree with THL's conclusions that by deriving (9) they have proved that $H(t)$ increases monotonically with t (for brevity we use $H(t)$ to denote H $[F(t)]$). We note that $H(t_3) \geqslant H(t_1)$ and $H(t_2) \geqslant H(t_1)$ for $t_3 > t_2 > t_1$, *do not* imply that $H(t_3) \geqslant H(t_2)$. In other words, inequality (9) does not imply that $H(t)$ is monotonically increasing function of t, even though H takes its smallest value at $t = t_1$, and this is only because of the assumption $f = F$ at $t = t_1$. We have shown that there is no arrow of time in the problem.

We also wish to point out that if the evolution of the system was collisionless for $t < t_1$, THL's proof of (9) would imply that $H(t) \geqslant H(t_1)$ for $t < t_1$ also. Therefore the

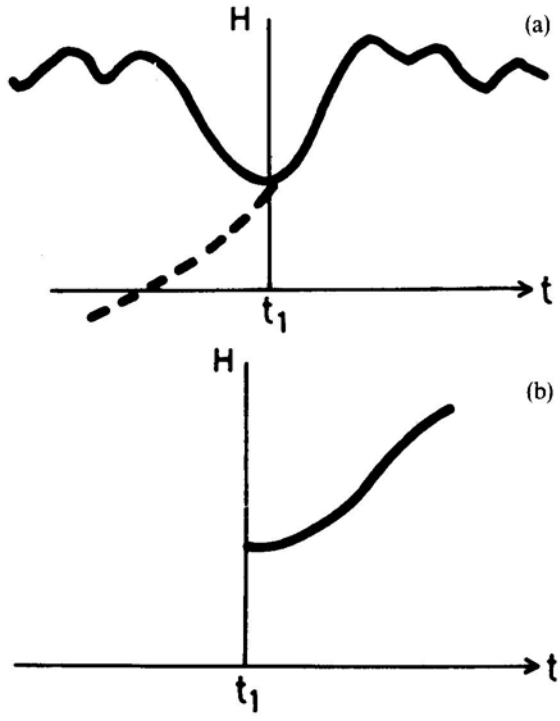

Figure 1. General behaviour of H as a function of time; (a) the solid curve is for a system showing unmixing behaviour and the dashed curve is for a system showing mixing for $t < t_1$, while (b) shows H for a mixing system.

general behaviour of H is like the solid curve in Fig. 1a rather than Fig. 1b as claimed by THL. THL do not discuss H(t) for $t < t_1$ They assume that the system was formed at t_1 If the processes that brought about the special state $f=F$ were collisional (*e.g.* the formation of the stellar system from gas clouds) then the general form of H could be like the dashed curve in Fig. 1a for $t < t_1$. For $t > t_1$, H is still the solid curve. In the next section we present a simple model which might clarify the issues involved.

4. A model showing unmixing behaviour*

Let us consider an ensemble of anharmonic oscillators each of whose members is described by a Hamiltonian

$$E = E(J) \tag{10}$$

J, θ are action-angle variables. The equations of motion are

$$\dot{J} = 0, \ \dot{\theta} = \frac{\mathrm{d}E}{\mathrm{d}J}. \tag{11}$$

The evolution in time of this ensemble is shown in Fig. 2 where $t_c > t_b > t_a$. It is assumed that $\mathrm{d}E/\mathrm{d}J > 0$. The precise functional form of $E(J)$ is unimportant. The members of the ensemble are distributed in phase-space (*i.e.* the J–θ plane) with density $f(J, \theta, t)$. For simplicity we define coarse-graining as integration over J to get the coarse-grained distribution function

$$F(\theta, t) = \int_0^\infty f(J, \theta, t) \, \mathrm{d}J. \tag{12}$$

THL's coarse-graining scheme applied to our ensemble would involve averaging over some (macro)cells with some spread in both J and θ, while we have chosen to integrate over J to get the coarse-grained function. The purpose of this example is to show that H does not monotonically increase with t, *i.e.* unmixing behaviour. The differences between THL's method and our method of coarse-graining will not affect our conclusions.

H-functions are defined in a straightforward manner

$$H(t) = -\int_{-\pi}^{\pi} C[F(\theta, t)] \, \mathrm{d}\theta \tag{13}$$

where $C(F)$ is a convex function. The Hamiltonian evolution of the ensemble preserves phase volumes and densities just like the collisionless evolution of stellar systems. $H(t)$ defined in (13) takes its smallest value at $t = t_a$ when the system is in a specially prepared initial state. This is analogous to the special initial state $f = F$ at $t = t_1$ in THL's paper. It is easily verfied from Fig. 2b and Fig. 2c that $H(t_b) > H(t_a)$ and $H(t_c) > H(t_a)$ where $t_c > t_b > t_a$. This is analogous to THL's derivation of (9). We wish to point out that our model shows unmixing behaviour: $H(t_c) < H(t_b)$ even though $t_c > t_b$. This is easily verified from the functional form of F sketched in Fig. 2b and c (we note that $\int_{-\pi}^{\pi} F(\theta, t) \, \mathrm{d}\theta$ is conserved in time). So $H(t)$ is not a monotonically increasing function of t. This is a special example, but enough to show that the general form of $H(t)$ is like the solid curve in Fig. 1a rather than Fig. 1b.

* This example is due to Rajaram Nityananda.

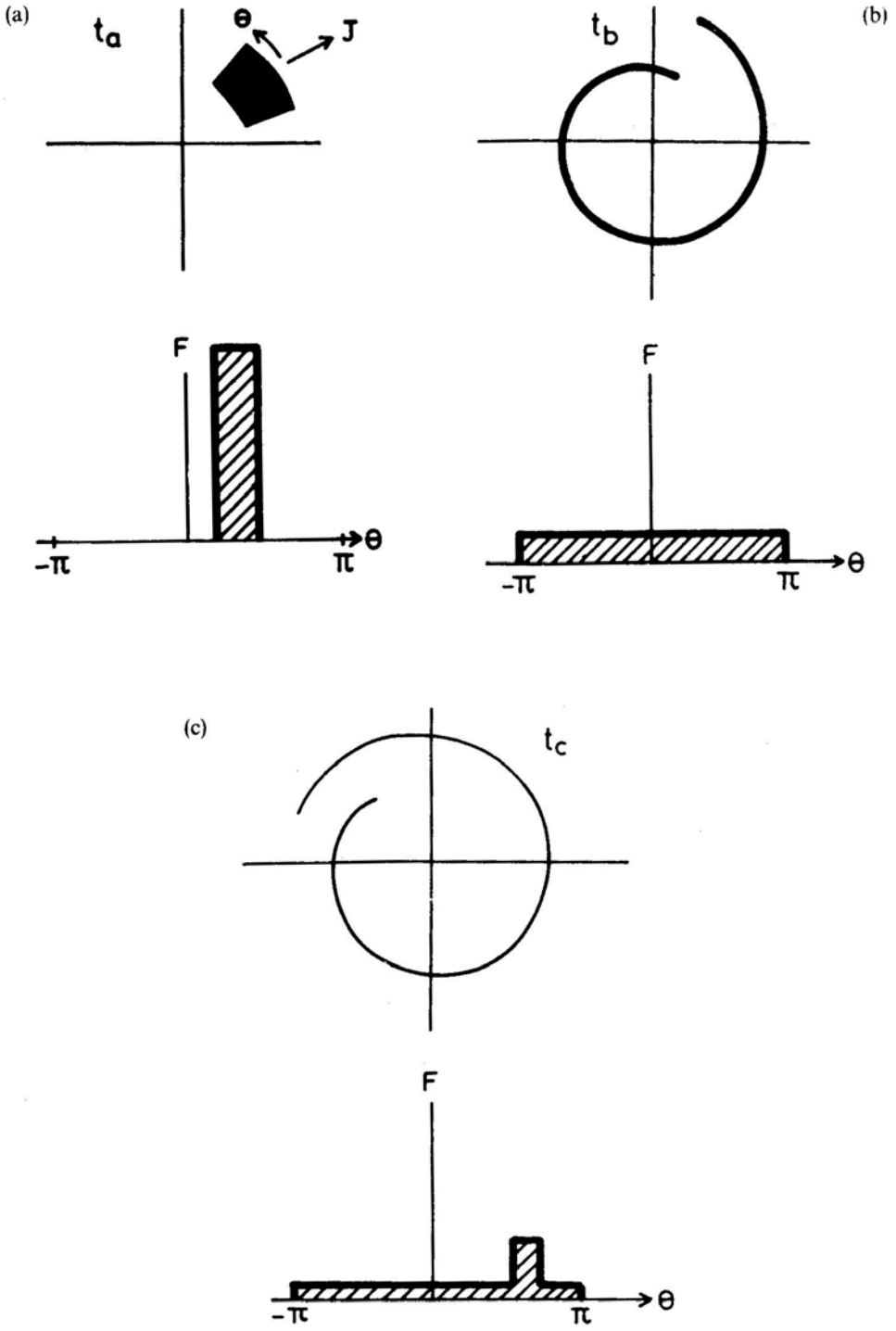

Figure 2. Evolution in time of an ensemble of anharmonic oscillators; (a) the specially prepared initial state at t_a for which H is minimum, (b) ensemble at t_b for which H is maximum, (c) ensemble at a later time t_c for which H takes an intermediate value.

5. Conclusions

THL state that all the properties of H-functions presented in their paper are well known and that only the applications to stellar dynamics is new. In our opinion THL's applications of their theorem to stellar dynamics is questionable to the extent that they have not proved that $H(t)$ increases monotonically with t even for their special choice of initial state. The situation is entirely parallel to attempts made early in this century (Tolman 1938; Ehrenfest 1912) to discuss entropy increase from Liouville's equation (which is a collisionless equation in $6N$ dimensions). All these discussions show that the general behaviour of H must be like Fig. 1a (solid curve). But this does not detract from the practical usefulness of the principle and the same could be true in the present case. Unmixing behaviour like Fig. 2 may be transient and rare but this is an additional hypothesis.

Independently of this work de Jonghe (1987) has pointed out that $H(t)$ need not be a monotonic function and noticed the difficulties with the THL interpretation of their entropy theorem.

Acknowledgements

It is a pleasure to thank Rajaram Nityananda for many discussions, Subhash Karbelkar for reading through the manuscript and making many useful comments and the Raman Research Institute for extending excellent research facilities.

A brief version of these results was presented earlier at the XI session of the Astronomical Society of India (ASI) held on 7 December 1986 in Bangalore; the abstract has appeared in the Bulletin of the ASI (1987, **15,** 44).

References

de Jonghe, H. 1987, preprint.

Ehrenfest,P., Ehrenfest, T.1912. *The Conceptual Foundations of the Statistical Approach in Mechanics,* 1959, Cornell Univ. Press, New York.

Lynden-Bell, D.1967, *Mon. Not. R. astr. Soc.,* **136,** 101.

Tolman, R. C. 1938, *The Principles of Statistical Mechanics,* Clarendon Press, Oxford.

Tremaine, S., Henon, M., Lynden-Bell, D. 1986, *Mon. Not. R. astr. Soc.,* **219,** 285.

J. Astrophys. Astr. (1987) **8,** 263–270

Study of Electron Energy and Angular Distributions and Calculations of X-ray, EUV Line Flux and Rise Times

Ranjna Bakaya, Sunil Peshin, R. R. Rausaria & P. N. Khosa
Department of Physics, Regional Engineering College, Hazratbal, Srinagar, Kashmir 190006

Received 1986 December 27; accepted 1987 June 7

Abstract. Evolution of energy and angular distributions of electrons has been studied by combining small-angle analytical treatment with large-angle Monte Carlo calculations as a function of column density for initially monoenergetic and monodirectional electrons. The incident electron energies considered are 20, 30 and 60 keV at 0°, 30° and 60° angles of incidence. Using these distributions, time evolution of extreme ultraviolet (EUV) spectrum has been studied. The slopes of the curves calculated compare well with the experimentally observed curve.

Key words: Sun, X-ray bursts—Sun, EUV flares

1. Introduction

One of the most interesting properties of solar hard X-ray bursts, is their synchronism with the impulsive extreme ultraviolet (EUV) flare emissions observed by means of their effect on the ionosphere which manifests itself in the form of sudden frequency deviations (SFD's) in radio transmission (Kane 1974; Donnelly 1970; Kane & Donnelly 1971). The hard X-ray bursts ($\gtrsim$ 10 ke V) are generally attributed to collisional bremsstrahlung of nonthermal electrons in the flare plasma while the EUV emissions are thought to arise thermally by free-bound and line transitions in the broad wavelength range (10–1030 A) to which the ionosphere is sensitive. Thus the study of these synchronous emissions provides valuable insight into the connection between the nonthermal and thermal aspects of the flare.

Kane & Donnelly (1971) studied the relationship between impulsive solar EUV bursts observed by means of SFD's and hard X-ray bursts (energies $\geqslant$10 keV) recorded mainly by single-channel ionization chambers aboard OGO 1 and OGG 3, and in a few cases by the OGO 5 multichannel measurements.

Generally, the EUV bursts show very good time coincidence with the nonthermal hard X-ray and the impulsive microwave bursts (Fig. 1). If the hard component is not present in the X-ray enhancement, an EUV burst may still be observed, but such a burst is usually weaker and rises more slowly to the maximum than the EUV bursts associated with impulsive X-ray events. Therefore, as in the X-ray, region, the bursts appear to have two components—one of nonthermal and impulsive nature, and the other of quasi-thermal and gradual character (Castelli & Richards 1971; Wood & Noyes 1972; Donnelly *et al.* 1973). Since very little is known about the relatively weak

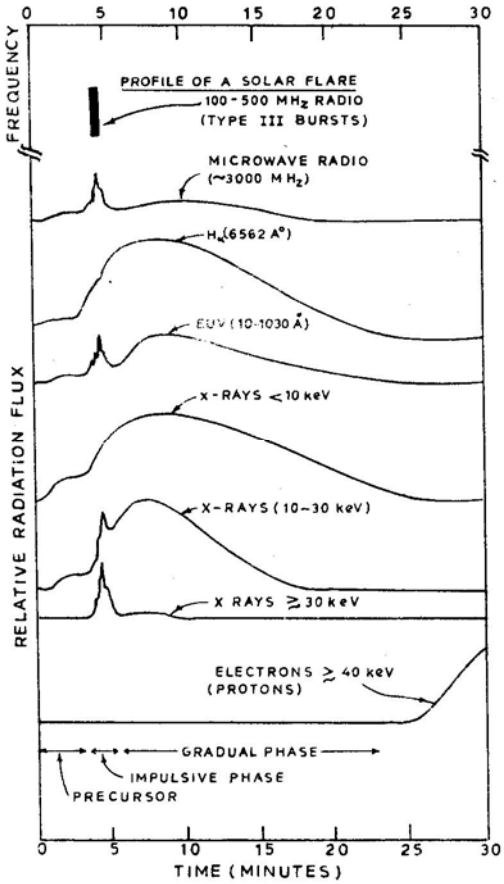

Figure 1. Schematic representation of the different phases of a solar flare as observed in the electromagnetic and particle radiation (after Kane 1974).

gradual EUV bursts that accompany the soft X-ray bursts and microwave post-burst increase, we shall confine our discussion only to the typical impulsive EUV enhancements.

The EUV emission appears in many Spectral lines ranging from those of neutral hydrogen and oxygen to highly ionized species such as Si XII and Fe XV and Fe XVI as well as in the recombination continua of neutral hydrogen and helium. In strong events, continuous emission other than radiative recombination continua also contributes to EUV burst. X-ray emissions from solar flares in the spectral range 1–10 keV is usually interpreted as being produced by a thermal plasma at several million degrees of temperature. Furthermore, line emission of these photon energies cannot be explained in terms of isothermal models of flares and instead multitemperature models have to be postulated (Meekins *et al.* 1970; Neupert 1971). For these reasons, it seems necessary to investigate the ionization and recombination processes which occur in ä plasma whose electrons follow a non-Maxwellian energy distribution. The EUV flux depends on the nature of electron energy distributions. The EUV generation due to power law spectrum has been studied by Landini, Monsignori Fossi & Pallavicini (1973) and

Haug (1979). However, in these studies the effect of multiple scattering on electron energy distributions has not been considered. The intent of the present paper is to study the EUV emission with the help of nonthermal distributions accounting for the dispersion in electron energy and angles resulting from multiple collisions.

2. Electron Energy and Angular Distributions

Usually, the energy spectrum of the nonthermal electrons is deduced from measured X-ray spectra. The electron energy spectrum above 10 keV is taken to be of a power law form. We have considered initially monoenergetic incident beams of electrons having energies 20, 30 and 60 keV characterized by a velocity vector $\hat{\mathbf{n}}$. The choice of monoenergetic beam is justified by the fact that the power law shape of distribution can be obtained by giving suitable weights to monoenergetic electrons. The components of $\hat{\mathbf{n}}$ in a co-ordinate system with z-axis are $\sin\alpha\cos\phi$, $\sin\alpha\sin\phi$ and $\cos\alpha$ where α is the angle of incidence with respect to vertical direction and becomes the pitch angle in the presence of a magnetic field. We consider the electrons directed towards the chromosphere, from the acceleration site situated in corona at 0°, 30° and 60° angles of incidence. Electron transport has been calculated as a function of column density/ height in the atmosphere.

We consider a fully ionized thermal plasma consisting of protons and electrons. It is assumed that the relativistic electron beam will be influenced only by Coulomb forces between the beam electrons and the thermal protons and electrons. Since for chromospheric and coronal plasma, the mean free path as determined by the minimum scattering-angle, is only a small fraction of a centimetre, it is not possible to treat all the small-angle deflections in a pure Monte Carlo procedure. The path of electrons is, therefore, divided into two parts: a condensed history of the small-angle scattering processes treated analytically, followed by Monte Carlo calculations of a single large-angle collision process. Details of the calculations are given in Haug, Elwert & Rausaria (1985) and Koul *et al.* (1985).

In the condensed history, the numerous collision processes with small energy losses are taken into account by mean energy loss rates. We have considered electrons starting at the location $S = 0$, which is taken as the acceleration site situated high up in the corona. In the case of horizontal stratification, S is the height in the atmosphere counted positive downwards (towards the chromosphere). The relation between S and path length is $S = l\cos\theta$ where θ is the angle between electron direction and gradient $\hat{\mathbf{n}}$. The random walk of each electron is followed towards the chromosphere until it has lost nearly its total energy ($E < E_{\min}$); $E_{\min}$ is ~ 5 per cent of the initial energy E_0. It is turned out that for all scale heights used the results depend only on column density $N(S) = \int_0^S n(S)\mathrm{d}S$, the number of protons/cm^2 or electrons/cm^2 within the column traversed. By this procedure we determine the electron energy and angular distributions at different heights (See Haug, Elwert & Rausaria 1985 for detail). A look at the distributions shows that electrons coming at 60° incidence are stopped at higher heights (lower column density) and electrons with 0° incidence are stopped at lower heights (higher column density) (Koul *et al.* 1985). However, the general trend of energy and angular distributions remains the same, becoming broader with the increase in the depth of penetration for all the incidence angles and energies of electrons (Koul *et al:* 1985; Haug, Elwert & Rausaria 1985). The number of backscattered electrons,

however, increases for higher incidence angles. Some examples of electron-energy distributions at different heights for given initial energy and incident angle are shown in Fig. 3. The number of particles followed is 10^4.

3. Calculations of Line Flux and its Comparison with Experimental Data

We have considered Si xiv and Fe xxv for the calculation of EUV flux. For such highly ionized atoms, it is sufficient to evaluate the strength of an emission line in a two-level approximation including the ground and the excited level, *i.e.,* neglecting cascades via energetically higher configurations. Following the reasoning on the lines of Haug (1979) in this work also, it is assumed that the ionization equilibrium of the coronal plasma is established predominantly by thermal processes and is not much influenced by direct ionization due to nonthermal electrons. The flux of line photons including the backscattering correction factor C_R is given by Haug (1979) as

$$F_{kl}=\frac{3\pi}{16\alpha^3}\frac{B_{lk}}{g_k}\frac{N_{iz}}{N_i}\frac{\varepsilon_i}{\sum_i \varepsilon_1 z_i}\frac{\gamma-1}{B(\gamma-1,\frac{1}{2})}\frac{k}{C_R}E_{kl}^{-(\gamma-1)}\langle\Omega_{kl}\rangle$$

$$=1.11\times10^6\frac{B_{lk}}{g_k}\varepsilon_i\frac{N_{iz}}{N_i}\frac{\gamma-1}{B(\gamma-1,\frac{1}{2})}\frac{k}{C_R}E_{kl}^{-(\gamma-1)}\langle\Omega_{kl}\rangle \tag{1.1}$$

where the symbols have the same meaning as in Haug (1979). Haug (1979) has further shown that the same expression is valid for thick target geometry also.

Using Equation (1.1) and the electron energy distributions we have studied F_{kl} as function of column density. We have calculated the electron energy and angular distribution with a given initial energy and incidence angle. Initially the calculations have been done for monoenergetic electrons. Then we have extended the calculations to incorporate the power-law nature of the electron distribution. In this case also to start with we take a constant value of spectral index. However, as the electrons penetrate the deeper layers of the Sun, there is dispersion in energy of the electron as a result the spectral index changes. At each column we have computed the change in the spectral index and have used this value for calculation of line flux. To check the validity of our calculations, we have compared the line flux with OSO-5 observations. The results are given in Tables 1–3. From the tables one can see that the calculated values are close to observations showing that the contribution of nonthermal electrons for the production of X-ray and EUV line flux is significant.

4. Rise times

The rise of EUV emission is compared with the rise of hard X-ray emission for the various energy bands of the OGO 5 measurements for three flares in Fig. 2, where the fluxes were corrected by removing the pre-flare background. The rise of impulsive EUV emission was found to be usually similar to that of the 9.6–19.2 keV X-rays. In some flares, this close agreement extended to the 19.2-32 keV X-rays, while in other bursts,

Table 1. Line flux F_{kl} for Si xiv.

S. No.	γ	Column density	Electrons incident at 0°	30°	60°
I	3	0.16×10^{20}	1.84×10^{5}	1.79×10^{5}	2.25×10^{5}
		0.62×10^{20}	4.23×10^{5}	3.63×10^{5}	5.89×10^{5}
		0.89×10^{20}	5.42×10^{5}	6.74×10^{5}	9.12×10^{5}
II	4	0.16×10^{20}	1.18×10^{4}	1.12×10^{4}	1.46×10^{4}
		0.62×10^{20}	3.22×10^{4}	2.85×10^{4}	5.26×10^{4}
		0.89×10^{20}	4.76×10^{4}	5.95×10^{4}	9.76×10^{4}
III	5	0.16×10^{20}	6.30×10^{2}	6.90×10^{2}	8×10^{2}
		0.62×10^{20}	2.03×10^{3}	1.85×10^{3}	3.91×10^{3}
		0.89×10^{20}	3.45×10^{3}	4.37×10^{3}	8.7×10^{3}

Table 2. Line flux F_{kl} for Fe xxv.

S. No.	γ	Column density	Electrons incident at 0°	30°	60°
I	3	0.16×10^{20}	1.17×10^{3}	1.10×10^{3}	1.56×10^{3}
		0.62×10^{20}	2.69×10^{3}	2.31×10^{3}	3.75×10^{3}
		0.89×10^{20}	3.47×10^{3}	4.29×10^{3}	5.81×10^{3}
II	4	0.16×10^{20}	7.54×10^{1}	7.14×10^{1}	9.30×10^{1}
		0.62×10^{20}	2.06×10^{2}	1.81×10^{2}	3.88×10^{2}
		0.89×10^{20}	3.03×10^{2}	3.79×10^{2}	4.72×10^{2}
III	5	0.16×10^{20}	0.40×10^{1}	0.38×10^{1}	0.50×10^{1}
		0.62×10^{20}	1.3×10^{1}	1.18×10^{1}	2.49×10^{1}
		0.89×10^{20}	1.82×10^{1}	2.78×10^{1}	5.56×10^{1}

Table 3. Line flux F_{kl} for $\gamma = 4$.

S. No.	λ(Å)	Column density	Electrons incident at 0°	30°	60°
Fe xxv:					
I	1.850	0.62×10^{20}	3.25×10^{2}	3.42×10^{2}	1.17×10^{3}
		0.89×10^{20}	5.25×10^{2}	8.73×10^{2}	1.73×10^{3}
II	1.513	0.62×10^{20}	3.10×10^{2}	2.99×10^{2}	9.59×10^{2}
		0.89×10^{20}	4.80×10^{2}	7.75×10^{2}	1.48×10^{3}
Si xxv:					
I	2.01	0.76×10^{20}	1.38×10^{5}	3.32×10^{5}	5.36×10^{5}
		0.89×10^{20}	1.88×10^{5}	4.58×10^{5}	8.1×10^{5}

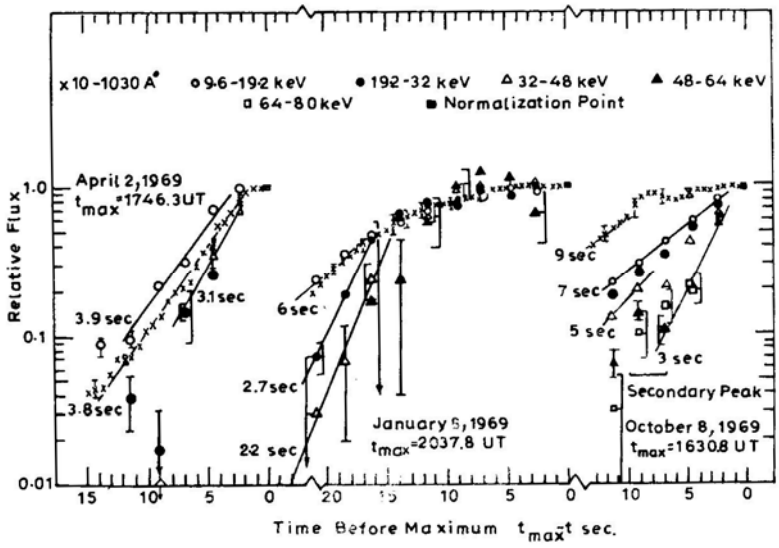

Figure 2. Impulsive solar EUV and hard X-ray bursts—rise time comparisons.

the rise of EUV emission was slower than that in hard X-rays for energy bands greater than 32 keV. These results are independent of the small uncertainity in the EUV rise resulting from uncertainities in the ionospheric electron loss rates involved in the analysis of each particular SFD.

The fact that the impulsive EUV emission rises and decays slower than the X-ray above 32 keV should not be interpreted to mean that these EUV emissions are like the slow flare emissions observed at soft X-ray and EUV wavelengths. The rise times for the impulsive bursts discussed above range from several seconds to several tens of seconds, while the time constants for the slow soft X-ray and EUV emission are typically several minutes for rise times and upto several tens of minutes for decay times.

5. Results and discussion

Using the electron distributions calculated in Section 2 we have studied the rise times of EUV bursts. A look at the observed time profiles of EUV shows that it is steeper in the beginning and becomes flatter afterwards. To explain this, we have taken electron energy distributions in a fixed energy interval with initial electron energies of 20, 30, 60 keV as function of height. By taking slopes of energy distributions we find that it has the same trend as the observed one. This can be explained theoretically using the fact that in the beginning, the number of low-energy electrons is smaller and it increases with an increase in column density. With the increase of low-energy electrons at higher column density, the curve becomes flatter. The same results are obtained over a range of electron and photon energies. However, the calculations are found to be sensitive to the choice of density models. A beam of high-energy electrons injected towards the photosphere will be absorbed in a fraction of seconds. However, we find that rise times are often of the order of afew seconds. There can be two possibilities. First the electrons

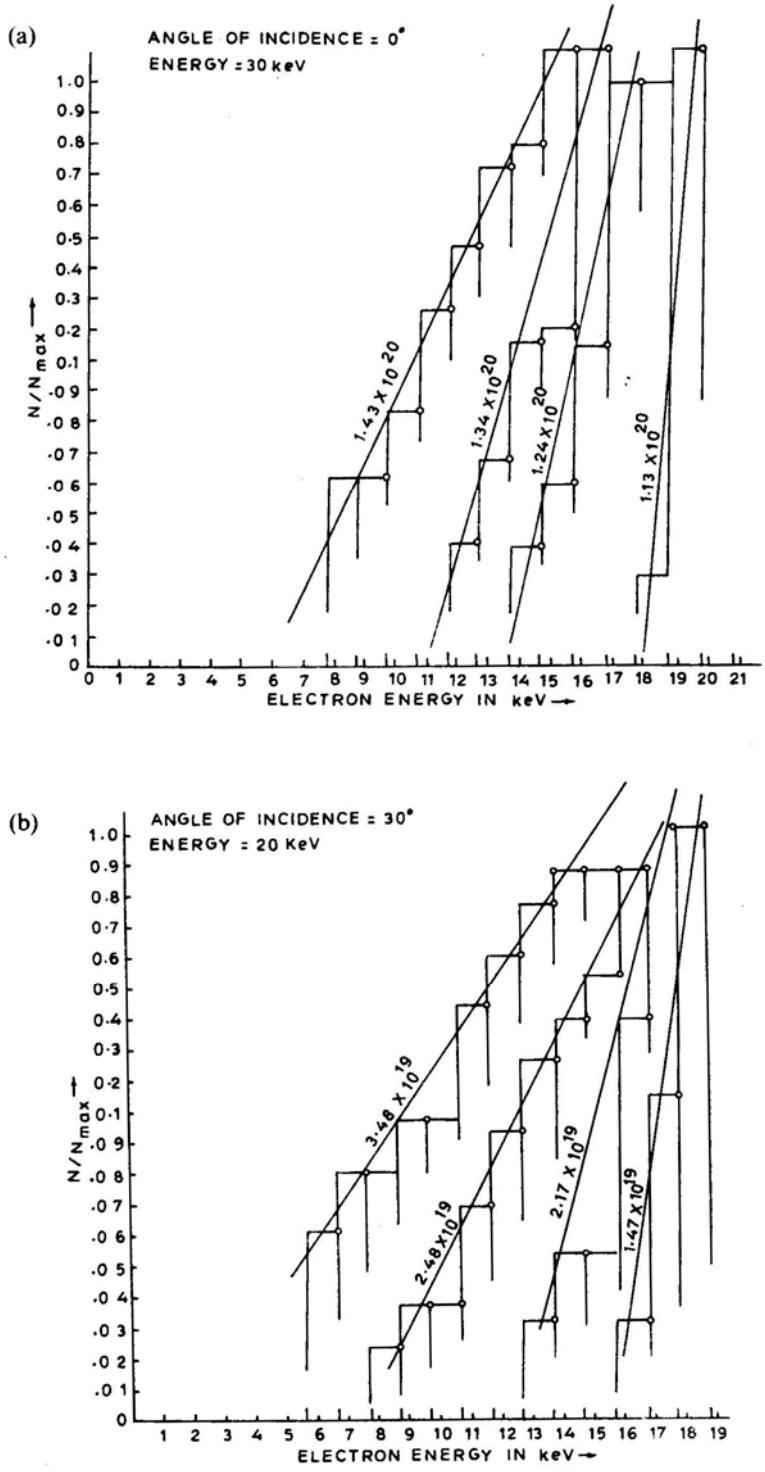

Figure 3. Continued.

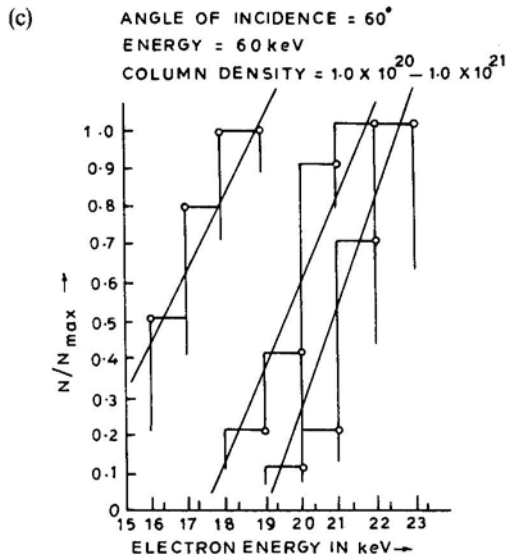

Figure 3. Variation of electron energy distributions and slopes for initial electron energy 20,30, 60 keV incident at 0°, 30° and 60° incidence angles.

coming at higher incidence angles will remain trapped and will keep moving between two conjugate points. Second possibility is that there is continuous injection of the electron beams. The second possibility seems to be more reasonable. Our calculations of hard X-ray spectra and EUV rise times carried out so far favour nonthermal and thick target.

Acknowledgements

We are thankful to Dr. O. N. Kaul, Principal, Regional Engineering College, Srinagar for his keen interest in the work. This work is supported by ISRO Grant No. 10/2/134.

References

Castelli, J. P., Richards, D. W. 1971, *J. Geophys. Res.,* **76,** 8409.
Donnelly, R. F. 1970, ESSA Techn. Rep. ERL 169-SDL 14.
Donnelly, R. F., Wood, A. T., Jr., Noyes, R. W. 1973, *Solar Phys.,* **29,** 107.
Haug, E. 1979, *Solar Phys.,* **61,** 129.
Haug, E., Elwert, G., Rausaria, R. R. 1985, *Astr. Astrophys.,* **146,** 159.
Kane, S. R. 1974, *Space Sci. Lab. Series,* **14,** issue 76.
Kane, S. R., Donnelly, R. F. 1971, *Astrophys. J.,* **164,** 151.
Koul, P. K., Moza, K. L., Khosa, P. N., Rausaria, R. R. 1985, *Astrophys.* J., **292,** 725.
Landini, M., Monsignori Fossi, B. C., Pallavicini, R. 1973, *Solar Phys.,* **29,** 93.
Meekins, J. F., Doschek, G. A., Friedman, H., Chub, T. A., Kreplin, R. W. 1970, *Solar Phys.,* **13,** 198.
Neupert, W. M. 1971, *Solar Phys.,* **18,** 474.
Wood, A. T., Noyes, R. W. 1972, *Solar Phys.,* **24,** 180.

J. Astrophys. Astr. (1987) **8,** 271–274

Atmospheric Noise on the Bispectrum in Optical Speckle Interferometry

S. N. Karbelkar *Joint Astronomy Programme, Physics Department, Indian Institute of Science, Bangalore 560012*

Rajaram Nityananda *Raman Research Institute, Bangalore 560080*

Received 1987 May 16; accepted 1987 July 27

Abstract. Based on a simple picture of speckle phenomena in optical interferometry it is shown that the recent signal-to-noise ratio estimate for the so called bispectrum, due to Wirnitzer (1985), does not possess the right limit when photon statistics is unimportant. In this wave-limit, which is true for bright sources, his calculations over-estimate the signal-to-noise ratio for the bispectrum by a factor of the order of the square root of the number of speckles.

Key words: speckle interferometry—bispectrum—signal-to-noise ratio

1. Introduction

Though large ground-based optical telescopes have large light collecting capacity, the Earth's turbulent atmosphere degrades their resolution (smallest detectable angular separation) to a value far poorer than the Rayleigh limit corresponding to their diameter. Random density fluctuations associated with the atmospheric turbulence offer random refractive-index inhomogeneities to the incoming light waves. The telescope then behaves as if it were aberrated. These aberrations due to the atmosphere vary on both spatial (typically 10 cm) as well as temporal (about ten milliseconds) scales.

Let $I(x)$ be the focal plane distribution of intensity which is the convolution of the source structure $S(x)$ and the system (telescope + atmosphere) response $R(x)$. Equivalently, in the Fourier representation

$$I_u = R_u S_u \tag{1}$$

where u, v are spatial frequencies. As mentioned before, due to atmospheric turbulence, R_u is random in u and in time. If one integrates the image over times much longer than about ten milliseconds then the average response $\langle R_u \rangle$ is significantly different from zero only for spatial frequencies less than about one (arcsec) $^{-1}$, which corresponds to resolution of about one arcsec. A 10-m telescope, in the absence of the atmosphere, should have a resolution of about ten milliarcsec, *i.e.,* the diffraction-limited response should be significant for spatial frequencies upto 100 (arcsec) $^{-1}$.

The stochastic nature of the system response requires one to use statistical methods of image restoration. Bispectrum analysis is one such method. In this note we point out

that when photon noise is unimportant, previous calculations due to Wirnitzer (1985) overestimate the signal-to-noise ratio for the bispectrum.

2. Statistical methods of image restoration

To get the information about the source structure for higher spatial frequencies it is necessary to measure those correlations of the I_u's for which corresponding correlations of the system responses, R_u' s, are nonzero right upto the diffraction limit of the telescope. Labeyrie (1970) proposed and successfully demonstrated (Gezari, Labeyrie & Stachnik 1972) the use of the second order correlation (power spectrum)

$$\langle I_u I_{-u} \rangle \tag{2}$$

in high-resolution astronomy. This form of speckle-interferometry has the limitation that it yields only the modulus of the Fourier coefficients and not their phases. It is known (Dainty & Greenaway 1979) that, for bright sources, the signal-to-noise ratio for the power spectrum measurements is of the order of unity, in one realization:

$$\mathrm{SNR}_{|Iu|} \sim 1 \tag{3}$$

To reconstruct the phase of the object Fourier transform is important and Weigelt (1977) has proposed the use of the so-called bispectrum

$$\langle I_u I_v I_{-u-v} \rangle \tag{4}$$

a third-order correlation, which is nonzero upto the diffraction limit of the telescope. This method, discussed in detail by Bartlet, Lohmann & Wirnitzer (1984), has been applied with some success to astronomical interferometry (Lohmann, Weigelt & Wirnitzer 1983).

Wirnitzer (1985) has calculated the SNR for the bispectrum as well as for phase restoration for general light levels. For bright sources and one frame of data his results can be summarized as follows:

$$\mathrm{SNR}_{\mathrm{Bispectrum}} \sim 1, \tag{5}$$

$$\mathrm{SNR}_{\mathrm{Phase}} \sim N^{1/2}, \tag{6}$$

where N is the average number of speckles per frame. Note (also from Fig. 3 of Wirnitzer 1985) that the SNR for the bispectrum is of the same order as that for the power spectrum. Paradoxically, it appears that the phase of a Fourier coefficient is better determined (Eq. 6) than the amplitude (Eq. 3)! This paradox is removed below.

3. Present calculations

In this section we use an extremely simplified picture of the speckle phenomenon to estimate the SNR for the bispectrum in the wave limit. The system response $R(x)$ can be considered to contain N speckles, each with roughly the diffraction-limited size, spread over an area about a square arcsec. The number of speckles is about 100 D^2 where D is the diameter of the telescope in metres. The intensity of each speckle is random, but in the following we shall regard it a constant, say I_0. The position x_j of each speckle is

random and uncorrelated to every other. Thus for the system response we use

$$R(x) = I_0 \sum_{j=1}^{N} \delta(x - x_j)$$

or

$$R_u = R_0 \sum_{j=1}^{N} \exp(iux_j). \tag{7}$$

We see that the system response function in the Fourier representation, R_u, is just a sum of N uncorrelated complex numbers. Because of the assumption of randomness, the average of all these numbers is zero. In this simple picture the triple product $R_u R_v R_{-u-v}$ is given by

$$R_u R_v R_{-u-v}/R_0^3 = \sum_{j=1}^{N} \exp[iux_j] \sum_{k=1}^{N} \exp[ivx_k] \sum_{l=1}^{N} \exp[i(-u-v)x_l]$$

$$= \sum_{j=1}^{N} 1 \qquad N \text{ terms} \tag{8.1}$$

$$+ \sum_{\substack{j=k \\ j \neq l}} \exp[i(u+v)(x_j - x_l)] \qquad N(N-1) \text{terms} \tag{8.2}$$

$$+ \sum_{\substack{j=l \\ k \neq l}} \exp[iv(x_k - x_l)] \qquad N(N-1) \text{ terms} \tag{8.3}$$

$$+ \sum_{\substack{k=l \\ j \neq l}} \exp[iu(x_j - x_l)] \qquad N(N-1) \text{ terms} \tag{8.4}$$

$$+ \sum_{\substack{j,k,l \\ \text{all distinct}}} \exp[iu(x_j - x_l) + iv(x_k - x_l)] \qquad N(N-1)(N-2) \text{terms} \tag{8.5}$$

Note that the triple product $R_u\ R_u\ R_{-u-u}$ contains N deterministic terms and $N(N^2 - 1)$ random terms whose average is zero. It is then clear that for the average of the bispectrum it is the terms like (8.1) which contribute:

$$\langle R_u R_v R_{-u-v} \rangle \sim N R_0^3. \tag{9}$$

Now, consider the modulus of the bispectrum:

$(R_u\ R_v\ R_{-u-v})(R_u\ R_v\ R_{-u-v})^*$

$= (N + N\,(N^2 - 1)$ random terms$)\ (N + N\,(N^2 - 1)$ random terms$)^*$

$= (N^2 + N\,(N^2 - 1) +$ cross-terms with nonzero phase factors.

The cross-terms, which have nonzero phase factors, vanish on averaging. Thus:

$$\langle |R_u R_v R_{-u-v}|^2 \rangle \sim N^2 + N(N^2 - 1) \sim N^3 \quad \text{as } N \gg 1. \tag{10}$$

This gives us the SNR for the bispectrum, apart from a factor which depends on the S_u's:

$$\text{SNR}_{\text{Bispectrum}} \sim N/N^{3/2} = N^{-1/2} \sim (10D)^{-1} \tag{11}$$

where D is the diameter of the telescope in metres. The approximation of a speckle pattern by a sum of delta functions may appear drastic and has been chosen only to

illustrate the scaling with N in the simplest possible way. It is easy to see that allowance for the finite size of the speckles and the fact that their intensities and shapes vary cannot alter this scaling. Similar approximations, for a speckle image, have recently been used in high-resolution optical astronomy (see for example: Roddier 1986 and Christou *et al.* 1986) arid are known to reproduce, qualitatively, the results based on more refined models of the speckle image.

The number of independent points in the image, or number of spatial frequencies, is of the order of N. The number of points in the bispectrum, which is a function of two independent spatial frequencies, is proportional to N^2 (Wirnitzer 1985). Thus the phase information is contained redundantly in the bispectrum. This is expected (Wirnitzer 1985) to lead to a significant improvement, by a factor $N^{1/2}$ as seen from the equations 5 and 6, for recovering the phase of the object Fourier transform.

4. Conclusion

With our estimate (Eq. 11) of the SNR for the bispectrum one should then get the SNR for phase restoration as about unity which is similar to that for the amplitude, thus resolving the paradox. We emphasize that this result does not question the significance of the bispectrum for optical interferometry. A SNR of the order unity per frame in the wave limit, for phase restoration, would still make the triple correlation very useful in high-resolution astronomy. In this note, however, we do not consider further the question of phase retrieval from the bispectrum.

A brief version of these results was presented earlier (Karbelkar & Nityananda 1986).

Acknowledgements

We are grateful to an anonymous referee for bringing it to our notice that approximations for. the speckle image, similar to the one used in this paper, have been used recently, and also for other useful comments. SNK thanks the Raman Research Institute for extending research facilities.

References

Bartelt, H., Lohmann, A. W., Wirnitzer, B. 1984, *Appl. Opt.,* **23,** 3121.
Christou, J. C., Ribak, E., Hege, E. K., Freeman, J. D. 1986, *Opt. Engg,* **25,** 724.
Dainty, J. C., Greenaway, A. H. 1979, *J. opt. Soc. Am.,* **69,** 786.
Gezari, D. Y., Labeyrie, A., Stachnik, R. V. 1972, *Astrophys. J.,* **173,** L1.
Karbelkar, S. N., Nityananda, R. 1986, XI meeting of astr. Soc. India: abstract in *Bull. astr. Soc. India.* 1987,**15,** (in press).
Labeyrie, A. 1970, *Astr. Astrophys.,* **6,** 85.
Lohmann, A. W., Weigelt, G., Wirnitzer, B. 1983, *Appl. Opt.,* **22,** 4028.
Roddier, F. 1986, *Opt. Commun.,* **60,** 145.
Weigelt, G. P. 1977, *Opt. Commun.,* **21,** 55.
Wirnitzer, B. 1985, *J. Opt. Soc. Am.,* Series 2, **A2,** 14.

J. Astrophys. Astr. (1987) **8,** 275–280

Horizon Problem and Inflation

T. Padmanabhan & T. R. Seshadri *Astrophysics Group, Tata Institute of Fundamental Research, Homi Bhabha Road, Bombay 400005*

Received 1987 March 16; accepted 1987 June 24

Abstract. We show that, the part of the universe that is observable today (in principle), could not have evolved out of a domain which was causally connected in the past. This and other issues related to horizon problem in inflationary models are discussed.

Key words: cosmology, inflationary models—universe, horizon problem

1. Introduction

Models for the inflationary universe have enjoyed immense popularity in the last few years. The original model for inflation proposed by Guth is quite elegant and simple. It was originally invoked to explain: (i) the homogeneity of the surface of last scattering (LSS) and the consequent isotropy of cosmic microwave background radiation (CMBR), (ii) the closeness of the rate of expansion of the universe to that of a spatially flat universe ('flatness problem') and (iii) the absence of GUT monopoles. Unfortunately the model turned out to be unworkable due to other reasons—it produced a universe very different from what we observe.

In the subsequent years several other models for inflation were proposed. It was also discovered that any inflationary model can produce density inhomogeneities out of the inherent quantum fluctuations of the field responsible for inflation. All these models are, however, unnatural in the sense that dimensionless parameters have to be fine-tuned to very low values for the model to produce an acceptable universe. (Thus, in order to avoid fine-tuning of initial conditions we have to invoke fine-tuning of theoretical parameters.) It is generally believed that, once this fine-tuning of the theoretical model is accepted, inflation would provide a natural explanation to (i) and (ii) of the previous paragraph.

In this paper, we examine the claim that 'inflation solves the horizon problem'. To motivate the discussion, consider a conventional inflationary scenario: The universe evolves from a singularity at $t = 0$, and is radiation dominated until $t = t_i$; it inflates for $t_i < t < t_f$ and is radiation dominated for $t_f < t$. The proper distance to the horizon — which is the linear extent of the causally connected domain—is given by

$$d_H(t) \equiv S(t) \int_0^t \frac{dx}{S(x)} \tag{1}$$

where $S(t)$ is the expansion factor. Thus $d_H(t)$ also represents the size of the observable universe. At any time t, an observer at the origin can receive signals from proper

distances up to $d_H(t)$. The reader, at this stage, is invited to decide for himself the correctness (or otherwise) of the following statements:

1. In a model with sufficient inflation, the currently observable part of the universe has evolved out of a region which was causally connected in the past. In other words, the observable universe is causally connected (Turner 1983: p. 237, lines 6–9; Linde 1984: p. 946, lines 6–8).
2. Perturbations at some wavelengths can grow bigger than the horizon during the inflationary phase and reenter the horizon at a later stage.
3. Inflation can explain the isotropy of the CMBR in a natural manner.

In this paper we shall discuss the above claims and show: (a) The only way to make the whole of observable universe causally connected is to have a horizon-free model, *i.e.* choose a model with infinite $d_H(t)$ for all $t > 0$. (This can be realized if, for example, $S(t) \sim t^n$ with $n > 1$ near $t = 0$.) (b) The second statement is incorrect if 'horizon' is defined as $d_H(t)$. Unfortunately, the term 'horizon' is used in literature to denote two very different objects: $d_H(t)$ and the inverse Hubble distance $H^{-1}(t) = (S/\dot{S})^{-1}$. For $S(t) \sim t^n$, with $n \sim 0$ (1) both $H^{-1}(t)$ and $d_H(t)$ are proportional to t and are of the same order of magnitude. But during an inflationary epoch, they behave very differently. The statement (2) is correct if horizon is interpreted as 'inverse Hubble distance'—which is the sense in which the term 'horizon' is used in literature dealing with perturbations. (c) The explanation of the isotropy of CMBR in inflationary models involves a surprising fine tuning.

2. Horizons in RW cosmology

Consider a $k = 0$, Robertson-Walker universe with an expansion factor $S(t)$. (Since we are not interested in 'flatness problem' we shall set $k = 0$; our results are independent of this assumption.) This proper distance to the horizon, $d_H(t)$, is defined by (1). Let t_0 denote the present moment (10^{18} s) and $\lambda(t_0) = \lambda_0$ be any proper length scale in the present day universe, which would correspond to the size

$$\lambda(t) = \lambda_0 \frac{S(t)}{S(t_0)} \tag{2}$$

at any other epoch t. We are interested in the ratio,

$$r(t) \equiv \frac{d_H(t)}{\lambda(t)} = \frac{S_0}{\lambda_0} \int_0^t \frac{dx}{S(x)} \qquad (t \leqslant t_0). \tag{3}$$

A particular scale λ_0 is 'within the horizon' at some time t if $r(t) > 1$ and is 'outside the horizon' if $r(t) < 1$. We can rewrite (3) as,

$$r(t) = \frac{S_0}{\lambda_0} \left\{ \int_0^{t_0} \frac{dx}{S(x)} - \int_t^{t_0} \frac{dx}{S(x)} \right\} = r(t_0) - \frac{S_0}{\lambda_0} \int_t^{t_0} \frac{dx}{S(x)}. \tag{4}$$

The complete, observable, region of the universe today corresponds to a length scale $\lambda_u(t_0) = d_H(t_0)$. In other words, for this scale $r(t_0) = 1$. From (4) it follows that,

$$\frac{d_H(t)}{\lambda_u(t)} = 1 - \frac{S_0}{\lambda_u(t_0)} \int_t^{t_0} \frac{dx}{S(x)} < 1 \quad (t \leqslant t_0). \tag{5}$$

Notice that $\lambda_u(t)$ represents the size of that region at time *t,* which expands to form the currently observable region of the universe. Equation (5) shows that the horizon size will always be smaller than the size of the region which evolves to form the currently observable universe. *In other words, it is simply impossible for the observable universe to have evolved out of a single causally connected domain in the past.* Statement 1 is false, in spite of repeated assertions to the contrary in the literature (Turner 1983: p. 237, lines 6–9; Linde 1984: p. 946, lines 6–8).

It is clear from the definition that, for $t_1 \leqslant t_2$

$$r(t_1) \leqslant r(t_2). \tag{6}$$

So if $r(t_2) < 1$ (the scale is outside the horizon at $t = t_2$) then $r(t)$ must be less than unity for all $0 \leqslant t_1 \leqslant t_2$ ('the scale must be outside the horizon in the past'). In other words no scale can grow bigger than the horizon and 'go outside the horizon' sometime in the past. (To do so, one would require $r(t_2) < 1$ and $r(t_1) > 1$ with $t_2 > t_1$; this is impossible.) Thus the claim in statement 2 is impossible if 'horizon' is taken to mean $d_H(t)$. We will come back to this point later.

The validity or otherwise of statement 3 depends on the specific form of $S(t)$ used. We shall take $S(t)$ to be,

$$S(t) = \begin{cases} S_i\left(\dfrac{t}{t_i}\right)^{1/2} & 0 < t \leqslant t_i \quad (7) \\ S_i \exp\left[H(t-t_i)\right] & t_i \leqslant t \leqq t_f \quad (8) \\ S_i Z\left(\dfrac{t}{t_f}\right)^{1/2} & t_f < t < t_0 \quad (9) \end{cases}$$

where $Z = \exp H(t_f - t_i)$. (We have neglected the matter-dominated epoch after recombination, but this hardly changes the results.) The coordinate length along the surface of last scattering (which is observable today) is,

$$l(t_0, t_{rec}) = \int_{t_{rec}}^{t_0} \frac{dx}{S(x)} \tag{10}$$

coordinate horizon distance at $t = t_{rec}$ is,

$$l(t_{rec}, 0) = \int_0^{t_{rec}} \frac{dx}{S(x)}. \tag{11}$$

Therefore, the number of causally disconnected volumes in CMBR is about $\sim N^3$ with,

$$N = \frac{l(t_0, t_{rec})}{l(t_{rec}, 0)} = \frac{l(t_0, 0)}{l(t_{rec}, 0)} - 1. \tag{12}$$

Using (7)–(9) we can easily compute $l(t,0)$. For $t > t_f$, this is given by,

$$l(t,0) = \frac{1}{S_i z}\left\{(2t_i + H^{-1})Z - H^{-1} + 2\sqrt{t_f}(\sqrt{t} - \sqrt{t_f})\right\} \tag{13}$$

$$\simeq \frac{1}{S_i z}\left\{4t_i z + 2\sqrt{t t_f}\right\}. \tag{14}$$

In arriving at (14) we have made the usual assumptions regarding inflation: $2t_i \simeq H^{-1}$

($\simeq 10^{10}$ GeV)$^{-1}$), Z $\gg$ 1 and have taken $t \gg t_f$. Using (14) in (12) we get,

$$N = \frac{\sqrt{t_f}(\sqrt{t_0} - \sqrt{t_r})}{2t_i Z + \sqrt{t_f t_r}} \simeq \frac{\sqrt{t_f t_0}}{2t_i Z + \sqrt{t_f t_r}}. \tag{15}$$

If the whole of CMBR has to be within a causally connected patch, then $N \leqslant 1$. In other words,

$$\sqrt{t_f}(\sqrt{t_0} - \sqrt{t_{rec}}) \simeq \sqrt{t_f t_0} < 2t_i Z \tag{16}$$

or equivalently,

$$Z \geqslant \left(\frac{t_f}{t_i}\right)^{1/2} \left(\frac{t_0}{t_i}\right)^{1/2} \tag{17}$$

(Guth 1981). The value of right-hand side in conventional models is $\sim 3 \times 10^{27}$. So the usual inflation with $z \simeq 10^{29}$ will make CMBR homogeneous.

There is however, a surprise hidden in (17). Let us rewrite (17) in the form,

$$t_0 < t_i Z^2 (t_i/t_f) = \frac{t_i^2}{t_f} \exp[2H(t_f - t_i)]. \tag{18}$$

Now, all the parameters on the right-hand side of (18) are fixed by microscopic physics at a very early epoch. (All the parameters t_i, t_f and H are fixed in terms of the fundamental theory producing inflation.) *The isotropy of CMBR will hold true only as long as the age of the universe* t_0 (*the 'present' epoch*) *is smaller than the pre-decided timescale on the right-hand side!* CMBR may appear to be isotropic today; but may appear anisotropic sometime in future!

There is another way of presenting the same result: Given a microscopic theory Z, t_i, t_f are fixed. One can now violate (17) by simply taking a sufficiently large t_0. Thus, if we wait long enough, CMBR will appear to be anisotropic. (The same result can be restated in terms of T_0 the CMBR temperature at the present epoch. We also would like to stress the fact our results are independent of various approximations invoked in the discussion.)

3. Comparison and conclusions

The apparent contradiction between the Standard lore of inflation and our results above demands a comparison, which we shall now provide.

Let us begin with statement 2. The growth of perturbations is actually governed by the scale (inverse Hubble distance).

$$h(t) \equiv H^{-1}(t) = \left(\frac{\dot{S}}{S}\right)^{-1} \tag{19}$$

rather than by $d_H(t)$. Bounds like (6) are not applicable to the ratio $[d_H(t)/h(t)]$. There are, however, two aspects related to this issue that require comment: (i) It is sometimes stated in literature that only perturbations smaller than the 'horizon' (meaning $h(t)$) are physically relevant *because* they are inside *the causally connected region.* This is clearly untrue because $h(t)$ is much smaller than $d_H(t)$. Wavelengths in the range $h(t) < \lambda(t) < d_H(t)$ are well within the causally connected domain but outside the

Hubble distance. The validity of the statement 'microphysics cannot operate at scales $\lambda(t) > h(t)$, is not obvious in inflationary models with $d_H(t) \gg h(t)$. (Brandenberger 1985: p. 46; Turner 1985: p. 243). The issue is somewhat subtle, (ii) The behaviour of $\lambda(t)$, $h(t)$ and $d_H(t)$ are shown in Fig. 1, for an inflationary model described by (7)–(9). Note the exponential growth of $\lambda(t)$ during $t_i < t < t_f$.

In a simplified picture described by (7)–(9), $h(t)$ will be discontinuous at $t = t_f$. Proper discussion of reheating is necessary to smoothen this discontinuity.

Let us now consider statement 1. This statement is simply false. To understand how it is conventionally tackled, let us estimate $d_H(t_0)$—the size of the horizon today. It is easily computed to be,

$$d_H(t_0) = \left(\frac{t_0}{t_f}\right)^{1/2} [(2t_i + H^{-1})z - H^{-1} + 2\sqrt{t_f}(\sqrt{t_0} - \sqrt{t_f})] \tag{20}$$

$$\simeq (4t_i)Z\left(\frac{t_0}{t_f}\right)^{1/2} + 2t_0 \tag{21}$$

for $Z \gg 1$, $t \gg t_f$, $2t_i \simeq H^{-1}$ Taking $t_i \simeq 10^{-35}$ s, $t_f \simeq 10^{-33}$ s, $Z \simeq 10^{29}$, and $t_0 \simeq 10^{18}$ s we get

$$d_H(t_0) \simeq 3 \times 10^{30} \text{ cm}. \tag{22}$$

In Standard inflationary lore, the size of observable universe is taken to be $\lambda(t_0) \simeq 10^{28}$ cm $\ll d_H(t_0)$. Such a scale would have been inside the causally connected domain all the way down to $t = t_i$. At the end of inflation, ($t = t_f$) $d_H(t_f) \simeq 10^5$ cm while $\lambda(t_f) \simeq 3 \times 10^2$ cm; at the beginning of inflation ($t = t_i$), $d_H(t_i) \simeq 10^{-24}$ cm while $l(t_i) \simeq 3 \times 10^{-27}$ cm. The arguments in (5)–(7), of course, are not applicable if $r(t_0) > 1$.

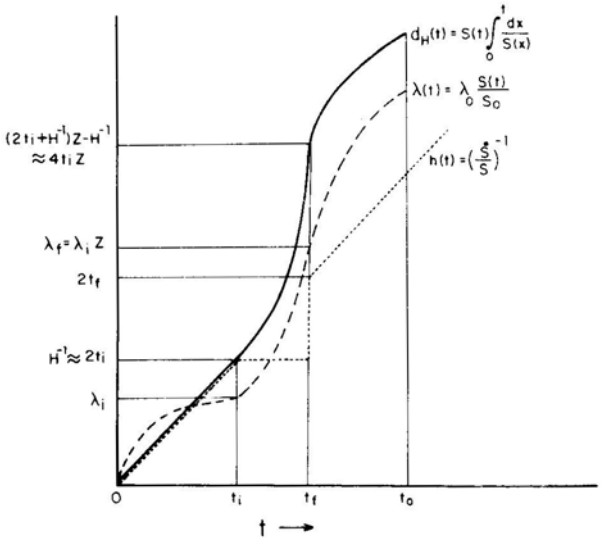

Figure 1. Evolution of various lengthscales with time. Thick line denotes the evolution of the particle horizon, dashed line denotes the growth of a comoving length scale and dotted line represents H^{-1}.

But what is *the* size of observable universe today? All the region in the universe that is causally connected to *us are observable in principle.* Thus the size of the region which is observable by us today (in principle) is $\lambda_u(t_0) = d_H(t_0)$. *This region would have been outside the horizon for all* $t < t_0$.

The claim that 'observable universe has a size of 10^{28} cm' arises from the existence of a last scattering surface (LSS) at $Z \simeq 10^3$. It is usual to say that universe at higher redshifts is 'opaque' and unobservable. Such a statement is misleading, to say the least. If cosmic neutrino background is discovered, one can proceed to redshifts $Z \gg 10^3$. Nothing—in principle—precludes the possible existence of one exotic relic particles which decoupled at very large Z. Therefore, it is more proper to consider $d_H(t_0)$ to be the size of observable universe.

If the above definition is accepted, the following conclusion is inescapable: Inflation can never produce the observable region of the universe from a single causally connected region. It can only be achieved in models which are strictly horizon-less. (This happens in many quantum gravitational models; for example, see Narlikar & Padmanabhan 1983, 1985.)

Lastly, we repeat that the conventional inflation does explain the homogeneity of CMBR. But only because our universe is still young, *i.e.,* t_0 is less than some predecided value.

Acknowledgement

We thank Professor J. V. Narlikar for persuading us to air the above misgivings and for a critical reading of the manuscript.

References

Brandenberger, R. H. 1985, *Rev. of Mod. Phys.,* **57,** 1.

Guth, A. H. 1981, *Phys. Rev.,* **D23,** 347.

Linde, A. D.1984, *Rep. Prog. Phys.,* **47,** 925.

Narlikar, J. V., Padmanabhan, T. 1983, *Ann. Phys.* **150,** 289.

Narlikar, J. V., Padmanabhan, T. 1985, *Phys. Rev.,* **D32,** 1928.

Turner, M. 1983, *Fourth Workshop on Grand Unification,* Univ. Pennsylvania, Eds H. A. Weldon, P. Langacker & P. J. Steinhardt, Birkhauser.

Turner, M. 1985, Fermi Lab. preprint no. 85/153-A.

J. Astrophys. Astr. (1987) **8,** 281–294

Ionospheric Refraction Effects on Radio Interferometer Phase

S. Sukumar *Radio Astronomy Centre, Tata Institute of Fundamental Research, Post Box 8, Ootacamund 643001*

Received 1986 November 22; revised 1987 May 24; accepted 1987 June 27

Abstract. The refraction of radio waves as they traverse through the terrestrial ionosphere and troposphere introduces a differential phase path which results for a radio interferometer in variations of the visibility phase. Though refraction due to troposphere is significant for synthesis radio telescopes operating at 1.0 GHz and above, ionospheric refraction is dominant at lower frequencies. This problem is important in the case of Ooty Synthesis Radio Telescope (OSRT) operating at 326.5 MHz, due to its proximity to the magnetic equator. This paper deals with the nature of phase variations suffered by OSRT due to refraction and explains the methodology evolved to alleviate them.

Key words: radio interferometers—visibility—ionosphere—refraction

1. Introduction

"Atmosphere" refers to two sections *viz*., "troposphere" and "ionosphere". The region up to 50 km from the surface of earth is called troposphere and the ionosphere typically extends from 70 km up to 3000 km above earth's surface. For single antenna radio telescopes, refraction suffered by radio waves in the atmosphere has generally amounted to apparent positional shifts of astronomical sources, which could easily be corrected in most cases. But interferometric observations suffer differential phase paths between the radio waves received at different interferometer elements due to the curved structure/shape of the refracting medium. Also irregularities within the refracting medium introduce further phase variations in the visibility phase observed with a radio interferometer.

For the tropospheric refraction, it has been adequate to assume an exponential variation for the refractive index as a function of height above ground and solve analytically for the differential phase path. This procedure could further be simplified by invoking a slab approximation for the troposphere (Brouw 1971; Hinder & Ryle 1971). For a radio telescope such as the Ooty Synthesis Radio Telescope (OSRT) having antennas at different heights above ground, an additional phase path is introduced due to tropospheric refraction between the signals received at various antennas. These effects are relatively simpler to correct and hence we will not discuss them. However, we will show that a simplified slab approximation does not adequately correct for ionospheric refraction effects and instead present a numerical approach making use of electron density distributions in the ionosphere.

One may assume, for the purpose of evaluating refraction corrections, that the ionosphere consists of two components, (i) an undisturbed regular ionosphere without any movements of electron density irregularities and (ii) a disturbed ionosphere having movements of electron density irregularities of varying spatial and time scales. Though it is not possible to take care of the effects of disturbed ionosphere by simple means, refraction effects due to regular ionosphere can be corrected by assuming simple models for the ionosphere. Some analytical methods assuming simple gradients in the electron density of the ionosphere have been discussed by Komesaroff (1960) and Hagfors (1976). The numerical method to correct ionospheric refraction effects for the Westerbork Synthesis Radio Telescope has been described by Spoelstra (1983). We discuss here a correction procedure developed for OSRT, located at 76° E and 11° N. Owing to its proximity to the magnetic equator wherein abnormal conditions of the ionosphere could often be encountered, a synthesis radio telescope like OSRT operating at 327 MHz (Swarup 1984) especially requires an ionospheric refraction correction procedure. Besides, the OSRT has phased arrays in the focal lines of its antennas adding further complexities and without correcting for ionospheric refraction, it is difficult to evaluate the baselines to any reasonable accuracy. In this paper, we discuss a methodology evolved to compute the differential phase path corrections due to refraction through undisturbed ionosphere and present some observational effects noticed with OSRT during disturbed ionospheric conditions.

2. Ionospheric refraction

The refractive index of ionosphere varies as a function of height depending upon the electron density (number of electrons m^{-3}) and can be expressed as

$$n(h) = [1 - 81\ N(h)/f^2]^{1/2} \tag{1}$$

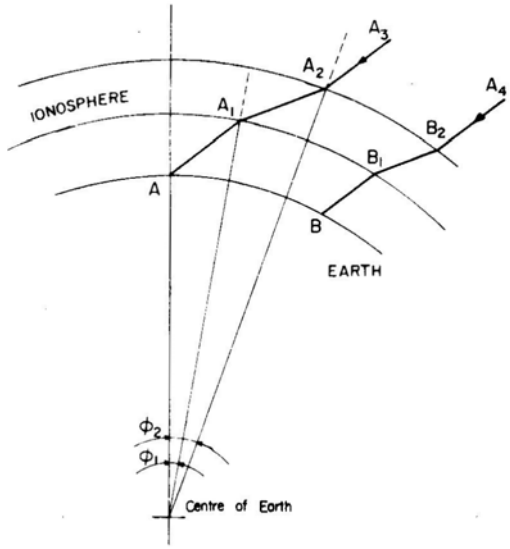

Figure 1. Curved ionosphere geometry for differential phase path.

where h is the height above earth's surface (metres), $n(h)$ the refractive index as a function of height, N (h) the electron density as a function of height (m^{-3}), and f the observing frequency (Hz).

From Equation 1, it can be realized that $n(h)$ has a maximum value of unity and generally it is less than unity. At f =327 MHz, the factor 81 $N(h)/f^2$ is very small ($<10^{-3}$) and hence we can write,

$$n(h) = 1 - 40.5\, N(h)/f^2. \tag{2}$$

In Fig. 1, we show the rays reaching two stations A and B on earth's surface traversing through the 'curved ionosphere' having uniform electron density. As seen, the path lengths A_2A_1 and B_2B_1 are not equal and the difference between them is termed as 'differential phase path' (DPP). It is important to realize that this effect arises purely due to curvature of earth. In the case of plane-parallel ionosphere, the incident and emergent rays at ionospheric boundaries will be parallel, making the path lengths equal.

3. Computation of differential phase path

3.1 *Slab Model for the Ionosphere*

In this model, the ionosphere is simply replaced by a slab of uniform electron density whose thickness is given by

$$S = N_t/N_{max} \tag{3}$$

where S is the slab thickness in metres, N_t the total electron content (number of electrons contained in a column of one square metre cross-sectional area extending all along the ionosphere), and N_{max} the maximum electron density in the ionosphere.

The approximate formula for the differential phase path in the slab model is given by

$$\Delta\Psi = \frac{2\pi(n-1)}{\lambda}\,\frac{L\cos A\cos Z\sin(\phi_2-\phi_1)}{\cos(Z-\phi_2)\cos(Z-\phi_1)}\ \text{rad} \tag{4}$$

where L is the baseline length in metres, λ the observing wavelength in metres, n the refractive index of ionosphere, Z the zenith angle of the source, A the angle between source azimuth and baseline azimuth, and ϕ_1, ϕ_2 the angles subtended at the centre of earth by normals drawn at the earth's surface, lower and upper boundaries of the ionosphere where the ray intersects (refer Fig. 1). Knowing the lower and upper limits of the slab ionosphere these angles can be calculated.

3.2 *Ray-Tracing Through Electron Density Profiles*

The lengths A_2A_1 and B_2B_1 may also be evaluated by 'ray-tracing' along a straight line through the ionosphere. Actually, this is only an approximation as the real electron density profile cannot be measured in the direction to the radio source and during the observations. The complete ray-tracing implies computation of refractive index at each point in the ionosphere, evaluating the refractive bending suffered by the

electromagnetic waves and iterating the computation all along the curved path traversed by the ray. Since this procedure involves enormous amount of computing time, we have approximated the curved path by a simple straight line. This approximation will not introduce errors greater than a few percent and will be adequate for our purpose. The excess length travelled by the ray is given by (at station A)

$$P(Z_A) = \int_0^\infty (n(h) - 1)\,\mathrm{d}s \tag{5}$$

where ds is the line element along the ray, given by

$$\mathrm{d}s = \mathrm{d}h \sec(Z_A) \tag{6}$$

where dh is the vertical component of ds and Z_A, the zenith angle of the source, measured at the subionospheric point over station A. Similarly for station B we write

$$P(Z_B) = \int_0^\infty (n(h) - 1)\,\mathrm{d}s. \tag{7}$$

The differential phase path is given by

$$\Delta P = P(Z_B) - P(Z_A). \tag{8}$$

To evaluate the integrals given by Equations 5 and 7 we should know the functional form of $n(h)$ which in turn is derived from the electron density distribution of the ionosphere.

4. Ionosphere models

Many models have been proposed to predict the electron density distribution of ionosphere at low geo-magnetie latitudes (equatorial regions). Some of them are theoretical (Hunt 1973), some are partly theoretical, partly observational (Somayajulu & Ghosh 1979), the rest are purely empirical (Bent *et al.* 1972; Bent *et al.* 1975; Rajaram & Rastogi 1977). Apart from these, International Reference Ionosphere (IRI) models are also available for low and mid geomagnetic latitudes.

All these models essentially use three parameters, namely $h_m F_2$ (height above ground at which maximum electron density occurs), $N_m F_2$ (maximum electron density in the F2 region), and Y_m (semi-thickness of bottomside ionosphere) to generate the electron density profiles. The parameters vary as functions of (i) geomagnetic latitude of the place, (ii) hour of the day, (iii) season (equinox, winter and summer), and (iv) solar activity.

Most of the models also describe the ways of deriving $h_m F_2$, $N_m F_2$ and Y_m. Measured parameters like $M(3000)F_2$ (maximum usable frequency over a distance of 3000 km on ground using reflection of the electromagnetic waves from the F2 layer of the ionosphere), f_0F_2 (critical frequency of the F2 region) are generally used to derive these parameters. In our case, the choice of a particular model is based on how good it accounts for the observed total electron content and considerations of computational ease, availability and reliability of the basic parameters used to generate the model *etc.*

We have chosen Bent ionospheric model. This empirical model is based on a vast amount of satellite measurements, F2 peak layer measurements and profiles from

ground stations. The prime objective of the Bent model is to keep the total electron content as accurate as possible in order to obtain reliable values of the path length and directional changes of a wave due to refraction. Tests with Faraday rotation data show that 75–90 per cent of the ionospheric effects can be accounted for by the model (Llewellyn & Bent 1973). The Bent model describes the mean ionosphere in terms of simple biparabolic, exponential layers and this simplicity results in less computing time to generate the model, thus making it more attractive. The complete description of this model can be found in Bent, Llewellyn & Schmidt (1972), Bent *et al.* (1975) and a brief description of it as applicable for OSRT can be found in Sukumar (1986).

5. Correction procedure

5.1 *Parameters of Equatorial Ionosphere*

As noted by Köhnlein (1978), the capability of Bent model can be improved if measured values of the total electron content or critical frequency f_0F_2 is incorporated along with the observation station and time information. The OSRT is situated close to magnetic equator at a geomagnetic latitude of 4° N and is well within the region exhibiting equatorial anomaly. Depending upon the presence of equatorial electrojet or counter electrojet the peak electron density region shifts towards the magnetic equator. This effect drastically changes the total electron content as well as other characteristics of the ionosphere over OSRT location. Hence it is preferable to generate Bent ionospheric profiles based on the parameters derived from ionograms obtained on the OSRT observational days from a closely situated ionospheric research station (B. V. Krishnamurthy, personal communication) such as Vikram Sarabhai Space Centre at Thumba or the Solar Observatory, Kodaikanal.

However, we also note that it is just not sufficient to generate ionospheric profiles for OSRT location alone since over the hour-angle and declination coverage of OSRT antennas, the rays reaching them meet the ionosphere at totally different sub-ionospheric latitudes belonging to different geographic locations. The ionospheric parameters at these locations could be quite different from that over OSRT. In principle, the different ionospheric profiles could be extrapolated from the ionograms obtained from Thumba provided the magnetic field variation over a large region is also known. This involves reduction of several ionograms and magnetograms obtained on the observational days, which is rather cumbersome. Besides, these differences show only second order effects resulting in deviations of about 10–20 per cent from the observed values of the ionospheric parameters. Hence we have resorted to a simplified procedure of deriving the ionospheric parameters from the monthly ionospheric predictions released by National Physical Laboratory (NPL), New Delhi (Laxmi, Shastri & Reddy 1981). The uncertainties that could arise due to this simplified method are briefly discussed later.

5.2 *Equivalence Method*

After generating the required profile, Equation 8 is numerically evaluated by ray-tracing along a straight line through the ionosphere. The cosine of the difference

between the source azimuth and baseline azimuth is multiplied with this to get the differential phase path. When we extend the phase correction program to different antennas (baselines) the computations become quite tedious. This is mainly because Equation 8 involves calculating zenith angles for different interferometer elements using the latitude, longitude of each antenna which proved impracticable. This problem has been circumvented by invoking the equivalence of differential phase path with the apparent change in zenith angle of the source due to refraction which is a baseline independent parameter (A. Pramesh Rao, personal communication). We briefly outline the method below.

The effect of refraction by a curved atmosphere on the observations of stars has been studied by Smart & Green (1977). The formula for the angle of refraction Δ is

$$\Delta = R_0 \mu_0 \sin Z \int_1^{\mu_0} \frac{\mathrm{d}\mu}{\mu (r^2\mu^2 - R_0^2 \mu^2 \sin^2 Z)^{1/2}} \tag{9}$$

where R_0 is the radius of earth, μ_0 the refractive index at the surface of the earth, Z the zenith angle of the star, μ the refractive index at a distance r from the centre of the earth at height h, and $r = R_0 + h$.

The integration limits are from $\mu = 1$; ($h = \infty$) to $\mu = \mu_0$; ($h = 0$).

For the ionosphere

$$\mu(h) = 1 - \frac{40.5\, N(h)}{f^2} = 1 - AN(h)$$

where $N(h)$ is the electron density as a function of height and we have assumed that $\mu(h) - 1 \ll 1$. Thus,

$$\mathrm{d}\mu(h) = -A\, \mathrm{d}N(h) = \frac{-A\, \mathrm{d}N(h)}{\mathrm{d}h} \mathrm{d}h.$$

Inserting this in Equation 9 and setting $\mu_0 \simeq \mu \simeq 1$, we get

$$\Delta = A R_0 \sin Z \int_0^{\infty} \frac{\mathrm{d}N(h)/\mathrm{d}h}{[(R_0 + h)^2 - R_0^2 \sin^2 Z]^{1/2}} \mathrm{d}h. \tag{10}$$

Integrating Equation 10 by parts we get,

$$\Delta = A R_0 \sin Z \left[\frac{N(h)}{[(R_0 + h)^2 - R_0^2 \sin^2 Z]^{1/2}} \Bigg|_{h=0}^{\infty} + \int_0^{\infty} \frac{(R_0 + h) N(h) \mathrm{d}h}{[(R_0 + h)^2 - (R_0^2 \sin^2 Z]^{3/2}} \right].$$

Since for the ionosphere $N(h) = 0$ at $h = 0$ and $h = \infty$ the first term is identically equal to zero leaving

$$\Delta = A R_0 \sin Z \int_0^{\infty} \frac{N(h)\mathrm{d}h}{(R_0 + h)^2 \left[1 - \dfrac{R_0^2}{(R_0 + h)^2} \sin^2 Z \right]^{3/2}}$$

$$= \frac{A \sin Z}{R_0} \int_0^{\infty} \frac{\alpha^2 N(h) \mathrm{d}h}{(1 - \alpha^2 \sin^2 Z)^{3/2}} \tag{11}$$

where $\alpha = R_0/(R_0 + h)$.

If we consider a plane formed by observer, the centre of the earth and the source, the effect of refraction is to displace the source from the zenith by an amount Δ. If we consider an interferometer with baseline L to be located on the surface of the earth in

this plane, the effect of refraction is to introduce an error in the position of the source. From Figs 2a and 2b, the path difference between the rays reaching the two antennas is given by

$$\Delta P = L\sin Z - L\sin(Z+\Delta)$$
$$= -L\cos Z\sin\Delta = -L\,\Delta\cos Z \quad \text{if} \quad \Delta \ll 1.$$

Inserting for Δ from Equation (11)

$$\Delta P = \frac{-AL\sin Z\cos Z}{R_0}\int_0^\infty \frac{\alpha^2 N(h)\,dh}{(1-\alpha^2\sin^2 Z)^{3/2}}.$$

Including the difference between source azimuth A_s and baseline azimuth A_b we get,

$$\Delta P = -\frac{AL\cos(A_s - A_b)\sin Z\cos Z}{R_0}\int_0^\infty \frac{\alpha^2 N(h)\,dh}{(1-\alpha^2\sin^2 Z)^{3/2}}. \tag{12}$$

The integral in Equation (12) is solved numerically assuming the factor L cos (A_s – A_b) to be unity and evaluating the zenith angle at the h_mF_2. The actual baseline length and the azimuth factor are later evaluated from the baseline parameters and appropriately multiplied with. The description of the computer programs written for this purpose can be found in Sukumar (1986).

5.3 *Results and Limitations*

In Fig. 3, we show the phase variation observed with OSRT for short and long baselines before and after correcting for ionospheric refraction.

Our calculations also show

(a) slab model overestimates the corrections by about 40 per cent. Table 1 shows the difference between differential phase path calculated by slab model and Bent ionospheric model;

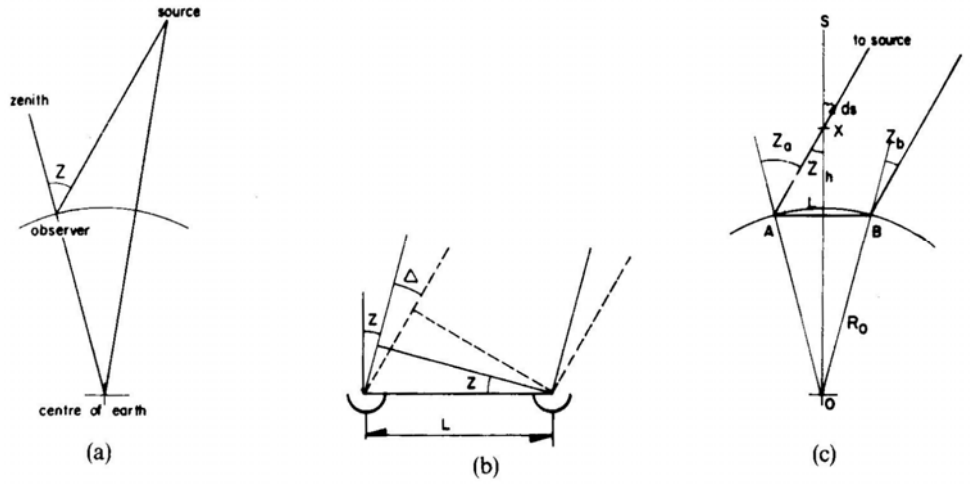

Figure 2. (a) source–observer geometry, (b) source–baseline geometry, and (c) ionosphere–baseline geometry.

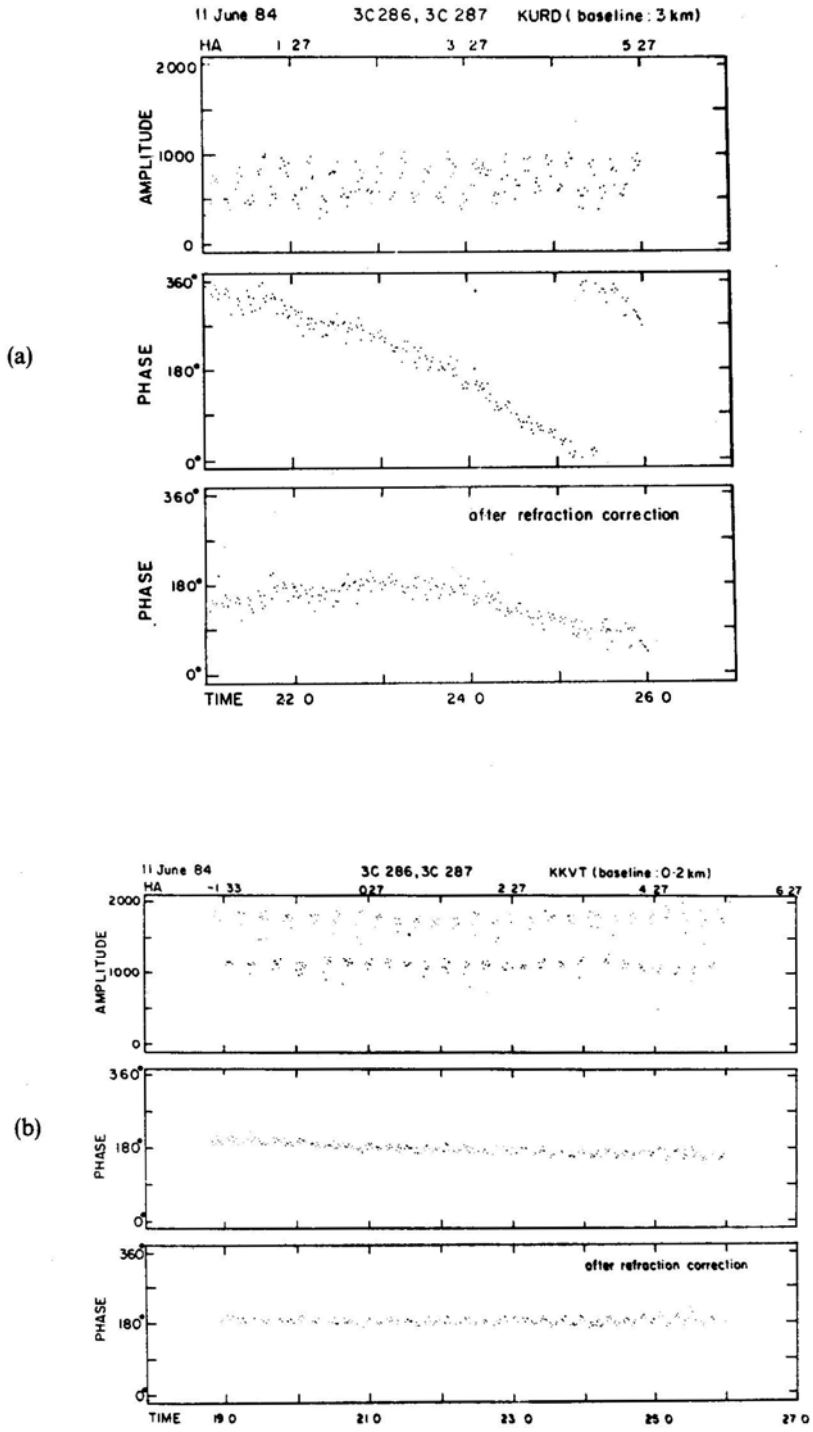

Figure 3. Phase variations observed during undisturbed conditions of the ionosphere.

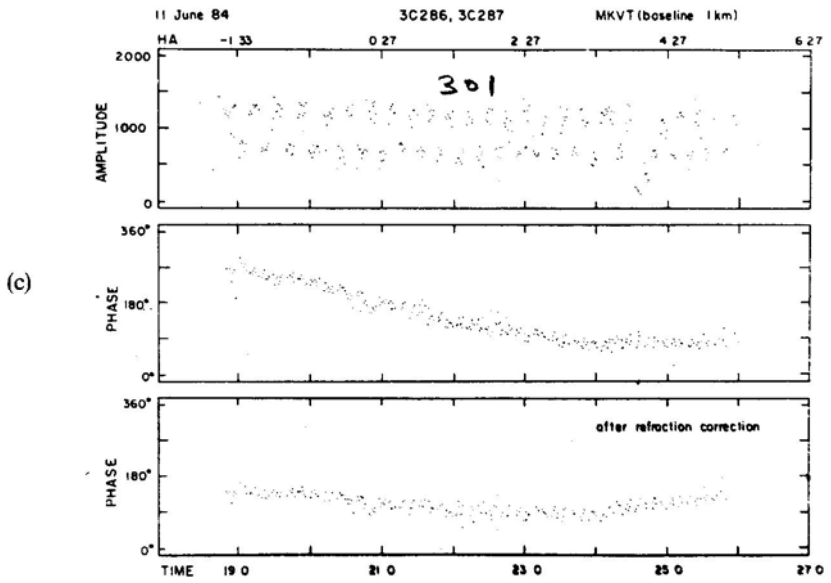

(c)

Figure 3. Continued.

Table 1. Comparison of differential phase path for slab and Bent models of the ionosphere.

Baseline (km)	Differential phase path (m) for elevation 5° slab	5° Bent	10° slab	10° Bent	20° slab	20° Bent	45° slab	45° Bent
1.0	0.021	0.013	0.032	0.021	0.030	0.020	0.008	0.007
10.0	0.202	0.113	0.294	0.188	0.240	0.183	0.080	0.071
100.0	2.200	1.300	2.950	1.933	2.380	1.820	0.800	0.720

(b) the numerical calculations are very sensitive to any variation in h_mF_2 and N_mF_2. Any change in these parameters changes the differential phase path approximately in the same proportion whereas in the case of Y_m, it is less by a factor of 2.

It may be noted that about 60 per cent of the ionospheric refraction occurs in a 400 km thick region placed symmetrically about h_mF_2. About 25 per cent occurs in the bottomside and the rest occurs in the topside between 1000–3000 km of the ionosphere.

Recently, Vikram Kumar & Rao (1985) have shown that the Bent model for equatorial daytime ionosphere is generally consistent with the observations in the topside, but does not agree in the bottomside. It uses the same semithickness for the bottomside parabolic segments while observations show that the semithickness for the bottomside is greater by a factor of 1.5 to 2.5. Hence we may introduce substantial

errors if the assumed Y_m deviates much from the true value. The optional approach to compute actual ionograms and use the values of Y_m derived from them will avoid this problem.

The NPL ionospheric predictions suffer from uncertainties greater than 25 per cent during sunrise and this effect is more pronounced for regions close to magnetic equator (refer Fig. 4). Accordingly, the correction coefficients computed from these predictions also inherit the errors and leave residual phase errors in the visibility data. This could perhaps be alleviated only by special calibration procedures like self-calibration, infield and frequent calibrations currently in wide use for reducing radio-astronomical data.

In our approach we are ray-tracing along a straight line which is not an 'actual ray-tracing' in the true sense. We need to compute the complicated path the ray will travel inside the ionosphere, which we have not attempted to do since the residual phase errors may be taken care of by suitable radio astronomical calibrations like infield and self-calibration.

6. Short period phase variations

Apart from the refraction of radio waves by regular undisturbed ionosphere, which introduces slow phase variations of about 2π radians (equivalent to path variation of one wavelength) over 6 hours period, we also encounter, short-period variations in the interferometer phase during disturbed conditions of the ionosphere. These phase variations result from movements of electron density irregularities having various scale sizes. The generation of ionospheric irregularities are attributed to the presence

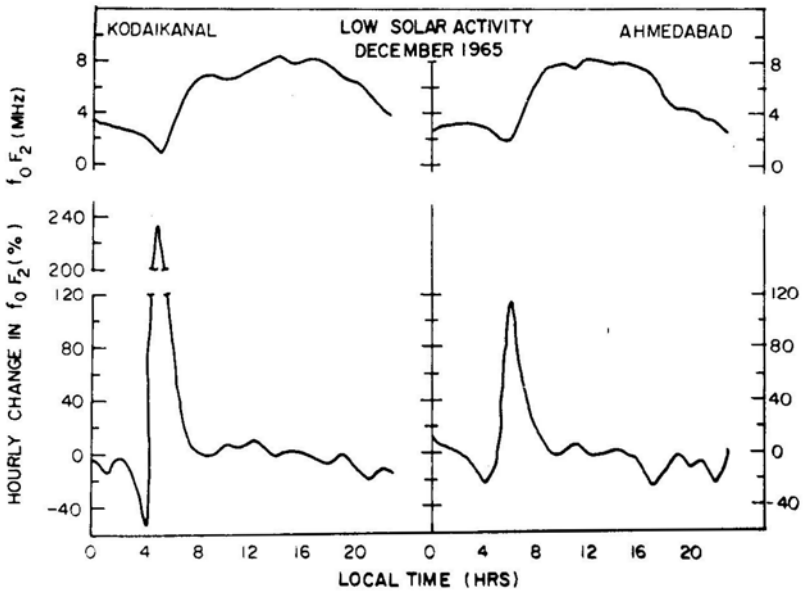

Figure 4. Variation in f_0F_2 during sunrise for low latitude and mid latitude stations (reproduced from Laxmi *et al.* 1979).

of acoustic gravity waves induced by various physical mechanisms (Yeh & Liu 1974). There are two kinds of irregularities which affect the interferometer phase:

(i) The medium scale travelling ionospheric disturbances (TIDs) have scale sizes ranging from 100 to 200 km and move with phase velocities of 100–200 m s^{-1}. We have generally observed phase variations of about 60° peak-to-peak in the visibility phase obtained over an interferometer baseline of 4 km, typically having periods of 12–20 min (see Fig. 5). Sometimes TID movements have been observed almost

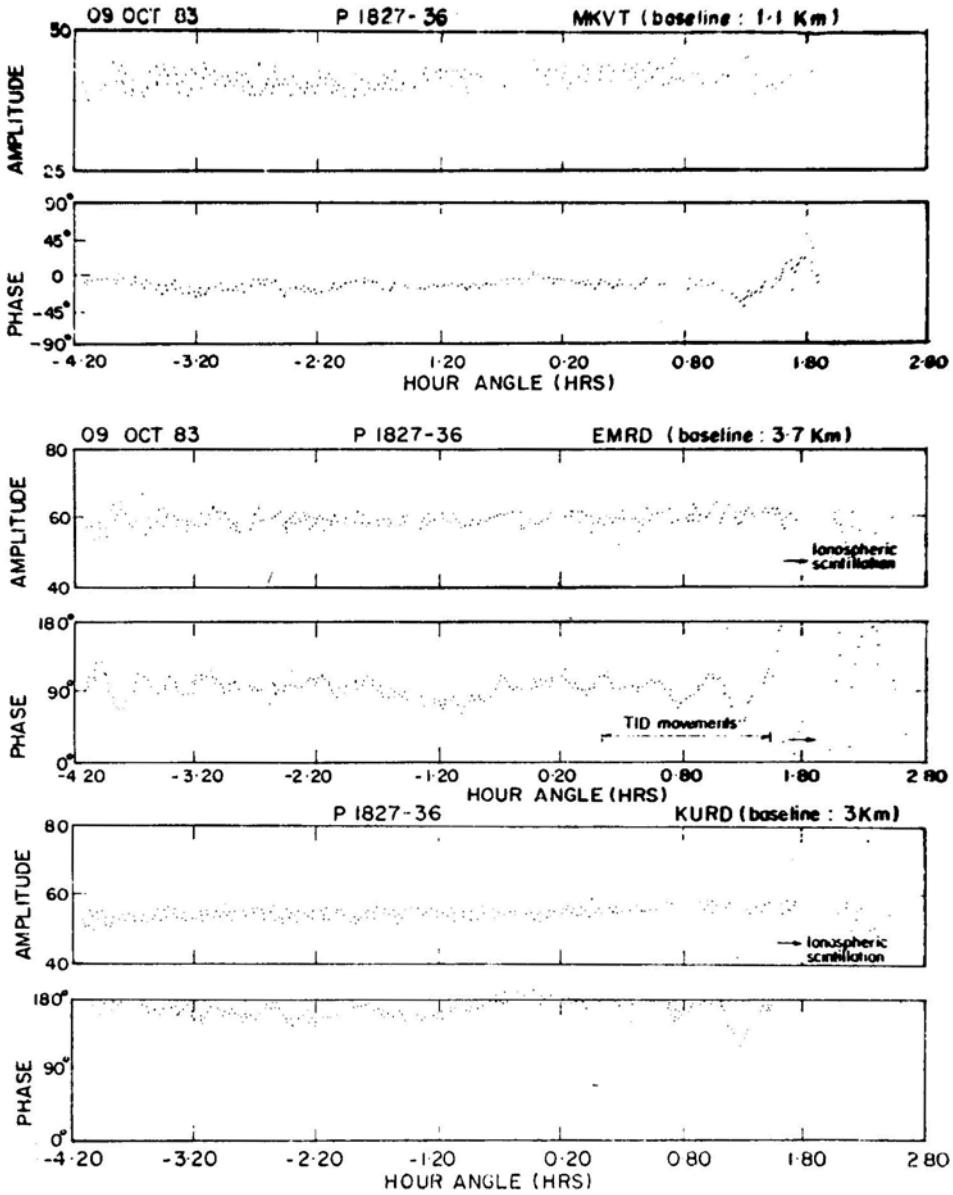

Figure 5. Phase variations observed during movements of medium scale traveling ionospheric disturbances in the ionosphere.

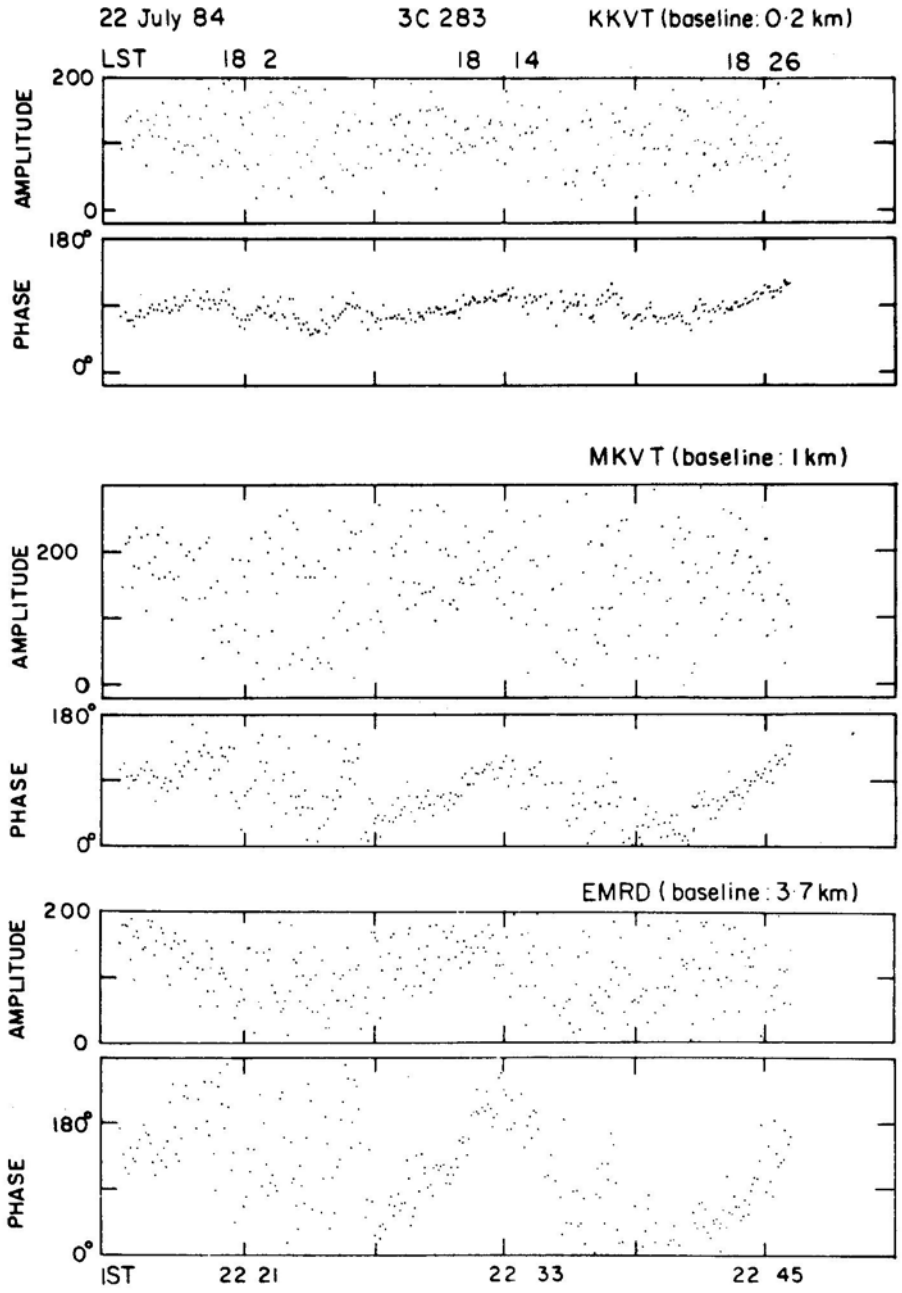

Figure 6. Phase variations observed during ionospheric scintillations.

throughout the day. The effects of such TIDs on the visibility phase can be minimized only by special calibration procedures, mentioned earlier.

(ii) The small-scale irregularities have average scale sizes of 600 m, travel at an average phase velocity of 500–600 m s^{-1} and introduce rapid fluctuations in the

signals received by an antenna. These fluctuations, also known as 'ionospheric scintillations', have been observed to occur over timescales in the range of 40 s to a few minutes. Generally, the scintillations are present during night times of the equinox months and are much dependent upon the solar activity. When the scintillations are strong, S_2 (ratio of rms fluctuations to the mean source strength) > 0.25, they result in severe decorrelation (depending upon the time constant of the radio receiver) among the radio signals received at different antennas. Only over short spacings of the antennas, the effect of scintillations are correlated. This could be seen from Fig. 6, wherein effects of both small-scale irregularities and movements of TIDs are shown together for different baselines. Though frequent calibration can remove some of the phase fluctuations observed with short spacings, it may not be straightforward to estimate the amplitude decorrelations during severe scintillations and hence the calibrations may be improper. Only a detailed ray-tracing through the disturbed ionosphere could solve this problem, which in any case is not simple to perform.

Acknowledgements

The author is very grateful to Professor N. C. Mathur, Indian Institute of Technology, Kanpur, for introducing him to the subject of ionosphere and also for his valuable guidance. This work could not have been completed but for the numerous suggestions and guidance the author received from many ionospheric researchers working in the National Physical Laboratory, New Delhi, and Vikram Sarabhai Space Centre, Thumba, Trivandrum. He also thanks Drs T. Velusamy, A. Pramesh Rao and T. Spoelstra for many interesting discussions and valuable suggestions. He is thankful to an anonymous referee for his various suggestions to improve the contents of this paper.

References

Bent, R. B., Llewellyn, S. K., Schmid, P. E. 1972, *Space Res.,* **12,** 1208.

Bent, R. B., Llewellyn, S. K., Nesterczuk, G., Schmid, P. E. 1975, in *Proc. Symp. Effect of Ionosphere on Space Systems and Communications,* p. 559.

Brouw, W. N. 1971, *PhD Thesis,* Univ. Leiden.

Hagfors, T. 1976, in *Methods of Experimental Physics,* **12B,** Ed. M. L. Meeks, New York, p. 119.

Hinder, R, Ryle, M. 1971, *Mon. Not. R. astr. Soc,* **154,** 229.

Hunt, B. G. J.1973, *Atmos. Terr. Phys.,* **35,** 1755.

Köhnlein, W.1978, *Rev. Geophys. Space Phys.,* **16(3),** 341.

Komesaroff, M. M. 1960, *Austr. J. Phys.,* **13,** 153.

Laxmi, D. R., Aggarwal, S., Pasricha, P. K., Reddy, B. M.1979, *Indian J. Radio Space Phys.,* **8,** 101.

Laxmi, D. R., Shastri, S., Reddy, B. M. 1981, Sci. Rep. RSD-114, National Phys. Lab., New Delhi.

Llewellyn, S. K., Bent, R. B. 1973, Rep SAMSO TR-73-252,Space and Missile Syst. Organ., Los Angeles.

Rajaram, G, Rastogi, R. G. 1977, *J. atmos. ten. Phys.,* **39,** 1175.

Smart, W. M., Green, R. M. 1977, *Text book on Spherical Astronomy,* Cambridge Univ. Press, Ch. III.

Somayajalu, T. N., Ghosh, A. B. 1979, *Indian J. Radio Space Phys.,* **8,** 47.

Spoelstra, T. A. T. 1983, *Astr. Astrophys.,* **120,** 313.

Sukumar, S. 1986, *PhD Thesis,* Univ. Bombay.
Swarup, G. 1984, *J. Astrophys. Astr.,* **5,** 139.
Vikram Kumar, B. T., Rao, P. B. 1985, *Proc. Indian Acad. Sci.*: *Earth Planet. Sci.,* **94,** 7.
Yeh, K. C, Liu, C. H. 1974, *Rev. Geophys. Space Phys.,* **12(2),** 193.

J. Astrophys. Astr. (1987) **8,** 295–303

Flare-associated Surge Prominence on 1980 October 30

Rajmal Jain & Barkat Sorathia* *Udaipur Solar Observatory, 11, Vidya Marg, Udaipur 313001*

Received 1987 February 13; accepted 1987 August 5

Abstract. The Hα observations of a flare-associated surge prominence on 1980 October 30 have been described. Morphology and dynamics of the surge prominence have been presented. From our observations and analysis we have estimated the magnetic field associated with surge material to be about 35 gauss which is in good agreement with the earlier result of Tandberg-Hanssen & Malville (1974). It has been determined that coronal pressure is not acting as a resistive force on the outward expansion of the surge into the corona. The kinetic energy of the surge was about 10^{28} erg, which is 2 orders less than required for the mass to escape the chromosphere. It appears that the flare-associated surge prominence was perhaps a result of kink instability in the flaring region.

Key words: solar flare—surge prominence—mass ejection—magnetic field —kink instability

1. Introduction

Quite often a solar flare is accompanied by gas ejections which manifest themselves as moving prominences on the limb. The majority of surge prominences is associated with small flares, *i.e.,* only with the flare at its base. This applies even to very large surges as pointed out by Gopasyuk & Ogir (1963). Near the solar limb it is seen that the surge is formed by a stretching of the base. When the surge attains maximum height the base flare disappears as if the whole flare material had been transformed completely into the surge (Bruzek 1969), which, however, keeps in contact with the chromosphere during its whole lifetime. After maximum extension the material returns to the chromosphere either along the trajectory of its ascent or along a large arch, thus obviously guided by the magnetic field.

The shape of a surge is either a straight or a curvilinear spike which moves upward from the chromosphere with velocities between 50 and 200 km s^{-1}. Lifetime of these spikes are mostly between 10 and 30 min (Westin 1969). The surge sources are usually situated close to the edges of sunspot penumbrae (Giovanelli & McCabe 1958). According to Rust (1968) the surge sources are usually located above small, changing, satellite sunspots which represent small 'islands' of polarity reversals near a large spot. However, according to Roy (1973) the surges appear to be related to rising flux of one polarity into a region of stronger opposite flux. The morphology of recurrent surge

* Permanent address: c/o Lion Om Methi, Kudva Line, Gondia 441601, Maharashtra.

activity with a quasi-periodicity of 5–30 min is described by Jain, Bhatnagar & Shelke (1984). A typical large surge has a mass of 10^{15}–10^{16} g and a mechanical energy of 10^{30}–10^{31} erg. Further, it is interesting to note that type II and type III radio bursts are more likely to occur if the associated flare is accompanied by a surge.

In this paper we present Hα observations made at Udaipur solar observatory, of a flare-associated surge prominence which occurred on 1980 October 30 at south-west limb of the Sun. The flare surge activity was observed to begin at 0720 UT and to end at 0745 UT. Associated with this activity, X-rays, SIDs and type III radio bursts were also observed.

2. Observations

On 1980 October 30, the Hale region 17212 gave rise to a flare of importance 1N beginning at 0720 UT and at a location S16 W89, *i.e.,* at the southwest limb of the Sun. This flare was accompanied by a surge prominence observed on the limb. We present in this paper a detailed study of the development of the surge prominence. Time-lapse observations of the flare-associated surge prominence were made at an interval of 5 s and 10 s in the Hα line centre, through a Halle filter of 0.7 Å passband in conjunction with a 15 cm aperture solar spar telescope. A total of 250 frames were obtained for the event.

Associated with the flare-surge event, X-ray flux enhancement in 0.5–4 Å and 1–8 Å bands were observed; also type III radio bursts were reported in metric band. Given in Table 1 is a summary of optical, X-ray and radio events (Solar Geophysical Reports No. 435-I; 436-I and 440-11).

3. Morphology

Shown in Fig. 1 is the development of the flare-associated surge prominence in Hα line centre. At 072032 UT two spikes S1 and S2 are associated with the flare at the base as shown in Fig. 1 (b). At this time S1 and S2 had already attained heights of 9500 and 15900 km respectively in the sky plane. Both were moving out with an average

Table 1. Summary of the time history of Hα flare-associated surge phenomenon.

Time UT	Optical	Radio metric bursts	X-ray & SID
0720	—	—	Beginning of flux enhancement
072022	Flare surge appearance	—	—
072530	Explosive phase	—	Maximum phase of X-ray
0726	—	—	Beginning of SID
0734	—	—	SID maximum
073648	—	Type III radio bursts start	—
0745	Surge prominence decayed	—	—

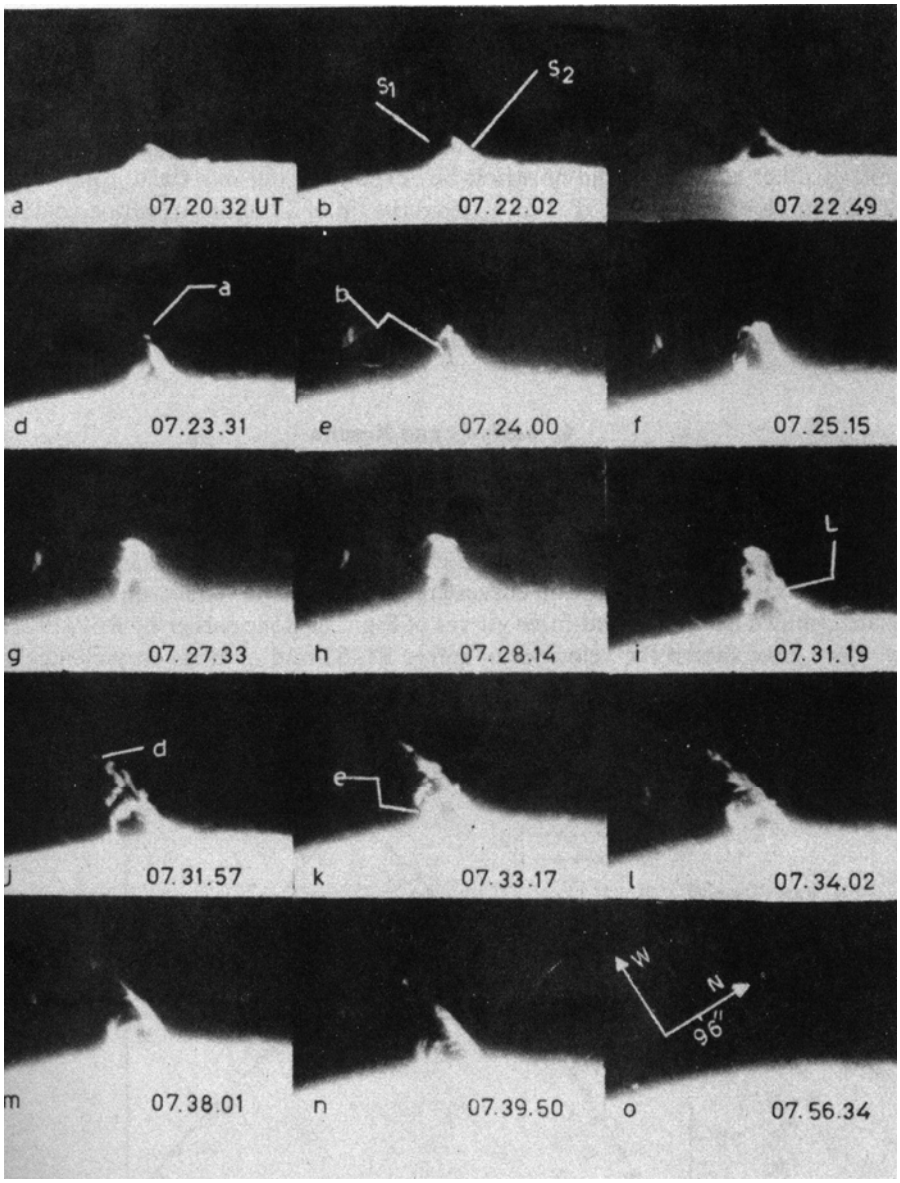

Figure 1. Sequence of Hα filtergrams, showing the development of the flare-associated surge prominence of 1980 October 30 at 0720 UT.

velocity of about 50 km s^{-1} At 072331 UT the tip of S2, called as 'a' (Fig. 1d) was shot out with a velocity of about 100 km s^{-1}. After reaching a maximum height of 34900 km the material in tip 'a' started flowing down in an arch manner and ultimately diffused. On the other hand, around 0723 UT, when spike S1 was moving down towards the limb, its tip, 'b' (Fig. le) was detached and started moving up with a velocity of about 200 km s^{-1} to join spike S2. However, around 0725 UT, large amounts of material were rising up in both spikes S1 and S2 (Fig. If), and mostly in S2

which was in fact composed of several individual bright spikes. The material then started flowing down on the other end in the form of arches, as shown in Fig. l g and onwards. This stage perhaps coincides with the exploding phase of the flare at the base as indicated in Table 1. Among several arches an arch 'L' was identified at a height of about 35000 km (Fig. 1i). This arch 'L' was seen at the same height until 0741 UT. Similarly other arches also did not show any expansion out into the corona. Around 0729 UT, a blob of material, 'd' (Fig. 1j) from the tip of S2, shot out with a velocity of about 50 km s^{-1}. After reaching a maximum height of 73000 km it started coming down, however, not in the same trajectory but along the other leg of the arch formed by S2. From 0728 to 0738 UT a clump of bright material 'e' was seen moving downwards along the southern leg of the loop with a velocity of about 100 km s^{-1}

4. Analysis and Results

A magnifying eyepiece with a millimetre scale of accuracy 0.05 mm (1500 km) was used for determining the positions of various features associated with the flare-surge event under study. Shown in Fig. 2 are positions of various features as a function of time whereas in Fig. 3 acceleration curves are presented. The velocity in the sky plane was determined from the hand-fitted curves of Fig. 2 as done earlier by Roy (1973). In Fig. 3, we have shown the velocities of spikes S1, S2 and of 'd' as they change with time. The values of acceleration are marked on the curve at various points. In fact an

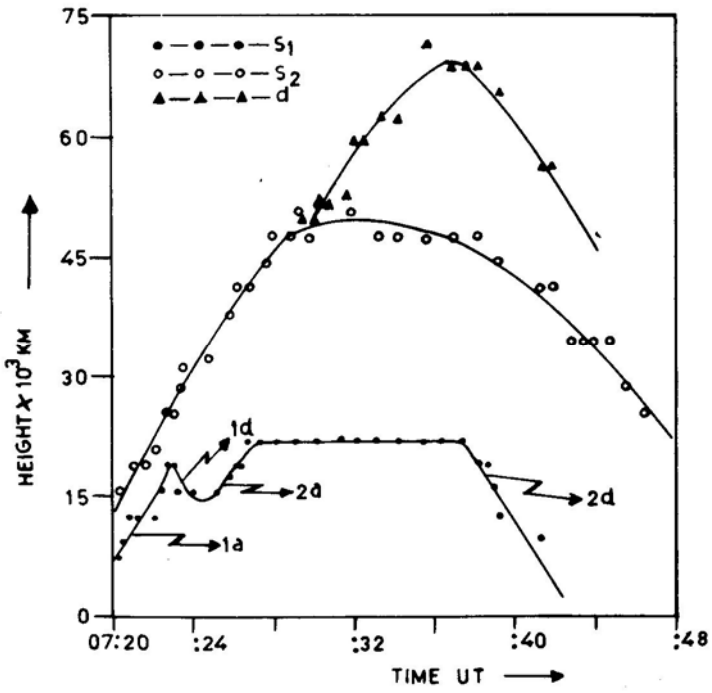

Figure 2. The height versus time plots, showing the positions of surge tops in sky plane as a function of time.

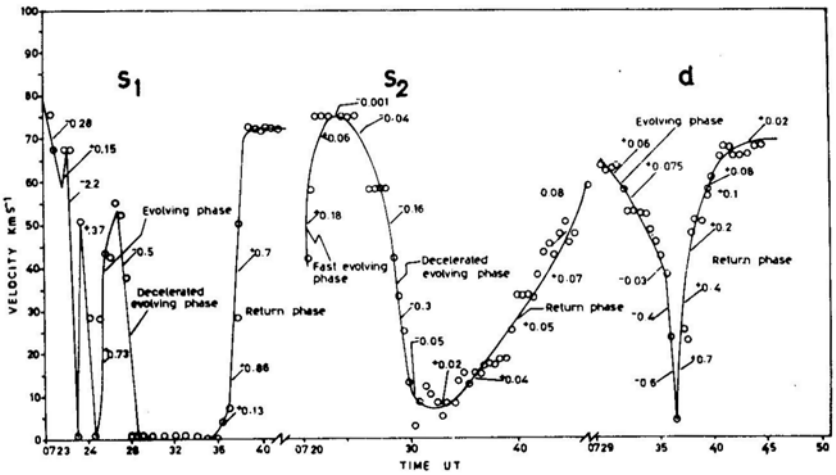

Figure 3. The velocity versus time plots of S1, S2 and 'd' features of surge prominence. Acceleration values (km s^{-2}) are also marked at various points.

evolving surge has three different phases—the fast ascending phase, the decelerated ascending phase, and the return phase. This can be seen best in the curve for spike S2. The feature 'd' shot out from spike S2 and thus it had only decelerated ascending phase and the descending phase. The velocity of spike S1 changes very rapidly with respect to time and hence the acceleration also does. However, this might be due to several unresolvable spikes with S1.

We have made another attempt to study the ascending and descending phase separately. The velocity decreased in spike S1 as the spike rose upwards and then declined, but after 0725 UT it again rose. We have thus designated two ascending phases 1A and 2A for spike S1. In Fig. 4 the velocity versus height plots of spikes S1,

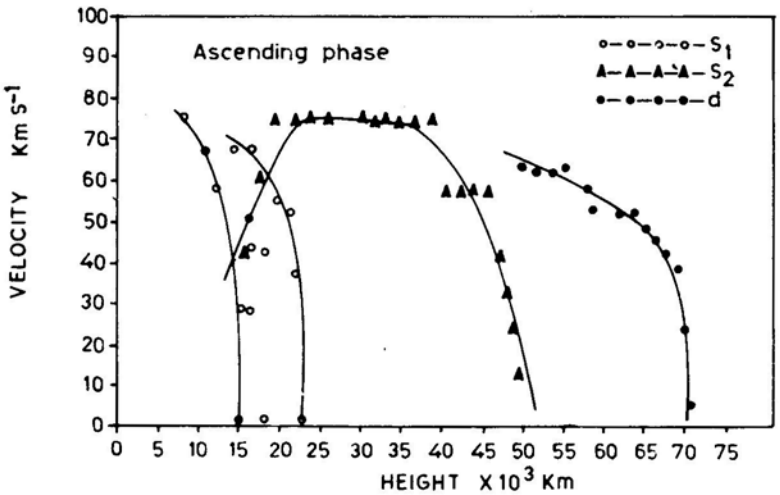

Figure 4. The velocity versus height curves for the ascending phase of the surge features S1, S2 and 'd'.

S2 and 'd' are shown during their ascending phase. In spike S2 the velocity increased in the beginning attaining 75 km s^{-1} when it reached a height of 22500 km; then it moved with zero acceleration up to a height of 35000 km; however, after that the velocity declined and reached 10 km s^{-1} at a height of 51500 km. Similarly in feature 'd' the velocity decreased during the ascending phase.

In the descending phase (Fig. 5) one can see that the velocity increased in all features, S1, S2 and 'd', as the material came down. This is perhaps caused by gravity.

5. Discussion

The material of the surge might become optically thin near the top or disappear perhaps either because of an expansion or because the material becomes excited by the hot ambient corona (Roy 1973). However, both possibilities are ruled out by Hα observations because the return phase shows that strong deceleration is a reality (Fig. 5). Thus very little material 'boils-off' at the surge tip. A surge moving into the corona is not travelling in vacuum but it is ploughing its way through a medium having a finite energy density due to thermal pressure of the gas. It is interesting to find whether the coronal gas pressure can resist the surge from moving outwards. The pressure exerted by surge material is $\frac{1}{2} m_H v^2 n_e$. We obtain, for $n_c = 10^{12}$ cm^{-3} and $v = 75$ km s^{-1}:

$$\tfrac{1}{2} m_H v^2 n_e \simeq 48 \text{ dynes cm}^{-2}. \quad (1)$$

The coronal gas pressure is NkT. For the corona $N = 10^{10}$ cm^{-3} and $T = 10^6$ K, which gives the gas pressure of about 1 dyne cm^{-2}. Thus the coronal gas pressure is insufficient as a resistive force to reduce the velocity of the moving surge material. In fact it is the kinetic energy converted from the thermal energy gained by the surge material from the flare at the base in the chromosphere. If the kinetic energy is not high enough, then the surge material will return in the same trajectory and if it is high it will travel along the magnetic arch. However, if the velocity of the moving material

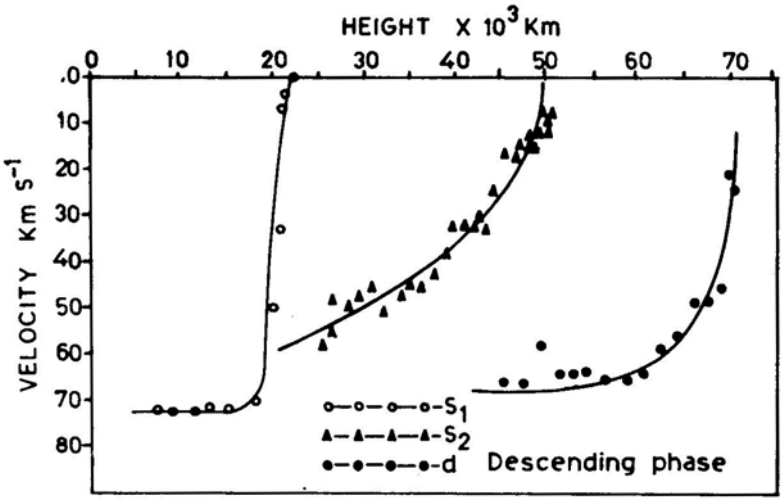

Figure 5. The velocity as a function of height of S1, S2 and 'd' during the returning phase.

exceeds the escape velocity, then the material moves out into the corona and is called a spray.

Our observations show that the surge material either returned along the same trajectory or travelled along the magnetic arch. Thus for the surge material driven and held by the expanding large-scale field, we require that $B_z^2/8\pi \geqslant \frac{1}{2}\rho v^2$.Using relation (1), we have,

$$B_z^2/8\pi \geqslant 48 \text{ dynes cm}^{-2}. \tag{2}$$

We obtain from this relation that the longitudinal magnetic field in the surge material under study is about 35 gauss, which lies within the limits given by Tandberg-Hanssen & Malville (1974).

The mass M_s in the surge is estimated as follows. $M_s = V_s \rho$ where V_s is the volume of surge spike S2. We determine the maximum height of spike S2 to be about 10800 km. With the help of enlargements made for the event on a scale 48 arcsec cm^{-1}, we estimate the thickness of the fine structure resolved in the spike to be about 1200 km. Thus we get $V_s \simeq 6.6 \times 10^{26}$ cm^3. In the surge $n_e = 10^{12}$ cm^{-3} and we get

$$M_s = \alpha(1.12 \times 10^{15})\text{g}, \tag{3}$$

where α is the filling factor less than unity. For the range of α between 0.1 and 0.9, the mass observed in Hα for spike S2 lies between 10^{14} g and 10^{15} g.

The maximum velocity in spike S2 observed in Hα is 75 km s^{-1}. Therefore the kinetic energy in the Hα surge prominence (spike S2) is

$$E_{kin} = 3.14 \times 10^{28} \text{ erg}. \tag{4}$$

With the associated mass of 10^{15} g and velocity of 75 km s^{-1} ($E_{kin} = 3 \times 10^{28}$ erg) the surge cannot move out because in order to escape it needs a kinetic energy of the order of 10^{30} erg taking $V_{esc} = 620$ km s^{-1}. On the other hand, magnetic field energy is one order higher; thus we observed that either the surge material was falling back along the same trajectory or moving along the loop so as to fall at the other end of the loop. Hence the material was guided along the magnetic loops. These observations emphasize the force-free fields in the loop. This assumption has been used later while calculating the current in the loop.

It is generally believed that solar flares and associated optical phenomena are caused by some kind of plasma instability in the coronal plasma permeated by magnetic fields. The stability of a magnetic flux loop embedded in the solar plasma is not fully understood quantitatively. General equilibrium properties of a magnetic flux tube in the solar atmosphere have been studied by Raadu (1972) and Parker (1975). Raadu showed, in the context of a solar flare that force-free cylindrical magnetic flux rope of finite length L with both ends rigidly fixed in dense material of the chromosphere is stable against the kink instability, provided the flux is not twisted more than one turn over the length L. The stability condition against the kink instability obtained by Raadu (1972) is

$$\frac{B_z}{B_\theta} \geqslant \frac{L}{2\pi a} \tag{5}$$

where B_z is the longitudinal magnetic field, B_θ is the azimuthal magnetic field and α is the radius of the cylindrical rope. The condition (5) just expresses the fact that for stability, the twisting of the magnetic field is less than one whole turn over the length

L. Expressing the azimuthal field in terms of the current I, ($B_\theta = 2I/ca$) in the inequality (5), we obtain the critical current for instability

$$I_c \simeq \frac{ca^2 B_z}{L}. \tag{6}$$

In the present case of surge prominence, *i.e.,* the maximum observed height of S2 is 51500 km (top of the flux rope) and from the fine structure in spike we find α = 600 km. With the longitudinal magnetic field B_z = 35 gauss, we get

$$I_c \simeq 7.8 \times 10^8 \text{ A}. \tag{7}$$

However, the stability condition was discussed above in relation (5), applies only to plasmas with very low β-values, i.e.,

$$\frac{8\pi n_e kT}{B_z^2} < 1.$$

In the present flare-associated surge prominence, $\beta \simeq 0.02$, if we consider $T = 10^4$ K. But the value estimated for β is sensitive to the value chosen for B_z. According to Cheng (1977) when β ranges from 0.015 to 0.39 for B_z = 30 gauss, the kink instability is certain to occur, no matter how small the current in the arch is. However, the current in the loop is calculated employing the following relation in a force-free magnetic field (Alfvén & Fälthammer 1963)

$$I = \tfrac{1}{2} fca B_z \tag{8}$$

where f is a numerical constant whose value is ~ 2.6. We estimated the current in the loop (I) to be of the order of 1.4×10^{10} A which is almost two orders higher than the critical current (I_c) needed for kink instability. This implies that the flare-associated surge prominence under study is a result of kink instability. This also implies that the increased current might be produced by a twisting of the foot points of the loop due to sub-photospheric motions which have been proposed by several authors. A similar conclusion was drawn earlier by Cheng (1977). However, it is interesting to find how much the temperature was increased due to increase in the current in the loop. We have found in this case that the kink instability occurred either due to $\beta \ll 1$ or $I \gg I_c$. However, if we consider kink instability due to $I \gg I_c$, then

$$I^2 = 200\pi a^2 n_e kT. \tag{9}$$

On putting $I = 10^{10}$ A; $n_c = 10^{12}$, we find $T \simeq 4 \times 10^5$K. This shows that the temperature of the plasma was high enough for the arches to be observable in Hα in the beginning. Perhaps due to this reason we could not observe the Hα loops until 0730 UT. However, after 0730 UT, when the temperature possibly decreased to 10^4 K, the loops were easily identified. Thus the possibility of kink instability in the present case due to high value of β ($\gg$ *i.e.* due to increased temperature, also cannot be ignored as $\beta \gg 1$ is a more favourable condition for instability against relation 5.

Acknowledgements

We are very thankful to Dr. A. Bhatnagar for his keen interest in this work and encouragement. We are grateful also to Prof. J. L. Leroy and an anonymous referee

for their helpful comments and suggestions. BS is thankful to ASI for offering him a fellowship under popularization of astronomy programme and to Lion's club, Gondia, for providing him the travel grant. We are thankful to Mr. Laxmi Lal for preparing good prints of this event. Financial support for this work has come from the Dept. of Science & Technology, Govt. of India, under SERC scheme.

References

Alfvén, H., Falthammer, C. 1963, in *Cosmic Electrodynamics,* Oxford Univ. Press, London, p. 198.

Bruzek, A. 1969, in *COSPAR Symp. Solar Flares and Space Research,* Eds C. de Jager & Z. Svestka, p. 61.

Cheng, C. C. 1977, *Astrophys. J.,* **213,** 558.

Giovanelli, R. G., McCabe, M. 1958, *Austr. J. Phys.,* **11,** 1981.

Gopasyuk, S. J., Ogir, M. B. 1963, *Izv. Krym. astrofiz. Obs.,* **30,** 185.

Jain, R., Bhatnagar, A., Shelke, R. N. 1984, *Bull. astr. Soc. of India,* **12,** 162.

Parker, E. N. 1975, *Astrophys. J.,* **201,** 494.

Raadu, M. A. 1972, *Solar Phys.,* **22,** 425.

Roy, J. R. 1973, *Solar phys.,* **32,** 139.

Rust, D. M. 1968, in *IAU Symp.* 35: *Structure and Development of Solar Active Regions,* Ed. K. O. Kiepenheur, D. Reidel, Dordrecht, p. 77.

Tandberg-Hanssen, E., Malville, J. M. 1974, *Solar Phys.,* **28,** 477.

Westin, H. 1969, *Solar Phys.,* **7,** 393.

J. Astrophys. Astr. (1987) **8,** 305–314

Thermosolutal-Convective Instability in a Stellar Atmosphere

R. C. Sharma *Department of Mathematics, Himachal Pradesh University, Shimla 171005*

Bakshis Singh *S.V.S.D. College, Bhatoli, P.O. Naya Nangal, Himachal Pradesh*

Received 1987 April 28; accepted 1987 August 17

Abstract. The thermosolutal-convective instability of a stellar atmosphere is studied in the presence of suspended particles. The criteria for monotonic instability are derived and are found to hold good also in the presence of uniform rotation and uniform magnetic field on the thermosolutal-convective instability. The thermosolutal-convective instability of a stellar atmosphere is also studied in the presence of suspended particles and radiative transfer effects and the criteria for monotonic instability are obtained in terms of source function.

Key words: stellar atmosphere—thermosolutal-convective instability—suspended particles

1. Introduction

Defouw (1970) has found that an inviscid stellar atmosphere is unstable if

$$D = \frac{1}{C_p}(L_T - \rho\alpha L_\rho) + \kappa k^2 < 0, \tag{1}$$

where L is the heat-loss function (the energy lost minus the energy gained per gram per second), α the coefficient of thermal expansion, ρ the density, k the coefficient of thermometric conductivity, k the wave number of the perturbation, C_p the specific heat at constant pressure, L_T the partial derivative of L with respect to temperature T, and L_p the partial derivative of L with respect to density ρ, both evaluated in equilibrium state. Defouw (1970) has generalized the Schwarzschild criterion for convection to include departures from adiabatic motion and has shown that a thermally unstable atmosphere is also convectively unstable, irrespective of the atmospheric temperature gradient. 'Thermal-convective instability' is termed as the instability in which motions are driven by buoyancy forces of a thermally unstable atmosphere. In general, the instability due to inequality (1) may be either oscillatory or monotonic. Defouw (1970) has also shown that inequality (1) is a sufficient condition for monotonic instability in the presence of magnetic field and rotation on thermal-convective instability.

The conditions under which convective motions are important in stellar atmospheres are usually far removed from the consideration of a single component fluid and rigid boundaries and therefore it is desirable to consider one gas component acted on by solute concentration gradient and free boundaries. Keeping such situations in mind, Sharma & Misra (1986a) have considered the thermosolutal-convective instability in a stellar atmosphere and have also studied the effects of uniform rotation

and variable/uniform magnetic field on the instability. In a separate study, Sharma & Misra (1986b) have considered the thermosolutal-convective instability in the presence of finite Larmor radius and Hall effects. The criteria for monotonic instability are found to hold true in the presence of above effects.

Recent spacecraft observations have confirmed that dust particles play an important role in the dynamics of the Martian atmosphere as well as in the diurnal and surface variations in the temperature of the Martian weather (Pollack 1975). It is, therefore, of interest to study the presence of suspended (fine dust) particles in astrophysical situations. Sharma, Prakash & Dube (1976) have studied the effect of suspended particles on the onset of Bénard convection in hydromagnetics and have found that the effect of suspended particles is to destabilize the layer. A detailed account of thermal convection, under varying assumptions of hydrodynamics and hydromagnetics, has been given by Chandrasekhar (1981).

The present paper deals with the thermosolutal-convective instability of a stellar atmosphere in the presence of suspended particles. The Coriolis forces and magnetic field play important roles in astrophysical situations. The problem is, therefore, also studied in the presence of rotation and magnetic field. The effects of radiative transfer arise when self-absorption is not negligible. The radiative transfer effect is also considered on the thermosolutal-convective instability of a stellar atmosphere in the presence of suspended particles. These aspects form the subject matter of the present paper.

2. Formulation of the problem: perturbation equations

Consider an infinite horizontal fluid-particle layer of thickness d heated from above and subjected to a stable solute concentration gradient so that the temperatures and solute concentrations at the bottom surface ($z = 0$) are T_0 and C_0 and at the upper surface ($z = d$) are T_1 and C_1, respectively, z-axis being taken as vertical. This layer is acted on by gravity force g(0, 0, –g). Let $\rho, p, T, C,$ ν ($u, v,$ w), u (l, r, s), g, α, α', ν, k and k' denote respectively the density, pressure, temperature, solute concentration, fluid velocity, particle velocity, gravitational acceleration, thermal coefficient of expansion, an analogous solvent coefficient of expansion, kinematic viscosity, thermal diffusivity and solute diffusivity. The suffix zero refers to values at the reference level $z = 0$. Then the equations governing the motion of the fluid, following Boussinesq approximation, are

$$\frac{\partial \mathbf{v}}{\partial t} + (\mathbf{v}\cdot\nabla)\mathbf{v} = -\frac{1}{\rho_0}\nabla p + \nu\nabla^2\mathbf{v} + \mathbf{g}\left(1 + \frac{\delta\rho}{\rho_0}\right) + \frac{KN}{\rho_0}(\mathbf{u} - \mathbf{v}), \tag{2}$$

$$\nabla\cdot\mathbf{v} = 0, \tag{3}$$

$$\frac{\partial C}{\partial t} + (\mathbf{v}\cdot\nabla)C = \kappa'\nabla^2 C, \tag{4}$$

$$\rho = \rho_0[1 - \alpha(T - T_0) + \alpha'(C - C_0)]. \tag{5}$$

Here Equations (2)–(4) express the conservation of momentum, mass and solute mass concentration, respectively. Equation (5) represents the equation of state. $\delta\rho$ is the perturbation in density, N (x, t) is number density of particles and K (= $6\pi\rho_0\nu\varepsilon$), ε being particle radius, is the Stokes' drag. In the equations of motion for the fluid, the presence of particles adds an extra force term, proportional to the velocity difference

between particles and fluid. Since the force exerted by the fluid on the particles is equal and opposite to that exerted by the particles on the fluid, there must be an extra force term, equal in magnitude but opposite in sign, in the equations of motion for the particles. The buoyancy force on the particles is neglected. Interparticle reactions are also not considered for we assume that the distances between particles are quite large compared with their diameters. If mN is the mass of particles per unit volume, then the equations of motion and continuity for the particles, under the above assumptions, are

$$mN\left[\frac{\partial \mathbf{u}}{\partial t}+(\mathbf{u}\cdot\nabla)\mathbf{u}\right]=K_1 N(\mathbf{v}-\mathbf{u}), \tag{6}$$

$$\frac{\partial N}{\partial t}+\nabla\cdot(N\mathbf{u})=0. \tag{7}$$

The steady state solution is

$$\begin{aligned}&\mathbf{v}=0,\quad \mathbf{u}=0,\quad T=T_0+\beta z,\quad C=C_0-\beta' z,\\ &\rho=\rho_0(1-\alpha\beta z-\alpha'\beta' z),\quad N_0=\text{constant}\end{aligned} \tag{8}$$

where $\beta = (T_1 - T_0)/d$ and $\beta' = (C_0 - C_1)/d$ are the magnitudes of uniform temperature and concentration gradients.

Consider a small perturbation on the steady-state solution and let **v, u,** θ, γ, $\delta\rho$ and $\delta\rho$ denote the perturbations in fluid velocity, particle velocity, temperature, solute concentration, pressure and density, respectively, so that the change in density $\delta\rho$, caused by the perturbations θ and γ in temperature and concentration, is given by

$$\delta\rho=-\rho_0(\alpha\theta-\alpha'\gamma). \tag{9}$$

Then Equations (2)–(7) on linearization give

$$\frac{\partial \mathbf{v}}{\partial t}=-\frac{1}{\rho_0}\nabla\delta p+\nu\nabla^2\mathbf{v}-\mathbf{g}(\alpha\theta-\alpha'\gamma)+\frac{KN}{\rho_0}(\mathbf{u}-\mathbf{v}), \tag{10}$$

$$\nabla\cdot\mathbf{v}=0, \tag{11}$$

$$\left(\tau\frac{\partial}{\partial t}+1\right)\mathbf{u}=\mathbf{v}, \tag{12}$$

$$\frac{\partial M}{\partial t}+\nabla\cdot\mathbf{u}=0, \tag{13}$$

$$\frac{\partial\gamma}{\partial t}-\kappa'\nabla^2\gamma=\beta' w, \tag{14}$$

where $\tau = m/K_1$ and $M = N/N_0$.

If L, q, C_v and t denote, respectively, the heat-loss function, the thermal conductivity, the specific heat at constant volume and the time, then the first law of thermodynamics may be written as

$$C_v\frac{\mathrm{d}T}{\mathrm{d}t}=-L+\frac{q}{\rho}\nabla^2 T+\frac{p}{\rho^2}\frac{\mathrm{d}\rho}{\mathrm{d}t}. \tag{15}$$

The linearized perturbation form of Equation (15), following Defouw (1970), is

$$\frac{\partial\theta}{\partial t}+\frac{1}{C_p}(L_T-\alpha\rho L_\rho)\theta-\kappa\nabla^2\theta=-\left(\beta+\frac{g}{C_p}\right)w, \tag{16}$$

where C_p is the specific heat at constant pressure and k (= $q/\rho_o\ C_v$) is the thermal diffusivity.

The density changes arise principally from thermal effects. Consider the case in which both boundaries are free as well as perfect conductors of both heat and solute concentration. The case of two free boundaries is the most appropriate for stellar atmospheres. The boundary conditions appropriate for the problem are

$$w = \frac{\partial^2 w}{\partial z^2} = \theta = \gamma = 0. \tag{17}$$

3. Dispersion relation and discussion

Analyzing in terms of normal modes, we seek solutions whose dependence on x, y, z and t is of the form

$$(\sin k_z z)\exp(ik_x x + ik_y y + nt), \tag{18}$$

where $k_z = s\pi/d$ (s being any integer and d the thickness of the layer), n is the growth rate and $k(=\sqrt{k_x^2+k_y^2+k_z^2})$ is the wave number of the perturbation.
is the wave number of the perturbation.

Equations (10)–(12), (14) and (16) give

$$L_2\frac{\partial}{\partial t}\nabla^2 w = gL_2\left(\frac{\partial^2}{\partial x^2}+\frac{\partial^2}{\partial y^2}\right)(\alpha\theta-\alpha'\gamma)+\nu L_2\nabla^4 w-\frac{KN\tau}{\rho_0}\frac{\partial}{\partial t}\nabla^2 w, \tag{19}$$

$$\left(\frac{\partial}{\partial t}-\kappa'\nabla^2\right)\gamma=\beta' w, \tag{20}$$

$$\left(\frac{\partial}{\partial t}+D\right)\theta = -\left(\beta+\frac{g}{Cp}\right)w, \tag{21}$$

where $L_2 = 1+\tau\frac{\partial}{\partial t}$.

Eliminating θ, γ from Equations (19)–(21) and using (18), we obtain the dispersion relation

$$\begin{aligned}
&\tau n^4+\left[1+\frac{KN\tau}{\rho_0}+\tau(D+k^2\overline{\nu+\kappa'})\right]n^3\\
&+\left[D+\kappa'k^2(1+\tau D)+\Gamma\left(\beta+\frac{g}{C_p}\right)\tau+\Gamma'\beta'\tau+\nu k^2(\kappa'k^2\tau+\tau D+1)\right.\\
&\left.+\frac{KN\tau}{\rho_0}(D+\kappa'k^2)\right]n^2\\
&+\left[\kappa'k^2D\left(1+\frac{KN\tau}{\rho_0}+\nu k^2\tau\right)+\Gamma\left(\beta+\frac{g}{C_p}\right)(1+\kappa'k^2\tau)+\Gamma'\beta'(1+\tau D)\right.\\
&\left.+\nu k^2(D+\kappa'k^2)\right]n\\
&+\left[\Gamma\left(\beta+\frac{g}{C_p}\right)\kappa'k^2+(\nu\kappa'k^4+\Gamma'\beta')D\right]=0,
\end{aligned} \tag{22}$$

where $\Gamma = g\alpha(k_x^2 + k_y^2)/k^2$ and $\Gamma' = g\alpha'(k_x^2 + k_y^2)/k^2$.

If
$$D < 0 \quad \text{and} \quad |(\nu\kappa' k^4 + \Gamma'\beta')D| > \Gamma\left(\beta + \frac{g}{C_p}\right)\kappa' k^2, \tag{23}$$

the constant term in Equation (22) is negative. The product of the roots must, therefore, be negative. Hence at least one root of Equation (22) is positive and one root is negative. The occurrence of positive root implies monotonic instability. We thus obtain the criteria that a stellar atmosphere in the presence of solute concentration gradient and suspended particles is unstable if

$$D < 0 \quad \text{and} \quad |(\nu\kappa' k^4 + \Gamma'\beta')D| > \Gamma\left(\beta + \frac{g}{C_p}\right)\kappa' k^2.$$

4. Effect of magnetic field

Here we consider an infinite horizontal viscous and finitely conducting fluid-particle layer subjected to a stable solute concentration gradient and acted on by a uniform vertical magnetic field **H** (0, 0, *H*) and gravity force **g**(0, 0, – *g*). This layer is heated such that a steady temperature gradient β (= *dT/dz*) is maintained. The linearized perturbed equations of motion and Maxwell's equations are

$$\frac{\partial \mathbf{v}}{\partial t} = -\frac{1}{\rho_0}\nabla\delta p + \nu\nabla^2\mathbf{v} - \mathbf{g}(\alpha\theta - \alpha'\gamma) + \frac{KN}{\rho_0}(\mathbf{u} - \mathbf{v}) + \frac{\mu_e}{4\pi\rho_0}(\nabla \times \mathbf{h}) \times \mathbf{H}, \tag{24}$$

$$\nabla \cdot \mathbf{h} = 0, \tag{25}$$

$$\frac{\partial \mathbf{h}}{\partial t} = \nabla \times (\mathbf{v} \times \mathbf{H}) + \eta\nabla^2\mathbf{h}, \tag{26}$$

where **h** (h_x, h_y, h_z) is the perturbation in magnetic field **H**. μ_e and η denote the magnetic permeability and the resistivity respectively. Equations (11), (12), (14) and (16) remain unchanged. Equations (11), (12), (14), (16) and (24)–(26) give

$$L_2\left[\frac{\partial}{\partial t}\nabla^2 w - \nu\nabla^4 w - g\left(\frac{\partial^2}{\partial x^2} + \frac{\partial^2}{\partial y^2}\right)(\alpha\theta - \alpha'\gamma) - \frac{\mu_e H}{4\pi\rho_0}\nabla^2\frac{\partial h_z}{\partial z}\right] = \frac{KN\tau}{\rho_0}\frac{\partial}{\partial t}\nabla^2 w, \tag{27}$$

$$\left(\frac{\partial}{\partial t} - \eta\nabla^2\right)h_z = H\frac{\partial w}{\partial z}, \tag{28}$$

together with Equations (20) and (21). Eliminating h_z, θ and γ from Equations (20), (21), (27) and (28) and using (18), we obtain

$$\tau n^5 + \left[1 + \tau\left\{D + \frac{KN}{\rho_0} + k^2(\nu + \eta + \kappa')\right\}\right]n^4$$

$$+\left[D+k^2(\nu+\eta+\kappa')+\tau\left\{k^2D(\nu+\kappa'+\eta)+k^4(\nu\kappa'+\nu\eta+\eta\kappa')+\Gamma\left(\beta+\frac{g}{C_p}\right)\right.\right.$$
$$\left.\left.+\Gamma'\beta'+k_z^2V_A^2+\frac{KN}{\rho_0}(D+k^2\overline{\kappa'+\eta})\right\}\right]n^3$$
$$+\left[\nu\eta k^4+\kappa'k^2D+k^2(\nu+\eta)(D+\kappa'k^2)+\Gamma\left(\beta+\frac{g}{C_p}\right)(1+k^2\tau\overline{\kappa'+\eta})\right.$$
$$+\eta k^4\tau(\nu\kappa'k^2+D\overline{\nu+\kappa'})+\Gamma'\beta'(1+\tau\overline{D+\eta k^2})+k_z^2V_A^2(1+\tau\overline{D+\kappa'k^2})$$
$$\left.+\frac{KN\tau}{\rho_0}(\eta\kappa'k^4+k^2D\overline{\kappa'+\eta})\right]n^2$$
$$+\left[\kappa'k^4D(\nu+\eta)+\Gamma\left(\beta+\frac{g}{C_p}\right)k^2(\eta+\kappa'+\eta k^2\kappa'\tau)+\Gamma'\beta'(D+\eta k^2\overline{1+D\tau})\right.$$
$$\left.+(D+\kappa'k^2)(\nu\eta k^4+k_z^2V_A^2)+\kappa'k^4D\tau\left(\nu\overline{1+\eta k^2}+\frac{KN}{\rho_0}\eta\right)\right]n$$
$$+k^2\left[\nu\eta\kappa'k^4D+\eta\kappa'k^2\Gamma\left(\beta+\frac{g}{C_p}\right)+\Gamma'\beta'\eta D+k_z^2V_A^2\kappa'D\right]=0, \tag{29}$$

where $V_A^2=\mu_e H^2/4\pi\rho_0$.

If the inequalities (23) are satisfied, the constant term in Equation (29) is negative. Equation (29), therefore, involves one change of sign and hence contains one positive root. The occurrence of positive root implies monotonic instability. The criteria for monotonic instability (23), thus, hold good in the presence of uniform vertical magnetic field and suspended particles on thermosolutal-convective instability in a stellar atmosphere.

5. Effect of rotation

Here we consider an infinite horizontal fluid-particle layer heated from above and solute concentrated from below but acted on by a uniform rotation $\mathbf{\Omega}(0,\ 0,\ \Omega)$ and gravity force $\mathbf{g}(0,0,-g)$. The linearized perturbed equations of motion become

$$\frac{\partial\mathbf{v}}{\partial t}=-\frac{1}{\rho_0}\nabla\delta p+\nu\nabla^2\mathbf{v}-\mathbf{g}(\alpha\theta-\alpha'\gamma)+\frac{KN}{\rho_0}(\mathbf{u}-\mathbf{v})+2(\mathbf{v}\times\mathbf{\Omega}), \tag{30}$$

whereas Equations (11)–(14) and (16) remain unaltered. Equations (11), (12), (14), (16) and (30) give

$$L_2\left[\frac{\partial}{\partial t}\nabla^2w-\nu\nabla^4w-g\left(\frac{\partial^2}{\partial x^2}+\frac{\partial^2}{\partial y^2}\right)(\alpha\theta-\alpha'\gamma)+2\Omega\frac{\partial w}{\partial z}\right]$$
$$=-\frac{KN\tau}{\rho_0}\frac{\partial}{\partial t}\nabla^2w, \tag{31}$$

$$\left(L_2\frac{\partial}{\partial t}-L_2\nu\nabla^2+\frac{KN\tau}{\rho_0}\frac{\partial}{\partial t}\right)\zeta=2\Omega L_2\frac{\partial w}{\partial z}, \tag{32}$$

together with Equations (20) and (21). $\zeta = \frac{\partial v}{\partial x} - \frac{\partial u}{\partial y}$ denotes the z-component of vorticity. Eliminating ζ, θ and γ from Equations (20), (21), (31) and (32) and using (18), we obtain

$$A_6 n^6 + A_5 n^5 + A_4 n^4 + A_3 n^3 + A_2 n^2 + A_1 n + A_0 = 0, \tag{33}$$

where

$$A_6 = \tau^2,$$

$$A_5 = \tau\left[2 + k^2\tau\overline{2v+\kappa'} + \tau D + \frac{KN\tau}{\rho_0}\right],$$

$$A_4 = 1 + \tau\Bigg[2D + k^2 D\tau(2v+\kappa') + 2k^2(2v+\kappa') + vk^4(1+\kappa\tau+\kappa'\tau)$$
$$+ \frac{KN}{\rho_0}\left\{2(1+D\tau) + \frac{KN\tau}{\rho_0} + 2k^2\tau(v+\kappa')\right\} + \tau\left\{\Gamma\left(\beta + \frac{g}{C_p}\right) + \Gamma'\beta' + 4\Omega^2\frac{k_z^2}{k^2}\right\}\Bigg],$$

$$A_3 = D + k^2(2v+\kappa') + \tau\{k^2 D(4v+2\kappa') + 3v\kappa' k^4 + v^2 k^4(1+\kappa k^2) + 2v\kappa' k^4 D$$
$$+ v\kappa k^4 D\tau + v^2 k^4 D\tau\} + \frac{4\Omega^2 k_z^2\tau}{k^2}(2 + \tau\overline{D+\kappa' k^2})$$
$$+ \tau\Gamma\left(\beta + \frac{g}{C_p}\right)\left(2 + k^2\tau\overline{v+\kappa} + \frac{KN\tau}{\rho_0}\right) + \tau\Gamma'\beta'\left(2 + \tau\overline{D + vk^2 + \frac{KN}{\rho_0}}\right)$$
$$+ \frac{KN\tau}{\rho_0}\left\{2D + 2k^2(v+\kappa') + 2k^2 D\tau(v+\kappa') + 2v\kappa' k^4\tau + \frac{KN\tau}{\rho_0}(D+\kappa' k^2)\right\},$$

$$A_2 = v^2 k^4 + \kappa' k^2 D + 2vk^2(D+\kappa' k^2) + \frac{4\Omega^2 k_z^2}{k^2}\{1 + 2\tau(D+\kappa' k^2) + \kappa' k^2\tau^2 D\}$$
$$+ \Gamma\left(\beta + \frac{g}{C_p}\right)\left\{1 + k^2\tau\overline{2v+\kappa+\kappa'} + v\kappa k^4\tau^2 + \frac{KN\tau}{\rho_0}(1+\kappa k^2\tau)\right\}$$
$$+ \Gamma'\beta'\left\{1 + \tau\left(2D + vk^2 + \frac{KN}{\rho_0}\right) + \tau^2 D\left(vk^2 + \frac{KN}{\rho_0}\right)\right\}$$
$$+ \tau\Bigg[vk^4 D(\kappa+\kappa') + v^2 k^4(D+\kappa' k^2) + \frac{KN}{\rho_0}\left\{2k^2 D(v+\kappa') + v\kappa' k^4(D+2)\right.$$
$$\left. + \frac{KN\tau}{\rho_0}\kappa' k^2 D\right\}\Bigg],$$

$$A_1 = v^2 k^4(D+\kappa' k^2) + v\kappa' k^4 D + \Gamma\left(\beta + \frac{g}{C_p}\right)\left\{k^2(v+\kappa') + vk^4\tau(\kappa+\kappa') + \frac{KN\tau}{\rho_0}\kappa' k^2\right\}$$
$$+ \Gamma'\beta'\left(D + vk^2 + 2vk^2 D\tau + \frac{KN\tau}{\rho_0}D\right) + v^2\kappa k^6 D\tau + \frac{KN\tau}{\rho_0}vk^4 D(\kappa+\kappa')$$
$$+ \frac{4\Omega^2 k_z^2}{k^2}(D + \kappa' k^2 + 2\kappa' k^2 D\tau),$$

$$A_0 = vk^2\left\{(v\kappa' k^4 + \Gamma'\beta')D + \kappa' k^2\Gamma\left(\beta + \frac{g}{C_p}\right)\right\} + 4\Omega^2 k_z^2\kappa' D. \tag{34}$$

If the criteria (23) are satisfied, the constant term in Equation (33) is negative. Equation (33), therefore, contains one positive real root. The occurrence of positive root implies monotonic instability. The criteria for monotonic instability, thus, hold good in the presence of rotation and suspended particles on thermosolutal-convective instability in a stellar atmosphere.

6. Radiative transfer effect

The effects of radiative transfer arise when self-absorption is not negligible. In considering the heat-loss function $L(\rho, T)$ to be dependent only on the local values of density and temperature, it is assumed that the gas is optically thin. We shall study radiative transfer with the Eddington approximation which is accurate in both the optically thick and optically thin limits as pointed out by Unno & Spiegel (1966).

The heat equation for a grey gas, using the Eddington approximation, may be written as

$$\rho C_v \frac{dT}{dt} - \frac{p}{\rho}\frac{d\rho}{dt} = \nabla\cdot\left[\frac{1}{3m\rho}\nabla\left\{\frac{1}{m\rho}\left(\rho C_v \frac{dT}{dt} - \frac{p}{\rho}\frac{d\rho}{dt}\right) + 4\pi S\right\}\right], \tag{35}$$

where m is the mass absorption coefficient and S is the source function.

Since the layer depth is small and the temperature gradient maintained is also small so that their product is very small in comparison with the temperature of the lower boundary, the temperature at an intermediate point may be approximately taken as the temperature of the lower boundary. The source function S and the mass absorption coefficient m may, therefore, be treated as independent of height in the equilibrium state. Then the linearized perturbation form of Equation (35) may be obtained as

$$\begin{aligned} 3m^2\rho^2\frac{\partial\theta}{\partial t} - \frac{4\pi m}{C_p}(S_T - \rho\alpha S_\rho)\nabla^2\theta - \frac{\partial}{\partial t}\nabla^2\theta \\ = -\left(\beta + \frac{g}{C_p}\right)(3m^2\rho^2 w - \nabla^2 w), \end{aligned} \tag{36}$$

where S_T and S_ρ denote, respectively, the partial derivatives of S with respect to T and ρ.

Equation (36), using expression (18), may be written as

$$(n+E)\theta = -\left(\beta + \frac{g}{C_p}\right)w, \tag{37}$$

where

$$E = \frac{4\pi m}{C_p}\cdot\frac{(S_T - \rho\alpha S_\rho)}{(1 + 3m^2\rho^2/k^2)}. \tag{38}$$

Eliminating γ and θ from Equations (19), (20) and (37) and using expression (18), we

obtain the dispersion relation

$$\tau n^4 + \left\{1 + \tau\left(E + \kappa' k^2 + \frac{KN}{\rho_0}\right)\right\} n^3$$
$$+ \left[E + \kappa' k^2 + \nu k^2 (1 + E\tau + \kappa' k^2 \tau) + \tau\left\{\kappa k^2 E + \Gamma\left(\beta + \frac{g}{C_p}\right) + \Gamma' \beta'\right.\right.$$
$$\left.\left. + \frac{KN}{\rho_0}(E + \kappa k^2)\right\}\right] n^2$$
$$+ \left[\kappa' k^2 E\left(1 + \frac{KN\tau}{\rho_0}\right) + \Gamma\left(\beta + \frac{g}{C_p}\right)(1 + \kappa' k^2 \tau) + \Gamma' \beta' (1 + E\tau)\right.$$
$$\left. + \nu k^2 (E + \kappa' k^2 \overline{1 + E\tau})\right] n$$
$$+ \left[(\nu\kappa' k^4 + \Gamma' \beta') E + \kappa' k^2 \Gamma\left(\beta + \frac{g}{C_p}\right)\right] = 0. \tag{39}$$

If

$$S_T - \frac{\rho}{T} S_\rho < 0 \quad \text{and} \quad |(\nu\kappa' k^4 + \Gamma' \beta') E| > \kappa' k^2 \Gamma\left(\beta + \frac{g}{C_p}\right), \tag{40}$$

the constant term in Equation (39) is negative. The product of the roots must, therefore, be negative. This implies that at least one root of Equation (39) is negative and one positive. The occurrence of a positive root implies monotonic instability.

We thus obtain the criteria that a stellar atmosphere in the presence of stable solute concentration gradient, radiative transfer and suspended particle effects is unstable if

$$S_T - \frac{\rho}{T} S_\rho < 0 \quad \text{and} \quad |(\nu\kappa' k^4 + \Gamma' \beta') E| > \kappa' k^2 \Gamma\left(\beta + \frac{g}{C_p}\right).$$

7. Discussion

The Schwarzschild criterion is applicable in the interior of a star, where the photon mean free path is small, the assumption that the motion is adiabatic is justified. The departure from adiabatic motion may be significant in the outer layers of a stellar atmosphere, where the effective heat transfer is no longer prevented by opacity. The instability in which motions are driven by buoyancy forces, of a thermally unstable atmosphere has been termed as thermal-convective instability. The stellar chromospheres, coronae and the interstellar medium may exhibit thermal-convective instability. The conditions under which convective motions are important in stellar atmospheres are usually far removed from the consideration of a single component fluid. Recent spacecraft observations have confirmed that dust particles play an important role in the dynamics of the Martian atmosphere as well as in the diurnal and surface variations in the temperature of the Martian weather (Pollack 1975). It is, therefore, of interest to study the presence of suspended (fine dust) particles in astrophysical situations. Keeping in mind such astrophysical situations, we have studied the

thermosolutal-convective instability (thermal-convective instability in the presence of a stable solute gradient) of a stellar atmosphere in the presence of suspended particles. The criteria for monotonic instability have been derived. The Coriolis force and magnetic field play important role in astrophysical problems and so the present problem is also considered in the presence of magnetic field and rotation. The criteria for monotonic instability have been found to hold good in the presence of magnetic field, rotation and suspended particles on thermosolutal-convective instability in a stellar atmosphere. The thermosolutal-convective instability of a stellar atmosphere in the presence of suspended particles is also considered to include radiative transfer effect with the Eddington approximation and the criteria for monotonic instability have been derived. The criteria for monotonic instability (23), in the absence of solute gradient, reduce to inequality (1) which is a sufficient criterion for an inviscid stellar atmosphere to be monotonically unstable. The criteria for monotonic instability hold true in the presence of suspended particles.

References

Chandrasekhar, S. 1981, *Hydrodynamic and Hydromagnetic Stability,* Dover, New York.
Defouw, R. J. 1970, *Astrophys. J.,* **160,** 659.
Pollack, J. B. 1975, *Scient. Am.,* **233,** 107.
Sharma, R. C, Prakash, K., Dube, S. N. 1976, *Acta phys. Hungarica,* **40,** 3.
Sharma, R. C, Misra, J. N. 1986a, *Astrophys. Space Sci.,* **126,** 21.
Sharma, R. C, Misra, J. N. 1986b, *Astrophys. Space Sci.,* **126,** 223.
Unno, W., Spiegel, E. A.1966, *Publ. astr. Soc. Japan,* **18,** 85.

J. Astrophys. Astr. (1987) **8,** 315–329

E (B – V) Determination from an UV-Visual Two-Colour Diagram: O and B Stars in the Catalogue of Stellar Ultraviolet Fluxes

R. K. Gulati *International Centre for Theoretical Physics, Strada Costiera 11, 1-34100 Trieste, Italy* and *Dipartimento di Astronomia,Universitá degli Studi di Trieste, Via Tiepolo 11, 1-34131 Trieste, Italy*

M. L. Malagnini *Dipartimento di Astronomia, Universita degli Studi di Trieste, Via Tiepolo 11, I-34131 Trieste, Italy*

C.Morossi *Osservatorio Astronomico, P.O. Box Succursale Trieste 5, Via Tiepolo 11, I-34131 Trieste, Italy*

Received 1987 July 5; accepted 1987 September 15

Abstract. We present here, for the O and B type stars in the Catalogue of Stellar Ultraviolet Fluxes, an approach which does not require a precise knowledge of spectral type and luminosity class for deriving $E(B - V)$ colour excesses. The method is based on the use of an UV-visual two-colour diagram; galactic variations in the interstellar extinction law are analyzed and fully taken into account. Our results have been compared with those derived by using the differences between observed and intrinsic colours for stars with known spectral classification. The very good agreement in a large number of cases (94 per cent) demonstrates that our approach permits the derivation of reliable colour excess values for early type stars even if only a rough spectral classification is available.

Key words: interstellar medium, extinction—stars, colours of—ultraviolet observations.

1. Introduction

The HR diagram is a fundamental tool in the comparison of stellar evolutionary models with observations. In particular, an accurate positioning of early-type field stars, O and B, on the theoretical HR diagram would permit astronomers to test different hypotheses of models for massive stars, to complete the upper main sequence for the solar neighbourhood, to support the determination of the initial mass function in the form derived from clusters and associations (Lequeux 1985; Scalo 1986). However, since theory provides quantities such as absolute luminosities and effective temperatures, while observations provide apparent magnitudes or fluxes and/or spectral classifications, links between these different sets of data must be carefully investigated. In fact, the tests sought by the theory may require not only accuracy on the observational side, but also uniqueness in the relationships between ‘observables’ and physical quantities.

Along this line, the most relevant difficulties to be expected are due to the following problems:

1. derivation, for a star, of actual apparent magnitude values from the observed one (or from the fluxes) through correction for interstellar extinction;
2. derivation of effective temperature from photometric or spectroscopic data and/or spectral classification;
3. determination of absolute luminosities or bolometric magnitudes from 'observables', different kind of measurements, distance determinations, and, in general, bolometric corrections.

In previous works devoted to the determination of effective temperatures and bolometric corrections, Malagnini *et al.* (1986, and references therein), resorted to the use of intrinsic colours for dereddening the stellar fluxes. This choice was not particularly critical because they were dealing with bright stars slightly reddened, and spectral classification could be carefully checked individually, due to the limited number of objects under study. On the other hand, the application of such a method to very large data bases becomes impractical because it is almost impossible to check spectral classifications and to guarantee their overall consistency and homogeneity, especially for poorly studied stars. We faced this problem when analyzing the data of Thompson *et al.* (1978, hereafter Thompson Catalogue), for the project of deriving the HR diagram for early-type field stars. Interstellar extinction can not be ignored since, due to the absolute high brightness of O and B stars, very highly reddened objects are expected to be present in the Thompson Catalogue which contains also stars with $V > 9$ mag.

In fact, the knowledge of interstellar extinction is of paramount importance for many different applications, such as distance determination, derivation of flux distribution, calibration of photometric data as a function of stellar physical parameters, comparison between theoretical and observed fluxes. Interstellar extinction depends on both the characteristics and the column density of interstellar matter lying in between the star and the observational apparatus.

It is usual to give a global measure of extinction at a specific wavelength, A_λ, as the product between a dimensionless wavelength-dependent term, k_λ, and a sort of reference scale factor, the colour excess $E(B-V) = A_B - A_V$ (mag). While the same set of k_λ's, which represents the interstellar reddening law, may hold valid for different objects, the $E(B-V)$ value has to be estimated for every object under study.

Among the different methods devised in order to determine $E(B-V)$, the following are most widely applied:

1. computing the difference between the observed colour, $(B-V)$, and the intrinsic colour, $(B-V)_0$;
2. making use of two-colour diagrams, like $(U-B)$ versus $(B-V)$;
3. comparing star-to-star;
4. ironing out of the 2200 Å bump.

In the first case, intrinsic colours are obtained from compilations such as that of FitzGerald (1970), once spectral classification has been assessed. Obviously, reliable classification and accurate photometry are needed in order to avoid large errors in $E(B-V)$.

The second method requires the knowledge of the loci of sequences of unreddened stars and of the slope of the reddening line in the two-colour diagram. If the reference sequence results are different for different luminosity classes, then reliable spectral classification, in addition to accurate photometry, is also required.

In the third case, magnitude differences between nearby and distant stars of the same type are measured in a set of spectral bands. $E(B - V)$ can be obtained, once the galactic interstellar reddening law is assumed. Mismatch error in spectral type and/or luminosity class must be carefully checked.

Eventually, $E(B - V)$ can be derived by applying a mean extinction law, such as that by Nandy *et al.* (1975), to the spectral flux energy distribution with varying values of $E(B - V)$ until the bump at 2200 Å due to interstellar absorption is ironed out. In this case we should be certain about the exactness of the applied extinction law.

We present here, for the O and B stars in the Thompson Catalogue, a particular two-colour diagram devised for the purpose of obtaining the $E(B - V)$ colour excesses without an accurate *a priori* knowledge of their spectral classification.

The input data are described in section 2; the two-colour diagrams with reference sequences and reddening line slopes are presented in section 3 for twelve different regions in the galaxy; results and comparison with determinations of colour excess by the intrinsic colour method are given in section 4.

2. The input data

The Catalogue of Stellar Ultraviolet Fluxes (Thompson *et al.* 1978) contains the amplest collection of stellar absolute ultraviolet fluxes collected by the S2/68 ultraviolet sky survey telescope aboard the ESRO TD-1 satellite. The magnetic tape version of this catalogue, prepared by United Kingdom Science Research Council, is the result of merging the Thompson Catalogue with a consistent set of catalogues (see Carnochan 1982) providing information on other relevant stellar quantities. It was prepared at University College London (UCL) and provided to us by the NASA World Data Center. It contains the absolute fluxes and their one-sigma errors in four UV passbands, centred on 1565 Å, 1965 Å, 2365 Å, and 2740 Å for 31290 stars; the broadband fluxes have been calculated by combining the individual data points, obtained with a resolution of about 20 Å, which fall within the bandwidth of 330 Å.

The stars have been selected with the constraint that the signal-to-noise ratio (S/N) should be at least 10.0 in any one of the passbands.

The following complementary ground-based information, if available, is also provided on the magnetic tape: (i) HD number, DM number, SAO number, Bright Star number and the name of the star; (ii) right ascension (RA) and declination (Dec); (iii) proper motion in RA and Dec; (iv) *UBV* photometry; (v) Strömgren parameters; (vi) Spectral classification; (vii) peculiarity; (viii) radial and rotational velocities.

It is worth remembering that the entry referring to spectral classification, if present, may come from different sources, and represents either the only determination found in the literature, or the average of more than one determination, or the result of Carnochan's choice in the case of stars classified in very different ways by different researchers.

All the UV fluxes and errors were transformed into magnitudes by using the Hayes & Latham (1975) absolute calibration of Vega.

From the Thompson catalogue we have selected the magnitude at 1965 Å wavelength to define a new colour, i.e. ($m_{1965} - V$). This colour should be more appropriate than the classical Johnson ($U - B$) colour in analyzing especially O and B type stars. In fact the ($m_{1965} - V$) colour permits us to extend the wavelength coverage of the star's energy distribution to the ultraviolet region where most of the flux is emitted by early-type stars. Moreover, the ($U - B$) colour includes residual atmospheric extinction (Johnson 1963) which introduces uncertainties and inaccuracies in the ($U - B$) versus ($B - V$) two-colour diagram.

Among the four UV bands we have preferred the magnitude at 1965 Å due to the following reasons: (1) the absolute calibration of the 1965 Å band of TD-1 satellite is in good agreement with that of the IUE satellite, which is considered the most accurate and reliable. In fact, in its wavelength region the correction factors needed to convert individual TD-1 fluxes to the IUE absolute scale are very close to 1 and only slightly dependent on wavelength (see Table 2 in Bohlin & Holm 1984); (2) the 2740 Å band is very likely to be affected by calibration errors which cannot be easily corrected for by introducing a constant scale factor (Faraggiana & Malagnini 1984). Therefore the colour excesses obtained by using two-colour diagrams based on the 2740 Å fluxes, as for instance the one presented in the Thompson Catalogue (page XVI), may be affected by unpredictable and non-negligible errors; (3) over the 2365 Å band the correction factors needed to convert individual TD-1 fluxes to the IUE absolute scale depend significantly on wavelength (see Table 2 in Bohlin & Holm 1984); moreover, this band includes the maximum of the 2200 Å bump due to interstellar extinction that causes heavily reddened stars to have very low signal-to-noise ratios. The situation is obviously better in the 1965 Å band, even if it is affected by the interstellar bump, because here the intrinsic fluxes for O and B type stars are expected to be higher; (4) the 1565 Å band includes strong resonance lines such as those due to C IV and Si IV which are critically sensitive to luminosity and mass loss effects.

Galactic coordinates (l^{II}, b^{II}) have been computed for each star starting from right ascension and declination and the whole sample was divided into twelve different regions (see Table 1) analogously to the regions defined by Meyer & Savage (1981, hereafter MS) in order to compare our results with theirs. Region A includes stars in the Scorpius-Ophiuchus; regions B, E, F, G, and H include stars along the galactic plane whereas region K includes stars from Orion region. The other regions are included so as to cover the rest of the sky.

3. Two-colour diagram

Instead of preparing an ($m_{1965} - V$) versus ($B - V$) colour diagram we decided to use, by analogy with the Johnson colour factor Q, a reddening-free quantity defined as

$$Q_{UV} = (m_{1965} - V) - (k_{1965} - R)\,(B - V)$$

where k_{1965} is the coefficient of interstellar extinction at 1965 Å band, $A_{1965}/E(B - V)$, and R is $A_V/E(B - V)$.

Since the interstellar extinction is different in different regions of our galaxy (see for example Koorneef 1978; MS; Carnochan 1986) the proper extinction coefficient ($k_{1965} - R$), hereafter denoted as c, was derived in each region. To derive c values, plots of $E(1965 - V)$ versus $E(B - V)$ have been prepared for stars with available

Table 1. The extinction coefficients and intrinsic colour line parameters for the twelve regions of the sky used in this paper.

Name	l^{II}, b^{II}	No.	c	2σ	a	2σ	b	2σ
A	90 to 30 6 to 90	38	4.94	0.14	0.176	0.005	0.086	0.007
B	330 to 30 −6 to 6	22	5.04	0.17	0.179	0.005	0.088	0.008
C	280 to 30 −90 to −6	28	5.33	0.10	0.190	0.006	0.094	0.008
D	30 to 60 −90 to −6	31	4.57	0.22	0.166	0.005	0.082	0.007
E	60 to 90 −6 to 6	28	4.44	0.28	0.162	0.004	0.080	0.007
F	90 to 160 −6 to 6	22	5.08	0.17	0.180	0.005	0.088	0.008
G	160 to 230 −6 to 6	47	5.36	0.30	0.191	0.006	0.095	0.008
H	230 to 330 −6 to 6	54	4.78	0.17	0.171	0.005	0.085	0.007
J	230 to 280 −90 to −6	49	4.56	0.39	0.165	0.005	0.082	0.007
K	185 to 230 −90 to −6	50	5.22	0.25	0.185	0.006	0.090	0.008
L	60 to 185 −90 to −6	59	5.32	0.10	0.189	0.006	0.094	0.008
M	60 to 290 6 to 90	31	5.37	0.10	0.191	0.006	0.095	0.008

No. = number of stars, $c = (k_{1965} - R)$, $(B - V)_0 = a \times Q_{uv} + b$.

spectral classification. The intrinsic colours used to compute $E(1965 - V)$ and $E(B - V)$ are from Carnochan (1982); the following selection criteria were adopted to arrive at the appropriate c values for each region. According to Bless & Savage (1972) O and early B type stars with the same spectral type and intrinsic visual colours exhibit similar relative flux distributions in the UV while this does not hold valid for later spectral types. In fact the UV flux decreases steeply with decreasing temperature, and the spread in temperature for different stars of the same spectral subclass causes significant differences in the UV colours for late B and A stars, thus preventing well-defined intrinsic $(m_{1965} - V)_0$ values. To overcome this problem related to the coarseness of the spectral type classification, only stars classified as B3 or earlier were selected to arrive at c values. The stars with very blue $E(1965 - V)$ were omitted and only stars having S/N more than 10 in the 1965 Å band were retained.

The linear least-squares fits through the data were performed with an iterative procedure such that points away from the linear relation by more than 2 times the root-mean-square error of the fit were rejected. A first check on the values of the intercepts was performed and, since in all the cases intercepts were not significantly different from zero, the slopes derived with the above-described method have been accepted as reliable estimates of the extinction coefficients. They were actually found to be significantly different for different regions by using a Student t-test, thus confirming the variation of the interstellar extinction along different directions of

observation in our Galaxy in good agreement with the MS determinations at ANS wavelengths (see Fig. 1). In fact, in each region, the extinction coefficient at 1965 Å band lies in between the two values derived by MS from the ANS bands at 1800 and 2200 Å, respectively, if the two-sigma error bars are taken into account. These results are shown in Table 1 and, for an illustration, the data and the linear least-squares fit for one of the regions is shown in Fig. 2.

For each of the twelve regions defined in Table 1, the proper c extinction coefficient has been used together with intrinsic colours from Carnochan's (1982) Tables 3 and 29, to prepare the twelve intrinsic two-colour diagrams, namely one Q_{uv} versus $(B - V)_0$ diagram for each region (see Fig. 3 as an example). In all the plots, referring to the different galactic regions, the points corresponding to the eleven different

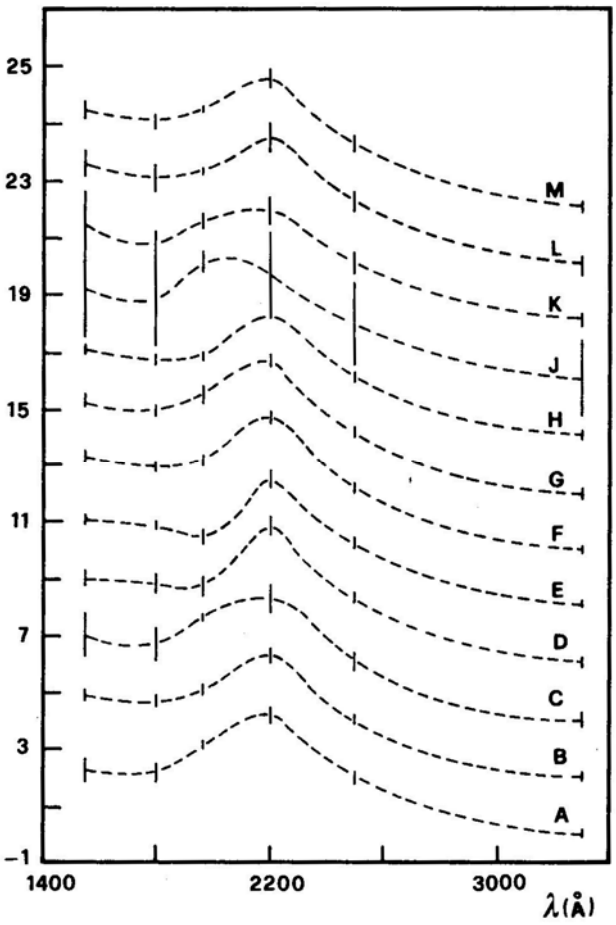

Figure 1. Extinction coefficients (c) at 1965 Å and two-sigma error bars are. plotted for the twelve regions given in Table 1 together with the extinction coefficients for the ANS passbands at 1550, 1800, 2200, 2500, and 3300 Å from Table 3 in Meyer & Savage (1981). The extinction coefficients for the ith region have been shifted by putting the value at 3300 Å equal to $(i - 1) \times 2$. Smooth dashed lines through the points have been drawn by hand just to make the figure more readable.

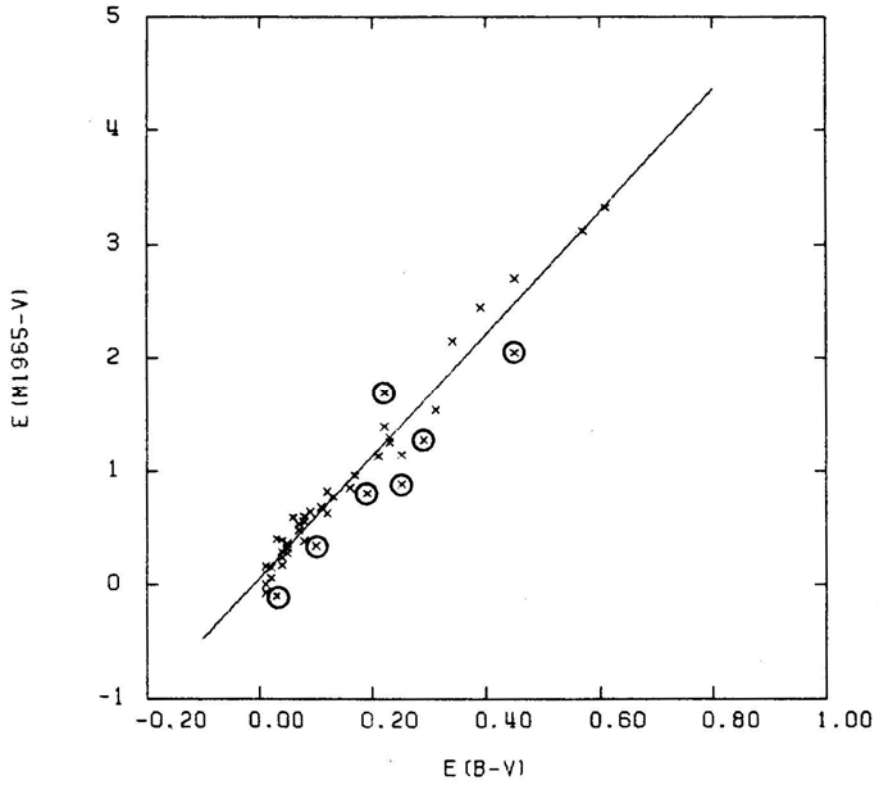

Figure 2. Correlation between $E(1965 - V)$ and $E(B - V)$ for stars in region M. The encircled points have not been used in deriving the slope of the L.M.S. straight line (see text) which is also shown. As expected the L.M.S. line passes very close to the origin.

luminosity classes (*i*.e. V, IV–V, IV, III–IV, III, II–III, II, Ib–II, Ib, lab, la) listed in Carnochan (1982), do not build up clearly separated sequences but are mixed together. Only three points fall away from the main bulk of data; they correspond to the intrinsic colours for the spectral classes B9 II, B9.5 II and A0 II, and have been obtained by Carnochan (1982) by interpolating the data for the very few luminosity class II stars at his disposal. It is very likely that their anomalous positions in the two-colour diagrams are due to the poor statistics for this luminosity class and do not reflect intrinsic properties. For these reasons, we decided to ignore them in the following analysis.

We can see that, for spectral types earlier than B8.5 ($Q_{UV} < -0.80$), at any fixed Q_{UV} value the spread in the corresponding intrinsic colours $(B - V)_0$'s due to the presence of different luminosity classes is always less than 0.04 mag. This figure is equivalent to twice the actual uncertainty on $(B - V)_0$, therefore an unique mean relationship between the two colours can be adopted without introducing significant systematic additional errors. By fitting a least-squares straight line through the points in each of the twelve diagrams, we found the mean relations, $(B - V)_0$ versus Q_{UV}, which permit us to give an estimation of $(B - V)_0$ starting from a Q_{UV} value. This estimate is independent of spectral type and luminosity class, and is affected by an uncertainty of ± 0.02 mag, which is comparable to the figure given in FitzGerald's (1967) Table 6.

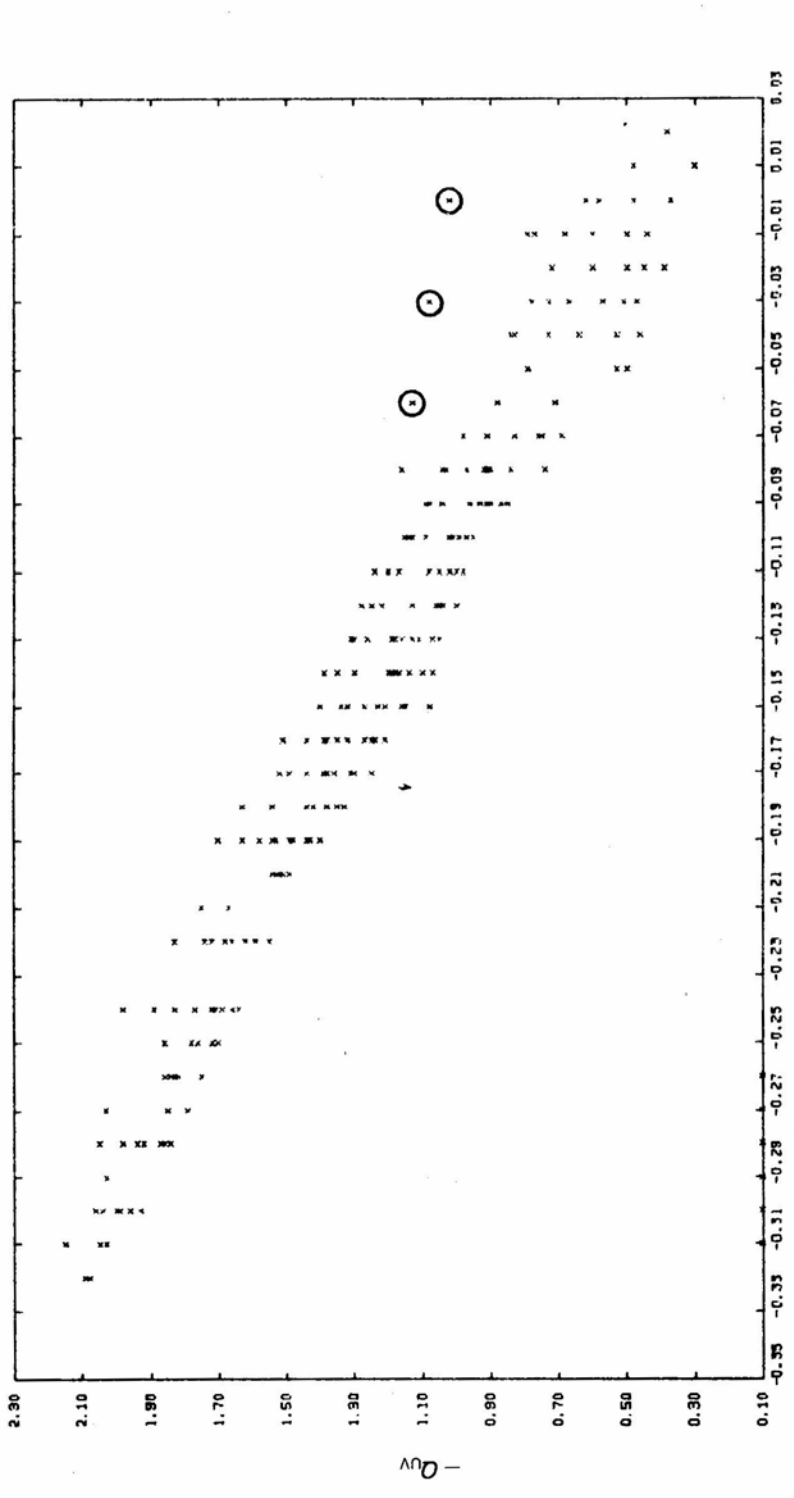

Figure 3. An example of intrinsic two-colour diagrams, $-Q_{UV}$ versus $(B-V)_0$. The interstellar extinction coefficient for region M, and Carnochan's (1982, Tables 3 and 29) intrinsic colours ($m_{1965}-V$) and $(B-V)_0$ have been used. The encircled points, corresponding to spectral classes B9 II, B9.5 II and A0 II, have not been used in deriving the values of the parameters a and b given in Table 1 (see text).

For each region the parameters a and b (slopes and intercepts) of the linear relations between $(B-V)_0$ and Q_{UV} are given in Table 1, together with their uncertainties. It is now possible to use these relationships to assign intrinsic $(B-V)_0$ colours to actual stars: from the observed values of $(B-V)$ and $(m_{1965}-V)$ we derive Q_{UV}, taking into account the position of the star in the sky so that the appropriate value for the extinction coefficient c can be used. Finally, the following relation is used to derive $E(B-V)$:

$$E(B-V) = (B-V) - (B-V)_i \tag{1}$$

where

$$(B-V)_i = a \times Q_{UV} + b$$

and

$$Q_{UV} = (m_{1965} - V) - c \times (B-V).$$

In order to estimate the accuracy of our determinations of $E(B-V)$ we took into account the following sources of uncertainties:

(a) photometric errors in the observed $(B-V)$ and V, which are on the order of 0.02 and 0.05 mag, respectively (see Blanco *et al.* 1968);
(b) photometric errors in m_{1965} from the Thompson Catalogue;
(c) uncertainties in the parameters a and b, and in the interstellar extinction coefficient c as given in Table 1.

Hence the final error in $E(B-V)$ was derived by using the standard propagation of errors:

$$\begin{aligned}\sigma^2(E(B-V)) = {} & (1 + c \times a)^2 \times \sigma^2(B-V) \\ & + ((m_{1965} - V) - c \times (B-V))^2 \times \sigma^2(a) \\ & + a^2 \times \sigma^2(m_{1965}) + a^2 \times \sigma^2(V) \\ & + (a \times (B-V))^2 \times \sigma^2(c) + \sigma^2(b).\end{aligned} \tag{2}$$

It is worth noting that the main contributions to the actual errors on $E(B-V)$ are the photometric errors on $(B-V)$ and m_{1965}. The 0.02 mag uncertainty on $(B-V)$ causes an uncertainty on $E(B-V)$ of 0.04 mag, while the errors on m_{1965} start to be important only when the signal-to-noise ratio in this band is lower than 7.

4. Results and discussion

We applied formulae 1 and 2, for each region separately, to the 1155 O and B type stars (the values obtained are available on request) whose spectral classifications are given in the Thompson Catalogue. This figure of 1155 stars comes from the full set of 31290 stars contained in the magnetic tape version of such a catalogue by adopting the following selection criteria based on the information contained in the catalogue itself:

(1) no indication of peculiarity, variability and/or duplicity;
(2) presence of both spectral type and luminosity class;
(3) positive values for both the flux and the corresponding error at 1965 Å band;
(4) presence of $(B-V)$ colour and V magnitude;

(5) computed Q_{UV} value smaller than – 0.80 (to reject stars for which the spread in the intrinsic two-colour diagrams, due to luminosity effect, is larger than the observational uncertainties in the photometric quantities).

The fulfillment of the criterion 2 for these 1155 stars permitted us to compare our results, EBV, with those, EBVF, obtained from the difference of observed colour, $(B - V)$, and intrinsic colour, $(B - V)_0$, taken from FitzGerald (1970) according to the listed spectral classification. There is a very good agreement between the EBV's and EBVF's values in most of the cases (see for example in Fig. 4 the plot of EBV versus EBVF referring to the stars in region M).

In order to identify the discordant cases, we defined a 'diagonal distance', D, which is related to the uncertainties on EBV and EBVF, namely

$$D = [\sigma^2(\mathrm{EBV}) + \sigma^2(\mathrm{EBVF})]^{1/2};$$

here σ(EBVF) was assumed to be 0.04 mag because of uncertainty of 0.02 mag in both $(B - V)$ *and* $(B - V)_0$.

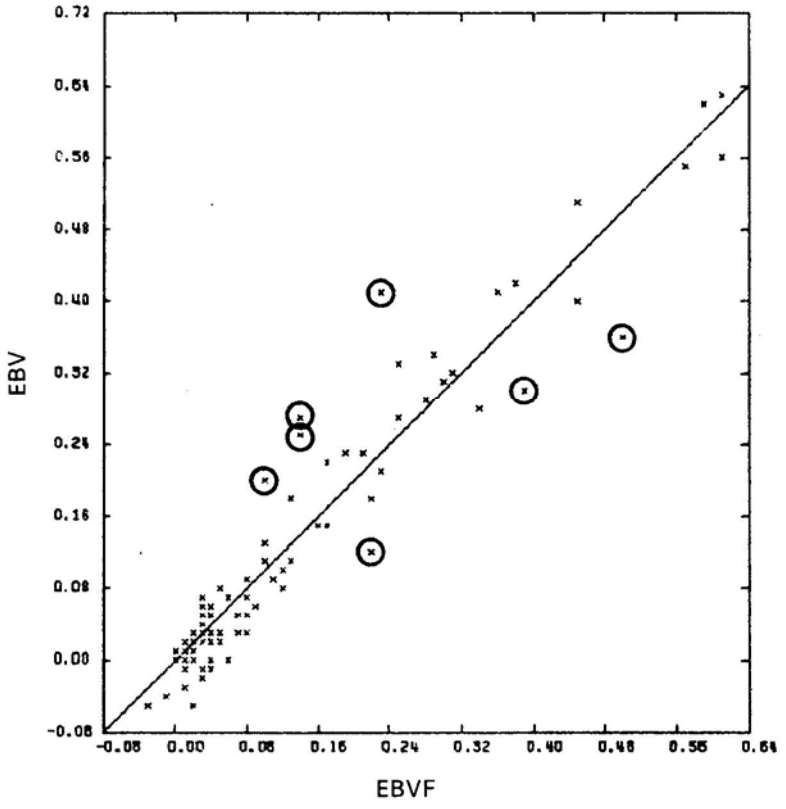

Figure 4. Comparison of $E(B - V)$ derived in this paper with those obtained by using FitzGerald's intrinsic $(B - V)_0$ for the stars in region M. Points with significant discrepancy in the two colour excess determinations are encircled and the line at 45 degrees is also plotted.

A check on the ratio of actual distance (d) from the line at 45 degrees to the diagonal distance (D) was made. We found 67 cases (6 per cent of the total) for which the ratios d/D are larger than 1 and the list of the corresponding stars is given in Table 2 with some remarks. Out of 67 stars, one star has d/D greater than 3, five stars have ratios between 2 and 3 and the rest of the stars have ratios between 1 and 2. These too large d/D values can be attributed to one or more of the following reasons: (i) wrong spectral classification: it causes a mistake in the EBVF estimation; (ii) anomalous photometric data reported in the Thompson Catalogue which will effect both EBV and EBVF determinations; (iii) underestimation of errors on EBV and EBVF values: it will effect the ratio between the actual and diagonal distance; (iv) peculiar extinction for the stars, which effects the c value used in the EBV determination; (v) presence of binary stars or multi-component systems; (vi) stellar peculiarity and/or variability.

Investigating the first possibility, thirty-two out of the 67 stars are found to have some classifications in the literature different from that given in the Thompson Catalogue. By choosing properly one of these, a good agreement between EBV and EBVF determinations can be achieved in twenty-three cases. If we add the fact that we could not check the reliability of spectral classification for those stars with only one determination, we can be confident that the inaccuracy of spectral classification will attribute most of the cases in Table 2 to wrong EBVF estimates. Therefore the advantage of our method, which does not require accurate knowledge of the stellar spectral type and luminosity class, is clearly confirmed and particularly evident.

The second and third possibilities seem to be less important. We have found no large differences between all the *UBV* photometric values given in the literature and those reported in the Thompson Catalogue. Therefore, both our estimates of Q_{UV} and D should be correct. But we have to recall that in some of the cases only one set of *UBV* photometric data has been found, thus preventing any check on their reliability.

Massa, Savage & Fitzpatrick (1983) and Camochan (1986) have deeply analyzed individual stars to study deviations from the mean extinction law and they concluded that some of the stars have actually peculiar extinction. Comparing their list of peculiar extinction stars with Table 2, we found five stars in common with Carnochan and one star in common with Massa, Savage & Fitzpatrick (1983). Hence the fourth possibility cannot be excluded.

As far as possibilities (v) and (vi) are concerned, we looked in the literature for any indication of variability, duplicity and/or peculiarity of all the stars listed in Table 2 even if they are classified as single normal stars in the Thompson Catalogue. Actually we found three binaries, one Be-shell, two variables and two chemically peculiar stars. It is possible that the use of non-simultaneous observations in the UV and in the visible produce spurious results for these kinds of objects (probably with the exception of chemically peculiar stars): in general, results for undetected variables or binaries may be unpredictable.

In conclusion, we can say not only that our method of estimating $E(B - V)$ gives reliable results as compared to those from the standard intrinsic colour method but also that, if for some stars discrepancies arise, this can be considered as a good indication that these objects are worth deeper analysis.

The main advantage of this method is that it makes it possible to estimate the colour excess for a much larger number of objects than usual, since it requires only a very rough indication of spectral type.

Table 2. List of stars for which the colour excess value computed in the present paper (EBV) differs significantly from the value obtained by using FitzGerald's intrinsic colour calibration (EBVF).

HD	EBVF	EBV	σ	D	d	d/D	Sp.	Remarks
9695	0.17	0.29	0.05	0.07	0.09	1.29	B9 III	A0, B8 III
14220	0.21	0.12	0.05	0.06	0.03	1.06	B2 V	
20961	0.13	0.25	0.05	0.07	0.09	1.30	A0 V	A1 V, B9.5 V
24129	0.17	0.33	0.05	0.07	0.11	1.74	B9.5 II–III	B9 II, B9 III, A0 III, B8 III
33189	0.20	0.33	0.05	0.06	0.09	1.48	B9 V	
34792	0.35	0.50	0.05	0.06	0.11	1.67	B9 V	
35329	0.41	0.61	0.05	0.07	0.14	2.12	B9 V	
37366	0.34	0.47	0.05	0.06	0.09	1.54	B1.5 V	B3, O9.5 V
38087	0.31	0.45	0.04	0.06	0.10	1.68	B4 V	B3, pec. extinction
38658	0.37	0.51	0.05	0.07	0.10	1.52	B3 II	
41831	0.36	0.52	0.05	0.06	0.11	1.80	B3 V	
42966	0.27	0.46	0.05	0.06	0.14	2.19	B9 V	
43025	0.13	0.22	0.05	0.06	0.06	1.01	B9 V	
43836	0.51	0.75	0.06	0.07	0.17	2.45	B9.5 II	A0 II, B9 II
43954	0.35	0.66	0.05	0.07	0.22	3.25	A0 V	
44290	0.38	0.61	0.05	0.06	0.16	2.56	B9 V	Ap, B9 V Cr Eu
45337	0.14	0.25	0.05	0.06	0.08	1.29	B5 V	
46592	0.23	0.41	0.05	0.06	0.13	2.10	B5 V	
48038	0.29	0.15	0.04	0.06	0.10	1.74	B1 V	
48282	0.50	0.61	0.06	0.07	0.08	1.11	B3 III	Be and shell
52382	0.38	0.47	0.05	0.06	0.06	1.06	B1.5 Ib	B2, B1 Ib
52533	0.20	0.29	0.04	0.06	0.06	1.09	B0.5 V	B6, O8.5 V, O9 V
52559	0.22	0.11	0.04	0.06	0.08	1.33	B2 IV–V	pec. extinction
57109	0.10	0.20	0.05	0.06	0.07	1.11	B9 V	
69253	0.16	0.27	0.04	0.06	0.08	1.42	B4 V	B3 V, B5 V

71609	0.39	0.28	0.04	0.06	0.08	1.33	B0 V	B2/3 II, B3 II
86606	0.11	0.20	0.05	0.06	0.06	1.06	B1 Ib	B0, B0.5 III/IV, B2 Ib
96261	0.35	0.48	0.06	0.07	0.09	1.33	B1 Ib–II	B0.5 III
112481	0.20	0.35	0.05	0.07	0.11	1.63	B2 Ib	B2 II/III
117856	0.46	0.56	0.04	0.06	0.07	1.20	B0 Ib	B0/1 III, B0 II, O9.5 III
124471	0.12	0.23	0.04	0.06	0.08	1.42	B2 Ib–II	B2 III/IV, B1.5 III, B2 III
137569	0.40	0.56	0.05	0.06	0.11	1.80	B5 III	
151310	0.19	0.31	0.05	0.06	0.09	1.40	B5 V	B8, B2 V, B3 V
151865	0.28	0.40	0.06	0.07	0.09	1.24	B8.5 V	B9, B8 V
155217	0.21	0.33	0.05	0.06	0.09	1.42	B3 V	B5, B2 II/III, B1 V, B1.5 III
155506	0.14	0.24	0.04	0.06	0.07	1.23	B3 V	B5, B2 V, B1 V, B1.5 V
156004	0.21	0.31	0.04	0.06	0.07	1.23	B3.5 V	B5, B2 II, B2 V, B1 V, B0.5 III
159831	0.14	0.27	0.05	0.06	0.09	1.43	A0 V	
166192	0.44	0.55	0.05	0.06	0.08	1.29	B2 V	
166787	0.68	0.82	0.06	0.07	0.10	1.35	B1 Ib	B3, B0.5 Ib-II
168302	0.36	0.47	0.05	0.07	0.08	1.18	B5 V	
170580	0.34	0.26	0.04	0.06	0.06	1.03	B2 V	binary, pec. extinction
170650	0.08	0.00	0.04	0.05	0.06	1.05	B4 IV–V	B6 IV
174403	0.44	0.58	0.05	0.06	0.10	1.62	B6 IV	variable
175156	0.34	0.25	0.04	0.06	0.06	1.11	B4.5 III	B5 II, He abnormal
176254	0.28	0.20	0.04	0.06	0.06	1.03	B2 IV	
183561	0.41	0.30	0.04	0.06	0.08	1.37	B2 III	pec. extinction
186536	0.27	0.18	0.04	0.06	0.06	1.13	B2 V	
187879	0.22	0.12	0.04	0.06	0.07	1.23	B1 III–IV	B2 II, variable, sp. binary (?)
188504	0.20	0.30	0.05	0.06	0.07	1.18	B9 III	B7 III, A4 Ia, binary (?)
191201	0.43	0.29	0.05	0.06	0.10	1.64	B0 III–IV	O9.5 IV, B2 V
191423	0.47	0.38	0.04	0.06	0.06	1.11	O9 V	O9 III, A9 V:
191456	0.29	0.21	0.04	0.06	0.06	1.03	B1.5 III	B0.5 III, B3, B0.5 IV, B0.5 II–III, pec. e
191746	0.25	0.15	0.04	0.05	0.07	1.31	B2 IV	
192517	0.14	0.03	0.04	0.05	0.08	1.44	B0.5 V	
192539	0.36	0.24	0.04	0.06	0.09	1.53	B2 III	
195556	0.15	0.05	0.04	0.05	0.07	1.32	B2 V	
197511	0.14	0.06	0.04	0.05	0.06	1.06	B2 V	
198784	0.30	0.19	0.04	0.06	0.08	1.42	B2 V	
200804	0.52	0.63	0.05	0.06	0.08	1.29	B3 IV	B2 II

Table 2. Continued

HD	EBVF	EBV	σ	D	d	d/D	Sp.	Remarks
205139	0.39	0.30	0.04	0.06	0.06	1.08	B0.5 II	B0, B1 II
206636	0.28	0.43	0.05	0.06	0.11	1.77	B7 V	
208218	0.50	0.36	0.05	0.07	0.10	1.52	B1 III	
213322	0.22	0.09	0.05	0.06	0.09	1.48	B2 IV	
250310	0.40	0.54	0.05	0.06	0.10	1.54	B3 V	
256413	0.51	0.67	0.06	0.07	0.11	1.54	B5 III	
290385	0.13	0.24	0.05	0.06	0.08	1.27	B8 V	

d = distance of the star's position in the EBV versus EBVF plot from the 45 degrees line;
$D = (\sigma^2(\text{EBV}) + \sigma^2(\text{EBVF}))^{1/2}$;
Sp = Spectral classification given in Thompson Catalogue.
Spectral types in the remarks are from Blanco *et al.* (1968), Buscombe (1968, 1977, 1980, 1981, 1984), Kennedy & Buscombe (1974), Houk (1978, '8, ouk (1978, 1982), Houk & Cowley (1975), Jaschek & Egret (1982).
By using the spectral types underlined, the new d/D ratios are lower than 1.

Acknowledgements

The facilities of the Astronet Center of Trieste on the Vax 11/750 were used for the computations. The NASA World Data Center is acknowledged for providing the UCL Ultraviolet Star Catalogue on magnetic tape through the Astronomical Data Center. Partial supports from a CNR-GNA grant, from the Universitá degli Studi di Trieste (MPI 60 per cent grant), and from ICTP are acknowledged. R.K.G. appreciates the hospitality given to him by the Osservatorio Astronomico di Trieste during his stay in Trieste while working on the present project. We are grateful to Prof. M. Hack of the Astronomy Department of Trieste University for critically going through the manuscript, for helpful comments and suggestions.

References

Blanco, V. M., Demers, S., Douglass, G. G., FitzGerald, M. P. 1968, *Photoelectric Catalogue,* Publ. U.S. Naval Obs., **21.**

Bless, R. C, Savage, B. D. 1972, *Astrophys. J.,* **171,** 293.

Bohlin, R. C, Holm, A. V. 1984, *NASA IUE Newsletter,* No. 24, p. 74

Buscombe, W. 1968, *M K Spectral Classification,* Northwestern Univ., Evanston.

Buscombe, W. 1977, *M K Spectral Classification,* Vol. 3, Northwestern Univ., Evanston.

Buscombe, W. 1980, *MK Spectral Classification,* Vol. 4, Northwestern Univ., Evanston.

Buscombe, W. 1981, *MK Spectral Classification,* Vol. 5, Northwestern Univ., Evanston.

Buscombe, W. 1984, *M K Spectral Classification,* Vol. 6, Northwestern Univ., Evanston.

Carnochan, D. J. 1982, *Mon. Not. R. Astr. Soc,* **201,** 1139.

Carnochan, D. J. 1986, *Mon. Not. R. Astr. Soc,* **219,** 903.

Faraggiana, R., Malagnini, M. L. 1984, *Astr. Astrophys.,* **137,** 149.

FitzGerald, M. P. 1967, *Doctoral Thesis,* Case Inst. Tech.

FitzGerald, M. P. 1970, *Astr. Astrophys.,* **4,** 234.

Hayes, D. S., Latham, D. W. 1975, *Astrophys. J.,* **197,** 593.

Houk, N. 1978, *Michigan Spectral Catalogue,* Vol. 2, Univ. Michigan.

Houk, N. 1982, *Michigan Spectral Catalogue,* Vol. 3, Univ. Michigan.

Houk, N., Cowley, A. P. 1975, *Michigan Spectral Catalogue,* Vol. 1, Univ. Michigan.

Jaschek, M., Egret, D. 1982, Catalog of Stellar Groups, Part one: The earlier groups, Centre Donnèes Stellaires, Strasbourg.

Johnson, H. L. 1963, in *Basic Astronomical Data,* Ed. K. Aa. Strand, Univ. Chicago Press, p. 204.

Kennedy, P. M., Buscombe, W. 1974, *M K Spectral Classification,* Northwestern Univ., Evanston.

Koorneef, J. 1978, *Astr. Astrophys.,* **68,** 139.

Lequeux, J. 1985, in *Birth and Infancy of Stars,* Ed. R. Lucas, A. Omont & R. Stora, North-Holland, Amsterdam, p. 3.

Malagnini, M. L., Morossi, C, Rossi, L., Kurucz, R. L. 1986, *Astr. Astrophys.,* **162,** 140.

Massa, D., Savage, B. D., Fitzpatrick, E. L. 1983, *Astrophys. J.,* **266,** 662.

Meyer, D. M., Savage, B. D. 1981, *Astrophys. J.,* **248,** 545.

Nandy, K., Thompson, G I., Jamar, C, Monfils, A., Wilson, R. 1975, *Astr. Astrophys.,* **44,** 195.

Scalo, J. M. 1986, *Fund. Cosmic Phys.,* **11,** 1.

Thompson, G. I., Nandy, K., Jamar, C, Monfils, A., Houziaux, L., Carnochan, D. J., Wilson, R. 1978, *Catalogue of Stellar Ultraviolet Fluxes,* UK Science Research Council (for the magnetic tape version).

J. Astrophys. Astr. (1987) **8,** 331–341

On an Unharmonic Oscillator Potential for Elliptical Galaxies

N. Caranicolas *Astronomy Department, University of Thessaloniki, 54006 Thessaloniki, Greece*

M. Gousidou-Koutita *Department of Mathematics, University of Thessaloniki, 54006 Thessaloniki, Greece*

Received 1987 July 20; accepted 1987 September 23

Abstract. Using a direct numerical procedure we approximate a 'realistic' potential for an elliptical galaxy by that of a perturbed harmonic oscillator. The quality of fitting is checked using two criteria. First by computing the value of the fitting parameter f, and second by comparing the behaviour of orbits for the two potentials. Both criteria suggest that the fitting is good when the total energy h is smaller than the energy of escape in the unharmonic potential.

Key words: galactic potentials—elliptical galaxies—stellar dynamics

1, Introduction

In the last three decades many papers have been devoted to the study of orbits in galactic type potentials made up of perturbed harmonic oscillators. The general form of such a potential in two dimensions is

$$V = \tfrac{1}{2}(Ax^2 + By^2) + \varepsilon V_1, \tag{1}$$

where ε gives the strength of the perturbation and V_1 is a polynomial containing terms of third or fourth degree in the variables or both (see Contopoulos 1960; Henon & Heiles 1964; Caranicolas & Barbanis 1982; Verlhust 1979).

On the other hand, it is generally believed that such models are comparable to realistic potentials only in a small region near an equilibrium point (Martinet & Mayer 1975). Therefore it seems of interest to see, how well and how far from the equilibrium point a realistic potential can be represented by that of an unharmonic oscillator.

In the present work we shall try to make a first step in this rather difficult problem. In order to keep things simple we have chosen the logarithmic potential with a softening parameter $c > 0$

$$V = \tfrac{1}{2}\ln(x^2 + \alpha y^2 + c), \tag{2}$$

where $1 \leqslant \alpha \leqslant 2$. Potential (2) was used by Richstone (1980, 1982) to model elliptical galaxies. In the above papers, potential (2) is considered as a realistic galaxy potential.

We shall refer to potential (2) as 'realistic'. We consider the following form for the potential of the perturbed harmonic oscillator

$$\tilde{V} = c_1 x^2 + c_2 y^2 + c_3 x^4 + c_4 x^2 y^2 + c_5 y^4. \tag{3}$$

Our aim is to find the values of c_1, c_2, c_3, c_4, c_5 for given values of α, c so that the potential surfaces V and $\tilde{V}$ will be as close as possible for a set of points (x_i, y_j). The method of fitting is described in Section 2. In Section 3 we compare the orbital characteristics of the potentials V, $\tilde{V}$ using the Poincaré surface of section, while in Section 4 we present the conclusions of this work.

2. The numerical model of the approximation

We take the constant value of $V=h$ and define a set of points (x_i , y_j), i, j= 1,2,..., n + 1 where n is the number of subintervals in the intervals $[x_{\min}, x_{\max}]$ and $[y_{\min}, y_{\max}]$ with

$$x_{\max}=(e^{2h}-c)^{1/2}=-x_{\min},$$
$$y_{\max}=[(e^{2h}-c)/\alpha]^{1/2}=-y_{\min}. \tag{4}$$

That is, we define the partitions

$$\Delta_x=\{x_1=x_{\min},\ x_i=x_1+i\delta x,\quad x_{n+1}=x_{\max};\qquad \delta x=(x_{\max}-x_{\min})/n\}$$
$$\Delta_y=\{y_1=y_{\min},\ y_j=y_1+j\delta y,\quad y_{n+1}=y_{\max};\qquad \delta y=(y_{\max}-y_{\min})/n\}. \tag{5}$$

For each value of x_i we take into account only the ordinates y_j that are inside the elliptic area $x^2+\alpha y^2 \leqslant e^{2h}-c$.

If we denote by V_{ij}, $\tilde{V}_{ij}$ the values of V and $\tilde{V}$ at the point (x_i, y_j) then the 'method of least squares' in three dimensions requires that

$$S(c_1, c_2, c_3, c_4, c_5)=\sum_i\sum_j (V_{ij}-\tilde{V}_{ij})^2=\text{minimum}. \tag{6}$$

The corresponding system of 'normal equations' is

$$\frac{\partial S}{\partial c_k}=0 \qquad (k=1, 2, \ldots, 5). \tag{7}$$

The solution of system (7) defines the coefficients c_k(k= 1, 2,. . . , 5). This solution is obtained by a direct numerical procedure using Gauss partial pivoting method with scaling in order to avoid numerical instabilities with minimum computational work and time.

It is more convenient to write potential (3) in the form

$$\tilde{V}=\tfrac{1}{2}(Ax^2+By^2)-\varepsilon(a_1x^4+2a_2x^2y^2+a_3y^4), \tag{8}$$

where ε is taken equal to 0.01. Then we choose c=1.0 and five values for the flattening parameter α namely the values 1.01, 1.25, 1.5, 1.75, 2.0. For each value of α we take a large number of values of h in the range $0.25 \leqslant h \leqslant 1.0$. Table 1 shows the values of A, B, a_1, a_2, a_3 when α is equal to 1.01 and 1.5 for three values of the total energy h. As a measure of the quality of the fitting we use the quantity

$$f=\max_{i,\,j}|V_{ij}-\tilde{V}_{ij}|/h. \tag{9}$$

The values of f are given in the last column of Table 1.

Table 1. Coefficients of the potential for different values of flattening parameter (α) and total energy (h).

α	h	A	B	a_1	a_2	a_3	f
	0.250	0.965852	0.978990	15.270854	15.643508	15.946167	0.00541
1.01	0.500	0.876289	0.894488	8.817660	9.124294	9.360752	0.02009
	0.625	0.816985	0.836895	6.550308	6.797898	6.994680	0.02990
	0.250	0.965843	1.453852	15.270193	23.225658	35.157233	0.00542
1.50	0.500	0.876342	1.327211	8.819726	13.526344	20.580536	0.01978
	0.625	0.816854	1.244042	6.547179	10.106868	15.472193	0.02983
Taylor	—	$1/c$	α/c	$25/c^2$	$25\alpha/c^2$	$25\alpha^2/c^2$	—

In the same table we also give the coefficients of the Taylor expansion. As expected, these coefficients are close to the ones obtained by the global fitting method, only for small values of the energy h. Results not shown here give differences of order 1–2 per cent when $0.001 \leqslant h \leqslant 0.01$.

Figs 1 and 2 show the potential surfaces: (a) $V(x, y)$ and (b) $\tilde{V}(x, y)$ when $\alpha = 1.50$, $c = 1.0$ for $h = 0.25$ and $h = 0.625$, respectively. We can see that the fitting is better for small h. It is also important to note that the numerical calculations suggest that the value of α does not affect significantly the quality of the fitting.

3. Orbital behaviour in the potentials V and $\tilde{V}$

Now we proceed to compare the orbital characteristics of the potentials V and $\tilde{V}$. For this purpose we use the Poincaré surface of section x–$\dot{x}$.

Figs 3a, b show the surfaces of section for the dynamical systems V and $\tilde{V}$ respectively, when $\alpha = 1.01$, $c = 1.0$, $h = 0.25$. It is interesting to observe that the two surfaces of section appear very similar. If we change the value of the flattening parameter α we get the same results. This can be seen in Fig. 4 where α is changed to 1.50. Although the topology of the surface of section appears different from that of Fig. 3 the similarity of the patterns is evident.

Figs 5a, b show the surfaces of section for potentials V and $\tilde{V}$ respectively when $\alpha = 1.01$, $h = 0.625$. We can see now some differences between the two surfaces of section. The first difference is that in potential $\tilde{V}$ there are two additional nearly straight-line periodic orbits going through the origin, whereas the x-axis is an unstable periodic orbit. The second difference is that in potential $\tilde{V}$ stars moving in box orbits go almost in every part of the galaxy and cross the x-axis only in a small region near the centre, whereas in potential V, box orbits belong to stars moving near the x-axis which is a stable periodic orbit. This is probably due to the fact that the box orbits 'touch' the zero velocity curve and therefore approach the region where the fitting is not very good (see Fig. 2). On the contrary, the rest of the surface or section covered by invariant curves giving the tube orbits appears very similar in both potentials. On this basis we can conclude that the general orbital behaviour is not much affected by the above differences (see also Caranicolas & Vozikis 1986).

Figs 6a, b show the surfaces of section when $\alpha = 1.5$ and $h = 0.625$. As we see, in both potentials the tube orbits are confined in the central regions while box orbits are

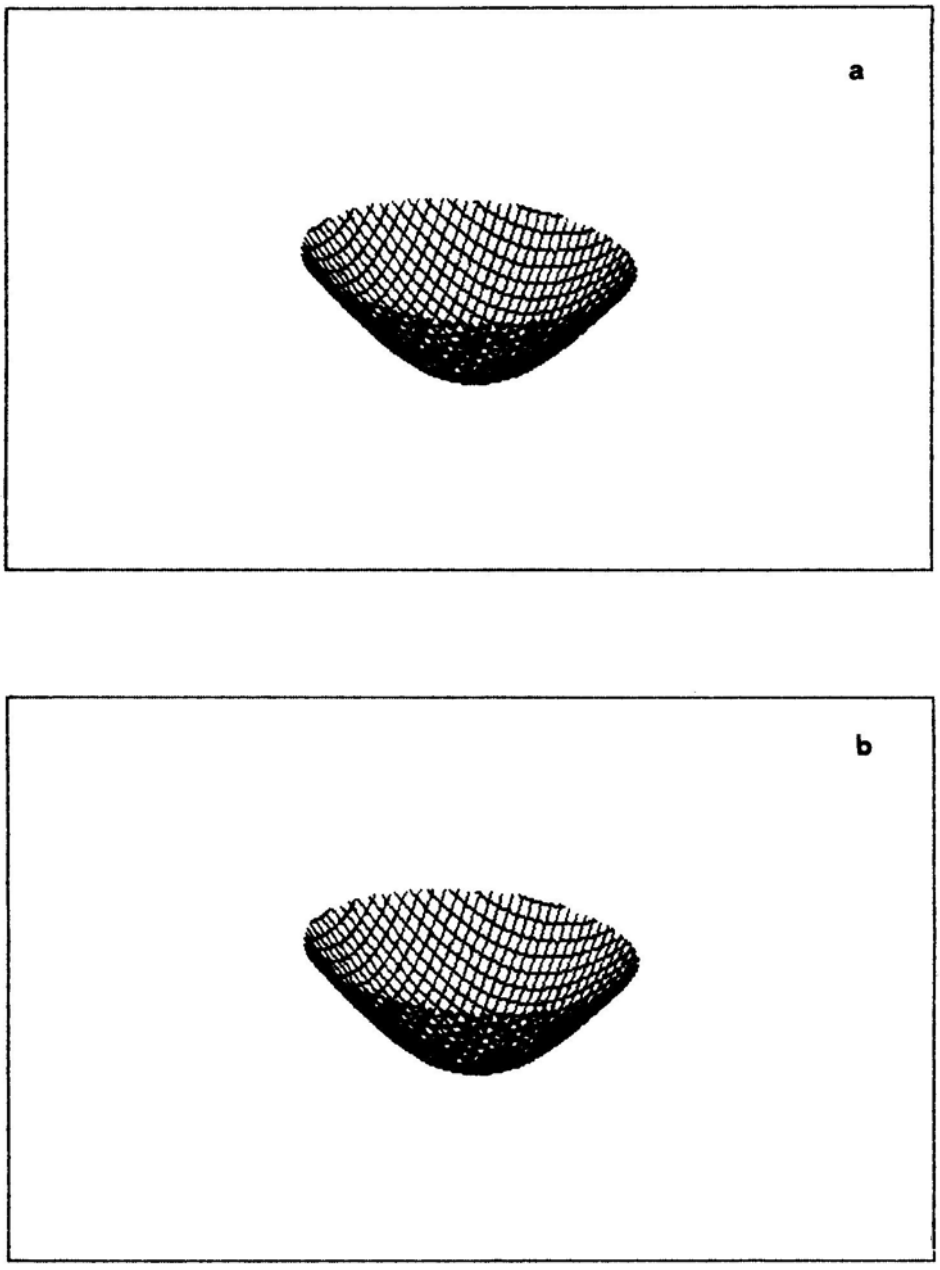

Figure 1. Potential surfaces (a) $V(x,y)$, (b) $V(x,y)$, for $\alpha = 1.50$, $c = 1.0$, $h = 0.25$.

found in the outer parts of the surface of section. Furthermore, in potential $\widetilde{V}$ one can see a set of small islands. This is due to the appearance of higher order resonances as the energy h increases (see Caranicolas & Barbanis 1982).

If we go on increasing the value of the energy h then we have to face the difficulty that in potential V the zero velocity curves will open. Then it is not possible to

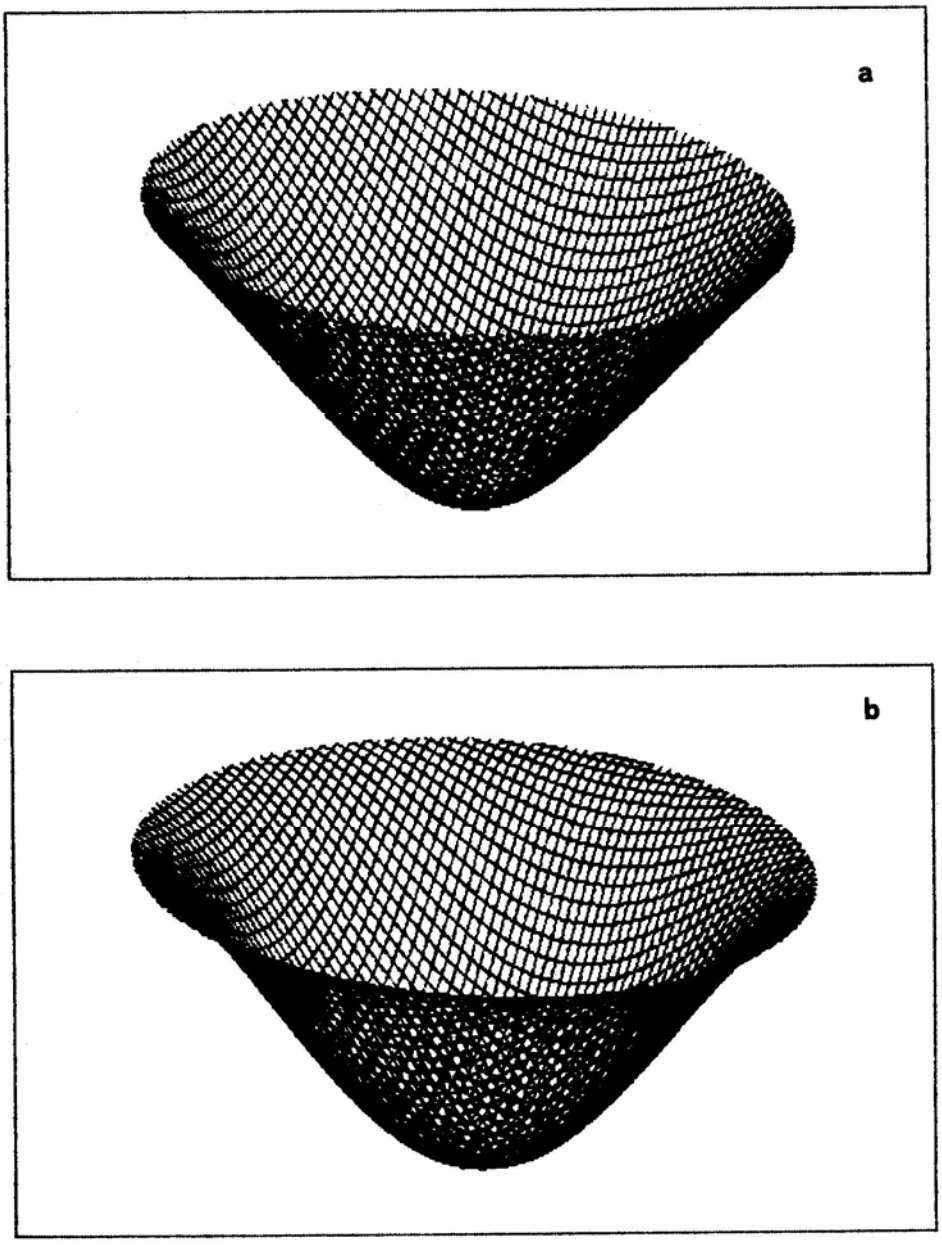

Figure 2. Potential surfaces (a) $\tilde{V}(x, y)$, (b) $\tilde{V}(x, y)$ for α = 1.50, c = 1.0, h = 0.625.

compare the two surfaces of section because many orbits escape to infinity. The energy of escape for the potential $\tilde{V}$ is given by the relations

$$\text{hesc}_1 = \frac{A^2}{16\varepsilon a_1}, \qquad \text{hesc}_2 = \frac{B^2}{16\varepsilon a_3}, \tag{10}$$

whichever is smaller (see Caranicolas & Varvoglis 1984).

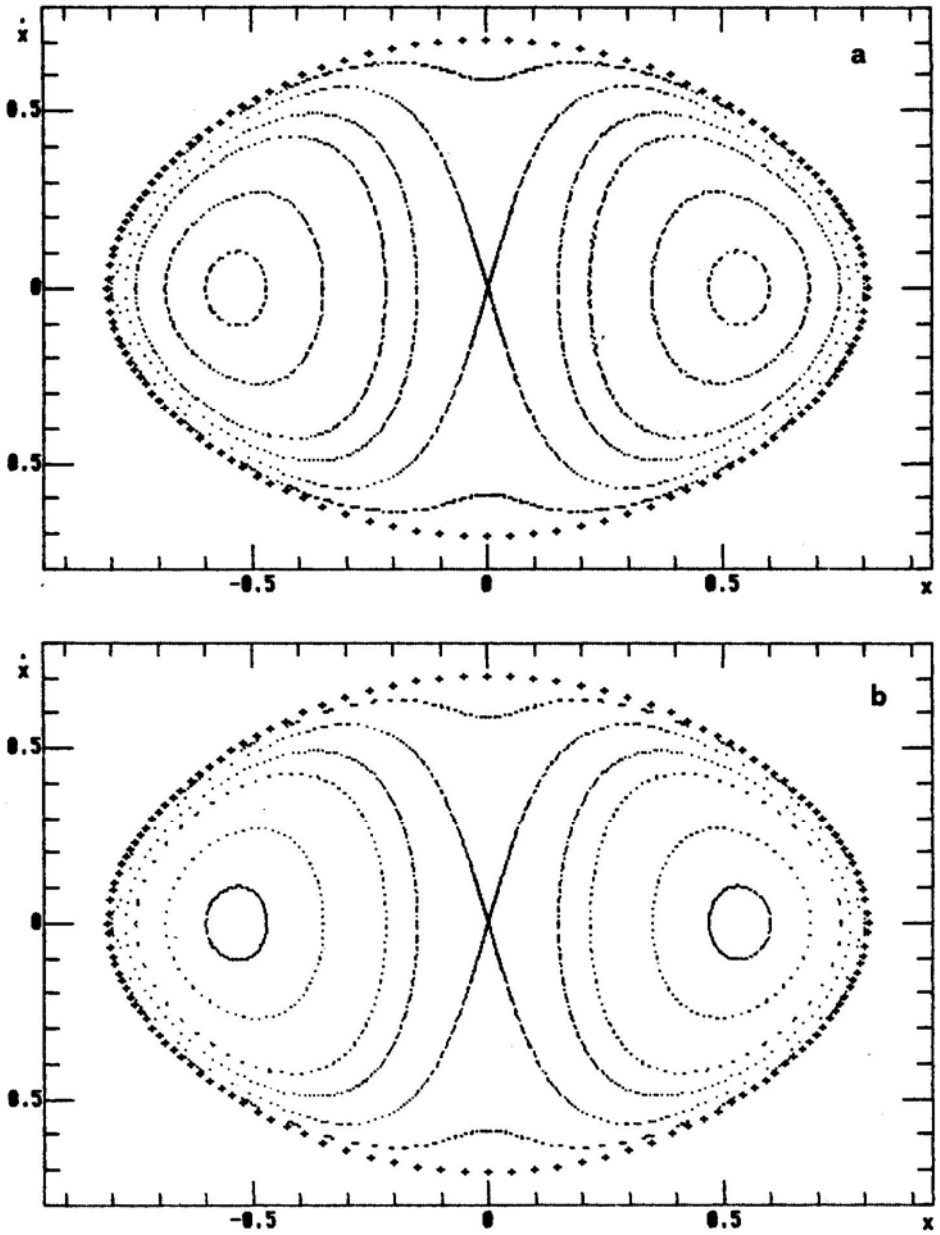

Figure 3. Poincaré surfaces of section for the potentials (a) V, and (b) $\widetilde{V}$ for α = 1.01, c=1.0, h=0.25.

As we do not know *α priori* the values of A, B, a_1, a_2, a_3 , the values of hesc_1 and hesc_2 cannot be found using relations(10). Therefore the value of hesc (hesc_1, hesc_2) is determined numerically by the program used to find the values of A, B, a_1, a_2, a_3. Table 2 gives the values of hesc for three values of α when h=0.625, c = 1.0. It is important to note that these values of hesc are very close to the value of the energy h = 0.625 for all three values of α.

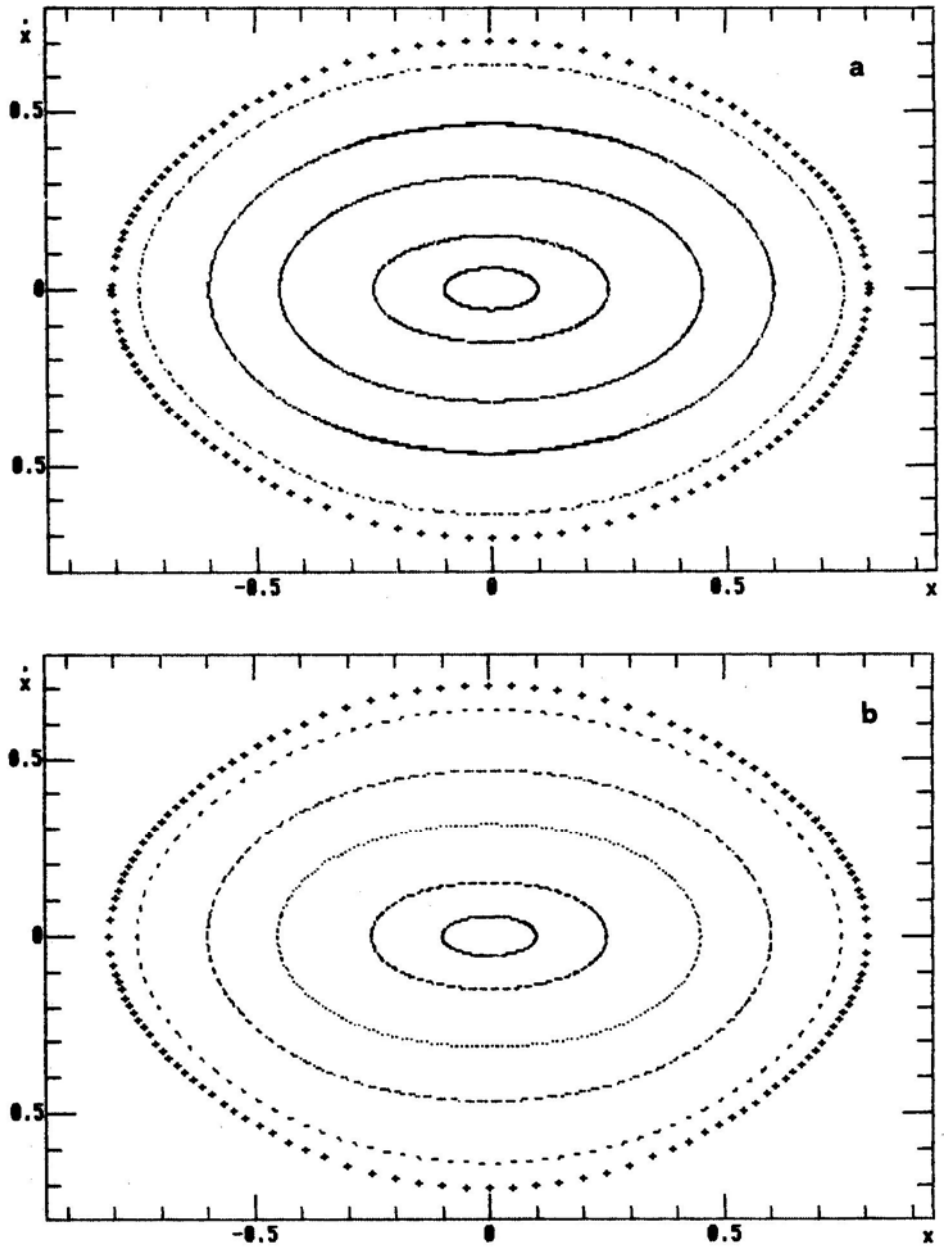

Figure 4. Poincaré surfaces of section for the potentials (a) V, and (b)$\widetilde{V}$ for α = 1.50, c= 1.0, h= 0.25.

All the above results refer to fixed energy levels. In order to make a more complete study we have also computed a number of surfaces of section in both potentials for a range of energy levels with fixed values of A, B, a_1, a_2, a_3, given in the first row of Table 1. The numerical calculations show that the surfaces of section in the potentials V and $\widetilde{V}$ are very similar for small values of h. For values of h near the energy of escape

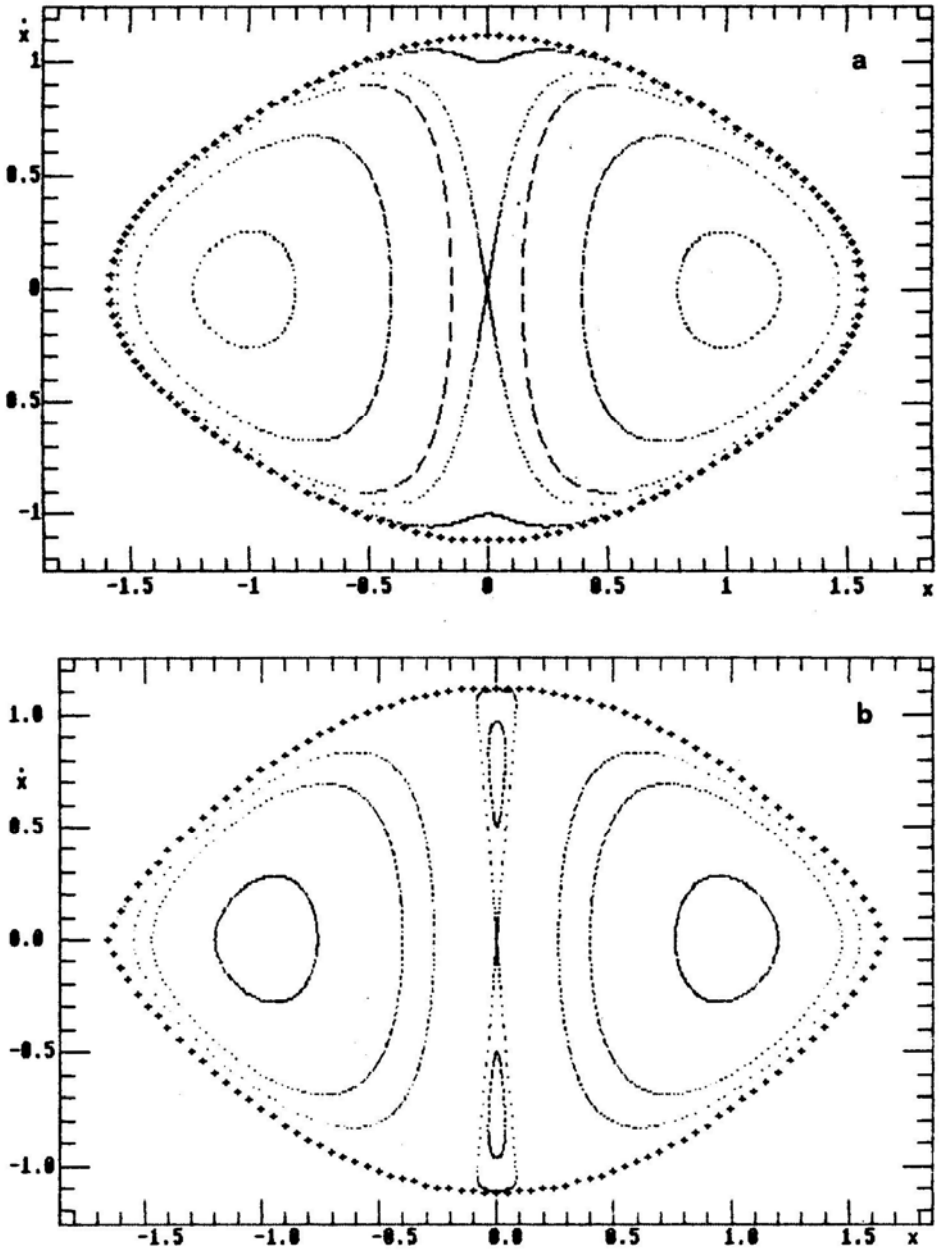

Figure 5. Poincaré surfaces of section for the potentials (a) V, and (b) $\widetilde{V}$ for α= 1.01, c = 1.0, h=0.625.

(in this case equal to 0.375647) the differences observed in the surfaces of section are analogous to those observed in the already described cases of fixed energy (see Fig. 5).

In general we can say that the differences in the surfaces of section appear in orbits approaching the zero velocity curve where the fitting is not very good.

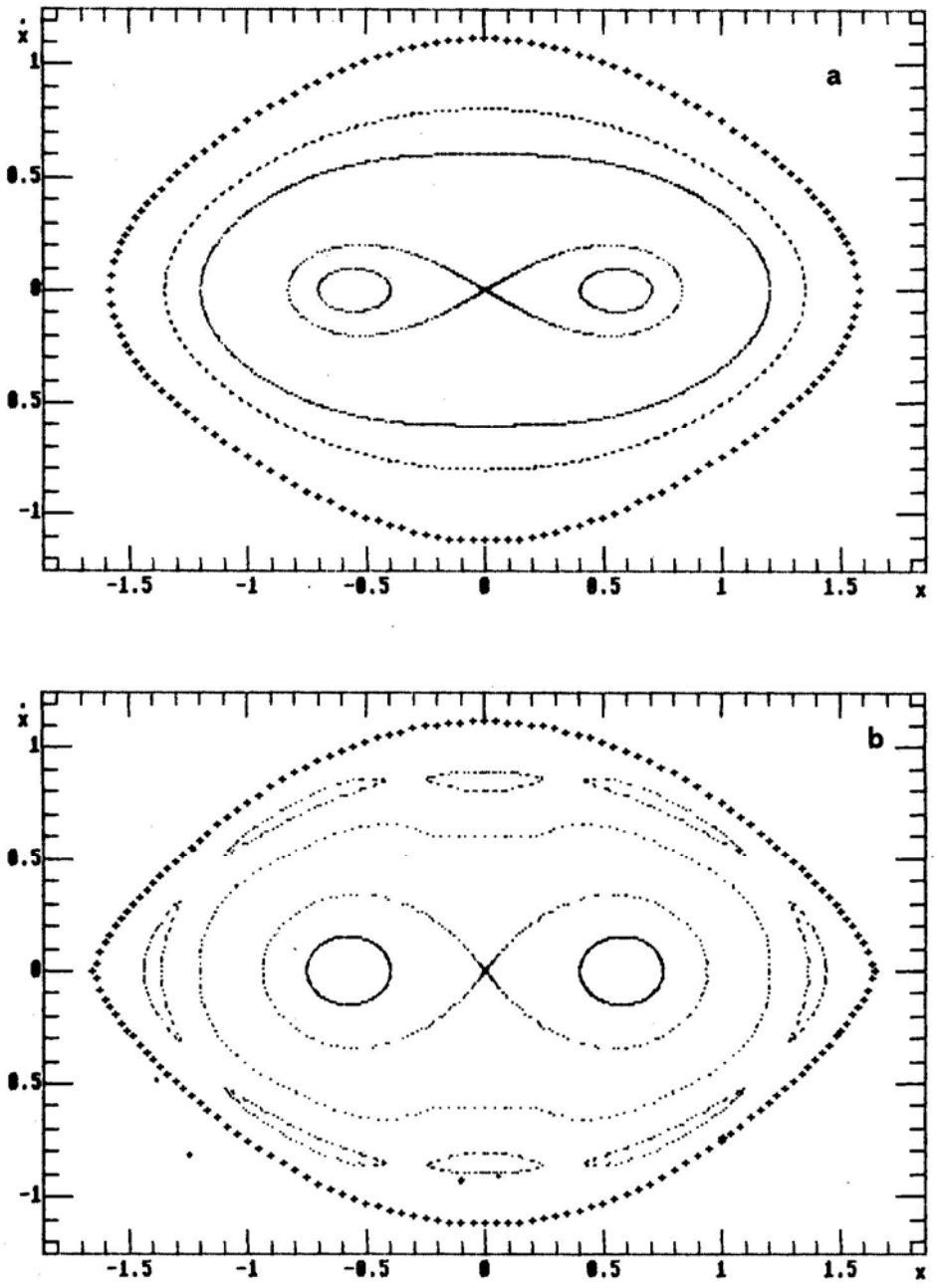

Figure 6. Poincaré surfaces of section for the potentials (a) V, and (b) $\widetilde{V}$ for $\alpha = 1.50$, c=1.0, h =0.625.

It is well known (Richstone 1982) that the stochasticity zones in potential (2) are negligible. On the other hand all the corresponding surfaces of section in potential $\widetilde{V}$ look integrable. We believe that this makes the comparison of the results given by the two potentials easier.

Table 2. Values of hesc for three sets of values (h, α).

h	α	hesc
0.625	1.01	0.625826
0.625	1.50	0.625170
0.625	2.00	0.625713

4. Discussion and conclusions

The aim of the present paper has been to approximate a simple 'realistic' logarithmic potential by that of an unharmonic oscillator. This work is of interest for three reasons.

The first reason is that though the unharmonic oscillators have been used in many problems of stellar dynamics in order to approximate realistic potentials, yet our knowledge is very poor about the 'quality' and the 'quantity' of this approximation. The second reason is that, as far as the authors know, the number of papers on this kind of research is very small (Innanen, personal communication 1985).

Although the present quartic fit seems to have no value for numerical calculations, since these can be done as quickly in the original potential, it is of great use if it is employed for analytic studies, which might give interesting information regarding the orbital behaviour (see de Zeeuw & Merritt 1983). This is the third argument to justify our study.

Furthermore, the interesting work of de Zeeuw and Lyhden-Bell (1985) is worth mentioning. In that paper the authors consider the problem of local and global fitting of a general potential with one of Stäckel form and cite many references.

The numerical methods used in the present paper suggest that the 'quality' of the fitting decreases slowly as the total energy h increases. When h=1.0 which is about 60 per cent greater than the energy of escape, the value of f is around 0.0650 for all tested values of the parameter α.

On the other hand, the term 'quantity' of the fitting characterizes the percentage of the surface of section in the two potentials V and V covered by the same kind of invariant curves. This quantity factor seems to be around 1 when $h \leqslant 0.30$ while for values of h near hesc seems to be 0.70 or 0.80. It is worth noting that the particular choice of α does not affect the above results significantly.

References

Binney, J. 1982, in *Morphology and Dynamics of Galaxies*, Eds L. Martinet & M. Mayor, Geneva Observatory, p. 3.

Caranicolas, N., Barbanis, B.1982, *Astr. Astrophys.,* **114,** 360.

Caranicolas, N.,Varvoglis, H.1984, *Astr. Astrophys.,* **141,** 383.

Caranicolas, N., Vozikis, Ch. 1986, *Cel. Mech.,* **39,** 85.

Contopoulos, G. 1960, Z. *Astrophys.,* **49,** 273.

de Zeeuw, T., Merritt, D. 1983, *Astrophys. J.,* **267,** 571.

de Zeeuw, P. T., Lynden-Bell, D. 1985, *Mon. Not. R. astr. Soc.,* **215,** 713.

Henon**,** M., Heiles, C. 1964, *Astr. J.,* **69,** 73.
Martinet, L., Mayer, F. 1975, *Astr. Astrophys.,* **44,** 45.
Richstone, D. 1980, *Astrophys. J.,* **238,** 103.
Richstone, D. 1982, *Astrophys. J.,* **252,** 496.
Verhulst, F. 1979, *Phil. Trans. R. Soc. Land. A,* **290,** 435.

J. Astrophys. Astr. (1987) **8,** 343–350

An Analytical Approximation of the Hubble Space Telescope Monochromatic Point Spread Functions

O. Bendinelli *Dipartimento di Astronomia, Università di Bologna, Via Zamboni 33, 40126 Bologna, Italy*

G. Parmeggiani *Osservatorio Astronomico di Bologna, Via Zamboni 33, 40126 Bologna, Italy*

F. Zavatti *Dipartimento di Astronomia, Università di Bologna, Via Zamboni 33, 40126 Bologna, Italy*

Received 1987 June 16; accepted 1987 October 7

Abstract. A mixture of off-centred Gaussians is used to approximate the predicted monochromatic point spread functions (PSFs) of Hubble space telescope (HST) at long wavelengths, and also, with a reduced number of parameters, the wide-band PSFs. The usefulness of the approximation in simulation and analysis of HST data is shown by means of application to image centring and convolution-deconvolution problems.

Key words: HST, point spread function—image centring—image deconvolution

1, Introduction

The basic information on the expected image quality of the Hubble space telescope (HST) is reported in the last Announcement of Opportunity (NASA 1984, A.O.No.OSSA-4-84, hereinafter AO). The resulting wavelength-dependent point spread functions (PSFs) are characterized (see Figs 2-E to 14-E in AO) by an irregular oscillatory behaviour due to superposition of the diffraction patterns of primary and secondary mirrors, a total wavefront error of 0.05 wavelength RMS (at 633 nm), and an estimated pointing instability which causes image motion with 0.007 arcsec rms. As noted by Bendinelli *et al.* (1985), the oscillatory behaviour at longer wavelengths does not disappear after PSF integration over pixel surface and bandwidth, though it evidently becomes smoother. Also, because the pixel size is comparable with the separation of adjacent maxima, centring of HST images is critical for various problems such as, for instance, the detection of a faint star imbedded in the outer rings of a brighter one, or the determination of the dimensions of a nearby galaxy nucleus. For these reasons the attainment of a specific research objective by HST requires an 'ad hoc' data analysis, which must be improved on, awaiting for ST launch, by means of reliable simulations. Very comprehensive software packages for simulation of HST observations, taking into account of all known physical effects on images, are now available at the Space Telescope Science Institute (Burrows & Hasan 1986) and at the Space Telescope European Coordinating Facility (Rosa & Baade 1986). Nevertheless,

simulations can be performed more easily and in a less time-consuming way if simple analytical approximations of the PSF are available.

The purpose of this work is to provide a model of on-axis PSFs with circular symmetry, as in first approximation the WF/PC images could be, showing its usefulness by some examples of application to HST data analysis. Also, the search of a bidimensional approximation of the expected off-axis PSFs is in progress, based on the analysis of azimuthally asymmetric star images generated by the above simulation packages.

2. Monochromatic PSF approximation

2.1 *Long-wavelength PSFs*

The multimodal behaviour of the monochromatic PSFs of the space telescope at long wavelength suggests that their radial profiles $f(r)$ may be approximated by a mixture of N off-centred Gaussian functions, *i.e.*,

$$f(r)=(a_1/2\pi\sigma_1^2)\exp(-r^2/2\sigma_1^2)+\sum_{i=2}^{N} a_i k_i \exp[-(r-b_i)^2/2\sigma_i^2]. \quad (1)$$

In this equation a_i $\left(\text{with } \sum_{i=1}^{N} a_i = 1\right)$ is the repartition coefficient of the ith Gaussian, σ_i its dispersion parameter, b_i its distance from the centre of the whole image (note $b_1 = 0$) and k_i the normalization factor explicitly expressed by

$$k_i=[2\pi\sigma_i^2\exp(-b_i^2/2\sigma_i^2)+\pi^{3/2}\sqrt{2}\sigma_i b_i \operatorname{erfc}(-b_i/\sigma_i\sqrt{2})]^{-1}. \quad (2)$$

The capability of Equation (1) to give a very good approximation of the space telescope monochromatic PSFs is shown in Fig. 1, where the PSF at 552 nm is considered. It is evident that small differences are present only in the minima.

The $3N$–2 parameters involved in Equation (1) are obtained by means of the Newton-Gauss Regularized method (see Bendinelli *et al.* 1988, hereafter BA) which, in the present case, is very easy to apply. In fact, the contribution of the ith Gaussian becomes negligible outside the radial range $b_i \pm 3\sigma_i$ so that, breaking down the data, the parameters of a limited number of Gaussians must be estimated at any one time. The values of the parameters, obtained for a set of chosen wavelengths, are reported in Table 1.

The well-defined trend of parameter values at long wavelengths must be noted. It enables us to derive approximately the PSF at intermediate wavelengths by Interpolation.

Though monochromatic PSFs may be used for the simulation of some HST observations (and also for data reduction if the mechanical stress at the launch does not cause defocusing and misalignment), the majority of observations will be performed by wide-band filter. To define the mean PSF of a particular, wide-band image, the monochromatic PSFs must be weighted (see Westphal 1982; Macchetto 1982), accounting for the spectral type of the source, filter transmission, quantum efficiency of the telescope and light detector, as was done in the accurate work of Rosa & Baade (1986). This means that, rigorously, there is a PSF for any HST observation proposed,

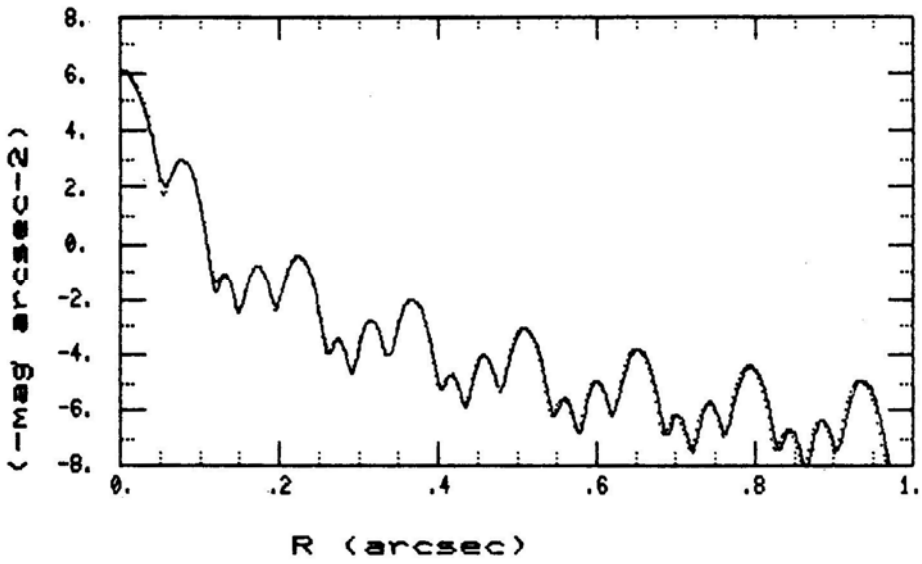

Figure 1. Comparison of the PSF at 552.5 nm (solid line) and its fit by off-centred Gaussians (dots).

and the more delicate the problem tackled the better must the PSF be known. Fortunately, the total weighting effect results in a general smoothing (increased by pixel integration), so that wide-band PSFs can be approximated by a reduced number of Gaussians. This happens since the smallest diffraction features are smeared out, as is shown in Fig. 2, where a rough weighted mean of the PSF in the *V* band is fitted with the parameters reported in Table 2.

2.2 *Short-wavelength PSFs*

It is known that at short wavelengths the effects of wavefront error and image motion are larger than the features of diffraction patterns, so that the expected monochromatic PSFs could be better described by smooth functions such as those proposed by Moffat (1959) and King (1983). But as is shown in BA, any smooth monotonically decreasing distribution can be fitted very well by a mixture of centred Gaussians, so that centring and convolution-deconvolution of nearly circular HST images does not present difficulties.

3. Two applications

In this section, two of the many problems concerning the analysis of HST data are briefly discussed based on the present monochromatic PSF approximation. Obviously they can be approached in the same way (and with less trouble) if wide-band observations and the Gaussian fit of their PSF are available.

Table 1. Computed coefficients for four monochromatic wavelengths.

	552.5 nm				656.3 nm			
	K	*a*	*σ*	*b*	*K*	*a*	*σ*	*b*
1	408.00	0.670E+00	0.185E−01	0.000	297.40	0.672E+00	0.216E−01	0.000
2	62.61	0.250E+00	0.130E−01	0.078	46.22	0.250E+00	0.148E−01	0.093
3	59.19	0.595E−02	0.811E−02	0.132	44.26	0.621E−02	0.916E−02	0.157
4	32.53	0.149E−01	0.113E−01	0.172	245.30	0.149E−02	0.126E−02	0.205
5	21.01	0.318E−01	0.135E−01	0.224	15.53	0.320E−01	0.153E−01	0.267
6	27.11	0.151E−02	0.851E−02	0.275	20.69	0.155E−02	0.939E−02	0.327
7	18.27	0.431E−02	0.110E−01	0.316	13.69	0.437E−02	0.124E−01	0.375
8	12.82	0.123E−01	0.135E−01	0.368	9.48	0.124E−01	0.153E−01	0.437
9	17.37	0.739E−03	0.874E−02	0.418	13.29	0.743E−03	0.963E−02	0.496
10	12.80	0.193E−02	0.108E−01	0.459	9.62	0.196E−02	0.121E−01	0.545
11	9.22	0.661E−02	0.135E−01	0.510	6.81	0.670E−02	0.154E−01	0.606
12	12.67	0.469E−03	0.894E−02	0.561	9.66	0.483E−03	0.987E−02	0.666
13	9.94	0.104E−02	0.106E−01	0.601	7.49	0.106E−02	0.119E−01	0.714
14	7.20	0.418E−02	0.135E−01	0.653	5.32	0.425E−02	0.154E−01	0.776
15	9.87	0.342E−03	0.915E−02	0.703	7.52	0.352E−03	0.101E−01	0.835
16	8.19	0.626E−03	0.104E−01	0.744	6.18	0.640E−03	0.116E−01	0.884
17	5.90	0.290E−02	0.135E−01	0.795	4.35	0.296E−02	0.155E−01	0.945
18	8.05	0.272E−02	0.933E−02	0.846				
19	6.99	0.404E−03	0.102E−01	0.886				
20	5.01	0.214E−02	0.135E−01	0.938				

	680.0 nm				815.0 nm			
	K	*a*	*σ*	*b*	*K*	*a*	*σ*	*b*
1	278.20	0.672E+00	0.223E−01	0.00	197.50	0.674E+00	0.263E−01	0.000
2	43.36	0.251E+00	0.153E−01	0.096	31.01	0.252E+00	0.178E−01	0.115
3	41.84	0.623E−02	0.936E−02	0.162	30.76	0.638E−02	0.106E−01	0.194
4	22.97	0.150E−01	0.130E−01	0.213	16.78	0.151E−01	0.149E−01	0.255
5	14.57	0.321E−01	0.158E−01	0.276	10.46	0.324E−01	0.183E−01	0.331
6	19.52	0.156E−02	0.961E−02	0.338	14.38	0.160E−02	0.109E−01	0.405
7	12.90	0.437E−02	0.127E−01	0.389	9.36	0.444E−02	0.146E−01	0.466
8	8.88	0.125E−01	0.158E−01	0.453	6.37	0.126E−01	0.184E−01	0.542
9	1.25	0.763E−02	0.985E−01	0.514	9.22	0.784E−03	0.112E−01	0.616
10	9.06	0.196E−02	0.124E−01	0.564	6.58	0.200E−02	0.143E−01	0.677
11	6.39	0.672E−02	0.158E−01	0.628	4.58	0.685E−02	0.184E−01	0.753
12	9.11	0.485E−03	0.101E−01	0.690	6.82	0.494E−03	0.113E−01	0.827
13	7.04	0.107E−02	0.122E−01	0.740	4.74	0.115E−02	0.151E−01	0.888
14	4.99	0.426E−02	0.158E−01	0.804				
15	7.23	0.350E−03	0.101E−01	0.865				
16	5.34	0.685E−03	0.130E−01	0.916				

3.1 *Centring of a star image*

An HST star image contains a large fraction of the total luminosity within the first minimum of diffraction pattern, hence its off-centring with respect to the central pixel (that of local maximum intensity) can be determined by the method proposed in BA (see also Chiu 1980), taking $N = 1$, *i.e.,* considering only the light distribution in the

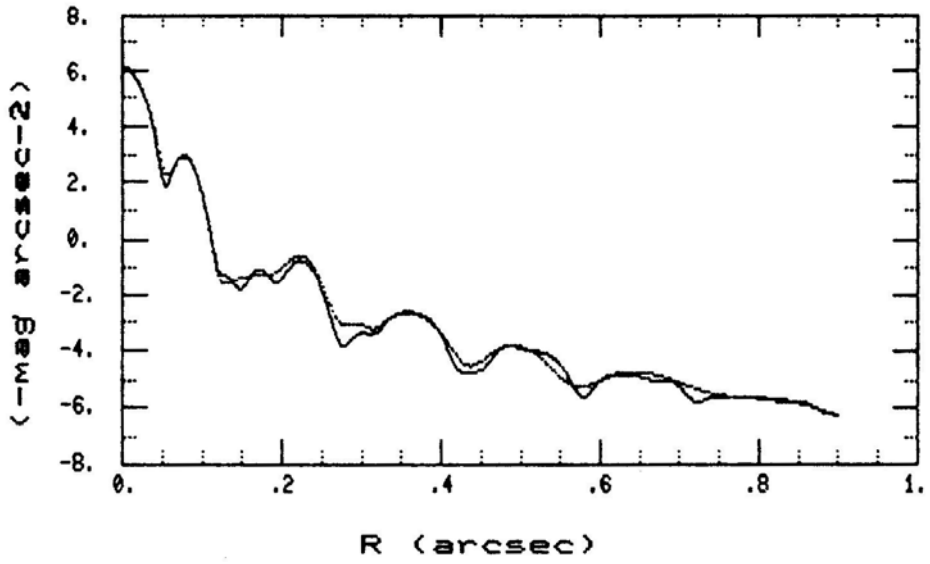

Figure 2. Comparison of the *V*-band PSF (solid line) and its fit (dots).

Table 2. Computed coefficients for *V*-band.

	K	*a*	*σ*	*b*
1	410.90	0.669E+00	0.186E−01	0.000
2	60.92	0.248E+00	0.135E−01	0.077
3	7.01	0.425E−01	0.538E−01	0.168
4	16.77	0.248E−01	0.169E−01	0.224
5	16.84	0.172E−02	0.128E−01	0.294
6	5.33	0.167E−01	0.332E−01	0.359
7	3.52	0.828E−02	0.367E−01	0.491
8	1.91	0.580E−02	0.520E−01	0.639
9	0.81	0.680E−02	0.994E−01	0.793

Airy disc. It must be stressed that the presence of b_i terms in Equation (1) prevents (as far as we know) expressing the complete marginal distributions by an analytical function, so that the BA method cannot be used to derive off-centring and all PSF parameters from the whole star image at the same time. In other words, the centring algorithm developed in BA for analysis of ground-based CCD star images is not applicable to HST frames to test if the wings of the in-orbit PSF are like their predictions. Nevertheless, at least in principle since handling of real noisy data may be considerably more difficult, the complete description of an HST star image—*i.e.* simultaneous estimate of off-centring, PSF parameters and background—can be derived considering the pixel-to-pixel intensity distribution along two orthogonal diameters crossing at the central pixel of the image.

If $2l$ is the pixel size and x_c, y_c (both $\leqslant l$) the offset of the centre of the star image with respect to the central pixel (x_p, y_p), the intensity level $i(x_n, y_m)$ of a pixel centred at (x_n,y_m) is given by

$$i(x_n, y_m) = L_T \sum_{i=1}^{N} a_i k_i \int_{x_0}^{x_F} \int_{y_0}^{y_F} \exp[-(\sqrt{x'^2 + y'^2} - b_i)^2/2\sigma_i^2]\,dx'dy' + f(x_n, y_m), \quad (3)$$

where

$$x_0 = x_n - l - x_c, \qquad y_0 = y_m - l - y_c,$$
$$x_F = x_n + l - x_c, \qquad y_F = y_m + l - y_c,$$
$$L_T = \sum_{nm} i(x_n, y_m) \qquad (n = 1,2, \ldots, M;\ m = 1, 2, \ldots, M),$$

and finally $f(x_n, y_m)$ is the background distribution.

We consider now the partial pixel sums along the x-diameter, which result in

$$S_x(x_n) = \sum_{r=1}^{n} i(x_r, y_p). \quad (4)$$

These sums can be rigorously expressed by means of an integral equation like Equation (3), with suitable integration limits, or in an approximate way, taking into account the reduced range of variability of y', by

$$S_x(x_n) \simeq L_T \sum_{i=1}^{N} a_i k_i \int_{-\infty}^{x_F} \exp[-(x' - b_i)^2/2\sigma_i^2]\,dx' + f(x_n - x_1) \quad (5)$$

$$= \Sigma_i A_i \{1 + \mathrm{erf}[(x_F - b_i)/\sqrt{2}\sigma_i]\} + f(x_n - x_1), \quad (6)$$

with $A_i = (2\pi)^{1/2}/lL_T\sigma_i a_i k_i$.

Since Equation (6) is differentiable with respect to the parameters x_c, A_i, σ_i, b_i and those of the background model, these can be derived by the Newton–Gauss regularized method (see BA for details).

Evidently, also $S_y(y_m)$, the sums along the y-axis, can be treated like $S_x(x_n)$, so that by comparison of analogous parameters it can be inferred if the in-orbit PSF is like the expected one.

3.2 *Convolution-deconvolution of small objects*

Convolution effects cannot be disregarded in the analysis of HST images of objects of small angular dimensions such as globular clusters in external galaxies, nuclei of nearby galaxies, overall profiles of normal and active galaxies at cosmological distances, and so on.

Dealing with non-undersampled objects, *i.e.,* those in which the searched features are not much smaller than pixel size, it can be easily derived that their apparent brightness profile $f(r)$ is related to the true radially symmetric profile $F(r)$ (including cosmological effects, if required) by the integral equation

$$f(r) = \sum_{i=1}^{N} 2a_i k_i \int_0^{\infty} sF(s)\Phi(r, s, \sigma_i, b_i)\,ds, \quad (7)$$

where, using the Gaussian mixture approximation of the PSF,

$$\Phi(r, s, \sigma_i, b_i) = \int_0^{\pi} \exp[-(s^2 + r^2 - 2rs\cos\theta + b_i^2 - 2b_i\sqrt{s^2 + r^2 - 2rs\cos\theta})/2\sigma_i^2]\,\mathrm{d}\theta \tag{8}$$

is evaluated by numerical integration. (For a remark on the analysis of undersampled data, see Section 4.2.)

Evidently Equation (7) can be used either to provide a set of convolved models of globular clusters or galaxies, as seen by HST, or for deconvolution (see Bendinelli, Parmeggiani & Zavatti 1986) of HST observations of the same objects.

In this case the resolution given by the pixel size may be insufficient, being comparable to the $\sigma\, i$; but a subpixel resolution is attainable by a set of frames, slightly shifted by a pixel fraction, obtained by exploiting the HST astrometric potential (see for instance Jefferys *et al.* 1985). Another possibility consists in determining *a posteriori* the relative displacements of the extended object with respect to the central pixels in a set of frames, by means of the off-centring of some stars around the object. It is worth noting that this procedure does not require the parallel use of one of the fine guidance sensors (FGS), and further that algebraic deconvolution works well even if the data are unequally spaced.

4. Concluding remarks

The usefulness of the present approximation of on-axis PSFs should have been sufficiently demonstrated by the examples of application shown, if the expected image quality will be kept in orbit. Nevertheless, some points deserve further comments.

4.1 *The wide-band PSFs*

In view of the importance of wide-band observations by the WF/PC camera in all astrophysical fields (see for instance 'The GTO observing program', STScI, October 1985) the parameters of the PSF multi-Gaussian model must be accurately re-calculated and the model compared with expected PSFs generated by the ST/ECF simulation code. This will be done in a future paper.

4.2 *HST resolution for extragalactic research*

Basically, the pixel size will give the resolution of a single HST observation, but if a set of images of the same object are obtained in conjunction with one of the FGS, or subjected to an astrometric analysis as outlined in Section 3.2), the resulting resolution would be a fraction of a pixel. Deconvolution of features of these dimensions seems therefore possible, improving the HST resolution. Further, a realistic PSF model can be of aid in reaching reliable inferences on the structure of a unresolved source (such as the nucleus of an external galaxy or the whole profile of a very distant one). A set of source models, in effect, can be easily convolved with PSF, integrated on pixel surface and compared with real undersampled data to select the most probable model.

Acknowledgements

We wish to thank G. G. C. Palumbo for careful reading of the manuscript and helpful comments, G. S. Djorgovski and an anonymous referee for their constructive criticism which has much improved the presentation of the paper, D. Iorio-Fili and P. Benvenuti for providing the ST/ECF simulation code. The Italian Piano Spaziale Nazionale is acknowledged for partial financial support (Contract PSN-85-078).

References

Bendinelli, O., Di Iorio, A., Parmeggiani, G., Zavatti, F.1985, *Astr. Astrophys*., **153,** 265.

Bendinelli, O.,Parmeggiani, G., Piccioni, A.,Zavatti, F.1988, *Astr. J.,* in press (BA).

Bendinelli, O., Parmeggiani, G., Zavatti, F. 1986, *Astrophys. J.,* **308,** 611.

Burrows, C, Hasan, H. 1986, preprint.

Chiu, L. T. G., 1980, *Celestial Mechanics,* **22,** 191.

Jefferys, W. H., Benedict, G. F., Hemenway, P. D., Shelus, P. J., Duncombe, R. L. 1985, *Celestial Mechanics,* **37,** 299.

King, I R. 1983, *Publ. astr. Soc. Pac,* **95,** 163.

Macchetto, F. 1982, in *The Space Telescope Observatory,* Ed. D. N. B. Hall, STScI, Baltimore, p. 40.

Moffat, A. F. J. 1969, *Astr. Astrophys.,* **3,** 455.

Rosa, M., Baade, D.1986, *The Messenger,* **45,** 22.

Westphal, J. A.1982, in *The Space Telescope Observatory,* Ed. D. N. B. Hall, STScI, Baltimore, p. 28.

J. Astrophys. Astr. (1987) **8,** 351–367

Experiments with CP Stars*

L. O. Lodén *Astronamiska Observatoriet, Box 515, S-75120 Uppsala, Sweden*

A. Sundman *Stockholms Observatorium, S-13300 Saltsjöbaden, Sweden*

Received 1987 March 31; revised 1987 August 4; accepted 1987 October 7

Abstract. Described here is a preliminary and tentative application of a method for fine-classification of stars, selected for studies of galactic structure. The present investigation is based on about 100 stars within the approximate spectral type range B6–A5, for which both spectra and *UBV* photometry have been obtained.

The motivation of the project is the following: For the study of galactic fine-structure it is essential to use as many members as possible of stellar agglomerations of various type for a statistical treatment of the material. A-type stars are fairly numerous and reasonably bright, but if all chemically peculiar stars, fast rotators or multiple systems have to be omitted there is generally too little left for a relevant investigation. Here we perform some experiments in order to find a method for fine-classification of A stars, both normal and chemically peculiar, within the framework of the M K system.

In this connection it is desirable to reduce the present multitude of CP classifications to a manageable number. It is shown here that, independenttly of the definition of the degree of peculiarity, there is no sharp borderline separating the CP stars from the 'normal' ones.

Also it is found that spectral classification can on an average be performed with almost the same accuracy for CP stars as for the 'normal' ones provided cases of extreme peculiarity are avoided.

Key words: spectral classification—CP stars—galactic structure

1. Introduction

For a study of galactic fine-structure, *i.e.*, the distribution of stars (and interstellar matter) within 2 kpc, the A-type stars represent a compromise between frequency and visibility. Hotter main-sequence stars are visible well at considerable distances but too few for statistical purposes, whereas the cooler ones are very frequent but generally too faint for successful performance of the investigation.

A-type stars are not free from problems, however. Spectroscopic multiplicity, fast rotation and chemical peculiarity (CP) interfere with the study of galactic structure.

The multiplicity may introduce various types of errors depending on the structure and arrangement of the system. If for instance, the components cannot be resolved due

* Based on observations collected at European Southern Observatory, La Silla, Chile

to Doppler effect and also happen to be more or less identical, there will be a direct misestimation of the spectroscopic parallax, and in case of a composite spectrum an uncertainty in the classification will occur, indirectly causing the same result. Rapidly spinning stars—or more correctly, stars with high $v \sin i$ values—present a corresponding difficulty by blurring spectral lines critical for the classification. When the CP stars are concerned it is difficult to know to what extent one can apply the same effective temperature and luminosity criteria that have been derived or calibrated for more 'normal' stars.

The basic idea here is to find out if there might be some limit in the 'degree of peculiarity' up to which 'normal star criteria' can be used without too great risk of misclassification and subsequent misestimation of the relevant parameters.

In practice this will imply an attempt to classify the A-type stars according to some parameter indicating the 'degree of peculiarity' rather than to give a separation between—in the first instance—normal and peculiar stars and—in a second step—between various types and subtypes of peculiarities. The CP phenomenon itself and the investigation of the physical mechanisms behind it, although highly interesting and urgent, will not be considered here.

2. The material

The observational material consists of slit spectra of altogether 103 stars obtained with the 193 cm telescope at Observatoire de Haute-Provence in 1981 May (dispersion 9.4 Å mm^{-1}) and with the 153 cm telescope at the European Southern Observatory in 1981 August and 1983 March (dispersion 20 Å mm^{-1}).*UBV* photometry of northern objects has been taken from Kennedy & Buscombe (1974) while for the southern ones it has partly been secured by Lodén with the 50 cm ESO telescope and the 61 cm Bochum telescope at a La Silla and partly compiled from Engberg (1983), Hoag *et al.* (1961) and Koelbloed (1959). All spectra have been subject to microphotometry in the Grant Machine at the ESO Headquarters in Garching, and by means of photometric standardization (ETA) the photometer readings have been directly transformed to intensity. For reduction methods, see Lodén (1983).

About a third of the objects are more or less well-established peculiar A stars according to literature, purposely selected for the investigation. The remaining ones constitute a comparison collection of relatively 'normal' A stars, partly selected exclusively for the investigation and partly leftovers from preceeding programmes (Lodén 1983, 1984).

Table 1 gives some basic data about these stars. The following comments may be appropriate: An N in column 7 indicates 'normal'. Spectral types in column 8 have been compiled from literature. The figures in columns 9 and 10 refer to the legend at the bottom of the table. The number of components indicated in column 11 is the *suspected* number estimated from the multiplicity of lines, not the actual one. The last column gives the number of spectra obtained for each star.

Although the discordance between various CP classifications is considerable, it should be possible to obtain a preliminary subdivision of the objects selected as representatives for the Ap and Am groups. The result shown in column 7. of Table 1 is not particularly satisfactory, however. Already in this selection there are at least 12 different CP characteristics according to literature compilation.

Table 1. Basic data on the material.

Nr.	Id. HD or CD	V	$B-V$	$U-B$	Sp. (litt.)	Character	Prel. Acc. Sp	Source of phot.	Source of character	Comp.	n sp.
1	87696	4.49	0.18	0.07	A5–7 V	N	A7 V	20	19		1
2	90569	6.03	−0.06	−0.10	B9	SiCrSr	B9	20	10, 28		1
3	90852	9.93	−0.05	−0.26	B8 IV	N	B8 V?	24	17	3	1
4	90871	9.35	0.01	−0.05	B9 V	N	A0 V	24	17	3	1
5	−55°3475	10.05	0.06	0.09		N	A1 V	24	24	2	1
6	90979	9.39	0.08	0.04	A0 V	N	A0 V	24	17		1
7	−56°3415	9.36	0.13	0.10		N	A1 V	24	24	1–2	1
8	„ comp					Si?	A5 V	—	24		1
9	91002	9.70	0.14	0.13	A1 V	N	A1 V	24	17	2	1
10	91051	9.16	−0.02	−0.09	B9 IV	N	B9 V?	24	17	2–3	1
11	91052	8.86	0.00	−0.02	A0 V	N	A0 V	24	17	$\geqslant 3$	2
12	91071	9.44	−0.02	−0.23	B8 III	N	B8 V?	24	17	2	2
13	91126	9.41	−0.04	−0.21	B9 V	N	B9 V	24	17	2–3	1
14	93821	7.93	−0.09	−0.28	B8	Si	B8	24	6, 17		3
15	95418	2.37	−0.02	0.00	A1 V	N	A1 V	20	8		1
16	97603	2.56	0.12	0.11	A4–5 V	N	A4 V	20	8		1
17	98329	7.01	−0.14	−0.40	B9 II/III	N	B9	24	17	3	2
18	98340	7.14	−0.06	−0.21	B9 IV	SiCr	B9	24	17		2
19	103287	2.44	0.00	0.02	A0 V	N	A0 V	20	14		1
20	104671	4.40	0.28	0.01	A3–8	(m)	A3–5	24	17		1
21	104810	7.33	0.02	−0.35	B8	Si	B8	24	6, 8, 17		3
22	−60°3750	9.97	0.23	−0.28		N	B6 V	24	24	2–4	1
23	105339	8.89	0.11	−0.34	B5/7 III/IV	N	B6 V	24	24		1
24	−60°3764	10.03	0.15	−0.20		N	B9 V	24	24	2	1
25	−60°3766	10.04	0.17	0.04		P?	B9 V	24	24		1
26	−60°3787	10.21	0.20	0.10		N	A0 V	24	24	$\geqslant 4$	1
27	−60°3790	10.09	0.13	0.10		N	A0 V	24	24	4	1
28	105581	8.66	0.08	−0.17	B9	N	B8–9 V	24	24	2–3	1

Table 1. Continued.

Nr.	Id. HD or CD	V	$B-V$	$U-B$	Sp. (litt.)	Character	Prel. Acc. Sp	Source of phot.	Source of character	Comp.	n sp.
29	105777	8.65	0.22	0.17	A1 V	N	A0 V	24	17	2–4	1
30	„ comp					N	A2 V	—	24	2–4	1
31	109387	3.89	−0.14	−0.57	B6 III	P amb.	B6	20	8, 21	2–4	1
32	109536	5.13	0.21	0.07	A5–7 IV/V	P amb. m	A5	20	8, 17, 25	2	2
33	111397	5.77	0.00	0.05	A2 V	N	A1 V	20	8		1
34	112185	1.77	−0.02	0.01	A0 V	CrEu	A0 V	20	2, 19		2
35	112381	6.51	−0.10	−0.15	B9.5	SiCr	B9.5	24	6, 17		3
36	112412	5.60	0.34	−0.03	F0 V	N	F0 V	20	19		1
37	112413	2.89	−0.12	−0.32	B9–A0	SiCrEuHg	A0	20	2, 8, 10, 28		1
38	115331	5.83	0.19	0.12	A2–4	m (Sr)	A2.5	24	2, 17		2
39	116656	2.27	0.02	−0.01	A1 V	m amb.	A1 V	20	14		3
40	116657	3.95	0.13	0.09	A1–7	m	A2	20	2, 10		3
41	116842	4.02	0.16	0.08	A5 V	N	A5 V	20	19		1
42	117025	6.07	0.10	0.05	A1–2	P amb.	A3	20	3, 16		1
43	118022	4.94	0.04	−0.02	A1–2	CrSrEu	A1–2	20	2, 10		3
44	118214	5.56	−0.04	−0.08	B9–A0	P amb.	B9	20	8		1
45	119938	5.90	0.27	0.07	A3–F0	m	A5	24	5, 17		1
46	120025	6.71	0.34	0.15	A	m amb.	A9	24	3, 5		1
47	120198	5.65	−0.05	−0.13	B8–A2	SiCrSrEu	B8–9	20	2, 10, 29		1
48	121409	5.69	−0.03	−0.07	B8–A0 V	N	A0 V	20	8		1
49	125158	5.18	0.26	0.15	A1–F2	m	A9	24	2, 5, 9, 18, 22		1
50	126504	5.82	0.31	0.15	A1–F2	m	A9	24	2, 5, 18, 22		1
51	135730	6.29	0.18	0.11	A2–7	m	A2	24	10		1
52	137160	8.02	0.08	0.01		CrSrEu	A5	24	6, 17		2
53	138413	5.52	0.16	0.12	A2	m	A2	24	5, 10, 18		4
54	139006	2.24	−0.02	−0.03	A0 V	N	A0 V	20	19		1
55	140160	5.33	0.04	0.05	A0–2	CrSrEu	A0	20	2, 10		1

56	142049	5.82	0.34	0.12	A3+F–G	m amb.	A3	24	3, 5, 16, 18, 22	2	2
57	144197	4.73	0.22	0.14	A3–9	m	A7	24	2, 3, 5, 11, 16		2
58	146998	9.55	0.66	0.37	A2–9	Sr(Cr)	A8	24	5, 13		1
59	147105	8.81	0.50	0.33	A5	CrSrEu	A5	24	5, 13		1
60	148112	4.59	−0.02	−0.03	B9–A1	CrEu	A0	20	2, 10, 23		1
61	148321	6.97	0.20	0.12	A1–7	m P(Sr)	A3	24	2, 3, 13, 18		2
62	152044	9.04	0.20	0.14	A1 V	CrSrEu	A2	24	5, 6, 17	2	2
63	152107	4.81	0.08	0.05	A2–4	CrSrEu	A2	24	2, 10		1
64	−34°12194	8.99	0.22	0.11		N	A4 V	15	24	2–3	2
65	−34°12195	9.20	0.19	0.11	A3 V	N	A3 V	15	1	2–3	1
66	−34°12196	9.30	0.21	0.15	A3 V	N	A4 V	15	1	2–3	1
67	162576	6.97	0.04	−0.21	B9.5 (8/9)	SiCr	B9 V	15	1	2	2
68	162586	6.17	−0.03	−0.35	B8 V	N	B9 V	15	1		2
69	162630	7.61	0.00	−0.16	B9 V	N	B9 V	15	1	1–2	2
70	−34°12210	9.06	0.15	0.11	A2 V	N	A2 V	15	1	2–3	1
71	−34°12211	8.93	0.36	0.10	A8 V	m	A5 V	15	1	2	1
72	162631	7.37	0.07	0.00	B9.5 V	N	A0 V	12, 15, 24	1	2	2
73	162656	8.21	0.04	0.01	B.9.5 V	N	A0 V	15	1		2
74	162678	6.38	0.00	−0.06	B9 V	N	B9 V	15	1		2
75	(19)	9.01	0.16	0.08		N	A2 V	15	24	3–4	1
76	162679	7.16	0.03	−0.20	B9 V	N	B9 V	15	1		1
77	162680	7.76	0.08	0.02	A1 V	N	A0 V	15, 24	1	3	2
78	162724	5.96	−0.01	−0.10	B9 V	N	B9 V	15	1	2–3	2
79	162725	6.45	0.02	−0.07	A0	SiCr	A0 V	12, 15	1		3
80	320861	8.49	0.11	0.06	A1 V	N	A1 V	15	1	2	1
81	−34°12232	8.80	0.17	0.12		N	A3 V	15	24	3–4	3
82	162732	6.74	−0.15	−0.37	B8	P amb.	B8	20	7, 8, 30		2
83	162780	6.88	0.03	−0.05	B9 V	N	B9 V	15	1		3
84	162781	7.48	0.09	−0.02	A0 V	N	A0 V	12, 15	1	3–4	2
85	164429	6.48	−0.08	−0.20	B9	SiCrSr	B9	20	3, 10		1
86	169820	6.45	−0.03	−0.27	B9 V	N	B9 V	20	24		1
87	169853	5.74	0.11	0.16	A2 V	m	A2 V	24	5, 26		1
88	176232	5.87	0.25	0.08	A4–F0	CrSrEu	F0	20	2, 4, 10		1
89	197461	4.44	0.32	0.10	A9 F0 IV	m? P	A9	20	10, 16, 27		1
90	206653	7.19	−0.09	−0.32	B9	Si	B9	24	5, 6, 17		1

Table 1. Continued.

Nr.	Id. HD or CD	V	$B-V$	$U-B$	Sp. (litt.)	Character	Prel. Acc. Sp	Source of phot.	Source of character	Comp.	n sp.
91	208217	7.13	0.20	0.04	A0	CrSrEu	A0	24	5, 6, 17		1
92	208321	5.41	0.09	0.13	A2–3 V	N	A2 V	24	17		1
93	208384	7.85	0.20	0.16	A3	m amb.	A3	24	17		1
94	209142	7.74	0.25	0.16	A8 V	N	A8 V	24	17		1
95	209337	9.52	0.32	0.12	A0–F2	m	A6	24	17		1
96	209468	7.53	0.07	0.05	A1 V	N	A1 V	24	17	2	1
97	212385	6.85	0.16	0.13	A2	CrSrEu	A2	24	17, 18		1
98	212410	10.01	0.48	0.01	F3 V	N	F3 V	24	17		2
99	215966	7.88	−0.01	−0.03	B9	CrSrEu	B9.5	24	5, 17		2
100	215983	9.63	0.22	0.12	A0	Sr(CrEu)	A0	24	5, 17		1
101	217522	7.50	0.50	0.11	A5	SrEu(SiCr)	A5	24	5, 17		1
102	218495	9.36	0.26	0.14	A2	SrEu	A2	24	5, 17		1
103	218994	8.57	0.30	0.11	A3	Sr	A3	24	5, 17		2

Note to Table 1.
Sources of information:

1. Abt 1975
2. Bertaud 1959
3. Bertaud 1965
4. Bertaud & Floquet 1967
5. W. P. Bidelman 1984 personal communication
6. Bidelman & McConnel 1973
7. Bidelman & Svolopoulos 1960
8. Buscombe 1971
9. Cowley & Cowley 1964
10. Cowley, Cowley, Jaschek & Jaschek, 1969
11. Crawford, Barnes & Golson 1970
12. Engberg 1983
13. Garrison 1967
14. HD Catalogue
15. Hoag *et al.* 1961
16. Hoffleit 1964
17. Houk & Cowley: Mich. Cat., 1975–82
18. Jaschek & Jaschek 1960
19. Johnson & Morgan 1953
20. Kenndy & Buscombe 1974
21. Lesh 1968
22. Levato 1972
23. Lockwood 1968
24. L. O. Lodén 1983, 1984 and present programme
25. Lü 1982
26. Malaroda 1973
27. Morgan & Abt 1972
28. Osawa 1965
29. Palmer *et al.* 1968
30. Slettebak 1966

3. Classification parameters used in the present investigation

In a previous investigation (Lodén 1983) we have tested a series of parameters for internal comparison of a selection of stars representing various spectral types as well as various degrees of chemical peculiarity. Based on the experience from that investigation the following parameters have been selected for the present programme.

PL. *UBV* colours, *i.e.*, $(B–V)_0$ obtained from the reddening line in the two-colour diagram.
P2. Equivalent width of the Balmer lines—in this case the mean value for H_γ and H_δ
P3. Depth of Mg II 4481.23Å.
P4. Depth of Si II 4128.08, 4130.88Å (mean value).
P5. Depth of Ca I 4226.73Å.
P6. Equivalent width of Ca II *K*-line.
P7. Depth of Cr I 4254.36Å.
P8. Depth of Cr II 4111.01Å.
P9. Depth of Mn I 4030.76Å.
P10. Depth of Sr II 4077.72, 4215.52Å (mean value).
P11. Depth of Ba II 4554.04Å.
P12. Depth of Eu II 4205.05Å.

To this list we add the following comments on the parameters:

The *UBV* two-colour diagram is generally extremely useful for temperature determination of stars. Unfortunately the two-colour correlation with effective temperature is less sensitive within the most important region (A0–A5) and also somewhat ambiguous. However, most of the stars for which spectra may be obtained, have a *B–V* colour excess not exceeding 0.25, and misclassification due to ambiguity can be avoided. A more serious complication is introduced by the relatively high frequency of spectroscopic multiple systems.

The use of the Balmer lines in stellar classification is complicated by two annoying facts: (a) they are sensitive also to luminosity, (b) the temperature dependence is ambiguous as there is an intensity maximum around 9500 K, *i.e.*, in a very critical part of the spectral type interval.

The Ca II K-line is one of the most interesting lines. It is highly sensitive to effective temperature but also to various types of chemical peculiarity, and to some extent the apparently capricious behaviour gets contributions from other line systems within the wavelength range. So for instance it sometimes shows a very complicated structure for certain types of Ap stars (particularly CrEuSr). In spite of its apparent capriciousness, the K-line is relatively well suited as temperature classification parameter for all normal stars and for a large fraction of the CP stars (Floquet 1981).

In general, it is somewhat awkward to mix equivalent width and line depth in the same analysis, and under ideal conditions it should be avoided. Mainly because of stellar rotation the depth is not a unique function of the equivalent width. For the ultimate purpose of this investigation, however, the situation is different: As the observations will be extended to rather distant objects, one has to count upon decreased rather than increased dispersion, and for weak lines it will no more be realistic with calculated equivalent widths. When strong lines are concerned, like the Balmer lines, the equivalent width is, in a first approximation, independent of

rotation—but the depth is not. In the case of weaker lines this is no longer true, for several reasons. Therefore the depth will, sooner or later, become the only conceivable parameter at hand. The error due to high v sin i value may be considerable, but it can be corrected for (essentially by comparison with Mg II 4481Å line).

4. Calibration problems

Reviewing the literature, one finds a striking discordance between different sources when it comes to spectral classification and the connection between spectral type and physical parameters. These conditions are quite natural consequences of the historical background and the development of the definitions. Thus there is in fact no absolute reference point in the spectral type and effective temperature sequences although for several purposes we really need such a point of reference. However, it is possible to construct a provisional one, and in this investigation we have proceeded as follows:

For the 'normal' stars with spectral type indicated in literature a mean value of this type has been compiled and accepted according to Table 1. The translation from spectral type to effective temperature has then been calculated as a mean of the individual values given in various published sources according to Table 2. The scatter (obtained like an ordinary mean error; column 3 ='standard deviation') of the effective temperature indication for each spectral type is then considered as a reasonable value of the 'tolerance' for the temperature within the framework of the actual spectral type symbol. By means of this translation the temperatures for the 'normal' stars have been tentatively calibrated. This procedure is rather crude but with respect to the present circumstances it is also the only realistic one.

By means of this preliminary temperature calibration the mean value for each selected parameter has been estimated as a function of effective temperature for 'normal' stars. The concept 'normal' is here an idealized indication, supposed to cover the case of singular, nonvariable, nonrotating, main-sequence stars with an average chemical composition.

5. Notes on the effects of multiplicity, rotation and differences in luminosity

It has turned out that stellar multiplicity is a predominant obstacle in fine-classification of stellar spectra. If the multiplicity is revealed, some precaution may be taken, but inevitably one must count on a considerable fraction of misclassifications due to composite spectra. For high v sin i values all spectral lines are widened and blurred and many faint lines will disappear from spectra of low and intermediate dispersion, hence causing more or less serious misclassification (Slettebak, Kuzma & Collins 1980). Spectral variability has definitely to be taken into account but will not be discussed here.

Most of the spectral lines, traditionally used for luminosity class estimation, are highly sensitive also to chemical peculiarity. Therefore, at this stage, there is no unique and simple parameter available, by means of which the luminosity class can be obtained from direct calibration. It is highly probable that many misclassifications of stellar luminosity over the years could be excused as a consign of peculiar behaviour of the key lines. Sources of classification errors have been extensively discussed by

Table 2. Accepted mean values of effective temperature for actual spectral types.

Type	T_{eff}	Std. dev.	log T_{eff}
B5	16100	297	4.207
B6	14876	295	4.172
B7	13799	278	4.140
B8	12656	275	4.102
B9	11605	274	4.065
B9.5	10862	255	4.036
A0	10247	254	4.011
A1	9767	210	3.990
A2	9341	168	3.970
A3	8943	128	3.951
A4	8614	102	3.935
A5	8335	80	3.921
A6	8144	67	3.911
A7	7971	60	3.902
A8	7704	49	3.887
A9	7470	62	3.873
F0	7266	76	3.861
F1	7087	66	2.850
F2	6926	53	3.840
F3	6777	46	3.831
F4	6651	36	3.823
F5	6517	28	3.814
F6	6406	19	3.807
F7	6272	15	3.797
F8	6139	13	3.788

Source:
Böhm-Vitense 1981
Cramer 1984
Harris 1963
Keenan & Morgan 1951
Kuiper 1938
McNamara 1966
Popper 1980
Sandage 1957

Cowley & Jaschek (1969), Jaschek (1976), Slettebak & Kuzma (1979) and Slettebak, Kuzma & Collins (1980).

6. The spectral classification procedure

The tentative estimation of effective temperature and consequently of spectral type has been based on the following parameters:

Equivalent width of Balmer lines;
half-width of Balmer lines;
equivalent width of Ca II K-line;
depth of Ca I 4227 Å line;
UBV colours;

according to the calibration method mentioned in section 4. The Balmer versus effective temperature correlation is illustrated in Fig. 1a. We thus obtain five different

estimations of the temperature, and under ideal conditions the five estimations should give identical results. Under less ideal conditions there will be some scatter in the values and the magnitude of this scatter, *i.e.,* 'the standard deviation', gives an indication of the reliability of the procedure.

Since both the Balmer line versus temperature curve, and the colour versus temperature curve have maxima within the relevant spectral type range, neither of them is suitable as primary entrance parameter. Therefore the spectral range has first been subdivided into two parts which are treated separately. The first part corresponds to K-line equivalent width $K_{eq} \leqslant 2$ and the second one to $K_{eq} > 2$. Ideally the K_{eq}-value of 2 should correspond to spectral type A2 and to the top of the Balmer line versus temperature curve. The corresponding value of the depth of the Ca I 4227 Å line is 0.15 and in order to obtain a mean value we form the quantity

$$f(\mathrm{Ca}) = \text{“K”}/4+\text{”4227”}/0.3$$

where equivalent width of the K-line ("K") and the depth of Ca I 4227 ("4227") enter with approximately equal weight (Fig. lb).

By means of the average value thus obtained from the five estimations and the translation shown in Table 2 the tentative fine-classification spectral types in Table 3 (column 3) have been calculated. Compared to the spectral types of Table 1, column 6 it tends to be typically half a subclass earlier in the B8–A1 range while later types show

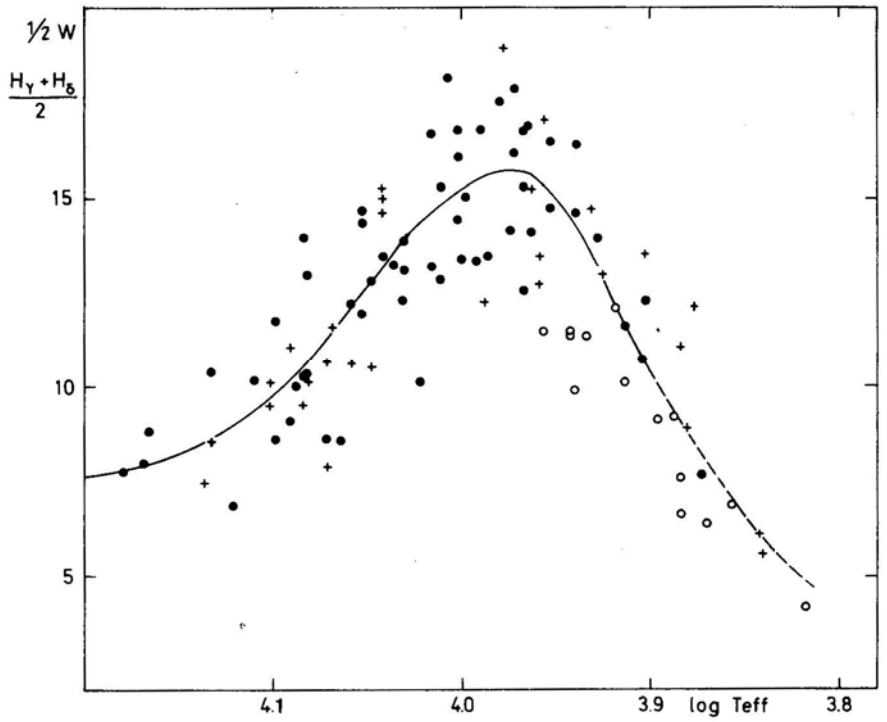

Figure 1a. Balmer line half-width versus effective temperature. Filled circle denotes normal star, plus symbol Ap star, and open circle Am star.

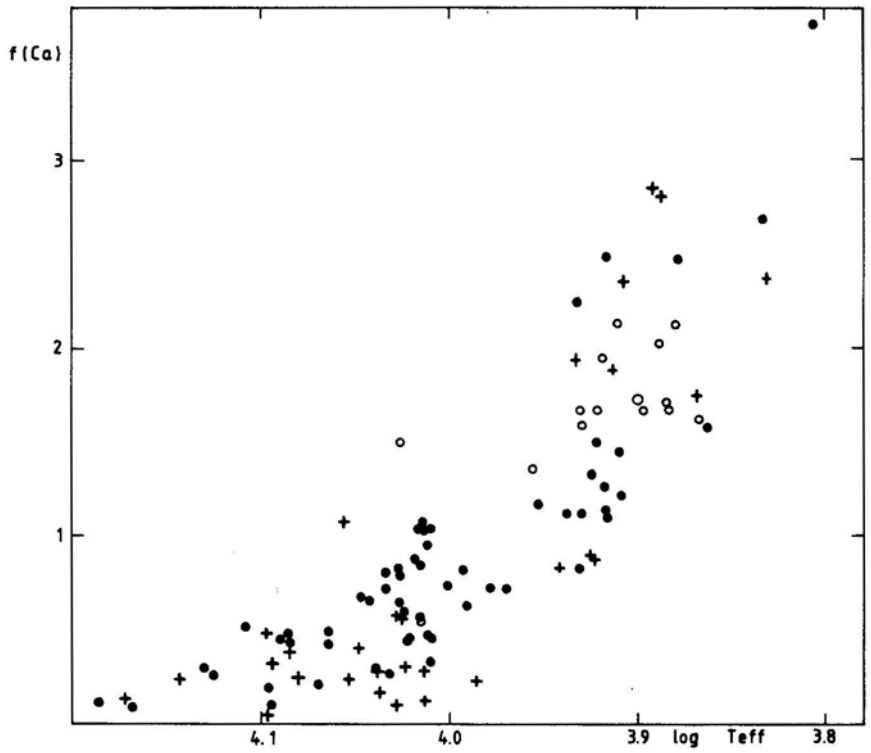

Figure 1b. *f*(Ca)—defined by the equivalent width of the K-line divided by 4 plus the depth of the Ca I 4227 line divided by 0.3—versus effective temperature. Filled circle denotes normal star, plus symbol Ap star and open circle Am star.

no clear tendency. The systematic difference betwen this classification and the one by Floquet (1981) for 9 stars in common is 0.03 of a subtype.

At this stage we have not tried to evaluate the fine classification presented in Table 3 in terms of 'resolution'. A comparison between this classification and *UBV* types should be performed. Since, however, the calibration of the classification parameters is based on the entire present material such a comparison would not be independent, and it is therefore postponed until a new set of programme stars can be discussed. At present we restrict the study to the scatter in the effective temperature estimates for various groups of A-type stars. This is illustrated in Table 4.

'Scatter' here means the average standard deviation from the mean value of effective temperature based on the five estimations listed in the beginning of this section. The relative scatter is the absolute value in degrees divided by the effective temperature value obtained for the star in question. Because of the discordance in the published classifications, the border lines between the groups are self-evidently rather diffuse, but the tendencies are clear, *i.e.,* there is in general a rather negligible difference between the scatter for the various groups. There is also, however, a significant indication that for extreme stars in the CrSrEu group one has a good reason for precaution.

Table 3. Fine classification and peculiarities of the programme stars.

Nr.	Id.	Sp.	Significant excess (+) or deficiency (−)							Degree of pec.
			Si II	Ca I	Cr I, II	Mn I	Sr II	Ba II	Eu II	
1	87696	A 4.7								0.46
2	90569	B 9.3	+		+	+	+			1.43
3	90852	B 8.2								0.73
4	90871	B 9.5								0.62
5	−55°3475	B 9.8								0.31
6	90979	A 3.6							−	0.86
7	−56°3415	A 1.1								0·15
8	„ comp.	A 4.9	+	+			+			0.93
9	91002	A 0.1						−	−	0.55
10	91051	B 8.3								0.26
11	91052	B 9.3								0.17
12	91071	B 8.3								0.58
13	91126	B 8.5								0.39
14	93821	B 7.8	+							0.74
15	95418	A 0.9								0.48
16	97603	A 3.5								0.53
17	98329	B 7.9		+						0.42
18	98340	B 8.6	+						+	0.81
19	103287	A 0.6							−	0.54
20	104671	A 8.9			−			+	−	0.87
21	104810	B 7.1	+							0.74
22	−60°3750	B 6.2		−						0.23
23	105339	B 6.2		−						0.48
24	−60°3764	B 7.1	+							0.45
25	−60°3766	B 8.6								0.11
26	−60°3787	A 0.5								0.45
27	−60°3790	A 0.5				+			+	1.14
28	105581	B 7.1		−						0.30
29	105771	B 9.6								0.42
30	„ comp.	A 2.2							+	0.54
31	109387	B 5.9		+						0.28
32	109536	A 5.5						+		0.78
33	111397	A 0.7								0.39
34	112185	B 9.0								0.39
35	112381	B 9.0	+		+		+			1.74
36	112412	F 2.7						−		0.94
37	112413	B 7.7							+	1.18
38	115331	A 3.3	+				+			0.78
39	116656	B 9.9								0.31
40	116657	A 3.9								0.71
41	116842	A 4.0								0.56
42	117025	A 0.1				+	+	−	+	2.52
43	118022	B 9.5			+	+	+		+	2.43
44	118214	B 9.3								0.37
45	119938	A 8.6			−			+	−	0.96
46	120025	A 9.3			+		+	+	+	2.04
47	120198	B 8.2					+			0.65
48	121409	B 9.3								0.24
49	125158	A 8.0	+				+	+	+	1.49
50	126504	A 8.7	+			+	+	+	+	2.08
51	135730	A 4.5	+			+	+	+	+	2.04
52	137160	B 8.3		−	+	+	+		+	2.06

Table 3. Continued.

Nr.	Id.	Sp.	Significant excess (+) or deficiency (−)							Degree of pec.
			Si II	Ca I	Cr I, II	Mn I	Sr II	Ba II	Eu II	
53	138413	A 5.5	+			+	+	+	+	1.38
54	139006	B 9.3								0.55
55	140160	A 1.4				+	+	−	+	1.10
56	142049	A 9.8	+			+	+	+	+	2.53
57	144197	A 6.4	+	+		+	+	+	+	3.32
58	146998	A 8.7					+	−	+	1.32
59	147105	B 9.5	+		+	+	+		+	1.79
60	148112	B 9.5								0.44
61	148321	A 4.9					+	+	+	2.03
62	152044	A 0.3					+			0.86
63	152107	B 9.0		−	+	+	+		+	1.96
64	−34°12194	A 4.1								0.20
65	−34°12195	A 2.7								0.31
66	−34°12196	A 4.1				−				0.69
67	162576	B 8.3	+		+					0.91
68	162586	B 7.6								0.54
69	162630	B 9.0								0.62
70	−34°12210	A 2.7						+	−	0.53
71	−34°12211	A 7.2						+		0.57
72	162631	B 9.9								0.32
73	162656	A 0.0								0.29
74	162678	B 9.2						+		0.59
75	(19)	A 2.9								0.29
76	162679	B 8.3	+							0.77
77	162680	B 9.9								0.50
78	162724	B 8.6								0.51
79	162725	B 8.2	+		+		+	+	+	1.38
80	320861	A 1.1							−	0.51
81	−34°12232	A 0.6								0.32
82	162732	B 6.5		+						0.14
83	162780	B 9.2								0.29
84	162781	B 9.5								0.28
85	164429	B 8.0								0.53
86	169820	B 7.9								0.36
87	169853	A 4.3	+			+	+	+		1.68
88	176232	A 8.1	+	+	+	+	+	+	+	3.40
89	197461	F 0.5				+	+	+	+	2.33
90	206653	B 6.6	+	−					+	1.56
91	208217	A 4.5	+		+	+	+	+	+	2.96
92	208321	A 2.7			−					0.72
93	208384	A 4.9	+			+	+	+	+	1.72
94	209142	A 6.9						+		0.92
95	209337	A 7.8	+		+	+	+	+	+	3.50
96	209468	A 2.7								0.38
97	212385	A 5.4	+		+	+	+		+	2.03
98	212410	F 6.8	+					−		0.93
99	215966	B 8.7	+		+		+	+	+	2.24
100	215983	A 3.4			+	+	+		+	2.05
101	217522	F 2.7	+				+	+	+	2.95
102	218495	A 6.0	+		+	+	+	+	+	2.90
103	218994	A 7.3			+	+	+		+	1.77

Table 4. Scatter in effective temperature estimates.

Type	Scatter (abs)	Scatter (rel)	*n*
normal	342	0.031	60
Ap, mild	377	0.034	13
Ap, extreme	463	0.045	15
Ap, Si	391	0.031	6
Ap, CrSrEu	524	0.049	14
Am, mild	170	0.021	5
Am, extreme	200	0.025	10

7. Classification of peculiarity

We have no proper zero-point indication on a sequence of stars arranged according to increasing peculiarity, *i.e.*, a definition of the concept 'extremely normal star' has no sense. According to experience gained by numerous other investigators the 'normal A star' is more or less a myth without any physical relevance (Abt & Moyd 1973; Jaschek & Jaschek 1974).

In order to obtain quantitative representation of the peculiarity we proceed as follows: The average correlations between the peculiarity-sensitive parameters and the estimated effective temperature is calculated for the 'normal' stars in the selection. The deviation (positive or negative) from the average value of a certain parameter for a given temperature is then a measure of the 'degree of peculiarity' for the star and the parameter in question. The total 'degree of peculiarity' is defined as the mean peculiarity for a certain selection of parameters.

Because of the influence from the irrelevant parameters mentioned in Section 5 the deviation has to become relatively large in order to be considered as significant. In Table 3 an indication of (+) for 'excess' and (–) for 'deficiency' is given for certain parameters. No attempt has been made to transform these indications into some qualitative classification system, however, as it would only increase the confusion for the stars already classified.

It must be emphasized that 'excess' or 'deficiency' should not be immediately interpreted as chemical overabundance or underabundance in strict terms. These concepts only refer to the relative deviation of observed spectral line intensity from the corresponding calculated mean value for the actual spectral type. An 'excess' in a certain line might for instance reflect line blend or spectral variability. For generally faint lines (like the Eu II ones) and for stars at both ends of the relevant spectral range the result may appear exaggerated (examples: star no. 9, no. 22 and no. 50). The abbreviated characterization of these stars (and a few more) should not be interpreted as a conclusive detailed information but rather as a hint to future investigators.

A quantitative classification may be used differently in future investigations but in the present case the only reason is to see if there might possibly be any discontinuity that suggests a frontier between 'more or less normal' and 'more or less peculiar' stars. In Fig. 2 all stars in the investigation have been arranged according to increasing peculiarity. The 'total degree' is here the mean value of the deviations from the mean depths for the lines indicated in Table 3 except Ca I 4227. Both excess and deficiency

enter with the same sign and the difference is adjusted to the mean depth in order to give all parameters equal weight. Fig. 2 shows no point that can represent a distinct border between normal and CP stars and hence no indication of the existence of two or more distinct branches of A-type stars. If such branches exist they are not pronounced enough to show up in the present material. This is in accordance with an investigation by Durrani (1970) of the silicon line strength in early-type stars, where no clear division between normal and peculiar stars could be established. However, one may safely state that below peculiarity degree 1 there is no indication of separation into normal and peculiar stars. The steep rise above peculiarity degree 1 shows that the extreme cases can be separated from the rest.

8. Conclusions

The result may be epitomized in the following points;

1. The opinion that there is no sharp borderline between 'normal' and 'peculiar' stars in the actual temperature range is supported. However, peculiarity degree 1

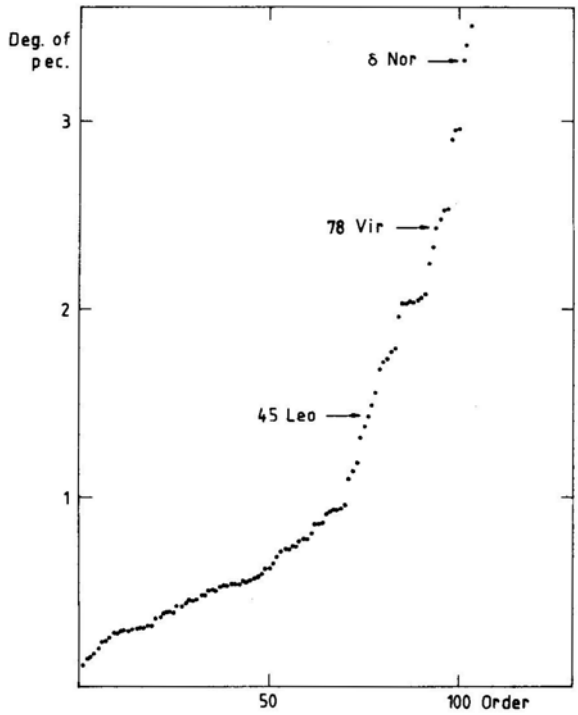

Figure 2. The increase of the calculated 'degree of peculiarity'. The points representing the stars in the present investigation are arranged according to increasing degree and the degree value is plotted against the order number. The position for three well-known objects are indicated. Roughly we may state that stars with lower degree than one are more or less normal and stars with higher degree are more or less peculiar, but it is difficult to find any point of dramatic change in the diagram.

can be applied as a division value between the more or less normal stars and the ones with more pronounced peculiarity.
2. It may be easier to classify the CP stars with respect to their degree of peculiarity than according to some kind of peculiarity type—although both parameters can be subject to periodic variations.
3. Temperature classification by means of criteria established for normal stars can be applied to peculiar stars provided extreme cases of peculiarity are avoided. Luminosity classification demands special care.
4. Concerning the CP phenomenon itself the only contribution is a further confirmation that the capricious behaviour of the K-line is a very typical CP characteristic (and that calcium in general should be regarded as the most interesting element in this connection.)
5. In addition, the suspicion that complicated CP structure, for instance combined Am and Ap characteristics, may be a consequence of multiplicity is strengthened although not definitely confirmed.

Acknowledgements

We thank the administrations and staffs of Observatoire de Haute-Provence and European Southern Observatory for allotment of observing time and for excellent service during these observations.

References

Abt, H. A. 1975, *Publ. astr. Soc. Pacific,* **87,** 417.
Abt, H. A., Moyd, K. I. 1973, *Astrophys. J.,* **182,** 809.
Bertaud, C.1959, *J. Observateurs,* **42,** 45.
Bertaud, C.1965, *J, Observateurs,* **48,** 211.
Bertaud, C, Floquet, M. 1967, *J. Observateurs,* **50,** 425.
Bidelman, W. P., McConnel, D. J. 1973, *Astr. J.,* **78,** 687.
Bidelman, W. P., Svolopoulos, S, N.1960, *Publ astr. Soc. Pacific,* **72,** 129.
Böhm-Vitense, E. 1981, *A. Rev. Astr. Astrophys.,* **19,** 295.
Buscombe, W.1971, *Astr. Soc. Pacific Leafl.,* 508.
Cowley, A. P., Cowley, Ch. R. 1964, *Publ. astr. Soc. Pacific,* **76,** 119.
Cowley, A. P., Cowley, Ch. R., Jaschek, M., Jaschek, C. 1969, *Astr. J.,* **74,** 375.
Cramer, N. 1984, *Astr. Astrophys.,* **132,** 283.
Crawford, D. L., Barnes, J. V., Golson, J. C. 1970, *Astr. J.*, **75,** 624.
Durrant, C. J. 1970, *Mon. Not. R. astr. Soc.,* **147,** 75.
Engberg, M.1983, *Astr. Astrophys. Suppl. Ser.,* **54,** 203.
Floquet, M.1981, *Astr. Astrophys.,* **101,** 176.
Garrison, F. R.1967, *Astrophys. J.,* **147,** 1003.
Harris, D. L. 1963, in *Stars and Stellar Systems,* Vol. Ill: *Basic Astronomical Data* Ed. K. Aa Strand, Univ. Chicago Press, p. 269.
Hoag, A. A., Johnson, H. L., Iriarte, B., Mitchell, R. I, Hallam, K. L., Sharpless, S. 1961, *Publ. U.S. Naval Obs.,* **17,** 343.
Hoffleit, D. 1964, *Catalogue of Bright Stars,* Yale Univ. Obs., New Haven.
Houk, N.1978, *University of Michigan Catalogue of two-dimensional spectral types for the HD stars.*
Houk, N. 1982, *University of Michigan Catalogue of two-dimensional spectral types for the HD stars.*

Houk, N., Cowley, A. P. 1975, *University of Michigan Catalogue of two-dimensional spectral types for the HD stars.*
Jaschek, M., Jaschek, C. 1960, *Publ. astr. Soc. Pacific.,* **72,** 500.
Jaschek, M., Jaschek, C. 1974, *Vistas Astr.,* **16,** 131.
Jaschek, C. 1976, in *IAU Symp.* 72: *Abundance Effects in Classification,* Ed. B. Hauck, & P. C. Keenan, D. Reidel, Dordrecht, p. 113.
Johnson, H. L., Morgan, W. W. 1953, *Astrophys.* J., **117,** 313.
Keenan, P. C, Morgan, W. W.1951, in *Astrophysics,* Ed. J. A. Hynek, McGraw-Hill, New York, p. 12.
Kennedy, P. M., Buscombe, W. 1974, *MK Spectral Classifications,* Evanston.
Koelbloed, D. 1959, *Bull. Astr. Inst. Nethl.,* **14,** 265.
Kuiper, G. P. 1938, *Astrophys. J.,* **88,** 429.
Lesh, J. R. 1968, *Astrophys. J. Suppl.,* **17,** 371.
Levato, O. H. 1972, *Publ. Astr. Soc. Pac,* **84,** 584.
Lockwood, G. W. 1968, *Astr. J.,* **73,** 14.
Lodén, L. O. 1983, *Astr. Astrophys. Suppl. Ser.,* **53,** 33.
Lodén, L. O. 1984, *Astr. Astrophys. Suppl. Ser.,* **58,** 595.
Lü, Ph. K. 1982, *Publ. astr. Soc. Pacific,* **94,** 304.
McNamara, D. H. 1966, in *IAU Symp.* 24; *Spectral Classification and Multicolour Photometry,* Eds K. Lodén, L. O. Lodén, U. Sinnerstad, Academic Press, London, p. 190.
Malaroda, S. 1973, *Publ. astr. Soc. Pacific,* **85,** 328.
Morgan, W. W., Abt, H. A. 1972, *Astr. J.,* **77,** 35.
Osawa, K. 1965, *A. Tokyo. astr. Obs.,* 2nd Ser. **9,** 123.
Palmer, D. R., Walker, E. N., Jones, D. H. P, Wallis, R. E. 1968, *R. Obs. Bull.,* **135.**
Popper, D. M. 1980, *A. Rev. Astr. Astrophys.,* **18,** 115.
Sandage, A. 1957, *Astrophys. J.,* **125,** 435.
Slettebak, A. 1966, *Astrophys. J.,* **145,** 121.
Slettebak, A., Kuzma, Th. J. 1979, in *IAU Coll. 47: Spectral Classification of the Future,* Eds M. F. McCarthy, A. G. D. Philip, G. V. Coyne, Vatican Obs. p. 87.
Slettebak, A., Kuzma, Th. J., Collins, G. W. 1980, *Astrophys. J.,* **242,** 171.

J. Astrophys. Astr. (1987) **8,** 369–387

Spectroscopic Evolution of Nova LW Serpentis 1978 during its Early Decline

T. P. Prabhu & G. C. Anupama *Indian Institute of Astrophysics Bangalore 560034*

Received 1987 May 28; accepted 1987 November 12

Abstract. Optical spectroscopic data are presented on nova LW Serpentis 1978, obtained during its decline from V 9.0 to $\simeq$ 10.2 (compared to a value of ~ 8.0 at recorded maximum). The spectrum and its evolution compare well with a typical nova, though the principal absorption (~ – 750 km s^{-1}) was very weak in comparison with the diffuse-enhanced absorption (~ –1300 km s^{-1}). The principal absorption could be identified only in the lines of O I $\lambda\lambda$7774, 8446, and in moderate-resolution observations of Hα. The salient features of spectral evolution follow: The near-infrared triplet of Ca II continuously weakened. O I λ8446 was always brighter than O I λ 7774, indicating continued importance of Lyman β fluorescence. The lines due to [O I], [N II] and N II brightened considerably near the end of our observations (37 days from maximum). The Hα emission line was asymmetric all through with more emission towards the red. Its emission profile showed considerable structure. Based on the individual peaks in the Hα line profile, a kinematical model is proposed for the shell of LW Ser. The model consists of an equatorial ring, and a polar cone on the side away from the earth. The nearer polar cone did not show significant emission of Hα during our observations. The polar axis of the shell is inclined at a small angle (~ 15°) to the line of sight.

Key words: stars, variable—stars, novae—spectroscopy, optical—stars, individual

1. Introduction

Nova LW Serpentis was discovered by Honda (1978) on 1978 March 1 at a photographic magnitude of 9.0. The nova was well-observed in the infrared band, and is one of the few novae in which the formation of optically thick dust shells has been well-studied (Szkody *et al.* 1979; Gehrz *et al.* 1980). On the other hand, the optical light curve was not monitored well except as visual estimates. The maximum recorded brightness was m_{pg} = 8.3 on March 4 (Kozai 1978). The available *UBV* data has been compiled by van den Bergh & Younger (1987).

The nature of the light curve places LW Ser among class II novae (in the nomenclature of Duerbeck 1981), exhibiting structured (as against class I: smooth) light curve. Duerbeck ascribes it the type Cb, similar to nova FH Ser 1970. Nova NQ Vul 1976 (Bb) also had a similar light curve. All these novae had fairly deep minima in

the transition stage and exhibited well-developed dust shells. The development of the dust shell in LW Ser bore a striking resemblance to that of NQ Vul (Bode & Evans 1983).

The optical spectrum of LW Ser was briefly described by Herbig (1978), and Prabhu (1978). Herbig measured on March 13.5 UT an Hα absorption velocity of –1500 km s^{-1}, whereas Prabhu obtained a mean absorption velocity of –1240 ± 60 kms^{-1} from several lines between March 10.92 and 11.97. On the other hand, Cohen & Rosenthal (1983) obtained an expansion velocity of ~ 600 km s^{-1} a few years later, based on the widths of emission lines.

LW Ser was monitored spectroscopically at the Vainu Bappu Observatory (VBO), Kavalur, for nearly a month following its maximum. A preliminary description of the spectrum was given recently by Prabhu & Anupama (1987). Detailed results are presented here together with the Hα profiles obtained at moderate resolution. A qualitative kinematical model of the shell is also constructed based on the structure of Hα profile.

2. Observations and reductions

Several spectra were recorded between 1978 March 10 and April 7 using the 1-m reflector and the Cassegrain spectrograph equipped with a Varo 8605 single-stage image intensifier at VBO. A set of gratings (80, 300, and 600 g mm^{-1}) were used in conjunction with a camera of focal length 175 mm, yielding reciprocal dispersions of 675, 166, and 83 Å mm^{-1} in the wavelength range of 3900–8800 Å mm^{-1} . Occasionally, the Hα line was observed at 30 Å mm^{-1} using a grating of 1800 g mm^{-1}. The journal of observations appears in Table 1.

Table 1. Journal of observations.

1978 UT	Exposure min	Wavelength range Å	Dispersion Å mm^{-1}
March 10.90	5	4600–8800	675
10.92	23	4000–8800	166
10.94	10	4000–8800	166
10.96	10	Hα	30
11.00	16	3900–6700	166
11.01	16	3900–6700	166
11.91	60	7000–8800	83
11.97	60	7000–8800	83
12.00	20	4900–7300	83
25.90	45	Hα	30
27.88	50	Hα	30
27.94	72	7000–8800	83
31.89	53	Hα	30
April 2.91	69	Hα	30
6.94	6	4600–8700	675
7.94	10	4600–8700	675

The spectra were recorded on Kodak Ila-D (except on one occasion when it was Kodak 103a-D) held in contact with the output fibre-optic face-plate of the image intensifier. All the spectra were calibrated to relative intensity scale using an auxiliary calibration spectrograph equipped with a rotating sector to yield 11 one-mm steps at relative exposure intervals of $\Delta \log E = 0.1$. No spectrophotometric standard star was observed, and hence no attempt is made to correct the spectra for instrumental response.

The spectrograms were digitized at 5 μm intervals using a 10 μm wide aperture on the PDS 1010M microdensitometer at the Indian Institute of Astrophysics (IIA), Bangalore, and analyzed using the software RESPECT (Prabhu, Anupama & Giridhar 1987), mostly at the VAX 11/ 780 system at VBO. Not all the spectrograms listed in Table 1 were digitized: A choice was made based on exposure and dispersion. Some of the spectrograms were measured on the Abbé comparator in order to derive absorption velocities.

3. The spectrum and its evolution

Observations with good spectral coverage were obtained only on three epochs: (1) on the nights of March 10–12 about 10 days after maximum, when LW Ser was at $V \simeq 9.0$ ($\lambda\lambda$3900–8800); (2) on March 27 at $V \simeq 9.5$ ($\lambda\lambda$7000–8800); and (3) on April 6–7 at $V \simeq 10.2$ ($\lambda\lambda$4600–8700). The Hα profile was recorded at better resolutions once on March 10, and four times between March 25 and April 2. We discuss in this section the nature and evolution of the spectrum at these epochs.

3.1 *The Line Identification and Equivalent Widths*

The emission lines in LW Ser were identified using the catalogue of Meinel, Aveni & Stockton (1975), and also by comparing with the spectra of some novae published in the literature. The large widths of emission lines (FWHM ~ 1200 kms^{-1}) and the consequent line-blending made the line identification a fairly difficult task, particularly shortward of Hα. Hence, whenever at least one bright line of a multiplet could be unambiguously identified, we have assumed the multiplet to be present. On April 6 and 7, we could record spectra only at low dispersions. The identification of lines in these spectra were carried out through a comparison with detailed spectra at earlier epochs.

The spectra reduced to continua are shown in Figs 1 and 2. The continuum was slightly underexposed on March 27, and considerably so on April 7. The line identifications and emission-line equivalent widths are listed in Tables 2a and b. The equivalent widths are rather uncertain when continua are underexposed. However, they illustrate the general trend in the evolution of the spectrum. Comments on individual elements follow.

Hydrogen: The Balmer series of hydrogen could be identified clearly only at Hα, Hβ, and Hγ in our spectra. H δ and Hε could be identified on the spectra recorded during March 10–12. Both these lines had blends towards longer wavelengths. Tin II (11) is a likely contributor to Hε, whereas Si II (3) is possibly present in the red wing of Hδ. The

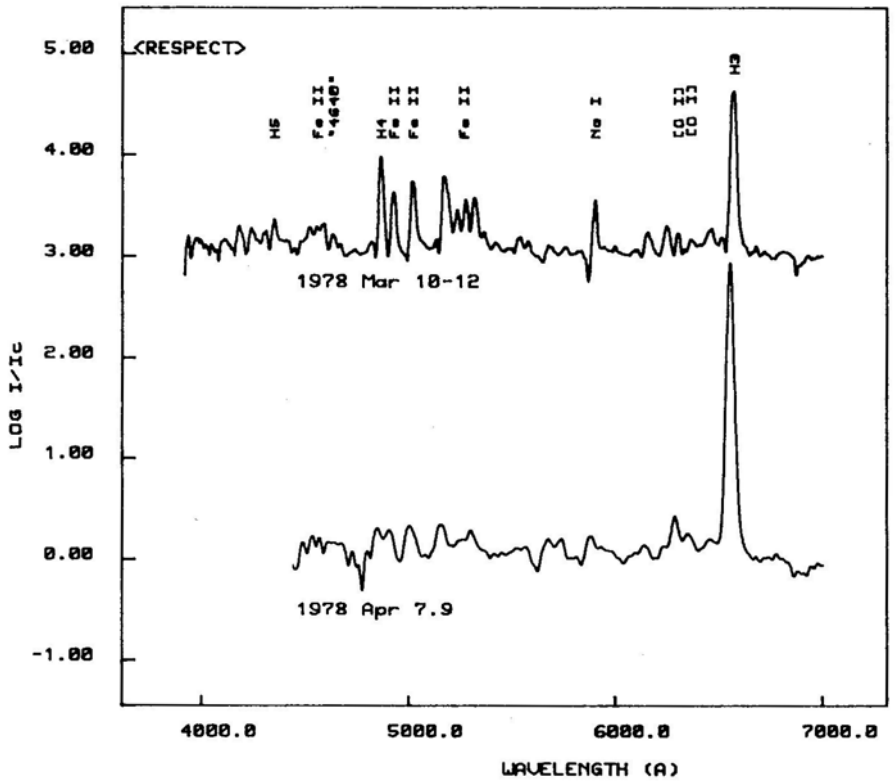

Figure 1. Spectra of LW Ser in the range λλ3900–7000 on 1978 March 10–12 and April 7, reduced to the continuum intensity. A bias of 3 has been added to the log(I/I_c) scale for the earlier spectrum.

presence of Ca II K near the edge of the recorded spectrum suggests that Ca II H contributed to Hε.

Carbon: C II λλ7231, 7236 (multiplet 3) and λλ7112–7119 (20) were the only lines of carbon easily seen in our spectra. The line at λ7236 appears to have increased in brightness with time. However, this line is blended with O I (20). Though there is some suggestion of C I λ8335(1) in Fig. 2, the spectrum is considerably underexposed in that region to enable definite identification.

Nitrogen: N I λλ8680–8728(1) feature was blended with Ca II λ18662, whereas N I λλ8184–8242(2) was clearly present, though affected by atmospheric absorption and blended with O I (34). The multiplet 3 at λλ7423–7468 was blended with Fe II (73) and O I (55). The lines at λλ8594, 8629 (8) were blended with the wings of Ca II λλ8542, 8662. The brighter of these (λ8629) was superposed over the P Cygni absorption of λ8662. The "4640" complex of O II (1), N II (5), N III (2) appeared flat-topped around April 7, on a rather underexposed spectrogram.

The best-seen lines of N II were λλ5452–5495 (2),λλ5666–5710 (3), and λλ5931–5952 (28). [N II] λ5755 (3) could also be identified all through.

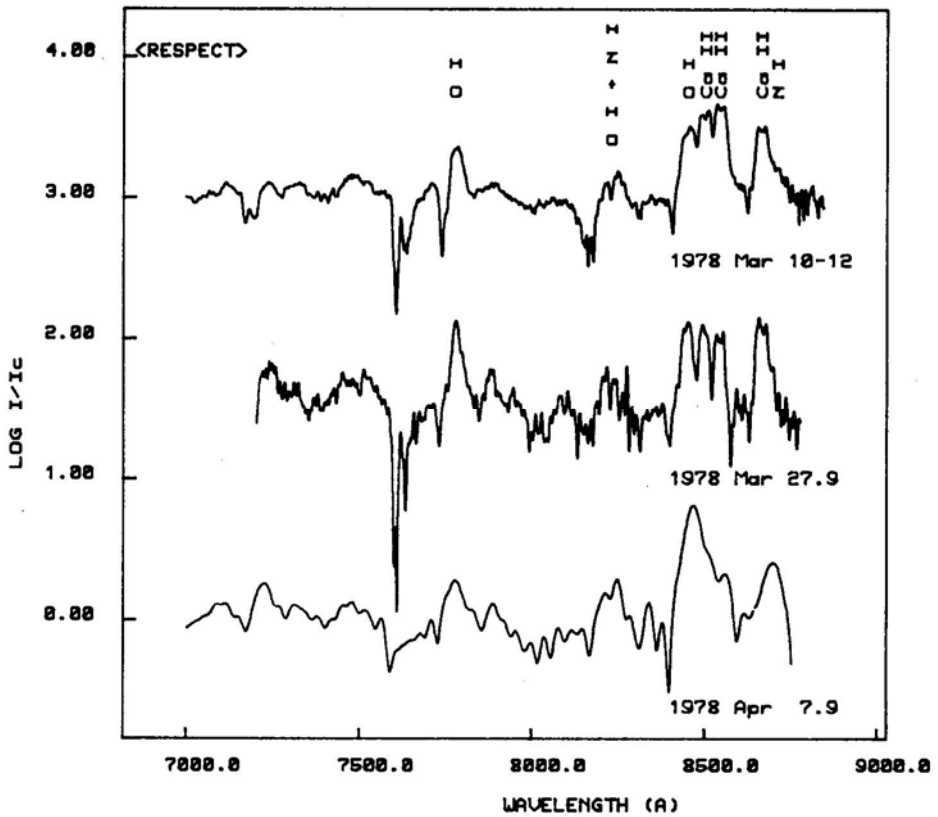

Figure 2. Spectra of LW Ser in the range $\lambda\lambda$7000–8800 on 1978 March 10–12, March 27 and April 7, reduced to the continuum intensity. Bias of 3 and 1.5 have been added to the log(I/I_c) scale for the first and second spectrum, respectively.

Table 2a. Line identifications and emission equivalent widths in the visual region.

Measured wavelength	Identification	Equivalent width (Å) March 10–12 (day 10)	Equivalent width (Å) April 7 (day 37)
3934	3933.66 Ca II K (1)	8	
3971	3968.47 Ca II H (1) 3970.07 Hε		
	4012.37 Ti II (11)* 4025.14 Ti II (11)* 4028.33 Ti II (87)*	27	
4056	4053.81 Ti II (87) 4056.21 Ti II (11)	7	
4108	4101.74 Hδ 4128.05 Si II (3)*		
	4130.88 Si II (3)* 4097.31 N III (1)* 4103.37 N III (1)*	23	

Table 2a. Continued.

Measured wavelength	Identification	Equivalent width (Å) March 10–12 (day 10)	April 7 (day 37)
4180	4178.86 Fe II (28) 4173.45 Fe(27)† 4177.70 Fe II (21)† 4185.46 O II (36)* 4189.79 O II (36)*	31	
4240	4233.17 Fe II (27) 4236.93 N II (48) 4237.05 N II (48) 4241.79 N II (48)	27	
4269:	4258.16 Fe II (28)* 4258.35 Fe II (21)* 4273.32 Fe II (27)*	8	
4300	4296.57 Fe II (28) 4303.17 Fe II (27)	23	
4351	4340.47 Hγ 4351.76 Fe II (27)	36	
4413:	4385.38 Fe II (27)* 4416.82 Fe II (27)* 4395.03 Ti II (19)* 4417.12 Ti II (40)*	22	
4446	4443.80 Ti II (19) 4447.03 N II (15)	4	
4478	4481.13 Mg II (4) 4481.33 Mg II (4)	14	
4520	4515.34 Fe II (37) 4520.23 Fe II (37) 4522.63 Fe II (38) 4501.27 Ti II (31)*	26	47
4556	4549.76 Fe II (38) 4555.89 Fe II (37) 4533.97 Ti II (50)* 4549.62 Ti II (82)* 4563.76 Ti II (50)* 4571.97 Ti II (82)*	25	
4587	4582.84 Fe II (37) 4583.83 Fe II (38) 4595.68 Fe II (38)	32	
4636	4629.34 Fe II (37) "4640" CNO Complex	19	44
4670	4666.75 Fe II (37) 4698.5 O II (40)	6	
4730	4731.44 Fe II (43) 4708.66 Ti II (49)*	6	2
4817	4825.71 Fe II (30) 4805.11 Ti II (92)*	14	3

Table 2a. Continued.

Measured wavelength	Identification	Equivalent width (Å) March 10–12 (day 10)	Equivalent width (Å) April 7 (day 37)
4866	4861.33 Hβ	180	45
4926	4923.92 Fe II (42)	83	44
5018	5018.43 Fe II (42)	132	65
5132	5129.14 Ti II (86)	11	
5174	5169.03 Fe II (42) 5175.89 N II (66) 5179.50 N II (66) 5185.90 Ti II (86)* 5197.57 Fe II (49)*	178	71
5236	5234.62 Fe II (49)	52	
5281	5275.99 Fe II (49) 5284.09 Fe II (41) 5264.80 Fe II (48)‡	69	
5319	5316.61 Fe II (49) 5325.56 Fe II (49)‡ 5316.78 Fe II (48)‡ 5336.81 Ti II (69)*	86	88
5365	5362.86 Fe II (48) 5381.02 Ti II (69)*	23	
5423	5414.09 Fe II (48) 5425.27 Fe II (49)† 5432.98 Fe II (55)	14	
5481	5452.12 N II (29) 5454.26 N II (29) 5462.62 N II (29) 5478.13 N II (29) 5480.10 N II (29) 5495.70 N II (29)	10	24
5539	5534.86 Fe II (55) 5530.27 N II (63) 5535.39 N II (63)	19	
5581	5577.35 [O I] (3)	11	14
5685	5666.64 N II (3) 5676.02 N II (3) 5679.56 N II (3) 5710.76 N II (3)	10	27
5755	5754.80 [N II] (3)	8	26
5823	5824.40 Fe II (58)	5	2
5901	5889.95 Na I (1) 5895.92 Na I (1)	52	33
5945:	5931.79 N II (28) 5940.25 N II (28) 5941.67 N II (28) 5952.39 N II (28)	8	21
5989:	5991.38 Fe II (46)	8	

Table 2a. Continued.

Measured wavelength	Identification	Equivalent width (Å) March 10–12 (day 10)	April 7 (day 37)
6100	6084.11 Fe II (46) 6113.33 Fe II (46)	6	7
6157	6147.74 Fe II (74) 6149.24 Fe II (74) 6155.99 O I (10) 6156.78 O I (10) 6158.19 O I (10) 6185.34 Fe II (46)*	27	18
6250	6247.56 Fe II (74) 6242.52 N II (57)†	34	9
6302	6300.23 [O I] (1)	16	71
6334	—	3	
6366	6363.88 [O I] (1) 6369.45 Fe II (40) 6379.63 N II (2)* 6347.09 Si II (2)* 6371.36 Si II (2)*	16	45
6400:	6407.30 Fe II (74)* 6416.91 Fe II (40)*	7	
6460	6456.38 Fe II (74) 6453.64 O I (9) 6456.01 O I (9) 6432.65 Fe II (40)* 6482.07 N II (8)*	44	39
6511	6516.05 Fe II (40) 6504.9 N II (45)*	14	
6568	6562.82 Hα	1074	over-exposed
6673	6678.15 He I	6	
6719		3	
6811		6	

Blended with the neighbouring feature.
† Minor contributor to the feature.
Multiplet numbers appear in parantheses.

The lines of nitrogen increased in strength by a factor of 3–4 with respect to the continuum, between March 10 and April 7.

Oxygen: The most prominent at all stages of the spectrum were O I λ8446 (4), enhanced by Lyman β fluorescence, and O I λ7774 (1). A few other lines of O I were also seen: λ6454 (9), λ6157 (10) as blends with Fe II; $\lambda\lambda$7982–7995 (19) and $\lambda\lambda$7947–7952 (35) blended with each other. O I (20) probably contributed to C II (3). The lines at $\lambda\lambda$7476–7480 (55) were present, blended with the lines of Fe II and N I. The forbidden lines [O I] $\lambda\lambda$6300, 6364 (1) and λ5577 (3) were seen more easily and

Table 2b. Line identifications and emission equivalent widths in the near-infrared region.

Measured wavelength	Identification	Equivalent width (Å) March 10–12 (day 10)	March 27 (day 26)	April 7 (day 37)
7116	7112.36 C II (20) 7115.13 C II (20) 7119.45 C II (20)	9		19
7236	7224.51 Fe II (73) 7231.12 C II (3) 7236.19 C II (3) 7254.19 O I (20) 7254.47 O I (20)	10	46	43
7314	7289.05 Fe II (72) 7301.57 Fe II (72) 7307.97 Fe II (73) 7310.24 Fe II (73) 7320.70 Fe II (73) 7291.46 [Ca II] (1) 7323.88 [Ca II] (1)	14	23	12
7423	7423.63 N I (3)	1	6	
7479	7442.28 N I (3) 7468.29 N I (3) 7476.45 O I (55) 7479.06 O I (55) 7480.66 O I (55) 7462.38 Fe II (73) 7515.88 Fe II (73) 7479.70 Fe II (72) 7533.42 Fe II (72)	32	69	20
7707	7711.71 Fe II (73)	7	under-exposed	
7782	7771.90 O I (1) 7774.18 O I (1) 7775.40 O I (1)	47	107	44
7882	7877.13 Mg II (8) 7896.37 Mg II (8) 7841.40 Fe II (72)*	14	30	8
7950	7947.56 O I (35) 7950.83 O I (35) 7952.18 O I (35) 7982.41 O I (19) 7987.00 O I (19) 7995.12 O I (19)		6	
8215 + 8249	8184.80 N I (2) 8187.95 N I (2) 8216.28 N I (2) 8223.07 N I (2) 8242.34 N I (2) 8221.84 O I (34) 8227.64 O I (34) 8230.01 O I (34) 8232.99 O I (34)	18:	28:	43:

Table 2b. Continued.

Measured wavelength	Identification	Equivalent width (Å) March 10–12 (day 10)	March 27 (day 26)	April 7 (day 37)
8338	8335.19 C I (10)			5:
8448	8446.35 O I (4)			
	8446.76 O I (4)	86:	110	
	8437.96 HP$_{18}$†			356
	8467.26 HP$_{17}$†			
8499	8498.02 Ca II (2)			
	8502.49 HP$_{16}$†	119:	85	
8544	8542.09 Ca II (2)		75	
	8545.38 HP$_{15}$†	149:		
8603:	8594.01 N I (8)		4:	
	8598.39 HP$_{14}$†			
8666	8662.14 Ca II (2)			
	8665.02 HP$_{13}$†	90		
	8629.24 N I (8)*			91
8711:	8680.24 N I (1)		130	
	8683.38 N I (1)			
	8686.13 N I (1)			
	8703.24 N I (1)	24		
	8711.69 N I (1)			
	8718.82 N I (1)			
	8728.88 N I (1)			
8810	8806.77 Mg I (7)	2:		

* Blended with the neighbouring feature.
† Minor contributor to the feature.
Multiplet numbers appear in parantheses.

appeared fairly strong on April 7. Si II (2), N II (2) and Fe II (40) were blended with [O I] (1) during the first epoch. N II (2) increased its contribution whereas the other blends weakened with time. O I λ8446 strengthened dramatically between March 10 and April 7.

Magnesium: The emissions at $\lambda\lambda$4478 and 7881 are possibly due to Mg I λ4481 (4), and $\lambda\lambda$7877, 7896 (8). Multiplet 7 (λ8806) was also possibly present. The lines due to Mg I have been identified in several novae (Andrillat & Houziaux 1987).

Sodium: Na I D $\lambda\lambda$5890, 5896 (1) were fairly bright all through the spectral evolution.

Silicon: The only identifiable lines of Si were Si II $\lambda\lambda$4128, 4130 (3) blended with H δ and $\lambda\lambda$6347, 6371 (20) blended with [O I] (1).

Calcium: The near-infrared triplet of Ca II $\lambda\lambda$8498, 8542, 8662 (2) was very bright on March 10–12, but faded considerably by April 6–7. H and K lines (1) were also seen in

the early spectrum. [Ca II] $\lambda\lambda$7291, 7323 (1) were possibly present during the later epochs.

Titanium: It is possible that several lines of Ti II were present; the only relatively unblended features were however λ4053 (87)+λ4056 (11), and λ5129 (86).

Iron: Lines of Fe II were particularly strong in the early spectrum, but faded with time. Strongest among these were multiplets 42, 48 and 49. Clearly visible were also multiplets 27, 28, 37, 38, 40, 46, 73 and 74.

3.2 *The Velocities*

Absorption velocities could be derived from comparator measurements at only one epoch (March 10–11≃ day 10). The derived velocities are listed in Table 3 together with a few values derived from the digitized data. The most conspicuous absorption system is identified with the diffuse-enhanced spectrum. The decreasing magnitude of this velocity with increasing quantum number for the Balmer lines is a phenomenon well-observed in novae. The comparator measurements of Fe II, Na I D, and O I λ7774 lines yield a mean absorption velocity of –1300 ± 60 km s^{-1}. This value agrees with the older, independent, measurements of the same plates, which gave a value of –1240 ± 60 kms^{-1} (Prabhu 1978).

The line profiles of O I $\lambda\lambda$7774, 8446 show weak absorption at –820 km s^{-1} (March 10–12), and –690 kms^{-1} (March 27). The Hα line profiles obtained at moderate resolution show similar absorption features around –700kms^{-1} (March 10–25). These, absorptions are identified with the principal velocity system. The Hα

Table 3. Absorption line velocities.

	Absorption velocity (km s^{-1})		
Emission line	March 10–12 (day 10)	March 27 (day 26)	April 7 (day 37)
4101 Hδ	(−1460:)		
4340 Hγ	−870		
4629 Fe II (37)	−1270		
4861 Hβ	−1319		
4924 Fe II (42)	−1401		
5018 Fe II (42)	(−1416)		
5169 Fe II (42)	−1281		
5893 Na I (1)	−1265		
6563 Hα	−1482		(−1770)*
	(−700)	(−700)	(−760)*
7774 O I (1)	−1279	(−1620)	(−1770)
	(−813)	(−662)	
8446 O I (4)	(−1395)	(−1646)	(−1797)
	(−830)	(−769)	
8662 Ca II (2)	(−1330)		

The values in parantheses were measured on the digitized spectra.
* On April 2.

line also showed an absorption at ~ – 1770 km s^{-1} on April 2, whereas the lines of O I $\lambda\lambda$7774, 8446 showed absorption at similar velocities on April 7. These may be ascribed to the Orion absorption system.

The absorption systems seen in LW Ser are in accordance with those observed in novae of moderate speed class (Gallagher & Starrfield 1978). However, the principal absorption system was rather weak in LW Ser.

3.3 *The Hα Line-Profile*

The Hα profiles on March 11, 25, 27 and April 2 are shown in Fig. 3, reduced to the continuum intensity, based on spectrograms obtained at 30 Å mm^{-1}, The continuum was not generally well-exposed. The absorption at –1480 km s^{-1} is barely visible on March 11. The profile of April 2 shows a shallow and broad absorption feature ~ –1770 km s^{-1}. The principal absorption is also visible.

At a very first glance the Hα profile is seen to be asymmetric with more emission towards the red. The centre of the profile lies at 300 kms^{-1}, an unlikely velocity for

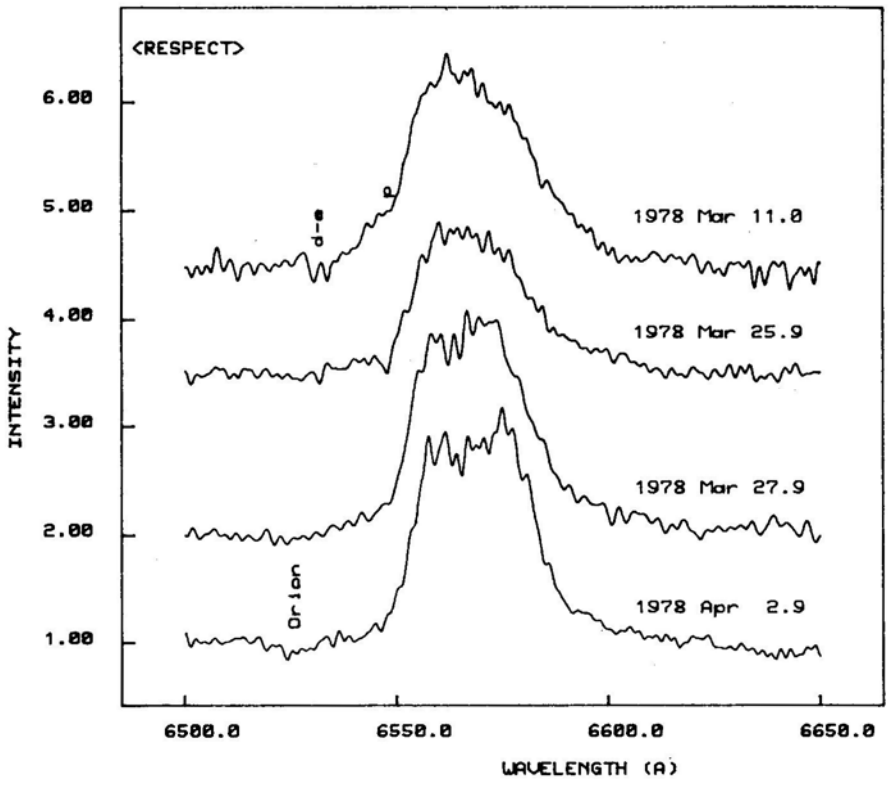

Figure 3. The line profiles of Hα between 1978 March 11 and April 2, reduced to the continuum intensity. The principal (p), diffuse-enhanced (d-e), and the Orion absorptions have been marked. Bias of 3.5, 2.5 and 1 have been added to the respective intensities of the first three spectra.

the system. Though the profile is very nearly flat-topped, some structure is evident near the peak, particularly after March 25.

It is likely that [N II] $\lambda\lambda$6548, 6584 contribute to the emission at Hα. In order to estimate their contribution, the profiles of Hα and [N II] were assumed to be similar, and a de-blending procedure in RESPECT was used. Fig. 4 shows the mean of observed profiles in intensity units, with the contributions due to Hα and [N II] shown separately. A ratio of 3 was assumed for [N II] λ6584/λ6548. The halfwidth of Hα line is now reduced to 1200 km s^{-1}. The asymmetry of the profile persists, though reduced in magnitude. The Hα/[N II] ratio of about 6 gives the best fit determined interactively.

More discussion on the Hα line profile appears in Section 4 where a qualitative, kinematical model is attempted.

3.4 *Comparison with other Novae*

McLaughlin (1960, and references therein) describes the spectral evolution of a 'typical' nova, with respect to the position on the light curve both in terms of

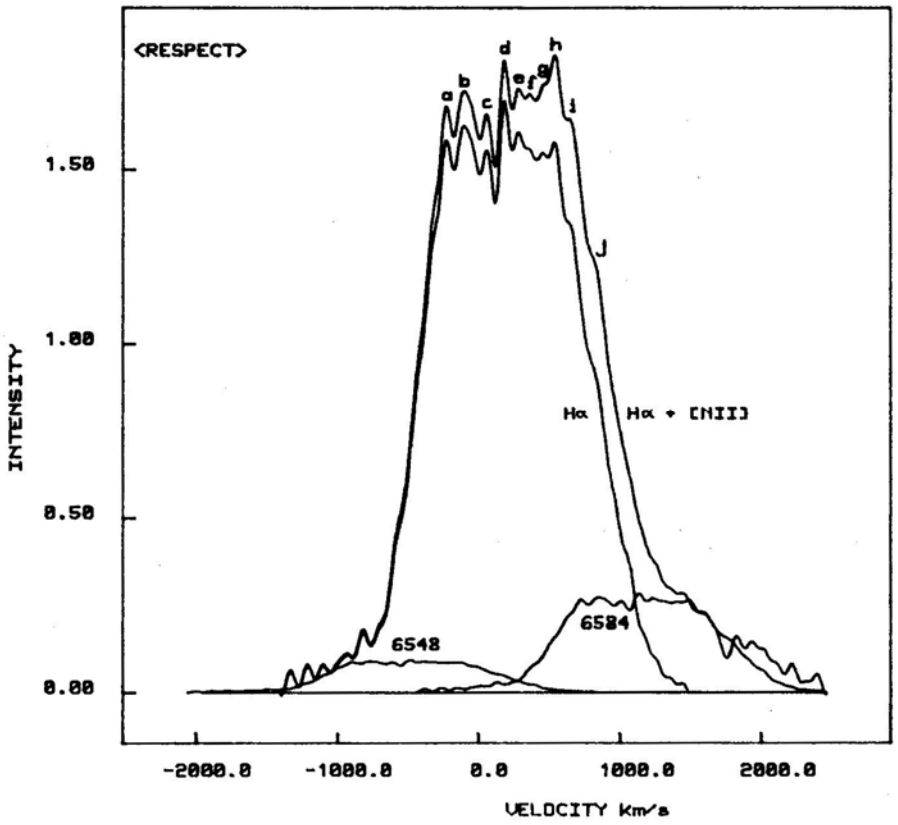

Figure 4. Mean Hα profile between 1978 March 25 and April 2. The contributions due to [N II] λ6548, Hα, and [N II] λ6584 have been separated out. The velocity scale refers to Hα. Peaks referred to in the text and Table 4 have been marked a–j.

magnitudes from the maximum, and with respect to a scaled time coordinate. One may compare the evolution of LW Ser with that of a typical nova, and also with other novae that exhibited a similar light curve—DQ Her (Stratton & Manning 1939), FH Ser (Andersen, Borra & Dubas 1971), and NQ Vul (Yamashita *et al.* 1977; Shcherbakov 1977; also unpublished VBO spectra).

The discovery magnitude of m_{pg} = 9 on 1978 March 1 UT, and the value of m_{pg}=8.3 on March 4.82 UT suggest that LW Ser reached its maximum between March 1 and 4. If we assume m_{pg} = 8.3 at the maximum and a colour index of 0.35 at this stage (Duerbeck 1981), we arrive at a visual magnitude of ~ 8.0. The three epochs of observation would then correspond to 1.0, 1.5 and 2.2 mag below maximum. For a typical nova spectrum, these stages would correspond approximately to (1) the principal spectrum, (2) advanced stages of the diffuse-enhanced spectrum, and (3) Orion absorption stage close to the onset of [O I] flash.

McLaughlin (1960) also describes evolution as a function of time expressed in the units of t_3, the time required to decline by three visual magnitudes. Duerbeck (1981) lists t_3 = 50 d for LW Ser. Assuming the zero of time to be March 1.5 (Gehrz *et al.* 1980), we obtain for the three epochs: (1) 10 days after maximum the diffuse-enhanced absorption would have just appeared; (2) 26 days after maximum, the nova was past the maximum of diffuse-enhanced phase, and the Orion absorption would have just appeared; (3) 37 days after maximum [O I] flash had just occurred.

The evolution of spectrum of LW Ser agrees generally with other novae of similar speed class. The major difference is in the weakness of the principal absorption in LW Ser and the early appearance and strength of diffuse-enhanced spectrum, if our identification of velocity systems is correct. The difference is particularly striking in comparison with NQ Vul, in which case the principal absorption was very strong.

4. Geometrical structure of the shell

High-resolution imaging and spectroscopy of shells around old novae indicate that a typical nova shell consists of an equatorial ring and a pair of polar caps. Particular examples are DQ Her and V603 Aql (Mustel & Boyarchuk 1970; Weaver 1974), and HR Del (Solf 1983). It also appears that these components are confined within a prolate ellipsoidal shell, the expansion velocity being smaller at the equator than at the poles.

A typical nova shell thus appears to consist of rings of matter at different latitudes with respect to an axis of symmetry. If there is continuous ejection of matter, these rings take the shape of hollow cones with different angles of opening with respect to a common axis (Solf 1983). The polar cap can be considered as a cone with a small angle of opening. We will refer to these components as cones in the following for convenience and uniformity of terminology.

4.1 *General Considerations*

Emission profile due to an individual cone is generally double-peaked, and is sharply bounded by the velocities

$$V_{r,b} = V_0 + V\cos(\phi \pm i) \quad (1)$$

where V_r, V_b are red and blue limits of the profile, V_0 is the systemic velocity, ϕ the semi-angle of opening, i the inclination of the polar axis to the line of sight, and V the velocity of expansion of the cone. V can be expressed as

$$V=(V_p^2\cos^2\theta+V_e^2\sin^2\theta)^{1/2} \tag{2}$$

where V_p, V_e are polar and equatorial expansion velocities and θ the parametric angle given by

$$\tan\theta=\frac{V_p}{V_e}\tan\phi. \tag{3}$$

The cones are assumed to be embedded in a prolate ellipsoidal shell with the longer axis making an angle i with the line of sight. The section of the ellipsoid in the plane defined by the line of sight and the longer axis would be an ellipse. The expansion velocities along the perimeter of the ellipse can be parametrized by

$$V_x = V_p\cos\theta\,\mathrm{cos}i - V_e\sin\theta\,\mathrm{sin}i, \tag{4a}$$

$$V_y = V_p\cos\theta\mathrm{sin}i + V_e\sin\theta\mathrm{cos}i, \tag{4b}$$

where the x-axis is chosen along the line of sight. The maximum velocity component along the line of sight would then be given by V_x such that

$$\frac{dV_x}{d\theta}=0, \tag{5a}$$

whereas the absorption velocity would correspond to V_x at

$$V_y=0. \tag{5b}$$

Obtaining the corresponding values of θ, and substituting in Equation (4a), it can be derived that emission from the shell is contained within

$$V_{max} = V_p(\cos^2 i + f^2\sin^2 i)^{1/2}, \tag{6}$$

where $f = V_e/V_p$, and that the absorption component is at

$$V_{abs} = -\frac{V_e}{(f^2\cos^2 i+\sin^2 i)^{1/2}}. \tag{7}$$

Eliminating ϕ and θ from Equations (1)–(3) One obtains the conditions

$$(x-\delta)^2 + y^2 = 1 \tag{8}$$

where $x=\frac{1}{2}(V_r+V_b)/V_p$ *cosi,* $y=\frac{1}{2}(V_r-V_b)/V_e$ sin *i,* and $\delta = V_0/V_p$ cosi. Thus, if the observed profile is separated into components corresponding to different cones, the values (x_i, y_i) lie on a unit circle with centre at $(\delta, 0)$. A least-squares fit can hence be obtained to derive optimal values of V_0, V_p, V_e and i. The values of ϕ can then be derived from

$$\tan\phi=\frac{fy}{x-\delta}. \tag{9}$$

4.2 *A Kinematical Model*

The fact that Hα profile showed structure on March 25 suggests that the shell had already broken into equatorial rings and polar cones. Since the material was still optically thick to line radiation it is difficult to model the line profile in terms of contributions due to individual cones. However, the velocities of peaks may be used to obtain a qualitative kinematical model following Section 4.1.

We use the averaged Hα profile so that the effect of residual noise is reduced in the identification of peaks. After correcting for [N II], the most prominent peaks in Hα profile were at velocities –240, –110, +50, +180, +270, and + 530 kms^{-1}. There appeared fainter peaks at 360 and 460 kms^{-1}. There were several undulations on the red wing of Hα+ [N II] profile. Prominent among these were at +640 and 840 kms $^{-1}$. All these features are marked a–j in Fig. 4.

Rms deviations of observed peaks from the, circle given by Equation (8) were obtained for all possible combinations of pairs (V_r, V_b) chosen from among the prominent six peaks. The nature of scaling of Equation (8) is such that rms deviations for different sets of parameters can be compared only if we define the rms residual as

$$\langle(\Delta s)^2\rangle^{1/2} = \langle[(\Delta x V_p \cos i)^2 + (\Delta y\, V_e \sin i)^2]\rangle^{1/2}. \quad (10)$$

The residuals were computed for V_p ranging between 600 and 1600kms^{-1}, i between 1° and 89°, and V_0 between –100 and +100 km s^{-1} . The value of f was fixed at 0.67 in analogy with the observed shell of DQ Her. The model with the least rms residual was chosen as the best model. An increase in the assumed value of f would decrease the derived value of inclination. An increase in the value of V_p would also have the same effect.

It was found that the residuals are sensitive to the choice of (V_r, V_b) pairs, but rather insensitive to the values of V_p. The best fit was obtained for pairs (–240, 50), (– 110, 180), (270, 530) kms^{-1}. The rms residual was $\lesssim$ 20kms^{-1} over the entire range of V_p.

The choice of V_p was made by constraining the model value of V_{abs} to the observed value of –750 km s^{-1} . The best fit model thus obtained is listed in Table 4. The model

Table 4. Model parameters for the shell of LW Ser.

		Model 1	Model 2
	V_p (km s^{-1})	800	1100
	f	0.67	0.67
	V_0 (km s^{-1})	40	−10
	i	16	11
	V_{max} (km s^{-1})	783	1089
	V_{abs} (km s^{-1})	−765	−1076
Identification in Fig. 4	Peak velocities (km s^{-1}) V_b	V_r	ϕ (deg)	
(a, c)	−240	50	101	98
(b, d)	−110	180	86	87
(e, h)	270	530	48	59

is clearly asymmetric, with no polar cone on the hemisphere facing the earth The polar axis subtends a small angle (11°–16°) to the line of sight. Furthermore, two of the rings are equatorial and the third could be termed polar. The minor peaks can be attributed to structure in the polar cone.

The presence of significant emission at Hα beyond ~ 800 kms^{-1} suggests that the value of V_p could be larger than this value. If the constraint on V_{abs} is removed—which is anyway based on a rather faint dip in the profile—one obtains the alternative model listed in Table 4 with V_p=1100kms^{-1}. The emission shortward of the dip ~ –750 kms s^{-1} as also the emission at $\gtrsim$ 800kms^{-1} can then be ascribed to the polar regions. However, there would remain significant emission at $\phi \sim 60°$ with only weak emission at $\phi \sim -60°$.

5. Discussion

LW Ser belongs to a class of novae that exhibit a moderate rate of decline, and a transition phase associated with infrared emission due to an optically thick dust shell.

Using the absolute-magnitude-rate-of-decline relationship, Gehrz *et al.* (1980) obtained an absolute magnitude of M_v= –7.2 at the maximum of LW Ser. Assuming A_v = 1.0, and m_v (max) $\simeq$ 7.9, they derived a distance of D = 6.3 kpc. Their infrared observations, however, yielded an angular diameter of 22.7 milli-arcsec 75 days from maximum, a value inconsistent with the above distance, and an assumed value of 1250 km s^{-1} for the velocity of expansion.

Van den Bergh & Younger (1987) derived mean values of $(B-V)_0$= –0.02 ±0.04 and M_v (15)= –5.23 ± 0.16 fifteen days after maximum for all but the fastest novae. The observed values of $(B-V)_0$ = 0.50 and V= 9.5 for LW Ser 15 days after estimated maximum (Gehrz *et al.* 1980) imply $E(B-V)$ = 0.52, A_v = 1.6 and D = 4.2± 0.4kpc. This value is in fair agreement with the distance suggested by Gehrz *et al.* (1980) assuming a value of 1250 kms^{-1} for expansion velocity.

On the other hand, Cohen & Rosenthal (1983) used an expansion velocity ~ 600 km s^{-1}, which reduced the implied distance to LW Ser by a factor of two, based on the observed angular diameter of the optically thick dust shell. The reduced distance implies that LW Ser reached only $M_v \simeq -5.0$ at recorded maximum.

From Fig. 5 of Cohen & Rosenthal (1983) it would appear that both NQ Vul and LW Ser were subluminous at maximum. Alternatively, distances derived from the infrared blackbody angular diameter and the ejection velocity of the principal shell are underestimated.

The extinction estimate for the relatively nearby nova FH Ser is 2.8 mag which brings it close to the standard absolute-magnitude-rate-of-decline relationship. NQ Vul also would fit in well if we assume a value of A_v=2.5 mag (Duerbeck 1981) based on polarization measurements, instead of 1.4 mag assumed by Cohen & Rosenthal. However, there is no evidence yet that the extinction to LW Ser is larger than 1.6 mag, whereas a value of ~ 3 mag is needed to make it appear normal at the nearer distance derived by Cohen & Rosenthal.

The velocity structure of the Hα profile suggests that the shell of LW Ser consisted of equatorial disc and polar cones. The polar axis was inclined at a small angle (~ 15°) to the line of sight. However, the line profile did not give clear indication of a polar cone at the pole nearer to the earth. For reasons of symmetry, we may assume that

such a cone was indeed present, but did' not contribute significantly near the peak Hα emission.

If one assumes that a nova shell is radiation-bound at least at early epochs (Ferland 1977), one would expect to see the nearer polar cone through considerable amount of neutral hydrogen. The neutral hydrogen may trap significant amount of Lα radiation resulting in an enhanced population of n = 2 level of H. This would imply a higher amount of absorption of Hα from the nearer polar cone compared to the farther one. We are extrapolating here from the model of the shell of V1500 Cygni due to Strittmatter *et al.* (1977). In the case of V1500 Cygni (t_3 = 3.6 d), the blue peaks brightened relative to the red ones between 25–115 days from maximum (Prabhu 1977). It is possible that a similar evolution would have taken place in LW Ser after our observations had stopped, and would have shown the nearer polar cap if observations could have been extended in time.

It is unlikely that the shell of LW Ser has expanded to over 1 arcsec angular size. Though the shell cannot be resolved yet, high spectral resolution observations of different emission lines would help in constructing a more accurate model of the shell, and to ascertain whether a symmetry is apparent in the shell at the present epoch.

Acknowledgements

We thank M. V. Mekkaden for obtaining some of the Hα plates. Some of the reductions were carried out with the VAX 11/780 system at the Raman Research Institute, Bangalore. We have greatly benefited from the critical comments of L. Rosino and an anonymous referee on an earlier version of the paper. TPP acknowledges helpful discussions with H. W. Duerbeck and W. C. Seitter.

References

Andersen, P. H., Borra, E. F., Dubas, O. V. 1971, *Publ. astr. Soc. Pacific*, **83,** 5.
Andrillat, Y., Houziaux, L. 1987, *Recent Results on Cataclysmic Variables*, ESA SP-236, L985, p. 187.
Bode, M. F., Evans, A. 1983, *Mon. Not. R. astr. Soc*, **203,** 285.
Cohen, J. G., Rosenthal, A. J. 1983, *Astrophys. J.*, **268,** 689.
Duerbeck, H. W. 1981, *Publ astr. Soc. Pacific*, **93,** 165.
Ferland, G. J. 1977, *Nature*, **267,** 597.
Gallagher, J. S., Starrfield, S. 1978, *A. Rev. Astr. Astrophys.*, **16,** 171.
Gehrz, R. D., Grasdalen, G. L., Hackwell, J. A., Ney, E. P. 1980, *Astrophys. J.*, **237,** 855.
Herbig, J. H. 1978, *I A U Cir.* 3198.
Honda, M. 1978, *I A U Cir.* 3186.
Kozai, Y. 1978, *I A U Cir.* 3188.
McLaughlin, D. B. 1960, in *Stellar Atmospheres*, Ed. J. L. Greenstein, Univ. Chicago Press, p. 585.
Meinel, A. B., Aveni, A. F., Stockton, M. W. 1975, *Catalog of Emission Lines in Astrophysical Objects*, Tech. Rep. No. 27, Optical Science Center, Univ. Arizona, Tucson.
Mustel, E. R., Boyarchuk, A. A. 1970, *Astrophys. Space Sci*, **6,** 183.
Prabhu, T. P. 1977, *Kodaikanal Obs. Bull, Ser. A.*, **2**, 75.
Prabhu, T. P. 1978, *I A U Cir.* 3201.
Prabhu, T, P., Anupama, G. C. 1987, *Astrophys. Space Sci.*, **131,** 479.
Prabhu, T. P., Anupama, G. C, Giridhar, S. 1987, *Bull astr. Soc. India*, **15**, 98.

Shcherbakov, A. G. 1977, *Sov. Astr. Lett,* **3,** 244.
Solf, J. 1983, *Astrophys. J.,* **273,** 647.
Stratton, F. J. M., Manning, W. H. 1939, *Atlas of Spectra of Nova Herculis* 1934, Solar Phys. Obs., Cambridge.
Strittmatter, P. A., Woolf, N. J., Thompson, R. I., Wilkerson, S., Angel, J. R. P., Stockman, H. S., Gilbert, G., Grandi, S. A., Larson, H., Fink, U. 1977, *Astrophys. J.,* **216,** 23.
Szkody, P., Dyck, H. M., Capps, R. W., Becklin, E. E., Cruickshank, D. P. 1979, *Astr.* J., **84,** 1359.
van den Bergh, S., Younger, P. F. 1987, *Astr. Astrophys. Suppl. Ser.,* **70**, 125.
Weaver, H. 1974, *Highlights of Astronomy,* **3,** 509.
Yamashita, Y., Ichimura, K., Nakagiri, M., Norimoto, Y., Maehara, H., Miyajima, K. 1977, *Publ. astr. Soc. Japan,* **29**, 527.

J. Astrophys. Astr. (1987) **8**, 389–395

The RS Canum Venaticorum Binary HD 116204

S. Mohin & A. V. Raveendran *Indian Institute of Astrophysics, Bangalore 560034*

Received 1987 July 30; accepted 1987 November 13

Abstract. *BV* photometry of HD 116204 obtained on 57 nights during 1983–84, 1984–85 and 1986–87 observing season is presented. A photometric period of 21.9 ± 0.2 d and a mean $(B - V) = 1.196 \pm 0.010$ are obtained. It is suggested that the binary HD 116204 has a mass ratio close to unity. Attempts are needed to detect the spectrum of secondary.

Key words: BV photometry—HD 116204—RS CVn systems

1. Introduction

A preliminary inspection of moderate-dispersion objective prism survey by Bidelman (1983) has shown the K2-type HD 116204 to be a Ca II emission star. In 1984 January we started observations of this star as part of a programme to study the photometric behaviour and chromospheric activity of late-type emission-line binaries. From the *U B V* photometry of this star its variability with a 21.7 day period has since been reported by Boyd, Genet & Hall (1984). Here we report on our *BV* photometric observations of HD 116204.

2. Observations

HD 1 16204 was observed on a total of 57 nights during the three observing seasons 1983–84 (13 nights), 1984–85 (7 nights), and 1986–87 (37 nights) with the 34-cm reflector of Vainu Bappu Observatory, Kavalur, using standard *B* and *V* filters. The comparison stars were HD 116494 (spectral type G5) and HD 115968 (spectral type K0). All observations were made differentially with respect to HD 116494 and transformed to the *UBV* system. The mean differential magnitudes and colours of the comparison stars, in the sense HD 116494 minus HD 115968, obtained during the three seasons are given in Table 1. Table 2 gives the results for the variable star HD 116204. Each value given in Table 2 is a mean of three to four independent measurements. The probable errors of the differential magnitudes and colours of the variable star for each observing season are also given in Table 2.

3. Results

Using the technique described by Raveendran, Mekkaden & Mohin (1982), we find a mean photometric period of 21.9 ± 0.2 d which agrees well with the value of 21.7 ±

Table 1. The mean differential magnitudes and colours of comparison stars, in the sense HD 116494 minus HD 115968.

Season	ΔV	$\Delta(B-V)$
1983–84	-0.512 ± 0.004	$+0.005 \pm 0.003$
1984–85	-0.510 ± 0.004	$+0.007 \pm 0.003$
1986–87	-0.515 ± 0.001	$+0.014 \pm 0.001$

Table 2. The differential magnitudes and colours of HD 116204. The probable errors for each season are also given.

JD (hel.)	ΔV	$\Delta(B-V)$
2440000 +		
5726.4105	-0.265 ± 0.017	0.444 ± 0.009
5727.4025	-0.256	0.437
5727.4449	-0.260	0.439
5730.4551	-0.234	
5781.2468	-0.244	0.482
5782.4091	-0.258	0.482
5790.4437	-0.270	
5792.3363	-0.262	
5820.2982	-0.269	0.463
5825.2607	-0.264	0.490
5826.3030	-0.261	0.483
5827.2297	-0.273	0.470
5828.2161	-0.288	
6084.4513	-0.259 ± 0.010	
6086.4721	-0.292	0.474 ± 0.007
6088.4925	-0.301	0.452
6090.4343	-0.303	0.462
6118.3211	-0.210	0.462
6120.3443	-0.194	0.480
6123.3203	-0.208	0.449
6803.4849	-0.201 ± 0.007	0.476 ± 0.006
6819.3930	-0.192	0.454
6820.4114	-0.214	0.456
6823.4156	-0.224	0.458
6823.4498	-0.227	0.458
6823.4847	-0.229	0.462
6824.4292	-0.214	0.452
6825.4224	-0.208	0.467
6825.4403	-0.205	0.464
6828.3993	-0.186	0.470
6830.4128	-0.178	0.473
6830.4373	-0.168	0.467
6831.3981	-0.163	
6832.3750	-0.177	0.460
6833.4560	-0.159	0.461

Table 2. Continued.

JD (hel.)	ΔV	$\Delta(B-V)$
2440000 +		
6834.3298	−0.171	0.447
6835.3314	−0.154	
6836.3176	−0.164	
6846.3321	−0.215	
6847.3287	−0.212	0.457
2440000 +		
6850.4092	−0.192	
6851.3670	−0.178	0.456
6852.3834	−0.173	0.468
6853.3914	−0.160	0.464
6857.3133	−0.161	
6858.3773	−0.162	
6859.4047	−0.167	0.464
6860.3200	−0.158	0.461
6861.3029	−0.173	0.461
6861.3464	−0.170	0.465
6861.3809	−0.172	0.473
6862.3375	−0.172	0.461
6862.3654	−0.174	0.459
6877.3104	−0.172	
6880.4389	−0.169	0.464
6883.3061	−0.192	
6884.3272	−0.196	0.461
6884.3566	−0.203	0.468
6885.4278	−0.210	0.461
6886.4238	−0.219	0.455
6887.2641	−0.212	0.463
6889.4350	−0.230	0.455
6890.4332	−0.226	0.454
6892.3746	−0.238	
6892.4041	−0.223	0.425
6893.3653	−0.228	
6893.3868	−0.217	0.424

0.2 d obtained by Boyd, Genet & Hall (1984). Only the observations obtained during 198687 season were used for the period analysis since they provide more data points necessary to have a better phase coverage. The times of minima in Figs 2 and 3 satisfy a 21.67 d period, whereas the time of minimum listed by Boyd, Genet &.Hall (1984), together with the minimum in Fig. 3 results in a period of 21.83 d. However, we note that in several latetype Ca II H and K emissionline objects, the phases of light maxima and minima are found to vary arbitrarily (*cf.* Mohin, Raveendran & Mekkaden 1986). The Heliocentric Julian days of observation given in Table 2 are converted to photometric phases using the ephemeris:

$$\text{J.D.(Hel.)} = 2446803.4849 + 21^{\text{d}}.9E, \quad (1)$$

where the initial epoch is arbitrary and the period is the photometric period mentioned above. The differential magnitudes ΔV and colours $\Delta(B–V)$, in the sense HD 116204 minus HD. 116494, given in Table 2 are plotted against photometric phases in Figs 1 to 3. During 1986–87 we found that on two nights (JD 2446892.3854 and JD 2446893.3791), HD 116204 was brighter than expected from the mean light curve, presumably due to a long duration flare up similar to that reported in the case of V711 Tau (Parthasarathy, Raveendran & Mekkaden 1981). The $(B–V)$ obtained on JD 2445726.4105 and JD 2445727.4237 (Fig. 1) were brighter compared to the other values, probably due to a similar long-duration flare up. The corresponding variation is not clearly seen in V because of the poor definition of the trend of the light curve. However, it is clear from Figs 1 to 3 that the light curve is highly variable: the mean light level varied from – 0.26 mag to – 0.19 mag during the three observing seasons. The amplitude of light variation was always small (0.05–0.10 mag). Here we note that the amplitude of 0.05 mag in V obtained during the 1983–84 season is consistent with the observations of Boyd, Genet & Hall (1984) during the same period.

4. Discussion

From the nature and phasing of the light minima it is evident that geometrical eclipses are not the cause of light variation. We obtain a mean $(B–V)$ = 1.196 ± 0.010, comparable to $(B–V)$ = 1.16 given by Walker (1971) who also gives $(U–B)$ = 1.00 for HD 116204. Assuming that the interstellar reddening is negligible, the colours to-

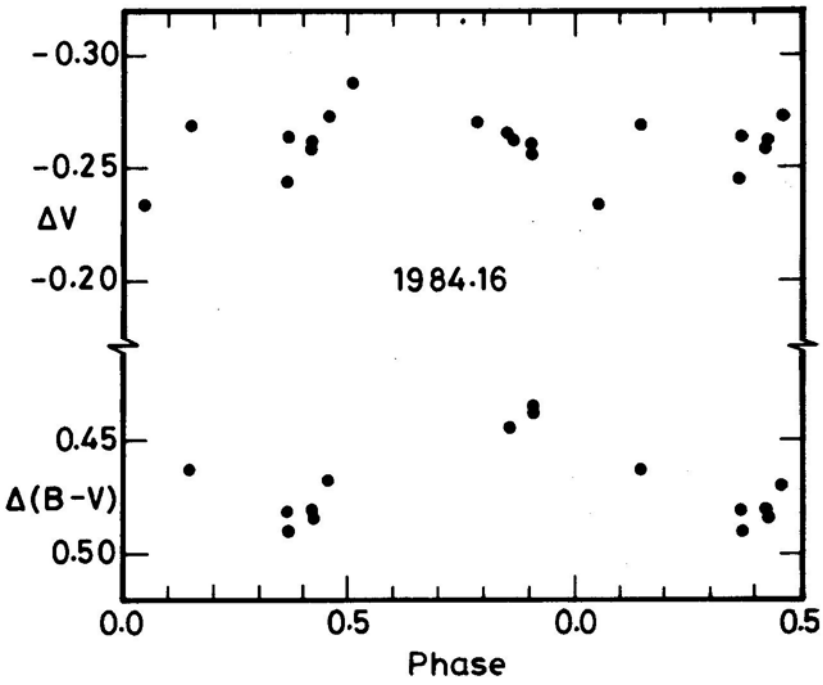

Figure 1. V and $(B–V)$ light curves of HD 116204 during 1983–84 season. Phases are reckoned from HJD 2446803.4849 and the photometric period 21.9d.

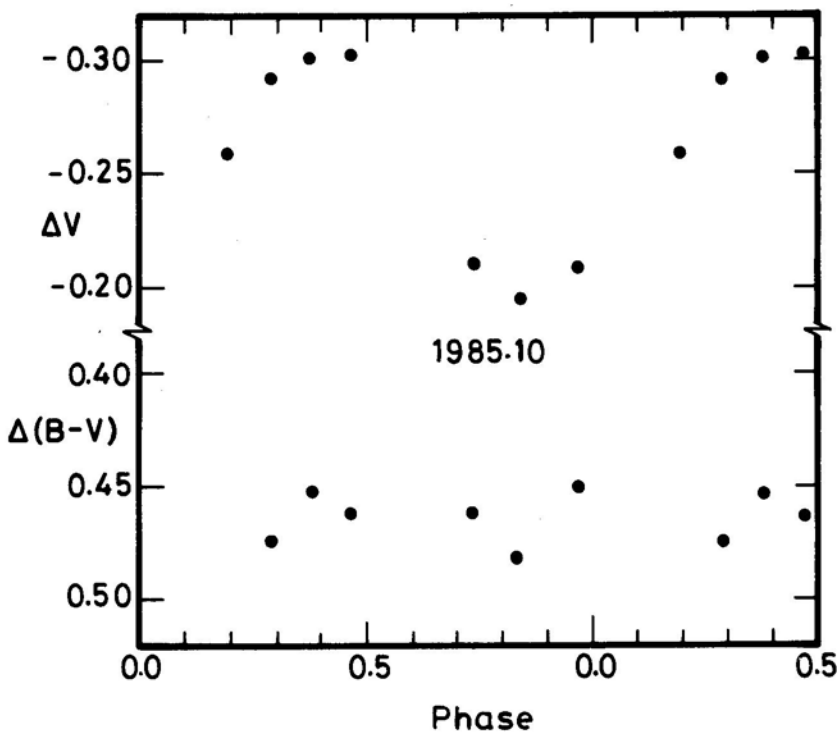

Figure 2. *V* and (*B–V*) light curves of HD 116204 during 198485 season. Phases are reckoned as in Fig. 1.

gether. with the spectral classification K2 imply that HD 116204 is a giant or a subgiant. Additional support for a giant classification comes from the *V* sin *i* measurements by Fekel, Moffett & Henry (1986), who arrive at a radius of 6 $R_\odot$ or more for HD 116204. The observed changes in the mean light level and amplitude of light variation are similar to the photometric characteristics of RS Canum Venaticorum systems, wherein the photometric variations are attributed to the presence of large-scale starspots on the giant/subgiant component which rotationally modulate the observed flux (Eaton & Hall 1979). If HD 116204 behaves similarly to the active component of RS CVn systems, then its photometric period is the rotation period of the star. The rotation period of 22 days, and the orbital period of 21 days found by Griffin (Fekel, Moffett & Henry 1986) suggest that the star is a member of a nearly-synchronous binary with the mass ratio close to unity (*cf. Zahn* 1977, Equation 6.1). A single K2 subgiant is expected to have a rotation period much larger than 22 d, which would also be the case of a K2 subgiant in a binary unaffected by the companion. Here we note that in the case of λ And (G8III–V+?) the rotation period is 56 d while the orbital period is 20.5 d (Hall 1976). As far as we know the orbital elements are not available in the literature except for a mention of the binary period (Fekel, Moffett & Henry 1986). Also it is not known whether HD 116204 is a single-lined spectroscopic binary or not. If the mass-ratio is close to unity; the secondary must be detectable spectroscopically.

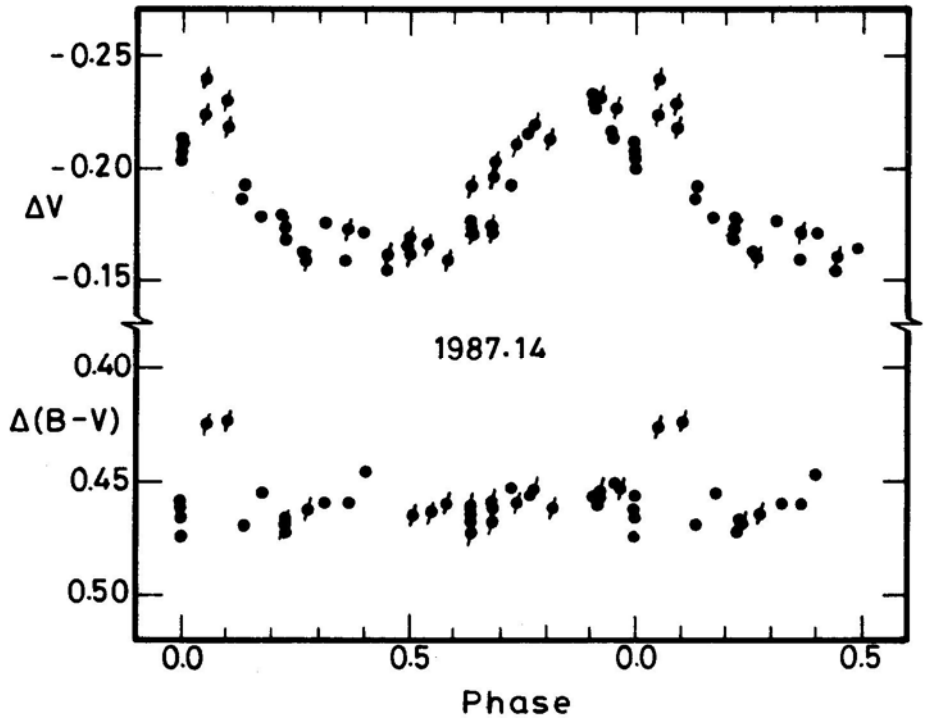

Figure 3. *V* and (*B–V*) light curves of HD 116204 during 1986–87 season. Phases are reckoned as in Fig. 1. Note that the observations obtained during the last two rotations (ϕ), of the five included in 1987.14 light curve, are systematically brighter, suggesting noticeable changes in the spot number and surface distribution.

An inspection of Fig. 3 shows that the observations obtained during the last two rotations, of the nearly five covered by our 1986–87 observations, are systematically brighter than the previous ones. This suggests a vertical shift of the entire light curve towards brighter magnitudes, as would occur due to a decrease of the spot covering factor and changes in their surface distribution. The low amplitude of light variations and the change in the mean light level of HD 116204 imply that the distribution of the spots is such that a major fraction of them is always presented on the star's hemisphere facing the observer. This suggests a low inclination of the rotation axis.

We did not attempt any quantitative modelling of the observed light curve and of its variation, since the large number of free parameters involved would render such a model ambiguous.

Acknowledgements

We are grateful to Prof. J. C. Bhattacharyya for his kind encouragement during the course of this work. We thank Mr. M. J. Rosario for obtaining photometric data on a few nights. We also thank Prof. R. K. Kochhar, and Prof. M. Rodono for their suggestions that led to an improvement of the paper.

References

Bidelman, W. P. 1983, *Astr. J.,* **88**, 1182.
Boyd, L. J., Genet, R. M., Hall, D. S. 1984, *Inf. Bull. Var. Stars,* No. 2546.
Eaton, J. A., Hall, D. S. 1979, *Astrophys. J*., **227**, 907.
Fekel, F. C., Moffett, T. J., Henry, G. W. 1986, *Astrophys. J. Suppl*., **60**, 551.
Hall, D. S. 1976, in *I A U Coll.* 29: *Multiple Periodic Variable Stars,* Ed. W. S. Fitch, D. Reidel, Dordrecht, p. 287.
Mohin, S., Raveendran, A. V., Mekkaden, M. V. 1986, *Bull astr. Soc. India,* **14**, 48.
Parthasarathy, M., Raveendran, A. V., Mekkaden, M. V. 1981, *Astrophys. Sp. Sci*., **74**, 87.
Raveendran, A. V., Mekkaden, M. V., Mohin, S. 1982, *Mon. Not. R. astr. Soc*., **199,** 797.
Walker,R.L.1971, *Publ. astr.Soc. Pac*., **83**,177.
Zahn, J. P. 1977, *Astr. Astrophys*., **57**, 383.